Systematic Tuning of Rhodamine Spirocyclization

Dissertation

Submitted to the
Combined Faculty of Mathematics, Engineering and Natural Science
University of Heidelberg, Germany
for the degree of
Doctor of Natural Sciences (Dr. rer. nat.)

Presented by
Nicolas Marcel Lardon (M. Sc.)

Dissertation

Submitted to the
Combined Faculty of Mathematics, Engineering and Natural Science
University of Heidelberg, Germany
for the degree of
Doctor of Natural Sciences (Dr. rer. nat.)

Presented by
Nicolas Marcel Lardon (M. Sc.)

Oral examination: April 12, 2022

Systematic Tuning of Rhodamine Spirocyclization

Examiners: Prof. Dr. Peter Comba

Prof. Dr. Kai Johnsson

“The structure known, but not yet accessible by synthesis, is to the chemist what the unclimbed mountain, the uncharted sea, the untilled field, the unreached planet, are to other men.”

Prof. Dr. Robert B. Woodward

This work was conducted under the supervision of Prof. Dr. Kai Johnsson and Prof. Dr. Peter Comba at the Max Planck Institute for Medical Research Heidelberg from March 2019 until March 2022. Single molecule localization microscopy data were recorded and analyzed by Aline Tschanz and Dr. Philipp Hoess at the European Molecular Biology Laboratory Heidelberg. Stimulated emission depletion microscopy was performed under the supervision of Dr. Elisa D'Este. The spontaneously blinking TMR derivative (**101**) was originally developed by Dr. Lu Wang. In the course of this thesis, **101** was synthesized on larger scale, characterized and its properties were examined. The fluorogenicity of the HIV-1 protease probes (**121** – **123**) was examined by Dr. Annica Flemming (University Hospital Heidelberg).

Parts of this work were published (N. Lardon, L. Wang, A. Tschanz, P. Hoess, M. Tran, E. D'Este, J. Ries, K. Johnsson, *J. Am. Chem. Soc.* **2021**, *143* (36), 14592.). Data thereof were adapted for this thesis.

Abstract

Fluorescence microscopy is a powerful method to examine cellular structures and biological processes with high spatial and temporal resolution. The development of novel microscopy techniques and labeling systems has expanded the limits of cellular imaging. However, this progress also relies on the availability of suitable fluorescent probes, thereby creating a need for new synthetic strategies that enable systematic modification of fluorophores. Rhodamine derivatives are widely used fluorophores, which exist in an equilibrium between a non-fluorescent, cell-permeable spirocyclic form and a fluorescent zwitterion. This spirocyclization equilibrium affects crucial properties of rhodamines regarding their applicability in cellular imaging, including fluorogenicity, cell-permeability and blinking behavior. Strategies that provide control over this equilibrium therefore hold the potential to generate suitable fluorescent probes for different microscopy techniques and labeling systems.

This thesis describes the development and application of a synthetic strategy, which allows systematic tuning of the spirocyclization equilibrium of rhodamines. To this end, the *ortho*-carboxy group of various rhodamine derivatives was transformed into amides with different substituents. Introduction of substituted acyl benzenesulfonamides enables to control the spirocyclization equilibrium with unprecedented precision and to specifically optimize the fluorogenicity for HaloTag and SNAP-tag labeling. The resulting probes show suitable properties for live-cell, no-wash confocal and stimulated emission depletion (STED) microscopy. Replacing the *ortho*-carboxy group with more electron-rich amides strongly shifts the position of the equilibrium toward the spirocyclic state and results in spontaneous blinking. This led to the development of fluorophores for single molecule localization microscopy (SMLM). The generality of this synthetic strategy allowed conversion of various rhodamine-based scaffolds into highly fluorogenic HaloTag and SNAP-tag probes as well as spontaneously blinking dyes. In addition to HaloTag and SNAP-tag labeling, fluorogenic probes for *Escherichia coli* dihydrofolate reductase (eDHFR), tubulin and human immunodeficiency virus-1 (HIV-1) protease were generated. The *ortho*-carboxy group was also used as a handle for further functionalization of rhodamines, thereby introducing a zinc ligand to form a localizable and fluorogenic zinc indicator. Altogether, differently colored fluorescent probes optimized for various microscopy techniques and labeling systems were developed. These results demonstrate the value of systematic modification of rhodamines for expanding the fluorophore palette in cellular imaging.

Zusammenfassung

Die Fluoreszenzmikroskopie ermöglicht die Untersuchung zellulärer Strukturen und biologischer Prozesse mit einer hohen räumlichen und zeitlichen Auflösung. Dabei birgt die Entwicklung neuer Mikroskopie- und Markierungstechniken das Potenzial, die Grenzen der zellulären Bildgebung zu erweitern. Dieser Fortschritt benötigt jedoch Fluoreszenzsonden mit maßgeschneiderten Eigenschaften und verlangt daher nach Methoden der systematischen Modifizierung von Fluoreszenzfarbstoffen. Rhodamine stellen eine weit verbreitete Klasse von Fluoreszenzfarbstoffen dar, welche ein Spirozyklisierungsgleichgewicht zwischen einer farblosen, zell-permeablen, geschlossenen Spiroform und einer fluoreszierenden, offenen Zwitterionform aufweist. Dieses Gleichgewicht beeinflusst die Fluorogenität, die Zell-Permeabilität und die Charakteristik des Blinkens und prägt somit wichtige Eigenschaften der Rhodamine hinsichtlich ihrer Anwendbarkeit in der zellulären Bildgebung. Daher ist eine Strategie zur Einstellung dieses Gleichgewichtes für die Entwicklung verbesserter Fluoreszenzsonden in unterschiedlichen Mikroskopie- und Markierungstechniken von besonderem Interesse.

Die vorliegende Arbeit beschreibt die Entwicklung und Anwendung einer chemischen Strategie, welche die systematische Einstellung des Spirozyklisierungsgleichgewichtes von Rhodaminen ermöglicht. Zu diesem Zweck wurde die *ortho*-Carbonsäure verschiedener Rhodamine in Amide mit unterschiedlichen Substituenten überführt. Die Einführung von Benzolsulfonamid-Derivaten dient einer präzisen Kontrolle des Gleichgewichtes und einer Optimierung der Fluorogenität bezüglich der Markierung des HaloTags und SNAP-tags. Dabei eignen sich die dargestellten Fluoreszenzsonden für die Anwendung in Konfokal- und STED-Mikroskopie lebender Zellen. Die Umwandlung in elektronenreichere Amide stabilisiert die geschlossene Form des Gleichgewichtes und das daraus resultierende stochastische Blinken dieser Rhodaminderivate kann für die Einzelmolekül-Lokalisationsmikroskopie (SMLM) genutzt werden. Auf Grund der breiten Anwendbarkeit dieser Strategie wurden verschiedene Rhodamine sowohl in fluorogene Farbstoffe zur Markierung des HaloTags und SNAP-tags als auch in blinkende Fluorophore umgewandelt. Neben fluorogenen Sonden für HaloTag und SNAP-tag wurden ebensolche fluorogenen Sonden zur Visualisierung der *Escherichia coli* Dihydrofolatreduktase (eDHFR), der Protease des humanen Immunodefizienzvirus-1 (HIV-1) und des Tubulins dargestellt. Die Funktionalisierung von Rhodaminen mittels Modifizierung der *ortho*-Carbonsäure wurde darüber hinaus untersucht, wobei durch die Einführung eines Zinkliganden ein fluorogener und lokalisierbarer Zinkindikator entwickelt wurde. Insgesamt brachte diese Arbeit Fluoreszenzsonden in verschiedenen Wellenlängenbereichen für unterschiedliche Mikroskopie- und Markierungstechniken hervor. Damit konnte umfangreich

gezeigt werden, dass die gezielte Modifizierung von Rhodaminen ein attraktives Konzept für die Entwicklung verbesserter Fluoreszenzsonden in der zellulären Bildgebung darstellt.

Acknowledgements

First, I would like to express my gratitude to Prof. Dr. Kai Johnsson for giving me the opportunity to pursue my PhD in his research group and to work on such fascinating and challenging projects at the interface of chemical synthesis and cellular imaging. I learned a lot from his broad knowledge and experience, which he generously imparted during numerous discussions. His guidance and the freedom to learn new methods and laboratory techniques allowed me to improve my expertise in the field of chemical biology and to grow as a scientist.

I am grateful to Prof. Dr. Peter Comba for being the first examiner and supervisor of my PhD. I really enjoyed the intriguing scientific discussions and the social activities with him and his research group. Furthermore, I would like to thank him and the other members of my TAC, Dr. Claire Deo and Dr. Elisa D'Este, for all their helpful advice. I also want to thank the other examiners for taking the time to be part of my examination committee and to review this work.

A special thanks goes to Dr. Lu Wang as his fundamental work and the development of the MaP strategy laid the foundation for this thesis. Working with him on different projects allowed me to learn from his expertise in the field of fluorescent probe development. I also thank him for investing a lot of time answering my questions, giving helpful advice and showing me new laboratory techniques.

I am grateful to the senior scientists in our group for their scientific and administrative support. Specifically, I thank Dr. Birgit Koch for introducing me to cell culture work and the use of confocal microscopy, Dr. Julien Hiblot for sharing his vast knowledge on the complex interactions between fluorescent probes and proteins and Dr. Richard Wombacher for all our discussions on fluorophores, microscopy and most importantly the world of cycling.

I would like to thank our technicians Bettina Réssy and Dominik Schmidt for the synthesis of precursors and Andrea Bergner for protein production. Furthermore, I am grateful to our secretary, Gwenaëlle Matthies, who never hesitated to help with administrative and organizational issues. I also want to thank Dr. Mai Tran for her synthetic contributions to the development of triplet-state quencher fluorophore conjugates, the MS-core facility comprising Dr. Sebastian Fabritz, Tatjana Rudi and Juliana Kling for measuring all the submitted compounds and Ioannis Karagiannis for his always enthusiastic help with the shipment of probes. Moreover, I am grateful for the privilege of supervising Johannes Dreizler, a talented and hard-working master student.

In the course of my PhD, I had the pleasure to collaborate with various brilliant scientists outside of our research group. A big thanks goes to Dr. Elisa D'Este (Optical Microscopy

Facility) for introducing me to STED microscopy and for her help with the optimization of imaging conditions. I also would like to thank Jasmine Hubrich (Optical Microscopy Facility) for providing cell samples, Dr. Jiri Schimer (Charles University, Prague) for the donation of HIV-1 protease binders and Dr. Annica Flemming (University Hospital Heidelberg) for analyzing the fluorogenicity of our HIV-1 protease probes. Moreover, I am grateful to our collaborators at EMBL Heidelberg, Aline Tschanz, Dr. Philipp Hoess and Dr. Jonas Ries, who investigated the blinking behavior of our probes and their applicability in SMLM.

I also want to thank Dr. Richard Wombacher, Dr. Michelle Frei, Dr. Julien Hiblot, Dr. Vincent Grenier, Dr. Fabio Raith, Dr. Veselin Nasufovic, Nicole Mertes and Stefanie Kühn for careful proofreading of this thesis and their constructive input. Moreover, I would like to thank Dr. Patrick Cieslik for helpful discussions regarding inorganic chemistry and, together with Simon Clemens, for outstanding barbecue sessions. I also want to express my appreciation to the members of our former office 216 (Dr. Aleksandar Salim, Dr. Michelle Frei, Nicole Mertes and Dr. Mai Tran) where I spent the first half of my PhD. It was a privilege sharing this office with such fantastic people. A special thanks thereby goes to Dr. Michelle Frei for all the advice on microscopy experiments, the insightful scientific discussions and - to the general amusement of the other group members - our Swiss-german conversations.

I would like to thank all other members of the Johnsson group, which I had not yet mentioned herein, for their helpfulness and for creating an outstanding working atmosphere.

I acknowledge the Max Planck School Matter to Life for financial support and for organizing social events that enabled interaction with many inspiring scientists.

With respect to the beginnings of my research, I would like to express my gratitude to Dr. Raphael Liffert and Dr. Chien-Chi Hsiao, who prepared me for the challenges that I encountered in the course of my PhD. I would also like to thank my fellow students from the University of Zurich (Lukas Hoff, Marin Nikolic, Allan Murphy, Max Bär, Clarissa Vögel and Marco Eicher) for all the good times during our studies and for staying in contact although our paths led us into different directions.

Finally, I want to thank my family and all my friends for their support during my PhD. From the bottom of my heart, I am deeply grateful to Pia for her patience and love, for accepting all my flaws and for always being there for me.

Heidelberg, February 2022

Nicolas Lardon

Abbreviations

A ..... absorbance
a ..... pixel size
ATP ..... adenosine triphosphate
b ..... photon background
BAPTA ..... 1,2-bis(*o*-aminophenoxy)ethane-*N,N,N',N'*-tetraacetic acid
BG ..... O^6-benzylguanine
Boc ..... *tert*-butyloxycarbonyl
Bu ..... butyl
CA ..... chloroalkane
COT ..... cyclooctatetraene
CP ..... benzylchloropyrimidine
d ..... doublet
dba ..... dibenzylideneacetone
DIPEA ..... *N,N*-diisopropylethylamine
DMA ..... dimethylacetamide
DMAP 4-dimethylaminopyridine
DMEM ..... Dulbecco's modified Eagle's medium
DMF ..... *N*,*N*-dimethylformamide
DMSO ..... dimethyl sulfoxide
DNA ..... deoxyribonucleic acid
DPA di-2-picolylamine
D_{50} ..... dielectric constant at half-maximum absorbance
EDC ..... 1-ethyl-3-(3-dimethylaminopropyl)carbodiimide
eDHFR ..... *Escherichia coli* dihydrofolate reductase
EDT 1,2-ethanedithiol
eq ..... equivalent
ER ..... endoplasmic reticulum
ESI ..... electrospray ionization
Et ..... ethyl
F ..... fluorescence
F_0 ..... maximal fluorescence signal in buffered solution
FBS ..... fetal bovine serum
F_{cyt} ..... cytosolic fluorescence signal
FlAsH ..... fluorescein arsenical hairpin binder
F_{nuc} ..... nuclear fluorescence signal

FP .....fluorescent protein
fPALM .....fluorescence photoactivation localization microscopy
$F_{protein}$ .....maximal fluorescence signal in the presence of the target protein
$F_{protein,Zn2+}$ .....maximal fluorescence signal in the presence of the target protein and zinc
fwhm ..... full-width-half-maximum
F_{Zn2+} ..... maximal fluorescence signal in the presence of zinc
g .....gram
GFP.....green fluorescent protein
h .....hour
hAGT.....human *O*^{6}-alkylguanine-DNA-alkyltransferase
HEPES ..... 4-(2-hydroxyethyl)-1-piperazineethanesulfonic acid
HIV ..... human immunodeficiency virus
HM .....hydroxymethyl
HOMO..... highest occupied molecular orbital
HPLC .....high performance liquid chromatography
HR.....high resolution
Hz .....hertz
I .....ionic strength
IC .....internal conversion
ISC..... intersystem crossing
J ..... coupling constant
JF ..... Janelia Fluor
k ..... kilo
K_d .....dissociation constant
L .....liter
LC .....liquid chromatography
LED ..... light emitting diode
LUMO.....lowest unoccupied molecular orbital
M .....mega
M .....molar
m .....meter
m .....milli
m ..... multiplet
MaP..... Max Planck
Me ..... methyl
min ..... minute
mol .....mole

MS ..... mass spectrometry
m/z ..... mass to charge ratio
N ..... number of replicates
n ..... nano
NADPH ..... nicotinamide adenine dinucleotide phosphate
NLS ..... nuclear localization sequence
NMR ..... nuclear magnetic resonance
Ox ..... oxidation
P ..... phosphorescence
p ..... para
PAINT ..... point accumulation for imaging in nanoscale topography
PALM ..... photoactivation localization microscopy
PBS ..... phosphate buffered saline
PEG ..... polyethylene glycol
PeT ..... photoinduced electron transfer
Ph ..... phenyl
POI ..... protein of interest
ppm ..... parts per million
PR ..... HIV-1 protease
PSF ..... point-spread function
PyBOP ..... benzotriazol-1-yloxytripyrrolidinophosphonium hexafluorophosphate
q ..... quadruplet
ReAsH ..... resorufin arsenical hairpin binder
Red ..... reduction
R_f ..... retention factor
RhoBo ..... rhodamine-based bisboronic acid
ROI ..... region of interest
RP ..... reverse phase
rt ..... room temperature
s ..... singlet
s ..... second
s.d. ..... standard deviation
SDS ..... sodium dodecyl sulfate
s.e.m. ..... standard error of the mean
s_G ..... standard deviation of the *Gaussian* fit
SiR ..... siliconrhodamine
SMLM ..... single molecule localization microscopy

STED ..... stimulated emission depletion
STORM .....stochastic optical reconstruction microscopy
S_0 .....singlet ground state
S_1 .....singlet first excited state
S_2 ..... singlet second excited state
t.....time
t.....triplet
T_1 .....triplet first excited state
Tf.....triflate
TFA ..... trifluoroacetic acid
THF .....tetrahydrofuran
TICT ..... twisted internal charge transfer
TLC .....thin layer chromatography
TMP .....trimethoprim
TMR ..... tetramethylrhodamine
TPEN ..... *N,N,N',N'*-tetrakis(2-pyridinylmethyl)-1,2-ethanediamine
TPP .....triphenylphosphonium
t_R ..... retention time
tRNA ..... transfer ribonucleic acid
TSQ.....triplet-state quenchers
TSTU..... *N*,*N*',*N*'-tetramethyl-*O*-(*N*-succinimidyl)uronium tetrafluoroborate
UAA.....unnatural amino acid
UV .....ultraviolet
VIS .....visible
VR..... vibrational relaxation
W .....watt
δ..... chemical shift
ε .....extinction coefficient
λ_{abs} ..... wavelength of maximal absorbance
λ_{em} .....wavelength of maximal emission
λ_{ex}.....excitation wavelength
μ.....micro
σ.....*Hammett* constant
σ_{LP} .....localization precision
Φ .....quantum yield
°C.....degree Celsius

Table of Contents

1. Introduction

1.1. Fluorescence and Fluorescence Microscopy

Examining cellular structures and biological processes with high spatial and temporal resolution is indispensable to gain a deep understanding of biology. Fluorescence microscopy is a powerful tool for this task as it is minimally invasive and enables one to look inside a living cell or tissue with high resolution and sensitivity.[1] For this purpose, the structure of interest is labeled with a fluorescent molecule and is irradiated with light of a suitable wavelength. Upon absorbance of a photon, the fluorophore is excited from its singlet ground state (S_0) via higher energy levels to its singlet first excited state (S_1) (Figure 1a).[2] By fluorescence emission the molecule returns to its ground state. The emitted light is red-shifted in comparison to the wavelength of the absorbed light since processes such as vibrational relaxation (VR), internal conversion (IC) and solvent reorganization lead to a reduced emission energy.[3-4] This change in wavelength is called *Stokes* shift after *G. G. Stokes*, who described this phenomenon in 1852 (Figure 1b).[5] The *Stokes* shift enables to separate excitation from emission light in a microscopy experiment and, thus, allows the detection of fluorescent molecules. The decay of S_1 to S_0 can also occur in a non-radiative fashion via processes, such as vibrational relaxation, photoinduced electron transfer (PeT), twisted internal charge transfer (TICT) and molecular collision.[6-8] Furthermore, intersystem crossing (ISC) from S_1 to the triplet excited state (T_1) can occur followed by non-radiative decay or phosphorescence. Fluorophores in T_1 can also interact with triplet oxygen to produce singlet oxygen or undergo redox reactions, which may cause their degradation.[9] These detrimental pathways therefore are important for the photostability of fluorescent dyes (Section 1.3.2.).[10]

The aforementioned sequence of processes leading to fluorescence endows fluorophores with several general, photophysical properties.[11] The wavelength of maximal absorbance (λ_{abs}) originates from the energy difference between S_0 and higher energy levels. The absorptivity at λ_{abs} is described with the extinction coefficient (ε). While λ_{abs} as well as ε can be determined by measuring the absorbance spectrum of a fluorophore, the wavelength of maximal emission (λ_{em}) can be read out of its emission spectrum (Figure 1b). Another essential characteristic of a fluorescent molecule is the quantum yield (Φ), which is defined as the ratio of emitted to absorbed photons.[11] Adjusting and optimizing the photophysical properties of fluorophores is crucial for their compatibility with the respective microscopy experiment and setup. Thus, a wide variety of synthetic strategies was developed to modulate these properties (Section 1.3.1.).[12]

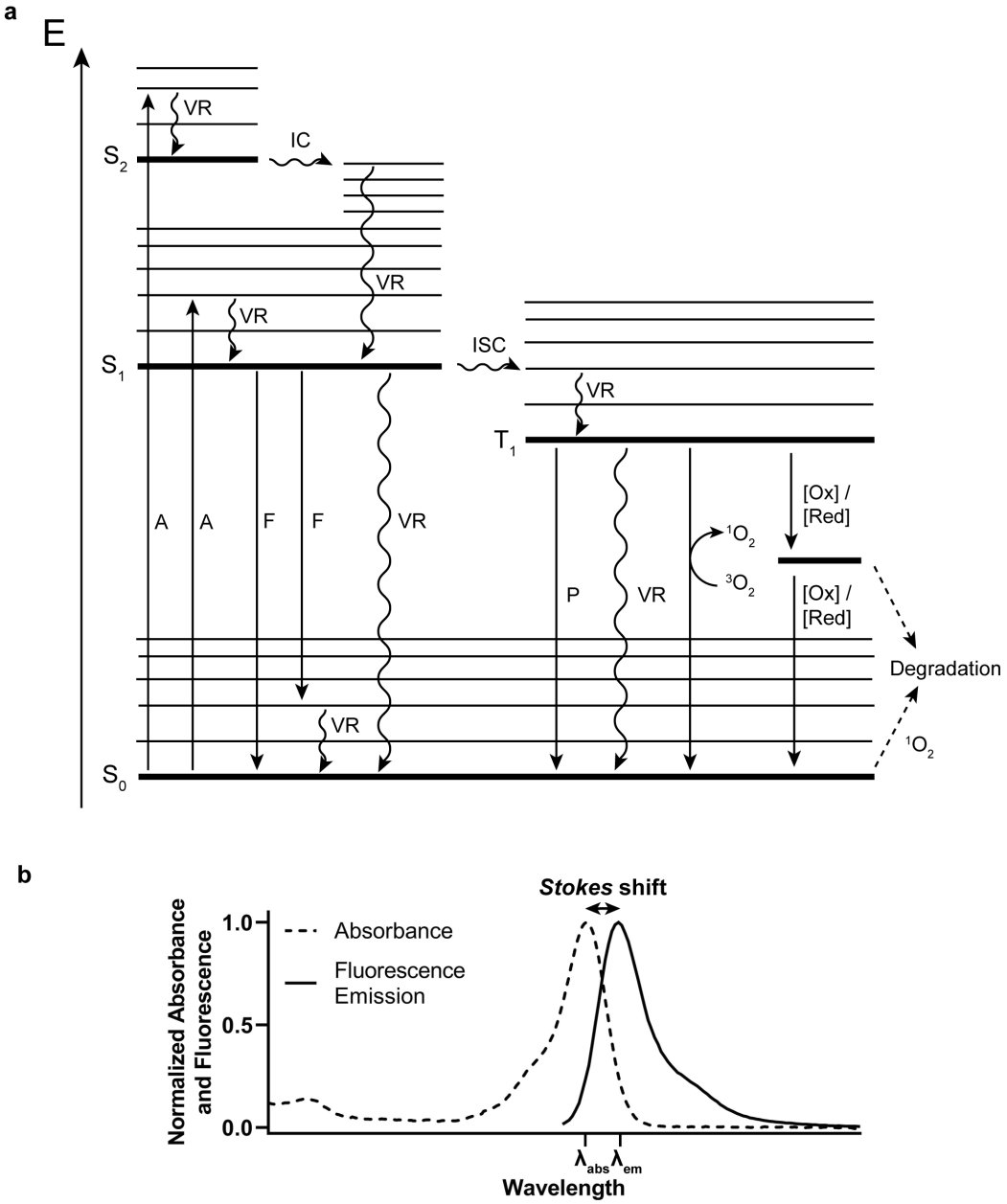

Figure 1: Jablonski diagram, absorbance and fluorescence emission spectrum of fluorophores. (a) Jablonski diagram representing important photophysical processes occurring upon excitation of a fluorophore. (b) Representative absorbance and fluorescence emission spectra of a fluorophore. A: absorbance, F: fluorescence emission, IC: internal conversion, ISC: intersystem crossing, λ_{abs}: wavelength of maximal absorbance, λ_{em}: wavelength of maximal emission, $^1O_2$: singlet oxygen, $^3O_2$: triplet oxygen, [Ox]: oxidation, P: phosphorescence emission, [Red]: reduction, S_0: singlet ground state, S_1: singlet first excited state, S_2: singlet second excited state, T_1: triplet first excited state, VR: vibrational relaxation.

Until super-resolution microscopy techniques were developed, the spatial resolution of fluorescence microscopy had been limited to approximately 200 nm due to the diffraction limit of light.[13] Fluorescent molecules that reside closer in proximity could not be distinguished in conventional fluorescence microscopy measurements. This also restricted the biological understanding since many cellular structures are smaller in size and therefore could not be resolved.[14] Different types of super-resolution microscopy have emerged to overcome the

diffraction limit. These include stimulated emission depletion (STED) microscopy as well as single molecule localization microscopy (SMLM).[1, 15] Both techniques rely on the switching of fluorophores between a fluorescent and a non-fluorescent state such that only a small subset of the dye population emits light at the same time, thereby achieving high resolution.[16]

1.1.1. STED Microscopy

STED microscopy applies, in addition to the excitation laser, a second beam to switch molecules into their non-fluorescent state. Therefore, a part of the fluorophores in the same diffraction area is kept in a dark state during the time in which the fluorescence of this area is recorded.[1] For this purpose, STED microscopy employs the phenomenon of stimulated emission.[17] The stimulating beam contains a longer wavelength and, thus, a lower energy compared to the excitation laser. Therefore, fluorophores are not excited, but stimulated to return from their excited state to their non-fluorescent ground state. Modifying this beam to obtain a donut-shape enables one to detect only the molecules in the center of the beam.[18] However, the high intensity of the stimulating laser and the propensity of exciting molecules into higher excited states creates a need for highly photostable and bright fluorophores in STED microscopy.[19] Therefore, various chemical strategies have been explored to enhance the performance of dyes by increasing their photostability and brightness (Section 1.3.).[18, 20-21]

Since the introduction of the concept of STED microscopy by *S. W. Hell* and *J. Wichmann* in 1994, the technique has evolved into a widely used tool for the examination of sub-cellular structures and functions.[17, 22] Live-cell STED microscopy with fluorescent proteins, self-labeling protein tags or probes containing specific ligands for cellular structures has been reported.[23-26] Furthermore, the development of fluorophores with suitable spectral properties enables multicolor STED microscopy.[14] Applying large *Stokes* shift dyes permits to use the same depletion wavelength for different fluorophores while distinguishing them by their difference in excitation.[27] Moreover, fluorophores can be distinguished regarding their emission spectra, fluorescence lifetime or photochromism.[28-30]

1.1.2. SMLM

A first breakthrough toward the development of SMLM was the optical detection of single molecules by *W. E. Moerner* and *L. Kador* in 1989.[31] In 1995, *E. Betzig* proposed a general method to distinguish individual fluorophores within the diffraction limit by sequentially identifying them.[32] In the following years, various classes of chromophores were reported to show blinking or switching behavior such as fluorescent proteins, polymers, nanocrystals as well as small-molecule organic dyes.[33-36] The development of robust photoactivatable and photoswitchable fluorophores was an important prerequisite for the progress in the field of

SMLM.[37-41] In 2006, four different groups published experimental proof for the applicability of SMLM within a period of only a few months. The group of *X. Zhuang* reported stochastic optical reconstruction microscopy (STORM).[42] *E. Betzig*, *H. F. Hess* and co-workers described photoactivated localization microscopy (PALM).[43] Furthermore, the group of *S. T. Hess* demonstrated fluorescence photoactivation localization microscopy (fPALM) and point accumulation for imaging in nanoscale topography (PAINT) was reported by the group of *R. M. Hochstrasser*.[44-45] While PALM, fPALM and STORM rely on the serial activation of individual fluorescent dyes or proteins, PAINT uses transient binding to a lipid membrane to activate fluorophores.[42-45] Although different acronyms are used to describe these methods, they all employ the sequential detection of single fluorophores within a diffraction-limited region.[37] Thus, all of them are summarized under the term SMLM in this work.

Obtaining a super-resolution image by SMLM requires the sequential collection of many localizations with a low position uncertainty. A key requirement for fluorophores in SMLM is the ability to switch between a fluorescent and a dark state where the majority of the dye population should remain in its non-fluorescent state at the same time. Moreover, a high contrast between the two states is crucial for the detection of single molecules.[46] Another important parameter is the duty cycle, which describes the fraction of time the fluorophore remains in its fluorescent state. A low duty cycle is a prerequisite for localization of individual molecules, and for avoiding artifacts that are caused by detecting multiple localizations at the same time within a diffraction-limited area.[47] However, low duty cycles often are at the expense of longer acquisition times. Furthermore, fluorophore brightness is essential for super-resolution image quality since the localization precision is inversely proportional to the square root of the number of detected photons.[48] To date, a wide variety of fluorophores exhibiting the aforementioned properties has been applied in SMLM including fluorescent proteins as well as synthetic organic dyes.[37]

1.2. Labeling Strategies

Investigating cellular processes and structures by fluorescence microscopy relies on the ability to distinguish cellular features. This can be achieved by orthogonal labeling with spectrally distinct fluorophores, such as genetically encoded fluorescent proteins. After the first report of applying green fluorescent protein (GFP) outside the original host (*Aequorea victoria*) by *M. Chalfie* and co-workers in 1994, the group of *R. Y. Tsien* elucidated its fluorescence mechanism and optimized its spectral properties.[49-52] The optimization of GFP, as well as the discovery and modification of other GFP-like proteins, transformed the family of fluorescent proteins (FPs) into powerful tools for fluorescence microscopy.[53-54] However, FPs also exhibit disadvantageous properties compared to organic fluorophores, such as lower brightness and photostability.[55] Therefore, a plethora of different labeling strategies has been developed to enable the application of small-molecule dyes in living cells.[56] In the following sections, selective labeling of unnatural amino acids, peptides or proteins fused to cellular targets as well as the direct labeling of cellular structures by means of targeting ligands are described.

1.2.1. Selective Labeling of Proteins

The selective labeling of proteins is a bioorthogonal reaction of two reactants: a small-molecule probe and a protein.[57] The first example of such a system relies on binding of the fluorescein arsenical hairpin binder (FlAsH) to a tetracysteine-containing peptide sequence.[58] To this end, a tetracysteine-tagged protein is expressed and labeled with the cell-permeable FlAsH-ethanedithiol (FlAsH-EDT_2, **1**) conjugate (Figure 2a). The non-fluorescent FlAsH-EDT_2 becomes fluorescent upon binding to the target peptide and, thus, provides high signal-to-background ratios.[59] Another advantage of this labeling system is the small size of the peptide tag, which potentially leads to less perturbation of the biological structure of interest compared to FPs. However, several limitations for this approach were reported.[60] As FlAsH binds non-specifically to proteins containing cysteine pairs, the sample has to be incubated with dithiols to inhibit unspecific staining. This limits the applicability of the system in animals. Furthermore, a reducing environment is required to enable the reaction with the thiol groups of cysteines and, therefore, the addition of strong reducing agents can be necessary.[60] To date, only a small number of probes for this labeling strategy has been developed, with resorufin arsenical hairpin binder (ReAsH) representing the most commonly used alternative to FlAsH.[61-63] Another related labeling system is based on the binding of a rhodamine-based bisboronic acid (RhoBo, **2**) to a tetraserine-containing peptide sequence (Figure 2b).[64] However, in contrast to the tetracysteine tag, the tetraserine motif is found in many human proteins, thereby limiting the specificity of the system.[65]

The use of unnatural amino acids (UAAs) enables labeling of a protein of interest with a label smaller than even the peptide tags - a single amino acid. An UAA can be introduced by means of an orthogonal aminoacyl-tRNA synthetase-tRNA pair.[66] The position of the UAA in the protein is determined by placing an Amber stop codon (UAG) at a certain site in a gene of interest. The employed tRNA then acts as an Amber suppressor and directs the incorporation of the unnatural amino acid at the site of the Amber stop codon.[67] The UAA can then be employed in a biorthogonal reaction and thereby allows labeling of the protein of interest. For this purpose, UAAs containing strained alkenes or alkynes were developed, which undergo a fast and selective inverse electron demand Diels–Alder reaction with tetrazine-based probes (**3**) (Figure 2c).[68-70] The application of bright and cell-permeable fluorescent tetrazine derivatives enables the use of this labeling system for live-cell labeling as well as super-resolution microscopy.[71-72] Despite various advantages, this labeling technique also has limitations, such as the presence of background signal due to the formation of non-specifically sticking complexes of UAAs and the possibility of natural Amber codon suppression.[73] The latter could become visible if proteins with low abundancy are examined.[74] Moreover, the experimental preparation is relatively laborious since it requires coexpression of the aminoacyl-tRNA synthetase, the tRNA and the protein of interest as well as addition of the UAA followed by the probe.[57]

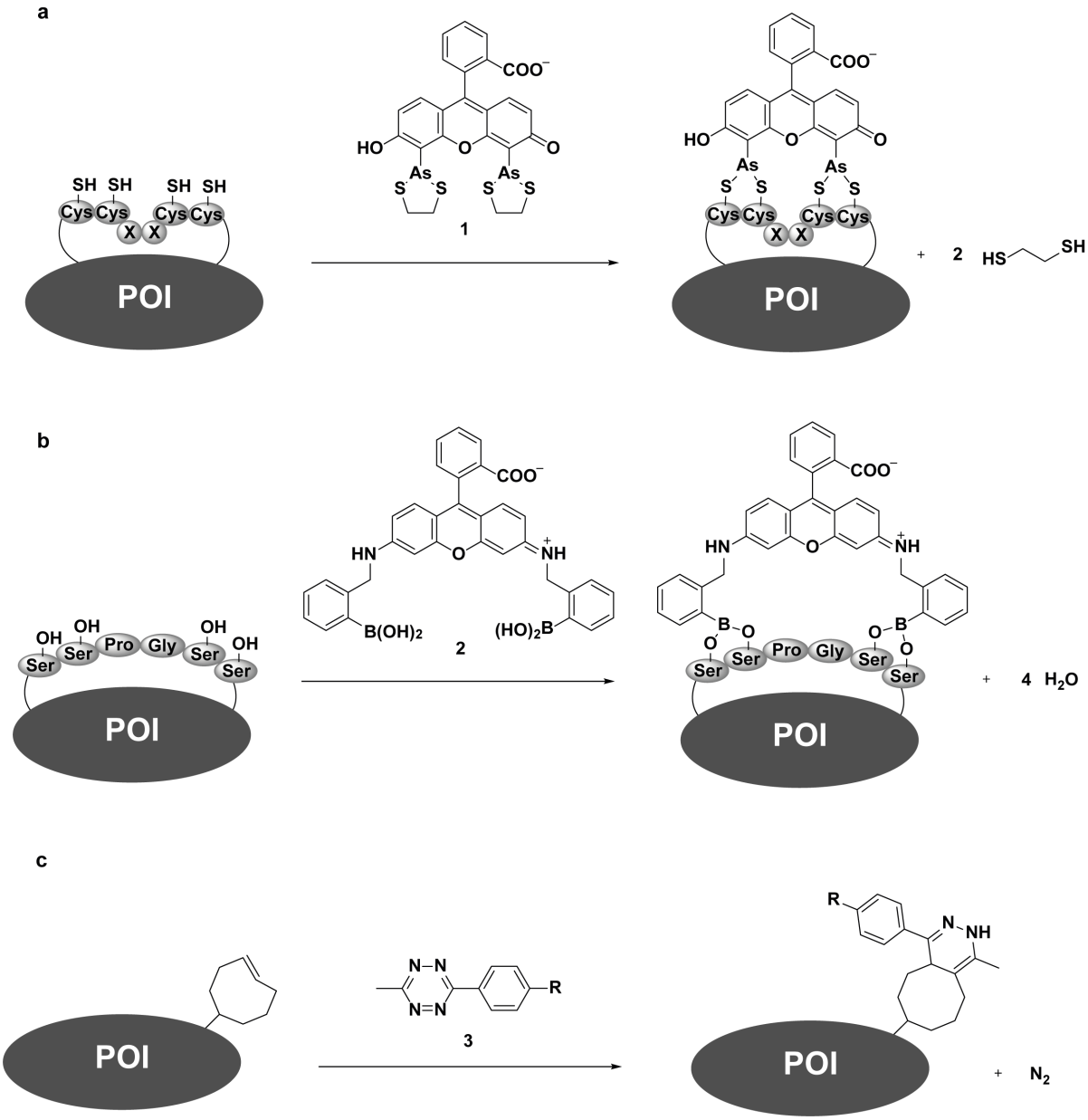

Figure 2: Schematic representation of the labeling of protein of interests (POIs) with small-molecule probes based on peptide tags and UAAs. (a) Binding of FlAsH-EDT$_2$ (**1**) to a tetracysteine-tagged POI. (b) Binding of RhoBo (**2**) to a tetraserine-tagged POI. (c) Inverse electron demand Diels–Alder reaction between a tetrazine derivative (**3**) and a *trans*-cyclooctene-containing UAA incorporated into a POI where R corresponds to a fluorophore.

Self-labeling proteins represent another widely used labeling strategy. Thereby, a small protein tag is fused to the protein of interest, which specifically reacts with a certain electrophile. A prominent example is the SNAP-tag. SNAP-tag was engineered from human O^6-alkylguanine-DNA-alkyltransferase (hAGT), a DNA repair enzyme transferring an alkyl group from O^6-alkylated guanines to its own active site cysteine.[75] Using conjugates of BG (**4**), a potent inhibitor of hAGT, as a substrate, the enzyme was evolved into a self-labeling protein tag (Figure 3a).[76-77] Further engineering of the SNAP-tag resulted in SNAPf bearing a single point mutation, E30R, which increases the labeling kinetics.[78] Additionally, CLIP-tag, an orthogonal self-labeling protein variant using O^2-benzylcytosine derivatives as substrates, was

evolved from SNAP-tag.[79] Moreover, the more cell-permeable benzylchloropyrimidine (CP) was also introduced as a ligand for SNAP-tag.[80] Another self-labeling protein, HaloTag, is based on the reaction between a chloroalkane (CA) derivative (**5**) and an engineered dehalogenase enzyme (Figure 3b).[81] It was further engineered to obtain enhanced stability and labeling kinetics and, in a recent study, to increase the brightness of the bound fluorophores as well as to induce a change in their fluorescence lifetime, thereby enabling fluorescence lifetime multiplexing.[82-83] The labelling kinetics of SNAP-tag and HaloTag reveal different substrate preferences. HaloTag preferentially reacts with certain rhodamine derivatives, while SNAP-tag shows a less pronounced substrate specificity.[84] Furthermore, various fluorophores conjugated to CA show enhanced cell-permeability compared to the corresponding BG derivatives.[85] Another important difference between HaloTag and SNAP-tag is the altered brightness of fluorogenic rhodamine-derived ligands. Various studies revealed that binding to either HaloTag or SNAP-tag leads to a different influence on the spirocyclization equilibrium of rhodamine derivatives (Section 1.4).[85-87] To date, a wide variety of SNAP-tag and HaloTag fusion proteins has been generated and applied to study biological function *in cellulo* as well as *in vivo*.[56] However, a major limitation of self-labeling protein tags is their considerable size, which might affect the function of the protein of interest. Moreover, it limits the precision with which the probe can be localized.[57]

The group of *V. W. Cornish* developed a protein tag-based method, which relies on the non-covalent interaction of a methotrexate-based probe and the *Escherichia coli* dihydrofolate reductase (eDHFR).[88] Subsequently, the system was optimized by replacing methotrexate (**6**) with trimethoprim (TMP, **7**), which shows a much higher affinity for eDHFR than for endogenous DHFR in mammalian cells (Figure 3c). Therefore, background signal and toxicity resulting from binding endogenous DHFR could be circumvented.[89] Further extensions of this labeling approach include the development of covalently binding and fluorogenic variants.[90-91] The high cell-permeability and specific binding of TMP conjugates endows the TMP-tag with suitable properties for live-cell imaging applications.[92] However, to date, it is still applied less widely than SNAP-tag or HaloTag.[93] Additionally, it is worth mentioning that the dependence of eDHFR labeling on its native cofactor NADPH can lead to different results in different cellular compartments.[94-96]

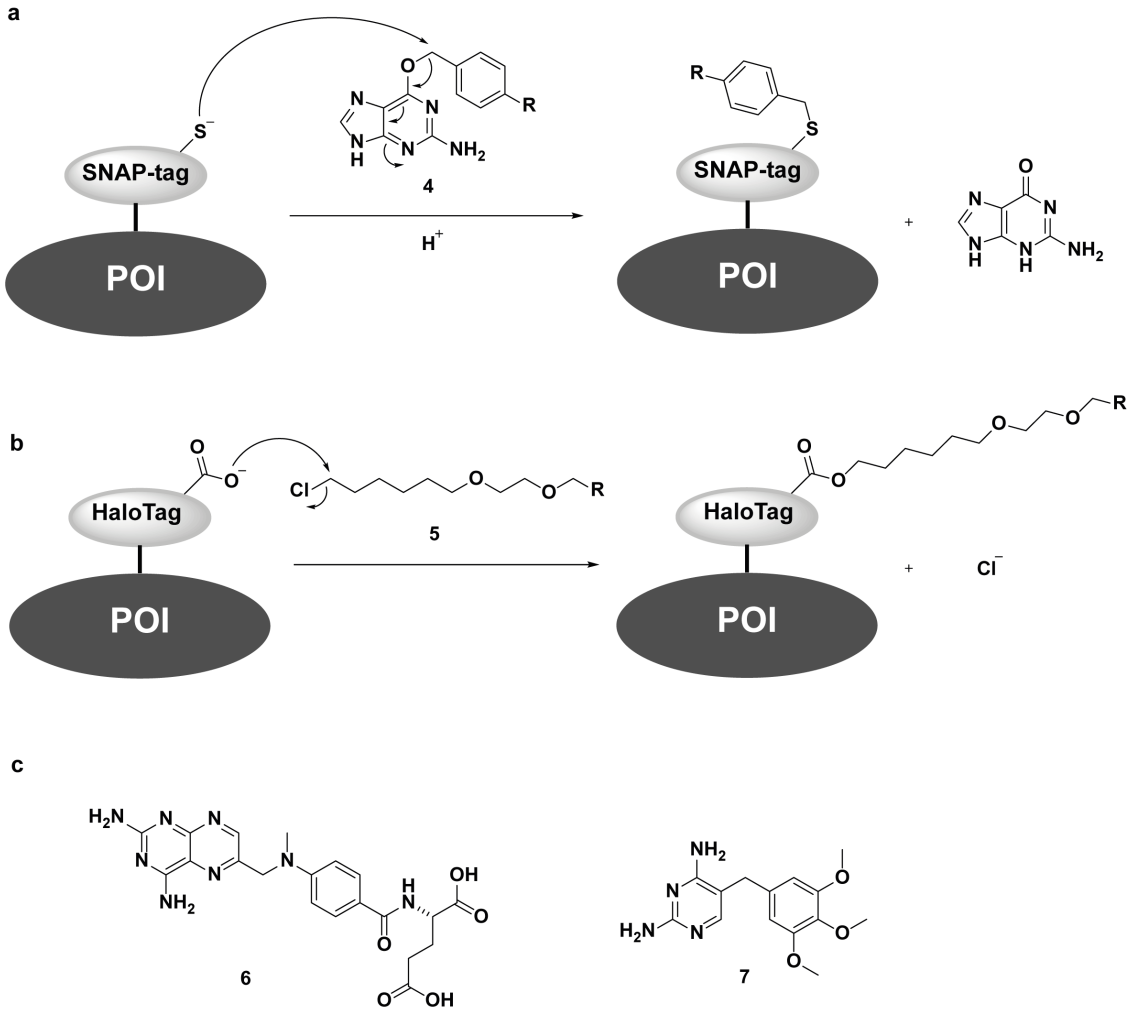

Figure 3: Labeling strategies based on fusion proteins. (a) Reaction mechanism between SNAP-tag fused to a protein of interest (POI) and a BG derivative (**4**). (b) Reaction mechanism between HaloTag fused to a POI and a CA derivative (**5**). For **4** and **5**, R represents a fluorophore. (c) Chemical structures of methotrexate (**6**) and TMP (**7**).

1.2.2. Direct and Non-Covalent Labeling of Cellular Structures

Advances in super-resolution microscopy have led to a level of optical resolution, where the size of the label can influence the precision of localization.[97-98] A straight-forward approach to minimize label size is the use of targeting ligands to directly label native cellular structures. The resulting probe should be non-toxic, cell-permeable, fluorogenic and should label the cellular target with high specificity and affinity. To date, several ligands that bind to different organelles and substructures have been reported.[99] Prominent examples include molecules that selectively target the nucleus, the cytoskeleton, the endoplasmic reticulum (ER), the Golgi apparatus, lysosomes and mitochondria. Labeling of the nucleus was achieved by means of Hoechst derivatives (**8**) containing a bisbenzimide core, for which different modes of interaction with DNA were reported, such as minor and major groove binding (Figure 4).[100-102] The Hoechst moiety itself can be used as a fluorophore.[103] However, such dyes require UV excitation, which can lead to cell damage and observation of auto-fluorescence. Thus, probes with suitable

excitation spectra were developed by conjugating Hoechst to more red-shifted fluorophores.[26, 104] Other widely used probes employ taxanes, including docetaxel (**9**) as well as cabazitaxel (**10**), for tubulin-binding and jasplakinolide-based ligands (**11**) for targeting of actin (Figure 4).[25, 105] Probes with high specificity for the ER could be developed by using Glibenclamide (**12**), which binds ATP-sensitive potassium channels that occur in the membrane of the ER (Figure 4).[106-107] Ceramide (**13**), which is a lipid-based targeting group, was applied to examine the Golgi apparatus (Figure 4).[108-110] Additionally, ceramide-based probes were also reported to localize to the ER.[111] Direct labeling of lysosomes was achieved by means of probes containing pepstatin A (**14**), which strongly binds to the lysosomal protease cathepsin D (Figure 4).[28, 112] A wide variety of mitochondrial probes take advantage of the negative potential at the inner mitochondrial membrane. Therefore, cationic targeting groups, such as triphenylphosphonium (TPP, **15**) cations, were used to study mitochondria (Figure 4).[27, 113] A general limitation for the direct labeling by means of targeting ligands includes potential toxicity and an effect on the biological function of the cellular target upon ligand binding.[25, 57] Furthermore, molecules with high affinity and specificity are not yet available for a large number of cellular structures.

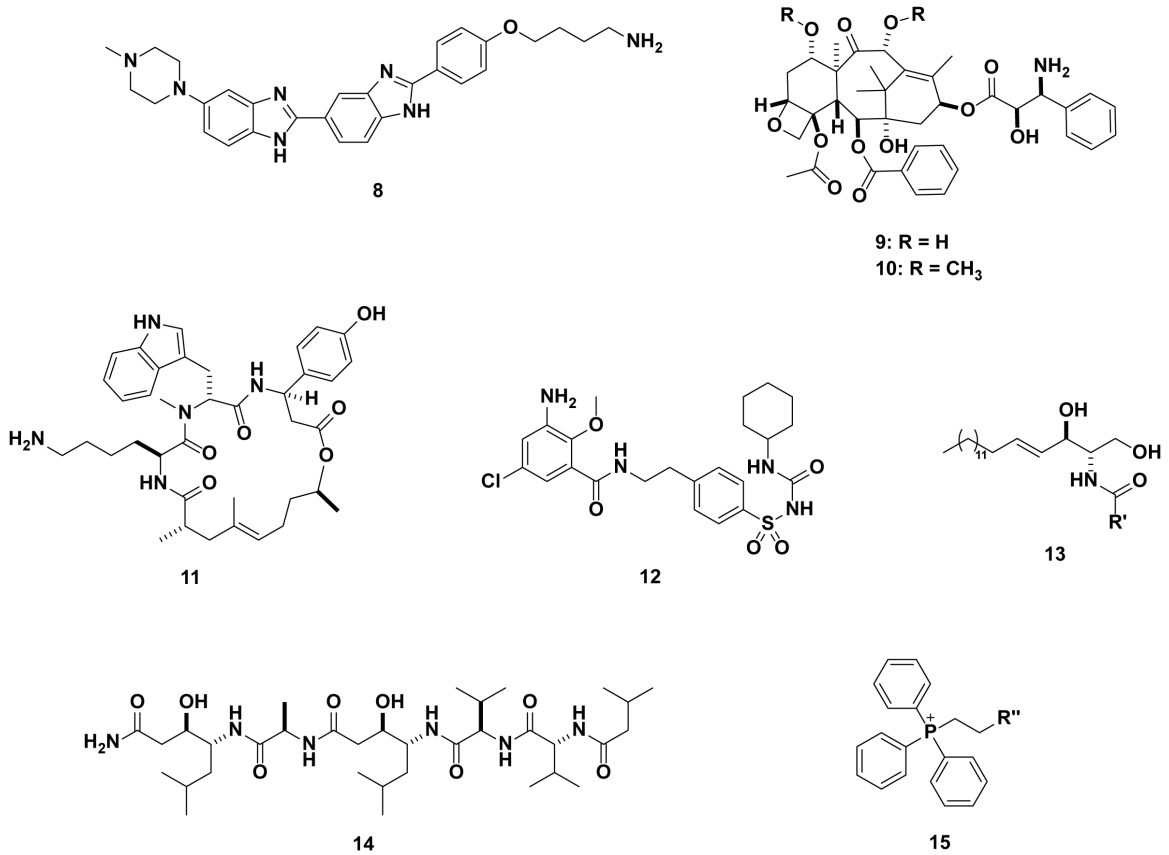

Figure 4: Chemical structures of targeting ligands for the direct labeling of different cellular structures.

1.3. Small-Molecule Fluorophores

The successful labeling and visualization of cellular structures strongly relies on the employed fluorophore. Crucial properties of dyes for fluorescence microscopy applications include brightness, cell-permeability, solubility, spectral compatibility, photostability, fluorogenicity as well as blinking character.[12] A main advantage of small-molecule fluorophores compared to fluorescent proteins is their increased brightness and photostability. Progress in super-resolution microscopy techniques and the examination of targets with endogenous expression levels has led to an increased demand for fluorophores with a higher photon budget.[114] Therefore, small-molecule fluorophores are essential tools for a wide variety of microscopy applications.

1.3.1. Rhodamine-Based Fluorophores

A prominent class of small-molecule fluorophores are rhodamine derivatives. Rhodamine-based dyes exist in an equilibrium between a spirocyclic (**16**) and a zwitterionic state (**17**) (Figure 5a). A detailed description of this spirocyclization equilibrium and its significance for microscopy applications will be provided in Section 1.4. In their spirocyclic form, rhodamines structurally consist of a xanthene system fused to an isobenzofuran. Therefore, the numbering of the fluorophore core is adapted from these two chemical moieties.[115] To date, a plethora of synthetic modifications has been reported to tune and optimize the properties of rhodamine-based dyes. Their solubility can be enhanced by sulfonation of the xanthene scaffold.[116] Furthermore, various strategies to increase fluorophore brightness and photostability have been developed. They rely on the suppression of pathways of non-radiative decay as well as processes causing fluorophore degradation, such as twisted internal charge transfer (TICT) and stepwise photooxidative *N*-dealkylation. TICT describes an electron transfer from the amino-substituents to the xanthene core leading to the formation of an amine radical cation with a twisted C-N bond. This radical state can either relax via non-radiative decay or undergo irreversible bleaching reactions.[6] Rigidification of the fluorophore by constraining the nitrogen atoms in ring systems fused to the xanthene core inhibits rotation of the C-N bond. Thus, this structural change leads to enhanced quantum yields, as reported for Q-rhodamine (**18**) (Figure 5b).[117-118] Moreover, replacing *N,N*-dialkylamino moieties with cyclic structures, including pyrrolidines (**19**) and azetidines (**20**), allows the suppression of TICT and, thus, yields an enhanced brightness and photostability (Figure 5c).[119-121] The increased ionization potential of these cyclic amines as well as a decreased steric repulsion with the xanthene core were reported as the main causes for these observations.[6, 122] Furthermore, the photooxidative *N*-dealkylation can be mitigated by introducing α-quaternary centers on the nitrogen atoms (di-*t*-butylrhodamine (**21**)) as well as by modification with electron-deficient substituents (rhodamine *500R* (**22**)) (Figure 5d).[20, 123] More recent developments in this field

include the work of the groups of *L. D. Lavis* as well as *J. Broichhagen*, who reported enhanced brightness and photostability upon deuteration of rhodamines.[124-125]

The maximal absorbance and emission wavelengths can be altered significantly by exchanging the bridging oxygen with other functionalities (X), thus covering a broad spectral range (Figure 5e).[126-129] Widely used fluorophores resulting from this transformation are carborhodamines and siliconrhodamines (SiR), which contain a *gem*-dimethyl carbon as well as a *gem*-dimethyl silicon respectively. Moreover, the wavelength maxima can be tuned with high precision by introducing different 3-substituted azetidine rings onto the 3'- and 6'-positions of the xanthene system (Figure 5e).[130] Additionally, an increase in *Stokes* shift was obtained upon attachment of a 1,4-diethyl-decahydro-quinoxaline moiety to the xanthene system. It was reported that this structural change leads to asymmetric electronic structures, thereby inducing strong internal conversion and a large difference between the wavelength of absorbed and emitted light.[131]

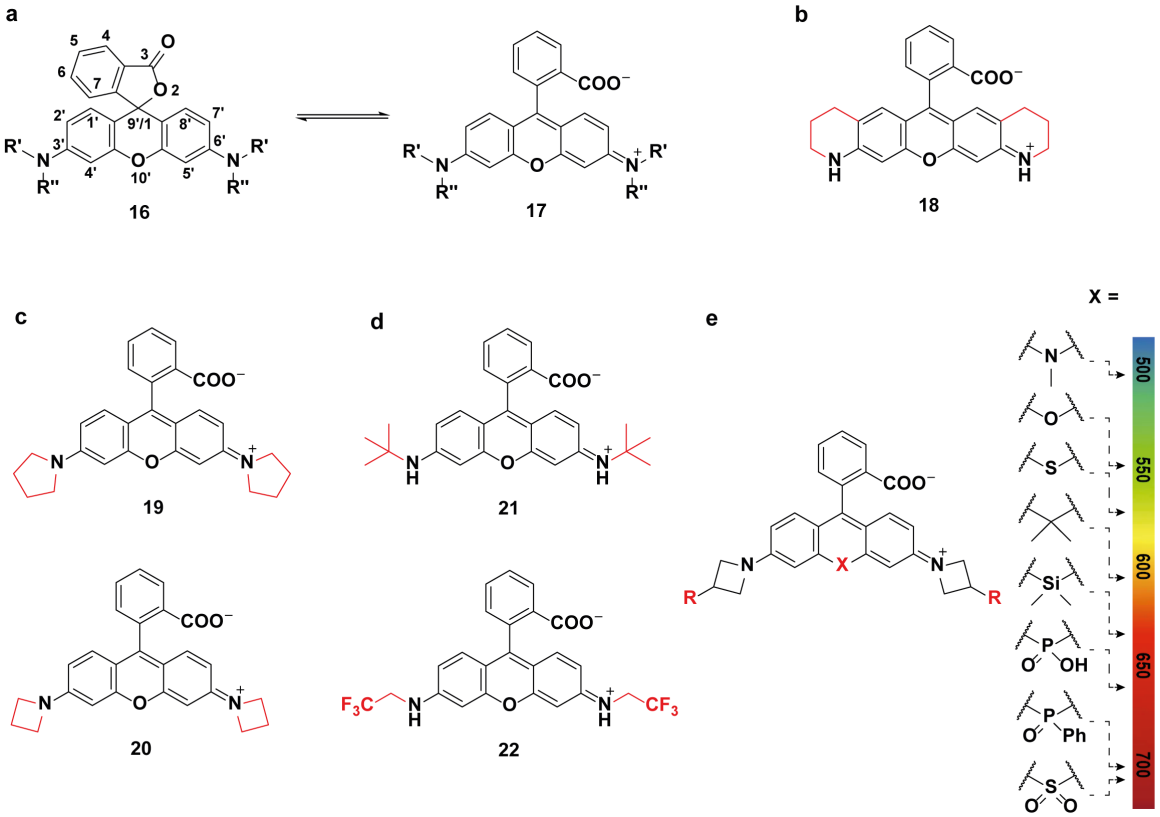

Figure 5: Rhodamine-based fluorophores and their modification to change as well as optimize their brightness, photostability and spectral properties. (a) The spirocyclization equilibrium and numbering of rhodamine derivatives. (b) Rigidification of the fluorophore structure. (c) Modifying rhodamines with cyclic amines. (d) Introduction of α-quaternary centers and electron-withdrawing groups onto the aniline nitrogen atoms. (e) Tuning the λ_{abs} of rhodamine derivatives by changing X or R.

The first rhodamine derivatives were originally synthesized employing century-old synthetic methods, including the acid-catalyzed formation of tetramethylrhodamine (TMR, **23**)

(Figure 6a).[132] Over the last decades, applications of more sophisticated chemical concepts, such as transition metal catalysis as well as organometallic reagents, have expanded the scope of fluorophore synthesis.[12] The *Buchwald-Hartwig* amination was used to introduce aniline nitrogen atoms with a wide variety of functionalities (Figure 6b).[20, 133] Furthermore, the reaction between metalated aryl species (**24**) and xanthone derivatives (**25**) yielded various rhodamine-based scaffolds with different spectral properties (Figure 6c).[121, 129, 134] However, this synthetic approach shows several limitations, such as tedious syntheses of commonly used xanthone derivatives. Furthermore, this route often leads to a mismatch between reactants if an electron-rich ketone electrophile reacts with an electron-poor metalated aryl nucleophile. Thus, relatively harsh reaction conditions are required, which are incompatible with various functional groups. To overcome these limitations, alternative synthetic methodologies were reported employing an electronically matched reaction between electron-rich bis(arylmetal) compounds (**26**) and electron-poor esters (**27**) or anhydrides (**28**) (Figure 6c).[135-136] Recently, the application of bis-aryllanthanum reagents has been reported to provide milder reaction conditions and a further expanded substrate scope.[137]

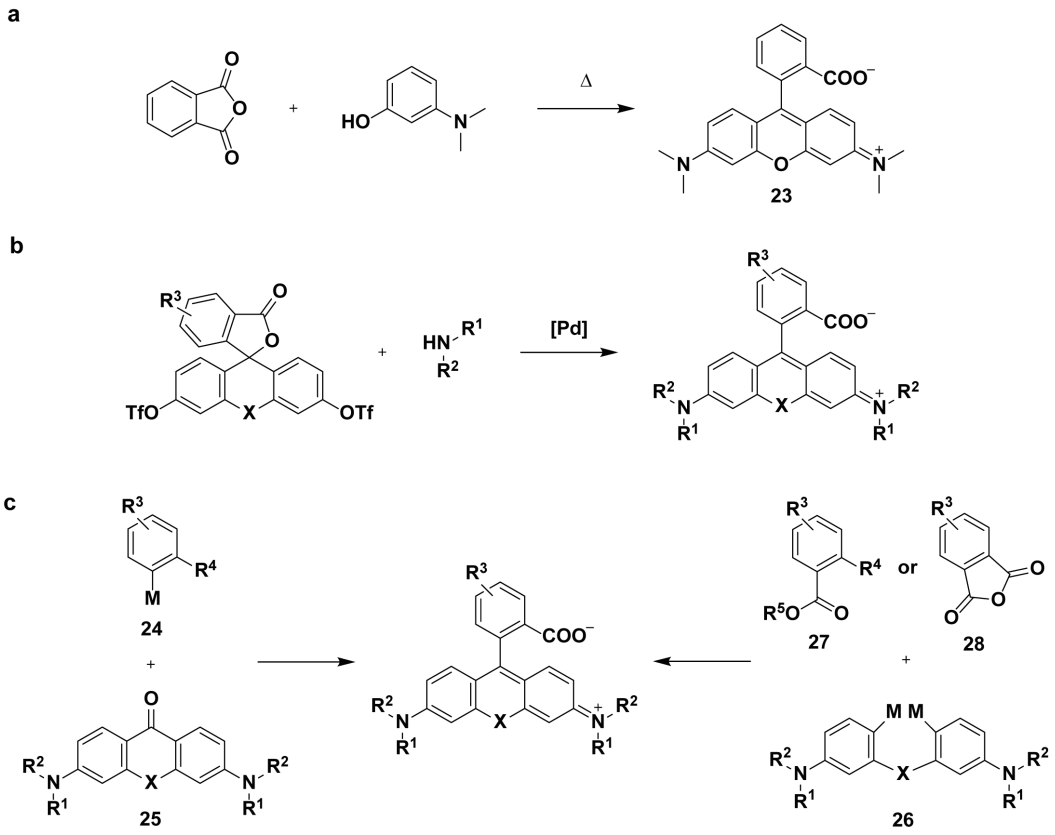

Figure 6: Synthetic strategies toward rhodamine derivatives. (a) Synthesis of TMR (**23**). (b) Introducing aniline nitrogen atoms with different substituents via *Buchwald-Hartwig* amination. (c) Different approaches to form the central C-C bond of rhodamine-based scaffolds.

1.3.2. Triplet-State Quencher Fluorophore Conjugates

Fluorophores can be excited into an excited triplet state (T_1) upon irradiation with light followed by intersystem crossing (ISC). Processes resulting from T_1, such as singlet oxygen formation or redox reactions, are a major source of degradation of small-molecule dyes (Figure 1a). Therefore, strategies to quench T_1 and inhibit related detrimental pathways have been developed.[9] Various compounds have been applied as triplet-state quenchers (TSQ), including cyclooctatetraene (COT, **29**), 4-nitrobenzyl alcohol (**30**) and 6-hydroxy-2,5-,7,8-tetramethylchroman-2-carboxylic acid (**31**) (Figure 7a). While **29** was reported to quench the triplet state via energy transfer, quenching by means of **30** and **31** is based on electron transfer.[138-140] Using these TSQs as additives is limited by the high concentrations that are required to enhance the photostability of dyes and the related toxicity. The group of *S. C. Blanchard* overcame this limitation by conjugating **29** – **31** to a cyanine dye (**32**) (Figure 7b).[141] The resulting probes showed significantly increased photostability and, thus, represent suitable tools for applications requiring long-lived fluorescence emission. Subsequent work with COT-fluorophore conjugates showed that their self-healing properties could be optimized by altering the linker length as well as the electronics of COT.[138, 142] Additionally, COT-conjugation was also reported to decrease the phototoxicity of cyanine dyes.[143]

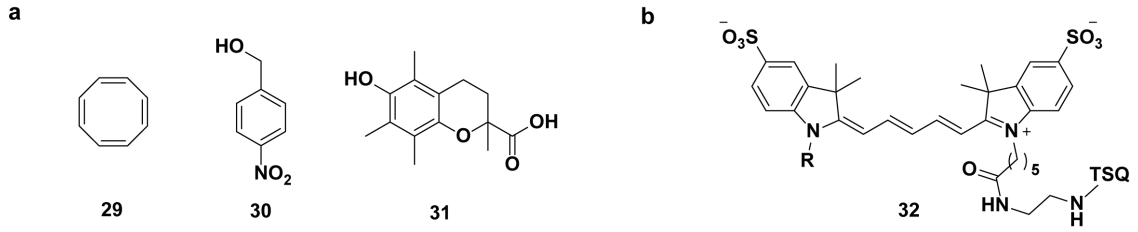

Figure 7: TSQs and their fluorophore conjugates. (a) Chemical structures of TSQs **29** – **31**. (b) Conjugation of TSQs to a cyanine dye (**32**).

1.4. The Spirocyclization Equilibrium of Rhodamines

Rhodamines exist in an equilibrium between a non-fluorescent, cell-permeable spirocyclic form (**33**) and a fluorescent zwitterion (**34**) (Figure 8a). This spirocyclization equilibrium is a key feature for the widespread use of rhodamine derivatives in fluorescence microscopy.[115] Controlling this equilibrium allows one to tune and optimize crucial fluorophore properties, such as their cell-permeability, blinking behavior and fluorogenicity.[144]

1.4.1. Strategies to Increase Fluorogenicity and Cell-Permeability

Fluorogenicity describes the ability of a fluorescent probe to increase fluorescence emission upon binding to its target.[145] Therefore, fluorogenic dyes show low background emission, and their use in fluorescence microscopy yields high contrast images without requiring washing steps.[14] The potential fluorogenicity and cell-permeability of rhodamine-based dyes results from the environmental sensitivity of the spirocyclization equilibrium. External factors, such as solvent polarity as well as pH, can influence this equilibrium.[146] Moreover, binding to a cellular structure often stabilizes the fluorescent, zwitterionic form.[72, 85] Thus, this dynamic equilibrium enables that certain fluorophores only exist as a fluorescent zwitterion if they are bound to their target, and otherwise reside in their hydrophobic, non-fluorescent state. This spirocyclic form can enter the cell more readily through passive diffusion compared to the zwitterion.[115] Consequently, the spirocyclization equilibrium endows probes with high fluorogenicity as well as cell-permeability and, therefore, makes them potent tools for live-cell fluorescence microscopy applications.[14]

Various strategies to enhance fluorogenicity and cell-permeability by shifting the spirocyclization equilibrium toward the spirocyclic state have been reported (Figure 8a).[144] The majority of these approaches relies on increasing the electrophilicity of the xanthene system. For instance, the equilibrium can be altered by replacing the bridging oxygen of rhodamines with other functional groups (X). Introducing a *gem*-dimethyl silicon moiety provides siliconrhodamine (SiR, **35**), a highly fluorogenic and cell-permeable dye scaffold (Figure 8b).[72] The shift in equilibrium toward the spirocyclic state is caused by a stabilization of the lowest unoccupied molecular orbital (LUMO) of the xanthene core and, thus, an enhanced electrophilicity.[147] This stabilization results from the interaction between the σ^* orbital of the exocyclic Si-C bonds and the π^* system of the adjacent carbons.[126, 148] SiR-based probes were developed for a wide variety of labeling systems and cellular targets, including self-labeling proteins, the cytoskeleton, DNA as well as genetically encoded unnatural amino acids.[25-26, 72] Furthermore, the group of *A. Jäschke* developed a SiR-binding aptamer to employ SiR and its favorable properties in RNA labeling.[149] However, the replacement of X also alters the spectral properties of the dye, including drastic changes in absorbance and emission wavelengths.[126]

Moreover, it causes strong shifts in spirocyclization equilibrium, and does not enable its fine-tuning. In the case of phosphine oxide (X) containing fluorophores, the stabilization of the spirocyclic state is very pronounced, such that they show low brightness. To enhance brightness, the position of the equilibrium was shifted toward the zwitterionic state by fluorination of the pendant phenyl ring.[127]

More precise control over the spirocyclization equilibrium is attained by altering R_1 and R_2 (Figure 8a). A prominent approach comprises the introduction of 3-substituted azetidine rings onto the 3'- and 6'-positions of the xanthene system.[130] However, electron-withdrawing substituents on the azetidine rings also lead to hypsochromic shifts in absorbance and emission maximum of the fluorophore. Another strategy employs fluorination of the xanthene system (R_3) to increase its electrophilicity and, thus, to shift the equilibrium toward the spirocyclic state (Figure 8a). A limitation of this approach is that significant decreases in quantum yield were observed for certain dye scaffolds upon fluorination, such as in the case of SiR and carborhodamine.[21] Combining fluorination of the xanthene core with the introduction of electron-deficient azetidines led to the development of a highly fluorogenic and cell-permeable fluorophore (JF_{526}, **36**) (Figure 8b).[150] **36** shows SiR-like features but shorter absorbance and emission wavelengths. Thus, it expands the spectrum of colors for fluorogenic and cell-permeable probes.

A general limitation of strategies, which rely on enhancing the electrophilicity of the xanthene core, is that its reactivity is not only increased toward an intramolecular nucleophile, but also toward intermolecular nucleophilic attack. Electron deficient xanthenes were reported to show enhanced reactivity toward intracellular nucleophiles, which can reduce the brightness of fluorophores.[151-153] Moreover, as xanthene modifications often are synthetically challenging, they have required the development of multistep syntheses and sophisticated methodologies (Section 1.3.1.).[20, 127, 135-137]

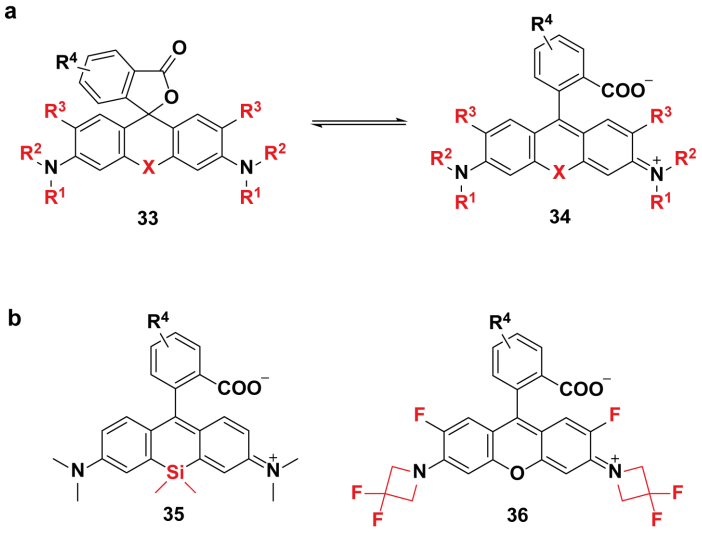

Figure 8: Strategies to shift the spirocyclization equilibrium toward the spirocyclic state upon modification of the xanthene system. (a) Chemical structures of the spirocyclic (**33**) and zwitterionic (**34**) form of rhodamine-based dyes. Positions at the xanthene core, which are modified to alter the spirocyclization equilibrium, are colored in red. (b) Chemical structures of prominent examples for fluorogenic and cell-permeable dyes (**35** and **36**).

An alternative and simple synthetic strategy was previously developed in our group and employs stronger intramolecular nucleophiles to shift the spirocyclization equilibrium toward the spirocyclic state. Transformation of the *ortho*-carboxy group into electron-poor amides, including acyl cyanamide (**37**), acyl sulfonamide (**38**) and acyl sulfamides (**39** and **40**), converted various rhodamine-based scaffolds into highly fluorogenic and cell-permeable dyes (Figure 9).[85] They were named MaP-dyes and include probes in different colors for various labeling systems and cellular targets, such as HaloTag, SNAP-tag, actin as well as tubulin. Furthermore, their applicability in live-cell, multicolor, no-wash STED microscopy was corroborated. The MaP-strategy enables to retain essential photophysical properties of the fluorophore, such as quantum yield, absorbance and emission wavelength, since the xanthene core is not modified. In comparison to many of the aforementioned approaches relying on xanthene modifications, the synthesis of the MaP-dyes is synthetically less challenging and more concise.[20, 127, 135-137] Recently, the MaP-strategy has been applied to enhance the emission ratio change of color-shifting dyes.[154-155]

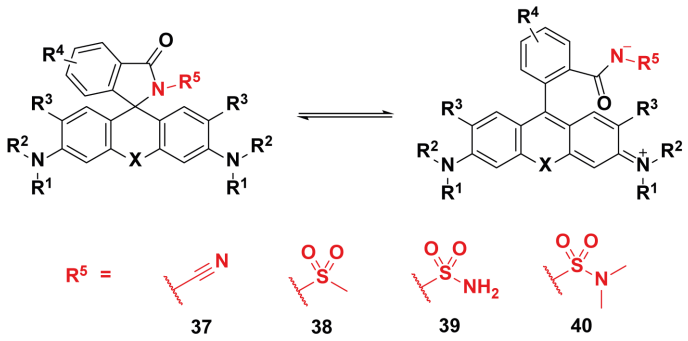

Figure 9: Shifting the spirocyclization equilibrium toward the spirocyclic state by introducing electron-deficient amides (**37 – 40**).

1.4.2. Strategies to Develop Probes for SMLM

The spirocyclization equilibrium is also essential to the design of rhodamine-based probes for SMLM applications.[37] These microscopy techniques are based on the accurate detection of individual molecules to obtain super-resolution images (Section 1.1.2.). Therefore, only a small portion of the fluorophore population should be fluorescent at the same time.[15] Various SMLM probes were developed, employing chemical modifications to shift the equilibrium strongly toward the spirocyclic state. A wide variety of rhodamines containing stable spirolactams were applied as photoactivatable probes.[156-160] In comparison to the aforementioned fluorogenic, electron-deficient amides (Section 1.4.1.), more electron-rich amides are required for SMLM, such that the majority of the dye population would be in its spirocyclic, non-fluorescent form. Irradiation with light of short wavelength enables a shift of the equilibrium toward the fluorescent state and, therefore, leads to the activation of a subset of the fluorophore population (Figure 10a).[161] Subsequently, thermal recyclization restores the spirocyclic state.[162] It was shown that the on-time of photoactivatable fluorophores as well as their single-molecule brightness could be increased by stabilization of the photoactivated zwitterion. To this end, a carboxy group was installed in close proximity to the spirolactam, which caused an intramolecular acidic environment.[160] A general limitation of photoactivatable probes is their need for intense laser irradiation of short wavelength, which often limits their applicability in live-cell imaging applications.[163]

Another prominent class of SMLM probes relies on exchanging the *ortho*-carboxy group of rhodamine derivatives with a more nucleophilic hydroxyl moiety. The resulting dyes can spontaneously interchange between their fluorescent form and their preferred spirocyclic state. The first member of this class of probes, hydroxymethyl siliconrhodamine (HMSiR, **41**), was developed by *Y. Urano* and co-workers (Figure 10b).[147] HMSiR shows blinking character without requiring intense laser irradiation of short wavelength or additives and, therefore, enables SMLM in living cells. In subsequent work, this dye was used to label different cellular targets, including mitochondria, ER, plasma membrane and DNA.[111, 164-165] Furthermore,

spontaneously blinking hydroxyl as well as spirolactam rhodamine derivatives with shorter absorbance and emission wavelengths have been developed.[150, 166-167] It was also observed that the blinking behavior of spontaneously blinking dyes strongly depends on their chemical environment.[111] To control the amount of fluorescent molecules independently from the environment, the group of *P. Rivera-Fuentes* used a combination of photoactivation and spontaneous blinking in their fluorophore design.[168] The resulting probe allows live-cell long time-lapse SMLM with minimal phototoxicity.

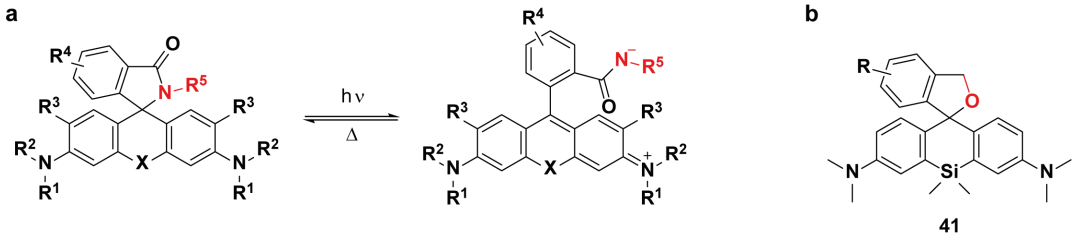

Figure 10: Rhodamine-based probes for SMLM. (a) Spirocyclization equilibrium of photoactivatable rhodamine spirolactams. (b) Chemical structure of HMSiR (**41**) in its spirocyclic form.

1.5. Fluorescein- and Rhodamine-Based Indicators

Metal ions play crucial roles in a wide variety of biological processes, such as metabolism, signaling, osmotic regulation and catalysis.[169] Therefore, measuring ion concentrations inside living cells is an essential part of unraveling biological systems. An efficient fluorescent indicator for live-cell applications should fulfill several requirements, including cell-permeability, solubility, brightness, high specificity for the ion of interest and an appropriate dissociation constant (K_d) for the examined system.[170] Furthermore, a change in fluorescence intensity or a shift in absorbance and emission wavelengths upon binding of the analyte are often used as a readout. Prominent scaffolds employed as small-molecule indicators are rhodamines as well as fluoresceins, which bear phenolic oxygens instead of the aniline nitrogens at the 3'- and 6'-positions of the xanthene system.[171] The development of a fluorescein-based pH indicator for live-cell applications by *E. Racker* and co-workers represents a milestone regarding the development of fluorescent indicators.[172] They exploited the pH sensitivity of fluorescein (pK_a = 6.3), which resides in an equilibrium between a highly fluorescent dianion (**42**) and a monoanion (**43**) with decreased fluorescence intensity (Figure 11a). An alternative approach is based on the conjugation of a fluorophore to a ligand with high specificity for a certain ion. This strategy has yielded sensors for a wide variety of analytes.[173] An early example (**44**) consists of a fluorescein-derivative fused to the calcium chelator 1,2-bis(*o*-aminophenoxy)ethane-*N,N,N',N'*-tetraacetic acid (BAPTA) (Figure 11b).[174-175] **44** shows a 40-fold increase in fluorescence emission upon coordinating calcium, as calcium binding to the BAPTA moiety reduces its photoinduced electron transfer (PeT)-based fluorescence quenching. Another turn-on mechanism for the detection of a wide variety of metal ions relies on shifting the spirocyclization equilibrium toward the fluorescent state by chelation with the analyte and/or an analyte-promoted reaction.[176] For this purpose, the *ortho*-carboxy group of rhodamine derivatives was replaced with an amide that is part of the ligand. Since the development of the first rhodamine-based copper (II) indicator (**45**), this strategy has been extended to sense various other metal ions (Figure 11c).[177-178]

1.5.1. Zinc Indicators

Zinc is a highly abundant transition metal in various biological systems, where it is used as a structural cofactor or Lewis acid, tightly bound to proteins.[179] Furthermore, free Zn^{2+} is involved in physiological processes, such as neuronal activity and pancreatic function.[180-181] Zn^{2+} concentrations have been found to be heterogeneous as well as dynamic, and range from 10^{-10} M in the cytosol up to 10^{-2} M in certain vesicles.[182-183] Due to the physiological importance of zinc, a wide variety of zinc indicators has been developed, including genetically encoded sensors and small-molecule probes.[169] A prominent design principle for small-molecule zinc indicators is based on di-2-picolylamine (DPA) derivatives as Zn^{2+} ligands. The *S. J. Lippard*

group introduced a series of probes based on this strategy. A dichlorofluorescein derivative bearing two DPA moieties on the xanthene core represents the first member of this series (**46**) (Figure 11d).[184] Mechanistically, the tertiary nitrogen of DPA quenches the fluorescence in the absence of Zn^{2+} via PeT. Zn^{2+} coordination to DPA changes its electronic structure and alleviates PeT quenching, leading to an increase in fluorescence intensity, which is then used as a readout.[185] In subsequent work, fluorination of the xanthene core as well as introduction of an aniline-based ligand tuned the nitrogen involved in PeT quenching less sensitive to protonation and, thus, reduced background signal.[186-187] *T. Nagano* and co-workers developed zinc indicators, such as **47**, with large turn-on responses and low background intensities by conjugating the DPA moiety to the pendant phenyl ring of the fluorescein scaffold (Figure 11d).[188] Moreover, synthetic strategies to alter the binding affinity of DPA derivatives for Zn^{2+} as well as the synthesis of a far-red SiR-based probe were reported.[126, 189-190] Targetable zinc indicators were developed by introducing the CA ligand for HaloTag labeling.[191-192] Recently, Zn^{2+} ligands with lower binding affinities have been used to develop probes with K_d values in the µM range. The resulting probes represent suitable tools to visualize biological processes involving high Zn^{2+} concentrations.[193]

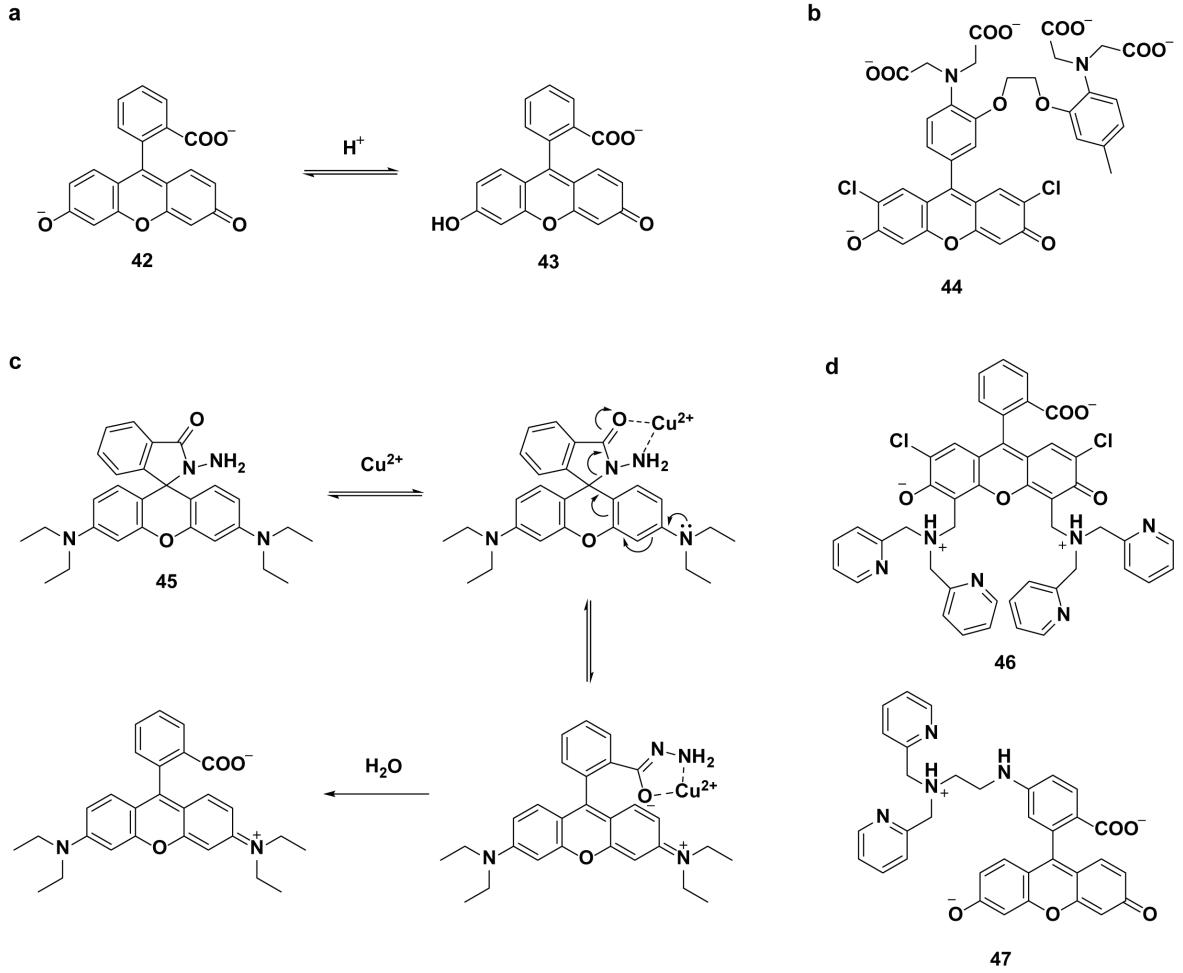

Figure 11: Fluorescein- and rhodamine-based indicators. (a) pH-dependent equilibrium between the dianionic (**42**) and the monoanionic (**43**) form of fluorescein. (b) Chemical structure of calcium indicator **44**. (c) Cu^{2+}-mediated hydrolysis of a rhodamine-hydrazide derivative (**45**). (d) Chemical structures of zinc indicators **46** and **47**.

2. Objectives

The main goal of this thesis was the development of a synthetic strategy to systematically tune the spirocyclization equilibrium of rhodamine derivatives with high precision and over a large range. It was envisioned that controlling this key feature of rhodamines by chemical means would enable the development of probes specifically optimized for different labeling systems and microscopy techniques. Ideally, this should be attained without altering crucial photophysical properties of the original fluorophore. To this end, the *ortho*-carboxy group of various rhodamine-based scaffolds was transformed into differently substituted amides. *In vitro* measurements were performed to examine the effect of these structural modifications on the spirocyclization equilibrium and the ability to retain crucial photophysical properties, such as quantum yield, maximal absorbance and emission wavelengths. Furthermore, the corresponding SNAP-tag and HaloTag probes were synthesized and tested *in vitro*, in live-cell, no-wash confocal as well as STED microscopy. Thereby, the significance of a precise control over the spirocyclization equilibrium for fluorogenicity and cell-permeability was investigated. Rhodamine derivatives exhibiting a strong shift in equilibrium toward the spirocyclic state were characterized for blinking behavior, and their applicability in SMLM was examined. In terms of other labeling systems and cellular targets, it was explored if fluorogenic probes for eDHFR, tubulin and HIV-1 protease could be created using fluorophores that had been developed in this as well as previous studies.[85]

Another aim of this thesis was to investigate if the *ortho*-carboxy group could serve as a handle for the functionalization of rhodamines to either improve their photostability or transform them into zinc indicators. To this end, triplet state quenchers and a zinc ligand were conjugated to the *ortho*-carboxy group of different rhodamine-based scaffolds and the properties of the resulting fluorophores were examined *in vitro*.

3. Systematic Tuning of the Spirocyclization Equilibrium of Rhodamines

The central idea of this thesis comprises the precise and broad manipulation of the spirocyclization equilibrium of rhodamine-based dyes. In order to retain crucial photophysical properties of the original fluorophore, the synthetic strategy was based on modifying the *ortho*-carboxy group. Functionalizing this position of rhodamine derivatives had previously been reported to alter the position of the spirocyclization equilibrium while retaining quantum yield as well as maximal absorbance and emission wavelengths (Section 1.4.1.).[85]

3.1. Tuning the Spirocyclization Equilibrium of Rhodamine *500R*

The systematic tuning of the spirocyclization equilibrium was first tested on rhodamine *500R* (**48**), which is a green fluorescent dye with high extinction coefficient and quantum yield but weak fluorogenic character.[21, 123] Therefore, a synthetic route for its derivatization was developed. The *t*-Bu-protected rhodamine *500R* scaffold (**49**) was synthesized by *Buchwald-Hartwig* amination of **50** in 72% yield (Figure 12a).[20] Amidation of the *ortho*-carboxy group of **49** by means of EDC in combination with DMAP followed by deprotection with TFA delivered a library of different spirolactams in yields of 20% – 83% (**51** – **65**) (Figure 12b).[194] Analogous to the MaP-strategy[85], acyl cyanamide **55**, acyl sulfonamide **60** and acyl dimethylsulfamide **61** were synthesized. Furthermore, rhodamine *500R* derivatives **51** – **54** and **56** – **59** were synthesized with acyl benzenesulfonamides that contain different substituents in para- or meta-position. Additionally, less electron-deficient amines were applied in the amidation of **49** to obtain **62** – **66**. This library of rhodamine *500R* spirolactams was then coupled to CA, BG or CP ligands, yielding probes for HaloTag as well as SNAP-tag labeling.

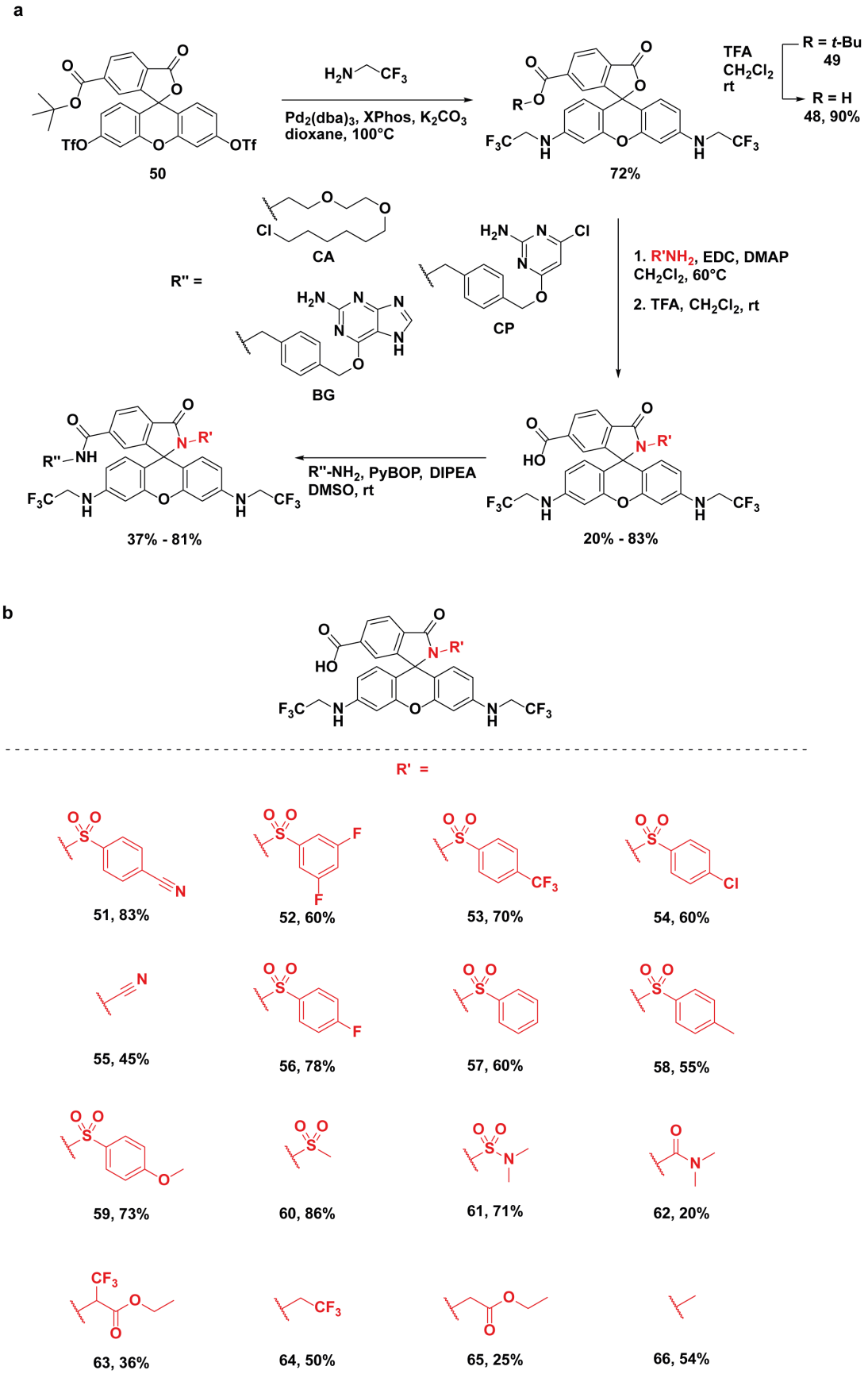

Figure 12: Rhodamine *500R* spirolactams and their synthesis. (a) Synthesis of rhodamine *500R*-derived probes. (b) Library of rhodamine *500R* spirolactams (**51 – 66**) and their combined yields after amidation and deprotection.

Transforming the *ortho*-carboxy group of rhodamine *500R* into different amides (Z) did not cause distinct changes in maximal absorbance and emission wavelengths (Table 1). Furthermore, **51** – **61** showed quantum yields ranging from 0.86 – 0.91, which are comparable to the one detected for *ortho*-carboxy derivative **48** (0.88). This confirms that the applied synthetic strategy enables to retain key photophysical properties of the original fluorophore.

Table 1: Photophysical properties of rhodamine *500R* derivatives (**48** and **51 – 61**).

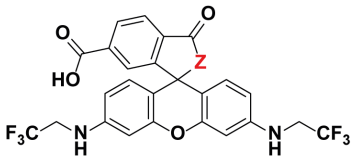

Z	Probe	λ_{abs} / λ_{em} (nm)	ε ($M^{-1}cm^{-1}$)	Φ	D_{50}
O	**48**	501_a / 527_a	82000_a	0.88_a	34_b
NSO_2PhCN	**51**	506_a / 529_a	79000_a	0.89_a	61_b
NSO_2PhF_2	**52**	506_a / 529_a	79000_a	0.90_a	63_b
NSO_2PhCF_3	**53**	506_a / 529_a	74000_a	0.91_a	65_b
NSO_2PhCl	**54**	507_a / 529_a	73000_a	0.91_a	68_b
NCN	**55**	504_a / 529_a	71000_a	0.86_a	69_b
NSO_2PhF	**56**	505_a / 529_a	72000_a	0.91_a	70_b
NSO2Ph	**57**	506_a / 529_a	67000_a	0.90_a	72_b
NSO_2PhCH_3	**58**	506_a / 527_a	49000_a	0.89_a	74_b
NSO_2PhOCH_3	**59**	506_a / 529_a	47000_a	0.90_a	76_b
NSO_2CH_3	**60**	505_a / 529_a	39000_a	0.89_a	78_b
$NSO_2N(CH_3)_2$	**61**	505_a / 527_a	7800_a	--	$>79_b$

$_a$ HEPES buffer (pH 7.3), $_b$ dioxane-water mixtures (v/v: 100/0 – 0/100); mean values from 3 experiments.

Another aim was to examine the position of the spirocyclization equilibrium of **48** and **51** – **61**. The spirocyclization equilibrium of rhodamines strongly depends on the chemical environment of the fluorophore (Section 1.4.).[144] Altering the dielectric constant of the solvent can change the equilibrium and, thereby cause a difference in absorbance.[72] Thus, absorbance spectra of the different rhodamine *500R* derivatives were measured in dioxane-water mixtures containing various dielectric constants.[195] The position of the spirocyclization equilibrium of **48** and **51** – **61** was compared by means of their D_{50} values, which correspond to the dielectric constant at half-maximum absorbance and, thus, to the dielectric constant at which half of the

respective dye population resides in the zwitterionic, fluorescent state.[21, 85, 130] **48** showed a D_{50} value of 34 (Table 1). Moreover, D_{50} values ranging from 61 to 71 were detected for acyl benzenesulfonamide derivatives **51** – **54** and **56** – **59**, indicating a shift in spirocyclization equilibrium toward the closed state compared to **48** (Table 1, Figures 13a and b). The small changes in D_{50} between the individual fluorophores led to the conclusion that the spirocyclization equilibrium of rhodamine *500R* can be tuned with high precision upon introduction of different acyl benzenesulfonamides (Figure 13b).

The use of meta- and para-substituted benzenesulfonamide derivatives was based on the idea of controlling the spirocyclization equilibrium by altering the electron density on the aromatic ring attached to the sulfonamide. Moreover, the distance between the substituents and the spirolactam should prevent a steric effect on the spirocyclization equilibrium upon modification. Higher D_{50} values and, therefore, stronger shifts toward the spirocyclic state were observed for acyl benzenesulfonamide derivatives containing electron-donating substituents compared to electron-poor benzenesulfonamides (Table 1 and Figure 13b). Furthermore, a linear correlation between the D_{50} values and the *Hammett* constants (σ) of the substituents at the aromatic ring was detected, where σ describes the electron-withdrawing or donating nature of the substituent (Figure 13c).[196-197] The correlation between σ and the D_{50} values therefore corroborates that the differences in spirocyclization equilibrium are solely caused by changes in electron density on the aromatic ring attached to the sulfonamide.

Coupling rhodamine *500R* to previously reported electron-poor amines resulted in a D_{50} value of 69 for **55** and 78 for **60** (Figures 13d, e and Table 1).[85] Furthermore, acyl dimethylsulfamide **61** dissolved in water showed only weak absorbance, leading to a D_{50} value higher than 79. The larger changes in D_{50} values obtained with these modifications indicate that the spirocyclization equilibrium could not be controlled with the same precision compared to the introduction of substituted acyl benzenesulfonamides (Figure 13d and e).[85] Prominent examples of other previously reported strategies to control the spirocyclization equilibrium comprise the fluorination of the xanthene system and the introduction of 3-substituted azetidine rings onto the 3'- and 6'-positions of the xanthene system (Section 1.4.1.).[21, 127, 130, 150] However, these strategies also caused larger changes in D_{50} values,[21, 130] thereby indicating that the use of substituted acyl benzenesulfonamides enables tuning of the spirocyclization equilibrium with an enhanced accuracy. Furthermore, modification of the xanthene core causes distinct changes of crucial photophysical properties, such as quantum yield, absorbance and emission wavelength.[21, 127, 130, 150]

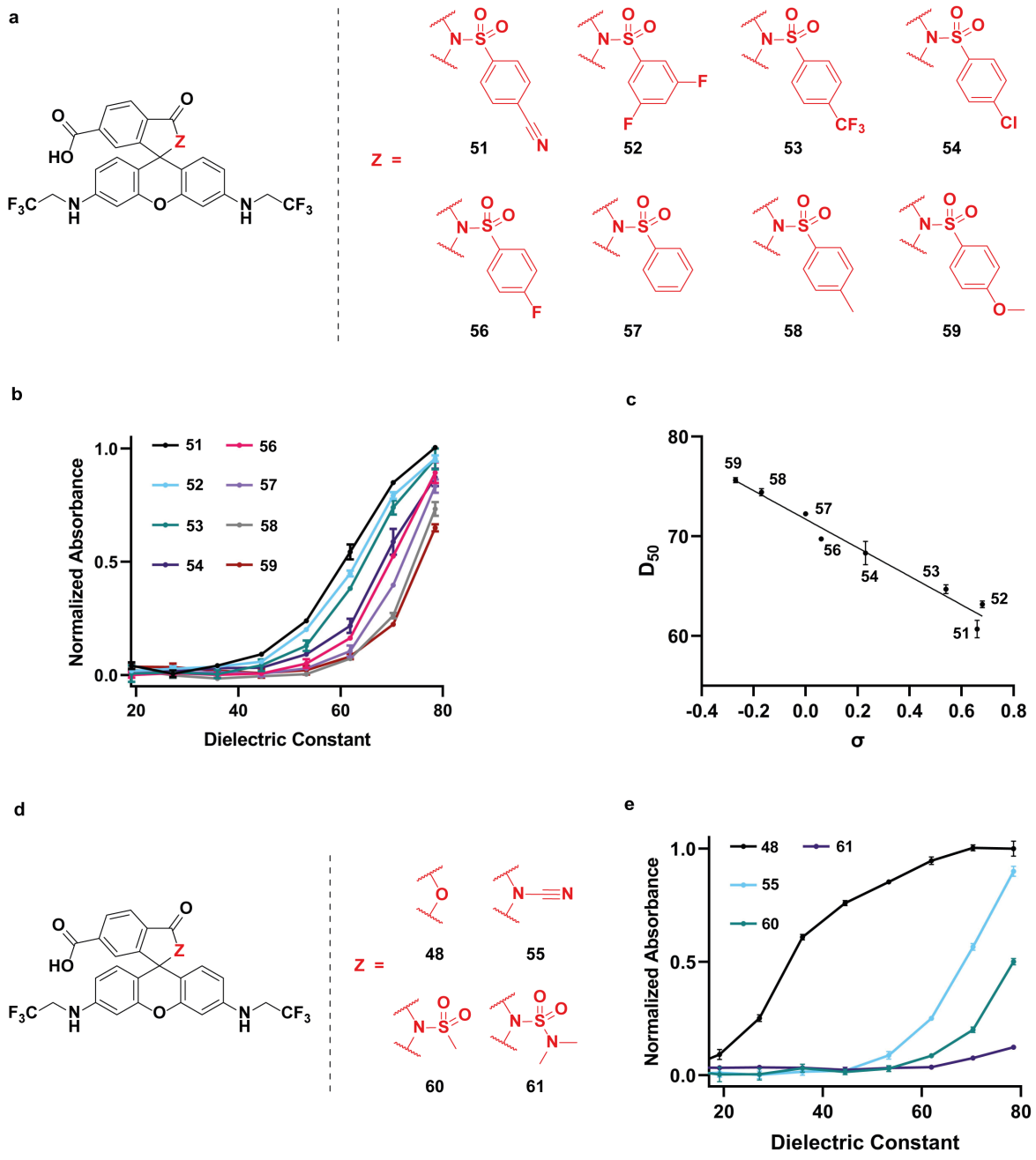

Figure 13: Position of the spirocyclization equilibrium of **48** and of the electron-deficient rhodamine *500R* spirolactams (**51 – 61**). (a) Chemical structures of acyl benzenesulfonamide rhodamine *500R* derivatives (**51 – 54** and **56 – 59**). (b) Normalized maximum absorbance of **51 – 54** and **56 – 59** (5 µM) in different dioxane-water mixtures as a function of their dielectric constant.[195] The absorbance of **51** – **54** and **56 – 59** was normalized to the maximal absorbance of **48**. (c) Correlation between D_{50} values of **51 – 54** and **56** – **59** and Hammett constants (σ) of the substituents of the benzenesulfonamide.[196] The line represents the linear regression (R^2 = 0.97). For acyl 3,5-difluorobenzenesulfonamide **52**, σ of the meta-fluorine substituent was doubled.[196, 198] (d) Chemical structures of **48**, **55**, **60** and **61**. (e) Normalized maximum absorbance of **48**, **55**, **60** and **61** (5 µM) in different dioxane-water mixtures as a function of their dielectric constant.[195] The absorbance of **48**, **55**, **60** and **61** was normalized to the maximal absorbance of **48**. Error bars show ± s.d. from 3 experiments.

With respect to the less electron-deficient rhodamine *500R* spirolactams **62** – **66**, a significant shift in spirocyclization equilibrium toward the non-fluorescent form compared to **48** was observed. While a high extinction coefficient was measured for **48** in aqueous solution of

neutral pH, no distinct absorbance in the visible range for **62** – **66** was detected under comparable conditions (Table 1, Figures 14a and b). It is known from previous reports that the spirocyclization equilibrium of rhodamine derivatives is pH dependent.[147, 166] Therefore, absorbance spectra were measured for **62** – **66** in PBS solutions containing different pH values to compare their state in spirocyclization equilibrium. No distinct absorbance in the visible spectrum was observed for **66** and **65** under all tested conditions. However, **62** – **64** showed an increase in absorbance above 500 nm below pH 4. These results indicate that **66** and **65** encounter the strongest shift toward the spirocyclic state followed by **64**, **63** and **62** (Figures 14a and b).

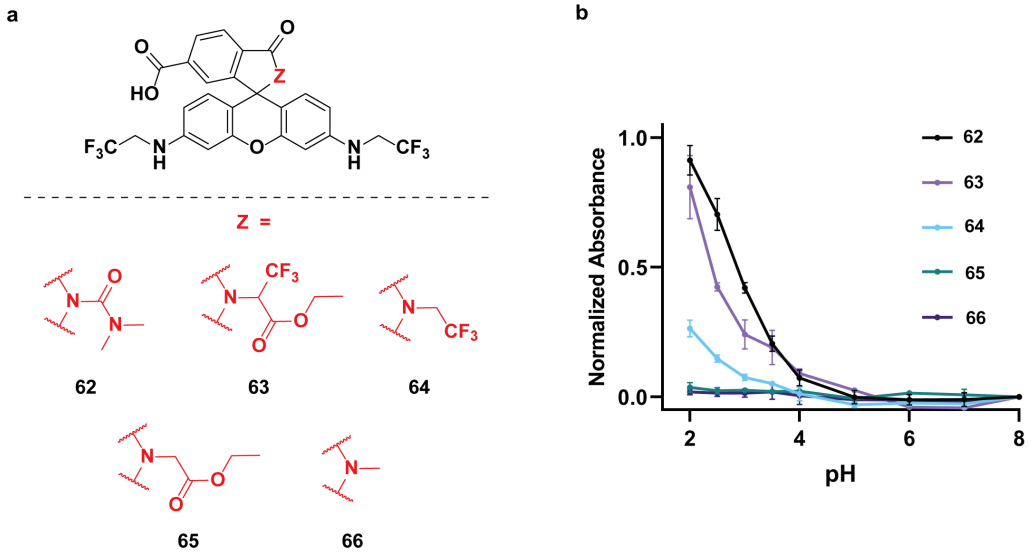

Figure 14: Position of the spirocyclization equilibrium of less electron-deficient rhodamine *500R* spirolactams (**62 – 66**). (a) Chemical structures of **62 – 66**. (b) Normalized maximal absorbance of **62 – 66** (5 µM) in phosphate-buffered saline (PBS) (10 µM) at different pH. The absorbance was normalized to the maximum absorbance of **48** (5 µM) in PBS (10 µM) at pH = 7.0. Error bars show ± s.d. from 3 experiments.

3.2. Optimization of Rhodamine *500R* for HaloTag Labeling

Another goal of this thesis was to investigate if the fine-tuning of the spirocyclization equilibrium also enables precise control over the fluorogenicity. This hypothesis was tested regarding the prominent self-labeling protein, HaloTag, which can be covalently labeled with fluorophore CA conjugates (Section 1.2.1.).[81] Fluorogenic HaloTag probes are powerful tools for live-cell fluorescence microscopy, since they allow to record images of high contrast without the need for washing steps.[14] In order to optimize the fluorogenicity of rhodamine *500R* for HaloTag labeling, the different acyl benzenesulfonamide derivatives (**51** – **54** and **56** – **59**) were coupled to the CA ligand, yielding HaloTag probes **68** – **71** and **73** – **76** (Figures 12 and 15). For comparison, HaloTag probes based on the original rhodamine *500R* dye (**67**) and MaP-derivatives (**72**, **77** and **78**) were synthesized.

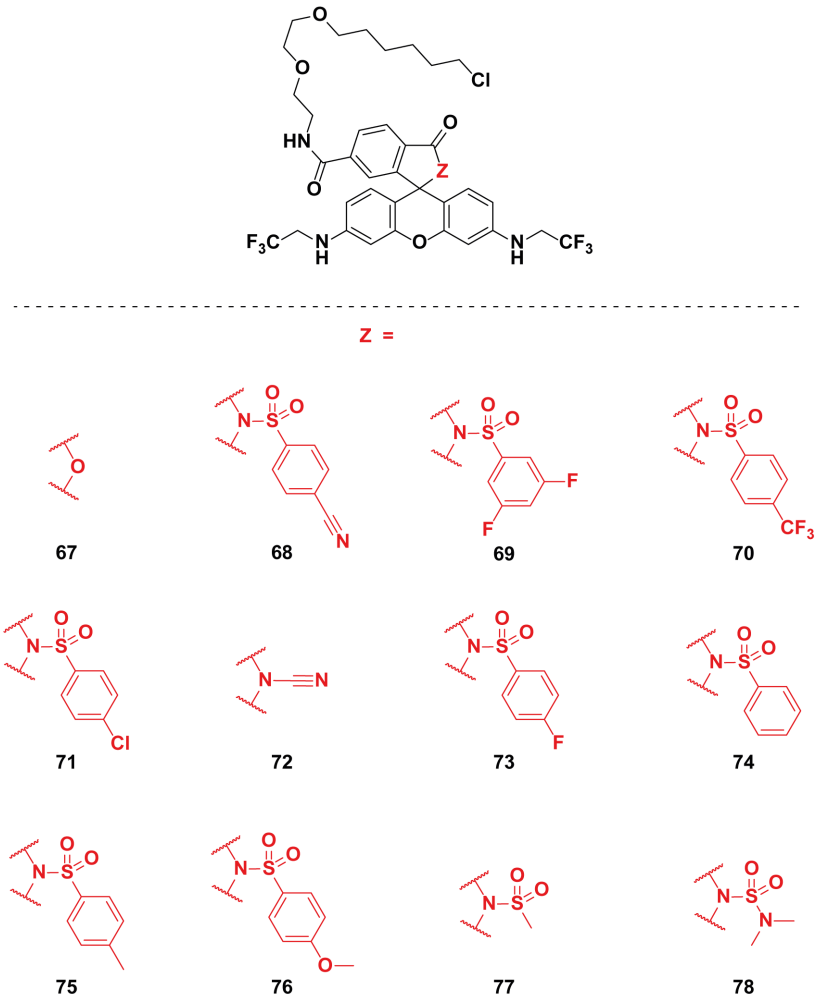

Figure 15: Chemical structures of rhodamine *500R* HaloTag probes (**67 – 78**).

First, the fluorogenicity of **67** – **78** was examined *in vitro*. To this end, their absorbance and fluorescence ($F_{protein}/F_0$) increase upon labeling of HaloTag was measured (Supplementary Figure 1). The original rhodamine *500R* HaloTag probe (**67**) exhibited a low fluorogenic

character with increases in fluorescence emission and absorbance of less than 2-fold upon labeling of HaloTag (Figure 16a). However, various highly fluorogenic probes among the analyzed rhodamine *500R* derivatives were identified (Supplementary Figure 1 and Table 2). The highest turn-on upon binding to HaloTag was detected for **75**, which showed a 54-fold increase in absorbance and an enhanced fluorescence emission of more than 130-fold (Figure 16b). Furthermore, the influence of the surfactant sodium dodecyl sulfate (SDS) on the position of the spirocyclization equilibrium of **67** – **78** was examined. An increase in absorbance and fluorescence signal was observed for **67** – **78** upon addition of SDS, indicating a shift in spirocyclization equilibrium toward the zwitterionic state (Supplementary Figure 1). This shift in spirocyclization equilibrium was also reported in previous studies, where SDS was used to investigate the fluorogenicity and the photophysical properties of fluorogenic probes.[28, 72] Potential mechanisms for the influence of SDS on the spirocyclization equilibrium include the inhibition of non-fluorescent aggregates and the stabilization of the fluorescent, zwitterionic form due to an interaction with the negatively charged SDS-micelle surface.[72, 150]

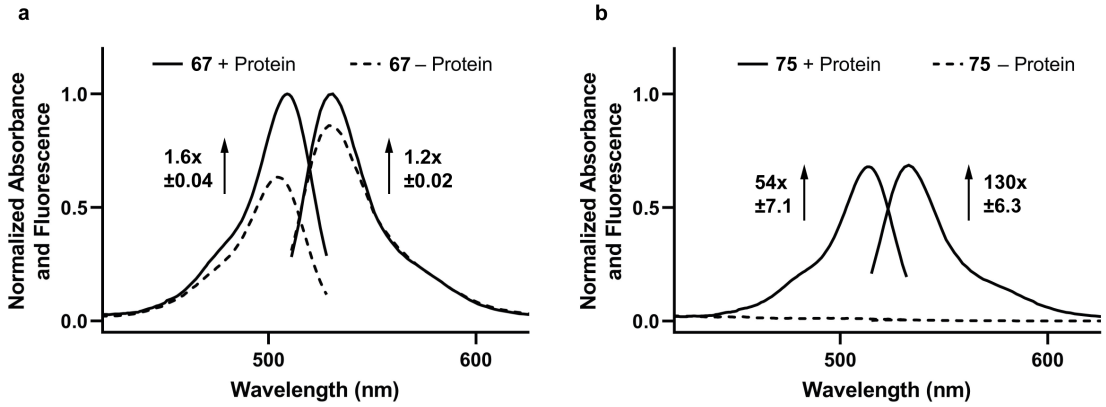

Figure 16: *In vitro* fluorogenicity measurements of rhodamine *500R* HaloTag probes **67** and **75**. Absorbance and fluorescence emission spectra of **67** (a) and **75** (b) (2.5 µM) in the presence (+ Protein) and absence (- Protein) of HaloTag (5 µM) after 2.5 h incubation normalized to the maximal absorbance and emission of **67**. Representative spectra from 3 experiments. Errors show s.d.

Next, it was investigated if the fluorogenic properties, which had been observed *in vitro*, could also be detected *in cellulo*. For this purpose, live-cell, no-wash confocal microscopy of U-2 OS cells that stably express a nuclear localized Halo-SNAP fusion protein and wild-type U-2 OS cells was performed.[85] The nuclear signal intensity (F_{nuc}) of these U-2 OS FlpIn Halo-SNAP-NLS-expressing cells was compared to the cytosolic signal intensity (F_{cyt}) of wild-type U-2 OS cells. The ratio between these fluorescence intensities (F_{nuc}/F_{cyt}) was then used as a read-out for the *in cellulo* fluorogenicity of **67** – **78**. Analogous to the *in vitro* experiments, **67** showed high background signal intensity and, therefore, no distinct fluorogenic behavior in live-cell, no-wash confocal microscopy (F_{nuc}/F_{cyt} = 2.7) (Figures 17a and b).

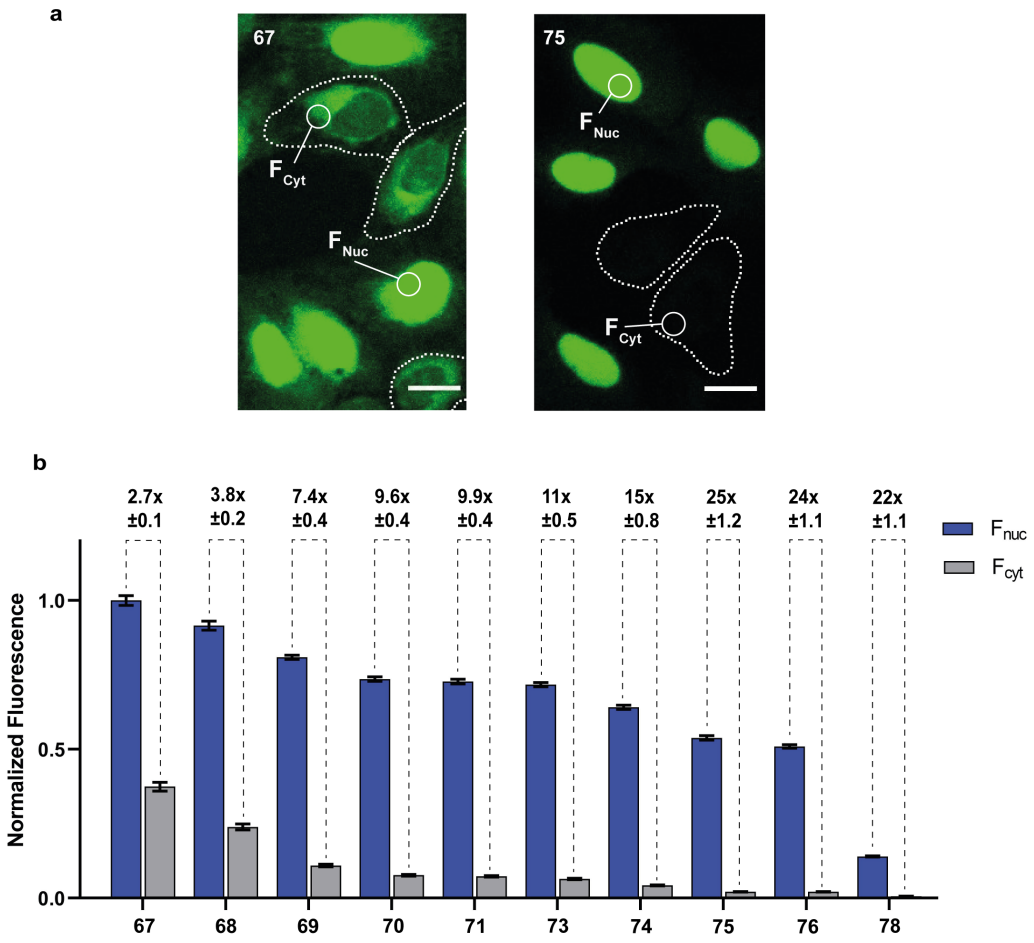

Figure 17: *In cellulo* fluorogenicity measurements of rhodamine *500R* HaloTag probes (**67** − **71, 73** − **76** and **78**). (a) Live-cell, no-wash confocal images of U-2 OS FlpIn Halo-SNAP-NLS-expressing cells and wild-type U-2 OS cells stained with **67** and **75** (200 nM) for 2.5 h. The dotted lines represent wild-type U-2 OS cells. Scale bar 20 µm. (b) Bar plot showing the F_{nuc}/F_{cyt} ratio of **67** − **71, 73** − **76** and **78** in live-cell, no-wash confocal microscopy. F_{nuc}: Nuclear rhodamine *500R* signal in U-2 OS FlpIn Halo-SNAP-NLS expressing cells normalized to the nuclear signal of SiR-BG. F_{cyt}: Cytosolic rhodamine *500R* signal in wild-type U-2 OS cells. U-2 OS FlpIn Halo-SNAP-NLS-expressing cells and wild-type U-2 OS cells were prelabeled with SiR-BG (500 nM) overnight followed by staining with **67** − **71, 73** − **76** and **78** (200 nM) for 2.5 h. In total, 180 cells were examined from 3 independent experiments for each probe. Error bars show ± s.e.m.

With respect to the acyl benzenesulfonamides (**68** – **71**, **73** – **76**), lower nuclear signal intensities were detected for probes with increased electron densities on the benzenesulfonamide (Figure 17b). This trend was also observed in *in vitro* experiments, where fluorophores containing more electron-rich benzenesulfonamides showed lower extinction coefficients upon labeling HaloTag (Table 2). However, enhancing the electron density on the benzenesulfonamide also led to a decrease in background signal. Therefore, the highest F_{nuc}/F_{cyt} ratio was detected for acyl *p*-toluenesulfonamide derivative **75** (F_{nuc}/F_{cyt} = 25) (Figures 17a and b). Furthermore, introducing amides with higher nucleophilicity led to a significantly decreased F_{nuc} and, thus, to a lower F_{nuc}/F_{cyt} ratio, as in the case of dimethylsulfamide **78**. Altogether, **75** showed high fluorogenicity *in vitro* as well as *in cellulo*, which could not be

attained with probes based on the MaP-strategy (**72**, **77** and **78**) (Figure 17b and Supplementary Figures 1 and 2).[85]

The shifts in spirocyclization equilibrium, which were detected in dioxane-water titrations of rhodamine *500R* acyl benzenesulfonamides (Figure 13b and Table 1), correspond with the *in vitro* and *in cellulo* fluorogenicity measurements of the respective HaloTag probes (Figure 17 and Table 2). Accordingly, the lower extinction coefficients, F_{nuc} and F_{cyt} values of more electron-rich acyl benzenesulfonamides could be explained by a stabilization of the non-fluorescent, spirocyclic state. In summary, transforming the *ortho*-carboxy group of rhodamine *500R* into different acyl benzenesulfonamides provided precise control over the spirocyclization equilibrium and the fluorogenicity of the respective HaloTag probes.

Table 2: Photophysical properties of rhodamine *500R* HaloTag probes (**67 – 78**).

Z	Probe	λ_{abs} / λ_{em} (nm)	ε ($M^{-1}cm^{-1}$)	Φ	$F_{protein}/F_0$	F_{nuc}/F_{cyt}
O	**67**	509[b] / 531[b]	42000[a] / 67000[b] / 76000[c]	0.85[b] / 0.95[c]	1.2 ±0.02[d]	2.7 ±0.1[e]
NSO_2PhCN	**68**	514[b] / 533[b]	2900[a] / 61000[b] / 66000[c]	0.90[b] / 0.97[c]	24 ±1.2[d]	3.8 ±0.2[e]
NSO_2PhF_2	**69**	514[b] / 533[b]	2400[a] / 63000[b] / 67000[c]	0.92[b] / 0.97[c]	33 ±1.1[d]	7.4 ±0.4[e]
NSO_2PhCF_3	**70**	514[b] / 533[b]	1400[a] / 56000[b] / 69000[c]	0.90[b] / 0.96[c]	51 ±4.3[d]	9.6 ±0.4[e]
NSO_2PhCl	**71**	515[b] / 533[b]	1300[a] / 54000[b] / 63000[c]	0.90[b] / 0.97[c]	62 ±1.1[d]	9.9 ±0.4[e]
NCN	**72**	512[b] / 533[b]	3200[a] / 59000[b] / 63000[c]	0.88[b] / 0.94[c]	20 ±0.6[d]	2.4 ±0.2[e]
NSO_2PhF	**73**	514[b] / 533[b]	1300[a] / 54000[b] / 64000[c]	0.92[b] / 0.97[c]	56 ±1.7[d]	11 ±0.5[e]
NSO2Ph	**74**	513[b] / 533[b]	1100[a] / 49000[b] / 63000[c]	0.92[b] / 0.98[c]	73 ±3.1[d]	15 ±0.8[e]
NSO_2PhCH_3	**75**	514[b] / 533[b]	830[a] / 45000[b] / 42000[c]	0.90[b] / 0.97[c]	133 ±6.3[d]	25 ±1.2[e]
NSO_2PhOCH_3	**76**	514[b] / 533[b]	770[a] / 43000[b] / 45000[c]	0.94[b] / 0.97[c]	117 ±3.8[d]	24 ±1.1[e]
NSO_2CH_3	**77**	513[b] / 533[b]	2300[a] / 45000[b] / 53000[c]	0.91[b] / 0.95[c]	28 ±2.8[d]	13 ±0.7[e]
$NSO_2N(CH_3)_2$	**78**	513[b] / 531[b]	580[a] / 13000[b] / 20000[c]	0.91[c]	87 ±2.9[d]	22 ±1.1[e]

[a] HEPES buffer (pH 7.3), [b] binding with HaloTag (2 eq) in HEPES buffer (pH 7.3), [c] 0.1% SDS in HEPES buffer (pH 7.3); mean values from 3 experiments, [d] ratio of maximum fluorescence intensities in the presence and absence of HaloTag (2 eq); errors show s.d. from 3 experiments, [e] fluorescence ratios; F_{nuc}: Nuclear rhodamine *500R* signal in U-2 OS FlpIn Halo-SNAP-NLS expressing cells normalized to the nuclear signal of SiR-BG; F_{cyt}: Cytosolic rhodamine *500R* signal in wild-type U-2 OS cells; in total, 180 cells from 3 independent experiments were examined for each probe; errors represent s.e.m.

An important property of probes for live-cell fluorescence microscopy is their cell-permeability. Analogous to the fluorogenicity, the cell-permeability of rhodamine-based probes also depends on the position of the spirocyclization equilibrium (Section 1.4.1.).[85, 130, 150] Therefore, the influence of modifying the *ortho*-carboxy group of rhodamine *500R* regarding the cell-permeability of the resulting probes was examined. To this end, the time period required to label HaloTag, expressed in the nucleus of U-2 OS cells, was measured. U-2 OS FlpIn Halo-SNAP-NLS-expressing cells were prelabeled with SiR-BG, followed by incubation with different rhodamine *500R* HaloTag probes (**67** − **71** and **73** − **78**). Saturation in fluorescence signal was detected after time periods ranging from less than 10 minutes up to 40 minutes (Figure 18). Numerous rhodamine *500R* spirolactams (**70**, **71**, **73**, **75**, and **76**) showed longer *in cellulo* labeling times compared to the *ortho*-carboxy probe **67**. Furthermore, no distinct correlation between *in cellulo* labeling time of the HaloTag probes and the D_{50} value of the respective fluorophore precursors (**48**, **51** – **54** and **56** – **61**) was detected (Figures 13 and 18). A potential explanation could be that the different substituents on the spirolactam also affect other properties of the probe, such as hydrophobicity, in addition to the position of the spirocyclization equilibrium. An enhanced hydrophobicity inhibits solubility and might increase the tendency of the probe for aggregation as well as sequestration in membranes and, thus, would require a longer labeling time.[127] Moreover, the *in cellulo* labeling time of a probe does not only depend on its cell-permeability, but also on the rate of the labeling reaction. Measuring the *in cellulo* labeling time therefore gives a rough estimate of the cell-permeability, but does not allow its exclusive comparison. As a future experiment, *in vitro* labeling kinetics could be additionally measured to distinguish between changes in labeling kinetics and cell-permeability.

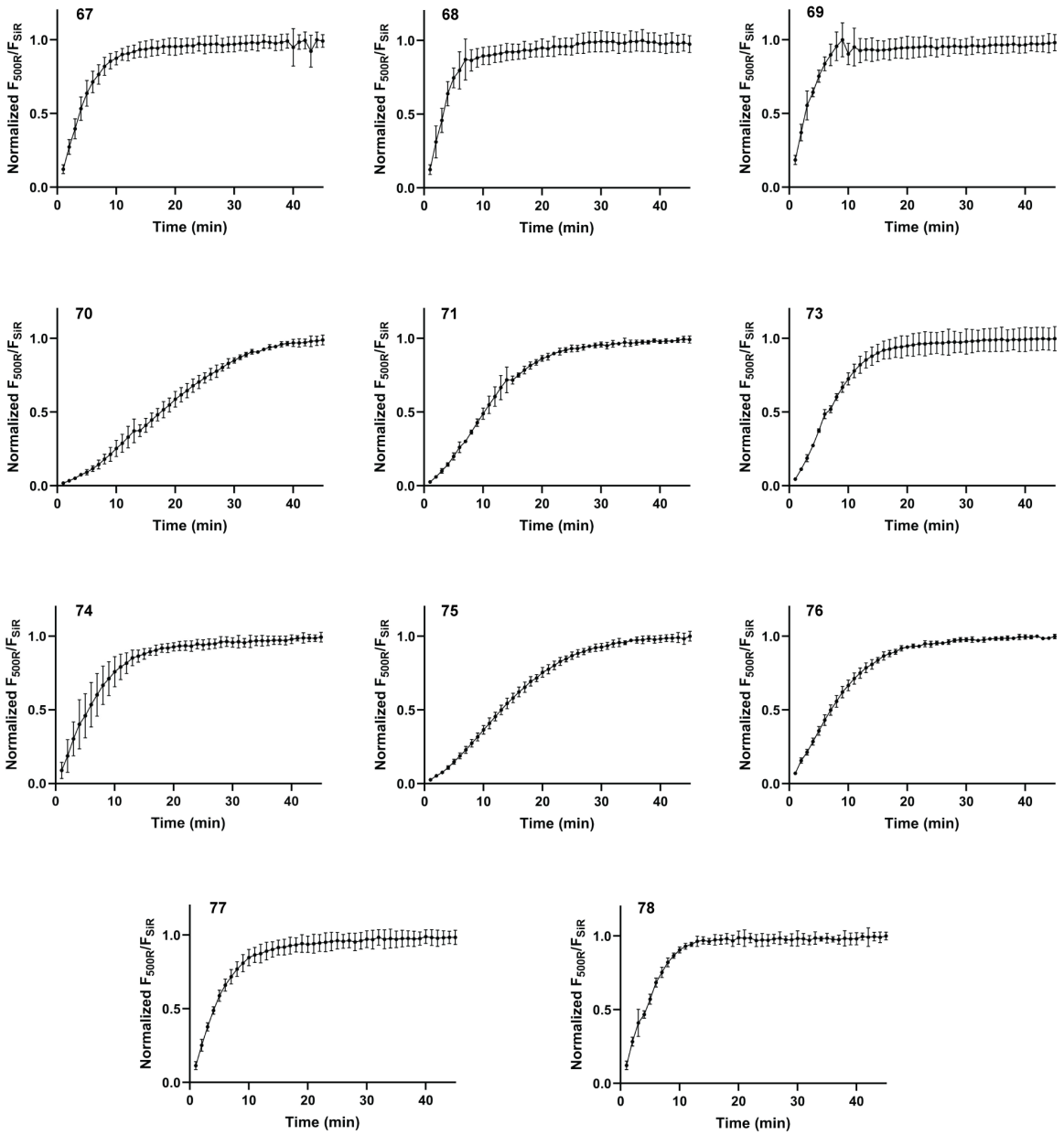

Figure 18: *In cellulo* HaloTag labeling with rhodamine *500R* HaloTag probes (**67** − **71** and **73** − **78**). U-2 OS FlpIn Halo-SNAP-NLS expressing cells were prelabeled with SiR-BG (500 nM) overnight, and incubated with **67** − **71** and **73** − **78** (200 nM). The normalized ratio of rhodamine *500R* fluorescence to the fluorescence signal of SiR-BG was plotted over time. In total, >51 cells were examined from technical triplicates for each probe. Error bars show ± s.e.m.

3.3. Optimization of Rhodamine *500R* for SNAP-tag Labeling

Another widely used self-labeling protein is the SNAP-tag, which can be covalently labeled with fluorophore BG derivatives (Section 1.2.1.).[76] After the transformation of rhodamine *500R* into a highly fluorogenic HaloTag probe (**75**), we aimed to investigate if the introduction of substituted acyl benzenesulfonamides would also enable the development of a suitable SNAP-tag probe for live-cell, no-wash fluorescence microscopy. In addition to the *ortho*-carboxy rhodamine *500R* BG derivative (**79**), acyl *p*-toluenesulfonamide **80** was synthesized, as this substituent gave the highest fluorogenicity for HaloTag labeling (**75**) (Figures 16b, 17 and 19a). **79** showed significant absorbance and fluorescence intensities in the absence of SNAP-tag, thus indicating a low fluorogenicity (Figure 19b and Supplementary Figure 3). In contrast to the *in vitro* turn-on experiments with HaloTag probe **75**, low signal intensities were observed for the corresponding SNAP-tag probe (**80**) after binding to the SNAP-tag (Figures 16b and 19c). This observation suggests that labeling HaloTag leads to a stronger shift in spirocyclization equilibrium toward the fluorescent zwitterion than SNAP-tag. This hypothesis is supported by previous reports, which described a reduced brightness of fluorogenic rhodamine-based probes upon labeling SNAP-tag compared to HaloTag.[85-86]

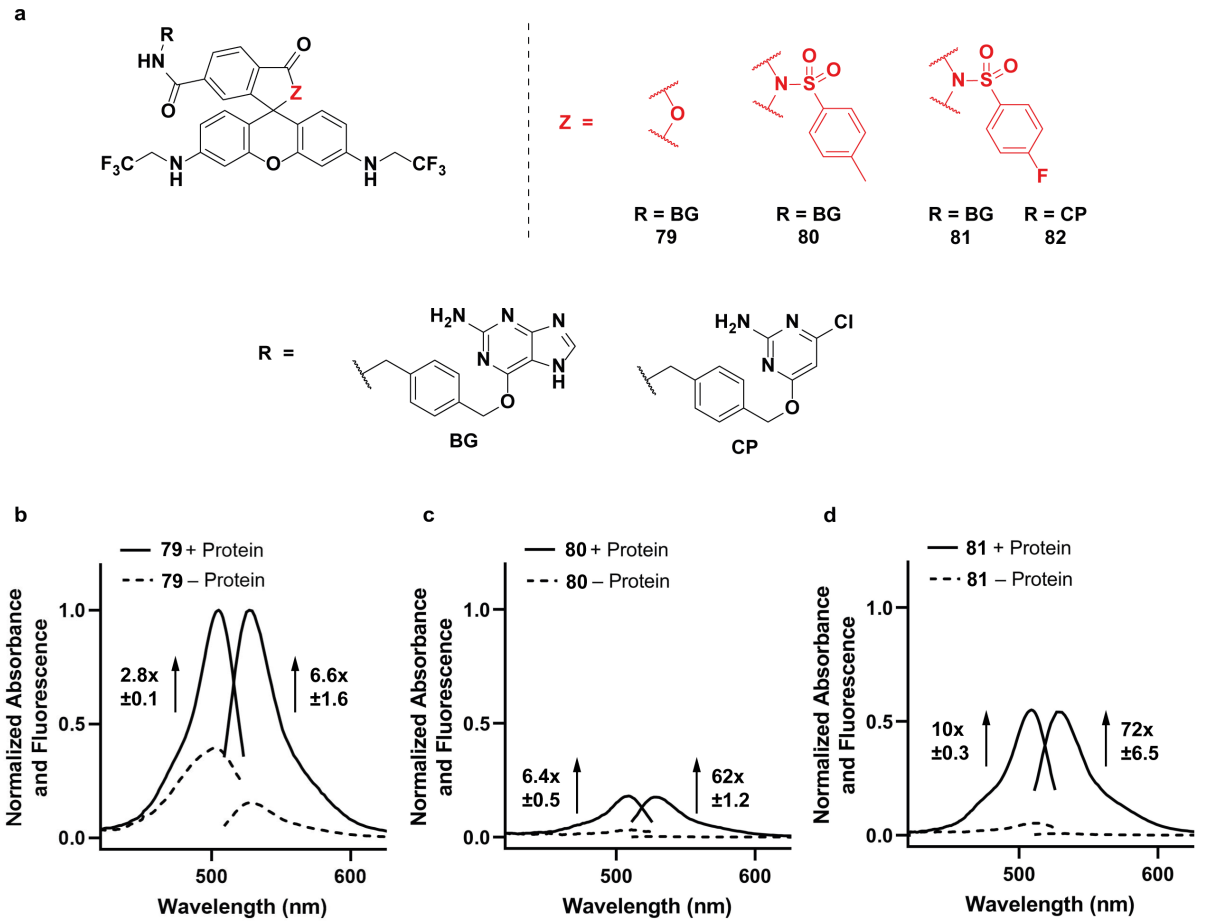

Figure 19: Chemical structures and *in vitro* fluorogenicity measurements of rhodamine *500R* SNAP-tag probes. (a) Chemical structures of **79 – 82**. (b) **–** (d) Absorbance and fluorescence emission spectra of **79** (b), **80** (c) and **81** (d) (2.5 µM) in the presence (+ Protein) and absence (- Protein) of SNAP-tag (5 µM) after 2.5 h incubation normalized to the maximal absorbance and emission of **79**. Representative spectra from 3 experiments. Errors show s.d.

To obtain enhanced brightness upon SNAP-tag labeling as well as maintain low background signal, a SNAP-tag probe based on a different rhodamine *500R* spirolactam was synthesized. It was envisioned using a slightly more electron-deficient acyl benzenesulfonamide derivative, such that the probe still would reside in its non-fluorescent state in the absence of SNAP-tag. However, binding to SNAP-tag should then lead to a stronger shift toward the fluorescent state compared to **80**. To this end, acyl 4-fluorobenzenesulfonamide **56** was coupled to BG, yielding SNAP-tag probe **81** (Figure 19a). Subsequently, the absorbance and fluorescence increase was measured upon labeling SNAP-tag with **81**. **81** showed higher absorbance and fluorescence intensity after binding to the SNAP-tag than **80** (Figure 19d and Table 3). Despite a reduced brightness compared to **79**, **81** yielded an increased turn-on due to a significantly lower signal in the absence of SNAP-tag. These results show that the fine-tuning of the spirocyclization equilibrium enables to enhance the fluorogenicity of rhodamine *500R* for SNAP-tag labeling *in vitro*.

Table 3: Photophysical properties of rhodamine *500R* SNAP-tag probes (**79 – 81**).

Z	Probe	λ_{abs} / λ_{em} (nm)	ε ($M^{-1}cm^{-1}$)	Φ	$F_{protein}/F_0$	F_{nuc}/F_{cyt}
O	**79**	505[b] / 527[b]	19000[a] / 54000[b] / 73000[c]	0.74[b] / 0.92[c]	6.6 ±1.6[e]	3.4 ±0.3[f]
NSO_2PhF	**81**	509[b] / 529[b]	2800[a] / 28000[b] / 64000[c]	0.78[b] / 0.94[c]	72 ±6.5[e]	25 ±1.8[f]
NSO_2PhCH_3	**80**	509[b] / 527[b]	1500[a] / 9900[b] / 43000[c]	0.95[c]	62 ±1.2[e]	--

[a] HEPES buffer (pH 7.3), [b] binding with SNAP-tag (2 eq) in HEPES buffer (pH 7.3), [c] 0.1% SDS in HEPES buffer (pH 7.3); mean values from 3 experiments, [d] ratio of maximum fluorescence intensities in the presence and absence of SNAP-tag (2 eq); errors show s.d. from 3 experiments, [e] fluorescence ratios; F_{nuc}: Nuclear rhodamine *500R* signal in U-2 OS FlpIn Halo-SNAP-NLS expressing cells normalized to the nuclear signal of SiR-CA; F_{cyt}: Cytosolic rhodamine *500R* signal in wild-type U-2 OS cells; in total, 180 cells from 2 independent experiments were examined for each probe; errors represent s.e.m.

Live-cell, no-wash confocal microscopy was then used to examine the *in cellulo* fluorogenicity and the cell-permeability of the different rhodamine *500R* SNAP-tag probes. Analogous to the analysis of the HaloTag probes, U-2 OS FlpIn Halo-SNAP-NLS-expressing cells were stained with **79** – **81** to measure the labeling time of SNAP-tag localized to the nucleus. Moreover, the fluorogenicity was investigated by comparing the nuclear signal intensity (F_{nuc}) of U-2 OS FlpIn Halo-SNAP-NLS-expressing cells to the cytosolic signal intensity (F_{cyt}) of wild-type U-2 OS cells. No saturation in fluorescence signal was detected after 6 hours of incubation with **79**, indicating a low cell-permeability (Figure 20a). Consistent with the *in vitro* turn-on experiments, a high F_{cyt} was observed for **79**, and **80** showed a low fluorescence intensity upon labeling SNAP-tag (Figures 20a – c and Supplementary Figure 4). With respect to **81**, a distinct increase in F_{nuc}/F_{cyt} ratio and a shorter *in cellulo* labeling time compared to **79** as well as a higher brightness than **80** were detected (Figures 20a – c). In previous work, the SNAP-tag ligand CP had shown improved cell-permeability compared to BG.[80] CP was therefore coupled to **56**, yielding SNAP-tag probe **82** (Figure 19a). However, preliminary microscopy experiments showed a significantly increased background signal intensity and a comparable labeling speed *in cellulo* for **82** compared to **81**. In summary, the introduction of acyl 4-fluorobenzenesulfonamide transformed rhodamine *500R* into a highly fluorogenic and cell-permeable SNAP-tag probe (**81**) and, thus, into a suitable tool for live-cell, no-wash fluorescence microscopy.

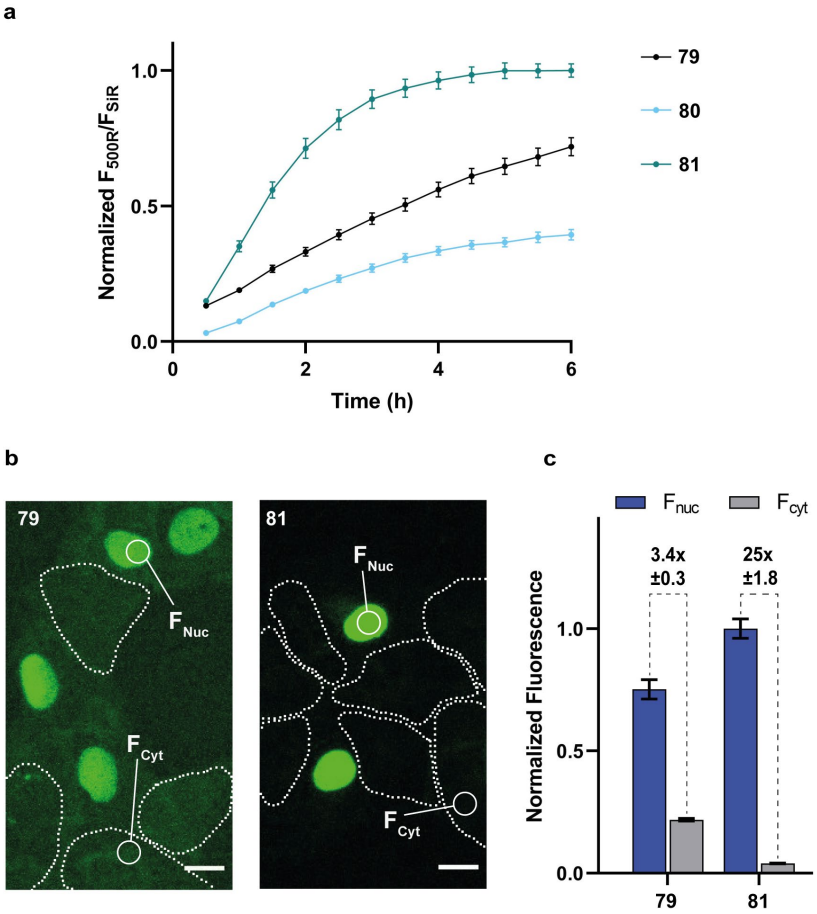

Figure 20: *In cellulo* labeling time and fluorogenicity measurements of rhodamine *500R* SNAP-tag probes (**79** − **81**). (a) *In cellulo* SNAP-tag labeling with **79** − **81**. U-2 OS FlpIn Halo-SNAP-NLS expressing cells were prelabeled with SiR-CA (200 nM) overnight, and incubated with **79** − **81** (500 nM). The normalized ratio of rhodamine *500R* fluorescence to the fluorescence signal of SiR-CA was plotted over time. In total, 90 cells were examined from 2 independent experiments for each probe. Error bars show ± s.e.m. (b) Live-cell, no-wash confocal images of U-2 OS FlpIn Halo-SNAP-NLS-expressing cells and wild-type U-2 OS cells stained with **79** and **81** (500 nM) for 5 h. The dotted lines represent wild-type U-2 OS cells. Scale bar 20 µm. (c) Bar plot showing the F_{nuc}/F_{cyt} ratio of **79** and **81** in live-cell, no-wash confocal microscopy. F_{nuc}: Nuclear rhodamine *500R* signal in U-2 OS FlpIn Halo-SNAP-NLS expressing cells normalized to the nuclear signal of SiR-CA. F_{cyt}: Cytosolic rhodamine *500R* signal in wild-type U-2 OS cells. U-2 OS FlpIn Halo-SNAP-NLS-expressing cells and wild-type U-2 OS cells were prelabeled with SiR-CA (200 nM) overnight followed by staining with **79** and **81** (500 nM) for 5 h. In total, 180 cells were examined from 2 independent experiments for each probe. Error bars show ± s.e.m.

The optimization of rhodamine *500R* for either HaloTag or SNAP-tag labeling revealed different properties for the corresponding probes. For instance, different trends were observed in terms of the required incubation time prior to imaging. The original rhodamine *500R* HaloTag probe (**67**) showed fast labeling of HaloTag *in cellulo*, and most modifications of the *ortho*-carboxy group led to increased *in cellulo* labeling times. With respect to SNAP-tag labeling, the incubation time required to obtain saturation in fluorescence signal could be significantly shortened by transforming the *ortho*-carboxy moiety into an acyl benzenesulfonamide derivative. Furthermore, a different position of the spirocyclization equilibrium was needed to obtain high fluorogenicity upon HaloTag or SNAP-tag labeling, respectively. A decreased stabilization of the zwitterionic, fluorescent state was observed upon binding to SNAP-tag.

Thus, a slightly more electron-deficient acyl benzenesulfonamide was necessary to receive sufficient brightness. Altogether, these findings corroborate that different labeling systems require different positions of the spirocyclization equilibrium, and precise control over this dynamic equilibrium therefore is essential for the development of suitable probes.

3.4. Development of a Rhodamine *500R* Probe for SMLM

In the previous sections, it was demonstrated that the spirocyclization equilibrium could be precisely adjusted, thereby transforming rhodamine *500R* into highly fluorogenic probes for live-cell, no-wash microscopy. The spirocyclization equilibrium also plays a crucial role in the development of probes for SMLM applications. SMLM techniques require an adjustment of the equilibrium, which retains the majority of the dye population in the non-fluorescent state to achieve high spatial resolution (Sections 1.1.2. and 1.4.2.).[37] With respect to live-cell SMLM, spontaneously blinking probes represent useful tools, since their on-off switching does not rely on strong irradiation with light of low wavelengths as well as additives.[147, 163] Inspired by previous reports of spontaneously blinking rhodamine spirolactams,[167-168] it was tested if the modification of the *ortho*-carboxy group of rhodamine *500R* enables the development of a spontaneously blinking probe for SMLM. Less electron-deficient rhodamine *500R* spirolactams compared to the fluorogenic probes were used, such that the position of the spirocyclization equilibrium was strongly shifted toward the spirocyclic, non-fluorescent state. This modification should then retain the majority of the dye population in the non-fluorescent state in an SMLM experiment. As discussed in Section 3.1., strong shifts toward the spirocyclic state were observed for rhodamine *500R* spirolactams **62** – **66** (Figure 14). Subsequently, **62** – **65** were coupled to CA, yielding HaloTag probes **83** – **86** (Figures 12 and 21a). Their blinking behavior as well as their applicability in SMLM was then examined by imaging fixed U-2 OS cells endogenously expressing HaloTag fused to Nup96, a protein of the nuclear pore complex.[199] As nuclear pores possess an internal diameter of approximately 100 nm, super-resolution microscopy is required to resolve their circular shape.[200] Upon incubation with **83**, **84** and **86**, no discernible nuclear pore structures were observed. However, applying **85** enabled visualization of the circular shape of nuclear pores (Figures 21b – d). **85** yielded an average photon count of each localization of 631 photons, and the localization precision peaked at 8.9 nm (Supplementary Figure 5). The applicability of **85** in SMLM was further evaluated by imaging U-2 OS cells stably expressing HaloTag fused to the microtubule binding protein Cep41.[201] Images were obtained that show fine tubulin structures with a full-width-half-maximum (fwhm) of 40.7 ± 5.7 nm (Figures 21e, f and Supplementary Figure 6). This value is in agreement with previous reports of microtubule diameter measurements and, thus, corroborates the suitability of **85** for SMLM.[201-202]

In the aforementioned SMLM experiments, cells were labeled with **85** overnight followed by fixation. To examine the required labeling time of **85**, U-2 OS FlpIn Halo-SNAP-NLS expressing cells were incubated with **85** for different durations followed by labeling with SiR-CA. The reduced SiR-signal was then used as a readout for the labeling of **85**. The experiment indicates that **85** reached saturation in labeling after 30 minutes incubation time (Figure 21g).

Based on these findings, SMLM of Nup96-Halo in fixed U-2 OS cells was performed after an incubation time of 30 minutes, which yielded comparable image quality as overnight labeling.

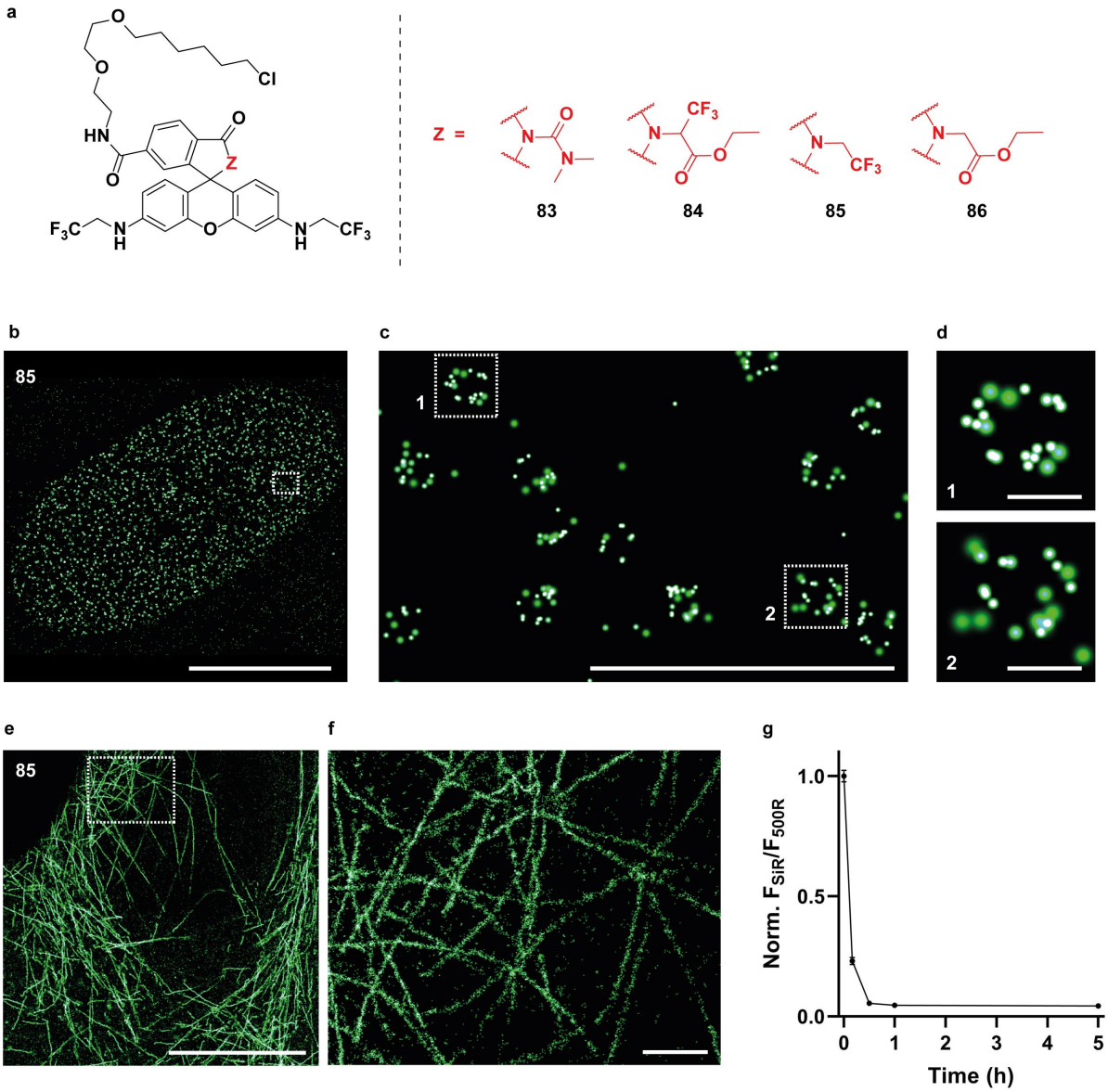

Figure 21: Highly closed rhodamine *500R* HaloTag probes (**83 – 86**) and their applicability in SMLM. (a) Chemical structures of **83 – 86**. (b) SMLM image of fixed U-2 OS cells endogenously expressing Nup96-Halo stained with **85** (1 µM) overnight. Scale bar 10 µm. (c) SMLM image of the marked region in (b). Scale bar 1 µm. (d) SMLM images of individual nuclear pores of the marked regions in (c). Scale bar 100 nm. (e) SMLM image of fixed U-2 OS cells stably expressing Cep41-Halo stained with **85** (1 µM) overnight. Scale bar 10 µm. (f) SMLM image of the marked region in (e). Scale bar 1 µm. (g) Live-cell labeling experiment. U-2 OS FlpIn Halo-SNAP-NLS expressing cells were prelabeled with **81** (500 nM, overnight), incubated with **85** (1 µM) for different amounts of time followed by labeling with SiR-CA (500 nM, 15 min). The SiR signal (normalized to the signal of **81**) was plotted over the different incubation times with **85** prior to addition of SiR-CA. For each time point, 90 cells were analyzed from technical triplicates. Error bars show ± s.e.m. SMLM images (b **–** f) were recorded and analyzed by Aline Tschanz (EMBL Heidelberg).

The blinking behavior of **85** was further investigated by labeling immobilized HaloTag on coated glass coverslips.[201] The single-molecule traces obtained from this experiment allowed the measurement of on- and off-times of **85** as well as its duty cycle, which corresponds to the

on-time divided by the sum of on- and off-time (Supplementary Table 1).[47] A duty cycle of $2.8 \cdot 10^{-5}$ was detected for **85**. According to previous reports, this value is low enough to localize individual molecules and to avoid artifacts that are caused by detecting multiple localizations at the same time within a diffraction-limited area.[37, 47] However, low duty cycles and short on-times can also be at the expense of smaller photon numbers and longer acquisition times, thereby limiting the temporal resolution.[37, 160] As a comparison, the on-time of **85** (3.6 ms) is significantly shorter than the one of HMSiR (96 ms), which is a readily used spontaneously blinking probe for live-cell SMLM.[147, 164-165] Furthermore, *Y. Urano* and co-workers postulated that an on-time between tens and hundreds of milliseconds is suitable to obtain sufficient photons for live-cell SMLM.[147]

In summary, the applicability of **85** in SMLM was demonstrated. **85** showed spontaneous blinking without the use of short-wavelength irradiation as well as any additive and enabled live-cell labeling. However to date, **85** has only been used in SMLM of fixed cells. Its short on-time and low duty cycle could lead to a low temporal resolution and, therefore, might limit its applicability in live-cell SMLM. Strategies to increase the on-time of fluorophores comprise the stabilization of the open, fluorescent state.[160] For instance, shifting the spirocyclization equilibrium toward the fluorescent state by changing the intramolecular nucleophile was reported to yield longer open lifetimes for different rhodamine derivatives.[147] Using less nucleophilic spirolactams, a shift in spirocyclization equilibrium toward the fluorescent state was detected for the precursors of **83** and **84** (**62** and **63**) compared to the precursor of **85** (**64**) (Figure 14). However, preliminary imaging experiments of U-2 OS cells endogenously expressing Nup96-Halo labeled with **83** and **84** did not result in satisfactory images.

3.5. Applying the Strategy to Other Rhodamine-Based Scaffolds

The modification of the *ortho*-carboxy group enabled the systematic tuning of the spirocyclization equilibrium of rhodamine *500R*. Thereby, this fluorophore scaffold was transformed into highly fluorogenic probes, specifically optimized for HaloTag and SNAP-tag labeling, as well as a spontaneously blinking dye for SMLM. Next, the generality of this approach was tested. To this end, it was applied to differently colored rhodamine-based dyes with various positions of the spirocyclization equilibrium, including SiR, carborhodamine and TMR.

3.5.1. Optimization of SiR for HaloTag Labeling

SiR shows a distinct shift in spirocyclization equilibrium toward the spirocyclic state compared to various other rhodamine derivatives (Section 1.4.1.).[21, 28] Therefore, SiR-based probes are endowed with high fluorogenicity and cell-permeability, such as the HaloTag probe SiR-CA.[72] A goal of this thesis was to investigate if a precise adjustment of its spirocyclization equilibrium could further enhance the fluorogenicity of SiR for HaloTag labeling.

Corresponding to the aforementioned shift in spirocyclization equilibrium, a higher D_{50} value was detected in dioxane-water titrations for 6-carboxy SiR (**87**) compared to rhodamine *500R* (**48**) (Figures 13e, 22a, b and Tables 1 and 4). These observations suggest that SiR would require the introduction of a more electron-deficient benzenesulfonamide derivative to obtain sufficient brightness upon HaloTag labeling. While transforming the *ortho*-carboxy group into the acyl *p*-toluenesulfonamide (**75**) yielded the highest fluorogenicity among the different rhodamine *500R*-based HaloTag probes, the more electron-poor 3,5-difluorobenzenesulfonamide was tested in the modification of SiR. For this purpose, the 6-carboxy group of **87** was protected using allyl bromide in the presence of Et_3N and K_2CO_3, delivering **88** in 86% yield (Figure 22c). No product formation was observed upon amidation of **88** by means of EDC in combination with DMAP.[194] A potential explanation for the different reactivity between rhodamine *500R* derivative **49** and the SiR-based compound **88** could be their shifted spirocyclization equilibria. However, formation of the acyl chloride using $POCl_3$ followed by nucleophilic acyl substitution with 3,5-difluorobenzenesulfonamide yielded the desired product, which was directly converted into **89** upon deprotection of the allyl ester.[85] **89** showed comparable maximal absorbance and emission wavelengths as well as a slightly increased quantum yield compared to **87**. (Table 4). Furthermore, a distinct shift in spirocyclization equilibrium toward the spirocyclic state was observed for **89** compared to **87** upon measuring their absorbance spectra in different dioxane-water mixtures (Figure 22b). Finally, CA was coupled to the 6-carboxy moiety of **89** to obtain HaloTag probe **90** in 78% yield.

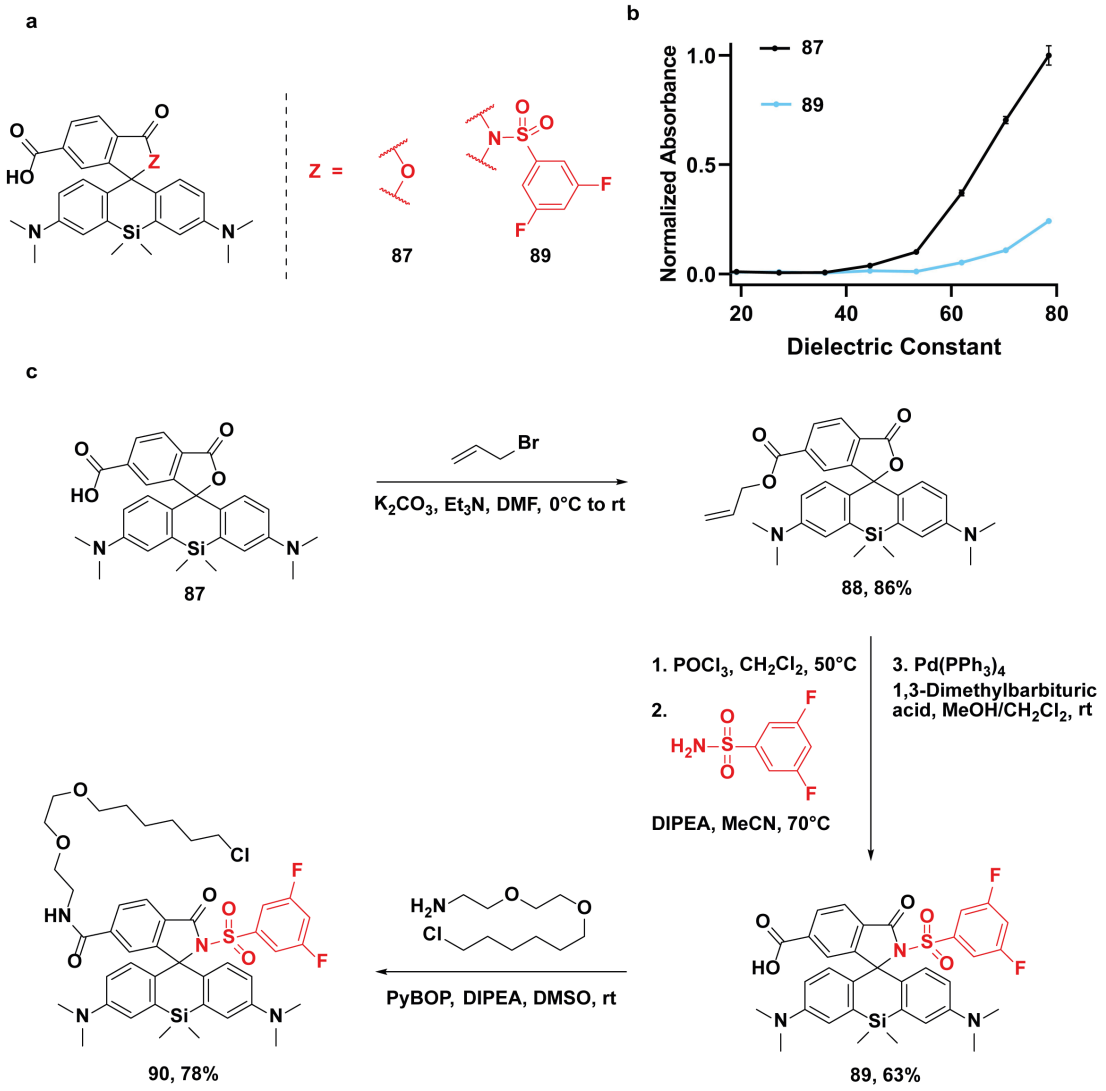

Figure 22: Synthesis and dioxane-water titrations of SiR derivatives. (a) Chemical structures of SiR derivatives **87** and **89**. (b) Normalized maximum absorbance of **87** and **89** (5 µM) in different dioxane-water mixtures as a function of their dielectric constant.[195] The absorbance of **87** and **89** was normalized to the maximal absorbance of **87**. Error bars show ± s.d. from 3 experiments. (c) Synthesis of SiR derivatives.

The fluorogenicity of **90** was examined *in vitro* and compared to SiR-CA (**91**) (Figure 23a). An increase in absorbance of 4.5-fold and fluorescence emission of 14-fold was detected for **91** upon labeling HaloTag (Figure 23b). **90** showed a significantly enhanced turn-on with an increase in fluorescence emission after binding to HaloTag of more than 1100-fold (Figure 23c). Moreover, the effect of SDS on the position of the spirocyclization equilibrium of **90** and **91** was investigated. While addition of SDS led to a strong turn-on for **91**, no distinct increase in absorbance and fluorescence was observed for **90** (Supplementary Figure 7 and Table 4). Similar observations were reported for other highly fluorogenic SiR and carborhodamine HaloTag probes, where labeling of HaloTag caused a significantly stronger shift in spirocyclization equilibrium toward the fluorescent, zwitterionic state than addition of SDS.[85] These findings show that the interaction of certain fluorophores with the surface of HaloTag

leads to an enhanced stabilization of the zwitterionic state compared to the interaction with the negatively charged SDS-micelle surface.

Table 4: Photophysical properties of SiR derivatives (**87**, **89 – 91**).

Z	Probe	λ_{abs} / λ_{em} (nm)	ε ($M^{-1}cm^{-1}$)	Φ	D_{50}	$F_{protein}/F_0$	F_{nuc}/F_{cyt}
O	**87**	646[a] / 668[a]	105000[a]	0.41[a]	65[d]	--	--
NSO_2PhF_2	**89**	648[a] / 666[a]	19000[a]	0.47[a]	>79[d]	--	--
O	**91**	651[b] / 668[b]	31000[a] / 139000[b] / 123000[c]	0.49[b] / 0.53[c]	--	14 ±4.9[e]	18 ±0.9[f]
NSO_2PhF_2	**90**	655[b] / 668[b]	650[a] / 113000[b] / 4700[c]	0.57[b]	--	1180 ±83[e]	150 ±8.3[f]

[a] HEPES buffer (pH 7.3), [b] binding with HaloTag (2 eq) in HEPES buffer (pH 7.3), [c] 0.1% SDS in HEPES buffer (pH 7.3), [d] dioxane-H_2O mixture (v/v: 100/0 – 0/100); mean values from 3 experiments [e] ratio of maximum fluorescence intensities in the presence and absence of HaloTag (2 eq); errors show s.d. from 3 experiments, [f] fluorescence ratios; F_{nuc}: Nuclear SiR signal in U-2 OS FlpIn Halo-SNAP-NLS expressing cells normalized to the nuclear signal of **81**; F_{cyt}: Cytosolic SiR signal in wild-type U-2 OS cells; in total, 180 cells from 2 independent experiments were examined for each probe; errors represent s.e.m.

Live-cell, no-wash confocal microscopy of U-2 OS FlpIn Halo-SNAP-NLS-expressing cells and wild-type U-2 OS cells was performed to test the *in cellulo* fluorogenicity of **90** and **91**. Significantly decreased background fluorescence and only slightly reduced nuclear signal intensities were observed for **90** compared to **91** (Figures 23 d, e and Supplementary Figure 8). Consequently, staining with **90** yielded a F_{nuc}/F_{cyt} ratio of 150, which is almost 10-fold higher than the one detected for **91**. Moreover, the *in cellulo* labeling time of **90** and **91** was measured upon staining U-2 OS FlpIn Halo-SNAP-NLS-expressing cells. The resulting microscopy data showed that **90** required a longer incubation time than **91** to reach saturation in fluorescence signal (Figures 23 f and g).

Altogether, the *in vitro* as well as *in cellulo* experimental data showed that transforming the *ortho*-carboxy group of SiR into an electron-deficient acyl benzenesulfonamide enhanced its fluorogenicity even further. However, this modification also had a disadvantageous effect on the *in cellulo* labeling time. As discussed in Section 3.2., a potential explanation for the lengthened *in cellulo* labeling time could be an increase in hydrophobicity upon modification of the *ortho*-carboxy group.

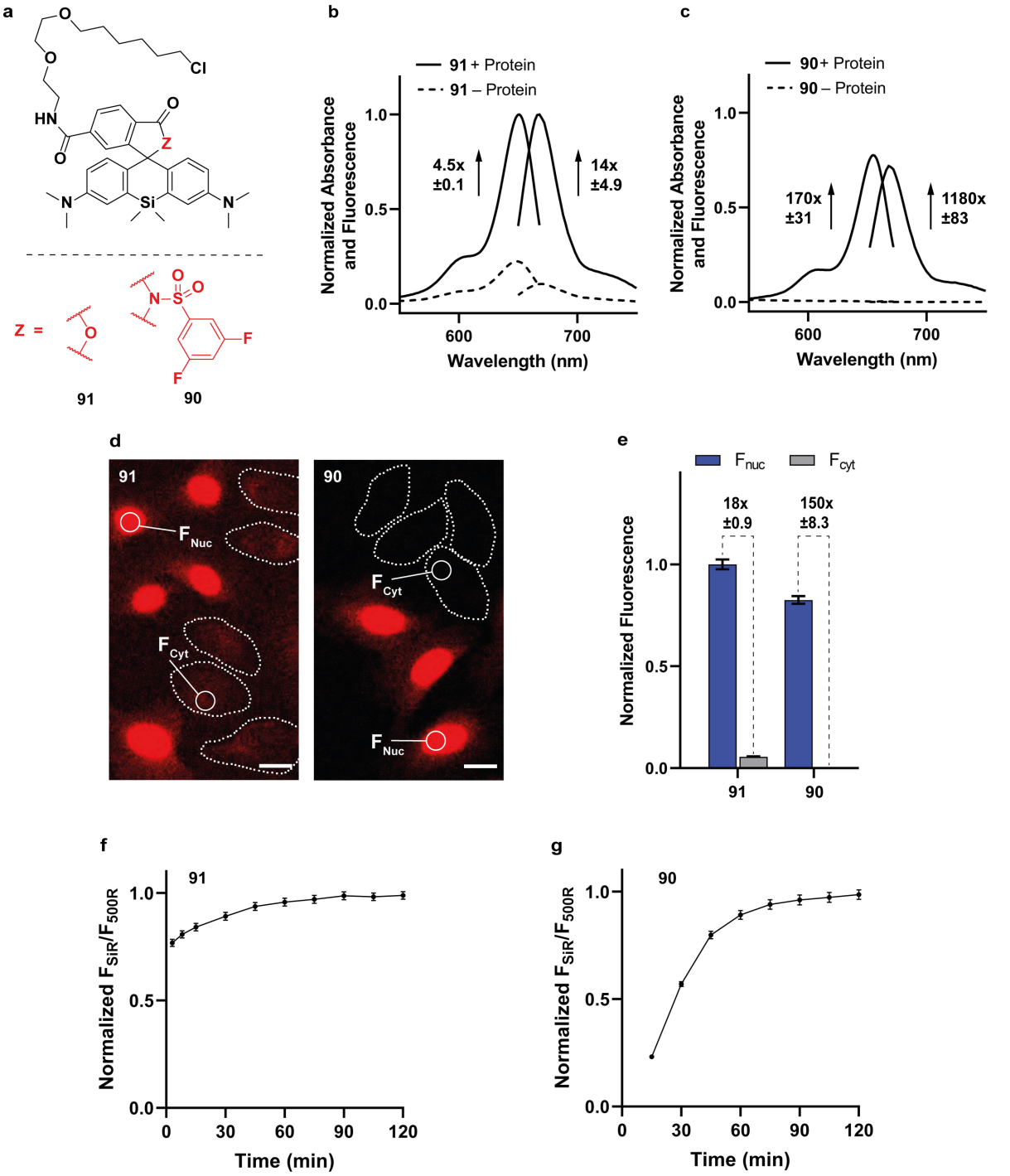

Figure 23: *In vitro* and *in cellulo* fluorogenicity measurements as well as *in cellulo* labeling time experiments of SiR HaloTag probes (**90** and **91**). (a) Chemical structures of **90** and **91**. (b) and (c) Absorbance and fluorescence emission spectra of **91** (b) and **90** (c) (2.5 µM) in the presence (+ Protein) and absence (- Protein) of HaloTag (5 µM) after 2.5 h incubation normalized to the maximal absorbance and emission of **91**. Representative spectra from 3 experiments. Errors show s.d. (d) Live-cell, no-wash confocal images of U-2 OS FlpIn Halo-SNAP-NLS-expressing cells and wild-type U-2 OS cells stained with **90** and **91** (500 nM) for 2.5 h. The dotted lines represent wild-type U-2 OS cells. Scale bar 20 µm. (e) Bar plot showing the F_{nuc}/F_{cyt} ratio of **90** and **91** in live-cell, no-wash confocal microscopy. F_{nuc}: Nuclear SiR signal in U-2 OS FlpIn Halo-SNAP-NLS expressing cells normalized to the nuclear signal of **81**. F_{cyt}: Cytosolic SiR signal in wild-type U-2 OS cells. U-2 OS FlpIn Halo-SNAP-NLS-expressing cells and wild-type U-2 OS cells were prelabeled with **81** (500 nM) overnight followed by staining with **90** and **91** (500 nM) for 2.5 h. In total, 180 cells were examined from 2 independent experiments for each probe. Error bars show ± s.e.m. (f) and (g) *In cellulo* HaloTag labeling with **91** (f) and **90** (g). U-2 OS FlpIn Halo-SNAP-NLS expressing cells were prelabeled with **81** (500 nM) overnight, and incubated with **90** and **91** (500 nM). The normalized ratio of SiR

fluorescence to the fluorescence signal of **81** was plotted over time. In total, 90 cells were examined from technical triplicates for each probe. Error bars show ± s.e.m.

3.5.2. Optimization of Carborhodamine for SNAP-tag Labeling

In previous work, the *ortho*-carboxy moiety of carborhodamine was replaced with an acyl dimethylsulfamide, yielding a highly fluorogenic HaloTag probe (MaP618-Halo).[85] However, the BG-conjugate of this fluorophore was reported to only show a slight increase in absorbance and fluorescence upon labeling SNAP-tag.[85] Therefore, it was herein tested if a systematic tuning of the spirocyclization equilibrium of carborhodamine could lead to the development of a fluorogenic SNAP-tag probe for live-cell, no-wash microscopy.

Comparable D_{50} values were detected for 6-carboxy carborhodamine (**92**) and rhodamine *500R* **48**, indicating a similar position of the spirocyclization equilibrium for these two fluorophore scaffolds (Figures 13e, 24a, b and Tables 1 and 5). Since introducing an acyl 4-fluorobenzenesulfonamide yielded a highly fluorogenic rhodamine *500R* SNAP-tag probe, the same modification was applied to carborhodamine. To this end, allyl-protection of the 6-carboxy group of **92** was performed to obtain **93** in 82% yield (Figure 24c). Subsequently, the *ortho*-carboxy moiety of **93** was converted into an acyl chloride using $POCl_3$.[85] Nucleophilic acyl substitution with 4-fluorobenzenesulfonamide and deprotection of the allyl ester using $Pd(PPh_3)_4$ and 1,3-dimethylbarbituric acid gave **94** in 78% yield over three steps. **94** showed comparable maximal absorbance and emission wavelengths as well as a slightly increased quantum yield compared to **92**. (Table 5). Furthermore, a distinct shift in spirocyclization equilibrium toward the spirocyclic state was observed for **94** compared to **92** in dioxane-water titrations, and comparable D_{50} values were detected for **94** and the corresponding rhodamine *500R* derivative (**56**) (Figure 24b, Tables 1 and 5). Finally, carborhodamine SNAP-tag probe **95** was formed in 65% yield upon coupling BG to the 6-carboxy group of **94**.

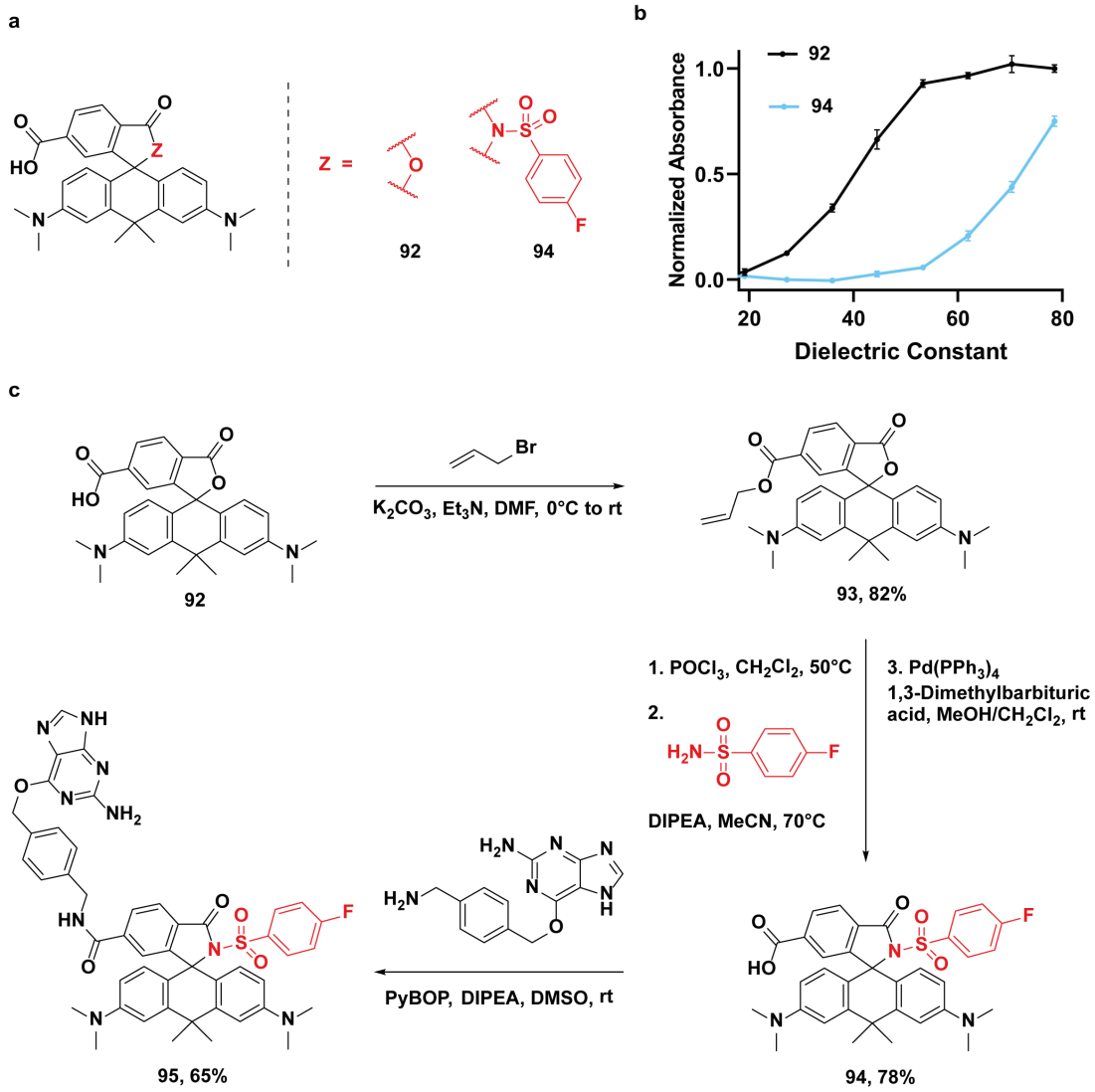

Figure 24: Synthesis and dioxane-water titrations of carborhodamine derivatives. (a) Chemical structures of carborhodamine derivatives **92** and **94**. (b) Normalized maximum absorbance of **92** and **94** (5 µM) in different dioxane-water mixtures as a function of their dielectric constant.[195] The absorbance of **92** and **94** was normalized to the maximal absorbance of **92**. Error bars show ± s.d. from 3 experiments. (c) Synthesis of carborhodamine derivatives.

The fluorogenicity of **95** was analyzed *in vitro* and compared to the original carborhodamine SNAP-tag probe (**96**) as well as MaP618-BG (**97**) (Figure 25a).[85] **96** showed intense background signal and, thus, yielded a low increase in absorbance (1.7-fold) and fluorescence emission (3-fold) upon SNAP-tag labeling (Figure 25b and Supplementary Figure 9). Furthermore, a significantly enhanced absorbance and fluorescence emission was detected for **95** after binding to SNAP-tag compared to **97** as well as a lower background signal intensity than for **96** (Figures 25b – d). Despite its reduced brightness, **95** exhibited an almost 20-fold higher turn-on in fluorescence emission than **96**. This increase in fluorogenicity was also detected by means of live-cell, no-wash confocal microscopy of U-2 OS FlpIn Halo-SNAP-NLS-expressing cells and wild-type U-2 OS cells (Figures 25e, f and Supplementary Figure 10). Analogous to the *in vitro* experiments, **95** showed reduced brightness compared to **96**.

However, since the decrease in background signal intensity was more distinct than the reduction of the nuclear brightness, a higher F_{nuc}/F_{cyt} ratio was observed for **95** (F_{nuc}/F_{cyt} = 65) than for **96** (F_{nuc}/F_{cyt} = 19). Next, the *in cellulo* labeling time of **95** and **96** was examined by staining U-2 OS FlpIn Halo-SNAP-NLS-expressing cells. The time needed to reach saturation in fluorescence signal was comparable for **95** and **96** (Figures 25g and h).

Table 5: Photophysical properties of carborhodamine derivatives (**92**, **94** – **97**).

Z	Probe	λ_{abs} / λ_{em} (nm)	ε ($M^{-1}cm^{-1}$)	Φ	D_{50}	$F_{protein}/F_0$	F_{nuc}/F_{cyt}
O	**92**	609[a] / 636[a]	116000[a]	0.51[a]	40[d]	--	--
NSO_2PhF	**94**	612[a] / 634[a]	74000[a]	0.59[a]	72[d]	--	--
O	**96**	614[b] / 638[b]	66000[a] / 112000[b] / 149000[c]	0.54[b] / 0.67[c]	--	3.0 ±0.1[e]	19 ±0.8[f]
NSO_2PhF	**95**	616[b] / 636[b]	5900[a] / 50000[b] / 59000[c]	0.56[b] / 0.72[c]	--	58 ±1.6[e]	65 ±4.1[f]
NSO_2NMe_2	**97**	616[b] / 636[b]	420[a] / 2700[b] / 7400[c]	--	--	22 ±0.4[e]	--

[a] HEPES buffer (pH 7.3), [b] binding with SNAP-tag (2 eq) in HEPES buffer (pH 7.3), [c] 0.1% SDS in HEPES buffer (pH 7.3), [d] dioxane-H_2O mixture (v/v: 100/0 – 0/100); mean values from 3 experiments [e] ratio of maximum fluorescence intensities in the presence and absence of SNAP-tag (2 eq); errors show s.d. from 3 experiments, [f] fluorescence ratios; F_{nuc}: Nuclear carborhodamine signal in U-2 OS FlpIn Halo-SNAP-NLS expressing cells normalized to the nuclear signal of **75**; F_{cyt}: Cytosolic carborhodamine signal in wild-type U-2 OS cells; in total, 180 cells from 2 independent experiments were examined for each probe; errors represent s.e.m.

In summary, a highly fluorogenic SNAP-tag probe (**95**), suitable for live-cell, no-wash microscopy, was developed by adjusting the spirocyclization equilibrium of carborhodamine. In terms of the *in cellulo* labeling time, a different effect upon introducing an acyl 4-fluorobenzenesulfonamide was observed for carborhodamine than for rhodamine *500R*. While this structural modification led to a significantly shortened *in cellulo* labeling time for rhodamine *500R*, a comparable incubation time was required for carborhodamines **95** and **96** to reach saturation in fluorescence signal (Figures 20a, 25g and h).

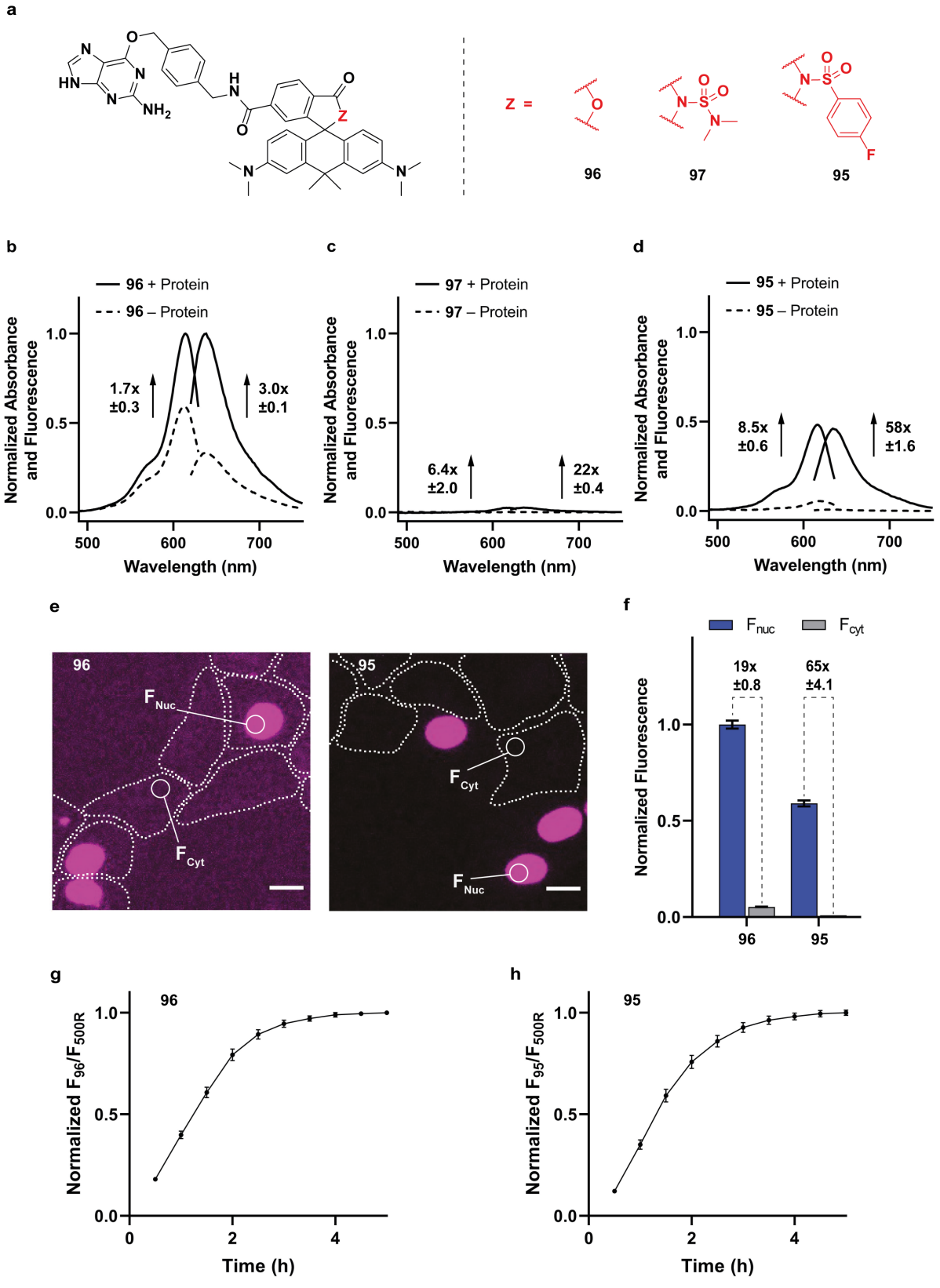

Figure 25: *In vitro* and *in cellulo* fluorogenicity measurements as well as *in cellulo* labeling time experiments of carborhodamine SNAP-tag probes (**95** – **97**). (a) Chemical structures of **95 – 97**. (b) – (d) Absorbance and fluorescence emission spectra of **96** (b), **97** (c) and **95** (d) (2.5 µM) in the presence (+ Protein) and absence (- Protein) of SNAP-tag (5 µM) after 2.5 h incubation normalized to the maximal absorbance and emission of **96**. Representative spectra from 3 experiments. Errors show s.d. (e) Live-cell, no-wash confocal images of U-2 OS FlpIn Halo-SNAP-NLS-expressing cells and wild-type U-2 OS cells stained with **96** and **95** (500 nM) for 4 h. The

dotted lines represent wild-type U-2 OS cells. Scale bar 20 µm. (f) Bar plot showing the F_{nuc}/F_{cyt} ratio of **96** and **95** in live-cell, no-wash confocal microscopy. F_{nuc}: Nuclear carborhodamine signal in U-2 OS FlpIn Halo-SNAP-NLS expressing cells normalized to the nuclear signal of **75**. F_{cyt}: Cytosolic carborhodamine signal in wild-type U-2 OS cells. U-2 OS FlpIn Halo-SNAP-NLS-expressing cells and wild-type U-2 OS cells were prelabeled with **75** (200 nM) overnight followed by staining with **96** and **95** (500 nM) for 4 h. In total, 180 cells were examined from 2 independent experiments for each probe. Error bars show ± s.e.m. (g) and (h) *In cellulo* SNAP-tag labeling with **96** (g) and **95** (h). U-2 OS FlpIn Halo-SNAP-NLS expressing cells were prelabeled with **75** (200 nM) overnight, and incubated with **96** and **95** (500 nM). The normalized ratio of carborhodamine fluorescence to the fluorescence signal of **75** was plotted over time. In total, 90 cells were examined from technical triplicates for each probe. Error bars show ± s.e.m.

3.5.3. Development of a TMR Probe for SMLM

In another extension of the systematic tuning of rhodamine spirocyclization, the *ortho*-carboxy moiety of TMR was modified to develop a spontaneously blinking probe for SMLM. To this end, the same modification was applied that had already endowed rhodamine *500R* with blinking character. The 6-carboxy group of **98** was protected by means of allyl bromide in the presence of Et_3N and K_2CO_3 (Figure 26). Amidation of the resulting fluorophore (**99**) using 2,2,2-trifluoroethylamine, EDC and DMAP followed by deprotection of the allyl ester gave **100** in 61% yield over two steps.[85, 194] Finally, CA was coupled to the 6-carboxy moiety of **100** to obtain HaloTag probe **101** in 55% yield.

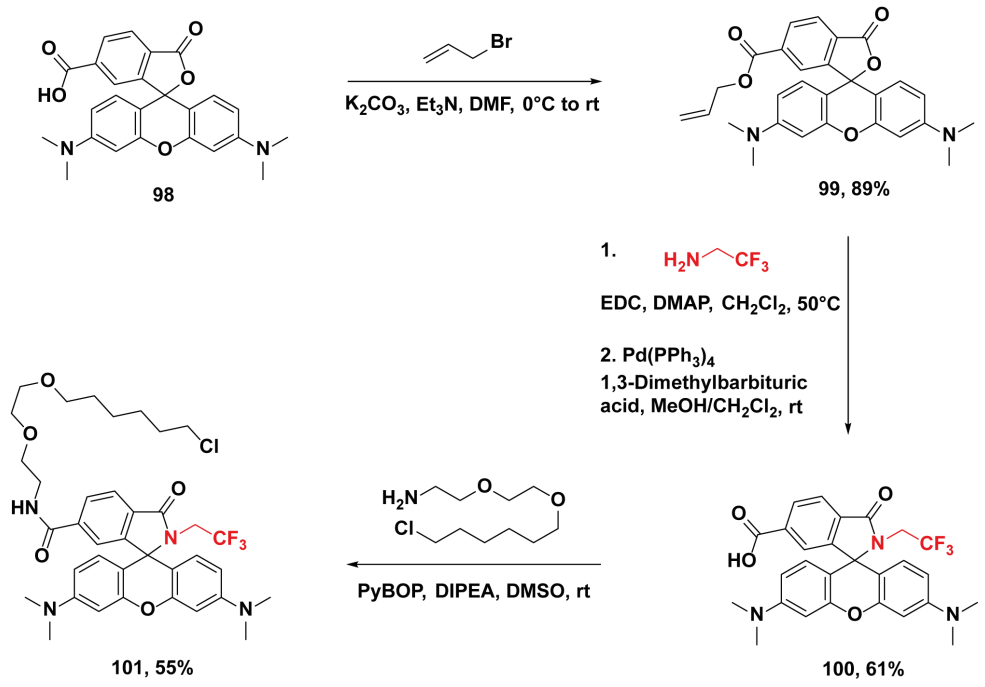

Figure 26: Synthesis of TMR derivatives.

The position of the spirocyclization equilibrium of **100** was analyzed by measuring the absorbance spectrum at various pH. **100** showed distinct absorbance in the visible range at higher pH compared to the corresponding rhodamine *500R* derivative (**64**), indicating a shifted position of the spirocyclization equilibrium toward the fluorescent form (Figures 14 and 27a). Next, the blinking behavior and applicability of **101** in SMLM was analyzed by imaging fixed U-2 OS cells endogenously expressing Nup96-Halo.[199] **101** showed spontaneous blinking, and

the resulting SMLM images revealed the circular structure of the nuclear pore (Figures 27b – d). Furthermore, **101** gave an average photon count of each localization of 2146, and the localization precision peaked at 3.6 nm (Supplementary Figure 5). The increased photon count of **101** compared to rhodamine *500R* **85** (631) could be explained by their shifted spirocyclization equilibria. Moreover, the different microscopy setup could have an influence on the brightness of the dyes. The laser line used for **101** (λ_{ex} = 561 nm, λ_{abs}(**100**) = 559 nm) was closer to the absorbance maximum of the fluorophore than in the case of **85** (λ_{ex} = 488 nm, λ_{abs}(**64**) = 512 nm) (Supplementary Table 2). **101** was also used to image U-2 OS Cep41-Halo expressing cells. A fwhm of 28.5 nm ± 5.8 nm was measured, which corresponds well to the reported microtubule diameter of 25 nm (Supplementary Figure 6).[202] The different fwhm measured with **85** and **101** could be due to their difference in localization precision (Supplementary Figures 5 and 6). In terms of the duty cycle measurement, a longer on-time was detected for **101** (13.1 ms) compared to **85** (3.6 ms) (Supplementary Table 1). Analogous to the enhanced photon count, a potential explanation for the increased on-time and duty cycle of **101** could be the shifted position of the spirocyclization equilibrium.

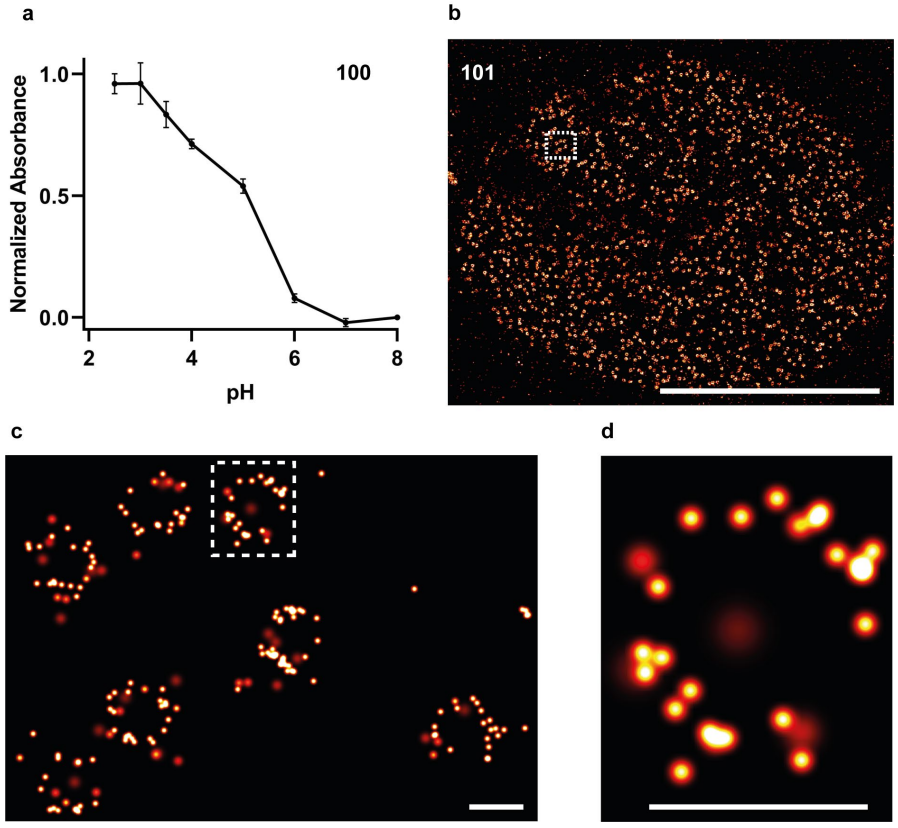

Figure 27: Analyzing the position of the spirocyclization equilibrium of TMR derivative **100** and the applicability of the corresponding HaloTag probe (**101**) for SMLM. (a) Normalized maximal absorbance of **100** (5 µM) in PBS (10 µM) at different pH. The absorbance was normalized to the maximum absorbance of **98** (5 µM) in PBS (10 µM) at pH = 7.0. Error bars show ± s.d. from 3 experiments. (b) SMLM image of fixed U-2 OS cells endogenously expressing Nup96-Halo stained with **101** (1 µM) overnight. Scale bar, 10 µm. (c) SMLM image of the marked region in (b). Scale bar, 100 nm. (d) Individual nuclear pore of the marked region in (c). Scale bar, 100 nm. SMLM images (b **–** d) were recorded and analyzed by Aline Tschanz and Dr. Philipp Hoess (EMBL Heidelberg).

With **101**, a second probe for SMLM was developed and, thus, the spectrum of colors for spontaneously blinking dyes was further expanded. However, it still remains to be determined if **101** is applicable to live-cell SMLM. While **101** showed a longer on-time than **85**, its on-time still is significantly lower than the one of the readily used live-cell SMLM probe HMSiR (96 ms).[147] Therefore, it needs to be tested if **101** allows the detection of sufficient photons in a short amount of time, thereby providing the required temporal resolution for live-cell SMLM.

3.6. STED Microscopy of Fluorogenic HaloTag and SNAP-tag Probes

Rhodamine *500R*, SiR and carborhodamine are endowed with compatible photophysical properties for STED microscopy.[21, 199] Transforming the *ortho*-carboxy group of these fluorophore scaffolds into different acyl benzenesulfonamides increased their fluorogenicity without significantly changing their photophysical properties. Thus, the corresponding acyl benzenesulfonamide HaloTag and SNAP-tag probes were tested in live-cell STED microscopy. To this end, U-2 OS cells stably expressing Vimentin-Halo were stained with rhodamine *500R*- and SiR-derived HaloTag probes **75** and **90**. With respect to carborhodamine-derived SNAP-tag probe **95**, U-2 OS Vimentin-SNAP expressing cells were labeled.[203] Confocal and STED imaging was performed without prior washing steps. While a 485 nm excitation laser was used in combination with a 595 nm STED laser for **75**, **90** was excited at 640 nm and depleted at 775 nm. Combinations of a 775 nm STED laser with 561 nm as well as 640 nm excitation lasers were tested for **95**, where excitation at 561 nm provided enhanced image quality. Moreover, laser powers and dwell time were optimized for each probe regarding signal intensity, photobleaching and spatial resolution. The resulting images showed bright filamentous structures with exceptionally low background intensities (Figures 28a, d and g). Comparing confocal and STED images enables visualization of the increased spatial resolution obtained in the STED channel (Figures 28a – i). Altogether, these results corroborate the high fluorogenicity of **75**, **90** and **95** as well as their applicability in live-cell, no-wash STED microscopy.

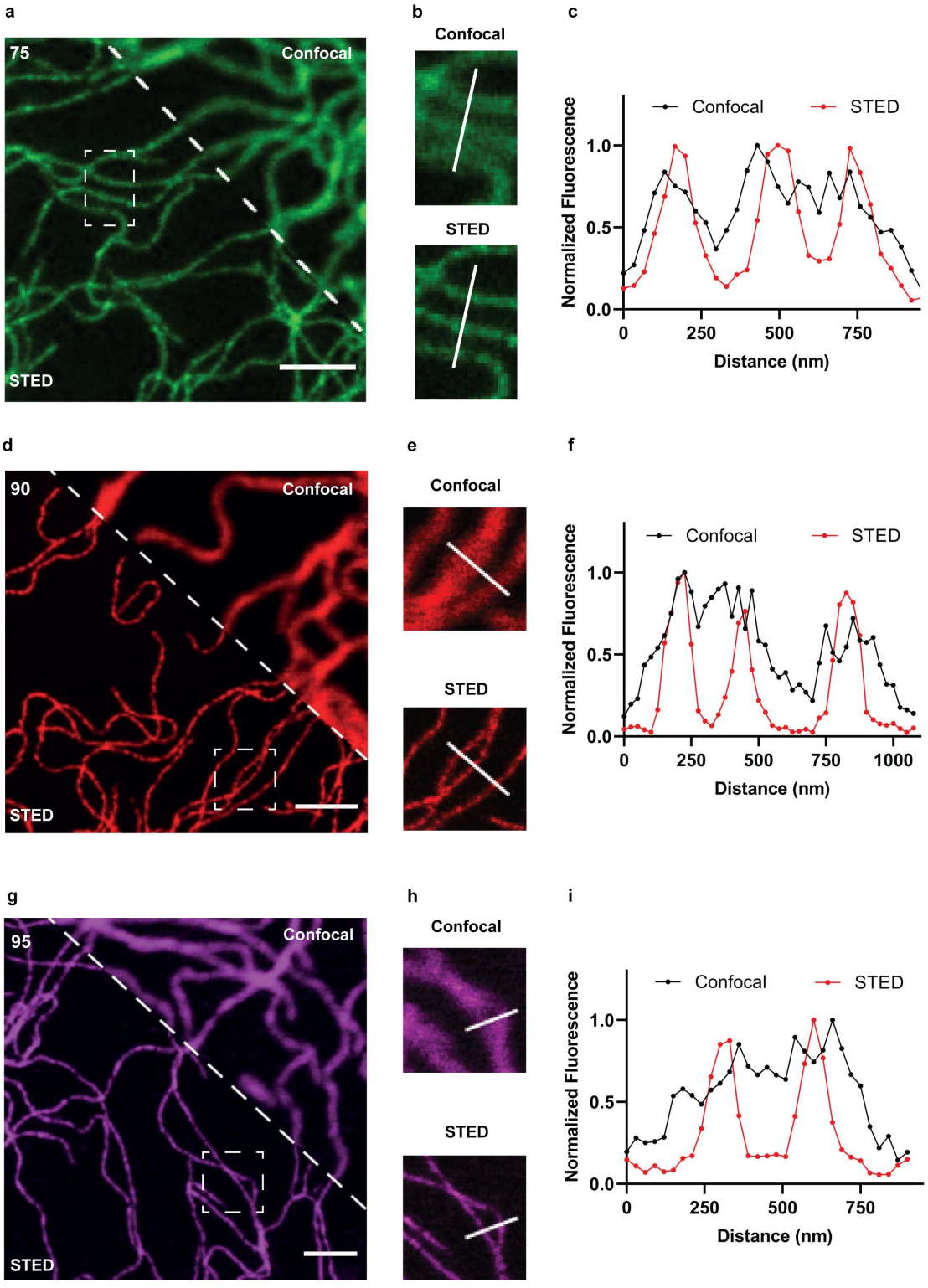

Figure 28: Live-cell, no-wash STED microscopy with rhodamine *500R* and SiR HaloTag probes (**75** and **90**) as well as carborhodamine SNAP-tag probe **95**. (a) Live-cell, no-wash confocal and STED images of U-2 OS Vimentin-Halo expressing cells labeled with **75** (200 nM) for 2 h. (b) Confocal and STED images of the marked region in (a). (c) Confocal and STED line profiles from (b). (d) Live-cell, no-wash confocal and STED images of U-2 OS Vimentin-Halo expressing cells labeled with **90** (500 nM) for 2 h. (e) Confocal and STED images of the marked region in (d). (f) Confocal and STED line profiles from (e). (g) Live-cell, no-wash confocal and STED images of U-2 OS Vimentin-SNAP expressing cells labeled with **95** (500 nM) for 4 h. (h) Confocal and STED images of the marked region in (g). (i) Confocal and STED line profiles from (h). Image data were smoothed with a 1-pixel low pass Gaussian filter. Scale bars, 1.5 µm. Images were recorded under the supervision of Dr. Elisa D'Este.

3.7. Fluorogenic Probes for Other Labeling Systems

Since the modification of the *ortho*-carboxy group allowed optimization of the fluorogenicity for HaloTag and SNAP-tag labeling, it was investigated if this strategy could be extended to other cellular targets and labeling systems. In the following sections, rhodamine *500R*- and SiR-derived spirolactams were transformed into probes for tubulin as well as eDHFR. Furthermore, HIV-1 protease probes were synthesized based on previously developed carborhodamine dyes.[85]

3.7.1. Fluorogenic Probes for Tubulin Labeling

While probes for HaloTag and SNAP-tag rely on covalent labeling, taxane derivatives, including cabazitaxel (**10**), directly and non-covalently label tubulin (Section 1.2.).[76, 81, 105] In order to investigate, which position of the spirocyclization equilibrium is required to obtain high fluorogenicity upon tubulin labeling, various rhodamine *500R* spirolactams with different D_{50} values were transformed into tubulin probes. To this end, rhodamine *500R* acyl 3,5-difluorobenzenesulfonamide (**52**), acyl 4-fluorobenzenesulfonamide (**56**), acyl *p*-toluenesulfonamide (**58**) and acyl methylsulfonamide (**60**) were coupled to 8-aminooctanoic acid after activation with TSTU, delivering **102** – **105** in yields of 76% – 83% (Figure 29).[25] Coupling of **102** – **105** to the tubulin ligand cabazitaxel (**10**) by means of PyBOP gave probes **106** – **109** in 62% – 76% yield. The linker length between fluorophore and ligand of **106** – **109** was based on previous studies regarding fluorescent tubulin probes.[25, 105]

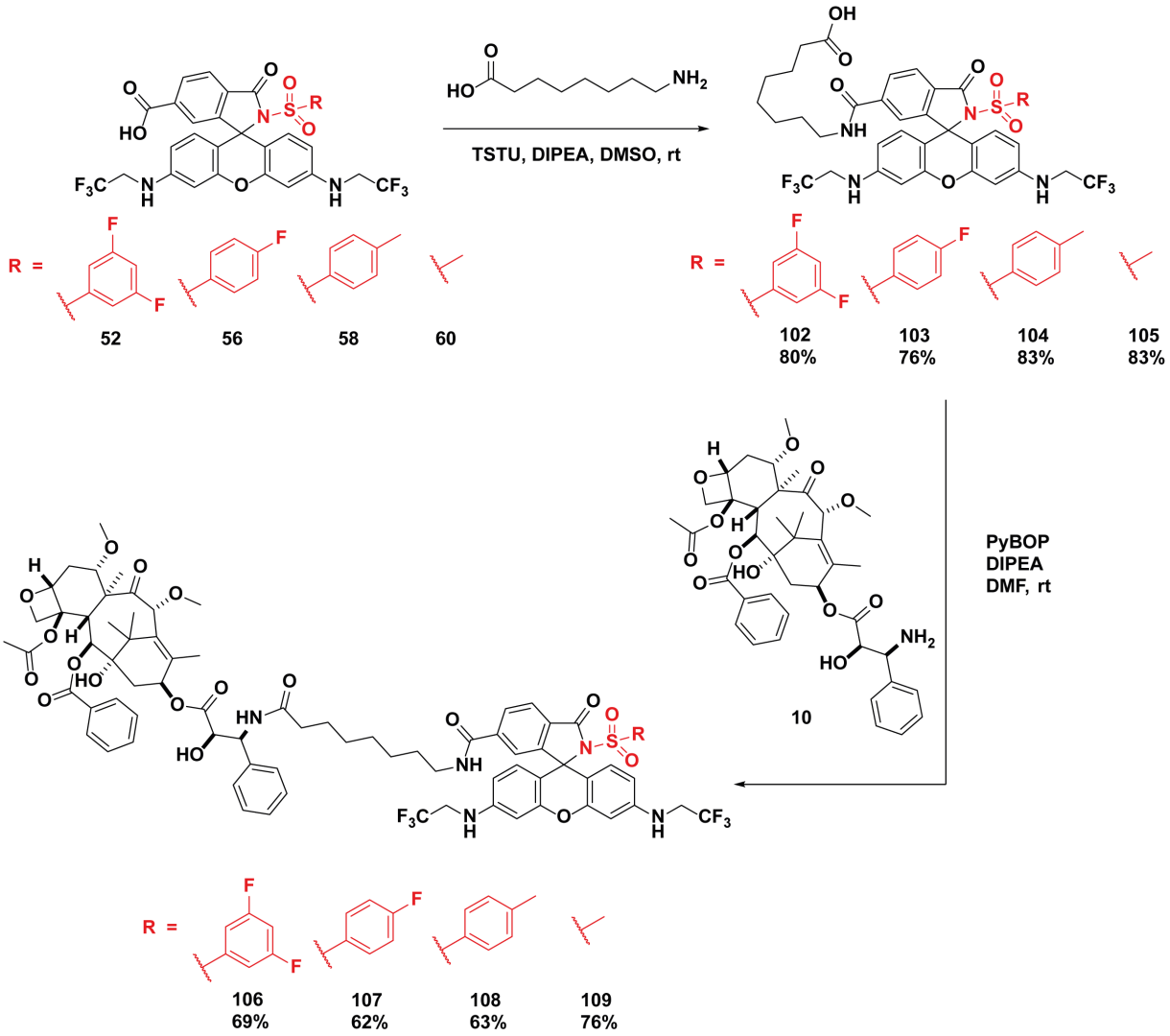

Figure 29: Synthesis of rhodamine *500R* tubulin probes **106** – **109**.

The fluorogenicity of **106** – **109** was examined by means of live-cell, no-wash confocal microscopy of wild-type U-2 OS cells. Staining with **106** showed bright filamentous structures (Figure 30a). A decreased brightness was observed upon labeling with the other rhodamine *500R* derivatives, where the reduction in signal intensity was more pronounced for **107** and **108** than for **109** (Figures 30b – d). Subsequently, the brightest probes, **106** and **109**, were further evaluated. By means of co-staining with the widely used tubulin probe SiR-tubulin, their signal specificity for tubulin was investigated.[25] Comparing the recorded images from the rhodamine *500R* and SiR channel revealed a significant amount of unspecific signal for **106** (Figures 30e – g). With respect to **109**, less unspecific staining was detected (Figures 30h – j). For all the presented tubulin imaging experiments, co-incubation with verapamil, an efflux-pump inhibitor, was performed since it was previously reported to enhance the labeling efficiency of fluorescent tubulin probes.[25, 204] Accordingly, preliminary microscopy data of **106**

– **109** recorded in the absence of verapamil showed significantly decreased signal intensities, indicating that efflux pumps affect their labeling efficiency.

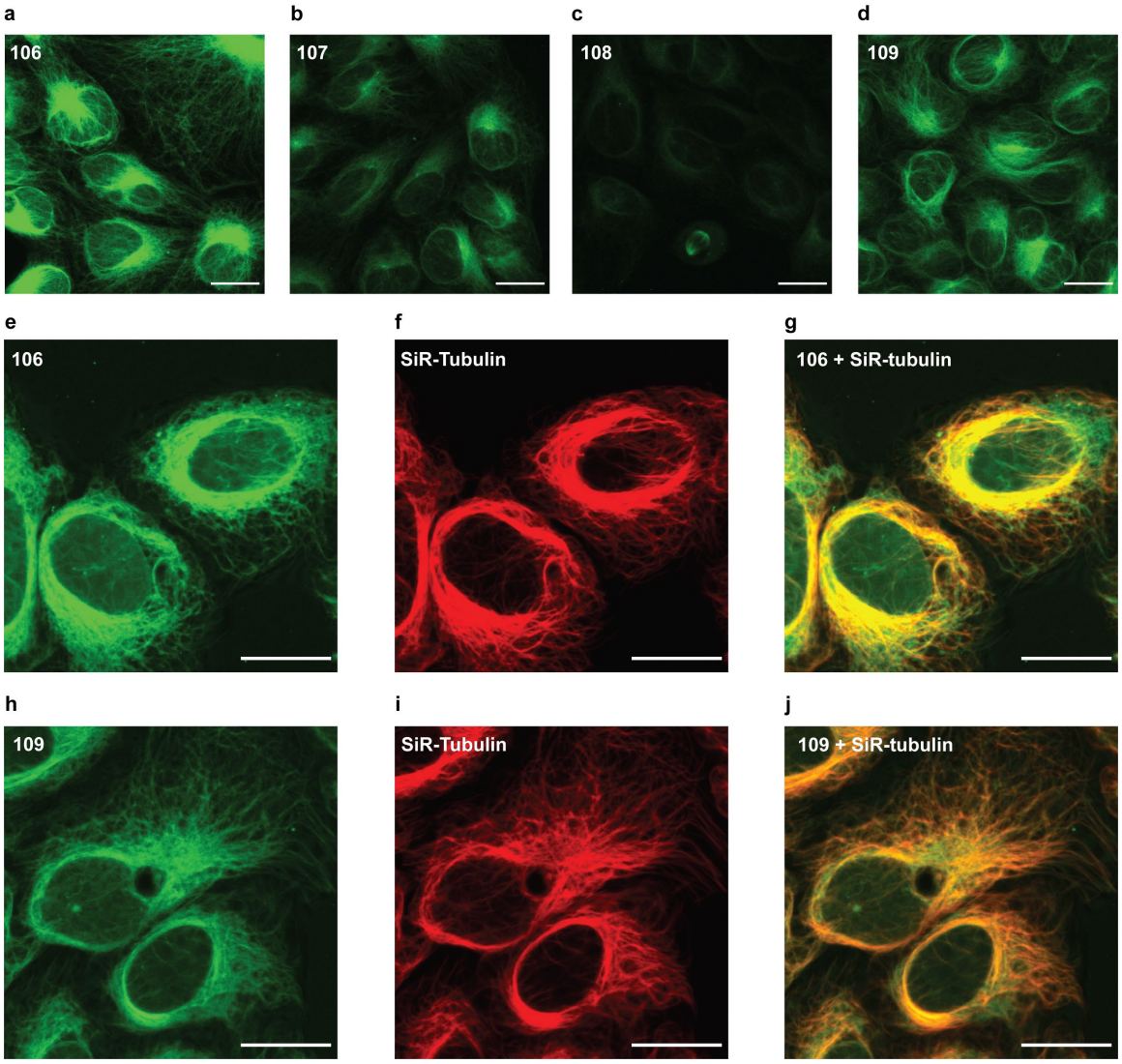

Figure 30: Live-cell, no-wash confocal microscopy with rhodamine *500R* tubulin probes **106 – 109**. (a) – (d) Live-cell, no-wash confocal images of wild-type U-2 OS cells incubated with **106 – 109** (500 nM) and verapamil (5 µM) for 3 h. (e) – (j) Live-cell, no-wash confocal images of wild-type U-2 OS cells incubated with **106** or **109** (500 nM) and verapamil (5 µM) for 1 h, followed by addition of SiR-tubulin (500 nM). After incubation for additional 2 h, images were recorded in the rhodamine *500R* (e, h) and SiR (f, i) channel, yielding merged images (g, j). Scale bars, 20 µm.

The higher signal intensity of **106** compared to the other tubulin probes (**107** – **109**) could be explained by their shifted spirocyclization equilibria. Acyl 3,5-difluorobenzenesulfonamide **52** showed a lower D_{50} value compared to the precursors of **107** – **109**, indicating a reduced stabilization of the spirocyclic state (Table 1). Consequently, binding of **106** to tubulin would lead to an enhanced formation of the fluorescent state. However, the increased brightness of **109** compared to **107** and **108** could not be explained by their positions of the spirocyclization equilibrium as acyl methylsulfonamide **60** exhibited a higher D_{50} value than acyl 4-fluorobenzenesulfonamide **56** and acyl *p*-toluenesulfonamide **58** (Table 1). A potential

explanation for the higher signal intensity of **109** could be a reduced hydrophobicity compared to **107** and **108**. A reduced hydrophobicity increases solubility and might decrease the tendency of the probe for aggregation as well as sequestration in membranes and, thus, could enhance the labeling efficiency and the specific signal intensity.[127] In order to further reduce the hydrophobicity, the aliphatic linker of **109** was replaced with a more hydrophilic polyethylene glycol (PEG) linker (**110**). For this purpose, **60** was coupled to **110** and subsequently to **10**, yielding tubulin probe **112** (Figure 31). However, no distinct change in image quality was observed by comparing the performance of **109** to **112** in live-cell, no-wash confocal microscopy of wild-type U-2 OS cells (Supplementary Figure 11).

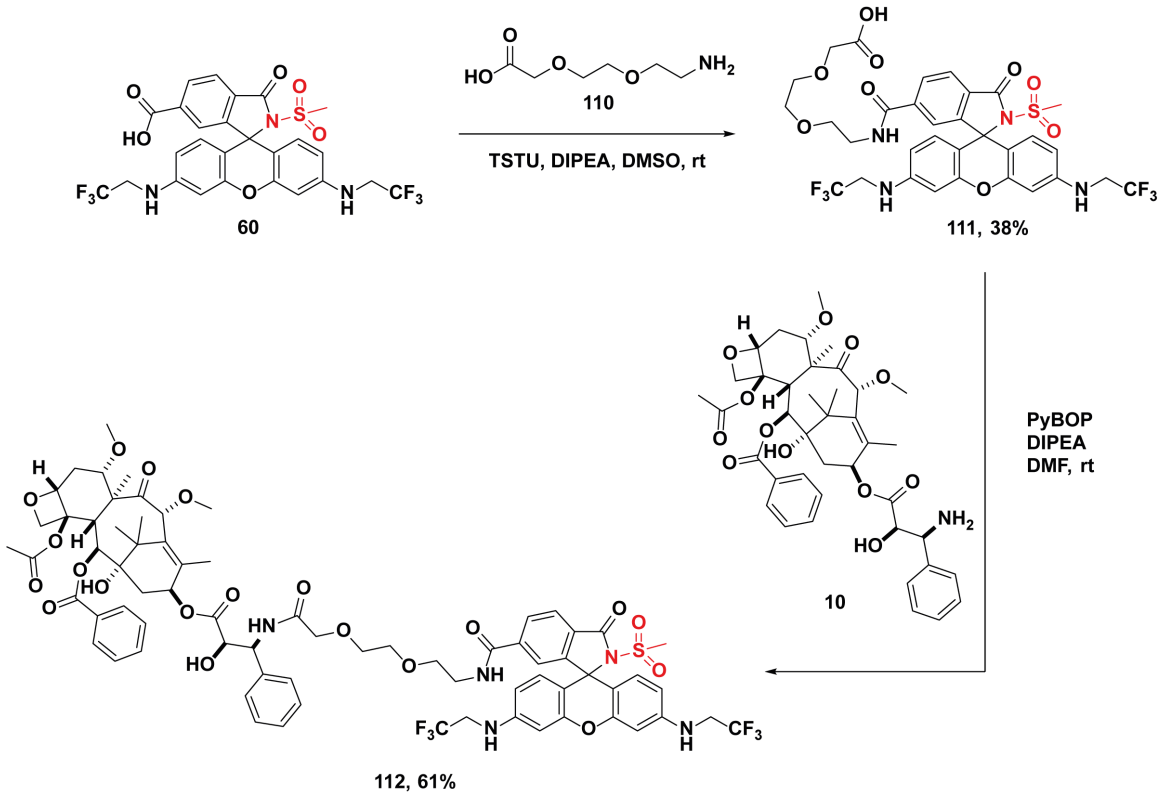

Figure 31: Synthesis of rhodamine *500R* tubulin probe **112**.

3.7.2. Fluorogenic Probes for eDHFR Labeling

In order to investigate if the modification of the *ortho*-carboxy group of rhodamines enables the development of fluorogenic probes for another protein tag-based method, eDHFR labeling was employed. In contrast to the covalent labeling of HaloTag and SNAP-tag, labeling of eDHFR by means of TMP derivatives relies on their non-covalent interaction (Section 1.2.1.).[89] With the aim of developing a fluorogenic rhodamine *500R*-derived eDHFR probe for live-cell, no-wash microscopy, acyl *p*-toluenesulfonamide **58** and acyl methylsulfonamide **60** were coupled to TMP ligand **113**, delivering eDHFR probes **114** and **115** (Figure 32a).[205] **58** and **60** were chosen, since the corresponding HaloTag (**75**) and tubulin (**109**) probes showed

high fluorogenicity and image quality in live-cell, no-wash microscopy (Sections 3.2. and 3.7.1.). The fluorogenicity of **114** and **115** was examined by live-cell, no-wash confocal microscopy of U-2 OS FlpIn SNAP-eDHFR-NLS expressing cells and wild-type U-2 OS cells (Figures 32b, c and Supplementary Figure 12). Both, **114** and **115** showed low background signal intensities and comparably high F_{nuc}/F_{cyt} ratios. As a comparison, the same cell line (U-2 OS FlpIn SNAP-eDHFR-NLS) was stained with a previously developed rhodamine *500R* SNAP-tag probe (**81**). **81** required a 3-fold lower excitation laser intensity to obtain comparable nuclear signal intensity to **114** and **115**, indicating a low brightness for **114** and **115** upon binding to eDHFR. Additionally, the time period required to label eDHFR, expressed in the nucleus of U-2 OS cells, was measured for **114**. A comparable incubation time was required to reach saturation in fluorescence signal for **114** as for the corresponding HaloTag probe (**75**) (Figures 18 and 32d). Altogether, the low background signal intensities of **114** and **115** and the acceptable *in cellulo* labeling time of **114** represent suitable features regarding their applicability in live-cell, no-wash microscopy. However, their low signal intensity after binding to eDHFR leaves room for improvement and will require further tuning of the spirocyclization equilibrium.

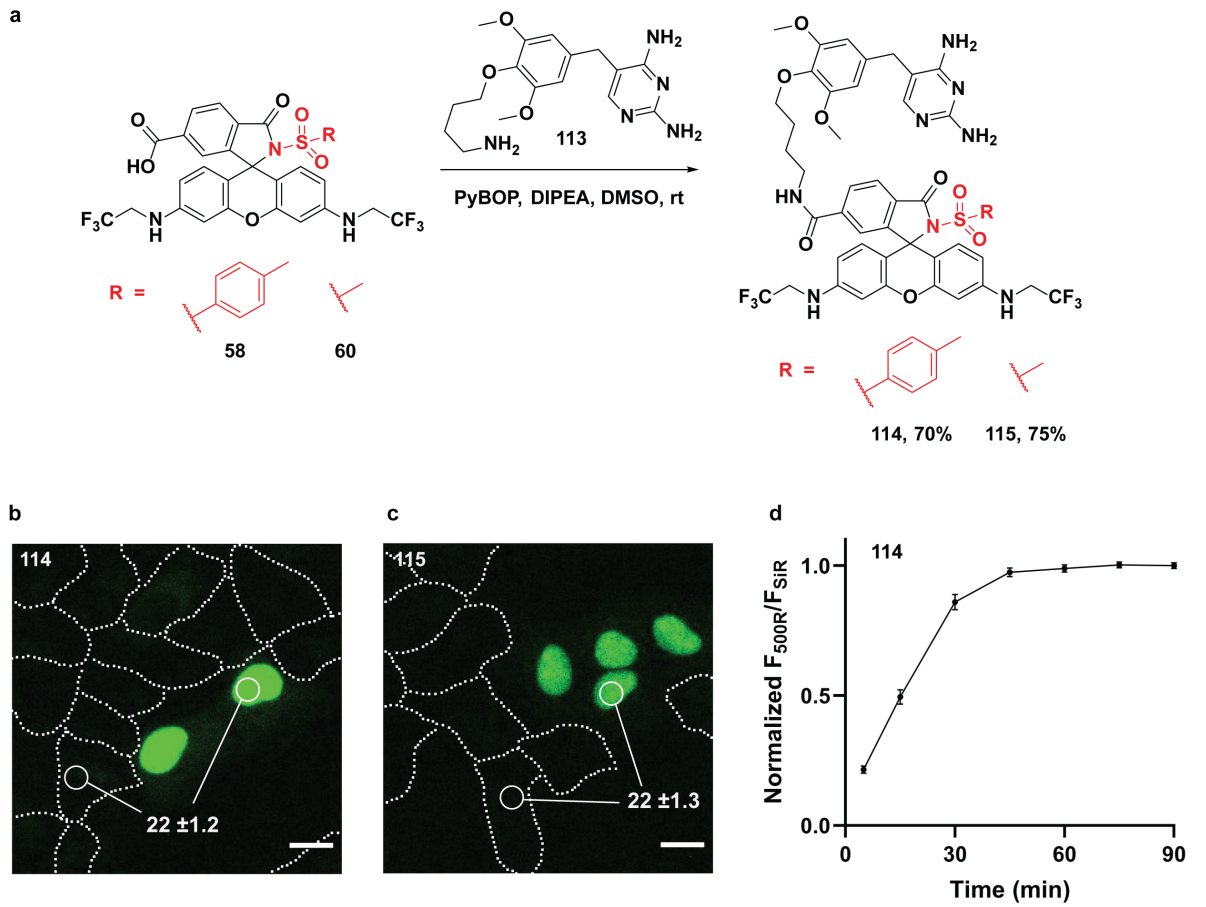

Figure 32: Synthesis, *in cellulo* fluorogenicity and labeling time experiments of rhodamine *500R* eDHFR probes (**114** and **115**). (a) Synthesis of **114** and **115**. (b) and (c) Evaluation of the fluorogenicity of **114** and **115** in live-cell,

no-wash confocal microscopy. Co-cultured U-2 OS FlpIn SNAP-eDHFR-NLS expressing cells and wild-type U-2 OS cells were labeled with SiR-BG (500 nM) overnight, and then labeled with **114** and **115** (200 nM) for 2.5 h. The numbers correspond to the fluorescence ratios F_{nuc}/F_{cyt}. F_{nuc}: Nuclear rhodamine *500R* signal in U-2 OS FlpIn SNAP-eDHFR-NLS expressing cells normalized to the nuclear signal of SiR-BG. F_{cyt}: Cytosolic rhodamine *500R* signal in wild-type U-2 OS cells. In total, 180 cells were examined from 2 independent experiments for each probe. Errors represent ± s.e.m. Wild-type U-2 OS cells are represented with dotted lines. Scale bars, 20 µm. (d) *In cellulo* eDHFR labeling with **114**. U-2 OS FlpIn SNAP-eDHFR-NLS expressing cells were prelabeled with SiR-BG (500 nM) overnight, and incubated with **114** (200 nM). The normalized ratio of rhodamine *500R* fluorescence to the fluorescence signal of SiR-BG was plotted over time. In total, 90 cells were examined from technical triplicates. Error bars show ± s.e.m.

In addition to rhodamine *500R*, it was examined if the modification of the *ortho*-carboxy group of SiR would yield a fluorogenic eDHFR probe, suitable for live-cell, no-wash microscopy. As the transformation of the *ortho*-carboxy group of SiR into an acyl 3,5-difluorobenzenesulfonamide led to the development of a highly fluorogenic HaloTag probe (**90**), eDHFR probe **116** was synthesized based on the same modification (Figure 33a). Therefore, **89** was coupled to TMP ligand **113** using PyBOP in the presence of DIPEA. The fluorogenicity of **116** was investigated in live-cell, no-wash confocal microscopy upon staining U-2 OS FlpIn SNAP-eDHFR-NLS expressing cells and wild-type U-2 OS cells. An outstanding fluorogenicity was observed for **116** *in cellulo* (F_{nuc}/F_{cyt} = 240) (Figure 33b and Supplementary Figure 13). In terms of brightness, preliminary microscopy experiments with U-2 OS FlpIn SNAP-eDHFR-NLS expressing cells showed a comparable nuclear signal intensity for **116** to the readily used SNAP-tag probe, SiR-BG.[72] Furthermore, the time period required to label eDHFR, expressed in the nucleus of U-2 OS cells, was measured for **116**. Saturation in fluorescence signal was detected after an incubation time of 30 minutes, which was significantly shorter than the *in cellulo* labeling time of the corresponding HaloTag probe (**90**) (Figures 23g and 33c). Both, the short *in cellulo* labeling time and the high fluorogenicity corroborate the applicability of **116** in live-cell, no-wash fluorescence microscopy.

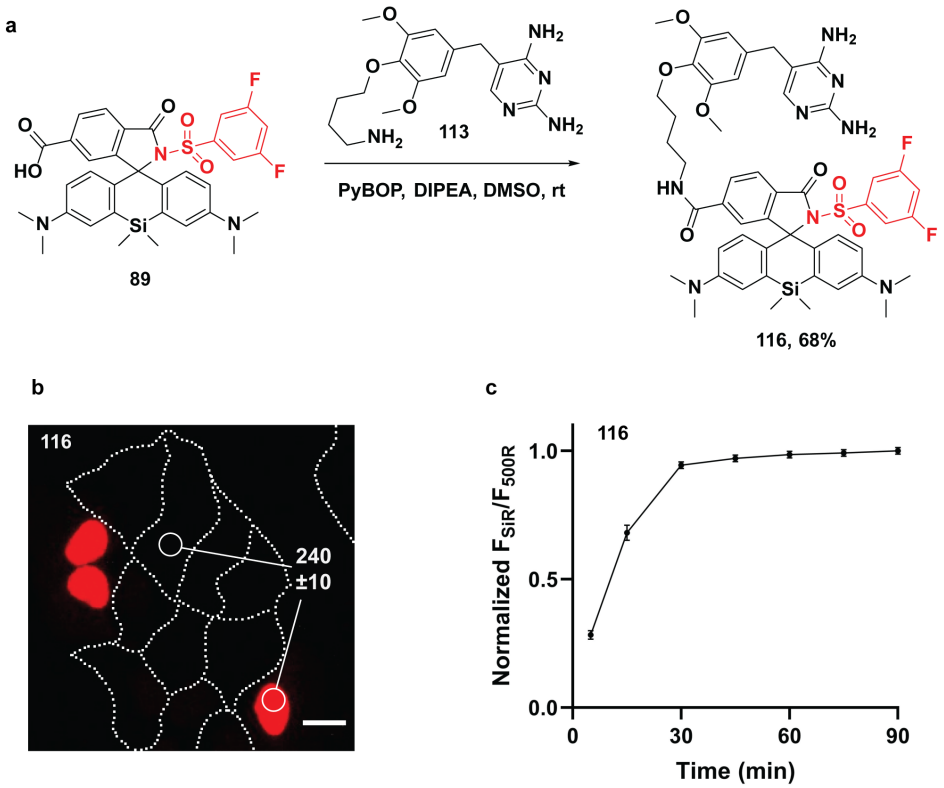

Figure 33: Synthesis, *in cellulo* fluorogenicity and labeling time experiments of SiR eDHFR probe (**116**). (a) Synthesis of **116**. (b) Evaluation of the fluorogenicity of **116** in live-cell, no-wash confocal microscopy. Co-cultured U-2 OS FlpIn SNAP-eDHFR-NLS expressing cells and wild-type U-2 OS cells were labeled with **81** (500 nM) overnight, and then labeled with **116** (200 nM) for 2.5 h. The numbers correspond to the fluorescence ratios F_{nuc}/F_{cyt}. F_{nuc}: Nuclear SiR signal in U-2 OS FlpIn SNAP-eDHFR-NLS expressing cells normalized to the nuclear signal of **81**. F_{cyt}: Cytosolic SiR signal in wild-type U-2 OS cells. In total, 180 cells were examined from 2 independent experiments. Errors represent ± s.e.m. Wild-type U-2 OS cells are represented with dotted lines. Scale bars, 20 µm. (c) *In cellulo* eDHFR labeling with **116**. U-2 OS FlpIn SNAP-eDHFR-NLS expressing cells were prelabeled with **81** (500 nM) overnight, and incubated with **116** (200 nM). The normalized ratio of SiR fluorescence to the fluorescence signal of **81** was plotted over time. In total, 90 cells were examined from technical triplicates. Error bars show ± s.e.m.

3.7.3. Fluorogenic Probes for HIV-1 Protease Labeling

Analogous to the labeling of tubulin, the aim was to directly and non-covalently label active HIV-1 protease (PR) by means of a targeting ligand. PR plays a crucial role in the replication cycle of HIV-1 and is essential for its infectivity.[206] In the late phase of HIV-1 replication, the polyprotein precursors assemble at the plasma membrane, where they are cleaved by PR and transformed into mature viral proteins.[207-208] In order to get a better understanding of the precise mechanism and kinetics of PR activation in relation to polyprotein assembly, a fluorogenic probe that specifically binds active PR was developed. Since this probe then would be applied in live-cell, no-wash microscopy experiments, a high fluorogenicity is required. To this end, probes based on previously reported highly fluorogenic carborhodamine spirolactams (**117** – **119**) conjugated to a derivative of the PR inhibitor ritonavir (**120**) were synthesized (Figure 34a).[85, 209-210] The synthesis started with the formation of allyl ester **93** as described in Section 3.5.2. Subsequently, the *ortho*-carboxy group of **93**

was transformed into an acyl cyanamide, acyl methylsulfonamide and acyl dimethylsulfamide followed by deprotection of the allyl ester by means of $Pd(PPh_3)_4$ and 1,3-dimethylbarbituric acid, delivering **117** – **119** in yields of 41% – 68% over three steps.[85] **117** – **119** were coupled to **120**, yielding PR probes **121** – **123** (Figure 34a).

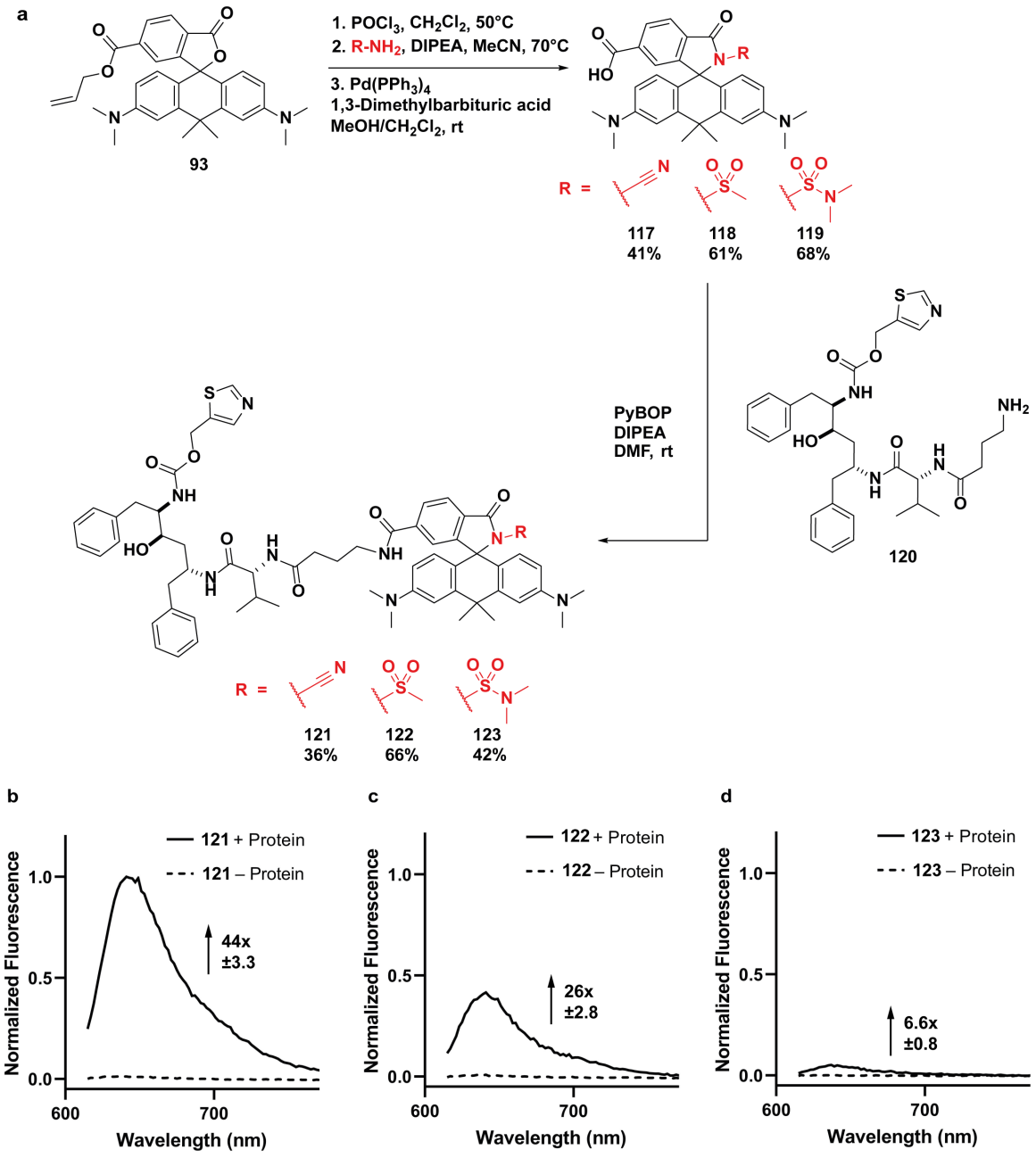

Figure 34: Synthesis and *in vitro* fluorogenicity experiments of carborhodamine HIV-1 protease probes **121 – 123**. (a) Synthesis of **121 – 123**. Carborhodamine derivative **119** was synthesized by Dr. Lu Wang. (b) – (d) Fluorescence emission spectra of **121** (b), **122** (c) and **123** (d) (500 nM) in the presence (+ Protein) and absence (- Protein) of HIV-1 protease (1.5 µM) normalized to the maximal emission of **121**. Representative spectra from 3 experiments. Errors show s.d. *In vitro* fluorogenicity experiments (b – d) were performed by Dr. Annica Flemming (University Hospital Heidelberg).

The fluorogenicity of **121** – **123** was examined *in vitro* by measuring the fluorescence increase upon addition of PR. The highest turn-on (44-fold) was observed for **121** (Figure 34b).

122 showed decreased signal intensity in the presence of PR, yielding a turn-on of 26-fold, and the lowest fluorescence increase was detected for **123** (6.6-fold) (Figures 34c and d). These observations could be explained by the fact that **121** – **123** show different positions of the spirocyclization equilibrium.[85] The less electron-withdrawing substituent at the spirolactam of **123** could cause an enhanced stabilization of the spirocyclic state. Consequently, a smaller shift in equilibrium toward the fluorescent form upon binding to PR was obtained with **123** compared to **121** and **122**. With respect to fluorescence microscopy applications, preliminary experiments indicated a higher fluorogenicity *in cellulo* for **122** compared to **121** and **123**. Further investigations regarding the formation of active PR using **122** are currently ongoing in the group of *B. Müller* (University Hospital Heidelberg).

4. The *Ortho*-Carboxy Group as Handle for Rhodamine Functionalization

While conversion of the *ortho*-carboxy group of rhodamines into different amides enables the systematic tuning of the spirocyclization equilibrium, it was investigated in the second part of this thesis if this modification could permit an increase in photostability and the development of zinc indicators. In the following sections, triplet state quenchers (TSQs) and a zinc ligand were conjugated to different fluorophore scaffolds via the *ortho*-carboxy moiety.

4.1. TSQ Rhodamine *500R* Conjugates

Previous reports demonstrated that the conjugation of the TSQs nitrobenzene and COT to cyanine dyes enhanced the photostability (Section 1.3.2.).[141-143] Herein, it was investigated if attaching these TSQs via the *ortho*-carboxy group to rhodamine *500R* could also lead to an increased photostability. Therefore, COT (**29**) was transformed into **124** in 86% yield by bromination using Br_2 followed by elimination with KO*t*Bu (Figure 35a).[141] Subsequently, the primary sulfonamide **125** was formed upon lithium-bromide exchange and reaction with the sulfinylamine reagent **126**.[211] **125** and 4-nitrobenzenesulfonamide were coupled to the *t*-Bu-protected rhodamine *500R* scaffold (**49**) by means of EDC and DMAP (Figure 35b).[194] Deprotection with TFA gave TSQ rhodamine *500R* conjugates **127** and **128** in yields of 64% and 70% over two steps. Finally, CA was coupled to the 6-carboxy moiety of **127** and **128** to obtain HaloTag probes **129** and **130** in 64% as well as 68% yield.

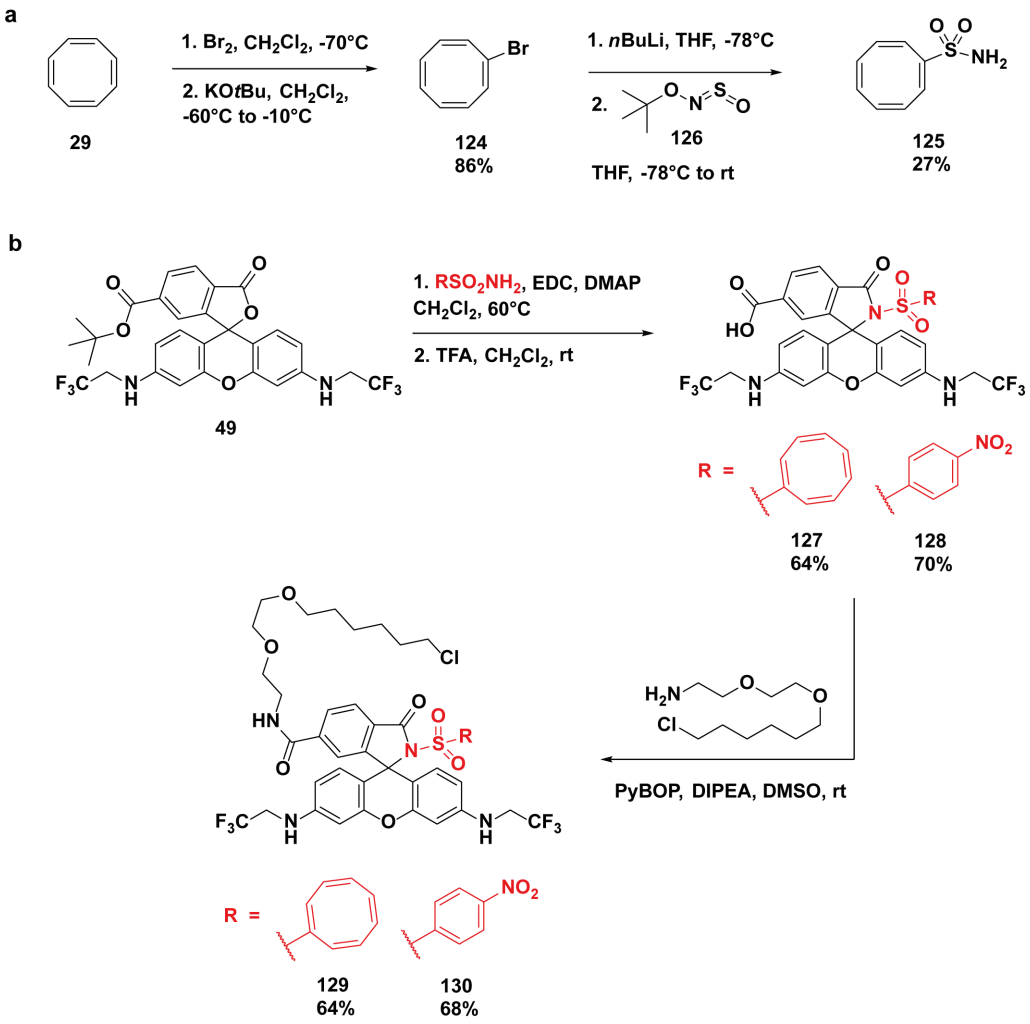

Figure 35: Synthesis of TSQ rhodamine *500R* conjugates (**129** and **130**). (a) Synthesis of COT sulfonamide **125**. (b) Synthesis of **129** and **130**.

In order to examine if the conjugation of COT and nitrobenzene to rhodamine *500R* led to an enhanced photostability, the photostability of **129** and **130** was tested *in vitro* and compared to the original rhodamine *500R* HaloTag probe (**67**) as well as the corresponding methylsulfonamide derivative (**77**). Furthermore, rhodamine *500R* COT conjugate **131**, which contains a longer linker between the fluorophore scaffold and COT than **129**, was included in this comparison (Figure 36a). HaloTag was labeled *in vitro* with **67**, **77**, **129**, **130** and **131** followed by irradiation with a light-emitting diode (LED). The decrease in maximal absorbance was measured after different time periods of illumination and was used to compare the photostability of the different HaloTag probes.[125] The most distinct decrease in maximal absorbance was detected for **67** and **129** (Figure 36b). **77** and **131** showed enhanced photostability, and **130** was identified as the HaloTag probe with the highest photostability.

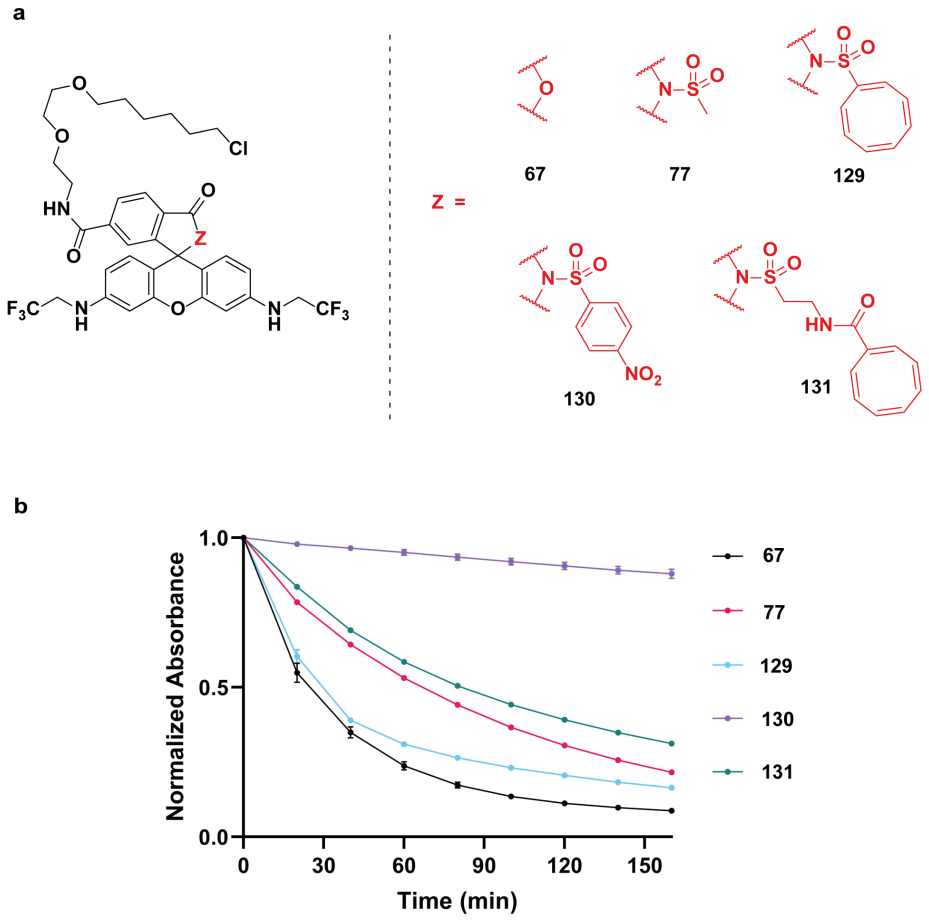

Figure 36: Photostability of rhodamine *500R* HaloTag probes **67**, **77**, **129**, **130** and **131**. (a) Chemical structures of **67**, **77**, **129**, **130** and **131**. **131** was synthesized by Dr. Mai Tran. (b) Normalized maximal absorbance of **67**, **77**, **129**, **130** and **131** (2.5 µM) in the presence of HaloTag (10 µM) after different durations of irradiation with a high power LED (525 nm, 2.4 W). The absorbance values were normalized to the maximal absorbance of the respective probe prior to irradiation. Error bars show ± s.d. from 3 experiments.

A potential explanation for the enhanced photostability of methylsulfonamide **77** compared to the original rhodamine *500R* HaloTag probe **67** could be their shifted position of

the spirocyclization equilibrium. Since the spirocyclic state was stabilized to a higher extent for **77**, a larger part of the fluorophore population would not absorb light of the LED. Thus, an enhanced protection from photobleaching would be obtained for **77**. Similar observations were reported for SiR derivatives where localization in a less polar environment favored the spirocyclic state and thereby led to an increased photostability.[110, 212] The comparable decrease in maximal absorbance of **131** to **77** indicates that conjugation of COT to rhodamine *500R* did not significantly increase the photostability. The enhanced photostability of **131** compared to **67** is potentially obtained due to a shift in spirocyclization equilibrium toward the spirocyclic state. Furthermore, shortening the linker length between the fluorophore scaffold and COT did not increase the photostability, as **129** showed a similar decrease in maximal absorbance as **67**. While the lowest decrease in maximal absorbance was observed for acyl 4-nitrobenzenesulfonamide derivative **130**, **130** also exhibited a significantly lower fluorescence quantum yield upon labeling HaloTag *in vitro* (Φ = 0.047) compared to other rhodamine *500R* acyl benzenesulfonamide HaloTag probes (**68** – **71** and **73** – **76**, Φ = 0.90 – 0.94) (Table 2). This finding indicates that the increased photostability is rather caused by the quenching of a fluorescent excited singlet state than of a triplet state. Previous reports, which described the fluorescence quenching of nitrobenzene derivatives, support this hypothesis.[213-214] Altogether, the TSQ rhodamine *500R* conjugates **129** – **131** either did not show a distinct increase in photostability compared to previously developed rhodamine *500R* HaloTag probes (**67** and **77**) or gave a significantly decreased fluorescence quantum yield.

4.2. Localizable and Fluorogenic Zinc Indicators

A wide variety of zinc indicators had been generated using the zinc ligand DPA (Section 1.5.1.).[126, 185, 188-189, 191-192] While previously developed DPA fluorophore conjugates rely on a reduced PeT quenching upon Zn^{2+} binding, it was herein investigated if a turn-on based on a combination of an alleviated PeT quenching and a shifted spirocyclization equilibrium could be obtained. To this end, a design principle was applied that had recently been used for the development of a family of localizable calcium indicators.[215] Thereby, DPA was conjugated via the *ortho*-carboxy group to the fluorophore such that coordination of Zn^{2+} would also lead to a shift in spirocyclization equilibrium toward the fluorescent state. This strategy was tested by modifying the fluorophore scaffolds TMR and rhodamine *500R*. The synthesis started with the formation of sulfamoyl chloride upon reaction of chlorosulfonyl isocyanate (**132**) and formic acid, followed by nucleophilic substitution with DPA to obtain DPA sulfonamide **133** in a yield of 54% (Figure 37a).[216] Coupling of **133** to the *ortho*-carboxy group of TMR derivative **99** and deprotection of the allyl ester gave **134** in 48% yield over two steps (Figure 37b).[85, 194] Subsequently, CA was coupled to the 6-carboxy moiety of **134**, forming HaloTag probe **135** in 76% yield. Analogous to the modification of TMR, the amidation of the *t*-Bu-protected rhodamine *500R* scaffold **49** was mediated by EDC and DMAP (Figure 37c).[194] Deprotection using TFA delivered **136**, which was coupled to CA to obtain HaloTag probe **137** in 75% yield.

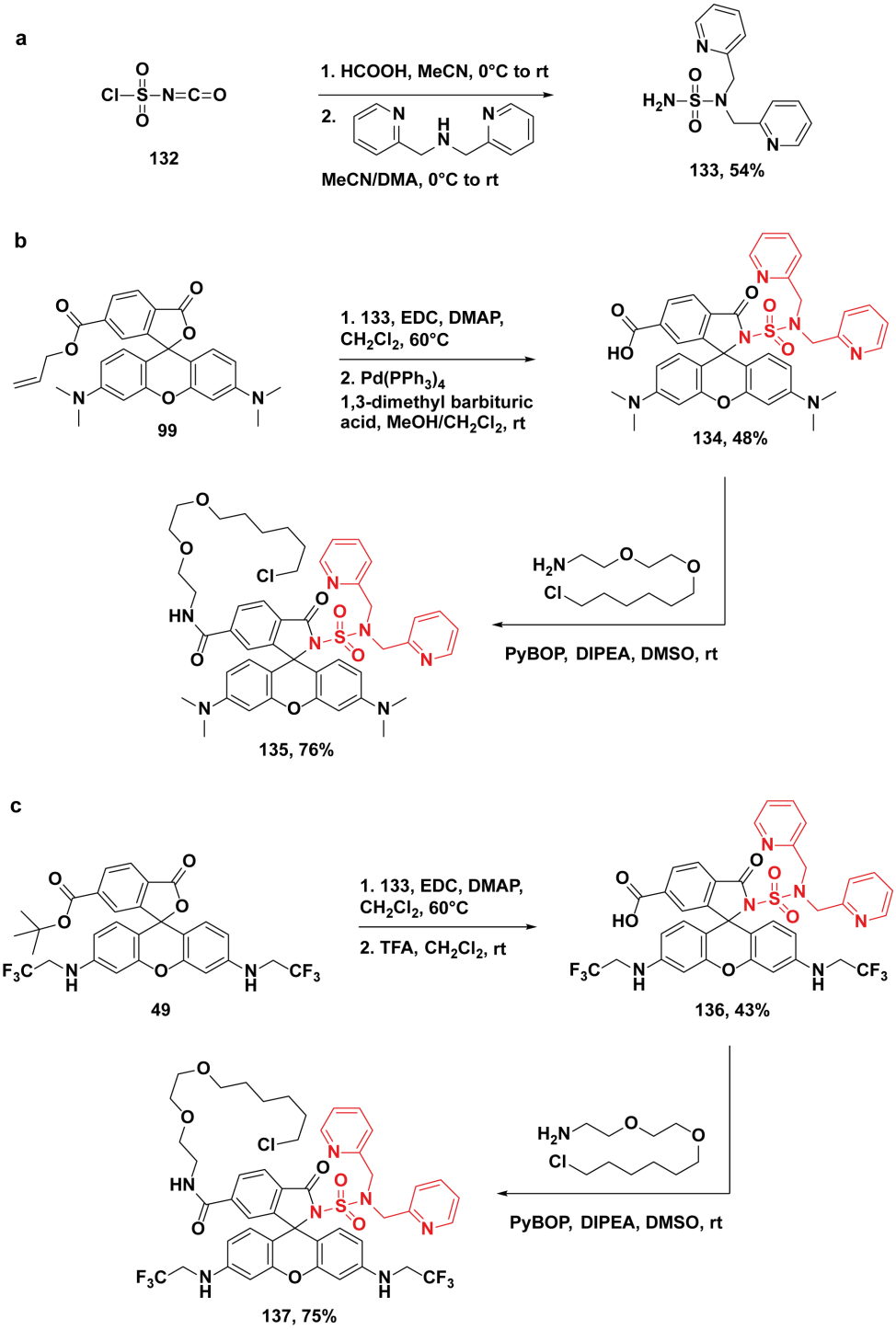

Figure 37: Synthesis of TMR and rhodamine *500R* DPA HaloTag probes **135** and **137**. (a) Synthesis of DPA sulfonamide **133**. (b) Synthesis of **135**. (c) Synthesis of **137**.

The increase in absorbance and fluorescence emission upon labeling HaloTag as well as binding of zinc was examined *in vitro* for **135** and **137**. Both, **135** and **137** showed small increases in absorbance and fluorescence emission after addition of Zn^{2+} in the absence of HaloTag (Figures 38a – e). Furthermore, a significant amount of background signal was observed for **135**. Comparing the maximal fluorescence emission in the presence and absence of HaloTag and Zn^{2+}, **135** showed a turn-on of less than 4-fold. With respect to **137**, this

fluorescence ratio was significantly higher ($F_{Protein,\ Zn2+}/F_0$ = 160). Measuring the fluorescence intensity after labeling HaloTag in the presence and absence of Zn^{2+}, a turn-on of 2.3-fold was detected for **137** and 1.3-fold for **135** ($F_{Protein,\ Zn2+}/F_{Protein}$). Furthermore, a titration experiment was performed to examine the affinity of **137** for Zn^{2+}, indicating a K_d of 119 µM (Figure 38f).

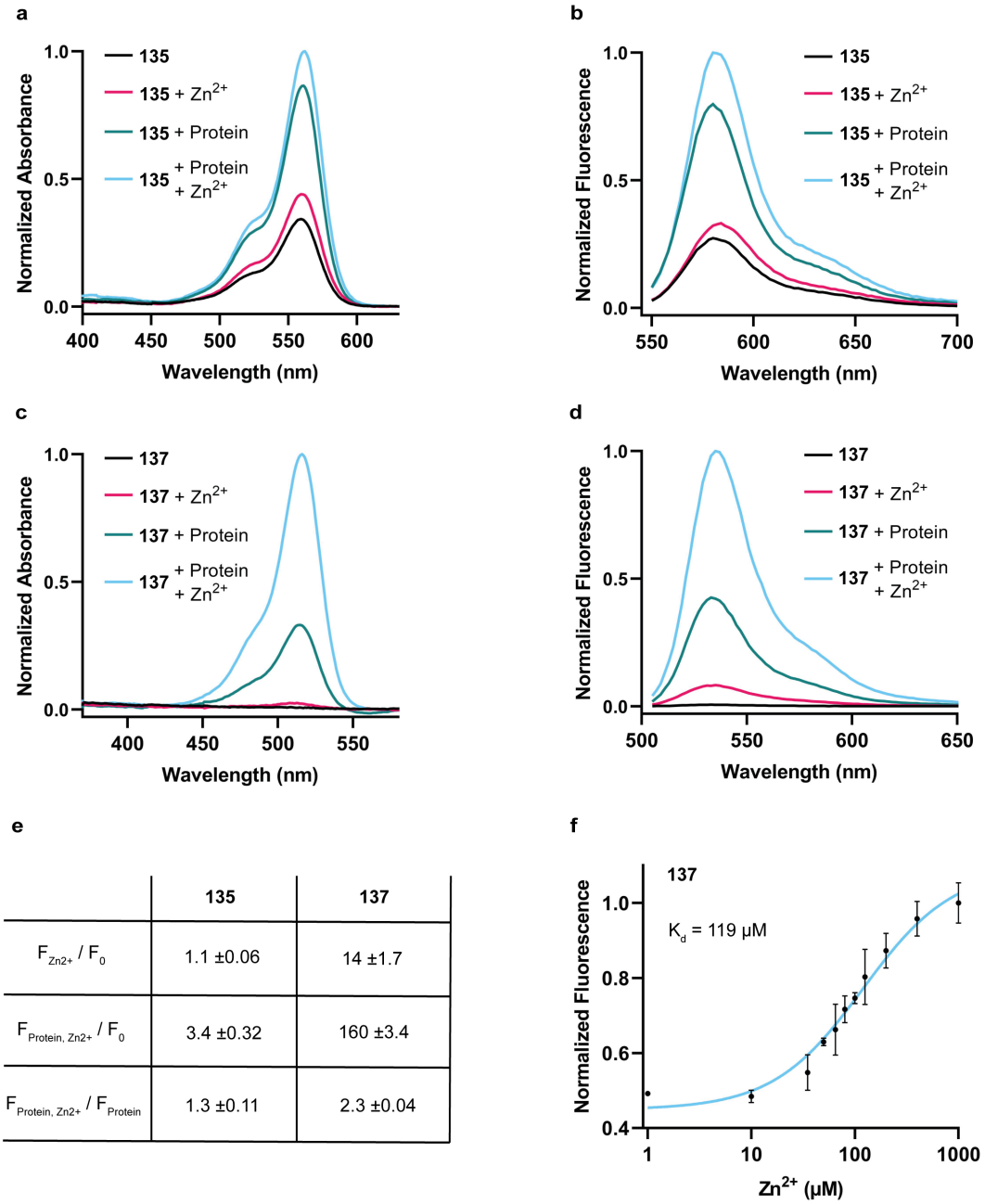

	135	137
F_{Zn2+} / F_0	1.1 ±0.06	14 ±1.7
$F_{Protein,\ Zn2+}$ / F_0	3.4 ±0.32	160 ±3.4
$F_{Protein,\ Zn2+}$ / $F_{Protein}$	1.3 ±0.11	2.3 ±0.04

Figure 38: *In vitro* fluorogenicity measurements and Zn^{2+} titration of TMR and rhodamine *500R* DPA HaloTag probes (**135** and **137**). (a) – (d) Normalized absorbance and fluorescence emission spectra of **135** (a, b) and **137** (c, d) in the presence and absence of HaloTag (+/- Protein) as well as $ZnSO_4$ (+/- Zn^{2+}). **135** and **137** (2.5 µM) were incubated for 2.5 h with or without HaloTag (10 µM) followed by addition of $ZnSO_4$ (1 mM). Representative spectra from 3 experiments. (e) Fluorescence ratios of **135** and **137**. Errors show s.d. from 3 experiments. F_0: Maximal fluorescence emission in the absence of HaloTag and $ZnSO_4$. F_{Zn2+}: Maximal fluorescence emission in the presence of $ZnSO_4$ (1 mM). $F_{Protein}$: Maximal fluorescence emission in the presence of HaloTag (10 µM). $F_{Protein,\ Zn2+}$: Maximal fluorescence emission in the presence of HaloTag (10 µM) and $ZnSO_4$ (1 mM). (f) Zn^{2+} titration. Normalized maximal fluorescence emission of **137** with different concentrations of $ZnSO_4$. **137** (1 µM) was incubated for 2.5 h with

HaloTag (5 µM) followed by addition of $ZnSO_4$ (different concentrations). Error bars show ± s.d. from 3 experiments and the blue line represents the fit.

The K_d determined for **137** (K_d = 119 µM) was significantly higher compared to the K_d of the previously reported DPA-based zinc indicators **46** (K_d = 0.7 nM) and **47** (K_d = 2.7 nM) (Section 1.5.1.).[184, 188] The lower affinity of **137** for Zn^{2+} could be explained by the electron-withdrawing character of the sulfonamide, which decreased the electron density of DPA. The comparable ratios in absorbance and fluorescence emission upon addition of Zn^{2+} indicate that the fluorescence turn-on of **135** and **137** originates from a shift in spirocyclization equilibrium and not from a reduced PeT quenching. This hypothesis was further corroborated since no distinct change in quantum yield was observed for **135** and **137** in the presence and absence of Zn^{2+}. A potential explanation for the absence of PeT quenching could be that the proximity of the electron-withdrawing sulfonamide to the DPA moiety decreases the energy level of the highest occupied molecular orbital (HOMO) of DPA, thereby disabling electron transfer to the HOMO of the fluorophore. Similar observations were reported regarding the fluorescence quenching of aminofluorescein derivatives.[188, 217] With respect to the observed turn-on upon addition of Zn^{2+}, the coordination of Zn^{2+} could reduce the electron-donating character of the DPA moiety, which leads to a shift in spirocyclization equilibrium of **135** and **137** toward the fluorescent state. A potential explanation for the higher $F_{Protein,\ Zn2+}/F_{Protein}$ ratio of **137** compared to **135** could be an enhanced stabilization of the spirocyclic state for rhodamine *500R* in comparison to TMR.[21, 85] Therefore, a smaller shift toward the fluorescent state was obtained after labeling HaloTag with **137**. Motivated by these findings, it was investigated if further stabilization of the spirocyclic state could increase the $F_{Protein,\ Zn2+}/F_{Protein}$ ratio. Since SiR shows a shift in spirocyclization equilibrium toward the spirocyclic state compared to rhodamine *500R* and TMR (Section 3.5.1.),[21, 28] a SiR-derived zinc indicator (**139**) was synthesized (Figure 39). To this end, **133** was coupled to the *ortho*-carboxy moiety of SiR derivative **88** via acyl chloride formation and nucleophilic acyl substitution, followed by deprotection of the allyl ester to obtain **138** in 54% yield over three steps.[85] Coupling of CA to the 6-carboxy group of **138** formed HaloTag probe **139** in a yield of 75%. However, preliminary *in vitro* fluorescence measurements with **139** showed a lower $F_{Protein,\ Zn2+}/F_{Protein}$ ratio compared to **137**. In summary, differently colored DPA fluorophore conjugates were synthesized with rhodamine *500R* derivative **137** exhibiting the highest turn-on upon zinc binding and a distinct fluorogenic character upon HaloTag labeling.

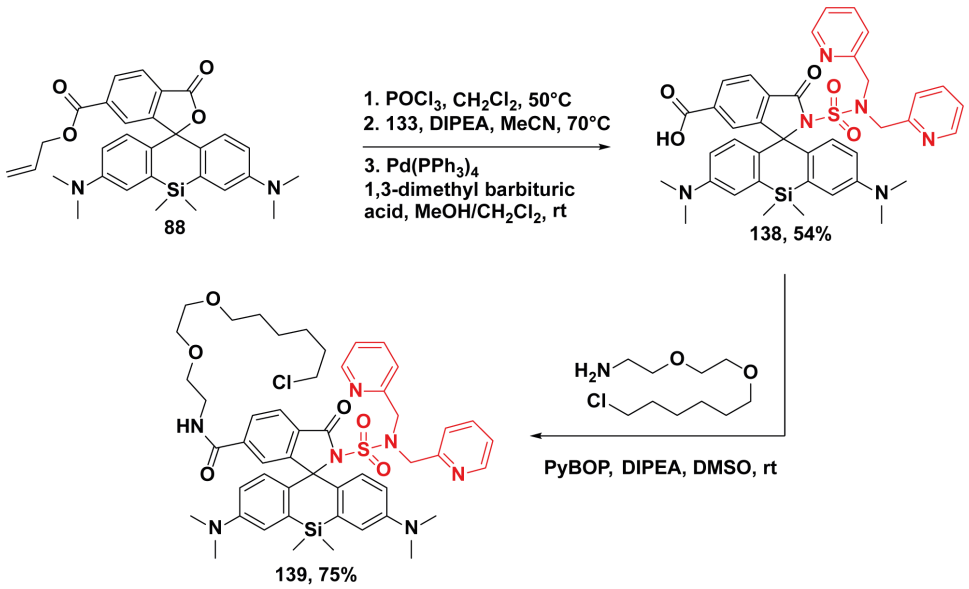

Figure 39: Synthesis of SiR DPA HaloTag probe **139**.

5. Conclusion and Outlook

5.1. Conclusion and Outlook - Systematic Tuning of the Spirocyclization Equilibrium of Rhodamines

A synthetic strategy was developed that allows tuning of the spirocyclization equilibrium of rhodamines with unprecedented accuracy and over a large range. This strategy comprises the transformation of the *ortho*-carboxy group into amides with different substituents and was first demonstrated on the fluorophore scaffold rhodamine *500R*. Introduction of substituted acyl benzenesulfonamides provides precise control over the spirocyclization equilibrium. Thereby, the fluorogenicity of rhodamine *500R* was specifically optimized for HaloTag and SNAP-tag labeling. The resulting rhodamine *500R* derivatives were examined *in vitro*, identifying **75** and **81** as the most fluorogenic HaloTag and SNAP-tag probe, respectively. Analogous to the trends found *in vitro*, **75** and **81** show largely enhanced signal-to-background ratios in live-cell no-wash microscopy compared to the original rhodamine *500R* HaloTag (**67**) and SNAP-tag (**79**) probe. Introduction of more electron-rich amides shifts the position of the spirocyclization equilibrium strongly toward the spirocyclic state and converted rhodamine *500R* into a spontaneously blinking dye (**85**) for SMLM. Subsequently, the synthetic strategy was extended to other differently colored rhodamine-based scaffolds. To this end, TMR was transformed into a spontaneously blinking dye (**101**) with suitable properties for SMLM. Moreover, the fluorogenicity of SiR and carborhodamine was optimized for HaloTag and SNAP-tag labeling, respectively. Both the resulting SiR-derived HaloTag probe **90** and carborhodamine-derived SNAP-tag probe **95** show a significantly enhanced fluorogenicity *in vitro* as well as *in cellulo* compared to the corresponding original dyes (**91** and **96**). Among all HaloTag and SNAP-tag probes developed in this work, **90** exhibits the highest fluorogenicity with a more than 1100-fold increase in fluorescence upon labeling HaloTag *in vitro* and a signal-to-background ratio in live-cell, no-wash microscopy of 150. In addition to their use in confocal microscopy, various HaloTag and SNAP-tag probes (**75**, **90** and **95**) were successfully applied in live-cell, no-wash STED imaging. In another extension of this strategy, it was set out to generate fluorogenic probes for HIV-1 protease, tubulin and eDHFR. HIV-1 protease probes were developed based on previously reported carborhodamine derivatives[85] and their fluorogenicity upon HIV-1 protease binding was demonstrated. Furthermore, various rhodamine *500R*-derived tubulin probes were synthesized and tested in live-cell, no-wash microscopy. Among the examined tubulin probes, the highest image quality was detected for **109** and **112**. With respect to eDHFR labeling, TMP conjugates of rhodamine *500R* (**114** and **115**) and SiR (**116**) were generated with suitable properties for live-cell, no-wash microscopy, including signal-to-background ratios of up to 240.

Previous strategies to tune the spirocyclization equilibrium include fluorination of the xanthene system, introduction of substituted azetidine rings onto the xanthene system and transformation of the *ortho*-carboxy group into an acyl cyanamide, acyl methylsulfonamide and acyl sulfamides (Section 1.4.1.).[21, 85, 127, 130, 150] Converting the *ortho*-carboxy group into substituted acyl benzenesulfonamides enables control over the spirocyclization equilibrium with enhanced accuracy compared to the aforementioned approaches, as demonstrated by means of dioxane-water titrations (Section 3.1.). While modifications of the xanthene system cause distinct changes in quantum yield, absorbance and emission wavelength,[21, 127, 130, 150] amidation of the *ortho*-carboxy group allows one to retain these crucial photophysical properties. Altering the xanthene system can also lead to an enhanced reactivity toward intracellular nucleophiles, as reported for electron deficient xanthenes.[151-153] Moreover, the amidation of the *ortho*-carboxy group is more concise and synthetically less challenging compared to most xanthene modifications (Sections 1.3.1. and 1.4.1.).[20, 127, 135-137] These findings corroborate the capacity of this novel synthetic strategy to develop suitable fluorescent probes. Nevertheless, previously reported approaches also generated highly fluorogenic dyes, which should be benchmarked against probes from this work. To this end, the increase in fluorescence upon binding to the target protein *in vitro* and the signal-to-background ratio in live-cell, no-wash microscopy could be measured. One could compare rhodamine *500R*-derived HaloTag (**75**) and tubulin (**109** and **112**) probes to MaP510-Halo as well as HaloTag and tubulin probes of JF_{526}.[85, 150] Furthermore, SiR-derived HaloTag probe **90** might be benchmarked against JF_{646} as well as JF_{635} and carborhodamine-derived SNAP-tag probe **95** against JF_{608} as well as JF_{585}.[121, 130] Analogous to **90**, transforming the *ortho*-carboxy group of SiR into an acyl 3,5-difluorobenzenesulfonamide also enabled the development of a highly fluorogenic eDHFR probe (**116**). Since SiR-based probes are widely used for different cellular targets and labeling systems, one might synthesize the corresponding acyl 3,5-difluorobenzenesulfonamide derivatives as well.[25-26, 72] Thereby, the effect of this structural modification on the fluorogenicity of SiR could be explored in various labeling systems. In another extension, this modification might be used to generate a fluorogenic SiR-derived HIV-1 protease probe. In addition to the carborhodamine derivatives described in Section 3.7.3., the resulting probe would further expand the spectrum of colors and would be compatible with commonly used laser lines.[218]

Results from this thesis and from previous studies show that the spirocyclization equilibrium of rhodamine derivatives is highly environmentally sensitive. Shifts in spirocyclization equilibrium were observed due to changes in pH and solvent polarity (Section 3.1.).[72, 146-147] Furthermore, the difference in brightness upon HaloTag or SNAP-tag labeling is also attributed to this environmental sensitivity (Sections 3.2. and 3.3.).[85-86] As a future

experiment, one could therefore investigate the effect of different cellular environments on the fluorogenicity. To this end, HaloTag could be expressed in various cellular compartments followed by labeling with our library of rhodamine *500R*-derived HaloTag probes (**67** – **78**) and analyzing the signal-to-background ratio. This systematic study would indicate if different positions of the spirocyclization equilibrium are required to obtain high fluorogenicity in different cellular compartments. The investigation of various cellular environments could also be of interest regarding the eDHFR probes since eDHFR labeling is dependent on the native cofactor NADPH, and different NADPH concentrations were reported for different cellular compartments.[94-96] In terms of a potential future application, eDHFR probes could be tested in STED microscopy. The high intensity of the stimulating laser applied in STED imaging causes photobleaching of fluorophores,[19] and the non-covalent binding to eDHFR could offer the possibility to replace bleached dyes with fluorescent ones.[219-220] Thus, a high number of frames could be recorded in live-cell STED microscopy prior to bleaching. Another rational for an enhanced photostability with a transiently binding dye could be based on a shift in spirocyclization equilibrium, thereby forming a large population of molecules that reside in their spirocyclic state. These molecules would not absorb photons of the excitation and stimulating laser and would therefore be protected from photobleaching.[110, 212] eDHFR probes **114** – **116** show low background signal intensities in live-cell, no-wash microscopy. However, rhodamine *500R* derivatives **114** and **115** exhibit relatively poor brightness upon binding to eDHFR (Section 3.7.2.). Thus, additional modifications of the *ortho*-carboxy group should be employed to shift the spirocyclization equilibrium slightly toward the fluorescent state. This might increase the signal intensity upon eDHFR labeling while retaining low background signal. One could therefore transform the *ortho*-carboxy group of rhodamine *500R* into a slightly more electron-deficient amide compared to acyl *p*-toluenesulfonamide **114** and acyl methylsulfonamide **115**.

To date, the fluorogenicity of the different HaloTag, SNAP-tag and eDHFR probes was analyzed using imaging experiments under protein over-expression. In terms of future experiments, the fluorogenicity could be explored at lower expression levels, such as in cells with endogenously expressed protein fusions.[199, 203, 221] These experiments would allow one to compare the performance of fluorogenic probes on more demanding targets and, thereby, would provide an enhanced evaluation of their applicability in future biological experiments.

With respect to the spontaneously blinking HaloTag probes **85** and **101**, their applicability in SMLM was demonstrated visualizing nuclear pores and microtubules in fixed cells. However, their use in live-cell SMLM has not yet been tested. As discussed in Sections 3.4. and 3.5.3., a potential limitation for the application of **85** and **101** in live-cell SMLM could be their relatively short on-time. In terms of a future modification, the pendant phenyl ring of **85** and **101** could be fluorinated to shift the spirocyclization equilibrium toward the fluorescent state and, thus, to

increase the on-time.[127] Furthermore, with HEtetTFER and HM-JF_{526}, two spontaneously blinking dyes with similar excitation and emission wavelengths to **85** already exist.[150, 166] Their performance in SMLM might be compared by measuring the localization precision as well as the photon count of the corresponding HaloTag probes under the same experimental conditions as for **85**. In order to further expand the existing palette of probes for SMLM, one might extend the use of spontaneously blinking spirolactams to other labeling systems than HaloTag. Analogous to what was observed for fluorogenic HaloTag and SNAP-tag probes (Sections 3.2. and 3.3.),[85-86] different labeling systems could also require a different position of the spirocyclization equilibrium to develop spontaneously blinking probes for SMLM. Consequently, further modifications of the spirolactam or the pendant phenyl ring would be necessary.

In conclusion, a general synthetic strategy was developed and applied to convert various rhodamine derivatives into probes optimized for different microscopy applications and labeling systems. It is expected that these fluorescent probes will serve as powerful tools in future examinations of cellular structures and biological processes. Furthermore, it is envisioned that the generality of this strategy will allow the conversion of numerous other rhodamine derivatives into probes that specifically match the requirements of the respective imaging experiment and labeling system. Altogether, this chapter demonstrates how the chemical modification of fluorophores can extend the existing toolbox for fluorescence microscopy.

5.2. Conclusion and Outlook - The *Ortho*-Carboxy Group as Handle for Rhodamine Functionalization

In this chapter, it was investigated if the modification of the *ortho*-carboxy group enables an enhanced photostability as well as the development of fluorogenic and targetable zinc indicators. TSQ rhodamine *500R* conjugates were synthesized, and their photostability was examined *in vitro*. While COT derivatives **129** and **131** did not show a distinct increase in photostability compared to previously developed rhodamine *500R* probes (**67** and **77**), a significantly enhanced photostability was observed for acyl 4-nitrobenzenesulfonamide **130**. However, the low quantum yield of **130** hampers its applicability as a fluorescent probe. This also indicates that the increased photostability of **130** results from quenching of an excited singlet state and not of a triplet state. With respect to future probe design, differently substituted acyl nitrobenzenesulfonamide derivatives could be synthesized to alter the energy level of the quenching moiety, thereby allowing interaction with the triplet state. In terms of COT rhodamine derivatives, the linker length and the electronic properties of COT might be altered. Previous studies applied such modifications to optimize triplet state quenching of cyanine dyes.[138, 142] In addition to the photostability, the effect of TSQ conjugation on the phototoxicity might be examined. To this end, **129** and **131** could be tested in long-term, live-cell microscopy, since these experiments require probes with a minimal phototoxicity.[143]

With the aim of developing differently colored localizable zinc indicators, the Zn^{2+} ligand DPA was coupled to the *ortho*-carboxy moiety and the HaloTag ligand CA to the 6-carboxy group of various rhodamine-based scaffolds. Among the resulting probes (**135**, **137** and **139**), the highest fluorescence turn-on upon addition of Zn^{2+} was observed for rhodamine *500R* derivative **137**. Additionally, HaloTag labeling also gave an increase in fluorescence emission, yielding an overall turn-on ($F_{Protein,\ Zn2+}/F_0$) of 160-fold for **137** *in vitro*. The high fluorogenicity of **137** could be favorable in terms of no-wash microscopy applications. Therefore, the fluorogenicity, cell-permeability and the turn-on upon Zn^{2+} binding should be tested *in cellulo*. Furthermore, the relatively low binding affinity of **137** for Zn^{2+} (K_d = 119 µM) could be useful regarding the examination of biological processes involving high Zn^{2+} concentrations.[193, 222] The probe design used in this study was based on the idea to obtain an increased fluorescence intensity by coordination of Zn^{2+} due to a shift in spirocyclization equilibrium as well as a reduced PeT quenching. However, no PeT quenching was observed for **135**, **137** and **139**, and a smaller fluorescence turn-on upon Zn^{2+} binding was detected compared to previously reported localizable zinc indicators.[191-192] With respect to future probe developments, an aliphatic linker could be installed between DPA and the sulfonamide. This modification could increase the energy level of the HOMO of DPA, thereby obtaining PeT quenching and an enhanced turn-on in the presence of Zn^{2+}.

The results presented in this chapter indicate the large potential, which the modification of the *ortho*-carboxy group offers for the development and the optimization of fluorescent probes. However as described above, further efforts will be necessary to fully exploit this potential.

6. Experimental Procedures

6.1. *In Vitro* and *In Cellulo* Experiments

Absorbance, Emission, Excitation Spectra and Quantum Yield Measurements

Fluorophores for spectroscopy were prepared as stock solutions (1.5 – 10 mM) in DMSO and diluted such that the DMSO concentration did not exceed 0.5% (v/v). Absorption spectra were recorded on a V-770 spectrophotometer (Jasco) in a Quartz cuvette. Emission and excitation spectra were measured on a Spark® microplate reader (Tecan) using a 96-well plate (Thermo Scientific Nunc with optical bottom). All measurements were performed at 25°C. Maximum absorption wavelength (λ_{abs}) and maximum emission wavelength (λ_{em}) were determined in 50 mM HEPES buffer containing 50 mM NaCl (pH 7.3) or in 10 µM PBS buffer (pH 2.0, 3.0). Absolute fluorescence quantum yields were recorded on a Quantaurus-QY spectrometer (model C11347, Hamamatsu). Measurements were carried out using diluted samples (A ≈ 0.1). The reported values for molar extinction coefficient (ε) and quantum yield (Φ) are averages (*N* = 3).

For absorbance, emission, excitation spectra and quantum yield measurements upon labeling of HaloTag and SNAP-tag, SNAP-Halo protein was diluted into HEPES buffer (50 mM HEPES, 50 mM NaCl, pH 7.3) to a final concentration of 5 µM. Fluorescent probes were diluted therein to a final concentration of 2.5 µM. The obtained mixtures were incubated until a consistent absorbance signal was observed (2.5 h). As a control experiment, the fluorescent probes (2.5 µM) were incubated together with 0.1% SDS in 50 mM HEPES buffer containing 50 mM NaCl (pH 7.3). The reported values are averages (*N* = 3).

For absorbance and emission spectra upon HaloTag and Zn^{2+} binding, SNAP-Halo protein was diluted into 100 µL HEPES buffer (50 mM HEPES, 50 mM NaCl, pH 7.3) to a concentration of 20 µM. Fluorescent probes were diluted therein to a concentration of 5 µM. The obtained mixtures were incubated until a consistent absorbance signal was observed (2.5 h). Subsequently, 100 µL of a $ZnSO_4$ (2 mM) solution in HEPES buffer (50 mM HEPES, 50 mM NaCl, pH 7.3) was added. Final concentrations: SNAP-Halo protein (10 µM), $ZnSO_4$ (1 mM) and fluorescent probes (2.5 µM). For conditions without Zn^{2+}, TPEN (10 µM) was added. The reported values are averages (*N* = 3).

Emission spectra with PR probes **121** – **123** were recorded by Dr. Annica Flemming (University Hospital Heidelberg). Solutions of 0.05% NP-40 in PBS were prepared and filtered using a nitrocellulose filter (0.22 µm pore size) prior to use. Measurements were performed at a final concentration of 500 nM probe. Where indicated, 1.5 µM of purified recombinant protein

(HIV-1 PR (wt)) was added to 500 nM probe in 0.05% NP-40/PBS. The reported values are averages (*N* = 3).

Absorbance Measurements in Dioxane-Water Mixtures

Dioxane-water mixtures containing 0%, 10%, 20%, 30%, 40%, 50%, 60%, 70%, 80%, 90% and 100% anhydrous dioxane (v/v) were prepared. The fluorophores were diluted in these dioxane-water mixtures to 5 µM and the absorbance spectra were measured on a Spark® microplate reader (Tecan) using a 96-well plate (Greiner Bio-One) at 25°C. The maximal absorbance values of the different fluorophores were normalized to the maximal absorbance of the corresponding *ortho*-carboxy derivative (rhodamine 500R: **48**, carborhodamine: **92**, SiR: **87**) in 100% water. The normalized absorbance values were plotted against the dielectric constants of the different dioxane-water mixtures.[195] The D_{50} values were calculated as the dielectric constant which yields 50% of the maximal absorbance of the corresponding ortho-carboxy derivative in 100% water. The reported values are averages (*N* = 3).

Absorbance Measurements at various pH

The pH values of PBS (10 µM) solutions were adjusted by addition of NaOH or HCl to 2.0, 2.5, 3.0, 3.5, 4.0, 5.0, 6.0, 7.0 and 8.0 using a pH meter. The fluorophores were diluted in these PBS mixtures to 5 µM and the absorbance spectra were measured on a Spark® microplate reader (Tecan) using a 96-well plate (Thermo Scientific Nunc with optical bottom) at 25°C. The maximal absorbance values of the different fluorophores were normalized to the maximal absorbance of the corresponding *ortho*-carboxy derivative (rhodamine *500R*: **48**, TMR: **98**) in PBS (10 µM, pH 7.0). The reported values are averages (*N* = 3).

***In Vitro* Photostability Measurements**

SNAP-Halo protein was diluted into HEPES buffer (50 mM HEPES, 50 mM NaCl, pH 7.3) to a final concentration of 10 µM. Fluorescent probes were diluted therein to a final concentration of 2.5 µM. The obtained mixtures were incubated until a consistent absorbance signal was observed (2.5 h). The measurements were performed in 1.5 mL quartz cuvettes (Hellma Analytics) on a JASCO V770 spectrophotometer with a Peltier element (PAC743R) at 25°C. The samples were irradiated directly inside the spectrophotometer during the ongoing experiment by means of an external high power LED (SOLIS-525C, THORLABS, 525 nm, 2.4 W). Absorbance spectra were measured every 20 min until 160 min after initiation of the irradiation.

Zn^{2+} Titration

HaloTag protein was diluted into 100 µL HEPES buffer (100 mM HEPES, I (KNO_3) = 0.1, pH 7.4) to a concentration of 10 µM. **137** was diluted therein to a concentration of 2 µM. The obtained mixtures were incubated until a consistent absorbance signal was observed (2.5 h). Subsequently, 100 µL of $ZnSO_4$ solutions of different concentrations in HEPES buffer (100 mM HEPES, I (KNO_3) = 0.1, pH 7.4) were added. Final concentrations: HaloTag protein (5 µM), $ZnSO_4$ (1 mM, 400 µM, 200 µM, 125 µM, 100 µM, 80 µM, 65 µM, 50 µM, 35 µM, 10 µM, 1 µM) and **137** (1 µM). Emission spectra were measured on a Spark® microplate reader (Tecan) using a 96-well plate (Thermo Scientific Nunc with optical bottom) at 25°C. The reported values are averages (*N* = 3). The resulting fluorescence (F) data were fit to equation (1).[193]

$$(1)\ F = \frac{F_{min}\,K_d + F_{max}[Zn^{2+}]}{K_d + [Zn^{2+}]}$$

Cell Culture, Labeling and Fixation

Wild-type U-2 OS cells, U-2 OS FlpIn Halo-SNAP-NLS[85], U-2 OS FlpIn SNAP-eDHFR, U-2 OS Vimentin-HaloTag[203] (cultured by Jasmine Hubrich) and Vimentin-SNAP-tag[203] (cultured by Jasmine Hubrich) expressing cells were cultured in Dulbecco's Modified Eagle Medium (DMEM, 4.5 g/L glucose) supplemented with 10% (v/v) fetal bovine serum (FBS), GlutaMAX and sodium pyruvate (all Life Technologies) in a humidified 5% CO_2 incubator at 37°C. Cells were split every 2 – 4 days or at confluency and regularly tested for mycoplasma contamination. Cells were seeded on 10-well glass bottom plates (Greiner Bio-One), 96-well glass bottom plates (Eppendorf) or glass coverslips 1 – 2 days before imaging. Prior to imaging, cells were labeled (see respective experiments for details) in imaging medium (phenol-red free DMEM supplemented with GlutaMAX, sodium pyruvate and 10% (v/v) FBS (all Life Technologies)).

The following cell culture, labeling and fixation procedures were performed by Aline Tschanz and Dr. Philipp Hoess (EMBL Heidelberg). U-2 OS Nup96-Halo cells[199] were cultured in DMEM (Gibco) growth medium containing 1x MEM NEAA (Gibco), 1x GlutaMAX (Gibco) and 10% (v/v) fetal bovine serum (Gibco). Stable U-2 OS Flp-In T-Rex Cep41-Halo cells[201] were cultured in DMEM/F-12 (Invitrogen) growth medium containing 10% (v/v) fetal bovine serum (Gibco) and 1x ZellShield (Minerva Labs). Both cell lines were cultured in a humidified incubator at 37°C and 5% CO_2 and split every 2 – 3 days to ensure confluency at approximately 60 – 70%. 2 days before imaging, cells were seeded at 60 – 70% confluency onto 24 mm round glass coverslips (No. 1.5H, Marienfeld). The coverslips were previously cleaned by overnight incubation in a MeOH:HCl mixture (50:50) while stirring. Then, they were rinsed with water until

a neutral pH was reached and placed in a laminar flow hood overnight to dry, followed by a 30 min UV sterilization step. In the case of the U-2 OS Cep41-Halo cells, expression was induced by addition of 1 µg mL^{-1} doxycycline (Sigma-Aldrich) to the growth medium. After 24 h, cells where incubated overnight at 37°C and 5% CO_2 in their respective growth medium containing 1 µM dye (**85** or **101**), followed by a 2 h incubation in growth medium without dye. The samples were then prefixed at rt for 30 s in 2.4% (w/v) formaldehyde (FA) in PBS. Permeabilization was achieved by incubating the sample at rt in 0.4% (v/v) Triton X-100 (Sigma) in PBS for 3 min before completing the fixation process at rt for 30 min in 2.4% (w/v) FA in PBS. The fixation was subsequently quenched by incubating the coverslips in 100 mM NH_4Cl (Sigma) in PBS. Sample preparation was finalized by washing three times in PBS for 5 min each.

Single-Molecule Assay

The single-molecule assay was performed by Dr. Philipp Hoess (EMBL Heidelberg). Sample preparation was adapted from a previously reported procedure.[201] Biotin-coated coverslips (MicroSurfaces) were glued on a glass slide (Carl Roth) with 2 strips of double-sided tape and fixed with two component silicone (Twinsil, Picodent, Wipperfürth, Germany) creating a ≈ 5 mm wide channel. The slides were made in batch and stored at -20°C. For attaching single molecules, the respective dyes (2.5 µM of **85** or **101** in DMSO) and BG-biotin (5 µM; SNAP-Biotin™, NEB) were coupled to a SNAP-Halo fusion protein (5 µM) in PBS for 1 h at rt. In parallel, 30 µL of 0.2 mg mL^{-1} streptavidin (Life Technologies) in PBS were flushed through the channel and incubated for 10 min. Then, the coverslip was washed with 200 µL PBS and 100 µL of diluted labeled protein solution (0.8 µL of a 1:10 dilution in 100 µL; final concentration: 4 nM) were flushed through the channel. After 10 min of incubation, the channel was washed with 400 µL of PBS. The sample was sealed with two component silicone (Twinsil, Picodent, Wipperfürth, Germany) and mounted for imaging.

Confocal Microscopy

Confocal microscopy was performed on a Leica DMi8 microscope (Leica Microsystems) equipped with a Leica TCS SP8 X scanhead, a SuperK white light laser, a HC PL APO CS2 20.0 x/0.75 objective, HC PL APO 63 x/1.47 oil objective or a HC PL APO 40.0 x/1.10 water objective and an incubator with CO_2 as well as temperature control (Life Imaging Services, 5%, 37°C). While for imaging of the nucleus the 20 x/0.75 objective was used, for tubulin imaging 63 x/1.47 and 40.0 x/1.10 objectives were applied.

Time-Dependent Intracellular HaloTag, SNAP-tag and eDHFR Labeling

For rhodamine *500R*-derived HaloTag probes (**67** – **71** and **73** – **78**), U-2 OS FlpIn Halo-SNAP-NLS expressing cells were pre-labeled with 500 nM of SiR-BG (overnight) and washed with imaging medium. Directly after labeling with 200 nM of **67** – **71** and **73** – **78**, images were recorded every minute over 45 min. Microscopy conditions: λ_{ex}: 510 nm and 645 nm, detection range: 520 – 600 nm and 655 – 720 nm, image size: 580.31 µm x 580.31 µm, pixel size: 567 nm, pixel dwell time: 0.86 µs. Mean values of rhodamine *500R* fluorescence of regions of interest (ROIs) within the nuclei were divided by the mean values of SiR fluorescence at the different time points. >51 cells were examined for each probe from technical triplicates (from 3 different wells).

For rhodamine *500R*-derived SNAP-tag probes (**79** – **81**), U-2 OS FlpIn Halo-SNAP-NLS expressing cells were pre-labeled with 200 nM of SiR-CA (overnight). Directly after labeling with 500 nM of **79** – **81**, z-stacks (stack size: 20 µm, number of steps: 30) were recorded every 0.5 h over 6 h. Microscopy conditions: λ_{ex}: 510 nm and 645 nm, detection range: 520 – 600 nm and 655 – 720 nm, image size: 580.31 µm x 580.31 µm, pixel size: 567 nm, pixel dwell time: 0.86 µs. The summed stacks were analyzed. Mean values of rhodamine *500R* fluorescence of ROIs within the nuclei were divided by the mean values of SiR fluorescence at the different time points. In total, 90 cells were examined for each probe in 2 independent experiments.

For rhodamine *500R*-derived eDHFR probes (**114** and **115**), U-2 OS FlpIn SNAP-eDHFR-NLS expressing cells were pre-labeled with 500 nM of SiR-BG (overnight). Directly after labeling with 200 nM of **114** and **115**, z-stacks (stack size: 20 µm, number of steps: 30) were recorded every 15 min over 90 min. Microscopy conditions: λ_{ex}: 510 nm and 645 nm, detection range: 520 – 600 nm and 655 – 720 nm, image size: 580.31 µm x 580.31 µm, pixel size: 567 nm, pixel dwell time: 0.86 µs. The summed stacks were analyzed. Mean values of rhodamine *500R* fluorescence of ROIs within the nuclei were divided by the mean values of SiR fluorescence at the different time points. In total, 90 cells were examined for each probe from technical triplicates (from 3 different wells).

For carborhodamine-derived SNAP-tag probes (**95** and **96**), U-2 OS FlpIn Halo-SNAP-NLS expressing cells were pre-labeled with 200 nM of **75** (overnight). Directly after labeling with 500 nM of **95** and **96**, z-stacks (stack size: 20 µm, number of steps: 30) were recorded every 0.5 h over 5 h. Microscopy conditions: λ_{ex}: 510 nm and 615 nm, detection range: 520 – 600 nm and 625 – 700 nm, image size: 580.31 µm x 580.31 µm, pixel size: 567 nm, pixel dwell time: 0.86 µs. The summed stacks were analyzed. Mean values of carborhodamine fluorescence of ROIs within the nuclei were divided by the mean fluorescence values of **75** at

the different time points. In total, 90 cells were examined for each probe from technical triplicates (from 3 different wells).

For SiR-derived HaloTag probes (**90** and **91**), U-2 OS FlpIn Halo-SNAP-NLS expressing cells were pre-labeled with 500 nM of **81** (overnight) and washed with imaging medium. Directly after labeling with 500 nM of **90** and **91**, z-stacks (stack size: 20 µm, number of steps: 30) were recorded every 15 min over 2 h. For **91**, further z-stacks were measured 3 and 8 min after labeling. Microscopy conditions: λ_{ex}: 510 nm and 645 nm, detection range: 520 – 600 nm and 655 – 720 nm, image size: 580.31 µm x 580.31 µm, pixel size: 567 nm, pixel dwell time: 0.86 µs. The summed stacks were analyzed. Mean values of SiR fluorescence of ROIs within the nuclei were divided by the mean fluorescence values of **81** at the different time points. In total, 90 cells were examined for each probe from technical triplicates (from 3 different wells).

For SiR-derived eDHFR probe (**116**), U-2 OS FlpIn SNAP-eDHFR-NLS expressing cells were pre-labeled with 500 nM of **81** (overnight) and washed with imaging medium. Directly after labeling with 200 nM of **116**, z-stacks (stack size: 20 µm, number of steps: 30) were recorded every 15 min over 90 min. Microscopy conditions: λ_{ex}: 510 nm and 645 nm, detection range: 520 – 600 nm and 655 – 720 nm, image size: 580.31 µm x 580.31 µm, pixel size: 567 nm, pixel dwell time: 0.86 µs. The summed stacks were analyzed. Mean values of SiR fluorescence of ROIs within the nuclei were divided by the mean fluorescence values of **81** at the different time points. In total, 90 cells were examined from technical triplicates (from 3 different wells).

Evaluating the Fluorogenicity - Live-Cell, No-Wash Confocal Microscopy

For rhodamine *500R*-derived HaloTag probes (**67** – **78**), co-cultured U-2 OS FlpIn Halo-SNAP-NLS expressing cells and wild-type U-2 OS cells (1:1) were pre-labeled with 500 nM of SiR-BG (overnight) and washed with imaging medium. 2.5 h after labeling with 200 nM **67** – **78**, z-stacks (stack size: 30 µm, number of steps: 40) were recorded. Microscopy conditions: λ_{ex}: 510 nm and 645 nm, detection range: 520 – 600 nm and 655 – 720 nm, image size: 446.02 µm x 446.02 µm, pixel size: 436 nm, pixel dwell time: 0.86 µs. The summed stacks were analyzed to measure the ratios between nuclear signal (F_{nuc}) and cytosolic background signal (F_{cyt}) of **67** – **78**. F_{nuc}: Mean values of rhodamine *500R* fluorescence of ROIs within the nuclei of U-2 OS FlpIn Halo-SNAP-NLS expressing cells normalized to the SiR fluorescence. F_{cyt}: Mean values of rhodamine *500R* fluorescence of ROIs within the cytosol of wild-type U-2 OS cells. Bright field images were used to locate wild-type U-2 OS cells. In total, 180 cells (90 U-2 OS FlpIn Halo-SNAP-NLS expressing cells and 90 wild-type U-2 OS cells) were examined from 3 independent experiments for each probe.

For rhodamine *500R*-derived eDHFR probes (**114** and **115**), co-cultured U-2 OS FlpIn SNAP-eDHFR-NLS expressing cells and wild-type U-2 OS cells (1:1) were pre-labeled with 500 nM of SiR-BG (overnight) and washed with imaging medium. 2.5 h after labeling with 200 nM of **114** and **115**, z-stacks (stack size: 30 µm, number of steps: 40) were recorded. Microscopy conditions: λ_{ex}: 510 nm and 645 nm, detection range: 520 – 600 nm and 655 – 720 nm, image size: 580.31 µm x 580.31 µm, pixel size: 567 nm, pixel dwell time: 0.86 µs. The summed stacks were analyzed as described above. In total, 180 cells (90 U-2 OS FlpIn SNAP-eDHFR-NLS expressing cells and 90 wild-type U-2 OS cells) were examined from 2 independent experiments for each probe.

For rhodamine *500R*-derived SNAP-tag probes (**79** and **81**), co-cultured U-2 OS FlpIn Halo-SNAP-NLS expressing cells and wild-type U-2 OS cells (1:1) were pre-labeled with 200 nM of SiR-CA (overnight) and washed with imaging medium. 5 h after labeling with 500 nM of **79** and **81**, z-stacks (stack size: 3 µm, number of steps: 40) were recorded. Microscopy conditions: λ_{ex}: 510 nm and 645 nm, detection range: 520 – 600 nm and 655 – 720 nm, image size: 580.31 µm x 580.31 µm, pixel size: 567 nm, pixel dwell time: 0.86 µs. The summed stacks were analyzed as described above. In total, 180 cells (90 U-2 OS FlpIn Halo-SNAP-NLS expressing cells and 90 wild-type U-2 OS cells) were examined from 2 independent experiments for each probe.

For carborhodamine-derived SNAP-tag probes (**95** and **96**), co-cultured U-2 OS FlpIn Halo-SNAP-NLS expressing cells and wild-type U-2 OS cells (1:1) were pre-labeled with 200 nM of **75** (overnight) and washed with imaging medium. 4 h after labeling with 500 nM of **95** and **96**, z-stacks (stack size: 30 µm, number of steps: 40) were recorded. Microscopy conditions: λ_{ex}: 510 nm and 615 nm, detection range: 520 – 600 nm and 625 – 700 nm, image size: 580.31 µm x 580.31 µm, pixel size: 567 nm, pixel dwell time: 0.86 µs. The summed stacks were analyzed as described above. In total, 180 cells (90 U-2 OS FlpIn Halo-SNAP-NLS expressing cells and 90 wild-type U-2 OS cells) were examined from 2 independent experiments for each probe.

For SiR-derived HaloTag probes (**90** and **91**), co-cultured U-2 OS FlpIn Halo-SNAP-NLS expressing cells and wild-type U-2 OS cells (1:1) were pre-labeled with 500 nM of **81** (overnight) and washed with imaging medium. 2.5 h after labeling with 500 nM of **90** and **91**, z-stacks (stack size: 30 µm, number of steps: 40) were recorded. Microscopy conditions: λ_{ex}: 510 nm and 645 nm, detection range: 520 – 600 nm and 655 – 720 nm, image size: 580.31 µm x 580.31 µm, pixel size: 567 nm, pixel dwell time: 0.86 µs. The summed stacks were analyzed as described above. In total, 180 cells (90 U-2 OS FlpIn Halo-SNAP-NLS expressing cells and 90 wild-type U-2 OS cells) were examined from 2 independent experiments for each probe.

For SiR-derived eDHFR probe (**116**), co-cultured U-2 OS FlpIn SNAP-eDHFR-NLS expressing cells and wild-type U-2 OS cells (1:1) were pre-labeled with 500 nM of **81** (overnight) and washed with imaging medium. 2.5 h after labeling with 200 nM of **116**, z-stacks (stack size: 30 µm, number of steps: 40) were recorded. Microscopy conditions: λ_{ex}: 510 nm and 645 nm, detection range: 520 – 600 nm and 655 – 720 nm, image size: 580.31 µm x 580.31 µm, pixel size: 567 nm, pixel dwell time: 0.86 µs. The summed stacks were analyzed as described above. In total, 180 cells (90 U-2 OS FlpIn SNAP-eDHFR-NLS expressing cells and 90 wild-type U-2 OS cells) were examined from 2 independent experiments.

Evaluating the Performance of Tubulin Probes

Wild-type U-2 OS cells were labeled with 500 nM of **106** – **109** as well as 5 µM verapamil for 3 h. Subsequently, z-stacks (stack size: 15 µm, number of steps: 35) were recorded. Microscopy conditions: λ_{ex}: 510 nm, detection range: 520 – 600 nm, image size: 145 µm x 145 µm, pixel size: 95 nm, pixel dwell time: 0.58 µs.

For the co-staining experiment, wild-type U-2 OS cells were labeled with 500 nM of **106** and **109** as well as 5 µM verapamil for 1 h followed by addition of SiR-tubulin (final concentration: 500 nM). After incubation for 2 h, z-stacks (stack size: 6 µm, number of steps: 15) were recorded. Microscopy conditions: λ_{ex}: 510 nm and 645 nm, detection range: 520 – 600 nm and 655 – 720 nm, image size: 73.9 µm x 73.9 µm, pixel size: 72 nm, pixel dwell time: 1.58 µs.

For comparison of **109** and **112**, wild-type U-2 OS cells were labeled with 500 nM of **109** and **112** as well as 5 µM verapamil for 3 h. Subsequently, z-stacks (stack size: 4 µm, number of steps: 20) were recorded. Microscopy conditions: λ_{ex}: 510 nm, detection range: 520 – 600 nm, image size: 82.9 µm x 82.9 µm, pixel size: 41 nm, pixel dwell time: 0.43 µs.

SMLM

SMLM experiments were performed by Aline Tschanz and Dr. Philipp Hoess (EMBL Heidelberg). SMLM data were acquired on a custom-built widefield setup described previously.[223-224] Briefly, the free output of a commercial laser box (LightHub, Omicron-Laserage Laserprodukte) equipped with Luxx 488 and Cobolt 561 lasers were coupled into a square multi-mode fiber (catalog no. M103L05, Thorlabs). The fiber was agitated as described previously.[225] The output of the fiber was magnified by an achromatic lens and focused into the sample to homogeneously illuminate an area of about 700 µm^2. The laser was guided through a laser cleanup filter (390/482/563/640 HC Quad, AHF) to remove fluorescence generated by the fiber. The emitted fluorescence was collected through a high numerical aperture (NA) oil immersion objective (HCX PL APO 160×/1.43 NA, Leica), filtered by a 525/50 (catalog no.

FF03-525/50-25, Semrock) bandpass filter (for imaging of **85**) or by a 600/60 (catalog no. NC458462, Chroma) bandpass filter (for imaging of **101**) on an EMCCD camera (Evolve 512, Photometrics). The z focus was stabilized by an infrared laser that was totally internally reflected off the coverslip onto a quadrant photodiode, which was coupled into closed-loop feedback with the piezo objective positioner (Physik Instrumente). The microscope hardware and data acquisition were handled via Micro-Manager 2.0 using custom-written software.[224, 226] Coverslips containing prepared samples were placed into a custom-built sample holder and 500 µL PBS were added. To image **85**, an excitation intensity at 488 nm of 17 kW cm^{-2} was used. For **101**, an excitation intensity at 561 nm of 23 kW cm^{-2} was used. The exposure time was 10 ms in both cases.

STED Microscopy

STED microscopy experiments were performed under the supervision of Dr. Elisa D'Este. STED imaging of **75** and **90** was performed on an Abberior easy3D STED/RESOLFT QUAD scanning expert line microscope (Abberior Instruments GmbH, Göttingen, Germany) built on a motorized inverted microscope IX83 (Olympus, Tokyo, Japan). The microscope is equipped with pulsed STED lasers at 595 nm and 775 nm, 355 nm, 405 nm, 485 nm, 561 nm, and 640 nm excitation lasers, and with 488 nm and 405 nm RESOLFT lines. **75** was super-resolved using λ_{ex} 485 nm and λ_{STED} 595 nm, while **90** was super-resolved using λ_{ex} 640 nm the λ_{STED} 775 nm depletion line. Spectral detection was performed with avalanche photodiodes (APD) in the following spectral windows: 505 – 580 nm (**75**), 650 – 770 nm (**90**). Images were acquired with a 100x/1.40 UPlanSApo Oil immersion objective lens (Olympus). Pixel size was 33 nm (**75**) and 25 nm (**90**). Laser powers and dwell times were optimized for each sample.

STED imaging of **95** was performed on an Abberior STED QUAD scanning expert line (Abberior Instruments GmbH, Göttingen, Germany) built on a motorized inverted microscope IX83 (Olympus, Tokyo, Japan). The microscope is equipped with pulsed STED lasers at 655 nm and 775 nm, with 520 nm, 561 nm, 640 nm, and multiphoton (Chameleon Vision II, Coherent, Santa Clara, USA) excitation lasers. Spectral detection was performed with two avalanche photodiodes (APD) in the spectral window 580 – 750 nm. Images were acquired with a 60x/1.42 Oil immersion objective lens (Olympus). Pixel size was 30 nm. Laser powers and dwell times were optimized for each sample.

Image Processing and Data Analysis

Images were processed by means of ImageJ/Fiji unless otherwise stated.[227-228] Imaging data in Figure 28 were smoothed with a 1-pixel low pass Gaussian filter in Imspector (Abberior

Instruments GmbH, Göttingen Germany). The line profiles represented in Figure 28 were measured with 2-pixel wide lines in ImageJ/Fiji before smoothing.

SMLM data were fitted and analyzed by Aline Tschanz and Dr. Philipp Hoess (EMBL Heidelberg). As previously described, a custom-written, open-source super-resolution microscopy analysis platform $SMAP_{21}$ in MATLAB (Mathworks, 2020b) was used.[229] The software is available at github.com/jries/SMAP. The localization precision (σ_{LP}) was calculated by means of equation (2) where a represents the pixel size, N the detected number of emitter photons, s the standard deviation of the point-spread function (PSF) and b the photon background.[48]

$$(2)\ \sigma_{LP}^2 = \frac{s^2 + \frac{a^2}{12}}{N}\left(\frac{16}{9} + \frac{8\pi\left(s^2 + \frac{a^2}{12}\right)b^2}{Na^2}\right)$$

The x, y positions were corrected for residual drift by a custom algorithm based on redundant cross-correlation. Localizations persistent over consecutive frames (detected within 35 nm from one another and with a maximum gap of one dark frame) were merged into one localization by calculating the weighted average of x and y positions and the sums of photons per localization and background photons. Localizations were filtered by the localization precision (0–20 nm) to exclude dim localizations, and by the fitted size of the PSF (0–150 nm laterally) to exclude localizations that were detected out-of-focus. Additionally, poorly fitted localizations were excluded if their log-likelihood was smaller than -1. Super-resolution images were constructed with every localization rendered as a two-dimensional elliptical Gaussian with a width proportional to the localization precision (factor 0.4). The reported average photon counts per localization were calculated based on these merged and filtered localizations.

For the quantification of microtubule width, a perpendicular line profile from a 250 nm long section of the microtubule was constructed. Subsequently, a Gaussian distribution was fitted (bin width 2 nm). *fwhm* was then calculated using equation (3) where s_G is the standard deviation of the Gaussian fit. Results were plotted in a boxplot (Supplementary Figure 6, N = 20 line profiles per dye).

$$(3)\ fwhm = 2\sqrt{2ln2}s_G \approx 2.36s_G$$

To estimate the duty cycle of **85** and **101**, SMLM data from the single-molecule assay were acquired, and individual molecules were clustered using the density-based spatial clustering of applications with noise algorithm (parameters: k = 3 and neighborhood radius eps = 20 nm).[230] Peaks were counted in single clusters that were separated by at least 10 frames and clusters with less than 2 peaks were discarded. Then, for each fluorophore in a

cluster the average on-and off-times per detection were determined, and the duty cycle was calculated by dividing the mean of the average on-time by the sum of the mean of the average on-time and the mean of the average off-time. In parallel, the duty cycle for each cluster was calculated by dividing the respective on-time by the sum of the on-and off-times per detection and then the median of this distribution was determined.

6.2. Chemical Synthesis and Characterization

General Information, Materials and Equipment

All chemical reagents and anhydrous solvents for synthesis were purchased from commercial suppliers (Sigma-Aldrich, TCI, Alfa Aesar, Acros, Merck, Carl Roth, Santa Cruz Biotechnology, Thermo Fisher, Cortex Organics, AAT Bioquest, AbMole BioScience) and were used without further purification or distillation. Reactions were monitored by thin-layer chromatography (TLC) performed on TLC-aluminum sheets (Silica gel 60 F254, Merck) or liquid chromatograph-mass spectrometry (LCMS-2020, Shimadzu). The analytical reversed-phase LC-MS was equipped with an SPD-20AV UV-VIS photodiode array detector for product visualization on a C18 1.9 µm, 2.1 x 50 mm column (Supelco) applying 10 – 95% MeCN/H_2O, linear gradient with constant 0.1% v/v formic acid additive in a 6 min run with 1 mL/min flow rate. Concentration under reduced pressure was performed by rotary evaporation at 40°C. Preparative RP-HPLC was performed on an UltiMate 3000 system (Thermo Fisher Scientific) on a C18 5 µm, 10 x 250 mm column (Supelco, flow rate 4 mL/min) or a C18 5 µm, 21.2 x 250 mm column (Supelco, flow rate 8 mL/min), solvent A: 0.1% v/v TFA or formic acid in H_2O, solvent B: MeCN. The compounds purified by Prep-HPLC were lyophilized on a lyophilizer (Christ) equipped with a vacuum pump (Vacuubrand). Flash column chromatography was performed with silica gel (230 – 400 mesh, Silicycle) on an automated purification system (Biotage Isolera One). Yields refer to purified, dried and spectroscopically pure compounds. ^{1}H and ^{13}C nuclear magnetic resonance (NMR) spectra were recorded on a Bruker DPX 400 at room temperature. Chemical shifts (δ-values) are reported in ppm, spectra were calibrated relative to the residual proton chemical shifts ($CDCl_3$, δ = 7.26; DMSO-d_6, δ = 2.50; MeOD-d_4, δ = 3.31) and carbon chemical shifts ($CDCl_3$, δ = 77.16; DMSO-d_6, δ = 39.52; MeOD-d_4, δ = 49.00) of the solvents, multiplicity is reported as follows: s = singlet, d = doublet, t = triplet, q = quartet, m = multiplet or unresolved and coupling constant J in Hz.[231] High-resolution mass spectra (HRMS) were measured on a maXis II™ ETD with electron spray ionization (ESI) (Bruker).

Synthetic Procedures

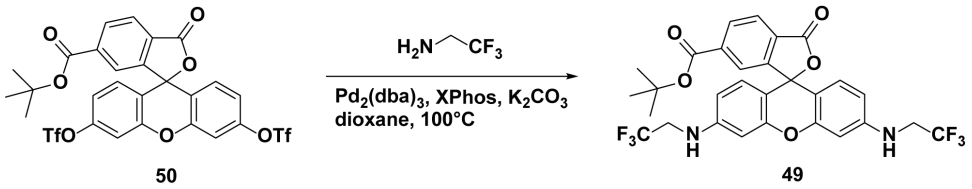

50 49

***Tert*-butyl 3-oxo-3',6'-bis((2,2,2-trifluoroethyl)amino)-3*H*-spiro[isobenzofuran-1,9'-xanthene]-6-carboxylate (49): 50** was synthesized by Bettina Réssy according to a previously reported procedure.[121] A *Schlenk* flask was dried with a heat gun *in vacuo* prior to dissolution of **50** (50.0 mg, 71.8 µmol, 1.0 eq) in dry 1,4-dioxane (2.5 mL). Potassium carbonate (47.6 mg, 345 µmol, 4.8 eq), 2,2,2-trifluoroethylamine (250 µL, 3.13 mmol, 43.6 eq), tris(dibenzylideneacetone)dipalladium (13.1 mg, 14.4 µmol, 0.20 eq) and 2-(dicyclohexylphosphino)-2',4',6'-triisopropylbiphenyl (10.3 mg, 21.5 µmol, 0.30 eq) were added. The reaction mixture was heated to 100°C and stirred at this temperature for 3 h. Subsequently, the mixture was allowed to cool down to rt and the solvent was evaporated under reduced pressure. The crude product was purified by flash column chromatography (CH_2Cl_2/MeOH 10:0 to 10:1) to give **49** (30.7 mg, 51.6 µmol, 72%) as a red solid.

TLC: R_f = 0.61 (SiO_2, CH_2Cl_2/MeOH 9:1).

^{1}H NMR (400 MHz, DMSO-d_6) δ 8.20 (d, J = 8.0, 1H), 8.09 (d, J = 8.0 Hz, 1H), 7.58 (s, 1H), 6.79 (t, J = 6.8 Hz, 2H), 6.65 (d, J = 1.8 Hz, 2H), 6.52 – 6.46 (m, 4H), 4.05 – 3.96 (m, 4H), 1.50 (s, 9H).

^{13}C NMR (101 MHz, DMSO-d_6) δ 167.9, 163.7, 152.5, 152.2, 150.0, 137.5, 130.7, 130.1, 128.7, 125.7 (q, $^1J_{CF}$ = 281 Hz), 125.2, 123.9, 110.2, 106.5, 97.9, 84.6, 82.3, 43.6 (q, $^2J_{CF}$ = 32 Hz), 27.6.

HRMS (ESI) Exact mass calculated for $C_{29}H_{24}N_2O_5F_6$ $[M+H]^+$: 595.1662, found: 595.1663.

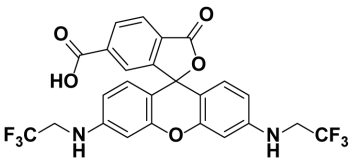

3-Oxo-3',6'-bis((2,2,2-trifluoroethyl)amino)-3H-spiro[isobenzofuran-1,9'-xanthene]-6-carboxylic acid (48): 49 (4.00 mg, 6.73 µmol, 1.0 eq) was dissolved in TFA/CH_2Cl_2 (1:4, 0.6 mL) and stirred at rt for 2 h. After the solvent was evaporated, the crude product was dissolved in DMSO (0.8 mL) and purified by preparative HPLC (8 mL/min, 30% to 90% MeCN/H_2O (0.1% TFA) in 55 min) to obtain **48** (3.26 mg, 6.06 µmol, 90%) as a red solid.

^{1}H NMR (400 MHz, DMSO-d_6) δ 8.21 (d, J = 8.0 Hz, 1H), 8.09 (d, J = 7.9 Hz, 1H), 7.63 (s, 1H), 6.80 – 6.75 (m, 2H), 6.65 (s, 2H), 6.52 – 6.47 (m, 4H), 4.05 – 3.96 (m, 4H).

^{13}C NMR (101 MHz, DMSO-d_6) δ 168.5, 166.5, 153.1, 152.6, 150.4, 137.6, 131.2, 130.4, 129.1, 126.2 (q, $^1J_{CF}$ = 281 Hz), 125.6, 124.8, 110.6, 107.1, 98.4, 84.9, 44.1 (q, $^2J_{CF}$ = 33 Hz).

HRMS (ESI) Exact mass calculated for $C_{25}H_{16}F_6N_2O_5$ $[M+H]^+$: 539.1036, found: 539.1036.

General Procedure A for 51:

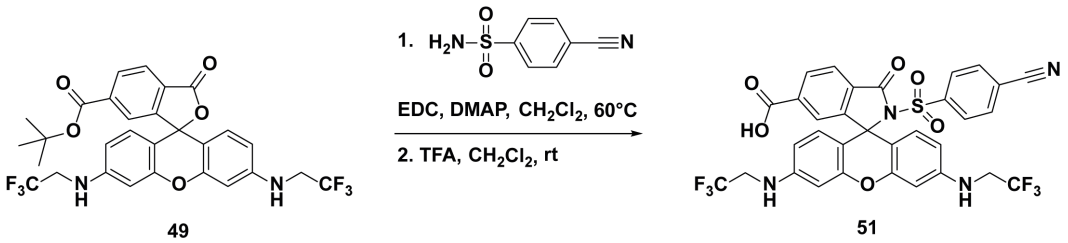

2-((4-Cyanophenyl)sulfonyl)-3-oxo-3',6'-bis((2,2,2-trifluoroethyl)amino)spiro[iso-indoline-1,9'-xanthene]-6-carboxylic acid (51): A solution of **49** (4.00 mg, 6.73 µmol, 1.0 eq), 4-cyanobenzenesulfonamide (6.15 mg, 33.7 µmol, 5 eq), 1-(3-dimethylaminopropyl)-3-ethylcarbodiimide hydrochloride (5.16 mg, 26.9 µmol, 4 eq) and 4-dimethylaminopyridine (3.29 mg, 26.9 µmol, 4 eq) in CH_2Cl_2 (0.6 mL) was heated to 60°C and stirred at this temperature for 12 h in a sealed tube. H_2O (1 mL) was added and the aqueous layer was extracted with CH_2Cl_2 (3x). The combined organic layers were dried over $MgSO_4$, filtered and concentrated. The residue was dissolved in TFA/CH_2Cl_2 (1:4, 0.6 mL) and stirred at rt for 2 h. After the solvent was evaporated, the crude product was dissolved in DMSO (0.8 mL) and purified by preparative HPLC (8 mL/min, 30% to 90% MeCN/H_2O (0.1% TFA) in 55 min) to obtain **51** (3.93 mg, 5.59 µmol, 83%) as a red solid.

^{1}H NMR (400 MHz, DMSO-d_6) δ 8.10 (dd, J = 8.1, 1.4 Hz, 1H), 7.98 (d, J = 8.0 Hz, 1H), 7.89 – 7.85 (m, 2H), 7.45 – 7.40 (m, 3H), 6.72 (t, J = 6.9 Hz, 2H), 6.65 (d, J = 2.2 Hz, 2H), 6.34 (dd, J = 8.7, 2.3 Hz, 2H), 6.27 (d, J = 8.7 Hz, 2H), 4.06 – 3.97 (m, 4H).

^{13}C NMR (101 MHz, DMSO-d_6) δ 165.9, 164.9, 152.5, 152.3, 149.6, 149.5, 142.0, 137.6, 132.7, 130.4, 130.2, 128.7, 128.2, 125.8 (q, $^1J_{CF}$ = 281 Hz), 124.8, 124.5, 117.4, 116.3, 109.6, 106.8, 98.2, 69.6, 43.8 (q, $^2J_{CF}$ = 32 Hz).

HRMS (ESI) Exact mass calculated for $C_{32}H_{20}F_6N_4O_6S$ $[M+H]^+$: 703.1081, found: 703.1077.

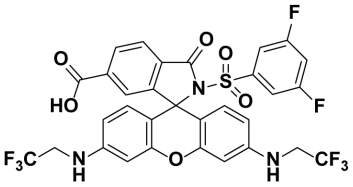

2-((3,5-Difluorophenyl)sulfonyl)-3-oxo-3',6'-bis((2,2,2-trifluoro-ethyl)amino)spiro-[isoindoline-1,9'-xanthene]-6-carboxylic acid (52): Following procedure A with 3,5-difluorobenzenesulfonamide (6.5 mg, 33.7 µmol, 5 eq), **52** (2.89 mg, 4.05 µmol, 60%) was obtained as a red solid.

^{1}H NMR (400 MHz, MeOD-*d*$_4$) δ 8.23 (d, *J* = 8.1 Hz, 1H), 8.02 (d, *J* = 8.0 Hz, 1H), 7.66 (s, 1H), 7.22 (tt, *J* = 8.7, 2.2 Hz, 1H), 7.00 – 6.96 (m, 2H), 6.67 (d, *J* = 1.5 Hz, 2H), 6.39 – 6.33 (m, 4H), 3.91 (q, *J* = 9.2 Hz, 4H).

^{13}C NMR (101 MHz, MeOD-*d*$_4$) δ 166.4, 165.5, 162.2 (dd, $^1J_{CF}$ = 253 Hz, $^3J_{CF}$ = 11 Hz), 153.9, 150.6, 142.0 (t, $^3J_{CF}$ = 9 Hz), 137.2, 131.8, 130.3, 128.7, 126.1, 125.4 (q, $^1J_{CF}$ = 280 Hz), 124.2, 111.2 (d, $^2J_{CF}$ = 28 Hz), 109.9, 108.8 (t, $^2J_{CF}$ = 25 Hz), 108.1, 98.3, 44.4 (q, $^2J_{CF}$ = 34 Hz).

HRMS (ESI) Exact mass calculated for $C_{31}H_{19}F_8N_3O_6S$ [M+H]$^+$: 714.0940, found: 714.0938.

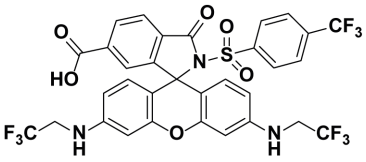

3-Oxo-3',6'-bis((2,2,2-trifluoroethyl)amino)-2-((4-(trifluoro-methyl)phenyl)sulfonyl)-spiro[isoindoline-1,9'-xanthene]-6-carboxylic acid (53): Following procedure A with 4-(trifluoromethyl)benzenesulfonamide (7.6 mg, 33.7 µmol, 5 eq), **53** (3.51 mg, 4.71 µmol, 70%) was obtained as a red solid.

^{1}H NMR (400 MHz, MeOD-*d*$_4$) δ 8.22 (dd, *J* = 8.0, 1.1 Hz, 1H), 8.00 (d, *J* = 8.0 Hz, 1H), 7.66 (d, *J* = 8.8 Hz, 3H), 7.61 (d, *J* = 8.5 Hz, 2H), 6.67 (s, 2H), 6.37 – 6.32 (m, 4H), 3.93 (q, *J* = 9.3 Hz, 4H).

^{13}C NMR (101 MHz, DMSO-*d*$_6$) δ 165.9, 164.8, 152.6, 152.4, 149.5, 142.1, 137.4, 133.4 (q, $^2J_{CF}$ = 33 Hz), 130.6, 130.2, 128.7, 128.5, 125.8 (q, $^1J_{CF}$ = 281 Hz), 125.8, 125.8, 124.8, 124.5, 123.2 (q, $^1J_{CF}$ = 273 Hz), 109.5, 106.8, 98.2, 69.5, 43.7 (q, $^2J_{CF}$ = 33 Hz).

HRMS (ESI) Exact mass calculated for $C_{32}H_{20}F_9N_3O_6S$ [M+H]$^+$: 746.1002, found: 746.0996.

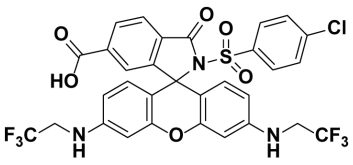

2-((4-Chlorophenyl)sulfonyl)-3-oxo-3',6'-bis((2,2,2-trifluoro-ethyl)amino)spiro[iso-indoline-1,9'-xanthene]-6-carboxylic acid (54): Following procedure A with 4-chlorobenzenesulfonamide (6.45 mg, 33.7 µmol, 5 eq), **54** (2.89 mg, 4.06 µmol, 60%) was obtained as a red solid.

^{1}H NMR (400 MHz, MeOD-*d*$_4$) δ 8.21 (dd, *J* = 8.0, 1.3 Hz, 1H), 7.99 (d, *J* = 8.1 Hz, 1H), 7.64 (s, 1H), 7.41 – 7.34 (m, 4H), 6.66 (d, *J* = 1.7 Hz, 2H), 6.38 – 6.32 (m, 4H), 3.93 (q, *J* = 9.3 Hz, 4H).

^{13}C NMR (101 MHz, DMSO-*d*$_6$) δ 165.9, 164.7, 152.5, 152.5, 149.5, 139.2, 137.3, 137.2, 130.6, 130.2, 129.6, 128.7, 128.6, 125.8 (q, $^1J_{CF}$ = 281 Hz), 124.8, 124.4, 109.5, 106.9, 98.2, 69.1, 43.8 (q, $^2J_{CF}$ = 33 Hz).

HRMS (ESI) Exact mass calculated for $C_{31}H_{20}ClF_6N_3O_6S$ $[M+H]^+$: 712.0738, found: 712.0734.

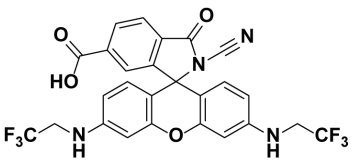

2-Cyano-3-oxo-3',6'-bis((2,2,2-trifluoroethyl)amino) spiro[iso-indoline-1,9'-xanthene]-6-carboxylic acid (55): Following procedure A with **49** (2.00 mg, 3.37 µmol, 1.0 eq) and cyanamide (1.42 mg, 33.7 µmol, 10 eq), **55** (0.850 mg, 1.51 µmol, 45%) was obtained as a red solid.

^{1}H NMR (400 MHz, MeOD-*d*$_4$) δ 8.28 (d, *J* = 8.1 Hz, 1H), 8.11 (d, *J* = 8.0 Hz, 1H), 7.71 (s, 1H), 6.61 (d, *J* = 2.3 Hz, 2H), 6.58 (d, *J* = 8.7 Hz, 2H), 6.51 (dd, *J* = 8.8, 2.4 Hz, 2H), 3.88 (q, *J* = 9.3 Hz, 4H).

HRMS (ESI) Exact mass calculated for $C_{26}H_{16}F_6N_4O_4$ $[M+H]^+$: 563.1149, found: 563.1148.

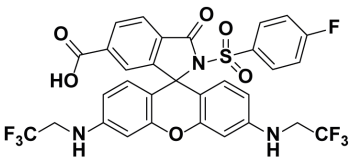

2-((4-Fluorophenyl)sulfonyl)-3-oxo-3',6'-bis((2,2,2-trifluoroethyl)amino)spiro[iso-indoline-1,9'-xanthene]-6-carboxylic acid (56): Following procedure A with 4-fluorobenzenesulfonamide (5.9 mg, 33.7 µmol, 5 eq), **56** (3.63 mg, 5.22 µmol, 78%) was obtained as a red solid.

^{1}H NMR (400 MHz, MeOD-*d*$_4$) δ 8.22 (dd, *J* = 8.0, 1.3 Hz, 1H), 7.99 (d, *J* = 8.1 Hz, 1H), 7.66 (s, 1H), 7.51 – 7.48 (m, 2H), 7.10 – 7.05 (m, 2H), 6.73 – 6.61 (m, 2H), 6.39 – 6.34 (m, 4H), 3.94 (q, *J* = 9.2 Hz, 4H).

^{13}C NMR (101 MHz, DMSO-*d*$_6$) δ 165.9, 165.0 (d, $^1J_{CF}$ = 254 Hz), 164.7, 152.5, 149.5, 137.2, 134.8, 134.8, 130.9 (d, $^3J_{CF}$ = 10 Hz), 130.7, 130.2, 128.6, 125.8 (q, $^1J_{CF}$ = 281 Hz), 124.8, 124.4, 115.8 (d, $^2J_{CF}$ = 23 Hz), 109.5, 106.9, 98.3, 69.0, 43.8 (q, $^2J_{CF}$ = 32 Hz).

HRMS (ESI) Exact mass calculated for $C_{31}H_{20}F_7N_3O_6S$ $[M+H]^+$: 696.1034, found: 696.1032.

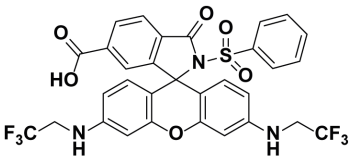

3-Oxo-2-(phenylsulfonyl)-3',6'-bis((2,2,2-trifluoro-ethyl)amino)spiro[isoindoline-1,9'-xanthene]-6-carboxylic acid (57): Following procedure A with benzenesulfonamide (5.29 mg, 33.7 µmol, 5 eq), **57** (2.73 mg, 4.03 µmol, 60%) was obtained as a red solid.

^{1}H NMR (400 MHz, MeOD-*d*$_4$) δ 8.22 (d, *J* = 8.1 Hz, 1H), 7.98 (d, *J* = 8.0 Hz, 1H), 7.66 (s, 1H), 7.56 (t, *J* = 7.4 Hz, 1H), 7.46 (d, *J* = 7.9 Hz, 2H), 7.35 (t, *J* = 7.8 Hz, 2H), 6.68 (s, 2H), 6.37 (s, 4H), 3.95 (q, *J* = 9.2 Hz, 4H).

^{13}C NMR (101 MHz, DMSO-*d*$_6$) δ 165.9, 164.6, 152.6, 149.4, 138.5, 137.2, 134.1, 130.8, 130.2, 128.6, 128.5, 127.7, 125.8 (q, $^1J_{CF}$ = 281 Hz), 124.8, 124.3, 109.5, 107.0, 98.3, 68.9, 43.8 (q, $^2J_{CF}$ = 32 Hz).

HRMS (ESI) Exact mass calculated for $C_{31}H_{21}F_6N_3O_6S$ [M+H]$^+$: 678.1128, found: 678.1123.

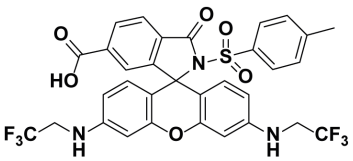

3-Oxo-2-tosyl-3',6'-bis((2,2,2-trifluoroethyl)amino) spiro[isoindoline-1,9'-xanthene]-6-carboxylic acid (58): Following procedure A with *p*-toluenesulfonamide (5.75 mg, 33.7 µmol, 5 eq), **58** (2.55 mg, 3.69 µmol, 55%) was obtained as a red solid.

^{1}H NMR (400 MHz, MeOD-*d*$_4$) δ 8.20 (dd, *J* = 8.1, 1.1 Hz, 1H), 7.97 (d, *J* = 8.0 Hz, 1H), 7.63 (s, 1H), 7.32 (d, *J* = 8.3 Hz, 2H), 7.15 (d, *J* = 8.1 Hz, 2H), 6.65 (s, 2H), 6.38 – 6.32 (m, 4H), 3.92 (q, *J* = 9.2 Hz, 4H), 2.36 (s, 3H).

^{13}C NMR (101 MHz, DMSO-*d*$_6$) δ 166.0, 164.6, 152.6, 152.5, 149.4, 144.8, 137.1, 135.7, 130.8, 130.1, 128.9, 128.6, 127.9, 125.8 (q, $^1J_{CF}$ = 281 Hz), 124.8, 124.2, 109.4, 107.1, 98.3, 68.7, 43.8 (q, $^2J_{CF}$ = 32 Hz), 21.1.

HRMS (ESI) Exact mass calculated for $C_{32}H_{23}F_6N_3O_6S$, [M+H]$^+$: 692.1285, found: 692.1284.

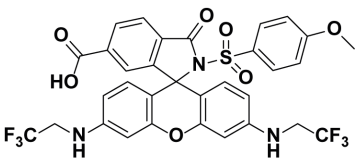

2-((4-Methoxyphenyl)sulfonyl)-3-oxo-3',6'-bis((2,2,2-trifluoro-ethyl)amino)spiro-[isoindoline-1,9'-xanthene]-6-carboxylic acid (59): Following procedure A with 4-

(methoxy)benzenesulfonamide (6.3 mg, 33.7 µmol, 5 eq), **59** (3.49 mg, 4.93 µmol, 73%) was obtained as a red solid.

^{1}H NMR (400 MHz, MeOD-*d*$_4$) δ 8.21 (d, *J* = 7.9 Hz, 1H), 7.97 (d, *J* = 8.0 Hz, 1H), 7.65 (s, 1H), 7.38 (d, *J* = 8.6 Hz, 2H), 6.83 (d, *J* = 8.9 Hz, 2H), 6.66 (s, 2H), 6.37 (s, 4H), 3.96 – 3.91 (m, 4H), 3.83 (s, 3H).

^{13}C NMR (101 MHz, DMSO-*d*$_6$) δ 166.0, 164.6, 163.4, 152.6, 152.5, 149.3, 137.0, 130.9, 130.2, 130.1, 130.1, 128.5, 125.8 (q, $^1J_{CF}$ = 281 Hz), 124.7, 124.2, 113.6, 109.5, 107.1, 98.2, 68.5, 55.7, 43.8 (q, $^2J_{CF}$ = 33 Hz).

HRMS (ESI) Exact mass calculated for $C_{32}H_{23}F_6N_3O_7S$ [M+H]$^+$: 708.1234, found: 708.1231.

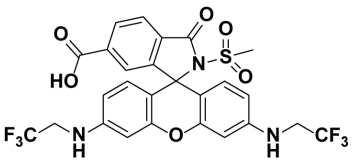

2-(Methylsulfonyl)-3-oxo-3',6'-bis((2,2,2-trifluoroethyl) amino)spiro[isoindoline-1,9'-xanthene]-6-carboxylic acid (60): Following procedure A with methanesulfonamide (3.20 mg, 33.7 µmol, 5 eq), **60** (3.56 mg, 5.78 µmol, 86%) was obtained as a red solid.

^{1}H NMR (400 MHz, MeOD-*d*$_4$) δ 8.25 (d, *J* = 7.8 Hz, 1H), 8.07 (d, *J* = 8.0 Hz, 1H), 7.68 (s, 1H), 6.64 – 6.60 (m, 4H), 6.50 (d, *J* = 7.5 Hz, 2H), 3.90 (q, *J* = 9.1 Hz, 4H), 2.95 (s, 3H).

^{13}C NMR (101 MHz, DMSO-*d*$_6$) δ 165.9, 165.6, 153.3, 152.0, 149.2, 137.1, 130.4, 130.0, 128.1, 125.8 (q, $^1J_{CF}$ = 281 Hz), 124.6, 124.5, 109.6, 106.8, 98.2, 68.0, 43.8 (q, $^2J_{CF}$ = 32 Hz), 42.0.

HRMS (ESI) Exact mass calculated for $C_{26}H_{19}F_6N_3O_6S$ [M+H]$^+$: 616.0972, found: 616.0969.

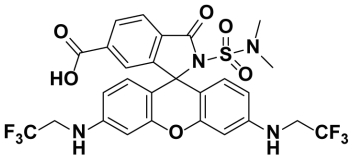

2-(*N,N*-Dimethylsulfamoyl)-3-oxo-3',6'-bis((2,2,2-trifluoroethyl)-amino)spiro-[isoindoline-1,9'-xanthene]-6-carboxylic acid (61): Following procedure A with *N,N*-dimethylsulfamide (4.18 mg, 33.7 µmol, 5 eq), **61** (3.07 mg, 4.76 µmol, 71%) was obtained as a red solid.

^{1}H NMR (400 MHz, DMSO-*d*$_6$) δ 8.12 (d, *J* = 8.0 Hz, 1H), 8.02 (d, *J* = 8.0 Hz, 1H), 7.40 (s, 1H), 6.61 – 6.58 (m, 2H), 6.53 (d, *J* = 1.9 Hz, 2H), 6.48 (d, *J* = 8.7 Hz, 2H), 6.40 (dd, *J* = 8.7, 2.1 Hz, 2H), 3.98 – 3.93 (m, 4H), 2.62 (s, 6H).

^{13}C NMR (101 MHz, DMSO-d_6) δ 166.5, 166.0, 153.9, 152.9, 149.5, 137.2, 131.3, 130.4, 129.1, 126.2 (q, $^{1}J_{CF}$ = 281 Hz), 125.3, 124.6, 109.8, 107.7, 98.5, 68.4, 44.3 (q, $^{2}J_{CF}$ = 33 Hz), 37.9.

HRMS (ESI) Exact mass calculated for $C_{27}H_{22}F_6N_4O_6S$ $[M+H]^+$: 645.1237, found: 645.1239.

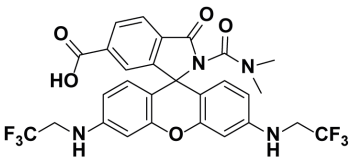

2-(Dimethylcarbamoyl)-3-oxo-3',6'-bis((2,2,2-trifluoroethyl) amino)spiro[iso-indoline-1,9'-xanthene]-6-carboxylic acid (62): Following procedure A with 1,1-dimethylurea (5.93 mg, 67.3 µmol, 10 eq), **62** (0.820 mg, 1.35 µmol, 20%) was obtained as a colorless solid.

^{1}H NMR (400 MHz, MeOD-d_4) δ 8.24 (d, *J* = 8.0 Hz, 1H), 8.03 (d, *J* = 8.0 Hz, 1H), 7.68 (s, 1H), 6.51 (d, *J* = 2.1 Hz, 2H), 6.47 (d, *J* = 8.6 Hz, 2H), 6.39 (dd, *J* = 8.7, 2.3 Hz, 2H), 3.87 – 3.80 (m, 4H), 2.80 (s, 6H).

HRMS (ESI) Exact mass calculated for $C_{28}H_{22}F_6N_4O_5$ $[M+H]^+$: 609.1567, found: 609.1572.

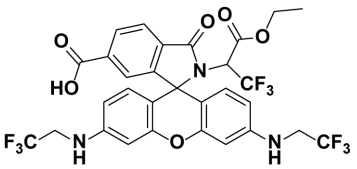

2-(3-ethoxy-1,1,1-trifluoro-3-oxopropan-2-yl)-3-oxo-3',6'-bis((2,2,2-trifluoroethyl)amino)spiro[isoindoline-1,9'-xanthene]-6-carboxylic acid (63): Following procedure A with ethyl 3,3,3-trifluoro-alaninate (14.0 mg, 67.3 µmol, 10 eq), **63** (1.71 mg, 2.47 µmol, 36%) was obtained as a colorless solid.

^{1}H NMR (400 MHz, DMSO-d_6) δ 8.13 (d, *J* = 8.5 Hz, 1H), 7.98 (d, *J* = 7.9 Hz, 1H), 7.49 (s, 1H), 6.68 – 6.60 (m, 2H), 6.55 (d, *J* = 8.6 Hz, 2H), 6.44 – 6.40 (m, 2H), 6.37 (d, *J* = 8.7 Hz, 1H), 6.31 (d, *J* = 8.7 Hz, 1H), 4.48 (q, *J* = 8.0 Hz, 1H), 3.98 – 3.93 (m, 6H), 1.05 (t, *J* = 7.1 Hz, 3H).

HRMS (ESI) Exact mass calculated for $C_{30}H_{22}F_9N_3O_6$ $[M+H]^+$: 692.1438, found: 692.1433.

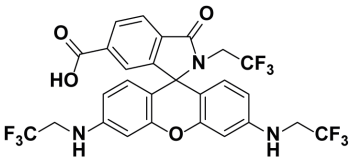

3-Oxo-2-(2,2,2-trifluoroethyl)-3',6'-bis((2,2,2-trifluoroethyl)-amino)spiro[isoindoline-1,9'-xanthene]-6-carboxylic acid (64): Following procedure A with 2,2,2-trifluoroethylamine (5.38 µL, 67.3 µmol, 10 eq) at 50°C, **64** (2.08 mg, 3.36 µmol, 50%) was obtained as a slightly red solid.

^{1}H NMR (400 MHz, DMSO-d_6) δ 8.10 (dd, J = 7.9, 1.1 Hz, 1H), 7.99 (d, J = 7.9 Hz, 1H), 7.46 (s, 1H), 6.64 (t, J = 6.1 Hz, 2H), 6.58 (d, J = 2.1 Hz, 2H), 6.44 (dd, J = 8.7, 2.2 Hz, 2H), 6.31 (d, J = 8.7 Hz, 2H), 4.00 – 3.92 (m, 4H), 3.75 (q, J = 9.6 Hz, 2H).

^{13}C NMR (101 MHz, DMSO-d_6) δ 167.2, 166.2, 153.7, 152.3, 149.2, 135.6, 132.1, 129.8, 128.3, 125.7 (q, $^{1}J_{CF}$ = 281 Hz), 124.4, 123.8 (q, $^{1}J_{CF}$ = 281 Hz), 123.5, 110.4, 105.3, 98.1, 64.9, 43.8 (q, $^{2}J_{CF}$ = 32 Hz), 41.3 (q, $^{2}J_{CF}$ = 35 Hz).

HRMS (ESI) Exact mass calculated for $C_{27}H_{18}F_9N_3O_4$ $[M+H]^+$: 620.1226, found: 620.1223.

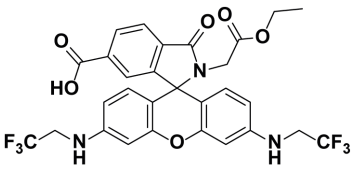

2-(2-Ethoxy-2-oxoethyl)-3-oxo-3',6'-bis((2,2,2-trifluoroethyl) amino)spiro[iso-indoline-1,9'-xanthene]-6-carboxylic acid (65): Following procedure A with glycine ethyl ester hydrochloride (4.70 mg, 33.7 µmol, 5 eq), **65** (1.04 mg, 1.67 µmol, 25%) was obtained as a colorless solid.

^{1}H NMR (400 MHz, MeOD-d_4) δ 8.21 (d, J = 7.9 Hz, 1H), 7.99 (d, J = 8.0 Hz, 1H), 7.66 (s, 1H), 6.54 (d, J = 1.6 Hz, 2H), 6.43 – 6.37 (m, 4H), 3.89 – 3.80 (m, 6H), 1.08 (t, J = 7.1 Hz, 3H).

HRMS (ESI) Exact mass calculated for $C_{29}H_{23}F_6N_3O_6$ $[M+H]^+$: 624.1564, found: 624.1562.

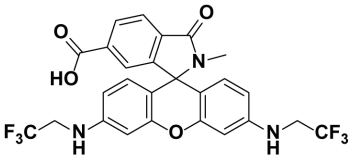

2-Methyl-3-oxo-3',6'-bis((2,2,2-trifluoroethyl)amino) spiro[isoindoline-1,9'-xanthene]-6-carboxylic acid (66): Following procedure A with **49** (8.00 mg, 13.5 µmol, 1.0 eq) and methylamine hydrochloride (4.54 mg, 67.3 µmol, 5 eq) **66** (4.03 mg, 7.31 µmol, 54%) was obtained as a colorless solid.

^{1}H NMR (400 MHz, DMSO-d_6) δ 8.03 (dd, J = 7.9, 1.3 Hz, 1H), 7.88 (d, J = 7.9 Hz, 1H), 7.42 – 7.42 (m, 1H), 6.64 – 6.60 (m, 4H), 6.45 (dd, J = 8.7, 2.3 Hz, 2H), 6.34 (d, J = 8.6 Hz, 2H), 4.00 – 3.91 (m, 4H), 2.53 (s, 3H).

^{13}C NMR (101 MHz, DMSO-d_6) δ 166.4, 165.8, 153.5, 152.3, 149.1, 149.0, 134.8, 133.4, 129.5, 127.3, 125.8 (q, $^{1}J_{CF}$ = 281 Hz), 123.7, 122.9, 110.2, 106.1, 106.1, 98.5, 63.7, 43.8 (q, $^{2}J_{CF}$ = 32 Hz), 24.5.

HRMS (ESI) Exact mass calculated for $C_{26}H_{19}F_6N_3O_4$ $[M+H]^+$: 552.1353, found: 552.1350.

General Procedure B for 67:

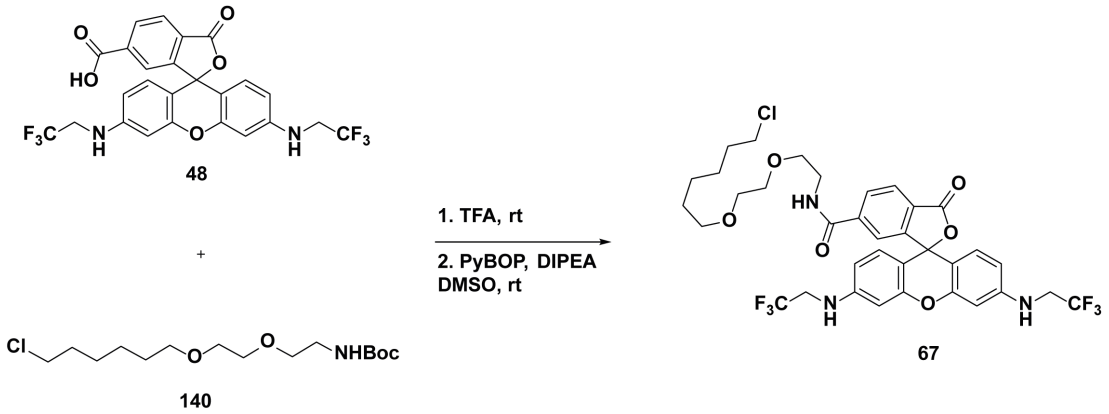

***N*-(2-(2-((6-chlorohexyl)oxy)ethoxy)ethyl)-3-oxo-3',6'-bis((2,2,2-trifluoroethyl)amino)-3*H*-spiro[isobenzofuran-1,9'-xanthene]-6-carboxamide (67): 140** was synthesized by Bettina Réssy according to a previously reported procedure.[232] A solution of **140** (2.98 mg, 9.19 µmol, 1.5 eq) in TFA (0.3 mL) was stirred at rt for 5 min. The solvent was evaporated, the residue dissolved in DMSO (0.3 mL) and transferred to a solution of **48** (3.30 mg, 6.13 µmol, 1.0 eq), PyBOP (4.15 mg, 7.97 µmol, 1.3 eq), and DIPEA (10.1 µL, 61.3 µmol, 10 eq) in DMSO (0.3 mL). The reaction mixture was stirred at rt for 40 min followed by purification using preparative HPLC (8 mL/min, 30% to 90% MeCN/H_2O (0.1% TFA) in 55 min) to obtain **67** (3.51 mg, 4.72 µmol, 77%) as a red solid.

^{1}H NMR (400 MHz, MeOD-d_4) δ 8.33 (d, *J* = 8.2 Hz, 1H), 8.20 (dd, *J* = 8.2, 1.6 Hz, 1H), 7.79 (d, *J* = 1.4 Hz, 1H), 7.14 (d, *J* = 9.2 Hz, 2H), 7.08 (d, *J* = 2.0 Hz, 2H), 6.95 (dd, *J* = 9.2, 2.2 Hz, 2H), 4.19 (q, *J* = 9.0 Hz, 4H), 3.66 – 3.54 (m, 8H), 3.52 (t, *J* = 6.6 Hz, 2H), 3.42 (t, *J* = 6.5 Hz, 2H), 1.71 (p, *J* = 6.7 Hz, 2H), 1.49 (p, *J* = 6.7 Hz, 2H), 1.43 – 1.36 (m, 2H), 1.34 – 1.28 (m, 2H).

HRMS (ESI) Exact mass calculated for $C_{35}H_{36}ClF_6N_3O_6$ $[M+H]^+$: 744.2270, found: 744.2268.

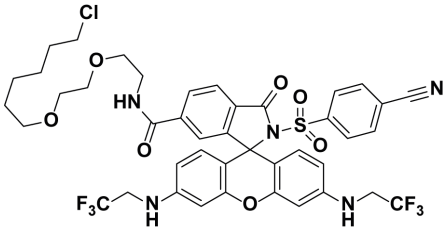

***N*-(2-(2-((6-Chlorohexyl)oxy)ethoxy)ethyl)-2-((4-cyanophenyl)sulfonyl)-3-oxo-3',6'-bis((2,2,2-trifluoroethyl)-amino)spiro [isoindoline-1,9'-xanthene]-6-carboxamide (68):** Following procedure B with **51** (3.93 mg, 5.59 µmol, 1.0 eq), **68** (1.90 mg, 2.09 µmol, 37%) was obtained as a red solid.

^{1}H NMR (400 MHz, DMSO-d_6) δ 8.71 (t, *J* = 5.4 Hz, 1H), 8.07 (d, *J* = 8.1 Hz, 1H), 7.95 (d, *J* = 8.0 Hz, 1H), 7.86 (d, *J* = 8.3 Hz, 2H), 7.55 (s, 1H), 7.41 (d, *J* = 8.3 Hz, 2H), 6.71 (t, *J* = 6.7 Hz,

2H), 6.64 (s, 2H), 6.33 (d, *J* = 8.7 Hz, 2H), 6.24 (d, *J* = 8.6 Hz, 2H), 4.06 – 3.97 (m, 4H), 3.57 (t, *J* = 6.6 Hz, 2H), 3.45 – 3.38 (m, 6H), 3.30 – 3.26 (m, 4H), 1.64 (p, *J* = 6.8 Hz, 2H), 1.43 – 1.36 (m, 2H), 1.33 – 1.28 (m, 2H), 1.25 – 1.20 (m, 2H).

HRMS (ESI) Exact mass calculated for $C_{42}H_{40}ClF_6N_5O_7S$ $[M+H]^+$: 908.2314, found: 908.2314.

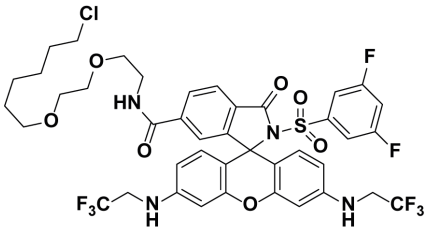

***N*-(2-(2-((6-Chlorohexyl)oxy)ethoxy)ethyl)-2-((3,5-difluorophenyl)sulfonyl)-3-oxo-3',6'-bis((2,2,2-trifluoroethyl)amino)spiro [isoindoline-1,9'-xanthene]-6-carboxamide (69):** Following procedure B with **52** (2.89 mg, 4.05 µmol, 1.0 eq), **69** (1.96 mg, 2.13 µmol, 53%) was obtained as a red solid.

^{1}H NMR (400 MHz, DMSO-*d*$_6$) δ 8.72 (t, *J* = 5.3 Hz, 1H), 8.08 (d, *J* = 8.1 Hz, 1H), 7.97 (d, *J* = 8.0 Hz, 1H), 7.64 (t, *J* = 8.8 Hz, 1H), 7.56 (s, 1H), 6.83 (d, *J* = 4.3 Hz, 2H), 6.72 (t, *J* = 6.0 Hz, 2H), 6.64 (s, 2H), 6.34 (d, *J* = 8.8 Hz, 2H), 6.27 (d, *J* = 8.6 Hz, 2H), 4.04 – 3.95 (m, 4H), 3.58 (t, *J* = 6.6 Hz, 2H), 3.45 – 3.39 (m, 6H), 3.33 – 3.27 (m, 4H), 1.64 (p, *J* = 6.8 Hz, 2H), 1.43 – 1.36 (m, 2H), 1.35 – 1.28 (m, 2H), 1.25 – 1.20 (m, 2H).

HRMS (ESI) Exact mass calculated for $C_{41}H_{39}ClF_8N_4O_7S$ $[M+H]^+$: 919.2173, found: 919.2175.

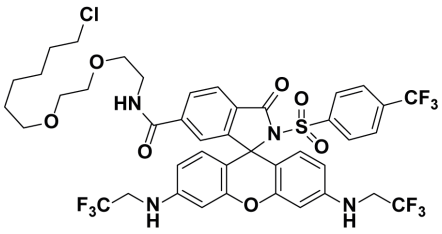

***N*-(2-(2-((6-Chlorohexyl)oxy)ethoxy)ethyl)-3-oxo-3',6'-bis((2,2,2-trifluoroethyl)amino)-2-((4-(trifluoromethyl)phenyl)sulfonyl)spiro[isoindoline-1,9'-xanthene]-6-carboxamide (70):** Following procedure B with **53** (3.51 mg, 4.71 µmol, 1.0 eq), **70** (2.90 mg, 3.05 µmol, 65%) was obtained as a red solid.

^{1}H NMR (400 MHz, DMSO-*d*$_6$) δ 8.71 (t, *J* = 5.5 Hz, 1H), 8.07 (d, *J* = 8.1 Hz, 1H), 7.95 (d, *J* = 8.1 Hz, 1H), 7.76 (d, *J* = 8.4 Hz, 2H), 7.55 (s, 1H), 7.48 (d, *J* = 8.3 Hz, 2H), 6.71 (t, *J* = 6.8 Hz, 2H), 6.65 (d, *J* = 1.6 Hz, 2H), 6.33 (dd, *J* = 8.7, 1.8 Hz, 2H), 6.26 (d, *J* = 8.6 Hz, 2H), 4.06 – 3.97 (m, 4H), 3.57 (t, *J* = 6.6 Hz, 2H), 3.45 – 3.38 (m, 6H), 3.34 – 3.26 (m, 4H), 1.64 (p, *J* = 6.7 Hz, 2H), 1.43 – 1.36 (m, 2H), 1.35 – 1.28 (m, 2H), 1.25 – 1.20 (m, 2H).

HRMS (ESI) Exact mass calculated for $C_{42}H_{40}ClF_9N_4O_7S$ $[M+H]^+$: 951.2235, found: 951.2233.

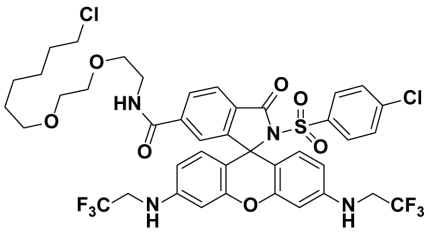

***N*-(2-(2-((6-Chlorohexyl)oxy)ethoxy)ethyl)-2-((4-chlorophenyl)sulfonyl)-3-oxo-3',6'-bis((2,2,2-trifluoroethyl)amino)spiro[isoindoline-1,9'-xanthene]-6-carboxamide (71):** Following procedure B with **54** (2.89 mg, 4.06 µmol, 1.0 eq), **71** (2.53 mg, 2.76 µmol, 68%) was obtained as a red solid.

^{1}H NMR (400 MHz, DMSO-d_6) δ 8.71 (t, *J* = 5.5 Hz, 1H), 8.06 (dd, *J* = 8.1, 1.0 Hz, 1H), 7.94 (d, *J* = 8.1 Hz, 1H), 7.54 (s, 1H), 7.46 (d, *J* = 8.7 Hz, 2H), 7.26 (d, *J* = 8.7 Hz, 2H), 6.70 (t, *J* = 6.6 Hz, 2H), 6.64 (d, *J* = 2.1 Hz, 2H), 6.35 (dd, *J* = 8.7, 2.2 Hz, 2H), 6.25 (d, *J* = 8.7 Hz, 2H), 4.06 – 3.97 (m, 4H), 3.57 (t, *J* = 6.6 Hz, 2H), 3.45 – 3.39 (m, 6H), 3.33 – 3.26 (m, 4H), 1.64 (p, *J* = 6.7 Hz, 2H), 1.43 – 1.36 (m, 2H), 1.35 – 1.28 (m, 2H), 1.25 – 1.18 (m, 2H).

HRMS (ESI) Exact mass calculated for $C_{41}H_{40}Cl_2F_6N_4O_7S$ $[M+H]^+$: 917.1972, found: 917.1966.

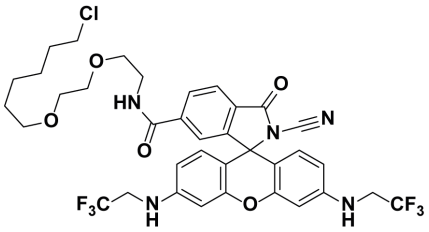

***N*-(2-(2-((6-Chlorohexyl)oxy)ethoxy)ethyl)-2-cyano-3-oxo-3',6'-bis((2,2,2-trifluoroethyl)amino)spiro[isoindoline-1,9'-xanthene]-6-carboxamide (72):** Following procedure B with **55** (0.930 mg, 1.65 µmol, 1.0 eq), **72** (1.03 mg, 1.34 µmol, 81%) was obtained as a red solid.

^{1}H NMR (400 MHz, DMSO-d_6) δ 8.77 (t, *J* = 5.5 Hz, 1H), 8.14 (d, *J* = 8.6 Hz, 1H), 8.09 (d, *J* = 7.9 Hz, 1H), 7.63 (s, 1H), 6.81 (t, *J* = 6.7 Hz, 2H), 6.63 – 6.60 (m, 4H), 6.52 (d, *J* = 8.6 Hz, 2H), 4.06 – 3.96 (m, 4H), 3.59 (t, *J* = 6.6 Hz, 2H), 3.47 – 3.39 (m, 6H), 3.32 – 3.27 (m, 4H) 1.65 (p, *J* = 6.8 Hz, 2H), 1.44 – 1.37 (m, 2H), 1.34 – 1.29 (m, 2H), 1.26 – 1.19 (m, 2H).

HRMS (ESI) Exact mass calculated for $C_{36}H_{36}ClF_6N_5O_5$ $[M+H]^+$: 768.2382, found: 768.2382.

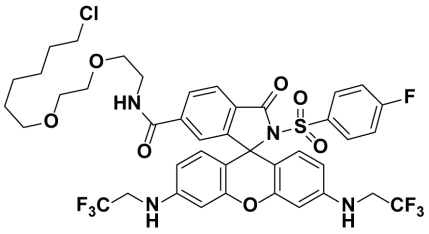

***N*-(2-(2-((6-Chlorohexyl)oxy)ethoxy)ethyl)-2-((4-fluorophenyl)sulfonyl)-3-oxo-3',6'-bis((2,2,2-trifluoroethyl)-amino)spiro[isoindoline-1,9'-xanthene]-6-carboxamide (73):** Following procedure B with **56** (2.80 mg, 4.03 µmol, 1.0 eq), **73** (2.27 mg, 2.52 µmol, 63%) was obtained as a red solid.

^{1}H NMR (400 MHz, DMSO-d_6) δ 8.71 (t, *J* = 5.5 Hz, 1H), 8.06 (dd, *J* = 8.0, 1.0 Hz, 1H), 7.94 (d, *J* = 8.1 Hz, 1H), 7.54 (s, 1H), 7.36 – 7.32 (m, 2H), 7.22 (t, *J* = 8.8 Hz, 2H), 6.70 – 6.67 (m, 2H), 6.64 (d, *J* = 2.1 Hz, 2H), 6.35 (dd, *J* = 8.7, 2.2 Hz, 2H), 6.23 (d, *J* = 8.7 Hz, 2H), 4.05 – 3.97 (m, 4H), 3.57 (t, *J* = 6.5 Hz, 2H), 3.45 – 3.38 (m, 6H), 3.33 – 3.26 (m, 4H), 1.64 (p, *J* = 6.7 Hz, 2H), 1.43 – 1.36 (m, 2H), 1.35 – 1.28 (m, 2H), 1.25 – 1.17 (m, 2H).

HRMS (ESI) Exact mass calculated for $C_{41}H_{40}ClF_7N_4O_7S$ $[M+H]^+$: 901.2267, found: 901.2269.

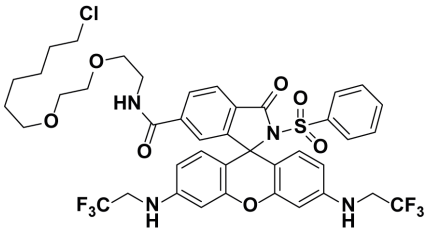

_N_-(2-(2-((6-Chlorohexyl)oxy)ethoxy)ethyl)-3-oxo-2-(phenylsulfonyl)-3',6'-bis((2,2,2-trifluoroethyl) amino)spiro[isoindoline-1,9'-xanthene]-6-carboxamide (74): Following procedure B with **57** (2.73 mg, 4.03 µmol, 1.0 eq), **74** (1.70 mg, 1.92 µmol, 48%) was obtained as a red solid.

^{1}H NMR (400 MHz, DMSO-d_6) δ 8.70 (t, *J* = 5.5 Hz, 1H), 8.05 (d, *J* = 8.1 Hz, 1H), 7.92 (d, *J* = 8.1 Hz, 1H), 7.64 (t, *J* = 7.4 Hz, 1H), 7.54 (s, 1H), 7.39 (t, *J* = 7.8 Hz, 2H), 7.29 (d, *J* = 7.8 Hz, 2H), 6.68 (t, *J* = 6.7 Hz, 2H), 6.64 (d, *J* = 1.7 Hz, 2H), 6.35 (dd, *J* = 9.0, 1.6 Hz, 2H), 6.23 (d, *J* = 8.6 Hz, 2H), 4.05 – 3.97 (m, 4H), 3.57 (t, *J* = 6.6 Hz, 2H), 3.45 – 3.39 (m, 6H), 3.31 – 3.27 (m, 4H), 1.64 (p, *J* = 6.8 Hz, 2H), 1.43 – 1.36 (m, 2H), 1.35 – 1.28 (m, 2H), 1.25 – 1.20 (m, 2H).

HRMS (ESI) Exact mass calculated for $C_{41}H_{41}ClF_6N_4O_7S$ $[M+H]^+$: 883.2361, found: 883.2362.

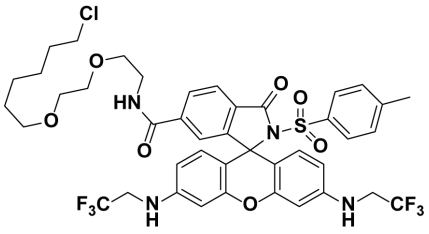

_N_-(2-(2-((6-Chlorohexyl)oxy)ethoxy)ethyl)-3-oxo-2-tosyl-3',6'-bis((2,2,2-trifluoroethyl) amino)spiro[isoindoline-1,9'-xanthene]-6-carboxamide (75): Following procedure B with **58** (2.55 mg, 3.69 µmol, 1.0 eq), **75** (2.26 mg, 2.52 µmol, 68%) was obtained as a red solid.

^{1}H NMR (400 MHz, DMSO-d_6) δ 8.70 (t, *J* = 5.6 Hz, 1H), 8.05 (dd, *J* = 8.1, 1.2 Hz, 1H), 7.91 (d, *J* = 8.1 Hz, 1H), 7.53 (s, 1H), 7.20 – 7.16 (m, 4H), 6.67 (t, *J* = 6.7 Hz, 2H), 6.63 (d, *J* = 2.2 Hz, 2H), 6.35 (dd, *J* = 8.7, 2.3 Hz, 2H), 6.23 (d, *J* = 8.7 Hz, 2H), 4.05 – 3.96 (m, 4H), 3.57 (t, *J* = 6.6 Hz, 2H), 3.46 – 3.39 (m, 6H), 3.33 – 3.27 (m, 4H), 2.33 (s, 3H), 1.65 (p, *J* = 6.7 Hz, 2H), 1.43 – 1.36 (m, 2H), 1.35 – 1.28 (m, 2H), 1.25 – 1.16 (m, 2H).

HRMS (ESI) Exact mass calculated for $C_{42}H_{43}ClF_6N_4O_7S$ $[M+H]^+$: 897.2518, found: 897.2518.

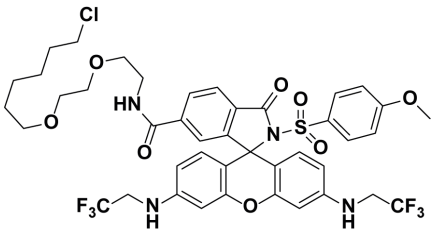

***N*-(2-(2-((6-Chlorohexyl)oxy)ethoxy)ethyl)-2-((4-methoxyphenyl)sulfonyl)-3-oxo-3',6'-bis((2,2,2-trifluoroethyl)amino)spiro [isoindoline-1,9'-xanthene]-6-carboxamide (76):** Following procedure B with **59** (3.49 mg, 4.93 µmol, 1.0 eq), **76** (3.03 mg, 3.32 µmol, 67%) was obtained as a red solid.

^{1}H NMR (400 MHz, DMSO-d_6) δ 8.70 (t, *J* = 5.3 Hz, 1H), 8.05 (d, *J* = 8.0 Hz, 1H), 7.91 (d, *J* = 8.0 Hz, 1H), 7.53 (s, 1H), 7.22 (d, *J* = 8.8 Hz, 2H), 6.87 (d, *J* = 8.9 Hz, 2H), 6.67 (t, *J* = 6.2 Hz, 2H), 6.63 (s, 2H), 6.35 (d, *J* = 8.7 Hz, 2H), 6.22 (d, *J* = 8.6 Hz, 2H), 4.05 – 3.97 (m, 4H), 3.80 (s, 3H), 3.57 (t, *J* = 6.6 Hz, 2H), 3.45 – 3.39 (m, 6H), 3.32 – 3.27 (m, 4H), 1.65 (p, *J* = 6.8 Hz, 2H), 1.43 – 1.36 (m, 2H), 1.34 – 1.28 (m, 2H), 1.26 – 1.20 (m, 2H).

HRMS (ESI) Exact mass calculated for $C_{42}H_{43}ClF_6N_4O_8S$ $[M+H]^+$: 913.2467, found: 913.2462.

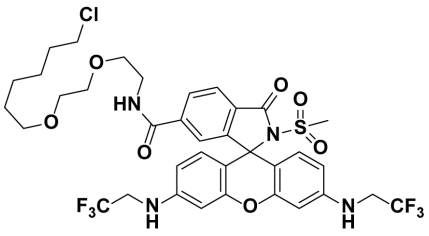

***N*-(2-(2-((6-Chlorohexyl)oxy)ethoxy)ethyl)-2-(methylsulfonyl)-3-oxo-3',6'-bis((2,2,2-trifluoroethyl)amino)spiro[isoindoline-1,9'-xanthene]-6-carboxamide (77):** Following procedure B with **60** (3.56 mg, 5.78 µmol, 1.0 eq), **77** (3.32 mg, 4.04 µmol, 70%) was obtained as a red solid.

^{1}H NMR (400 MHz, DMSO-d_6) δ 8.72 (t, *J* = 5.5 Hz, 1H), 8.08 (d, *J* = 8.1 Hz, 1H), 8.02 (d, *J* = 8.0 Hz, 1H), 7.50 (s, 1H), 6.62 (t, *J* = 6.6 Hz, 2H), 6.53 – 6.51 (m, 4H), 6.42 (dd, J = 8.7, 1.9 Hz, 2H), 4.01 – 3.91 (m, 4H), 3.59 (t, *J* = 6.6 Hz, 2H), 3.46 – 3.39 (m, 6H), 3.34 – 3.27 (m, 4H), 2.97 (s, 3H), 1.66 (p, *J* = 6.8 Hz, 2H), 1.44 – 1.37 (m, 2H), 1.35 – 1.29 (m, 2H), 1.27 – 1.20 (m, 2H).

HRMS (ESI) Exact mass calculated for $C_{36}H_{39}ClF_6N_4O_7S$ $[M+H]^+$: 821.2205, found: 821.2202.

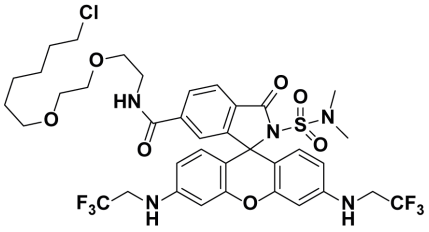

***N*-(2-(2-((6-Chlorohexyl)oxy)ethoxy)ethyl)-2-(*N*,*N*-dimethylsulfamoyl)-3-oxo-3',6'-bis((2,2,2-trifluoroethyl)amino)spiro [isoindoline-1,9'-xanthene]-6-carboxamide (78):** Following procedure B with **61** (3.07 mg, 4.76 µmol, 1.0 eq), **78** (2.11 mg, 2.48 µmol, 52%) was obtained as a red solid.

^{1}H NMR (400 MHz, DMSO-d_6) δ 8.70 (t, *J* = 5.4 Hz, 1H), 8.08 (d, *J* = 8.1 Hz, 1H), 7.98 (d, *J* = 8.0 Hz, 1H), 7.50 (s, 1H), 6.58 (t, *J* = 6.4 Hz, 2H), 6.52 (s, 2H), 6.45 (d, *J* = 8.6 Hz, 2H), 6.39 (d, *J* = 8.6 Hz, 2H), 4.01 – 3.90 (m, 4H), 3.59 (t, *J* = 6.6 Hz, 2H), 3.46 – 3.39 (m, 6H), 3.32 – 3.28 (m, 4H), 2.61 (s, 6H), 1.66 (p, *J* = 6.7 Hz, 2H), 1.44 – 1.37 (m, 2H), 1.35 – 1.29 (m, 2H), 1.27 – 1.21 (m, 2H).

HRMS (ESI) Exact mass calculated for $C_{37}H_{42}ClF_6N_5O_7S$ $[M+H]^+$: 850.2470, found: 850.2474.

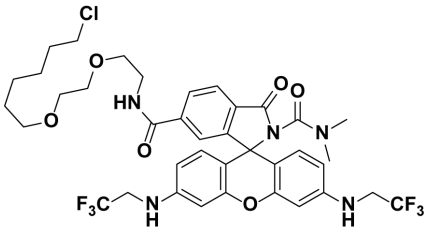

***N*^{6}-(2-(2-((6-Chlorohexyl)oxy)ethoxy)ethyl)-*N*^{2},*N*^{2}-dimethyl-3-oxo-3',6'-bis((2,2,2-trifluoroethyl)amino)spiro[isoindoline-1,9'-xanthene]-2,6-dicarboxamide (83):** Following procedure B with **62** (0.820 mg, 1.35 µmol, 1.0 eq), **83** (0.590 mg, 0.725 µmol, 54%) was obtained as a colorless solid.

^{1}H NMR (400 MHz, DMSO-d_6) δ 8.68 (t, *J* = 5.5 Hz, 1H), 8.06 (d, *J* = 8.0 Hz, 1H), 7.97 (d, *J* = 8.0 Hz, 1H), 7.52 (s, 1H), 6.53 (t, *J* = 6.9 Hz, 2H), 6.49 (d, *J* = 1.8 Hz, 2H), 6.41 (d, *J* = 8.7 Hz, 2H), 6.37 (dd, *J* = 8.7, 2.1 Hz, 2H), 3.98 – 3.89 (m, 4H), 3.58 (t, *J* = 6.6 Hz, 2H), 3.46 – 3.39 (m, 6H), 3.31 – 3.28 (m, 4H), 2.71 (s, 6H), 1.65 (p, *J* = 6.8 Hz, 2H), 1.44 – 1.37 (m, 2H), 1.35 – 1.29 (m, 2H), 1.24 – 1.21 (m, 2H).

HRMS (ESI) Exact mass calculated for $C_{38}H_{42}ClF_6N_5O_6$ $[M+H]^+$: 814.2801, found: 814.2801.

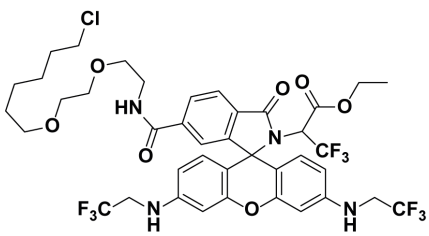

Ethyl 2-(6-((2-(2-((6-chlorohexyl)oxy)ethoxy)ethyl)-carbamoyl)-3-oxo-3',6'-bis((2,2,2-trifluoroethyl)amino)spiro[isoindoline-1,9'-xanthen]-2-yl)-3,3,3-trifluoropropanoate (84): Following procedure B with **63** (3.42 mg, 4.95 µmol, 1.0 eq), **84** (0.960 mg, 1.07 µmol, 22%) was obtained as a colorless solid.

^{1}H NMR (400 MHz, DMSO-d_6) δ 8.68 (t, *J* = 5.5 Hz, 1H), 8.09 (dd, *J* = 8.0, 1.1 Hz, 1H), 7.94 (d, *J* = 8.0 Hz, 1H), 7.58 (s, 1H), 6.63 (dt, *J* = 20.8, 6.9 Hz, 2H), 6.54 (dd, *J* = 8.7, 2.1 Hz, 2H), 6.41 (d, *J* = 10.1 Hz, 2H), 6.36 (t, *J* = 8.7 Hz, 1H), 6.29 (d, *J* = 8.7 Hz, 1H), 4.41 (q, *J* = 8.1 Hz, 1H), 4.00 – 3.91 (m, 6H), 3.58 (t, *J* = 6.6 Hz, 2H), 3.48 – 3.39 (m, 6H), 3.33 – 3.28 (m, 4H), 1.66 (p, *J* = 6.7 Hz, 2H), 1.44 – 1.37 (m, 2H), 1.37 – 1.29 (m, 2H), 1.26 – 1.21 (m, 2H), 1.04 (t, *J* = 7.1 Hz, 3H).

HRMS (ESI) Exact mass calculated for $C_{40}H_{42}ClF_9N_4O_7$ $[M+H]^+$: 897.2671, found: 897.2668.

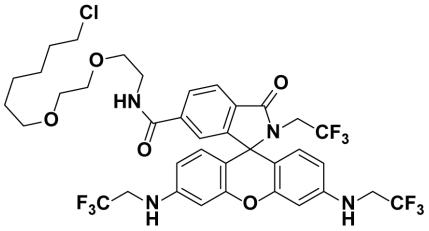

***N*-(2-(2-((6-Chlorohexyl)oxy)ethoxy)ethyl)-3-oxo-2-(2,2,2-trifluoroethyl)-3',6'-bis((2,2,2-trifluoroethyl)amino)spiro[isoindoline-1,9'-xanthene]-6-carboxamide (85):** Following procedure B with **64** (2.06 mg, 3.33 µmol, 1.0 eq), **85** (1.78 mg, 2.16 µmol, 65%) was obtained as a colorless solid.

^{1}H NMR (400 MHz, DMSO-d_6) δ 8.67 (t, *J* = 5.5 Hz, 1H), 8.05 (d, *J* = 8.0 Hz, 1H), 7.94 (d, *J* = 8.0 Hz, 1H), 7.54 (s, 1H), 6.62 (t, *J* = 6.7 Hz, 2H), 6.57 (d, *J* = 2.1 Hz, 2H), 6.43 (dd, *J* = 8.7, 2.2 Hz, 2H), 6.28 (d, *J* = 8.7 Hz, 2H), 4.00 – 3.91 (m, 4H), 3.72 (q, *J* = 9.6 Hz, 2H), 3.58 (t, *J* = 6.6 Hz, 2H), 3.46 – 3.40 (m, 6H), 3.33 – 3.28 (m, 4H), 1.66 (p, *J* = 6.7 Hz, 2H), 1.44 – 1.36 (m, 2H), 1.34 – 1.29 (m, 2H), 1.26 – 1.21 (m, 2H).

HRMS (ESI) Exact mass calculated for $C_{37}H_{38}ClF_9N_4O_5$ $[M+H]^+$: 825.2460, found: 825.2463.

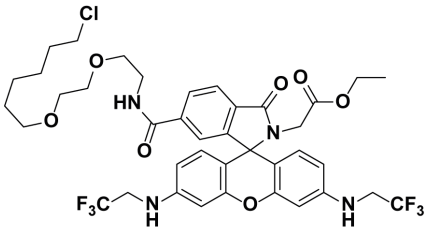

Ethyl 2-(6-((2-(2-((6-chlorohexyl)oxy)ethoxy) ethyl)-carbamoyl)-3-oxo-3',6'-bis((2,2,2-trifluoroethyl)amino)spiro-[isoindoline-1,9'-xanthen]-2-yl)acetate (86): Following procedure B with **65** (1.04 mg, 1.67 µmol, 1.0 eq), **86** (1.08 mg, 1.30 µmol, 78%) was obtained as a colorless solid.

^{1}H NMR (400 MHz, DMSO-d_6) δ 8.65 (t, *J* = 5.5 Hz, 1H), 8.03 (d, *J* = 8.0 Hz, 1H), 7.91 (d, *J* = 7.9 Hz, 1H), 7.53 (s, 1H), 6.60 (t, *J* = 6.8 Hz, 2H), 6.55 (d, *J* = 1.7 Hz, 2H), 6.41 (dd, *J* = 8.7, 1.8 Hz, 2H), 6.33 (d, *J* = 8.7 Hz, 2H), 3.99 – 3.90 (m, 4H), 3.76 (q, *J* = 7.1 Hz, 2H), 3.68 (s, 2H), 3.58 (t, *J* = 6.6 Hz, 2H), 3.47 – 3.39 (m, 6H), 3.31 – 3.28 (m, 4H), 1.66 (p, *J* = 6.8 Hz, 2H), 1.44 – 1.37 (m, 2H), 1.34 – 1.29 (m, 2H), 1.26 – 1.21 (m, 2H), 0.99 (t, *J* = 7.1 Hz, 3H).

HRMS (ESI) Exact mass calculated for $C_{39}H_{43}ClF_6N_4O_7$ $[M+H]^+$: 829.2797, found: 829.2799.

General Procedure C for 79:

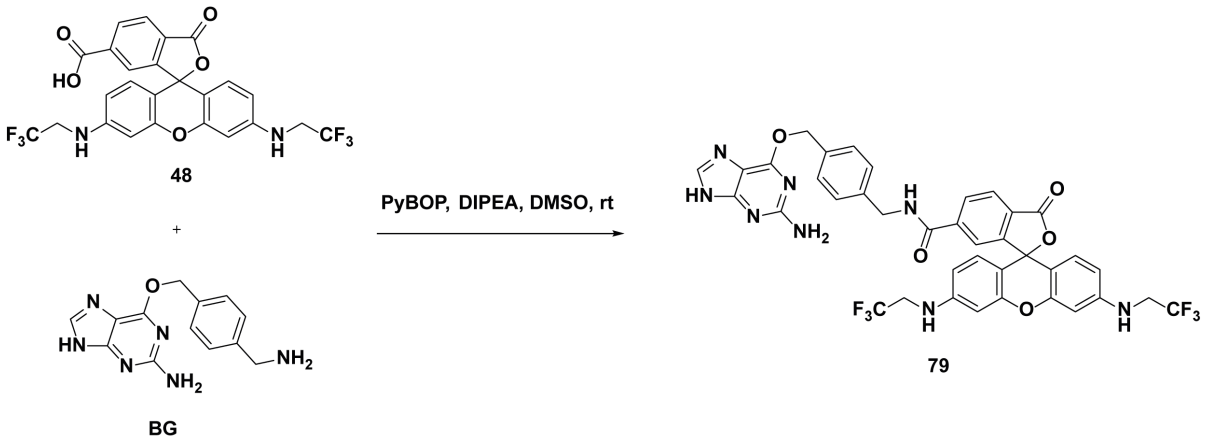

***N*-(4-(((2-amino-9*H*-purin-6-yl)oxy)methyl)benzyl)-3-oxo-3',6'-bis((2,2,2-trifluoroethyl)amino)-3*H*-spiro[isobenzofuran-1,9'-xanthene]-6-carboxamide (79):** **BG** (2.48 mg, 9.19 µmol, 1.5 eq) was added to a solution of **48** (3.30 mg, 6.13 µmol, 1 eq), PyBOP (4.15 mg, 7.97 µmol, 1.3 eq) and DIPEA (10.1 µL, 61.3 µmol, 10 eq) in DMSO (600 µL). The reaction mixture was stirred at rt for 30 min followed by purification using preparative HPLC (8 mL/min, 35% to 90% MeCN/H_2O (0.1% TFA) in 55 min) to obtain **79** (4.20 mg, 5.31 µmol, 87%) as a red solid.

^{1}H NMR (400 MHz, MeOD-d_4) δ 8.40 (d, *J* = 8.2 Hz, 1H), 8.23 (dd, *J* = 8.3, 1.8 Hz, 1H), 7.96 (d, *J* = 6.2 Hz, 1H), 7.84 (t, *J* = 1.9 Hz, 1H), 7.50 – 7.48 (m, 2H), 7.38 (d, *J* = 7.8 Hz, 2H), 7.18 (dd, *J* = 9.2, 1.3 Hz, 2H), 7.14 (d, *J* = 2.2 Hz, 2H), 7.01 – 6.98 (m, 2H), 5.55 (d, *J* = 2.5 Hz, 2H), 4.60 – 4.58 (m, 2H), 4.24 (q, *J* = 9.0 Hz, 4H).

HRMS (ESI) Exact mass calculated for $C_{38}H_{28}F_6N_8O_5$ $[M+2H]^{2+}$: 396.1116, found: 396.1113.

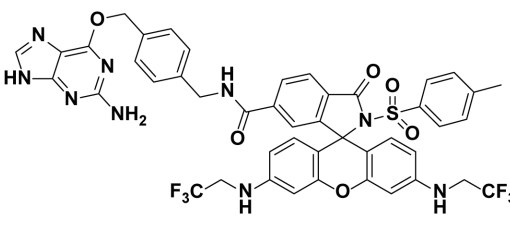

***N*-(4-(((2-Amino-*9H*-purin-6-yl)oxy)methyl) benzyl)-3-oxo-2-tosyl-3',6'-bis((2,2,2-trifluoro-ethyl)amino)spiro[isoindoline-1,9'-xanthene]-6-carboxamide (80):** Following procedure C with **58** (3.10 mg, 4.48 µmol, 1 eq), **80** (2.61 mg, 2.77 µmol, 62%) was obtained as a red solid.

^{1}H NMR (400 MHz, DMSO-d_6) δ 9.22 (t, *J* = 6.0 Hz, 1H), 8.37 (s, 1H), 8.09 (dd, *J* = 8.1, 1.5 Hz, 1H), 7.93 (d, *J* = 8.0 Hz, 1H), 7.55 (s, 1H), 7.44 (d, *J* = 8.1 Hz, 2H), 7.27 (d, *J* = 8.1 Hz, 2H), 7.22 – 7.13 (m, 4H), 6.67 (t, *J* = 7.0 Hz, 2H), 6.63 (d, *J* = 2.3 Hz, 2H), 6.35 (dd, *J* = 8.7, 2.4 Hz, 2H), 6.24 (d, *J* = 8.6 Hz, 2H), 5.47 (s, 2H), 4.37 (d, *J* = 5.8 Hz, 2H), 4.05 – 3.94 (m, 4H), 2.33 (s, 3H).

HRMS (ESI) Exact mass calculated for $C_{45}H_{35}N_9O_6F_6S$ $[M+2H]^{2+}$: 472.6240, found: 472.6236.

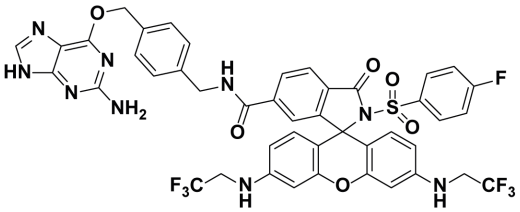

***N*-(4-(((2-Amino-*9H*-purin-6-yl)oxy)methyl)benzyl)-2-((4-fluorophenyl)sulfonyl)-3-oxo-3',6'-bis((2,2,2-trifluoroethyl)amino)spiro[isoindoline-1,9'-xanthene]-6-carboxamide (81):** Following procedure C with **56** (2.80 mg, 4.03 μmol, 1 eq), **81** (3.01 mg, 3.18 μmol, 79%) was obtained as a red solid.

^{1}H NMR (400 MHz, MeOD-d_4) δ 8.31 (s, 1H), 8.04 (dd, *J* = 8.1, 1.4 Hz, 1H), 7.97 (d, *J* = 8.1 Hz, 1H), 7.54 (s, 1H), 7.48 – 7.43 (m, 4H), 7.30 (d, *J* = 8.2 Hz, 2H), 7.10 – 7.04 (m, 2H), 6.61 (d, *J* = 2.1 Hz, 2H), 6.33 – 6.26 (m, 4H), 5.58 (s, 2H), 4.46 – 4.45 (m, 2H), 3.89 (q, *J* = 9.4 Hz, 4H).

HRMS (ESI) Exact mass calculated for $C_{44}H_{32}F_7N_9O_6S$ $[M+2H]^{2+}$: 474.6115, found: 474.6113.

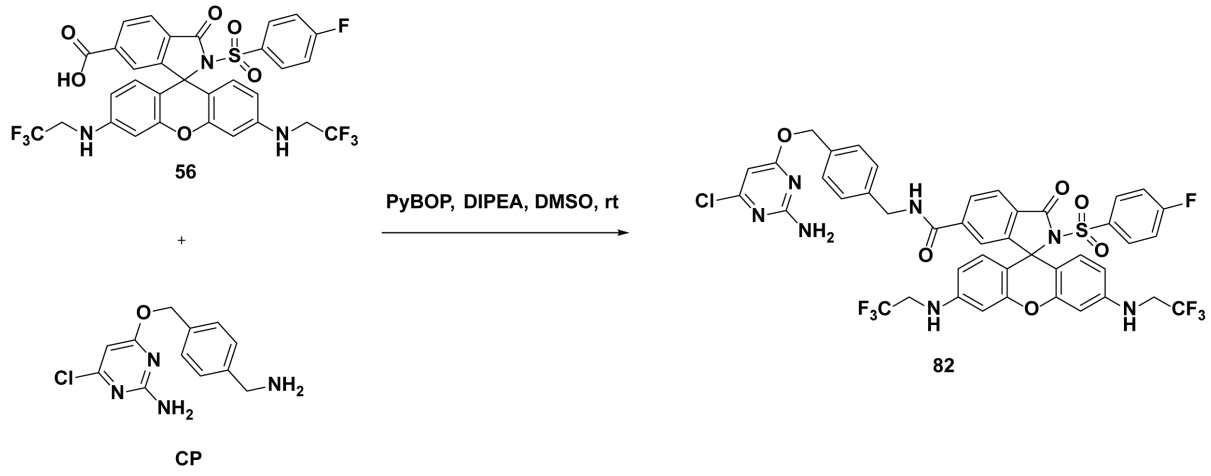

***N*-(4-(((2-amino-6-chloropyrimidin-4-yl)oxy)methyl)benzyl)-2-((4-fluorophenyl)sulfonyl)-3-oxo-3',6'-bis((2,2,2-trifluoroethyl)amino)spiro[isoindoline-1,9'-xanthene]-6-carboxamide (82): CP** (1.66 mg, 6.25 μmol, 1.5 eq) was added to a solution of **56** (2.90 mg, 4.17 μmol, 1 eq), PyBOP (2.82 mg, 5.42 μmol, 1.3 eq) and DIPEA (6.89 μL, 41.7 μmol, 10 eq) in DMSO (600 μL). The reaction mixture was stirred at rt for 30 min followed by purification

using preparative HPLC (8 mL/min, 35% to 90% MeCN/H_2O (0.1% TFA) in 55 min) to obtain **82** (2.80 mg, 2.97 µmol, 71%) as a red solid.

^{1}H NMR (400 MHz, DMSO-d_6) δ 9.22 (t, *J* = 5.9 Hz, 1H), 8.10 (dd, *J* = 8.1, 1.4 Hz, 1H), 7.95 (d, *J* = 8.1 Hz, 1H), 7.56 (s, 1H), 7.35 – 7.31 (m, 4H), 7.24 – 7.19 (m, 4H), 7.10 (s, 2H), 6.70 (t, *J* = 6.8 Hz, 2H), 6.63 (d, *J* = 2.3 Hz, 2H), 6.34 (dd, *J* = 8.7, 2.4 Hz, 2H), 6.24 (d, *J* = 8.6 Hz, 2H), 6.10 (s, 1H), 5.24 (s, 2H), 4.36 (d, *J* = 5.7 Hz, 2H), 4.05 – 3.97 (m, 4H).

HRMS (ESI) Exact mass calculated for $C_{43}H_{31}N_7O_6ClF_7S$ $[M+H]^+$: 942.1706, found: 942.1710.

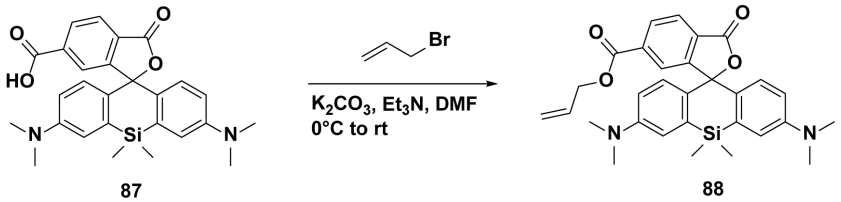

87 88

4-((Allyloxy)carbonyl)-2-(7-(dimethylamino)-3-(dimethyliminio)-5,5-dimethyl-3,5-dihydrodibenzo[b,e]silin-10-yl)benzoate (88): Potassium carbonate (40.8 mg, 295 µmol, 2.0 eq) and triethylamine (41.0 µL, 295 µmol, 2.0 eq) were added to a solution of **87** (70.0 mg, 147 µmol, 1.0 eq) in dry DMF (3 mL). The reaction mixture was cooled to 0°C and a solution of allyl bromide (19.3 µL, 221 µmol, 1.5 eq) in dry DMF (0.5 mL) was added dropwise. Afterward, the mixture was allowed to warm to rt and stirred for 2 h, before it was quenched with water and extracted with CH_2Cl_2 (3 x). The combined organic layers were dried over $MgSO_4$, filtered and concentrated. The residue was purified by flash column chromatography (CH_2Cl_2/MeOH 20:1) to give **88** (65.2 mg, 127 µmol, 86%) as a yellow solid.

TLC: R_f = 0.51 (SiO_2, CH_2Cl_2/MeOH 20:1).

^{1}H NMR (400 MHz, $CDCl_3$) δ 8.22 (dd, *J* = 8.0, 1.3 Hz, 1H), 8.02 (d, *J* = 8.0 Hz, 1H), 7.97 (s, 1H), 6.99 (d, *J* = 2.6 Hz, 2H), 6.82 (d, *J* = 8.9 Hz, 2H), 6.58 (dd, *J* = 8.9, 2.8 Hz, 2H), 6.04 – 5.94 (m, 1H), 5.40 – 5.35 (m, 1H), 5.30 – 5.27 (m, 1H), 4.79 (dt, *J* = 5.9, 1.2 Hz, 2H), 2.97 (s, 12H), 0.69 (s, 3H), 0.62 (s, 3H).

^{13}C NMR (101 MHz, $CDCl_3$) δ 170.0, 165.2, 155.2, 149.4, 136.7, 135.2, 131.8, 131.3, 130.2, 130.0, 128.0, 125.8, 125.7, 119.2, 116.8, 113.6, 92.1, 66.4, 40.4, 0.4, -1.1.

HRMS (ESI) Exact mass calculated for $C_{30}H_{32}N_2O_4Si$ $[M+H]^+$: 513.2204, found: 513.2197.

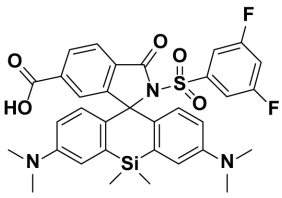

2'-((3,5-Difluorophenyl)sulfonyl)-3,7-bis(dimethylamino)-5,5-dimethyl-3'-oxo-*5H*-spiro[dibenzo[b,e]siline-10,1'-isoindoline]-6'-carboxylic acid (89): A *Schlenk* flask was dried with a heat gun *in vacuo* prior to dissolution of **88** (12.0 mg, 23.4 µmol, 1 eq) in dry CH_2Cl_2 (2 mL). Phosphorus oxychloride (32.7 µL, 351 µmol, 15 eq) was added, the mixture was heated to 50°C and stirred at this temperature for 2 h. Subsequently, 3,5-difluorobenzenesulfonamide (45.2 mg, 234 µmol, 10 eq) and DIPEA (116 µL, 702 µmol, 30 eq) dissolved in dry MeCN (2 mL) were added. After further dry MeCN (2 mL) was added, the mixture was stirred at 70°C for 10 min. The solvent was evaporated, H_2O (1 mL) was added and the aqueous layer was extracted with CH_2Cl_2 (3x). The combined organic layers were dried over $MgSO_4$, filtered and concentrated. The residue was dissolved in MeOH/CH_2Cl_2 (5:1, 1.8 mL) in a *Schlenk* flask which had been dried with a heat gun *in vacuo* before. 1,3-Dimethylbarbituric acid (11.0 mg, 70.2 µmol, 3 eq) and tetrakis(triphenylphosphine)palladium (13.5 mg, 11.7 µmol, 0.5 eq) were added and the reaction mixture was stirred at rt for 30 min. After the solvent was evaporated, the crude product was dissolved in DMSO (1.4 mL) and purified by preparative HPLC (8 mL/min, 50% to 80% MeCN/H_2O (0.1% formic acid) in 55 min) to obtain **89** (9.50 mg, 14.7 µmol, 63%) as a green solid.

^{1}H NMR (400 MHz, DMSO-d_6) δ 8.01 (s, 2H), 7.66 (tt, J = 9.0, 2.4 Hz, 1H), 7.16 (s, 1H), 6.96 (d, J = 2.9 Hz, 2H), 6.81 – 6.72 (m, 2H), 6.50 (dd, J = 9.1, 2.9 Hz, 2H), 6.32 (d, J = 9.0 Hz, 2H), 2.93 (s, 12H), 0.59 (s, 3H), 0.55 (s, 3H).

^{13}C NMR (101 MHz, DMSO-d_6) δ 165.9, 165.8, 161.4 (dd, $^1J_{CF}$ = 251 Hz, $^3J_{CF}$ = 11 Hz), 155.6, 148.6, 140.9 (t, $^3J_{CF}$ = 9 Hz), 137.4, 135.4, 129.6, 129.5, 129.3, 129.0, 124.7, 124.0, 115.1, 114.4, 111.3 (d, $^2J_{CF}$ = 28 Hz), 110.0 (t, $^2J_{CF}$ = 26 Hz), 75.6, 0.1, -1.0.

HRMS (ESI) Exact mass calculated for $C_{33}H_{31}F_2N_3O_5SSi$ $[M+H]^+$: 648.1795, found: 648.1790.

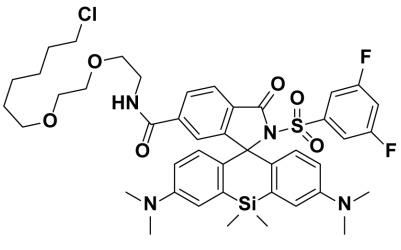

***N*-(2-(2-((6-Chlorohexyl)oxy)ethoxy)ethyl)-2'-((3,5-difluorophenyl)sulfonyl)-3,7-bis(dimethylamino)-5,5-dimethyl-3'-oxo-*5H*-spiro[dibenzo[b,e]siline-10,1'-isoindoline]-6'-carboxamide (90):** Following procedure B with **89** (2.30 mg, 3.55 µmol, 1 eq), **90** (2.37 mg, 2.78 µmol, 78%) was obtained as a green solid by preparative HPLC (8 mL/min, 55% to 90% MeCN/H_2O (0.1% TFA) in 55 min).

^{1}H NMR (400 MHz, DMSO-d_6) δ 8.70 (t, J = 5.6 Hz, 1H), 8.00 – 7.94 (m, 2H), 7.64 (tt, J = 9.1, 2.4 Hz, 1H), 7.15 (s, 1H), 6.97 (d, J = 2.9 Hz, 2H), 6.79 – 6.69 (m, 2H), 6.50 (dd, J = 9.1, 2.9 Hz,

2H), 6.30 (d, *J* = 9.0 Hz, 2H), 3.57 (t, *J* = 6.6 Hz, 2H), 3.44 – 3.37 (m, 6H), 3.30 – 3.25 (m, 4H), 2.93 (s, 12H), 1.68 – 1.61 (m, 2H), 1.42 – 1.27 (m, 4H), 1.24 – 1.17 (m, 2H), 0.59 (s, 3H), 0.57 (s, 3H).

HRMS (ESI) Exact mass calculated for $C_{43}H_{51}ClF_2N_4O_6SSi$ $[M+H]^+$: 853.3028, found: 853.3030.

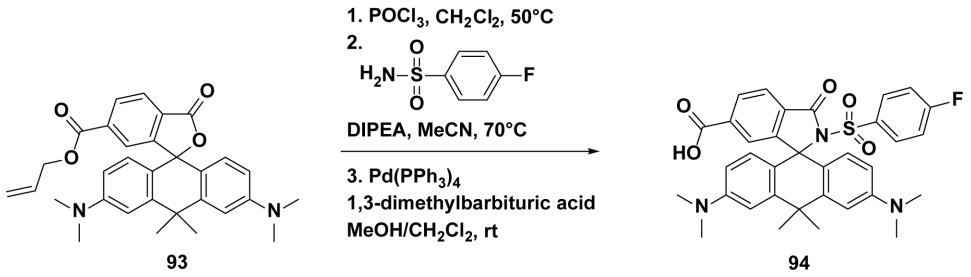

3,6-Bis(dimethylamino)-2'-((4-fluorophenyl)sulfonyl)-10,10-dimethyl-3'-oxo-*10H*-spiro[anthracene-9,1'-isoindoline]-6'-carboxylic acid (94): 93 was synthesized according to a previously reported procedure.[85] A *Schlenk* flask was dried with a heat gun *in vacuo* prior to dissolution of **93** (11.0 mg, 22.2 µmol, 1 eq) in dry CH_2Cl_2 (2 mL). Phosphorus oxychloride (31.0 µL, 332 µmol, 15 eq) was added, the mixture was heated to 50°C and stirred at this temperature for 2 h. Subsequently, 4-fluorobenzenesulfonamide (38.8 mg, 222 µmol, 10 eq) and DIPEA (110 µL, 665 µmol, 30 eq) dissolved in dry MeCN (2 mL) were added. After further dry MeCN (2 mL) was added, the mixture was stirred at 70°C for 10 min. The solvent was evaporated, H_2O (1 mL) was added and the aqueous layer was extracted with CH_2Cl_2 (3x). The combined organic layers were dried over $MgSO_4$, filtered and concentrated. The residue was dissolved in MeOH/CH_2Cl_2 (5:1, 1.8 mL) in a *Schlenk* flask which had been dried with a heat gun *in vacuo* before. 1,3-Dimethylbarbituric acid (10.4 mg, 66.5 µmol, 3 eq) and tetrakis-(triphenylphosphine)palladium (7.69 mg, 6.65 µmol, 0.3 eq) were added and the reaction mixture was stirred at rt for 30 min. After the solvent was evaporated, the crude product was dissolved in DMSO (1.4 mL) and purified by preparative HPLC (8 mL/min, 40% to 80% MeCN/H_2O (0.1% TFA) in 55 min) to obtain **94** (10.6 mg, 17.3 µmol, 78%) as a blue solid.

^{1}H NMR (400 MHz, DMSO-d_6) δ 8.02 – 7.96 (m, 2H), 7.43 – 7.40 (m, 2H), 7.31 (t, *J* = 8.8 Hz, 2H), 7.12 (s, 1H), 7.00 (s, 2H), 6.51 (d, *J* = 8.4 Hz, 2H), 6.33 (d, *J* = 8.8 Hz, 2H), 2.98 (s, 12H), 1.89 (s, 3H), 1.82 (s, 3H).

^{13}C NMR (101 MHz, DMSO-d_6) δ 165.9, 165.8, 165.1 (d, $^1J_{CF}$ = 254 Hz), 158.5, 158.1, 155.2, 149.5, 145.4, 137.1, 134.8, 131.2 (d, $^3J_{CF}$ = 10 Hz), 129.5, 129.5, 128.0, 124.6, 124.1, 115.9 (d, $^2J_{CF}$ = 23 Hz), 112.5, 110.5, 71.8, 40.5, 37.7, 36.1, 32.5.

HRMS (ESI) Exact mass calculated for $C_{34}H_{32}FN_3O_5S$ $[M+H]^+$: 614.2119, found: 614.2120.

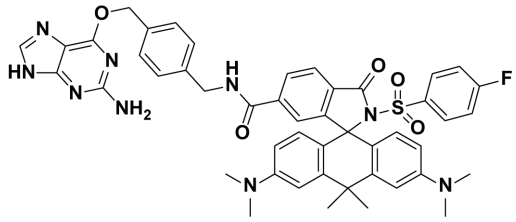

***N*-(4-(((2-Amino-*9H*-purin-6-yl)oxy)methyl) benzyl)-3,6-bis(dimethylamino)-2'-((4-fluorophenyl)sulfonyl)-10,10-dimethyl-3'-oxo-10H-spiro[anthracene-9,1'-isoindoline]-6'-carboxamide (95):** Following procedure C with **94** (4.00 mg, 6.52 µmol, 1 eq), **95** (3.66 mg, 4.23 µmol, 65%) was obtained as a blue solid.

^{1}H NMR (400 MHz, DMSO-d_6) δ 9.23 (t, *J* = 5.9 Hz, 1H), 8.31 (s, 1H), 7.99 (dd, *J* = 8.1, 1.3 Hz, 1H), 7.94 (d, *J* = 8.1 Hz, 1H), 7.43 – 7.38 (m, 4H), 7.30 – 7.23 (m, 4H), 7.12 (s, 1H), 6.92 (d, *J* = 2.4 Hz, 2H), 6.45 (dd, *J* = 8.9, 2.5 Hz, 2H), 6.28 (d, *J* = 8.8 Hz, 2H), 5.46 (s, 2H), 4.35 (d, *J* = 5.7 Hz, 2H), 2.95 (s, 12H), 1.89 (s, 3H), 1.82 (s, 3H).

HRMS (ESI) Exact mass calculated for $C_{47}H_{44}FN_9O_5S$ $[M+2H]^{2+}$: 433.6658, found: 433.6660.

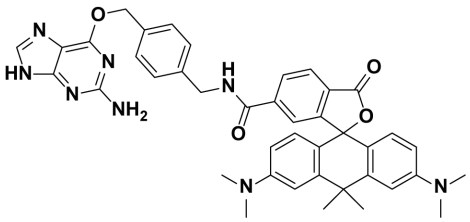

***N*-(4-(((2-amino-9*H*-purin-6-yl)oxy)methyl)benzyl)-3,6-bis(dimethylamino)-10,10-dimethyl-3'-oxo-3'*H*,10*H*-spiro[anthracene-9,1'-isobenzofuran]-6'-carboxamide (96):** Following procedure C with **92** (3.00 mg, 6.57 µmol, 1 eq), **96** (3.95 mg, 5.57 µmol, 85%) was obtained as a dark blue solid.

^{1}H NMR (400 MHz, MeOD-d_4) δ 9.29 (t, *J* = 5.9 Hz, 1H), 8.34 (d, *J* = 8.2 Hz, 1H), 8.16 (dd, *J* = 8.2, 1.7 Hz, 1H), 8.06 (s, 1H), 7.77 (d, *J* = 1.6 Hz, 1H), 7.48 (d, *J* = 8.1 Hz, 2H), 7.38 (d, *J* = 8.1 Hz, 2H), 7.22 (d, *J* = 2.4 Hz, 2H), 6.99 (d, *J* = 9.4 Hz, 2H), 6.78 (dd, *J* = 9.4, 2.5 Hz, 2H), 5.57 (s, 2H), 4.59 – 4.57 (m, 2H), 3.31 (s, 12H), 1.86 (s, 3H), 1.75 (s, 3H).

HRMS (ESI) Exact mass calculated for $C_{41}H_{40}N_8O_4$ $[M+2H]^{2+}$: 355.1659, found: 355.1659.

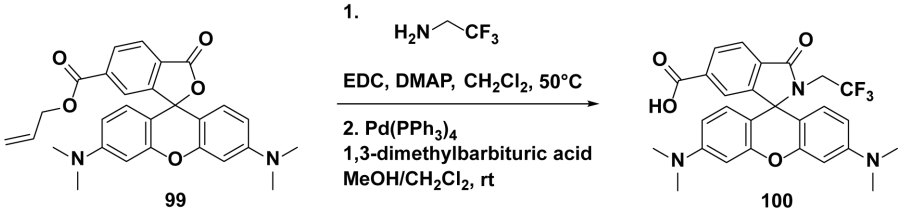

3',6'-Bis(dimethylamino)-3-oxo-2-(2,2,2-trifluoroethyl)spiro[isoindoline-1,9'-xanthene]-6-carboxylic acid (100): 99 was synthesized according to a previously reported procedure.[85] A solution of **99** (25.0 mg, 53.1 µmol, 1 eq), 2,2,2-trifluoroethylamine (84.9 µL, 1.06 mmol, 20 eq), 1-(3-dimethylaminopropyl)-3-ethylcarbodiimide hydrochloride (40.7 mg, 213 µmol, 4 eq) and 4-dimethylaminopyridine (26.0 mg, 213 µmol, 4 eq) in CH_2Cl_2 (1 mL) was heated to 50°C and stirred at this temperature for 12 h in a sealed tube. H_2O (2 mL) was added and the aqueous layer was extracted with CH_2Cl_2 (3x). The combined organic layers were dried over $MgSO_4$, filtered and concentrated. The residue was dissolved in MeOH/CH_2Cl_2 (5:1, 3 mL) in a *Schlenk* flask which had been dried with a heat gun *in vacuo* before. 1,3-Dimethylbarbituric acid (16.6 mg, 106 µmol, 2 eq) and tetrakis(triphenylphosphine)palladium (12.3 mg, 10.6 µmol, 0.1 eq) were added and the reaction mixture was stirred at rt for 30 min. After the solvent was evaporated, the crude product was dissolved in DMSO (3.2 mL) and purified by preparative HPLC (8 mL/min, 45% to 80% MeCN/H_2O (0.1% formic acid) in 55 min) to obtain **100** (16.7 mg, 32.6 µmol, 61%) as a slightly magenta solid.

^{1}H NMR (400 MHz, DMSO-d_6) δ 8.09 (dd, J = 7.9, 1.2 Hz, 1H), 7.98 (d, J = 7.9 Hz, 1H), 7.42 (s, 1H), 6.45 – 6.43 (m, 4H), 6.37 – 6.35 (m, 2H), 3.75 (q, J = 9.7 Hz, 2H), 2.92 (s, 12H).

^{13}C NMR (101 MHz, DMSO-d_6) δ 167.4, 166.3, 153.9, 152.4, 151.3, 136.0, 131.8, 129.7, 128.2, 124.4, 123.8 (q, $^1J_{CF}$ = 281 Hz), 123.4, 109.2, 104.2, 98.2, 64.9, 41.3 (q, $^2J_{CF}$ = 36 Hz).

HRMS (ESI) Exact mass calculated for $C_{27}H_{24}F_3N_3O_4$ $[M+H]^+$: 512.1792, found: 512.1793.

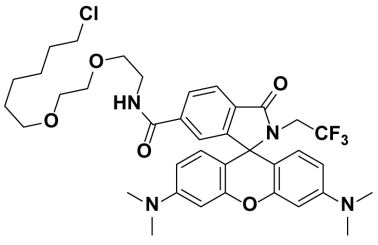

***N*-(2-(2-((6-Chlorohexyl)oxy)ethoxy)ethyl)-3',6'-bis(dimethylamino)-3-oxo-2-(2,2,2-trifluoroethyl)spiro[isoindoline-1,9'-xanthene]-6-carboxamide (101):** Following procedure B with **100** (4.00 mg, 7.82 µmol, 1 eq), **101** (3.10 mg, 4.32 µmol, 55%) was obtained as a colorless solid by preparative HPLC (8 mL/min, 60% to 95% MeCN/H_2O (0.1% formic acid) in 55 min).

^{1}H NMR (400 MHz, DMSO-d_6) δ 8.67 (t, J = 5.6 Hz, 1H), 8.04 (dd, J = 8.0, 1.3 Hz, 1H), 7.95 (d, J = 8.0 Hz, 1H), 7.49 (s, 1H), 6.45 – 6.42 (m, 4H), 6.36 – 6.33 (m, 2H), 3.72 (q, J = 9.7 Hz,

2H), 3.58 (t, *J* = 6.6 Hz, 2H), 3.47 – 3.43 (m, 4H), 3.41 – 3.39 (m, 2H), 3.31 – 3.27 (m, 4H), 2.92 (s, 12H), 1.66 (p, *J* = 6.7 Hz, 2H), 1.40 (p, *J* = 6.8 Hz, 2H), 1.36 – 1.19 (m, 4H).

HRMS (ESI) Exact mass calculated for $C_{37}H_{44}N_4O_5ClF_3$ $[M+H]^+$: 717.3025, found: 717.3019.

General Procedure D for 102:

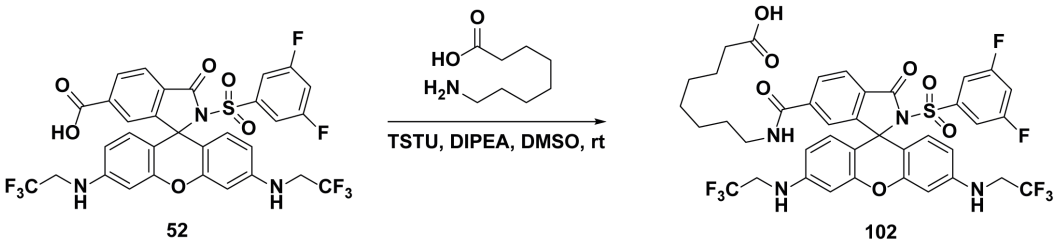

8-(2-((3,5-difluorophenyl)sulfonyl)-3-oxo-3',6'-bis((2,2,2-trifluoroethyl)amino)spiro[isoindoline-1,9'-xanthene]-6-carboxamido)octanoic acid (102): A solution of **52** (3.50 mg, 4.91 µmol, 1 eq), DIPEA (5.51 µL, 33.4 µmol, 6.8 eq) and TSTU (1.77 mg, 5.89 µmol, 1.2 eq) in DMSO (0.3 mL) was stirred at rt for 5 min. 8-Aminooctanoic acid (1.80 mg, 11.3 µmol, 2.3 eq) was added and the mixture was sonicated at rt for 15 min. Subsequently, H_2O (50 µL) was added and the mixture was stirred at rt for 15 min followed by purification using preparative HPLC (8 mL/min, 45% to 85% MeCN/H_2O (0.1% TFA) in 55 min) to obtain **102** (3.37 mg, 3.94 µmol, 80%) as a red solid.

^{1}H NMR (400 MHz, MeOD-*d*$_4$) δ 8.06 (dd, *J* = 8.1, 1.4 Hz, 1H), 8.00 (d, *J* = 8.1 Hz, 1H), 7.54 (s, 1H), 7.22 (tt, *J* = 8.7, 2.3 Hz, 1H), 7.00 – 6.96 (m, 2H), 6.69 – 6.63 (m, 2H), 6.39 – 6.34 (m, 4H), 3.92 (q, *J* = 9.2 Hz, 4H), 3.27 (t, *J* = 7.2 Hz, 2H), 2.24 (t, *J* = 7.4 Hz, 2H), 1.58 – 1.50 (m, 4H), 1.34 – 1.28 (m, 6H).

HRMS (ESI) Exact mass calculated for $C_{39}H_{34}F_8N_4O_7S$ $[M+H]^+$: 855.2093, found: 855.2100.

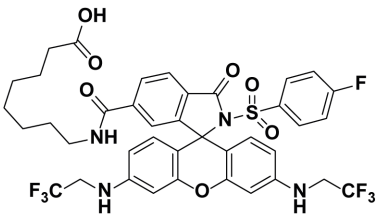

8-(2-((4-fluorophenyl)sulfonyl)-3-oxo-3',6'-bis((2,2,2-trifluoroethyl)amino)spiro[isoindoline-1,9'-xanthene]-6-carboxamido)octanoic acid (103): Following procedure D with **56** (3.10 mg, 4.46 µmol, 1 eq), **103** (2.82 mg, 3.37 µmol, 76%) was obtained as a red solid.

^{1}H NMR (400 MHz, MeOD-*d*$_4$) δ 8.03 (dd, *J* = 8.1, 1.3 Hz, 1H), 7.97 (d, *J* = 8.1 Hz, 1H), 7.52 – 7.47 (m, 3H), 7.10 – 7.07 (m, 2H), 6.66 – 6.64 (m, 2H), 6.37 – 6.32 (m, 4H), 3.93 (q, *J* = 9.1 Hz, 4H), 3.26 (t, *J* = 7.2 Hz, 2H), 2.24 (t, *J* = 7.4 Hz, 2H), 1.58 – 1.50 (m, 4H), 1.33 – 1.28 (m, 6H).

HRMS (ESI) Exact mass calculated for $C_{39}H_{35}F_7N_4O_7S$ [M+H]$^+$: 837.2187, found: 837.2189.

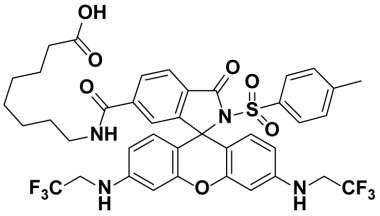

8-(3-oxo-2-tosyl-3',6'-bis((2,2,2-trifluoroethyl)amino)-spiro[isoindoline-1,9'-xanthene]-6-carboxamido)octanoic acid (104): Following procedure D with **58** (2.80 mg, 4.05 µmol, 1 eq), **104** (2.81 mg, 3.37 µmol, 83%) was obtained as a red solid.

^{1}H NMR (400 MHz, MeOD-*d*$_4$) δ 8.03 (d, *J* = 8.1 Hz, 1H), 7.95 (d, *J* = 8.1 Hz, 1H), 7.51 (s, 1H), 7.32 (d, *J* = 8.1 Hz, 2H), 7.15 (d, *J* = 8.2 Hz, 2H), 6.68 – 6.62 (m, 2H), 6.41 – 6.30 (m, 4H), 3.96 – 3.90 (m, 4H), 3.26 (t, *J* = 7.1 Hz, 2H), 2.36 (s, 3H), 2.24 (t, *J* = 7.4 Hz, 2H), 1.59 – 1.50 (m, 4H), 1.34 – 1.28 (m, 6H).

HRMS (ESI) Exact mass calculated for $C_{40}H_{38}F_6N_4O_7S$ [M+H]$^+$: 833.2438, found: 833.2445.

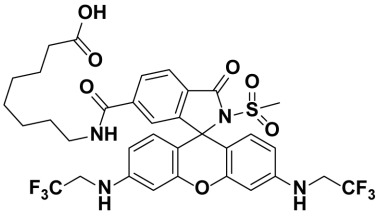

8-(2-(methylsulfonyl)-3-oxo-3',6'-bis((2,2,2-trifluoro-ethyl)amino)spiro[isoindoline-1,9'-xanthene]-6-carboxamido)octanoic acid (105): Following procedure D with **60** (3.20 mg, 5.20 µmol, 1.0 eq), **105** (3.25 mg, 4.30 µmol, 83%) was obtained as a red solid.

^{1}H NMR (400 MHz, MeOD-*d*$_4$) δ 8.08 – 8.04 (m, 2H), 7.52 (s, 1H), 6.60 – 6.56 (m, 4H), 6.47 – 6.45 (m, 2H), 3.87 (q, *J* = 9.0 Hz, 4H), 3.27 (t, *J* = 7.2 Hz, 2H), 2.95 (s, 3H), 2.24 (t, *J* = 7.4 Hz, 2H), 1.59 – 1.51 (m, 4H), 1.33 – 1.29 (m, 6H).

HRMS (ESI) Exact mass calculated for $C_{34}H_{34}F_6N_4O_7S$ [M+H]$^+$: 757.2125, found: 757.2126.

General Procedure E for 106:

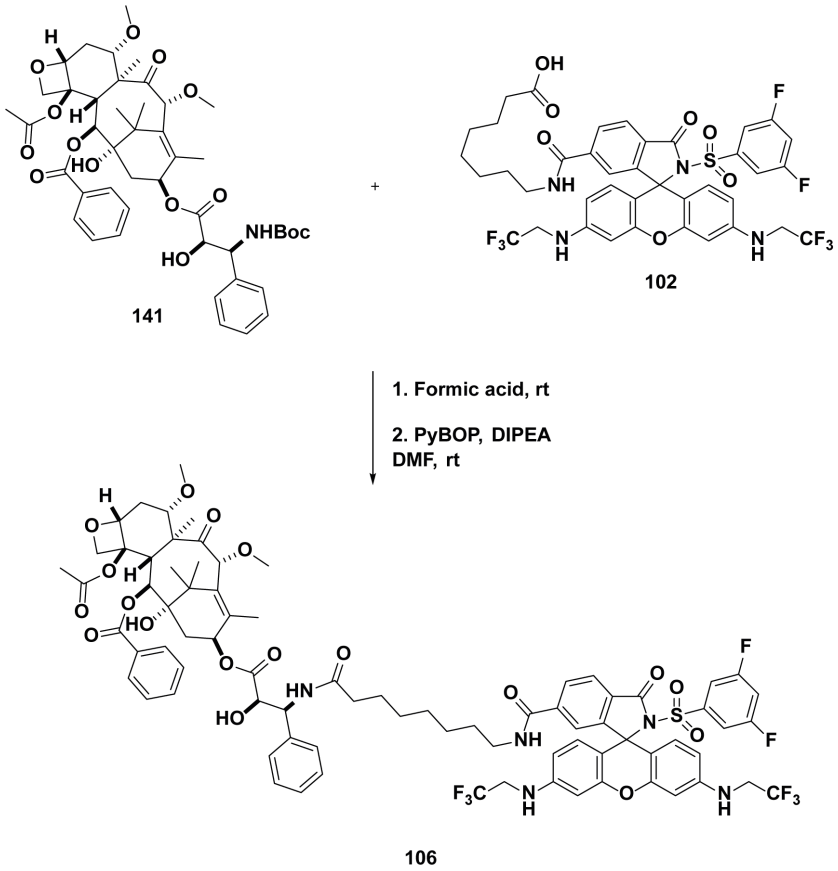

(2a*R*,4*S*,4a*S*,6*R*,9*S*,11*S*,12*S*,12a*R*,12b*S*)-12b-acetoxy-9-(((2*R*,3*S*)-3-(8-(2-((3,5-difluorophenyl)sulfonyl)-3-oxo-3',6'-bis((2,2,2-trifluoroethyl)amino)spiro[isoindoline-1,9'-xanthene]-6-carboxamido)octanamido)-2-hydroxy-3-phenylpropanoyl)oxy)-11-hydroxy-4,6-dimethoxy-4a,8,13,13-tetramethyl-5-oxo-2a,3,4,4a,5,6,9,10,11,12,12a,12b-dodecahydro-1*H*-[7,11]methanocyclodeca[3,4]benzo[1,2-b]oxet-12-yl benzoate (106): A solution of **141** (3.96 mg, 4.73 µmol, 1.2 eq) in formic acid (0.2 mL) was stirred at rt for 30 min followed by evaporation of the solvent and drying under high vacuum for 2 h. The residue was dissolved in DMF (0.4 mL) and added to a solution of **102** (3.37 mg, 3.94 µmol, 1 eq), DIPEA (6.52 µL, 39.4 µmol, 10 eq) and PYBOP (3.08 mg, 5.91 µmol, 1.5 eq) in DMF (0.4 mL). The reaction mixture was stirred at rt for 20 min followed by purification using preparative HPLC (8 mL/min, 45% to 85% MeCN/H_2O (0.1% TFA) in 55 min) to give **106** (4.26 mg, 2.71 µmol, 69%) as a red solid.

^{1}H NMR (400 MHz, DMSO-d_6) δ 8.64 (t, *J* = 5.3 Hz, 1H), 8.37 (d, *J* = 9.0 Hz, 1H), 8.07 (d, *J* = 8.1 Hz, 1H), 7.97 (d, *J* = 7.6 Hz, 3H), 7.69 – 7.57 (m, 4H), 7.52 (s, 1H), 7.37 – 7.28 (m, 4H), 7.18 (t, *J* = 7.1 Hz, 1H), 6.83 – 6.81 (m, 2H), 6.76 – 6.72 (m, 2H), 6.64 (d, *J* = 1.8 Hz, 2H), 6.34 (d, *J* = 8.8 Hz, 2H), 6.27 (dd, *J* = 8.7, 2.9 Hz, 2H), 5.92 (t, *J* = 8.8 Hz, 1H), 5.38 (d, *J* = 7.1 Hz, 1H), 5.28 – 5.25 (m, 1H), 4.95 (d, *J* = 9.9 Hz, 1H), 4.69 (s, 1H), 4.40 (d, *J* = 5.8 Hz, 1H), 4.02

– 3.96 (m, 6H), 3.77 – 3.72 (m, 1H), 3.62 (d, *J* = 7.0 Hz, 1H), 3.29 (s, 3H), 3.21 (s, 3H), 3.12 (q, *J* = 6.2 Hz, 2H), 2.69 – 2.62 (m, 1H), 2.24 (s, 3H), 2.16 – 2.07 (m, 3H), 2.00 – 1.92 (m, 1H), 1.86 – 1.80 (m, 4H), 1.51 (s, 3H), 1.46 – 1.37 (m, 5H), 1.23 – 1.17 (m, 7H), 1.01 (s, 3H), 0.96 (s, 3H).

HRMS (ESI) Exact mass calculated for $C_{79}H_{81}F_8N_5O_{18}S$ $[M+2H]^{2+}$: 786.7658, found: 786.7651.

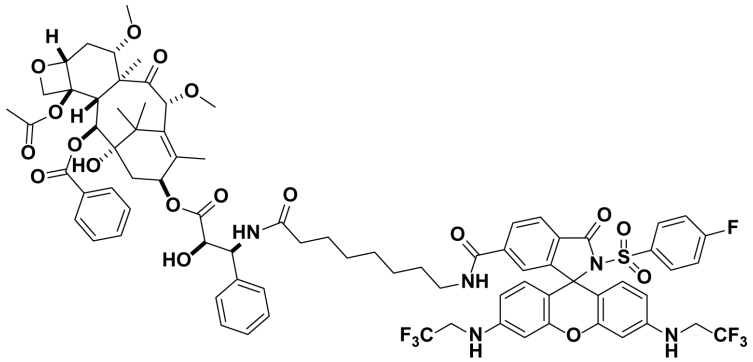

(2a*R*,4*S*,4a*S*,6*R*,9*S*,11*S*,12*S*,12a*R*,12b*S*)-12b-acetoxy-9-(((2*R*,3*S*)-3-(8-(2-((4-fluorophenyl)sulfonyl)-3-oxo-3',6'-bis((2,2,2-trifluoroethyl)amino)spiro[isoindoline-1,9'-xanthene]-6-carboxamido)octanamido)-2-hydroxy-3-phenylpropanoyl)oxy)-11-hydroxy-4,6-dimethoxy-4a,8,13,13-tetramethyl-5-oxo-2a,3,4,4a,5,6,9,10,11,12,12a,12b-dodecahydro-1*H*-[7,11]methanocyclodeca[3,4]benzo[1,2-b]oxet-12-yl benzoate (107): Following procedure E with **103** (2.82 mg, 3.37 µmol, 1 eq), **107** (3.27 mg, 2.10 µmol, 62%) was obtained as a red solid.

^{1}H NMR (400 MHz, DMSO-d_6) δ 8.63 (t, *J* = 5.4 Hz, 1H), 8.37 (d, *J* = 9.0 Hz, 1H), 8.05 (d, *J* = 8.2 Hz, 1H), 7.98 – 7.92 (m, 3H), 7.67 (t, *J* = 7.3 Hz, 1H), 7.58 (t, *J* = 7.5 Hz, 2H), 7.50 (s, 1H), 7.36 – 7.28 (m, 6H), 7.24 – 7.16 (m, 3H), 6.72 – 6.68 (m, 2H), 6.64 (d, *J* = 1.9 Hz, 2H), 6.34 (d, *J* = 8.7 Hz, 2H), 6.24 – 6.21 (m, 2H), 5.92 (t, *J* = 8.7 Hz, 1H), 5.38 (d, *J* = 7.1 Hz, 1H), 5.28 – 5.24 (m, 1H), 4.95 (d, *J* = 9.9 Hz, 1H), 4.69 (s, 1H), 4.40 (d, *J* = 5.8 Hz, 1H), 4.05 – 3.98 (m, 6H), 3.77 – 3.72 (m, 1H), 3.62 (d, *J* = 7.1 Hz, 1H), 3.29 (s, 3H), 3.21 (s, 3H), 3.11 (q, *J* = 6.0 Hz, 2H), 2.69 – 2.62 (m, 1H), 2.24 (s, 3H), 2.12 (t, *J* = 7.2 Hz, 2H), 2.02 – 1.91 (m, 2H), 1.86 – 1.80 (m, 4H), 1.51 (s, 3H), 1.46 – 1.38 (m, 5H), 1.27 – 1.16 (m, 7H), 1.01 (s, 3H), 0.96 (s, 3H).

HRMS (ESI) Exact mass calculated for $C_{79}H_{82}F_7N_5O_{18}S$ $[M+2H]^{2+}$: 777.7705, found: 777.7698.

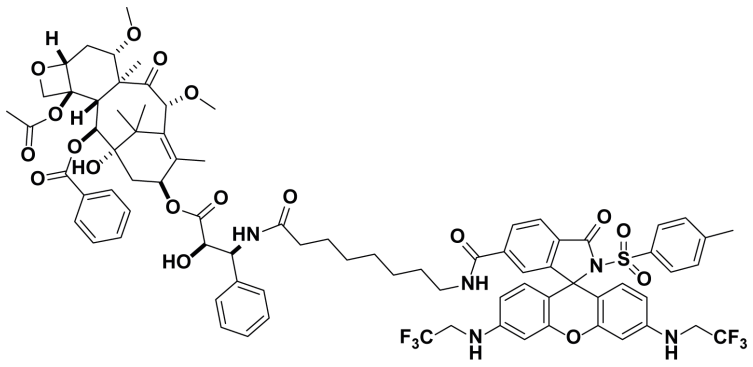

(2a*R*,4*S*,4a*S*,6*R*,9*S*,11*S*,12*S*,12a*R*,12b*S*)-12b-acetoxy-11-hydroxy-9-(((2*R*,3*S*)-2-hydroxy-3-(8-(3-oxo-2-tosyl-3',6'-bis((2,2,2-trifluoroethyl)amino)spiro[isoindoline-1,9'-xanthene]-6-carboxamido)octanamido)-3-phenylpropanoyl)oxy)-4,6-dimethoxy-4a,8,13,13-tetramethyl-5-oxo-2a,3,4,4a,5,6,9,10,11,12,12a,12b-dodecahydro-1*H*-[7,11]methanocyclodeca[3,4]benzo[1,2-b]oxet-12-yl benzoate (108): Following procedure E with **104** (2.81 mg, 3.37 μmol, 1 eq), **108** (3.32 mg, 2.14 μmol, 63%) was obtained as a red solid.

^{1}H NMR (400 MHz, DMSO-d_6) δ 8.63 (t, *J* = 5.4 Hz, 1H), 8.37 (d, *J* = 9.0 Hz, 1H), 8.04 (d, *J* = 8.2 Hz, 1H), 7.97 (d, *J* = 7.4 Hz, 2H), 7.90 (d, *J* = 8.1 Hz, 1H), 7.67 (t, *J* = 7.4 Hz, 1H), 7.58 (t, *J* = 7.5 Hz, 2H), 7.50 (s, 1H), 7.36 – 7.28 (m, 4H), 7.19 – 7.15 (m, 5H), 6.70 – 6.68 (m, 2H), 6.63 (d, *J* = 1.9 Hz, 2H), 6.35 (d, *J* = 8.7 Hz, 2H), 6.24 – 6.21 (m, 2H), 5.92 (t, *J* = 8.8 Hz, 2H), 5.38 (d, *J* = 7.1 Hz, 1H), 5.28 – 5.25 (m, 1H), 4.96 (d, *J* = 10.0 Hz, 1H), 4.69 (s, 1H), 4.40 (d, *J* = 5.8 Hz, 1H), 4.05 – 3.97 (m, 6H), 3.77 – 3.72 (m, 1H), 3.62 (d, *J* = 7.1 Hz, 1H), 3.29 (s, 3H), 3.21 (s, 3H), 3.11 (q, *J* = 6.3 Hz, 2H), 2.69 – 2.62 (m, 1H), 2.33 (s, 3H), 2.24 (s, 3H), 2.12 (t, *J* = 7.1 Hz, 2H), 2.02 – 1.91 (m, 1H), 1.86 – 1.82 (m, 4H), 1.51 (s, 3H), 1.46 – 1.34 (m, 5H), 1.23 – 1.17 (m, 7H), 1.01 (s, 3H), 0.96 (s, 3H).

HRMS (ESI) Exact mass calculated for $C_{80}H_{85}F_6N_5O_{18}S$ $[M+2H]^{2+}$: 775.7830, found: 775.7825.

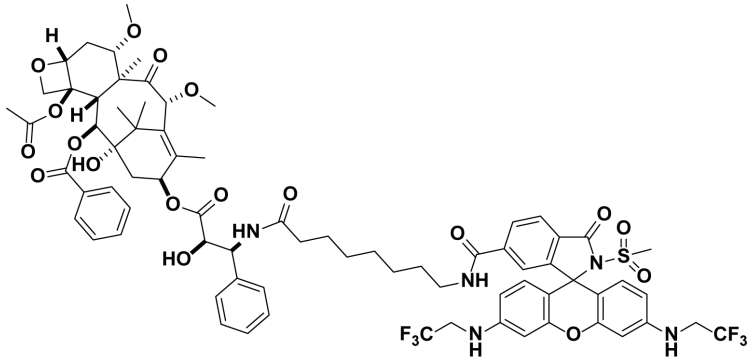

(2a*R*,4*S*,4a*S*,6*R*,9*S*,11*S*,12*S*,12a*R*,12b*S*)-12b-acetoxy-11-hydroxy-9-(((2*R*,3*S*)-2-hydroxy-3-(8-(2-(methylsulfonyl)-3-oxo-3',6'-bis((2,2,2-trifluoroethyl)amino)spiro[isoindoline-1,9'-xanthene]-6-carboxamido)octanamido)-3-phenylpropanoyl)oxy)-4,6-dimethoxy-4a,8,13,13-tetramethyl-5-oxo-2a,3,4,4a,5,6,9,10,11,12,12a,12b-dodecahydro-1*H*-[7,11]methanocyclodeca[3,4]benzo[1,2-b]oxet-12-yl benzoate (109): Following procedure E with **105** (3.25 mg, 4.29 µmol, 1 eq), **109** (4.80 mg, 3.26 µmol, 76%) was obtained as a red solid.

^{1}H NMR (400 MHz, DMSO-d_6) δ 8.65 (t, *J* = 5.4 Hz, 1H), 8.38 (d, *J* = 9.0 Hz, 1H), 8.07 (d, *J* = 8.1 Hz, 1H), 8.02 (d, *J* = 8.0 Hz, 1H), 7.98 (d, *J* = 7.3 Hz, 2H), 7.68 (t, *J* = 7.3 Hz, 1H), 7.59 (t, *J* = 7.6 Hz, 2H), 7.46 (s, 1H), 7.37 – 7.29 (m, 4H), 7.18 (t, *J* = 7.2 Hz, 1H), 6.68 – 6.60 (m, 2H), 6.53 – 6.50 (m, 4H), 6.43 – 6.40 (m, 2H), 5.93 (t, *J* = 8.9 Hz, 1H), 5.38 (d, *J* = 7.1 Hz, 1H), 5.29 – 5.25 (m, 1H), 4.96 (d, *J* = 9.8 Hz, 1H), 4.70 (s, 1H), 4.41 (d, *J* = 5.8 Hz, 1H), 4.02 – 3.94 (m, 6H), 3.77 – 3.73 (m, 1H), 3.62 (d, *J* = 7.1 Hz, 1H), 3.30 (s, 3H), 3.21 (s, 3H), 3.13 (q, *J* = 6.4 Hz, 2H), 2.96 (s, 3H), 2.69 – 2.62 (m, 1H), 2.24 (s, 3H), 2.17 – 2.05 (m, 3H), 2.00 – 1.92 (m, 1H), 1.86 – 1.80 (m, 4H), 1.51 (s, 3H), 1.46 – 1.36 (m, 5H), 1.23 – 1.18 (m, 7H), 1.01 (s, 3H), 0.96 (s, 3H).

HRMS (ESI) Exact mass calculated for $C_{74}H_{81}F_6N_5O_{18}S$ $[M+H]^+$: 1474.5274, found: 1474.5278.

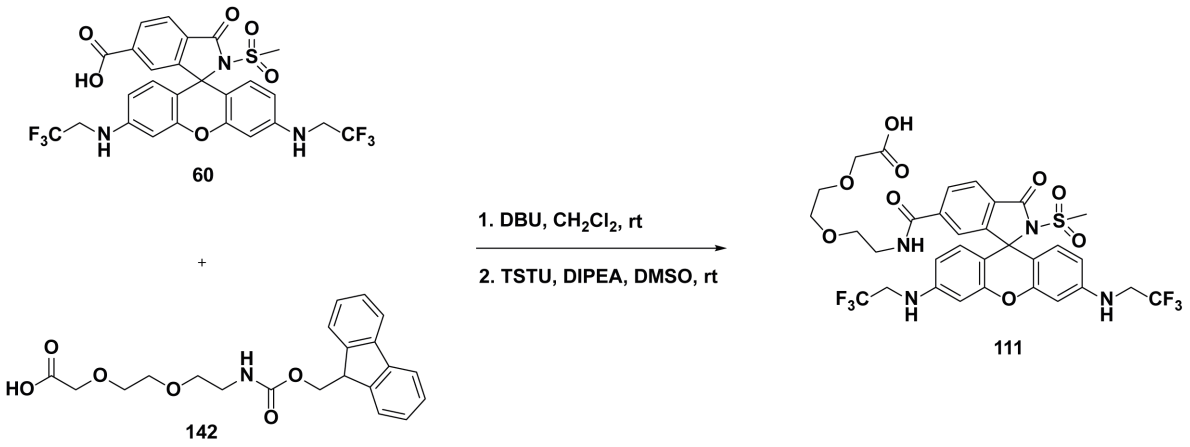

2-(2-(2-(2-(methylsulfonyl)-3-oxo-3',6'-bis((2,2,2-trifluoroethyl)amino)spiro[isoindoline-1,9'-xanthene]-6-carboxamido)ethoxy)ethoxy)acetic acid (111): A solution of **142** (6.05 mg, 15.7 µmol, 2.3 eq) and DBU (16.3 µL, 109 µmol, 16 eq) in CH_2Cl_2 (0.3 mL) was stirred at rt for 5 min. The solvent was evaporated under reduced pressure. The residue was dissolved in DMSO (0.3 mL) and added to a solution of **60** (4.20 mg, 6.82 µmol, 1 eq), DIPEA (7.67 µL, 46.4 µmol, 6.8 eq) and TSTU (2.47 mg, 8.19 µmol, 1.2 eq) in DMSO (0.4 mL) which had been stirred at rt for 5 min beforehand. The resulting mixture was stirred at rt for 15 min. Subsequently, H_2O (50 µL) was added and the mixture was stirred at rt for 15 min followed by purification using preparative HPLC (8 mL/min, 35% to 90% MeCN/H_2O (0.1% TFA) in 55 min) to obtain **111** (1.98 mg, 2.60 µmol, 38%) as a red solid.

^{1}H NMR (400 MHz, MeOD-*d*$_4$) δ 8.09 – 8.04 (m, 2H), 7.53 (s, 1H), 6.57 – 6.52 (m, 4H), 6.42 (dd, *J* = 8.6, 2.0 Hz, 2H), 4.01 (s, 2H), 3.85 (q, *J* = 9.2 Hz, 4H), 3.63 – 3.56 (m, 6H), 3.49 – 3.47 (m, 2H), 2.95 (s, 3H).

HRMS (ESI) Exact mass calculated for $C_{32}H_{30}F_6N_4O_9S$ $[M+H]^+$: 761.1710, found: 761.1716.

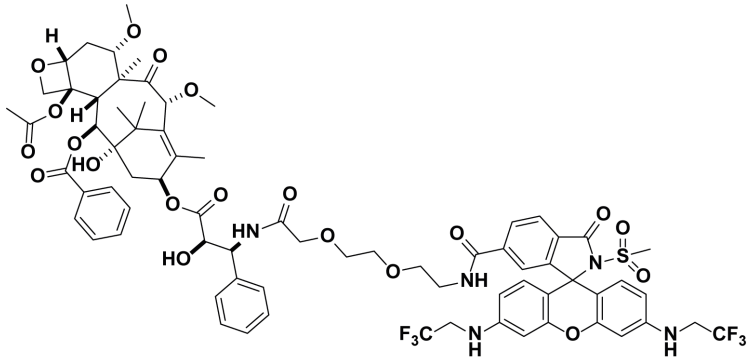

(2a*R*,4*S*,4a*S*,6*R*,9*S*,11*S*,12*S*,12a*R*,12b*S*)-12b-acetoxy-11-hydroxy-9-(((12*S*,13*R*)-13-hydroxy-1-(2-(methylsulfonyl)-3-oxo-3',6'-bis((2,2,2-trifluoroethyl)amino)spiro[isoindoline-1,9'-xanthen]-6-yl)-1,10-dioxo-12-phenyl-5,8-dioxa-2,11-diazatetradecan-14-oyl)oxy)-4,6-dimethoxy-4a,8,13,13-tetramethyl-5-oxo-2a,3,4,4a,5,6,9,10,11,12,12a,12b-dodecahydro-1*H*-[7,11]methanocyclodeca[3,4]benzo[1,2-b]oxet-12-yl benzoate (112): Following procedure E with **111** (2.40 mg, 3.16 μmol, 1 eq), **112** (2.86 mg, 1.93 μmol, 61%) was obtained as a red solid.

^{1}H NMR (400 MHz, DMSO-d_6) δ 8.75 (t, *J* = 5.5 Hz, 1H), 8.25 (d, *J* = 9.0 Hz, 1H), 8.08 (d, *J* = 8.1 Hz, 1H), 8.02 (d, *J* = 8.0 Hz, 1H), 7.97 (d, *J* = 8.1 Hz, 2H), 7.68 (t, *J* = 7.3 Hz, 1H), 7.59 (t, *J* = 7.7 Hz, 2H), 7.49 (s, 1H), 7.38 – 7.31 (m, 4H), 7.21 (t, *J* = 6.9 Hz, 1H), 6.64 (t, *J* = 5.5 Hz, 2H), 6.55 – 6.50 (m, 3H), 6.41 (dd, *J* = 8.7, 1.8 Hz, 2H), 6.15 (s, 1H), 5.95 (t, *J* = 8.9 Hz, 1H), 5.38 (d, *J* = 7.1 Hz, 1H), 5.30 – 5.26 (m, 1H), 4.95 (d, *J* = 9.9 Hz, 1H), 4.69 (s, 2H), 4.52 (d, *J* = 5.9 Hz, 1H), 4.04 – 3.87 (m, 7H), 3.77 – 3.72 (m, 1H), 3.62 – 3.56 (m, 6H), 3.47 – 3.45 (m, 2H), 3.36 – 3.31 (m, 2H), 3.30 (s, 3H), 3.20 (s, 3H), 2.97 (s, 3H), 2.69 – 2.61 (m, 1H), 2.22 (s, 3H), 2.00 – 1.91 (m, 1H), 1.86 – 1.80 (m, 4H), 1.51 – 1.46 (m, 4H), 1.28 – 1.23 (m, 1H), 1.02 (s, 3H), 0.96 (s, 3H).

HRMS (ESI) Exact mass calculated for $C_{72}H_{77}F_6N_5O_{20}S$ $[M+H]^+$: 1478.4860, found: 1478.4850.

General Procedure F for 114:

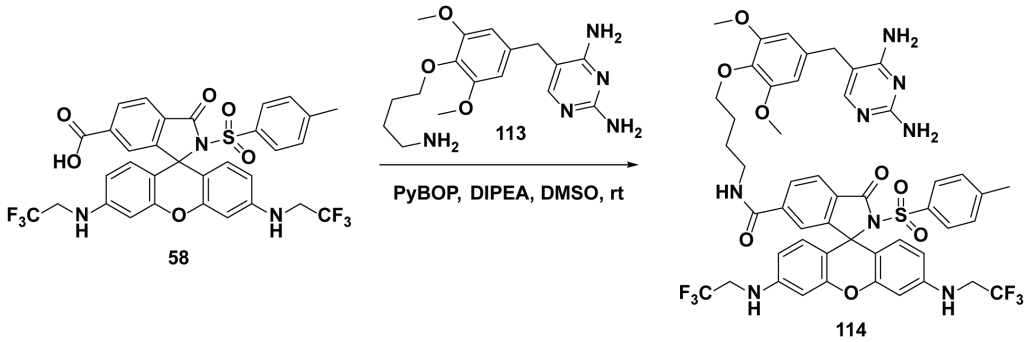

***N*-(4-(4-((2,4-diaminopyrimidin-5-yl)methyl)-2,6-dimethoxyphenoxy)butyl)-3-oxo-2-tosyl-3',6'-bis((2,2,2-trifluoroethyl)amino)spiro[isoindoline-1,9'-xanthene]-6-carboxamide (114):** **113** was synthesized by Christoph Popp according to a previously reported procedure.[205] **113** (2.69 mg, 7.74 µmol, 1.5 eq) was added to a solution of **58** (3.57 mg, 5.16 µmol, 1 eq), PyBOP (3.49 mg, 6.71 µmol, 1.3 eq) and DIPEA (8.53 µL, 51.6 µmol, 10 eq) in DMSO (600 µL). The reaction mixture was stirred at rt for 30 min followed by purification using preparative HPLC (8 mL/min, 25% to 85% MeCN/H_2O (0.1% TFA) in 55 min) to obtain **114** (3.69 mg, 3.61 µmol, 70%) as a red solid.

^{1}H NMR (400 MHz, MeOD-*d*$_4$) δ 8.67 (t, *J* = 5.5 Hz, 1H), 8.29 (s, 1H), 8.05 (d, *J* = 9.0 Hz, 1H), 7.92 (d, *J* = 8.1 Hz, 1H), 7.75 (s, 1H), 7.57 (s, 2H), 7.52 (s, 1H), 7.38 (s, 1H), 7.18 (d, *J* = 20.1 Hz, 4H), 6.70 (t, *J* = 6.7 Hz, 2H), 6.63 (d, *J* = 2.0 Hz, 2H), 6.57 (s, 2H), 6.36 (dd, *J* = 8.7, 2.1 Hz, 2H), 6.24 (d, *J* = 8.7 Hz, 2H), 4.02 (d, *J* = 37.2 Hz, 4H), 3.75 (d, *J* = 10.9 Hz, 2H), 3.67 (s, 6H), 3.57 (s, 2H), 3.21 (d, *J* = 17.9 Hz, 2H), 2.33 (s, 3H), 1.56 (s, 4H).

HRMS (ESI) Exact mass calculated for $C_{49}H_{46}F_6N_8O_8S$ $[M+2H]^{2+}$: 511.1605, found: 511.1605.

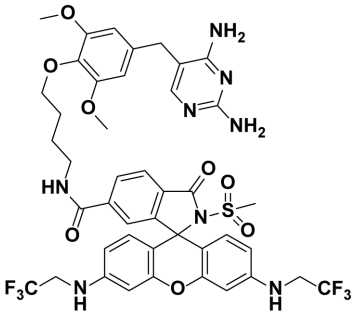

***N*-(4-(4-((2,4-diaminopyrimidin-5-yl)methyl)-2,6-dimethoxyphenoxy)butyl)-2-(methylsulfonyl)-3-oxo-3',6'-bis((2,2,2-trifluoroethyl)amino)spiro[isoindoline-1,9'-xanthene]-6-carboxamide (115):** Following procedure F with **60** (2.83 mg, 4.60 µmol, 1 eq), **115** (3.29 mg, 3.48 µmol, 75%) was obtained as a red solid.

^{1}H NMR (400 MHz, MeOD-*d*$_4$) δ 8.69 (t, *J* = 5.4 Hz, 1H), 8.29 (s, 1H), 8.08 (d, *J* = 8.4 Hz, 1H), 8.03 (d, *J* = 8.0 Hz, 1H), 7.76 (s, 1H), 7.57 (s, 2H), 7.48 (s, 1H), 7.38 (s, 1H), 6.64 (t, *J* = 6.6 Hz, 2H), 6.57 (s, 2H), 6.54 – 6.52 (m, 4H), 6.42 (dd, *J* = 8.7, 1.9 Hz, 2H), 4.02 – 3.91 (m, 4H), 3.77 – 3.74 (m, 2H), 3.68 (s, 6H), 3.57 (s, 2H), 3.24 – 3.20 (m, 2H), 2.97 (s, 3H), 1.57 (s, 4H).

HRMS (ESI) Exact mass calculated for $C_{43}H_{42}F_6N_8O_8S$ $[M+2H]^{2+}$: 473.1448, found: 473.1448.

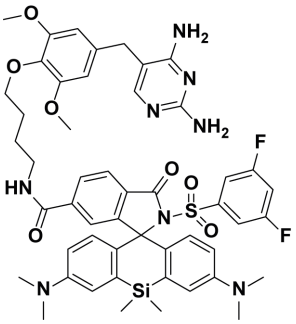

***N*-(4-(4-((2,4-diaminopyrimidin-5-yl)methyl)-2,6-dimethoxyphenoxy)butyl)-2'-((3,5-difluorophenyl)sulfonyl)-3,7-bis(dimethylamino)-5,5-dimethyl-3'-oxo-5H-spiro[dibenzo[b,e]siline-10,1'-isoindoline]-6'-carboxamide (116):** Following procedure F with **89** (2.50 mg, 3.86 µmol, 1 eq), **116** (2.57 mg, 2.63 µmol, 68%) was obtained as a green solid.

^{1}H NMR (400 MHz, MeOD-*d*$_4$) δ 8.68 (t, *J* = 5.5 Hz, 1H), 8.29 (s, 1H), 7.99 (d, *J* = 8.1 Hz, 1H), 7.95 (d, *J* = 9.0 Hz, 1H), 7.75 (s, 1H), 7.66 (tt, *J* = 8.9, 2.2 Hz, 1H), 7.56 (s, 2H), 7.39 – 7.38 (m, 1H), 7.13 (s, 1H), 6.96 (d, *J* = 2.8 Hz, 2H), 6.74 – 6.75 (m, 2H), 6.56 (s, 2H), 6.50 (dd, *J* = 9.1, 2.8 Hz, 2H), 6.30 (d, *J* = 9.0 Hz, 2H), 3.75 – 3.72 (m, 2H), 3.66 (s, 6H), 3.56 (s, 2H), 3.20 – 3.16 (m, 2H), 2.92 (s, 12H), 1.55 (s, 4H), 0.59 (s, 3H), 0.56 (s, 3H).

HRMS (ESI) Exact mass calculated for $C_{50}H_{54}N_8O_7F_2SSi$ $[M+H]^+$: 977.3646, found: 977.3646.

General procedure G for 122:

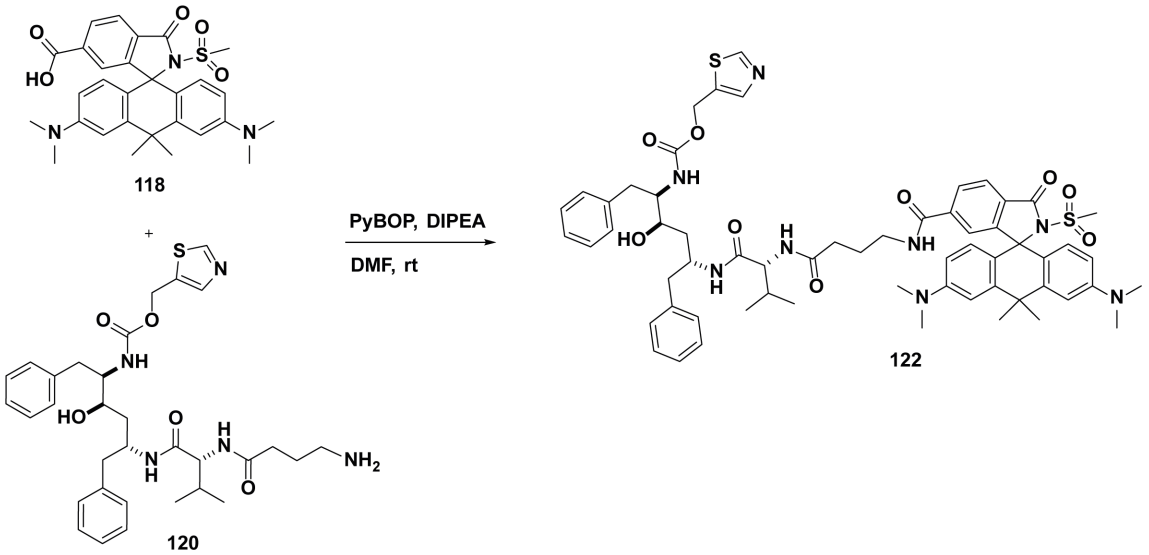

Thiazol-5-ylmethyl ((2*R*,3*R*,5*R*)-5-((*R*)-2-(4-(3,6-bis(dimethylamino)-10,10-dimethyl-2'-(methylsulfonyl)-3'-oxo-10*H*-spiro[anthracene-9,1'-isoindoline]-6'-carboxamido)butanamido)-3-methylbutanamido)-3-hydroxy-1,6-diphenylhexan-2-yl)carbamate (122): 118 was synthesized according to a previously reported procedure[85] and **120** was provided by Dr. J. Schimer (Charles University, Prague).[209] To a solution of **118** (1.77 mg, 3.32 µmol, 1.2 eq), **120** (2.00 mg, 2.77 µmol, 1 eq) and DIPEA (4.57 µL, 27.7 µmol, 10 eq) in

dry DMF (200 µL) was added PyBOP (2.16 mg, 4.15 µmol, 1.5 eq) dissolved in dry DMF (40 µL). The reaction mixture was stirred at rt for 40 min and purified by preparative HPLC (8 mL/min, 30% to 90% MeCN/H_2O (0.1% v/v TFA) in 55 min) to obtain **122** (2.06 mg, 1.83 µmol, 66%) as a blue solid.

^{1}H NMR (400 MHz, DMSO-d_6) δ 9.05 (s, 1H), 8.66 (t, *J* = 5.7 Hz, 1H), 8.03 (d, *J* = 8.0 Hz, 1H), 7.96 (d, *J* = 8.1 Hz, 1H), 7.85 (s, 1H), 7.71 (d, *J* = 8.6 Hz, 1H), 7.65 (d, *J* = 9.0 Hz, 1H), 7.26 – 6.97 (m, 11H), 6.89 – 6.86 (m, 3H), 6.62 – 6.56 (m, 4H), 5.18 – 5.10 (m, 2H), 4.16 – 4.09 (m, 1H), 4.01 (t, *J* = 8.1 Hz, 1H), 3.86 – 3.80 (m, 1H), 3.58 – 3.50 (m, 1H), 3.17 – 3.12 (m, 2H), 3.08 (s, 3H), 2.93 (s, 12H), 2.66 – 2.63 (m, 2H), 2.14 – 2.06 (m, 2H), 1.82 (s, 3H), 1.80 – 1.77 (m, 1H), 1.75 (s, 3H), 1.68 – 1.61 (m, 2H), 1.48 – 1.39 (m, 2H), 1.30 – 1.24 (m, 2H), 0.70 (d, *J* = 6.7 Hz, 6H).

HRMS (ESI) Exact mass calculated for $C_{61}H_{72}N_8O_9S_2$ $[M+2H]^{2+}$: 563.2505, found: 563.2500.

Analytical HPLC: t_R= 2.848 min >99% purity (5 cm × 2.1 mm 1.9 µm C18 column; 2 µL injection; 10 to 95% MeCN/H_2O, linear gradient, with constant 0.1% v/v formic acid additive; 6 min run; 1 mL/min flow; ESI; positive ion mode; detection at 254 nm).

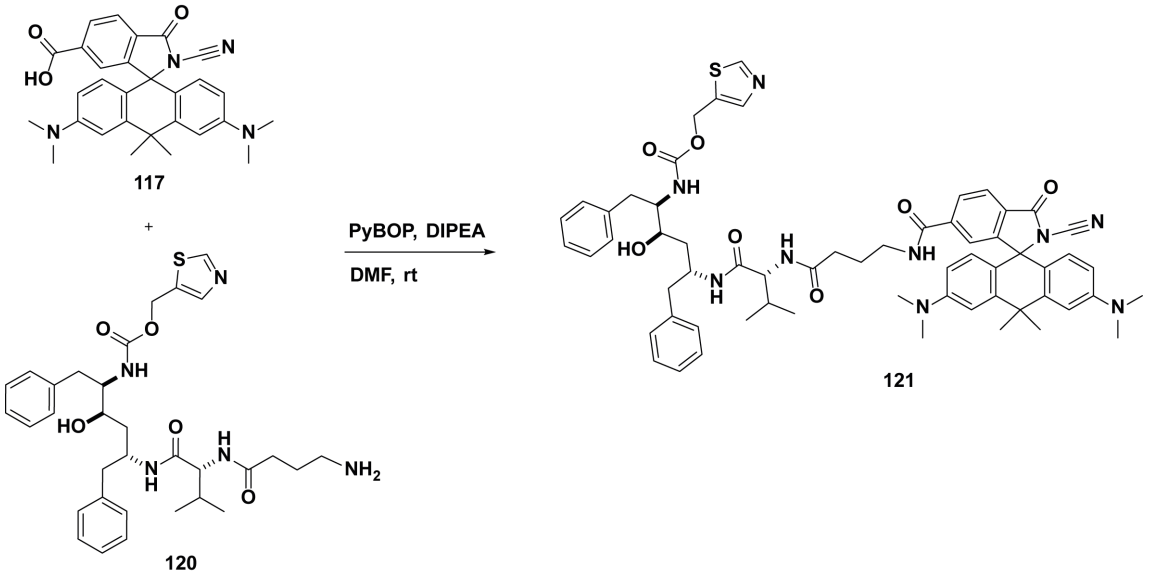

Thiazol-5-ylmethyl ((2*R*,3*R*,5*R*)-5-((*R*)-2-(4-(2'-cyano-3,6-bis(dimethylamino)-10,10-dimethyl-3'-oxo-10*H*-spiro[anthracene-9,1'-isoindoline]-6'-carboxamido)butan-amido)-3-methylbutanamido)-3-hydroxy-1,6-diphenylhexan-2-yl)carbamate (121): 117 was synthesized according to a previously reported procedure[85] and **120** was provided by Dr. J. Schimer (Charles University, Prague).[209] Following procedure G with **117** (1.60 mg, 3.32 µmol,

1.2 eq) and **120** (2.00 mg, 2.77 µmol, 1 eq), **121** (1.08 mg, 1.01 µmol, 36%) was obtained as a blue solid.

^{1}H NMR (400 MHz, DMSO-d_6) δ 9.05 (s, 1H), 8.72 (t, *J* = 5.7 Hz, 1H), 8.11 (d, *J* = 8.0 Hz, 1H), 8.08 (d, *J* = 8.1 Hz, 1H), 7.85 (s, 1H), 7.71 (d, *J* = 8.6 Hz, 1H), 7.65 (d, *J* = 8.9 Hz, 1H), 7.32 (s, 1H), 7.22 – 7.00 (m, 10H), 6.90 – 6.86 (m, 3H), 6.61 (dd, *J* = 9.0, 2.6 Hz, 2H), 6.54 (d, *J* = 8.9 Hz, 2H), 5.17 – 5.09 (m, 2H), 4.16 – 4.09 (m, 1H), 4.01 (t, *J* = 8.1 Hz, 1H), 3.85 – 3.79 (m, 1H), 3.57 – 3.54 (m, 1H), 3.19 – 3.12 (m, 2H), 2.95 (s, 12H), 2.66 – 2.62 (m, 2H), 2.13 – 2.08 (m, 1H), 2.03 – 1.97 (m, 1H), 1.84 (s, 3H), 1.78 (s, 3H), 1.77 – 1.73 (m, 1H), 1.69 – 1.61 (m, 2H), 1.48 – 1.40 (m, 2H), 1.30 – 1.26 (m, 2H), 0.70 (d, *J* = 6.7 Hz, 6H).

HRMS (ESI) Exact mass calculated for $C_{61}H_{69}N_9O_7S$ $[M+2H]^{2+}$: 536.7593, found: 536.7588.

Analytical HPLC: t_R= 3.123 min >95% purity (5 cm × 2.1 mm 1.9 µm C18 column; 2 µL injection; 10 to 95% MeCN/H_2O, linear gradient, with constant 0.1% v/v formic acid additive; 6 min run; 1 mL/min flow; ESI; positive ion mode; detection at 254 nm).

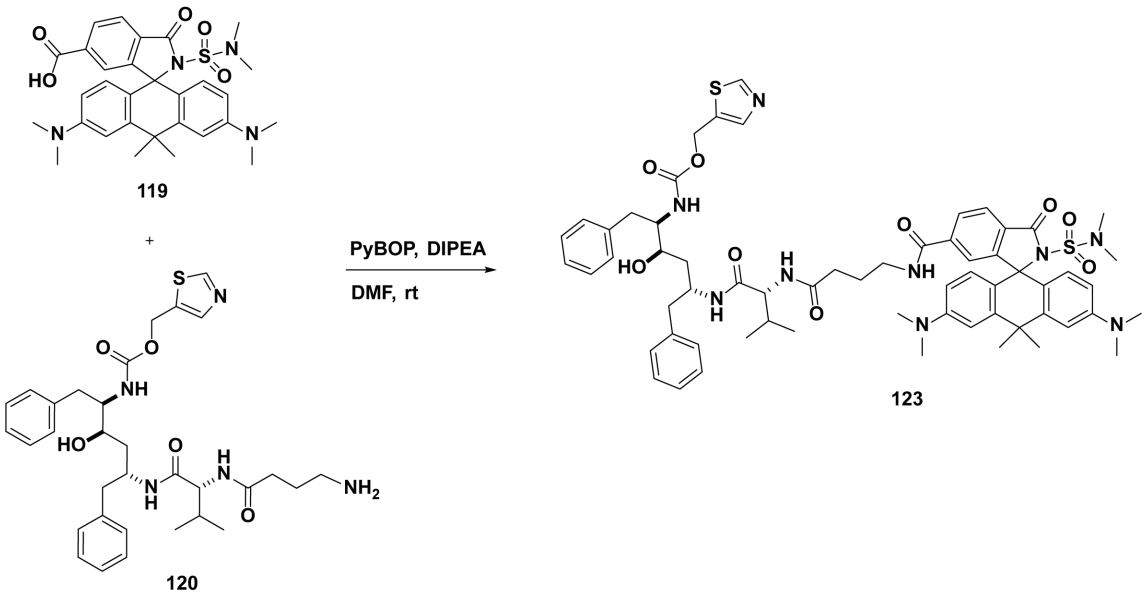

Thiazol-5-ylmethyl ((2*R*,3*R*,5*R*)-5-((*R*)-2-(4-(3,6-bis(dimethylamino)-2'-(*N*,*N*-dimethylsulfamoyl)-10,10-dimethyl-3'-oxo-10*H*-spiro[anthracene-9,1'-isoindoline]-6'-carboxamido)butanamido)-3-methylbutanamido)-3-hydroxy-1,6-diphenylhexan-2-yl)carbamate (123): 119 was synthesized by Dr. Lu Wang according to a previously reported procedure[85] and **120** was provided by Dr. J. Schimer (Charles University, Prague).[209] Following procedure G with **119** (1.87 mg, 3.32 µmol, 1.2 eq) and **120** (2.00 mg, 2.77 µmol, 1 eq), **123** (1.33 mg, 1.15 µmol, 42%) was obtained as a blue solid.

^{1}H NMR (600 MHz, DMSO-d_6) δ 9.05 (s, 1H), 8.65 (t, *J* = 5.8 Hz, 1H), 7.97 (d, *J* = 8.0 Hz, 1H), 7.95 (d, *J* = 8.2 Hz, 1H), 7.85 (s, 1H), 7.73 (d, *J* = 8.6 Hz, 1H), 7.67 (d, *J* = 9.0 Hz, 1H), 7.22 – 7.02 (m, 11H), 6.91 – 6.86 (m, 3H), 6.56 (s, 4H), 5.13 (q, *J* = 13.2 Hz, 2H), 4.15 – 4.10 (m, 1H), 4.02 – 3.99 (m, 1H), 3.84 – 3.80 (m, 1H), 3.57 – 3.54 (m, 1H), 3.16 – 3.09 (m, 2H), 2.92 (s, 12H), 2.68 (s, 6H), 2.66 – 2.61 (m, 1H), 2.56 – 2.54 (m, 1H), 2.12 – 2.06 (m, 1H), 2.02 – 1.97 (m, 1H), 1.80 (s, 3H), 1.79 – 1.77 (m, 1H), 1.76 (s, 3H), 1.64 – 1.62 (m, 2H), 1.47 – 1.40 (m, 2H), 1.30 – 1.25 (m ,2H), 0.69 (d, *J* = 6.8 Hz, 6H).

HRMS (ESI) Exact mass calculated for $C_{62}H_{75}N_9O_9S_2$ $[M+2H]^{2+}$: 577.7637, found: 577.7631.

Analytical HPLC: t_R= 2.935 min >99% purity (5 cm × 2.1 mm 1.9 µm C18 column; 2 µL injection; 10 to 95% MeCN/H_2O, linear gradient, with constant 0.1% v/v formic acid additive; 6 min run; 1 mL/min flow; ESI; positive ion mode; detection at 254 nm).

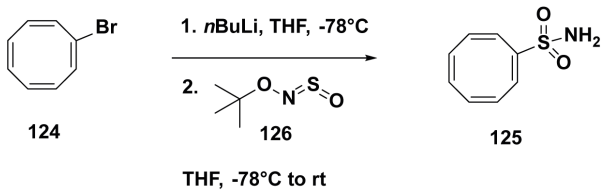

(1*E*,3*Z*,5*Z*,7*Z*)-cycloocta-1,3,5,7-tetraene-1-sulfonamide (125): 124 was synthesized according to a previously reported procedure.[141] **124** (110 mg, 600 µmol, 1 eq) was dissolved in anhydrous THF (3 mL) in a flame-dried *Schlenk* flask. At -78°C, *n*-butyllithium (1.6 M in hexanes, 450 µL, 720 µmol, 1.2 eq) was added dropwise and the reaction was stirred for 30 min at this temperature. **126** (97.3 mg, 720 µmol, 1.2 eq) dissolved in 0.5 mL anhydrous THF was added dropwise. Subsequently, the mixture was warmed to rt and stirred for 16 h. 2-Propanol (0.2 mL) was added and the solvent was evaporated under reduced pressure. The crude product was purified by flash column chromatography (hexanes/EtOAc 5:1 to 2:1) to give **125** (29.3 mg, 16.0 µmol, 27%) as a yellow oil.

TLC: R_f = 0.50 (SiO_2, hexanes/EtOAc 1:1).

^{1}H NMR (400 MHz, MeOD-d_4) δ 6.79 (d, *J* = 3.1 Hz, 1H), 6.17 (dd, *J* = 11.3, 3.0 Hz, 1H), 6.04 (d, *J* = 11.4 Hz, 1H), 5.98 – 5.83 (m, 4H).

^{13}C NMR (101 MHz, MeOD-d_4) δ 146.4, 138.4, 137.1, 135.1, 133.0, 132.8, 130.0, 126.4.

HRMS (ESI) Exact mass calculated for $C_8H_9NO_2S$ $[M+H]^+$: 184.0427, found: 184.0428.

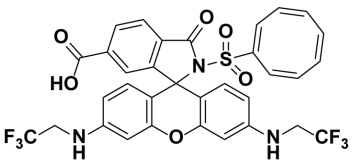

2-(((1*E*,3*Z*,5*Z*,7*Z*)-cycloocta-1,3,5,7-tetraen-1-yl)sulfonyl)-3-oxo-3',6'-bis((2,2,2-trifluoroethyl)amino)spiro[isoindoline-1,9'-xanthene]-6-carboxylic acid (127): Following procedure A with **49** (7.00 mg, 11.8 µmol, 1 eq) and **125** (10.8 mg, 58.9 µmol, 5 eq), **127** (5.30 mg, 7.53 µmol, 64%) was obtained as a red solid.

^{1}H NMR (400 MHz, MeOD-*d*$_4$) δ 8.26 (d, *J* = 8.5 Hz, 1H), 8.03 (d, *J* = 8.0 Hz, 1H), 7.69 (s, 1H), 6.62 – 6.50 (m, 7H), 5.91 – 5.72 (m, 5H), 5.51 (d, *J* = 11.1 Hz, 1H), 3.95 – 3.88 (m, 4H).

^{13}C NMR (101 MHz, DMSO-*d*$_6$) δ 166.0, 164.9, 152.8, 152.5, 149.3, 143.3, 140.8, 138.0, 137.1, 135.2, 132.4, 131.6, 130.9, 130.2, 129.0, 128.7, 125.8 (q, $^1J_{CF}$ = 281 Hz), 124.9, 124.4, 109.3, 107.0, 98.1, 68.8, 43.7 (q, $^2J_{CF}$ = 32 Hz).

HRMS (ESI) Exact mass calculated for $C_{33}H_{23}N_3O_6F_6S$ [M+H]$^+$: 704.1285, found: 704.1285.

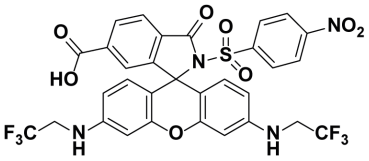

2-((4-nitrophenyl)sulfonyl)-3-oxo-3',6'-bis((2,2,2-trifluoroethyl)amino)spiro[isoindoline-1,9'-xanthene]-6-carboxylic acid (128): Following procedure A with **49** (8.00 mg, 13.5 µmol, 1 eq) and 4-nitrobenzenesulfonamide (13.6 mg, 67.3 µmol, 5 eq), **128** (6.76 mg, 9.36 µmol, 70%) was obtained as a red solid.

^{1}H NMR (400 MHz, DMSO-*d*$_6$) δ 8.21 – 8.17 (m, 2H), 8.11 (dd, *J* = 8.0, 1.3 Hz, 1H), 8.00 (d, *J* = 8.0 Hz, 1H), 7.53 – 7.49 (m, 2H), 7.46 (s, 1H), 6.76 (s, 2H), 6.66 (d, *J* = 2.2 Hz, 2H), 6.34 (dd, *J* = 8.7, 2.2 Hz, 2H), 6.28 (d, *J* = 8.7 Hz, 2H), 4.06 – 3.99 (m, 4H).

^{13}C NMR (101 MHz, DMSO-*d*$_6$) δ 166.0, 164.9, 152.6, 152.3, 150.3, 149.7, 143.4, 137.5, 130.5, 130.3, 129.1, 128.7, 125.9 (q, $^1J_{CF}$ = 281 Hz), 124.9, 124.6, 123.9, 109.6, 106.7, 98.2, 69.9, 43.7 (q, $^2J_{CF}$ = 33 Hz).

HRMS (ESI) Exact mass calculated for $C_{31}H_{20}N_4O_8F_6S$ [M+H]$^+$: 723.0979, found: 723.0976.

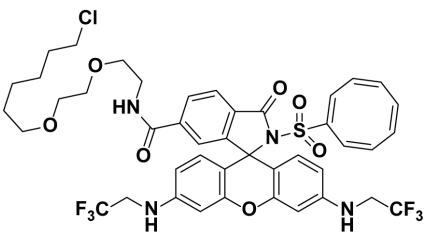

***N*-(2-(2-((6-chlorohexyl)oxy)ethoxy)ethyl)-2-(((1*E*,3*Z*,5*Z*,7*Z*)-cycloocta-1,3,5,7-tetraen-1-yl)sulfonyl)-3-oxo-3',6'-bis((2,2,2-trifluoroethyl)amino)spiro[isoindoline-1,9'-xanthene]-6-carboxamide (129):** Following procedure B with **127** (2.20 mg, 3.13 µmol, 1 eq), **129** (1.88 mg, 2.07 µmol, 66%) was obtained as a red solid.

^{1}H NMR (400 MHz, DMSO-d_6) δ 8.74 (t, *J* = 5.6 Hz, 1H), 8.09 (dd, *J* = 8.1, 1.1 Hz, 1H), 8.00 (d, *J* = 8.1 Hz, 1H), 7.53 (s, 1H), 6.64 (t, *J* = 6.8 Hz, 2H), 6.53 (s, 2H), 6.43 – 6.38 (m, 5H), 5.93 – 5.74 (m, 5H), 5.37 (d, *J* = 10.4 Hz, 1H), 4.02 – 3.92 (m, 4H), 3.59 (t, *J* = 6.6 Hz, 2H), 3.45 – 3.40 (m, 6H), 3.33 – 3.27 (m, 4H), 1.69 – 1.62 (m, 2H), 1.44 – 1.37 (m, 2H), 1.34 – 1.29 (m, 2H), 1.26 – 1.20 (m, 2H).

HRMS (ESI) Exact mass calculated for $C_{43}H_{43}N_4O_7ClF_6S$ $[M+H]^+$: 909.2518, found: 909.2517.

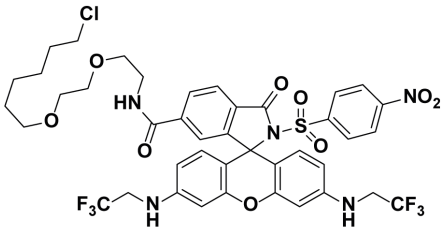

***N*-(2-(2-((6-chlorohexyl)oxy)ethoxy)ethyl)-2-((4-nitrophenyl)sulfonyl)-3-oxo-3',6'-bis((2,2,2-trifluoroethyl)amino)spiro[isoindoline-1,9'-xanthene]-6-carboxamide (130):** Following procedure B with **128** (3.46 mg, 4.79 µmol, 1 eq), **130** (3.03 mg, 3.26 µmol, 68%) was obtained as a red solid.

^{1}H NMR (400 MHz, DMSO-d_6) δ 8.72 (t, *J* = 5.6 Hz, 1H), 8.20 – 8.17 (m, 2H), 8.07 (dd, *J* = 8.1, 1.3 Hz, 1H), 7.96 (d, *J* = 8.1 Hz, 1H), 7.56 (s, 1H), 7.52 – 7.49 (m, 2H), 6.72 (t, *J* = 6.9 Hz, 2H), 6.65 (d, *J* = 2.2 Hz, 2H), 6.34 (dd, *J* = 8.7, 2.3 Hz, 2H), 6.25 (d, *J* = 8.7 Hz, 2H), 4.06 – 3.98 (m, 4H), 3.57 (t, *J* = 6.6 Hz, 2H), 3.45 – 3.37 (m, 6H), 3.29 – 3.26 (m, 4H), 1.68 – 1.61 (m, 2H), 1.43 – 1.36 (m, 2H), 1.35 – 1.27 (m, 2H), 1.25 – 1.19 (m, 2H).

HRMS (ESI) Exact mass calculated for $C_{41}H_{40}ClF_6N_5O_9S$ $[M+H]^+$: 928.2212, found: 928.2217.

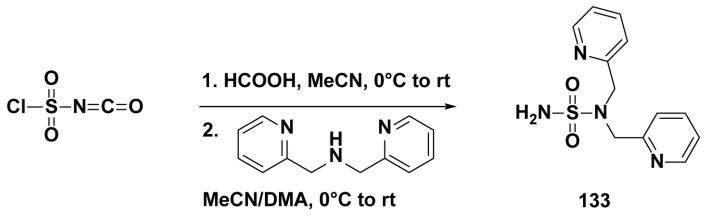

Bis(pyridin-2-ylmethyl)amine-sulfonamide (133): Chlorosulfonyl isocyanate (673 µL, 7.73 mmol, 2.2 eq) was dissolved in dry MeCN (1.5 mL) in a flame-dried *Schlenk* flask under argon and the solution was cooled to 0°C. Subsequently, formic acid (297 µL, 7.87 mmoles, 2.24 eq) was added dropwise leading to observed gas formation. The mixture was stirred at 0°C for 30 min followed by addition of dry MeCN (2.5 mL), warming of the solution to rt and stirring for additional 2 h. A solution of dipicolylamine (700 mg, 3.51 mmoles, 1 eq) in DMA (3 mL) was added dropwise at 0°C. The solution turned green and the formation of a precipitate was observed. After 10 min, the solution was warmed to rt and stirred for 16 h. Subsequently,

the mixture was filtered and the filter cake was washed with CH_2Cl_2. After dissolving the filter cake in H_2O (20 mL), NaOH (2 M) was added to adjust pH=10 followed by extraction with EtOAc. The combined organic layers were dried over $MgSO_4$, filtered and concentrated to obtain **133** (525 mg, 1.87 mmol, 54%) as a yellow oil.

TLC: R_f = 0.22 (SiO_2, CH_2Cl_2/MeOH 20:1).

^{1}H NMR (400 MHz, DMSO-d_6) δ 8.45 – 8.43 (m, 2H), 7.72 (td, *J* = 7.7, 1.8 Hz, 2H), 7.41 – 7.39 (m, 2H), 7.23 (ddd, *J* = 7.6, 4.8, 1.2 Hz, 2H), 7.10 (s, 2H), 4.39 (s, 4H).

^{13}C NMR (101 MHz, DMSO-d_6) δ 157.1, 148.8, 136.7, 122.4, 122.3, 53.5.

HRMS (ESI) Exact mass calculated for $C_{12}H_{14}N_4O_2S$ [M+H]$^+$: 279.0910, found: 279.0909.

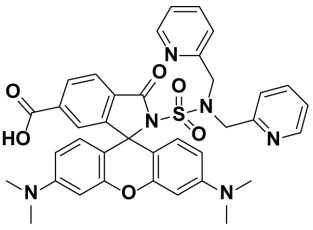

2-(*N*,*N*-bis(pyridin-2-ylmethyl)sulfamoyl)-3',6'-bis(dimethylamino)-3-oxospiro[isoindoline-1,9'-xanthene]-6-carboxylic acid (134): A solution of **99** (9.00 mg, 19.1 µmol, 1 eq), **133** (42.6 mg, 153 µmol, 8 eq), 1-(3-dimethylaminopropyl)-3-ethylcarbodiimide hydrochloride (22.0 mg, 115 µmol, 6 eq) and 4-dimethylaminopyridine (23.4 mg, 191 µmol, 10 eq) in CH_2Cl_2 (1 mL) was heated to 60°C and stirred at this temperature for 12 h in a sealed tube. H_2O (2 mL) was added and the aqueous layer was extracted with CH_2Cl_2 (3x). The combined organic layers were dried over MgSO4, filtered and concentrated. The residue was dissolved in MeOH/CH_2Cl_2 (5:1, 2.4 mL) in a Schlenk flask which had been dried with a heat gun in vacuo before. 1,3-Dimethylbarbituric acid (5.97 mg, 38.3 µmol, 2 eq) and tetrakis(triphenylphosphine)palladium (2.21 mg, 1.91 µmol, 0.1 eq) were added and the reaction mixture was stirred at rt for 30 min. After the solvent was evaporated, the crude product was dissolved in DMSO (1.8 mL) and purified by preparative HPLC (8 mL/min, 19% to 35% MeCN/H2O (0.1% TFA) in 55 min) to obtain **134** (6.40 mg, 9.27 µmol, 48%) as a magenta solid.

^{1}H NMR (400 MHz, MeOD-d_4) δ 8.63 – 8.61 (m, 2H), 8.36 (dd, *J* = 8.1, 1.6 Hz, 1H), 8.14 (dd, *J* = 8.1, 0.6 Hz, 1H), 7.97 (td, *J* = 7.8, 1.7 Hz, 2H), 7.89 (d, *J* = 1.0 Hz, 1H), 7.53 – 7.49 (m, 2H), 7.35 (d, *J* = 8.0 Hz, 2H), 6.98 (d, *J* = 9.2 Hz, 2H), 6.83 (dd, *J* = 9.2, 2.5 Hz, 2H), 6.73 (d, *J* = 2.5 Hz, 2H), 4.64 (s, 4H), 3.15 (s, 12H).

^{13}C NMR (101 MHz, MeOD-d_4) δ 168.3, 167.8, 157.4, 156.8, 156.7, 146.9, 142.2, 137.0, 136.7, 132.1, 131.2, 130.4, 128.3, 125.4, 125.1, 113.4, 112.0, 98.7, 54.8, 40.8.

HRMS (ESI) Exact mass calculated for $C_{37}H_{34}N_6O_6S$ [M+H]$^+$: 691.2333, found: 691.2325.

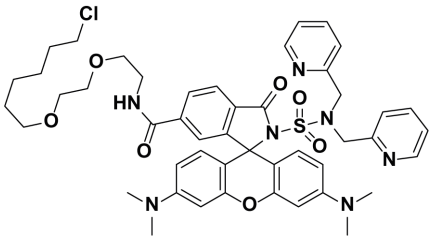

2-(*N*,*N*-bis(pyridin-2-ylmethyl)sulfamoyl)-*N*-(2-(2-((6-chlorohexyl)oxy)ethoxy)ethyl)-3',6'-bis(dimethylamino)-3-oxospiro[isoindoline-1,9'-xanthene]-6-carboxamide (135): Following procedure B with **134** (2.60 mg, 3.76 µmol, 1 eq), **135** (2.57 mg, 2.87 µmol, 76%) was obtained as a magenta solid by preparative HPLC (8 mL/min, 35% to 65% MeCN/H2O (0.1% TFA) in 55 min).

^{1}H NMR (400 MHz, DMSO-*d*$_6$) δ 8.73 (t, *J* = 5.6 Hz, 1H), 8.48 (d, *J* = 5.0 Hz, 2H), 8.13 (dd, *J* = 8.0, 1.4 Hz, 1H), 8.08 (d, *J* = 8.0 Hz, 1H), 7.78 – 7.74 (m, 2H), 7.51 (s, 1H), 7.33 – 7.30 (m, 2H), 7.12 (d, *J* = 7.9 Hz, 2H), 6.53 (d, *J* = 8.8 Hz, 2H), 6.41 (d, *J* = 2.5 Hz, 2H), 6.30 (dd, *J* = 8.9, 2.5 Hz, 2H), 4.46 (s, 4H), 3.59 (t, *J* = 6.6 Hz, 2H), 3.47 – 3.44 (m, 4H), 3.41 – 3.39 (m, 2H), 3.35 – 3.27 (m, 4H), 2.90 (s, 12H), 1.70 – 1.63 (m, 2H), 1.40 (p, *J* = 7.0 Hz, 2H), 1.35 – 1.29 (m, 2H), 1.27 – 1.21 (m, 2H).

HRMS (ESI) Exact mass calculated for $C_{47}H_{54}N_7O_7ClS$ $[M+H]^+$: 896.3567, found: 896.3571.

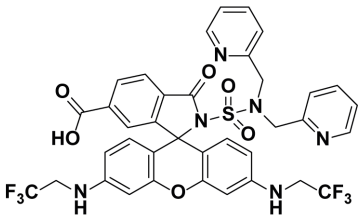

2-(*N*,*N*-bis(pyridin-2-ylmethyl)sulfamoyl)-3-oxo-3',6'-bis((2,2,2-trifluoroethyl)amino)spiro[iso-indoline-1,9'-xanthene]-6-carboxylic acid (136): Following procedure A with **49** (4.00 mg, 6.73 µmol, 1 eq) and **133** (9.36 mg, 33.6 µmol, 5 eq), **136** (2.33 mg, 2.92 µmol, 43%) was obtained as a red solid.

^{1}H NMR (400 MHz, MeOD-*d*$_4$) δ 8.70 (d, *J* = 5.3 Hz, 1H), 8.29 (dd, *J* = 8.0, 1.3 Hz, 1H), 8.12 (dd, *J* = 8.0, 0.7 Hz, 1H), 7.97 (tt, *J* = 7.8, 1.5 Hz, 2H), 7.66 – 7.65 (m, 1H), 7.55 – 7.51 (m, 2H), 7.27 (d, *J* = 8.0 Hz, 2H), 6.58 (d, *J* = 8.6 Hz, 2H), 6.48 – 6.42 (m, 4H), 4.77 (s, 4H), 3.85 (q, *J* = 9.3 Hz, 4H).

^{13}C NMR (101 MHz, MeOD-*d*$_4$) δ 168.0, 167.8, 156.9, 154.9, 154.6, 151.1, 146.8, 142.3, 138.7, 132.7, 131.7, 130.0, 127.2, 126.9 (q, $^1J_{CF}$ = 280 Hz), 125.4, 125.2, 125.0, 110.5, 108.9, 99.9, 72.0, 55.0, 45.8 (q, $^2J_{CF}$ = 34 Hz).

HRMS (ESI) Exact mass calculated for $C_{37}H_{28}N_6O_6F_6S$ $[M+H]^+$: 799.1768, found: 799.1769.

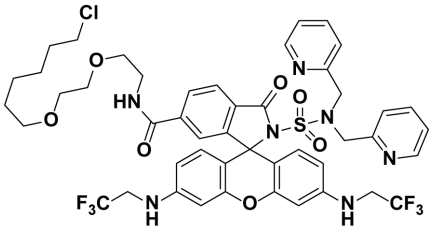

2-(*N*,*N*-bis(pyridin-2-ylmethyl)sulfamoyl)-*N*-(2-(2-((6-chlorohexyl)oxy)ethoxy)ethyl)-3-oxo-3',6'-bis((2,2,2-trifluoroethyl)amino)spiro[isoindoline-1,9'-xanthene]-6-carboxamide (137): Following procedure B with **136** (1.80 mg, 2.25 µmol, 1 eq), **137** (1.70 mg, 1.69 µmol, 75%) was obtained as a red solid.

^{1}H NMR (400 MHz, DMSO-d_6) δ 8.75 (t, *J* = 5.7 Hz, 1H), 8.38 (d, *J* = 4.9 Hz, 2H), 8.12 (dd, *J* = 8.0, 1.4 Hz, 1H), 8.06 (d, *J* = 8.0 Hz, 1H), 7.66 (td, *J* = 7.7, 1.7 Hz, 2H), 7.55 (s, 1H), 7.24 – 7.21 (m, 2H), 7.04 (d, *J* = 7.9 Hz, 2H), 6.59 (t, *J* = 6.9 Hz, 2H), 6.53 (d, *J* = 2.3 Hz, 2H), 6.47 (d, *J* = 8.7 Hz, 2H), 6.30 (dd, *J* = 8.7, 2.4 Hz, 2H), 4.38 (s, 4H), 3.99 – 3.89 (m, 4H), 3.59 (t, *J* = 6.6 Hz, 2H), 3.47 – 3.44 (m, 4H), 3.41 – 3.39 (m, 2H), 3.34 – 3.27 (m, 4H), 1.69 – 1.62 (m, 2H), 1.40 (p, *J* = 6.7 Hz, 2H), 1.35 – 1.29 (m, 2H), 1.27 – 1.21 (m, 2H).

HRMS (ESI) Exact mass calculated for $C_{47}H_{48}N_7O_7ClF_6S$ $[M+2H]^{2+}$: 502.6537, found: 502.6536.

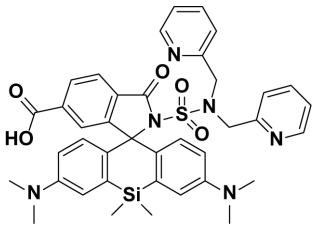

2'-(*N*,*N*-bis(pyridin-2-ylmethyl)sulfamoyl)-3,7-bis(dimethylamino)-5,5-dimethyl-3'-oxo-5*H*-spiro[dibenzo[b,e]siline-10,1'-isoindoline]-6'-carboxylic acid (138): A *Schlenk* flask was dried with a heat gun *in vacuo* prior to dissolution of **88** (14 mg, 27.3 µmol, 1 eq) in dry CH_2Cl_2 (2 mL). Phosphorus oxychloride (38.2 µL, 410 µmol, 15 eq) was added, the mixture was heated to 50°C and stirred at this temperature for 2 h. Subsequently, **133** (60.8 mg, 218 µmol, 8 eq) and DIPEA (135 µL, 819 µmol, 30 eq) dissolved in dry MeCN (2 mL) were added. After further dry MeCN (2 mL) was added, the mixture was stirred at 70°C for 10 min. The solvent was evaporated, H_2O (1 mL) was added and the aqueous layer was extracted with CH_2Cl_2 (3x). The combined organic layers were dried over $MgSO_4$, filtered and concentrated. The residue was dissolved in MeOH/CH_2Cl_2 (5:1, 1.8 mL) in a *Schlenk* flask which had been dried with a heat gun *in vacuo* before. 1,3-Dimethylbarbituric acid (8.53 mg, 54.6 µmol, 2 eq) and tetrakis(triphenylphosphine)palladium (3.16 mg, 2.73 µmol, 0.1 eq) were added and the reaction mixture was stirred at rt for 30 min. After the solvent was evaporated, the crude product was dissolved in DMSO (3 mL) and purified by preparative HPLC (8 mL/min, 22% to 45% MeCN/H_2O (0.1% TFA) in 55 min) to obtain **138** (10.8 mg, 14.7 µmol, 54%) as a green solid.

^{1}H NMR (400 MHz, DMSO-d_6) δ 8.51 – 8.49 (m, 2H), 8.10 (d, *J* = 8.0 Hz, 1H), 8.05 (dd, *J* = 8.0, 1.3 Hz, 1H), 7.78 (tt, *J* = 7.7, 1.6 Hz, 2H), 7.33 – 7.30 (m, 2H), 7.14 (s, 2H), 7.12 (s, 1H), 6.90 (d, *J* = 2.9 Hz, 2H), 6.65 (d, *J* = 9.0 Hz, 2H), 6.48 – 6.45 (m, 2H), 4.48 (s, 4H), 2.87 (s, 12H), 0.53 (s, 3H), 0.41 (s, 3H).

^{13}C NMR (101 MHz, DMSO-d_6) δ 166.8, 165.9, 156.1, 155.5, 148.3, 147.7, 138.2, 136.8, 135.2, 129.9, 129.8, 129.5, 129.2, 124.5, 124.2, 123.0, 122.3, 115.4, 114.3, 75.4, 52.8, 0.1, -0.9.

HRMS (ESI) Exact mass calculated for $C_{39}H_{40}N_6O_5SSi$ $[M+H]^+$: 733.2623, found: 733.2625.

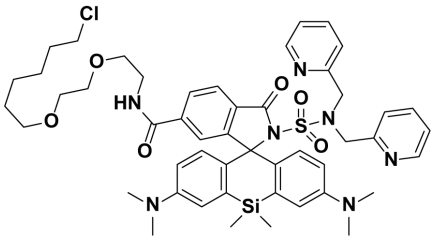

2'-(*N*,*N*-bis(pyridin-2-ylmethyl)sulfamoyl)-*N*-(2-(2-((6-chlorohexyl)oxy)ethoxy)ethyl)-3,7-bis(dimethylamino)-5,5-dimethyl-3'-oxo-5*H*-spiro[dibenzo[b,e]siline-10,1'-isoindoline]-6'-carboxamide (139): Following procedure B with **138** (5.80 mg, 7.91 µmol, 1 eq), **139** (5.59 mg, 5.96 µmol, 75%) was obtained as a slightly green solid by preparative HPLC (8 mL/min, 35% to 75% MeCN/H_2O (0.1% TFA) in 55 min).

^{1}H NMR (400 MHz, DMSO-d_6) δ 8.71 (t, *J* = 5.6 Hz, 1H), 8.54 (d, *J* = 4.7 Hz, 2H), 8.07 (d, *J* = 8.1 Hz, 1H), 7.99 (dd, *J* = 8.1, 1.4 Hz, 1H), 7.82 (td, *J* = 7.7, 1.8 Hz, 2H), 7.37 – 7.34 (m, 2H), 7.14 – 7.12 (m, 3H), 6.91 (d, *J* = 2.9 Hz, 2H), 6.61 (d, *J* = 9.0 Hz, 2H), 6.48 (dd, *J* = 9.1, 2.9 Hz, 2H), 4.48 (s, 4H), 3.58 (t, *J* = 6.6 Hz, 2H), 3.45 – 3.38 (m, 6H), 3.31 – 3.27 (m, 4H), 2.88 (s, 12H), 1.72 – 1.61 (m, 2H), 1.40 (p, *J* = 6.9 Hz, 2H), 1.35 – 1.29 (m, 2H), 1.27 – 1.19 (m, 2H), 0.54 (s, 3H), 0.38 (s, 3H).

HRMS (ESI) Exact mass calculated for $C_{49}H_{60}N_7O_6ClSSi$ $[M+H]^+$: 938.3856, found: 938.3854.

7. References

1. Hell, S. W., Nanoscopy with Focused Light (Nobel Lecture). *Angew. Chem. Int. Ed.* **2015,** *54* (28), 8054.
2. Lavis, L. D.; Raines, R. T., Bright building blocks for chemical biology. *ACS Chem. Biol.* **2014,** *9* (4), 855.
3. Abbyad, P.; Childs, W.; Shi, X.; Boxer, S. G., Dynamic Stokes shift in green fluorescent protein variants. *Proc. Natl. Acad. Sci. USA* **2007,** *104* (51), 20189.
4. Lichtman, J. W.; Conchello, J.-A., Fluorescence microscopy. *Nat. Methods* **2005,** *2* (12), 910.
5. Stokes, G. G., XXX. On the change of refrangibility of light. *Phil. Trans. R. Soc. Lon.* **1852,** *142*, 463.
6. Wang, C.; Chi, W.; Qiao, Q.; Tan, D.; Xu, Z.; Liu, X., Twisted intramolecular charge transfer (TICT) and twists beyond TICT: from mechanisms to rational designs of bright and sensitive fluorophores. *Chem. Soc. Rev.* **2021,** *50* (22), 12656.
7. Zelent, B.; Kuśba, J.; Gryczynski, I.; Johnson, M. L.; Lakowicz, J. R., Time-resolved and steady-state fluorescence quenching of N-acetyl-l-tryptophanamide by acrylamide and iodide1Dedicated to the memory of Professor Dr Tadeusz Latowski.1. *Biophys. Chem.* **1998,** *73* (1), 53.
8. de Silva, A. P.; Gunaratne, H. Q. N.; Gunnlaugsson, T.; Huxley, A. J. M.; McCoy, C. P.; Rademacher, J. T.; Rice, T. E., Signaling Recognition Events with Fluorescent Sensors and Switches. *Chem. Rev.* **1997,** *97* (5), 1515.
9. Minoshima, M.; Kikuchi, K., Photostable and photoswitching fluorescent dyes for super-resolution imaging. *J. Biol. Inorg. Chem.* **2017,** *22* (5), 639.
10. Zheng, Q.; Lavis, L. D., Development of photostable fluorophores for molecular imaging. *Curr. Opin. Chem. Biol.* **2017,** *39*, 32.
11. Lavis, L. D.; Raines, R. T., Bright Ideas for Chemical Biology. *ACS Chem. Biol.* **2008,** *3* (3), 142.
12. Lavis, L. D., Chemistry Is Dead. Long Live Chemistry! *Biochemistry* **2017,** *56* (39), 5165.
13. Abbe, E., Beiträge zur Theorie des Mikroskops und der mikroskopischen Wahrnehmung. *Arch. Mikr. Anat.* **1873,** *9* (1), 413.
14. Wang, L.; Frei, M. S.; Salim, A.; Johnsson, K., Small-Molecule Fluorescent Probes for Live-Cell Super-Resolution Microscopy. *J. Am. Chem. Soc.* **2019,** *141* (7), 2770.
15. Liu, Z.; Lavis, Luke D.; Betzig, E., Imaging Live-Cell Dynamics and Structure at the Single-Molecule Level. *Mol. Cell* **2015,** *58* (4), 644.
16. Sahl, S. J.; Hell, S. W.; Jakobs, S., Fluorescence nanoscopy in cell biology. *Nat. Rev. Mol. Cell Biol.* **2017,** *18* (11), 685.
17. Hell, S. W.; Wichmann, J., Breaking the diffraction resolution limit by stimulated emission: stimulated-emission-depletion fluorescence microscopy. *Opt. Lett.* **1994,** *19* (11), 780.
18. Vicidomini, G.; Bianchini, P.; Diaspro, A., STED super-resolved microscopy. *Nat. Methods* **2018,** *15* (3), 173.
19. Hotta, J.-i.; Fron, E.; Dedecker, P.; Janssen, K. P. F.; Li, C.; Müllen, K.; Harke, B.; Bückers, J.; Hell, S. W.; Hofkens, J., Spectroscopic Rationale for Efficient Stimulated-Emission Depletion Microscopy Fluorophores. *J. Am. Chem. Soc.* **2010,** *132* (14), 5021.
20. Butkevich, A. N.; Bossi, M. L.; Lukinavicius, G.; Hell, S. W., Triarylmethane Fluorophores Resistant to Oxidative Photobluing. *J. Am. Chem. Soc.* **2019**, *141* (2), 981.
21. Butkevich, A. N.; Mitronova, G. Y.; Sidenstein, S. C.; Klocke, J. L.; Kamin, D.; Meineke, D. N.; D'Este, E.; Kraemer, P. T.; Danzl, J. G.; Belov, V. N.; Hell, S. W., Fluorescent Rhodamines and Fluorogenic Carbopyronines for Super-Resolution STED Microscopy in Living Cells. *Angew. Chem. Int. Ed.* **2016,** *55* (10), 3290.
22. Bianchini, P.; Peres, C.; Oneto, M.; Galiani, S.; Vicidomini, G.; Diaspro, A., STED nanoscopy: a glimpse into the future. *Cell Tissue Res.* **2015,** *360* (1), 143.

23. Hein, B.; Willig, K. I.; Hell, S. W., Stimulated emission depletion (STED) nanoscopy of a fluorescent protein-labeled organelle inside a living cell. *Proc. Natl. Acad. Sci. USA* **2008,** *105* (38), 14271.
24. Hein, B.; Willig, K. I.; Wurm, C. A.; Westphal, V.; Jakobs, S.; Hell, S. W., Stimulated Emission Depletion Nanoscopy of Living Cells Using SNAP-Tag Fusion Proteins. *Biophys. J.* **2010,** *98* (1), 158.
25. Lukinavicius, G.; Reymond, L.; D'Este, E.; Masharina, A.; Gottfert, F.; Ta, H.; Guther, A.; Fournier, M.; Rizzo, S.; Waldmann, H.; Blaukopf, C.; Sommer, C.; Gerlich, D. W.; Arndt, H. D.; Hell, S. W.; Johnsson, K., Fluorogenic probes for live-cell imaging of the cytoskeleton. *Nat. Methods* **2014,** *11* (7), 731.
26. Lukinavičius, G.; Blaukopf, C.; Pershagen, E.; Schena, A.; Reymond, L.; Derivery, E.; Gonzalez-Gaitan, M.; D'Este, E.; Hell, S. W.; Wolfram Gerlich, D.; Johnsson, K., SiR–Hoechst is a far-red DNA stain for live-cell nanoscopy. *Nat. Commun.* **2015,** *6* (1), 8497.
27. Butkevich, A. N.; Lukinavičius, G.; D'Este, E.; Hell, S. W., Cell-Permeant Large Stokes Shift Dyes for Transfection-Free Multicolor Nanoscopy. *J. Am. Chem. Soc.* **2017,** *139* (36), 12378.
28. Lukinavicius, G.; Reymond, L.; Umezawa, K.; Sallin, O.; D'Este, E.; Gottfert, F.; Ta, H.; Hell, S. W.; Urano, Y.; Johnsson, K., Fluorogenic Probes for Multicolor Imaging in Living Cells. *J. Am. Chem. Soc.* **2016,** *138* (30), 9365.
29. Bückers, J.; Wildanger, D.; Vicidomini, G.; Kastrup, L.; Hell, S. W., Simultaneous multi-lifetime multi-color STED imaging for colocalization analyses. *Opt. Express* **2011,** *19* (4), 3130.
30. Willig, K. I.; Stiel, A. C.; Brakemann, T.; Jakobs, S.; Hell, S. W., Dual-Label STED Nanoscopy of Living Cells Using Photochromism. *Nano Lett.* **2011,** *11* (9), 3970.
31. Moerner, W. E.; Kador, L., Optical detection and spectroscopy of single molecules in a solid. *Phys. Rev. Lett.* **1989,** *62* (21), 2535.
32. Betzig, E., Proposed method for molecular optical imaging. *Opt. Lett.* **1995,** *20* (3), 237.
33. Dickson, R. M.; Cubitt, A. B.; Tsien, R. Y.; Moerner, W. E., On/off blinking and switching behaviour of single molecules of green fluorescent protein. *Nature* **1997,** *388* (6640), 355.
34. Bout, D. A. V.; Yip, W.-T.; Hu, D.; Fu, D.-K.; Swager, T. M.; Barbara, P. F., Discrete Intensity Jumps and Intramolecular Electronic Energy Transfer in the Spectroscopy of Single Conjugated Polymer Molecules. *Science* **1997,** *277* (5329), 1074.
35. Nirmal, M.; Dabbousi, B. O.; Bawendi, M. G.; Macklin, J. J.; Trautman, J. K.; Harris, T. D.; Brus, L. E., Fluorescence intermittency in single cadmium selenide nanocrystals. *Nature* **1996,** *383* (6603), 802.
36. Heilemann, M.; Margeat, E.; Kasper, R.; Sauer, M.; Tinnefeld, P., Carbocyanine Dyes as Efficient Reversible Single-Molecule Optical Switch. *J. Am. Chem. Soc.* **2005,** *127* (11), 3801.
37. Li, H.; Vaughan, J. C., Switchable Fluorophores for Single-Molecule Localization Microscopy. *Chem. Rev.* **2018,** *118* (18), 9412.
38. Patterson, G. H.; Lippincott-Schwartz, J., A Photoactivatable GFP for Selective Photolabeling of Proteins and Cells. *Science* **2002,** *297* (5588), 1873.
39. Chudakov, D. M.; Belousov, V. V.; Zaraisky, A. G.; Novoselov, V. V.; Staroverov, D. B.; Zorov, D. B.; Lukyanov, S.; Lukyanov, K. A., Kindling fluorescent proteins for precise in vivo photolabeling. *Nat. Biotechnol.* **2003,** *21* (2), 191.
40. Chudakov, D. M.; Verkhusha, V. V.; Staroverov, D. B.; Souslova, E. A.; Lukyanov, S.; Lukyanov, K. A., Photoswitchable cyan fluorescent protein for protein tracking. *Nat. Biotechnol.* **2004,** *22* (11), 1435.
41. Bates, M.; Blosser, T. R.; Zhuang, X., Short-Range Spectroscopic Ruler Based on a Single-Molecule Optical Switch. *Phys. Rev. Lett.* **2005,** *94* (10), 108101.
42. Rust, M. J.; Bates, M.; Zhuang, X., Sub-diffraction-limit imaging by stochastic optical reconstruction microscopy (STORM). *Nat. Methods* **2006,** *3* (10), 793.
43. Betzig, E.; Patterson, G. H.; Sougrat, R.; Lindwasser, O. W.; Olenych, S.; Bonifacino, J. S.; Davidson, M. W.; Lippincott-Schwartz, J.; Hess, H. F., Imaging Intracellular Fluorescent Proteins at Nanometer Resolution. *Science* **2006,** *313* (5793), 1642.

44. Hess, S. T.; Girirajan, T. P. K.; Mason, M. D., Ultra-High Resolution Imaging by Fluorescence Photoactivation Localization Microscopy. *Biophys. J.* **2006,** *91* (11), 4258.
45. Sharonov, A.; Hochstrasser, R. M., Wide-field subdiffraction imaging by accumulated binding of diffusing probes. *Proc. Natl. Acad. Sci. USA* **2006,** *103* (50), 18911.
46. Lelek, M.; Gyparaki, M. T.; Beliu, G.; Schueder, F.; Griffié, J.; Manley, S.; Jungmann, R.; Sauer, M.; Lakadamyali, M.; Zimmer, C., Single-molecule localization microscopy. *Nat. Rev. Methods Primers* **2021,** *1* (1), 39.
47. Dempsey, G. T.; Vaughan, J. C.; Chen, K. H.; Bates, M.; Zhuang, X., Evaluation of fluorophores for optimal performance in localization-based super-resolution imaging. *Nat. Methods* **2011,** *8* (12), 1027.
48. Mortensen, K. I.; Churchman, L. S.; Spudich, J. A.; Flyvbjerg, H., Optimized localization analysis for single-molecule tracking and super-resolution microscopy. *Nat. Methods* **2010,** *7* (5), 377.
49. Chalfie, M.; Tu, Y.; Euskirchen, G.; Ward, W. W.; Prasher, D. C., Green Fluorescent Protein as a Marker for Gene Expression. *Science* **1994,** *263* (5148), 802.
50. Heim, R.; Prasher, D. C.; Tsien, R. Y., Wavelength mutations and posttranslational autoxidation of green fluorescent protein. *Proc. Natl. Acad. Sci. USA* **1994,** *91* (26), 12501.
51. Heim, R.; Cubitt, A. B.; Tsien, R. Y., Improved green fluorescence. *Nature* **1995,** *373* (6516), 663.
52. Heim, R.; Tsien, R. Y., Engineering green fluorescent protein for improved brightness, longer wavelengths and fluorescence resonance energy transfer. *Curr. Biol.* **1996,** *6* (2), 178.
53. Matz, M. V.; Fradkov, A. F.; Labas, Y. A.; Savitsky, A. P.; Zaraisky, A. G.; Markelov, M. L.; Lukyanov, S. A., Fluorescent proteins from nonbioluminescent Anthozoa species. *Nat. Biotechnol.* **1999,** *17* (10), 969.
54. Shaner, N. C.; Campbell, R. E.; Steinbach, P. A.; Giepmans, B. N. G.; Palmer, A. E.; Tsien, R. Y., Improved monomeric red, orange and yellow fluorescent proteins derived from Discosoma sp. red fluorescent protein. *Nat. Biotechnol.* **2004,** *22* (12), 1567.
55. Marks, K. M.; Nolan, G. P., Chemical labeling strategies for cell biology. *Nat. Methods* **2006,** *3* (8), 591.
56. Yan, Q.; Bruchez, M. P., Advances in chemical labeling of proteins in living cells. *Cell Tissue Res.* **2015,** *360* (1), 179.
57. Xue, L.; Karpenko, I. A.; Hiblot, J.; Johnsson, K., Imaging and manipulating proteins in live cells through covalent labeling. *Nat. Chem. Biol.* **2015,** *11* (12), 917.
58. Griffin, B. A.; Adams, S. R.; Tsien, R. Y., Specific Covalent Labeling of Recombinant Protein Molecules Inside Live Cells. *Science* **1998,** *281* (5374), 269.
59. Albert Griffin, B.; Adams, S. R.; Jones, J.; Tsien, R. Y., Fluorescent labeling of recombinant proteins in living cells with FlAsH. In *Methods Enzymol.*, Thorner, J.; Emr, S. D.; Abelson, J. N., Eds. Academic Press: 2000; Vol. 327, pp 565.
60. Hoffmann, C.; Gaietta, G.; Zürn, A.; Adams, S. R.; Terrillon, S.; Ellisman, M. H.; Tsien, R. Y.; Lohse, M. J., Fluorescent labeling of tetracysteine-tagged proteins in intact cells. *Nat. Protoc.* **2010,** *5* (10), 1666.
61. Adams, S. R.; Campbell, R. E.; Gross, L. A.; Martin, B. R.; Walkup, G. K.; Yao, Y.; Llopis, J.; Tsien, R. Y., New Biarsenical Ligands and Tetracysteine Motifs for Protein Labeling in Vitro and in Vivo: Synthesis and Biological Applications. *J. Am. Chem. Soc.* **2002,** *124* (21), 6063.
62. Spagnuolo, C. C.; Vermeij, R. J.; Jares-Erijman, E. A., Improved Photostable FRET-Competent Biarsenical−Tetracysteine Probes Based on Fluorinated Fluoresceins. *J. Am. Chem. Soc.* **2006,** *128* (37), 12040.
63. Adams, S. R.; Tsien, R. Y., Preparation of the membrane-permeant biarsenicals FlAsH-EDT2 and ReAsH-EDT2 for fluorescent labeling of tetracysteine-tagged proteins. *Nat. Protoc.* **2008,** *3* (9), 1527.
64. Halo, T. L.; Appelbaum, J.; Hobert, E. M.; Balkin, D. M.; Schepartz, A., Selective Recognition of Protein Tetraserine Motifs with a Cell-Permeable, Pro-fluorescent Bis-boronic Acid. *J. Am. Chem. Soc.* **2009,** *131* (2), 438.

65. Lotze, J.; Reinhardt, U.; Seitz, O.; Beck-Sickinger, A. G., Peptide-tags for site-specific protein labelling in vitro and in vivo. *Mol. Biosyst.* **2016,** *12* (6), 1731.
66. Liu, C. C.; Schultz, P. G., Adding New Chemistries to the Genetic Code. *Annu. Rev. Biochem* **2010,** *79* (1), 413.
67. Davis, L.; Chin, J. W., Designer proteins: applications of genetic code expansion in cell biology. *Nat. Rev. Mol. Cell Biol.* **2012,** *13* (3), 168.
68. Lang, K.; Davis, L.; Torres-Kolbus, J.; Chou, C.; Deiters, A.; Chin, J. W., Genetically encoded norbornene directs site-specific cellular protein labelling via a rapid bioorthogonal reaction. *Nat. Chem.* **2012,** *4* (4), 298.
69. Plass, T.; Milles, S.; Koehler, C.; Szymański, J.; Mueller, R.; Wießler, M.; Schultz, C.; Lemke, E. A., Amino Acids for Diels–Alder Reactions in Living Cells. *Angew. Chem. Int. Ed.* **2012,** *51* (17), 4166.
70. Lang, K.; Davis, L.; Wallace, S.; Mahesh, M.; Cox, D. J.; Blackman, M. L.; Fox, J. M.; Chin, J. W., Genetic Encoding of Bicyclononynes and trans-Cyclooctenes for Site-Specific Protein Labeling in Vitro and in Live Mammalian Cells via Rapid Fluorogenic Diels–Alder Reactions. *J. Am. Chem. Soc.* **2012,** *134* (25), 10317.
71. Uttamapinant, C.; Howe, J. D.; Lang, K.; Beránek, V.; Davis, L.; Mahesh, M.; Barry, N. P.; Chin, J. W., Genetic Code Expansion Enables Live-Cell and Super-Resolution Imaging of Site-Specifically Labeled Cellular Proteins. *J. Am. Chem. Soc.* **2015,** *137* (14), 4602.
72. Lukinavicius, G.; Umezawa, K.; Olivier, N.; Honigmann, A.; Yang, G.; Plass, T.; Mueller, V.; Reymond, L.; Correa, I. R., Jr.; Luo, Z. G.; Schultz, C.; Lemke, E. A.; Heppenstall, P.; Eggeling, C.; Manley, S.; Johnsson, K., A near-infrared fluorophore for live-cell super-resolution microscopy of cellular proteins. *Nat. Chem.* **2013,** *5* (2), 132.
73. Nikić, I.; Estrada Girona, G.; Kang, J. H.; Paci, G.; Mikhaleva, S.; Koehler, C.; Shymanska, N. V.; Ventura Santos, C.; Spitz, D.; Lemke, E. A., Debugging Eukaryotic Genetic Code Expansion for Site-Specific Click-PAINT Super-Resolution Microscopy. *Angew. Chem. Int. Ed.* **2016,** *55* (52), 16172.
74. Nikić, I.; Kang, J. H.; Girona, G. E.; Aramburu, I. V.; Lemke, E. A., Labeling proteins on live mammalian cells using click chemistry. *Nat. Protoc.* **2015,** *10* (5), 780.
75. Pegg, A. E., Repair of O6-alkylguanine by alkyltransferases. *Mutat. Res. Rev. Mutat. Res.* **2000,** *462* (2), 83.
76. Keppler, A.; Gendreizig, S.; Gronemeyer, T.; Pick, H.; Vogel, H.; Johnsson, K., A general method for the covalent labeling of fusion proteins with small molecules in vivo. *Nat. Biotechnol.* **2003,** *21* (1), 86.
77. Damoiseaux, R.; Keppler, A.; Johnsson, K., Synthesis and Applications of Chemical Probes for Human O6-Alkylguanine-DNA Alkyltransferase. *ChemBioChem* **2001,** *2* (4), 285.
78. Sun, X.; Zhang, A.; Baker, B.; Sun, L.; Howard, A.; Buswell, J.; Maurel, D.; Masharina, A.; Johnsson, K.; Noren, C. J.; Xu, M.-Q.; Corrêa Jr., I. R., Development of SNAP-Tag Fluorogenic Probes for Wash-Free Fluorescence Imaging. *ChemBioChem* **2011,** *12* (14), 2217.
79. Gautier, A.; Juillerat, A.; Heinis, C.; Corrêa, I. R.; Kindermann, M.; Beaufils, F.; Johnsson, K., An Engineered Protein Tag for Multiprotein Labeling in Living Cells. *Chem. Biol.* **2008,** *15* (2), 128.
80. Correa, R. I.; Baker, B.; Zhang, A.; Sun, L.; Provost, R. C.; Lukinavic ius, G. z.; Reymond, L.; Johnsson, K.; Xu, M.-Q., Substrates for Improved Live-Cell Fluorescence Labeling of SNAP-tag. *Curr. Pharm. Des.* **2013,** *19* (30), 5414.
81. Los, G. V.; Encell, L. P.; McDougall, M. G.; Hartzell, D. D.; Karassina, N.; Zimprich, C.; Wood, M. G.; Learish, R.; Ohana, R. F.; Urh, M.; Simpson, D.; Mendez, J.; Zimmerman, K.; Otto, P.; Vidugiris, G.; Zhu, J.; Darzins, A.; Klaubert, D. H.; Bulleit, R. F.; Wood, K. V., HaloTag: A Novel Protein Labeling Technology for Cell Imaging and Protein Analysis. *ACS Chem. Biol.* **2008,** *3* (6), 373.
82. Encell, L. P.; Friedman Ohana, R.; Zimmerman, K.; Otto, P.; Vidugiris, G.; Wood, M. G.; Los, G. V.; McDougall, M. G.; Zimprich, C.; Karassina, N.; Learish, R. D.; Hurst, R.; Hartnett, J.; Wheeler, S.; Stecha, P.; English, J.; Zhao, K.; Mendez, J.; Benink, H. A.; Murphy, N.; Daniels, D. L.; Slater, M. R.; Urh, M.; Darzins, A.; Klaubert, D. H.; Bulleit, R. F.; Wood, K.

V., Development of a dehalogenase-based protein fusion tag capable of rapid, selective and covalent attachment to customizable ligands. *Curr. Chem. Genomics* **2012,** *6*, 55.
83. Frei, M. S.; Tarnawski, M.; Roberti, J.; Koch, B.; Hiblot, J.; Johnsson, K., HaloTag9: an engineered protein tag to improve fluorophore performance. *bioRxiv* **2021**, 2021.04.01.438024.
84. Wilhelm, J.; Kühn, S.; Tarnawski, M.; Gotthard, G.; Tünnermann, J.; Tänzer, T.; Karpenko, J.; Mertes, N.; Xue, L.; Uhrig, U.; Reinstein, J.; Hiblot, J.; Johnsson, K., Kinetic and Structural Characterization of the Self-Labeling Protein Tags HaloTag7, SNAP-tag, and CLIP-tag. *Biochemistry* **2021,** *60* (33), 2560.
85. Wang, L.; Tran, M.; D'Este, E.; Roberti, J.; Koch, B.; Xue, L.; Johnsson, K., A general strategy to develop cell permeable and fluorogenic probes for multicolour nanoscopy. *Nat. Chem.* **2020,** *12* (2), 165.
86. Erdmann, R. S.; Baguley, S. W.; Richens, J. H.; Wissner, R. F.; Xi, Z.; Allgeyer, E. S.; Zhong, S.; Thompson, A. D.; Lowe, N.; Butler, R.; Bewersdorf, J.; Rothman, J. E.; St Johnston, D.; Schepartz, A.; Toomre, D., Labeling Strategies Matter for Super-Resolution Microscopy: A Comparison between HaloTags and SNAP-tags. *Cell Chem. Biol.* **2019,** *26* (4), 584.
87. Lardon, N.; Wang, L.; Tschanz, A.; Hoess, P.; Tran, M.; D'Este, E.; Ries, J.; Johnsson, K., Systematic Tuning of Rhodamine Spirocyclization for Super-resolution Microscopy. *J. Am. Chem. Soc.* **2021**, *143* (36), 14592.
88. Miller, L. W.; Sable, J.; Goelet, P.; Sheetz, M. P.; Cornish, V. W., Methotrexate Conjugates: A Molecular In Vivo Protein Tag. *Angew. Chem. Int. Ed.* **2004,** *43* (13), 1672.
89. Miller, L. W.; Cai, Y.; Sheetz, M. P.; Cornish, V. W., In vivo protein labeling with trimethoprim conjugates: a flexible chemical tag. *Nat. Methods* **2005,** *2* (4), 255.
90. Gallagher, S. S.; Sable, J. E.; Sheetz, M. P.; Cornish, V. W., An In Vivo Covalent TMP-Tag Based on Proximity-Induced Reactivity. *ACS Chem. Biol.* **2009,** *4* (7), 547.
91. Jing, C.; Cornish, V. W., A Fluorogenic TMP-Tag for High Signal-to-Background Intracellular Live Cell Imaging. *ACS Chem. Biol.* **2013,** *8* (8), 1704.
92. Wombacher, R.; Heidbreder, M.; van de Linde, S.; Sheetz, M. P.; Heilemann, M.; Cornish, V. W.; Sauer, M., Live-cell super-resolution imaging with trimethoprim conjugates. *Nat. Methods* **2010,** *7* (9), 717.
93. Thorn, K., Genetically encoded fluorescent tags. *Mol. Biol. Cell* **2017,** *28* (7), 848.
94. Chen, Z.; Jing, C.; Gallagher, S. S.; Sheetz, M. P.; Cornish, V. W., Second-Generation Covalent TMP-Tag for Live Cell Imaging. *J. Am. Chem. Soc.* **2012,** *134* (33), 13692.
95. Sallin, O.; Reymond, L.; Gondrand, C.; Raith, F.; Koch, B.; Johnsson, K., Semisynthetic biosensors for mapping cellular concentrations of nicotinamide adenine dinucleotides. *eLife* **2018,** *7*, e32638.
96. Tao, R.; Zhao, Y.; Chu, H.; Wang, A.; Zhu, J.; Chen, X.; Zou, Y.; Shi, M.; Liu, R.; Su, N.; Du, J.; Zhou, H.-M.; Zhu, L.; Qian, X.; Liu, H.; Loscalzo, J.; Yang, Y., Genetically encoded fluorescent sensors reveal dynamic regulation of NADPH metabolism. *Nat. Methods* **2017,** *14* (7), 720.
97. Moore, R. P.; Legant, W. R., Improving probes for super-resolution. *Nat. Methods* **2018,** *15* (9), 659.
98. Balzarotti, F.; Eilers, Y.; Gwosch, K. C.; Gynnå, A. H.; Westphal, V.; Stefani, F. D.; Elf, J.; Hell, S. W., Nanometer resolution imaging and tracking of fluorescent molecules with minimal photon fluxes. *Science* **2017,** *355* (6325), 606.
99. Lin, J.; Yang, K.; New, E. J., Strategies for organelle targeting of fluorescent probes. *Org. Biomol. Chem.* **2021**, *19*, 9339.
100. Latt, S. A.; Wohlleb, J. C., Optical studies of the interaction of 33258 Hoechst with DNA, chromatin, and metaphase chromosomes. *Chromosoma* **1975,** *52* (4), 297.
101. Pjura, P. E.; Grzeskowiak, K.; Dickerson, R. E., Binding of Hoechst 33258 to the minor groove of B-DNA. *J. Mol. Biol.* **1987,** *197* (2), 257.
102. Bucevičius, J.; Keller-Findeisen, J.; Gilat, T.; Hell, S. W.; Lukinavičius, G., Rhodamine–Hoechst positional isomers for highly efficient staining of heterochromatin. *Chem. Sci.* **2019,** *10* (7), 1962.

103. Haraguchi, T.; Kaneda, T.; Hiraoka, Y., Dynamics of chromosomes and microtubules visualized by multiple-wavelength fluorescence imaging in living mammalian cells: effects of mitotic inhibitors on cell cycle progression. *Genes Cells* **1997,** *2* (6), 369.
104. Nakamura, A.; Takigawa, K.; Kurishita, Y.; Kuwata, K.; Ishida, M.; Shimoda, Y.; Hamachi, I.; Tsukiji, S., Hoechst tagging: a modular strategy to design synthetic fluorescent probes for live-cell nucleus imaging. *Chem. Commun.* **2014,** *50* (46), 6149.
105. Lukinavičius, G.; Mitronova, G. Y.; Schnorrenberg, S.; Butkevich, A. N.; Barthel, H.; Belov, V. N.; Hell, S. W., Fluorescent dyes and probes for super-resolution microscopy of microtubules and tracheoles in living cells and tissues. *Chem. Sci.* **2018,** *9* (13), 3324.
106. Vila-Carriles, W. H.; Zhao, G.; Bryan, J., Defining a binding pocket for sulfonylureas in ATP-sensitive potassium channels. *FASEB J.* **2007,** *21* (1), 18.
107. Wi, Y.; Le, H. T.; Verwilst, P.; Sunwoo, K.; Kim, S. J.; Song, J. E.; Yoon, H. Y.; Han, G.; Kim, J. S.; Kang, C.; Kim, T. W., Modulating the GSH/Trx selectivity of a fluorogenic disulfide-based thiol sensor to reveal diminished GSH levels under ER stress. *Chem. Commun.* **2018,** *54* (64), 8897.
108. Fan, L.; Wang, X.; Ge, J.; Li, F.; Zhang, C.; Lin, B.; Shuang, S.; Dong, C., A Golgi-targeted off–on fluorescent probe for real-time monitoring of pH changes in vivo. *Chem. Commun.* **2019,** *55* (47), 6685.
109. Pagano, R. E.; Martin, O. C.; Kang, H. C.; Haugland, R. P., A novel fluorescent ceramide analogue for studying membrane traffic in animal cells: accumulation at the Golgi apparatus results in altered spectral properties of the sphingolipid precursor. *J. Cell Biol.* **1991,** *113* (6), 1267.
110. Erdmann, R. S.; Takakura, H.; Thompson, A. D.; Rivera-Molina, F.; Allgeyer, E. S.; Bewersdorf, J.; Toomre, D.; Schepartz, A., Super-Resolution Imaging of the Golgi in Live Cells with a Bioorthogonal Ceramide Probe. *Angew. Chem. Int. Ed.* **2014,** *53* (38), 10242.
111. Takakura, H.; Zhang, Y.; Erdmann, R. S.; Thompson, A. D.; Lin, Y.; McNellis, B.; Rivera-Molina, F.; Uno, S.-n.; Kamiya, M.; Urano, Y.; Rothman, J. E.; Bewersdorf, J.; Schepartz, A.; Toomre, D., Long time-lapse nanoscopy with spontaneously blinking membrane probes. *Nat. Biotechnol.* **2017,** *35* (8), 773.
112. Chen, C.-S.; Chen, W.-N. U.; Zhou, M.; Arttamangkul, S.; Haugland, R. P., Probing the cathepsin D using a BODIPY FL–pepstatin A: applications in fluorescence polarization and microscopy. *J. Biochem. Bioph. Methods* **2000,** *42* (3), 137.
113. Ross, M. F.; Kelso, G. F.; Blaikie, F. H.; James, A. M.; Cochemé, H. M.; Filipovska, A.; Da Ros, T.; Hurd, T. R.; Smith, R. A.; Murphy, M. P., Lipophilic triphenylphosphonium cations as tools in mitochondrial bioenergetics and free radical biology. *Biochemistry (Mosc)* **2005,** *70* (2), 222.
114. Linde, S. v. d.; Heilemann, M.; Sauer, M., Live-Cell Super-Resolution Imaging with Synthetic Fluorophores. *Annu. Rev. Phys. Chem.* **2012,** *63* (1), 519.
115. Lavis, L. D., Teaching Old Dyes New Tricks: Biological Probes Built from Fluoresceins and Rhodamines. *Annu. Rev. Biochem.* **2017,** *86* (1), 825.
116. Boyarskiy, V. P.; Belov, V. N.; Medda, R.; Hein, B.; Bossi, M.; Hell, S. W., Photostable, Amino Reactive and Water-Soluble Fluorescent Labels Based on Sulfonated Rhodamine with a Rigidized Xanthene Fragment. *Chem. Eur. J.* **2008,** *14* (6), 1784.
117. Panchuk-Voloshina, N.; Haugland, R. P.; Bishop-Stewart, J.; Bhalgat, M. K.; Millard, P. J.; Mao, F.; Leung, W.-Y.; Haugland, R. P., Alexa Dyes, a Series of New Fluorescent Dyes that Yield Exceptionally Bright, Photostable Conjugates. *J. Histochem. Cytochem.* **1999,** *47* (9), 1179.
118. Grimm, J. B.; Klein, T.; Kopek, B. G.; Shtengel, G.; Hess, H. F.; Sauer, M.; Lavis, L. D., Synthesis of a Far-Red Photoactivatable Silicon-Containing Rhodamine for Super-Resolution Microscopy. *Angew. Chem. Int. Ed.* **2016,** *55* (5), 1723.
119. Vogel, M.; Rettig, W.; Sens, R.; Drexhage, K. H., Structural relaxation of rhodamine dyes with different N-substitution patterns: A study of fluorescence decay times and quantum yields. *Chem. Phys. Lett.* **1988,** *147* (5), 452.

120. Song, X.; Johnson, A.; Foley, J., 7-Azabicyclo[2.2.1]heptane as a Unique and Effective Dialkylamino Auxochrome Moiety: Demonstration in a Fluorescent Rhodamine Dye. *J. Am. Chem. Soc.* **2008,** *130* (52), 17652.
121. Grimm, J. B.; English, B. P.; Chen, J.; Slaughter, J. P.; Zhang, Z.; Revyakin, A.; Patel, R.; Macklin, J. J.; Normanno, D.; Singer, R. H.; Lionnet, T.; Lavis, L. D., A general method to improve fluorophores for live-cell and single-molecule microscopy. *Nat. Methods* **2015,** *12* (3), 244.
122. Cauletti, C.; Di Vona, M. L.; Gargano, P.; Grandinetti, F.; Galli, C.; Lillocci, C., Ring-size effects on the ionization potentials of N-substituted azacycloalkanes. *J. Chem. Soc. Perkin Trans. 2* **1986,** (5), 667.
123. Mitronova, G. Y.; Belov, V. N.; Bossi, M. L.; Wurm, C. A.; Meyer, L.; Medda, R.; Moneron, G.; Bretschneider, S.; Eggeling, C.; Jakobs, S.; Hell, S. W., New fluorinated rhodamines for optical microscopy and nanoscopy. *Chem. Eur. J.* **2010,** *16* (15), 4477.
124. Roßmann, K.; Akkaya, K. C.; Charbonnier, C.; Eichhorst, J.; Jones, B.; Lehmann, M.; Broichhagen, J., Deuterated rhodamines for protein labelling in nanoscopy. *bioRxiv* **2020**, 2020.08.17.253880.
125. Grimm, J. B.; Xie, L.; Casler, J. C.; Patel, R.; Tkachuk, A. N.; Falco, N.; Choi, H.; Lippincott-Schwartz, J.; Brown, T. A.; Glick, B. S.; Liu, Z.; Lavis, L. D., A General Method to Improve Fluorophores Using Deuterated Auxochromes. *JACS Au* **2021,** *1* (5), 690.
126. Koide, Y.; Urano, Y.; Hanaoka, K.; Terai, T.; Nagano, T., Evolution of group 14 rhodamines as platforms for near-infrared fluorescence probes utilizing photoinduced electron transfer. *ACS Chem. Biol.* **2011,** *6* (6), 600.
127. Grimm, J. B.; Tkachuk, A. N.; Xie, L.; Choi, H.; Mohar, B.; Falco, N.; Schaefer, K.; Patel, R.; Zheng, Q.; Liu, Z.; Lippincott-Schwartz, J.; Brown, T. A.; Lavis, L. D., A general method to optimize and functionalize red-shifted rhodamine dyes. *Nat. Methods* **2020,** *17* (8), 815.
128. Grzybowski, M.; Taki, M.; Senda, K.; Sato, Y.; Ariyoshi, T.; Okada, Y.; Kawakami, R.; Imamura, T.; Yamaguchi, S., A Highly Photostable Near-Infrared Labeling Agent Based on a Phospha-rhodamine for Long-Term and Deep Imaging. *Angew. Chem. Int. Ed.* **2018,** *57* (32), 10137.
129. Liu, J.; Sun, Y.-Q.; Zhang, H.; Shi, H.; Shi, Y.; Guo, W., Sulfone-Rhodamines: A New Class of Near-Infrared Fluorescent Dyes for Bioimaging. *ACS Appl. Mater. Interfaces* **2016,** *8* (35), 22953.
130. Grimm, J. B.; Muthusamy, A. K.; Liang, Y.; Brown, T. A.; Lemon, W. C.; Patel, R.; Lu, R.; Macklin, J. J.; Keller, P. J.; Ji, N.; Lavis, L. D., A general method to fine-tune fluorophores for live-cell and in vivo imaging. *Nat. Methods* **2017,** *14* (10), 987.
131. Ren, T.-B.; Xu, W.; Zhang, W.; Zhang, X.-X.; Wang, Z.-Y.; Xiang, Z.; Yuan, L.; Zhang, X.-B., A General Method To Increase Stokes Shift by Introducing Alternating Vibronic Structures. *J. Am. Chem. Soc.* **2018,** *140* (24), 7716.
132. Ceresole, M., Verfahren zur Darstellung von Farbstoffen aus der Gruppe des Meta-amidophenolphtaleïns. *German Patent* **1887,** *44002*.
133. Grimm, J. B.; Lavis, L. D., Synthesis of Rhodamines from Fluoresceins Using Pd-Catalyzed C–N Cross-Coupling. *Org. Lett.* **2011,** *13* (24), 6354.
134. Grimm, J. B.; Sung, A. J.; Legant, W. R.; Hulamm, P.; Matlosz, S. M.; Betzig, E.; Lavis, L. D., Carbofluoresceins and Carborhodamines as Scaffolds for High-Contrast Fluorogenic Probes. *ACS Chem. Biol.* **2013,** *8* (6), 1303.
135. Grimm, J. B.; Brown, T. A.; Tkachuk, A. N.; Lavis, L. D., General Synthetic Method for Si-Fluoresceins and Si-Rhodamines. *ACS Cent. Sci.* **2017,** *3* (9), 975.
136. Fischer, C.; Sparr, C., Direct Transformation of Esters into Heterocyclic Fluorophores. *Angew. Chem. Int. Ed.* **2018,** *57* (9), 2436.
137. Butkevich, A. N., Modular Synthetic Approach to Silicon-Rhodamine Homologues and Analogues via Bis-aryllanthanum Reagents. *Org. Lett.* **2021,** *23* (7), 2604.
138. Pati, A. K.; El Bakouri, O.; Jockusch, S.; Zhou, Z.; Altman, R. B.; Fitzgerald, G. A.; Asher, W. B.; Terry, D. S.; Borgia, A.; Holsey, M. D.; Batchelder, J. E.; Abeywickrama, C.; Huddle, B.; Rufa, D.; Javitch, J. A.; Ottosson, H.; Blanchard, S. C., Tuning the Baird aromatic

triplet-state energy of cyclooctatetraene to maximize the self-healing mechanism in organic fluorophores. *Proc. Natl. Acad. Sci. USA* **2020,** *117* (39), 24305.
139. Tinnefeld, P.; Cordes, T., 'Self-healing' dyes: intramolecular stabilization of organic fluorophores. *Nat. Methods* **2012,** *9* (5), 426.
140. Cordes, T.; Vogelsang, J.; Tinnefeld, P., On the Mechanism of Trolox as Antiblinking and Antibleaching Reagent. *J. Am. Chem. Soc.* **2009,** *131* (14), 5018.
141. Altman, R. B.; Terry, D. S.; Zhou, Z.; Zheng, Q.; Geggier, P.; Kolster, R. A.; Zhao, Y.; Javitch, J. A.; Warren, J. D.; Blanchard, S. C., Cyanine fluorophore derivatives with enhanced photostability. *Nat. Methods* **2012,** *9* (1), 68.
142. Zheng, Q.; Jockusch, S.; Zhou, Z.; Altman, R. B.; Zhao, H.; Asher, W.; Holsey, M.; Mathiasen, S.; Geggier, P.; Javitch, J. A.; Blanchard, S. C., Electronic tuning of self-healing fluorophores for live-cell and single-molecule imaging. *Chem. Sci.* **2017,** *8* (1), 755.
143. Yang, Z.; Li, L.; Ling, J.; Liu, T.; Huang, X.; Ying, Y.; Zhao, Y.; Zhao, Y.; Lei, K.; Chen, L.; Chen, Z., Cyclooctatetraene-conjugated cyanine mitochondrial probes minimize phototoxicity in fluorescence and nanoscopic imaging. *Chem. Sci.* **2020,** *11* (32), 8506.
144. Chi, W.; Qi, Q.; Lee, R.; Xu, Z.; Liu, X., A Unified Push–Pull Model for Understanding the Ring-Opening Mechanism of Rhodamine Dyes. *J. Phys. Chem. C* **2020**.
145. Nadler, A.; Schultz, C., The Power of Fluorogenic Probes. *Angew. Chem. Int. Ed.* **2013,** *52* (9), 2408.
146. Ramette, R. W.; Sandell, E. B., Rhodamine B Equilibria. *J. Am. Chem. Soc.* **1956,** *78* (19), 4872.
147. Uno, S. N.; Kamiya, M.; Yoshihara, T.; Sugawara, K.; Okabe, K.; Tarhan, M. C.; Fujita, H.; Funatsu, T.; Okada, Y.; Tobita, S.; Urano, Y., A spontaneously blinking fluorophore based on intramolecular spirocyclization for live-cell super-resolution imaging. *Nat. Chem.* **2014,** *6* (8), 681.
148. Fu, M.; Xiao, Y.; Qian, X.; Zhao, D.; Xu, Y., A design concept of long-wavelength fluorescent analogs of rhodamine dyes: replacement of oxygen with silicon atom. *Chem. Commun.* **2008,** (15), 1780.
149. Wirth, R.; Gao, P.; Nienhaus, G. U.; Sunbul, M.; Jäschke, A., SiRA: A Silicon Rhodamine-Binding Aptamer for Live-Cell Super-Resolution RNA Imaging. *J. Am. Chem. Soc.* **2019,** *141* (18), 7562.
150. Zheng, Q.; Ayala, A. X.; Chung, I.; Weigel, A. V.; Ranjan, A.; Falco, N.; Grimm, J. B.; Tkachuk, A. N.; Wu, C.; Lippincott-Schwartz, J.; Singer, R. H.; Lavis, L. D., Rational Design of Fluorogenic and Spontaneously Blinking Labels for Super-Resolution Imaging. *ACS Cent. Sci.* **2019,** *5* (9), 1602.
151. Umezawa, K.; Kamiya, M.; Urano, Y., A Reversible Fluorescent Probe for Real-Time Live-Cell Imaging and Quantification of Endogenous Hydropolysulfides. *Angew. Chem. Int. Ed.* **2018,** *57* (30), 9346.
152. Umezawa, K.; Yoshida, M.; Kamiya, M.; Yamasoba, T.; Urano, Y., Rational design of reversible fluorescent probes for live-cell imaging and quantification of fast glutathione dynamics. *Nat. Chem.* **2017,** *9* (3), 279.
153. Grzybowski, M.; Taki, M.; Senda, K.; Sato, Y.; Ariyoshi, T.; Okada, Y.; Kawakami, R.; Imamura, T.; Yamaguchi, S., A Highly Photostable Near-Infrared Labeling Agent Based on a Phospha-rhodamine for Long-Term and Deep Imaging. *Angew. Chem. Int. Ed.* **2018,** *57* (32), 10137.
154. Wang, L.; Hiblot, J.; Popp, C.; Xue, L.; Johnsson, K., Environmentally Sensitive Color-Shifting Fluorophores for Bioimaging. *Angew. Chem. Int. Ed.* **2020,** *59* (49), 21880.
155. Zhang, J.; Wang, L.; Jäschke, A.; Sunbul, M., A Color-Shifting Near-Infrared Fluorescent Aptamer–Fluorophore Module for Live-Cell RNA Imaging. *Angew. Chem. Int. Ed.* **2021,** *60* (39), 21441.
156. Belov, V. N.; Bossi, M. L.; Fölling, J.; Boyarskiy, V. P.; Hell, S. W., Rhodamine Spiroamides for Multicolor Single-Molecule Switching Fluorescent Nanoscopy. *Chem. Eur. J.* **2009,** *15* (41), 10762.

157. Fölling, J.; Belov, V.; Kunetsky, R.; Medda, R.; Schönle, A.; Egner, A.; Eggeling, C.; Bossi, M.; Hell, S. W., Photochromic Rhodamines Provide Nanoscopy with Optical Sectioning. *Angew. Chem. Int. Ed.* **2007,** *46* (33), 6266.
158. Belov, V. N.; Bossi, M. L., Photoswitching Emission with Rhodamine Spiroamides for Super-resolution Fluorescence nanoscopies. *Isr. J. Chem.* **2013,** *53* (5), 267.
159. Ho, S. H.; Tirrell, D. A., Enzymatic Labeling of Bacterial Proteins for Super-resolution Imaging in Live Cells. *ACS Cent. Sci.* **2019,** *5* (12), 1911.
160. Ye, Z.; Yu, H.; Yang, W.; Zheng, Y.; Li, N.; Bian, H.; Wang, Z.; Liu, Q.; Song, Y.; Zhang, M.; Xiao, Y., Strategy to Lengthen the On-Time of Photochromic Rhodamine Spirolactam for Super-resolution Photoactivated Localization Microscopy. *J. Am. Chem. Soc.* **2019,** *141* (16), 6527.
161. Knauer, K.-H.; Gleiter, R., Photochromism of Rhodamine Derivatives. *Angew. Chem. Int. Ed.* **1977,** *16* (2), 113.
162. Willwohl, H.; Wolfrum, J.; Gleiter, R., Kinetics and Mechanism of the Photochromism of N-Phenyl-Rhodaminelactame. *Laser Chem.* **1989,** *10*, 069709.
163. Wäldchen, S.; Lehmann, J.; Klein, T.; van de Linde, S.; Sauer, M., Light-induced cell damage in live-cell super-resolution microscopy. *Sci. Rep.* **2015,** *5* (1), 15348.
164. Werther, P.; Yserentant, K.; Braun, F.; Kaltwasser, N.; Popp, C.; Baalmann, M.; Herten, D.-P.; Wombacher, R., Live-Cell Localization Microscopy with a Fluorogenic and Self-Blinking Tetrazine Probe. *Angew. Chem. Int. Ed.* **2020,** *59* (2), 804.
165. Bucevičius, J.; Gilat, T.; Lukinavičius, G., Far-red switching DNA probes for live cell nanoscopy. *Chem. Commun.* **2020,** *56* (94), 14797.
166. Uno, S. N.; Kamiya, M.; Morozumi, A.; Urano, Y., A green-light-emitting, spontaneously blinking fluorophore based on intramolecular spirocyclization for dual-colour super-resolution imaging. *Chem. Commun.* **2017,** *54* (1), 102.
167. Macdonald, P. J.; Gayda, S.; Haack, R. A.; Ruan, Q.; Himmelsbach, R. J.; Tetin, S. Y., Rhodamine-Derived Fluorescent Dye with Inherent Blinking Behavior for Super-Resolution Imaging. *Anal. Chem.* **2018,** *90* (15), 9165.
168. Halabi, E. A.; Pinotsi, D.; Rivera-Fuentes, P., Photoregulated fluxional fluorophores for live-cell super-resolution microscopy with no apparent photobleaching. *Nat. Commun.* **2019,** *10* (1), 1232.
169. Carter, K. P.; Young, A. M.; Palmer, A. E., Fluorescent Sensors for Measuring Metal Ions in Living Systems. *Chem. Rev.* **2014,** *114* (8), 4564.
170. Domaille, D. W.; Que, E. L.; Chang, C. J., Synthetic fluorescent sensors for studying the cell biology of metals. *Nat. Chem. Biol.* **2008,** *4* (3), 168.
171. Zheng, H.; Zhan, X.-Q.; Bian, Q.-N.; Zhang, X.-J., Advances in modifying fluorescein and rhodamine fluorophores as fluorescent chemosensors. *Chem. Commun.* **2013,** *49* (5), 429.
172. Thomas, J. A.; Buchsbaum, R. N.; Zimniak, A.; Racker, E., Intracellular pH measurements in Ehrlich ascites tumor cells utilizing spectroscopic probes generated in situ. *Biochemistry* **1979,** *18* (11), 2210.
173. Lavis, L. D., Live and Let Dye. *Biochemistry* **2021**.
174. Minta, A.; Kao, J. P. Y.; Tsien, R. Y., Fluorescent indicators for cytosolic calcium based on rhodamine and fluorescein chromophores. *J. Biol. Chem.* **1989,** *264* (14), 8171.
175. Tsien, R. Y., New calcium indicators and buffers with high selectivity against magnesium and protons: design, synthesis, and properties of prototype structures. *Biochemistry* **1980,** *19* (11), 2396.
176. Kim, H. N.; Lee, M. H.; Kim, H. J.; Kim, J. S.; Yoon, J., A new trend in rhodamine-based chemosensors: application of spirolactam ring-opening to sensing ions. *Chem. Soc. Rev.* **2008,** *37* (8), 1465.
177. Dujols, V.; Ford, F.; Czarnik, A. W., A Long-Wavelength Fluorescent Chemodosimeter Selective for Cu(II) Ion in Water. *J. Am. Chem. Soc.* **1997,** *119* (31), 7386.
178. Chen, X.; Pradhan, T.; Wang, F.; Kim, J. S.; Yoon, J., Fluorescent Chemosensors Based on Spiroring-Opening of Xanthenes and Related Derivatives. *Chem. Rev.* **2012,** *112* (3), 1910.

179. Frederickson, C. J., Neurobiology of Zinc and Zinc-Containing Neurons. In *Int. Rev. Neurobiol.*, Smythies, J. R.; Bradley, R. J., Eds. Academic Press: 1989; Vol. 31, pp 145.
180. Que, E. L.; Domaille, D. W.; Chang, C. J., Metals in Neurobiology: Probing Their Chemistry and Biology with Molecular Imaging. *Chem. Rev.* **2008,** *108* (5), 1517.
181. Taylor, C. G., Zinc, the Pancreas, and Diabetes: Insights from Rodent Studies and Future Directions. *BioMetals* **2005,** *18* (4), 305.
182. Outten, C. E.; O'Halloran, a. T. V., Femtomolar Sensitivity of Metalloregulatory Proteins Controlling Zinc Homeostasis. *Science* **2001,** *292* (5526), 2488.
183. Formby, B.; Schmid-Formby, F.; Grodsky, G. M., Relationship Between Insulin Release and ⁶⁵Zinc Efflux from Rat Pancreatic Islets Maintained in Tissue Culture. *Diabetes* **1984,** *33* (3), 229.
184. Walkup, G. K.; Burdette, S. C.; Lippard, S. J.; Tsien, R. Y., A New Cell-Permeable Fluorescent Probe for Zn2+. *J. Am. Chem. Soc.* **2000,** *122* (23), 5644.
185. Burdette, S. C.; Walkup, G. K.; Spingler, B.; Tsien, R. Y.; Lippard, S. J., Fluorescent Sensors for Zn2+ Based on a Fluorescein Platform: Synthesis, Properties and Intracellular Distribution. *J. Am. Chem. Soc.* **2001,** *123* (32), 7831.
186. Chang, C. J.; Nolan, E. M.; Jaworski, J.; Burdette, S. C.; Sheng, M.; Lippard, S. J., Bright Fluorescent Chemosensor Platforms for Imaging Endogenous Pools of Neuronal Zinc. *Chem. Biol.* **2004,** *11* (2), 203.
187. Burdette, S. C.; Frederickson, C. J.; Bu, W.; Lippard, S. J., ZP4, an Improved Neuronal Zn2+ Sensor of the Zinpyr Family. *J. Am. Chem. Soc.* **2003,** *125* (7), 1778.
188. Hirano, T.; Kikuchi, K.; Urano, Y.; Higuchi, T.; Nagano, T., Highly Zinc-Selective Fluorescent Sensor Molecules Suitable for Biological Applications. *J. Am. Chem. Soc.* **2000,** *122* (49), 12399.
189. Komatsu, K.; Kikuchi, K.; Kojima, H.; Urano, Y.; Nagano, T., Selective Zinc Sensor Molecules with Various Affinities for Zn2+, Revealing Dynamics and Regional Distribution of Synaptically Released Zn2+ in Hippocampal Slices. *J. Am. Chem. Soc.* **2005,** *127* (29), 10197.
190. Nolan, E. M.; Ryu, J. W.; Jaworski, J.; Feazell, R. P.; Sheng, M.; Lippard, S. J., Zinspy Sensors with Enhanced Dynamic Range for Imaging Neuronal Cell Zinc Uptake and Mobilization. *J. Am. Chem. Soc.* **2006,** *128* (48), 15517.
191. Li, D.; Liu, L.; Li, W.-H., Genetic Targeting of a Small Fluorescent Zinc Indicator to Cell Surface for Monitoring Zinc Secretion. *ACS Chem. Biol.* **2015,** *10* (4), 1054.
192. Zastrow, M. L.; Huang, Z.; Lippard, S. J., HaloTag-Based Hybrid Targetable and Ratiometric Sensors for Intracellular Zinc. *ACS Chem. Biol.* **2020,** *15* (2), 396.
193. Zhang, J.; Peng, X.; Wu, Y.; Ren, H.; Sun, J.; Tong, S.; Liu, T.; Zhao, Y.; Wang, S.; Tang, C.; Chen, L.; Chen, Z., Red- and Far-Red-Emitting Zinc Probes with Minimal Phototoxicity for Multiplexed Recording of Orchestrated Insulin Secretion. *Angew. Chem. Int. Ed.* **2021**, *60*, 25846.
194. Chen, X.; Wu, Q.; Henschke, L.; Weber, G.; Weil, T., An efficient and versatile approach for the preparation of a rhodamine B ester bioprobe library. *Dyes Pigm.* **2012,** *94* (2), 296.
195. Critchfield, F. E.; Gibson, J. A.; Hall, J. L., Dielectric Constant for the Dioxane—Water System from 20 to 35°. *J. Am. Chem. Soc.* **1953,** *75* (8), 1991.
196. Hansch, C.; Leo, A.; Taft, R. W., A survey of Hammett substituent constants and resonance and field parameters. *Chem. Rev.* **1991,** *91* (2), 165.
197. Yau, H. M.; Haines, R. S.; Harper, J. B., A Robust, "One-Pot" Method for Acquiring Kinetic Data for Hammett Plots Used To Demonstrate Transmission of Substituent Effects in Reactions of Aromatic Ethyl Esters. *J. Chem. Educ.* **2015,** *92* (3), 538.
198. Bragato, M.; von Rudorff, G. F.; von Lilienfeld, O. A., Data enhanced Hammett-equation: reaction barriers in chemical space. *Chem. Sci.* **2020,** *11* (43), 11859.
199. Thevathasan, J. V.; Kahnwald, M.; Cieśliński, K.; Hoess, P.; Peneti, S. K.; Reitberger, M.; Heid, D.; Kasuba, K. C.; Hoerner, S. J.; Li, Y.; Wu, Y.-L.; Mund, M.; Matti, U.; Pereira, P. M.; Henriques, R.; Nijmeijer, B.; Kueblbeck, M.; Sabinina, V. J.; Ellenberg, J.; Ries, J., Nuclear pores as versatile reference standards for quantitative superresolution microscopy. *Nat. Methods* **2019,** *16* (10), 1045.

200. Szymborska, A.; Marco, A. d.; Daigle, N.; Cordes, V. C.; Briggs, J. A. G.; Ellenberg, J., Nuclear Pore Scaffold Structure Analyzed by Super-Resolution Microscopy and Particle Averaging. *Science* **2013,** *341* (6146), 655.
201. Frei, M. S.; Hoess, P.; Lampe, M.; Nijmeijer, B.; Kueblbeck, M.; Ellenberg, J.; Wadepohl, H.; Ries, J.; Pitsch, S.; Reymond, L.; Johnsson, K., Photoactivation of silicon rhodamines via a light-induced protonation. *Nat. Commun.* **2019,** *10* (1), 4580.
202. Ries, J.; Kaplan, C.; Platonova, E.; Eghlidi, H.; Ewers, H., A simple, versatile method for GFP-based super-resolution microscopy via nanobodies. *Nat. Methods* **2012,** *9* (6), 582.
203. Butkevich, A. N.; Ta, H.; Ratz, M.; Stoldt, S.; Jakobs, S.; Belov, V. N.; Hell, S. W., Two-Color 810 nm STED Nanoscopy of Living Cells with Endogenous SNAP-Tagged Fusion Proteins. *ACS Chem. Biol.* **2018,** *13* (2), 475.
204. Bellamy, W. T., P-Glycoproteins and Multidrug Resistance. *Annu. Rev. Pharmacool. Toxicol.* **1996,** *36* (1), 161.
205. Xue, L.; Prifti, E.; Johnsson, K., A General Strategy for the Semisynthesis of Ratiometric Fluorescent Sensor Proteins with Increased Dynamic Range. *J. Am. Chem. Soc.* **2016,** *138* (16), 5258.
206. Debouck, C.; Gorniak, J. G.; Strickler, J. E.; Meek, T. D.; Metcalf, B. W.; Rosenberg, M., Human immunodeficiency virus protease expressed in Escherichia coli exhibits autoprocessing and specific maturation of the gag precursor. *Proc. Natl. Acad. Sci. USA* **1987,** *84* (24), 8903.
207. Kräusslich, H. G.; Ingraham, R. H.; Skoog, M. T.; Wimmer, E.; Pallai, P. V.; Carter, C. A., Activity of purified biosynthetic proteinase of human immunodeficiency virus on natural substrates and synthetic peptides. *Proc. Natl. Acad. Sci. USA* **1989,** *86* (3), 807.
208. Pokorná, J.; Machala, L.; Řezáčová, P.; Konvalinka, J., Current and Novel Inhibitors of HIV Protease. *Viruses* **2009,** *1* (3), 1209.
209. Schimer, J.; Pávová, M.; Anders, M.; Pachl, P.; Šácha, P.; Cígler, P.; Weber, J.; Majer, P.; Řezáčová, P.; Kräusslich, H.-G.; Müller, B.; Konvalinka, J., Triggering HIV polyprotein processing by light using rapid photodegradation of a tight-binding protease inhibitor. *Nat. Commun.* **2015,** *6* (1), 6461.
210. Kempf, D. J.; Marsh, K. C.; Denissen, J. F.; McDonald, E.; Vasavanonda, S.; Flentge, C. A.; Green, B. E.; Fino, L.; Park, C. H.; Kong, X. P., ABT-538 is a potent inhibitor of human immunodeficiency virus protease and has high oral bioavailability in humans. *Proc. Natl. Acad. Sci. USA* **1995,** *92* (7), 2484.
211. Davies, T. Q.; Tilby, M. J.; Skolc, D.; Hall, A.; Willis, M. C., Primary Sulfonamide Synthesis Using the Sulfinylamine Reagent N-Sulfinyl-O-(tert-butyl)hydroxylamine, t-BuONSO. *Org. Lett.* **2020,** *22* (24), 9495.
212. Thompson, A. D.; Bewersdorf, J.; Toomre, D.; Schepartz, A., HIDE Probes: A New Toolkit for Visualizing Organelle Dynamics, Longer and at Super-Resolution. *Biochemistry* **2017,** *56* (39), 5194.
213. Sadhu, K. K.; Mizukami, S.; Lanam, C. R.; Kikuchi, K., Fluorogenic Protein Labeling through Photoinduced Electron Transfer-Based BL-Tag Technology. *Chem. Asian J.* **2012,** *7* (2), 272.
214. Kamikawa, Y.; Hori, Y.; Yamashita, K.; Jin, L.; Hirayama, S.; Standley, D. M.; Kikuchi, K., Design of a protein tag and fluorogenic probe with modular structure for live-cell imaging of intracellular proteins. *Chem. Sci.* **2016,** *7* (1), 308.
215. Mertes, N.; Busch, M.; Huppertz, M.-C.; Hacker, C. N.; Gürth, C.-M.; Kühn, S.; Hiblot, J.; Koch, B.; Johnsson, K., Fluorescent and bioluminescent calcium indicators with tuneable colors and affinities. *bioRxiv* **2021**, 2021.11.13.468356.
216. Bess, E. N.; DeLuca, R. J.; Tindall, D. J.; Oderinde, M. S.; Roizen, J. L.; Du Bois, J.; Sigman, M. S., Analyzing Site Selectivity in Rh2(esp)2-Catalyzed Intermolecular C–H Amination Reactions. *J. Am. Chem. Soc.* **2014,** *136* (15), 5783.
217. Hirano, T.; Kikuchi, K.; Urano, Y.; Higuchi, T.; Nagano, T., Novel Zinc Fluorescent Probes Excitable with Visible Light for Biological Applications. *Angew. Chem. Int. Ed.* **2000,** *39* (6), 1052.

218. Ikeno, T.; Nagano, T.; Hanaoka, K., Silicon-substituted Xanthene Dyes and Their Unique Photophysical Properties for Fluorescent Probes. *Chem. Asian J.* **2017,** *12* (13), 1435.
219. Spahn, C.; Hurter, F.; Glaesmann, M.; Karathanasis, C.; Lampe, M.; Heilemann, M., Protein-Specific, Multicolor and 3D STED Imaging in Cells with DNA-Labeled Antibodies. *Angew. Chem. Int. Ed.* **2019,** *58* (52), 18835.
220. Spahn, C.; Grimm, J. B.; Lavis, L. D.; Lampe, M.; Heilemann, M., Whole-Cell, 3D, and Multicolor STED Imaging with Exchangeable Fluorophores. *Nano Lett.* **2019,** *19* (1), 500.
221. Ratz, M.; Testa, I.; Hell, S. W.; Jakobs, S., CRISPR/Cas9-mediated endogenous protein tagging for RESOLFT super-resolution microscopy of living human cells. *Sci. Rep.* **2015,** *5* (1), 9592.
222. Formby, B.; Schmid-Formby, F.; Grodsky, G. M., Relationship Between Insulin Release and 65Zinc Efflux from Rat Pancreatic Islets Maintained in Tissue Culture. *Diabetes* **1984,** *33* (3), 229.
223. Deschamps, J.; Rowald, A.; Ries, J., Efficient homogeneous illumination and optical sectioning for quantitative single-molecule localization microscopy. *Opt. Express* **2016,** *24* (24), 28080.
224. Edelstein, A. D.; Tsuchida, M. A.; Amodaj, N.; Pinkard, H.; Vale, R. D.; Stuurman, N., Advanced methods of microscope control using μManager software. *J. Biol. Methods* **2014,** *1* (2), e10.
225. Schröder, D.; Deschamps, J.; Dasgupta, A.; Matti, U.; Ries, J., Cost-efficient open source laser engine for microscopy. *Biomed. Opt. Express* **2020,** *11* (2), 609.
226. Deschamps, J.; Ries, J., EMU: reconfigurable graphical user interfaces for Micro-Manager. *BMC Bioinform.* **2020,** *21* (1), 456.
227. Schindelin, J.; Arganda-Carreras, I.; Frise, E.; Kaynig, V.; Longair, M.; Pietzsch, T.; Preibisch, S.; Rueden, C.; Saalfeld, S.; Schmid, B.; Tinevez, J.-Y.; White, D. J.; Hartenstein, V.; Eliceiri, K.; Tomancak, P.; Cardona, A., Fiji: an open-source platform for biological-image analysis. *Nat. Methods* **2012,** *9* (7), 676.
228. Rueden, C. T.; Schindelin, J.; Hiner, M. C.; DeZonia, B. E.; Walter, A. E.; Arena, E. T.; Eliceiri, K. W., ImageJ2: ImageJ for the next generation of scientific image data. *BMC Bioinform.* **2017,** *18* (1), 529.
229. Ries, J., SMAP: a modular super-resolution microscopy analysis platform for SMLM data. *Nat. Methods* **2020,** *17* (9), 870.
230. Ester, M.; Kriegel, H.-P.; Sander, J.; Xu, X., A density-based algorithm for discovering clusters in large spatial databases with noise. In *kdd* **1996***, 96* (34) 226.
231. Gottlieb, H. E.; Kotlyar, V.; Nudelman, A., NMR Chemical Shifts of Common Laboratory Solvents as Trace Impurities. *J. Org. Chem.* **1997,** *62* (21), 7512.
232. Rubner, S.; Scharow, A.; Schubert, S.; Berg, T., Selective Degradation of Polo-like Kinase 1 by a Hydrophobically Tagged Inhibitor of the Polo-Box Domain. *Angew. Chem. Int. Ed.* **2018,** *57* (52), 17043.

8. Appendix

8.1. Supplementary Figures

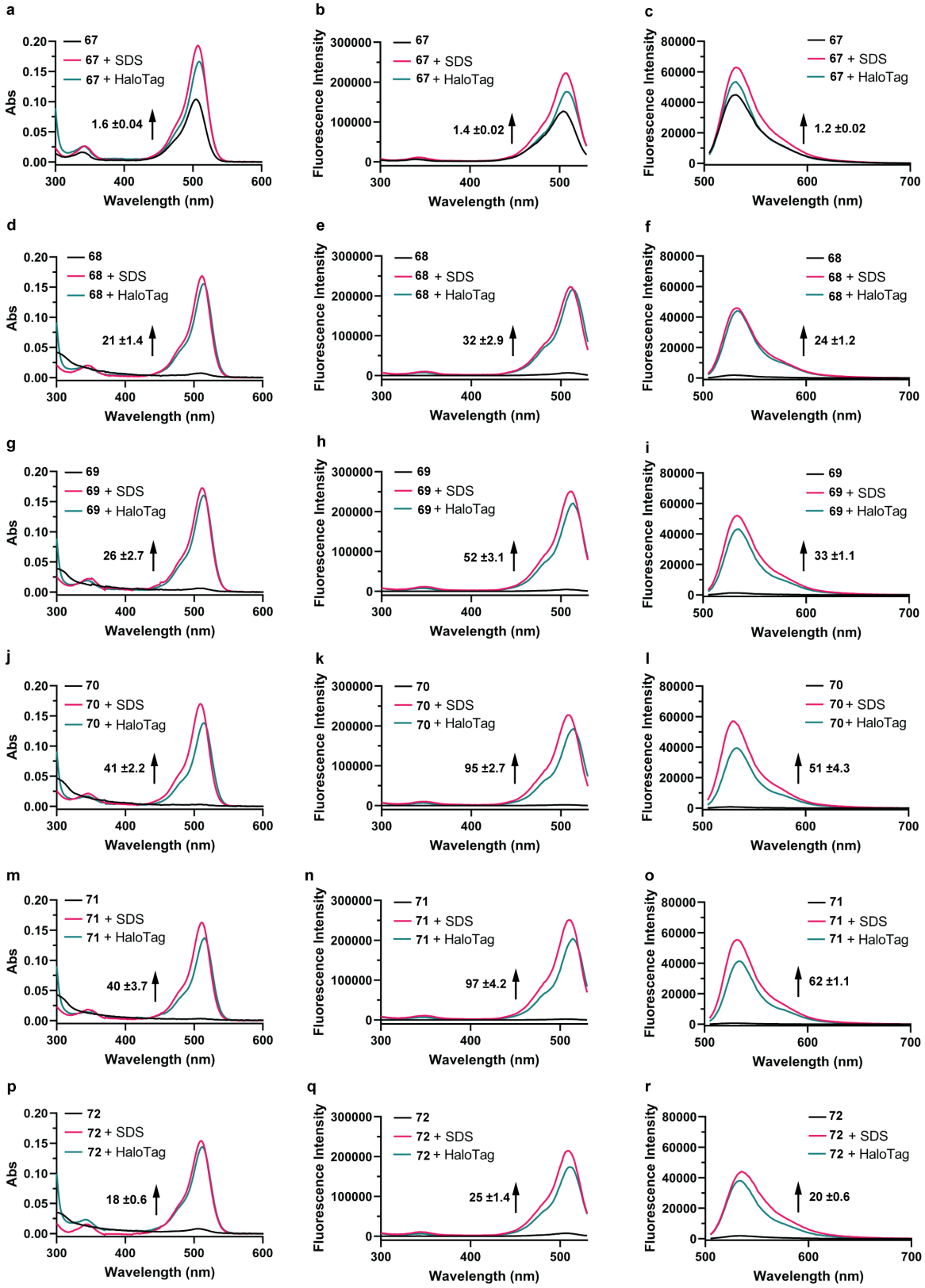

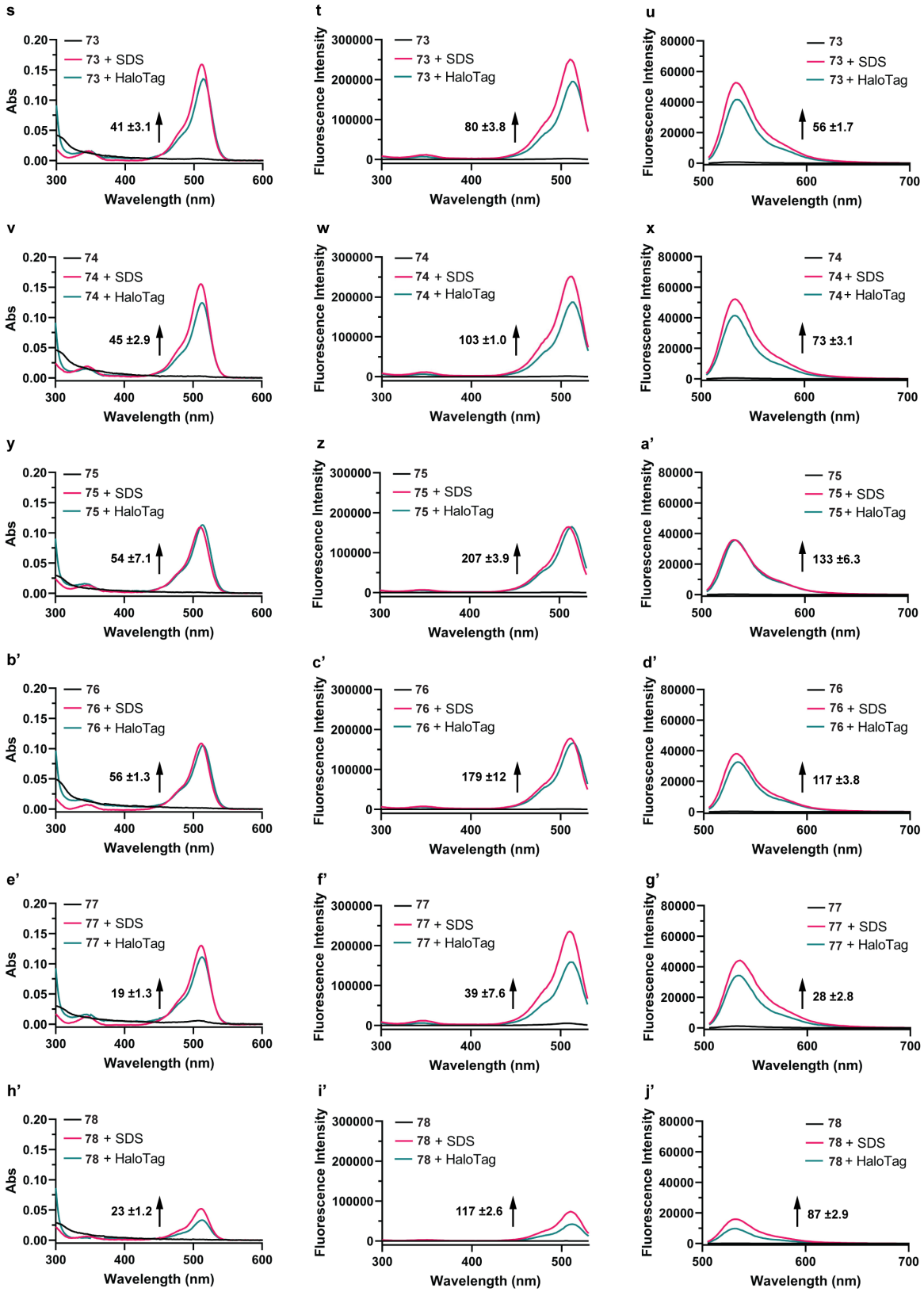

Supplementary Figure 1: Turn-on experiments of rhodamine *500R* HaloTag probes (**67** – **78**) upon labeling of HaloTag or interaction with SDS. Absorbance (a, d, g, j, m, p, s, v, y, b', e', h'), excitation (b, e, h, k, n, q, t, w, z, c', f', i') and emission (c, f, i, l, o, r, u, x, a', d', g', j') spectra of probes **67** – **78** (2.5 µM) measured in HEPES buffer (pH 7.3) in the absence and presence of HaloTag (5 µM) or SDS (0.1%) after 2.5 h incubation. The numbers show the ratio of maximal absorbance and fluorescence intensities ($F_{protein}/F_0$) (emission: λ_{ex}: 490 nm, excitation λ_{em}: 550 nm) in the presence and absence of the HaloTag. Representative data for 3 experiments. Errors show ± s.d.

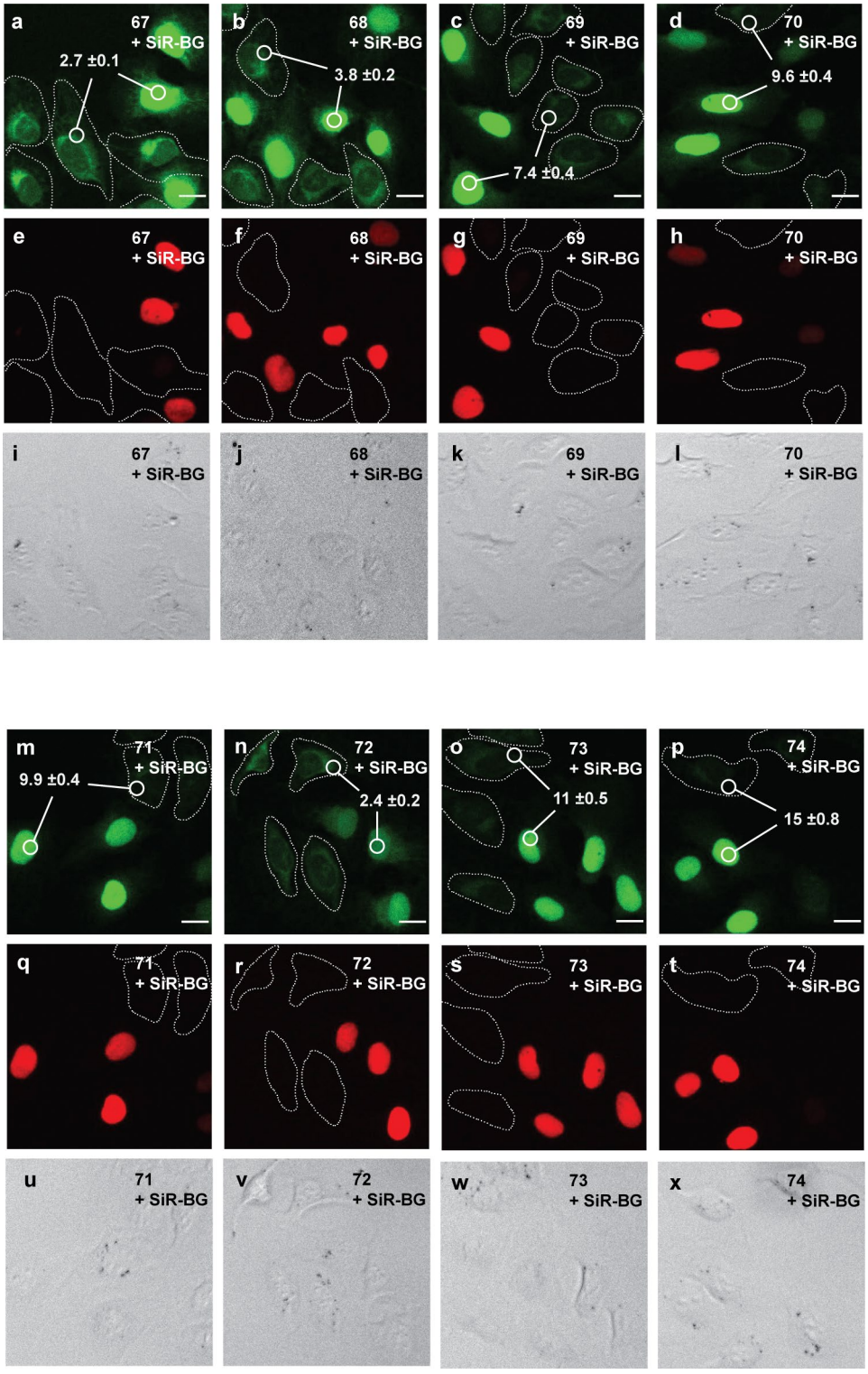
a
67
+ SiR-BG
2.7 ±0.1
b
68
+ SiR-BG
3.8 ±0.2
c
69
+ SiR-BG
7.4 ±0.4
d
70
+ SiR-BG
9.6 ±0.4
e
67
+ SiR-BG
f
68
+ SiR-BG
g
69
+ SiR-BG
h
70
+ SiR-BG
i
67
+ SiR-BG
j
68
+ SiR-BG
k
69
+ SiR-BG
l
70
+ SiR-BG
m
71
+ SiR-BG
9.9 ±0.4
n
72
+ SiR-BG
2.4 ±0.2
o
73
+ SiR-BG
11 ±0.5
p
74
+ SiR-BG
15 ±0.8
q
71
+ SiR-BG
r
72
+ SiR-BG
s
73
+ SiR-BG
t
74
+ SiR-BG
u
71
+ SiR-BG
v
72
+ SiR-BG
w
73
+ SiR-BG
x
74
+ SiR-BG

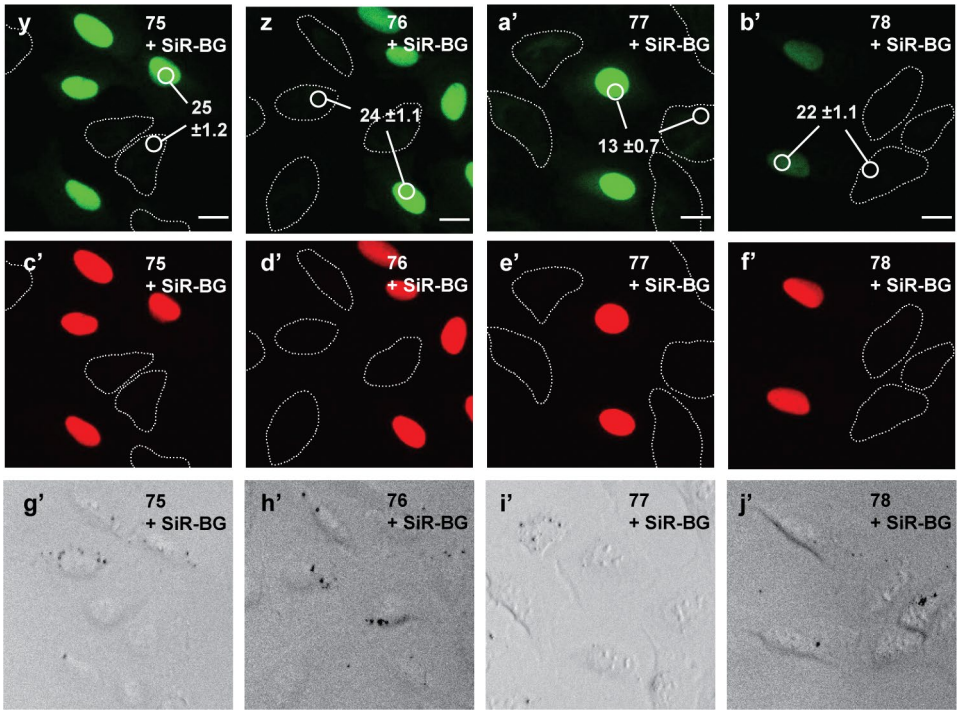

Supplementary Figure 2: Evaluation of fluorogenicity of rhodamine *500R* HaloTag probes (**67 – 78**) in live-cell, no-wash confocal microscopy. Co-cultured U-2 OS FlpIn Halo-SNAP-NLS expressing cells and wild-type U-2 OS cells were labeled with SiR-BG (500 nM) overnight,and then labeled with **67 – 78** (200 nM) for 2.5 h. (a) – (d), (m) – (p), (y) – (b') Live-cell, no-wash confocal images (sum projections of z-stacks) showing rhodamine *500R* fluorescence and (e) – (h), (q) – (t), (c') – (f') SiR fluorescence. Wild-type U-2 OS cells are represented with dotted lines. (i) – (l), (u) – (x), (g') – (j') Bright field images. The numbers correspond to the fluorescence ratios F_{nuc}/F_{cyt}. F_{nuc}: Nuclear rhodamine *500R* signal in U-2 OS FlpIn Halo-SNAP-NLS expressing cells normalized to the nuclear signal of SiR-BG. F_{cyt}: Cytosolic rhodamine *500R* signal in wild-type U-2 OS cells. In total, 180 cells were examined from 3 independent experiments for each probe. Errors represent ± s.e.m. Scale bar, 20 µm.

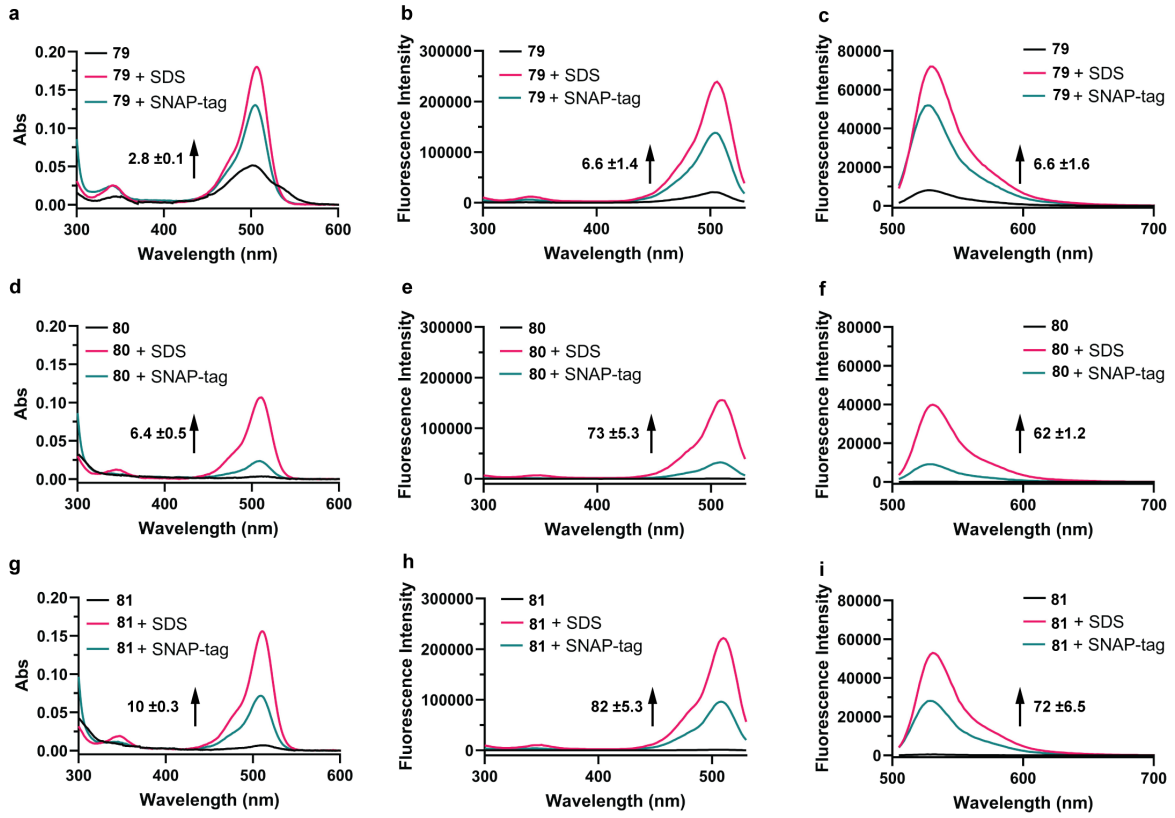

Supplementary Figure 3: Turn-on of rhodamine *500R* SNAP-tag probes (**79** – **81**) upon labeling of SNAP-tag and interaction with SDS. Absorbance (a, d, g), excitation (b, e, h) and emission (c, f, i) spectra of probes **79** – **81** (2.5 µM) measured in HEPES buffer (pH 7.3) in the absence and presence of SNAP-tag (5 µM) or SDS (0.1%) after 2.5 h incubation. The numbers represent the ratio of maximal absorbance and fluorescence intensities ($F_{protein}/F_0$) (emission: λ_{ex}: 490 nm, excitation λ_{em}: 550 nm) in the presence and absence of the SNAP-tag. Representative data for 3 experiments. Errors show ± s.d.

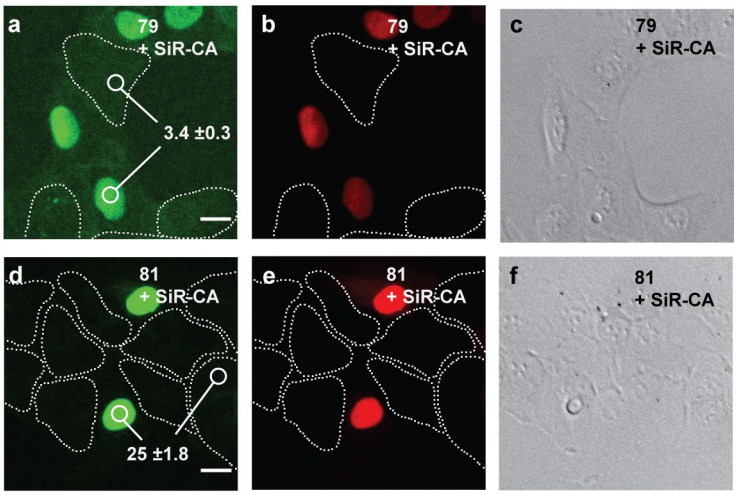

Supplementary Figure 4: Evaluation of fluorogenicity of rhodamine *500R* SNAP-tag probes (**79** and **81**) in live-cell, no-wash confocal microscopy. Co-cultured U-2 OS FlpIn Halo-SNAP-NLS expressing cells and wild-type U-2 OS cells were labeled with SiR-CA (200 nM) overnight and then labeled with **79** and **81** (500 nM) for 5 h. (a), (d) Live-cell, no-wash confocal images (sum projections of z-stacks) showing rhodamine *500R* fluorescence and (b), (e) SiR fluorescence. Wild-type U-2 OS cells are represented with dotted lines. (c), (f) Bright field images. The numbers correspond to the fluorescence ratios F_{nuc}/F_{cyt}. F_{nuc}: Nuclear rhodamine *500R* signal in U-2 OS FlpIn Halo-SNAP-NLS expressing cells normalized to the nuclear signal of SiR-CA. F_{cyt}: Cytosolic rhodamine *500R* signal in

wild-type U-2 OS cells. In total, 180 cells were examined from 2 independent experiments for each probe. Errors represent ± s.e.m. Scale bar, 20 µm.

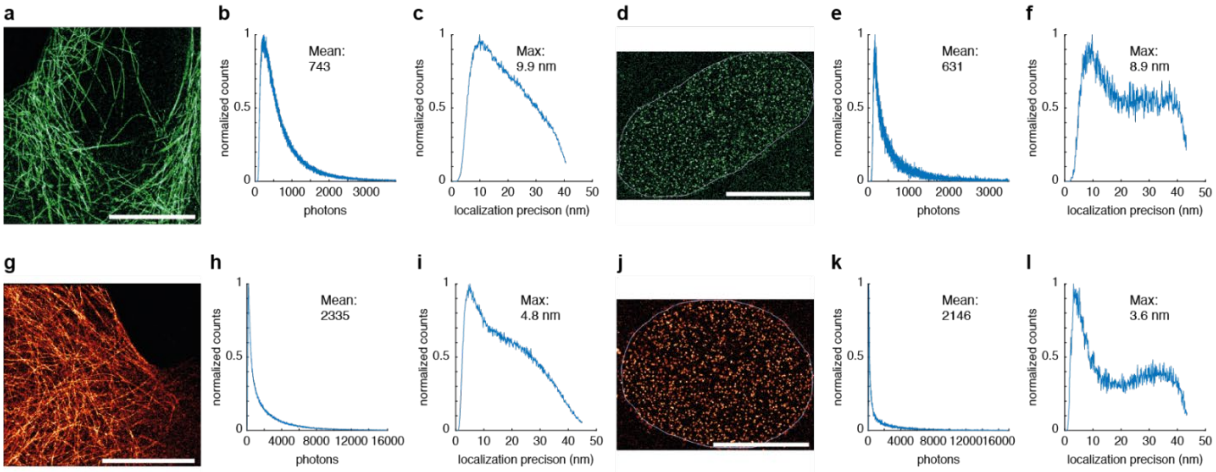

Supplementary Figure 5: Localization precision and photon count from SMLM with **85** and **101** (1 µM, overnight labeling). (a) – (c) Analysis of **85** blinking properties in U-2 OS Cep41-Halo cells. (a) SMLM image. (b) Photon count (mean: 743). (c) Localization precision (max: 9.9 nm). (d) – (f) Analysis of **85** blinking properties in U-2 OS Nup96-Halo cells. (d) SMLM image. (e) Photon count (mean: 631). (f) Localization precision (max: 8.9 nm). (g) – (i) Analysis of **101** blinking properties in U-2 OS Cep41-Halo cells. (g) SMLM image. (h) Photon count (mean: 2335). (i) Localization precision (max: 4.8 nm). (j) – (l) Analysis of **101** blinking properties in U-2 OS Cep41-Halo cells. (j) SMLM image. (k) Photon count (mean: 2146). (l) Localization precision (max: 3.6 nm). Scale bars, 10 µm. No filters were applied to the localizations for these reconstructions and analyses. SMLM data were recorded and analyzed by Aline Tschanz and Dr. Philipp Hoess (EMBL Heidelberg).

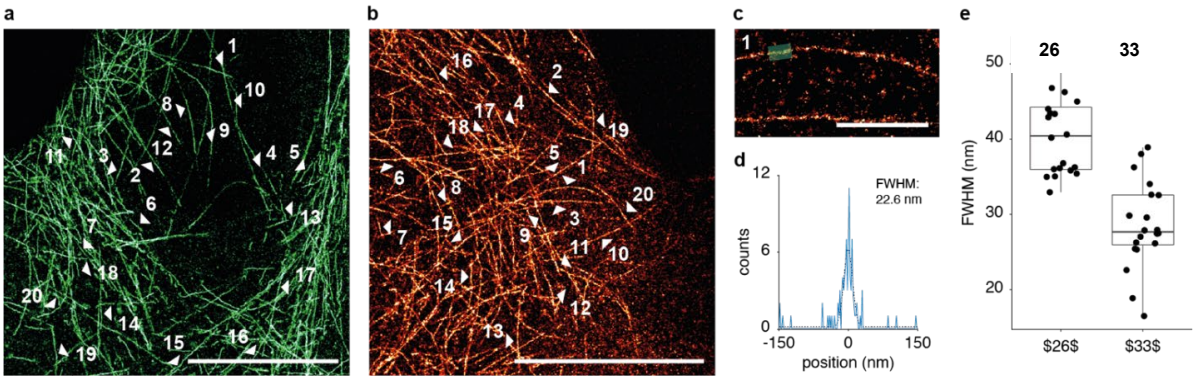

Supplementary Figure 6: Microtubule diameter estimation from SMLM with **85** and **101**. (a) SMLM image of U-2 OS Cep41-Halo cells, labeled with **85**. Arrows indicate the location of diameter estimation. Scale bar, 10 µm. (b) SMLM image of U-2 OS Cep41-Halo cells, labeled with **101**. Arrows indicate the location of diameter estimation. Scale bar, 10 µm. (c) Enlarged region of line profile 1 in (b), highlighted in green. Scale bar, 1 µm. (d) Example histogram (blue) of the line profile marked in (c). A Gaussian fit (dotted line) was used to estimate the fwhm of 22.6 nm. (e) Box-plots depicting the distribution of fwhm for both **85** (mean: 40.7 nm, s.d.: 5.7 nm) and **101** (mean: 28.5 nm, s.d.: 5.8 nm). box: 25th – 75th percentile, whiskers: 5th – 95th percentile, black line: median, individual data points in black, *N* = 20 tubules per data set. SMLM data were recorded and analyzed by Aline Tschanz and Dr. Philipp Hoess (EMBL Heidelberg).

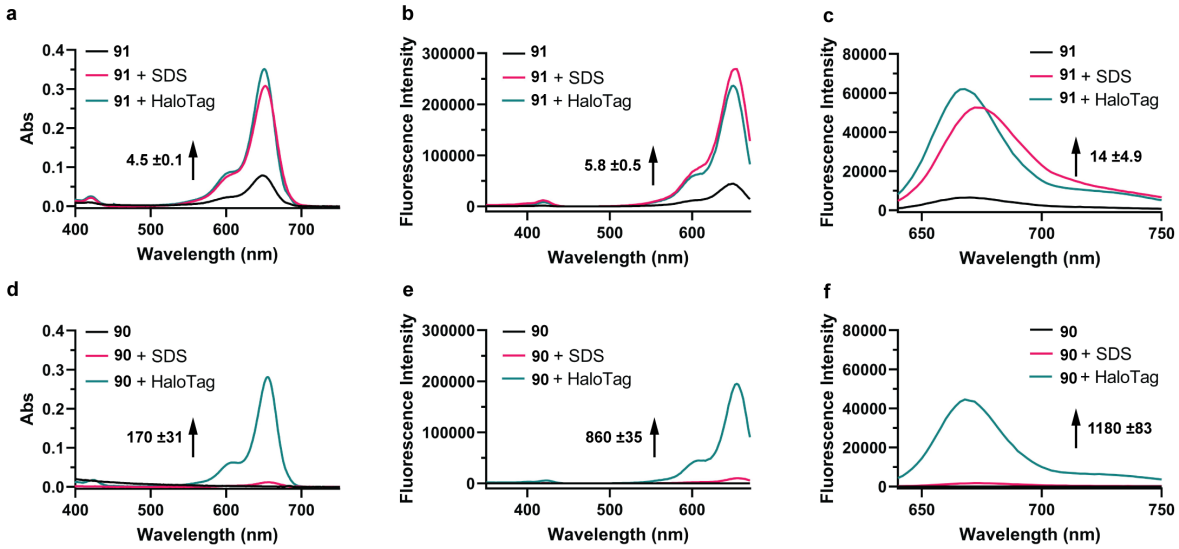

Supplementary Figure 7: Turn-on of SiR HaloTag probes (**90** and **91**) upon labeling of HaloTag and interaction with SDS. Absorption (a and d), excitation (b and e) and emission (c and f) spectra of probes **90** and **91** (2.5 µM) measured in HEPES buffer (pH 7.3) in the absence and presence of HaloTag (5 µM) or SDS (0.1%) after 2.5 h incubation. The numbers represent the ratio of maximal absorbance and fluorescence intensities ($F_{protein}/F_0$) (emission: λ_{ex}: 610 nm, excitation λ_{em}: 690 nm) in the presence and absence of the HaloTag. Representative data for 3 experiments. Errors show ± s.d.

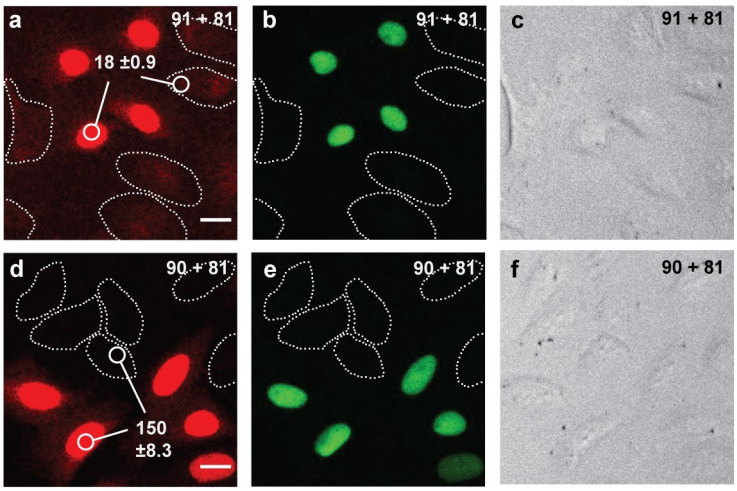

Supplementary Figure 8: Evaluation of fluorogenicity of SiR HaloTag probes (**90** and **91**) in live-cell, no-wash confocal microscopy. Co-cultured U-2 OS FlpIn Halo-SNAP-NLS expressing cells and wild-type U-2 OS cells were labeled with **81** (500 nM) overnight and then labeled with **90** and **91** (500 nM) for 2.5 h. (a), (d) Live-cell, no-wash confocal images (sum projections of z-stacks) showing SiR fluorescence and (b), (e) fluorescence of **81**. Wild-type U-2 OS cells are represented with dotted lines. (c), (f) Bright field images. The numbers correspond to the fluorescence ratios F_{nuc}/F_{cyt}. F_{nuc}: Nuclear SiR signal in U-2 OS FlpIn Halo-SNAP-NLS expressing cells normalized to the nuclear signal of **81**. F_{cyt}: Cytosolic SiR signal in wild-type U-2 OS cells. In total, 180 cells were examined from 2 independent experiments for each probe. Errors represent ± s.e.m. Scale bar, 20 µm.

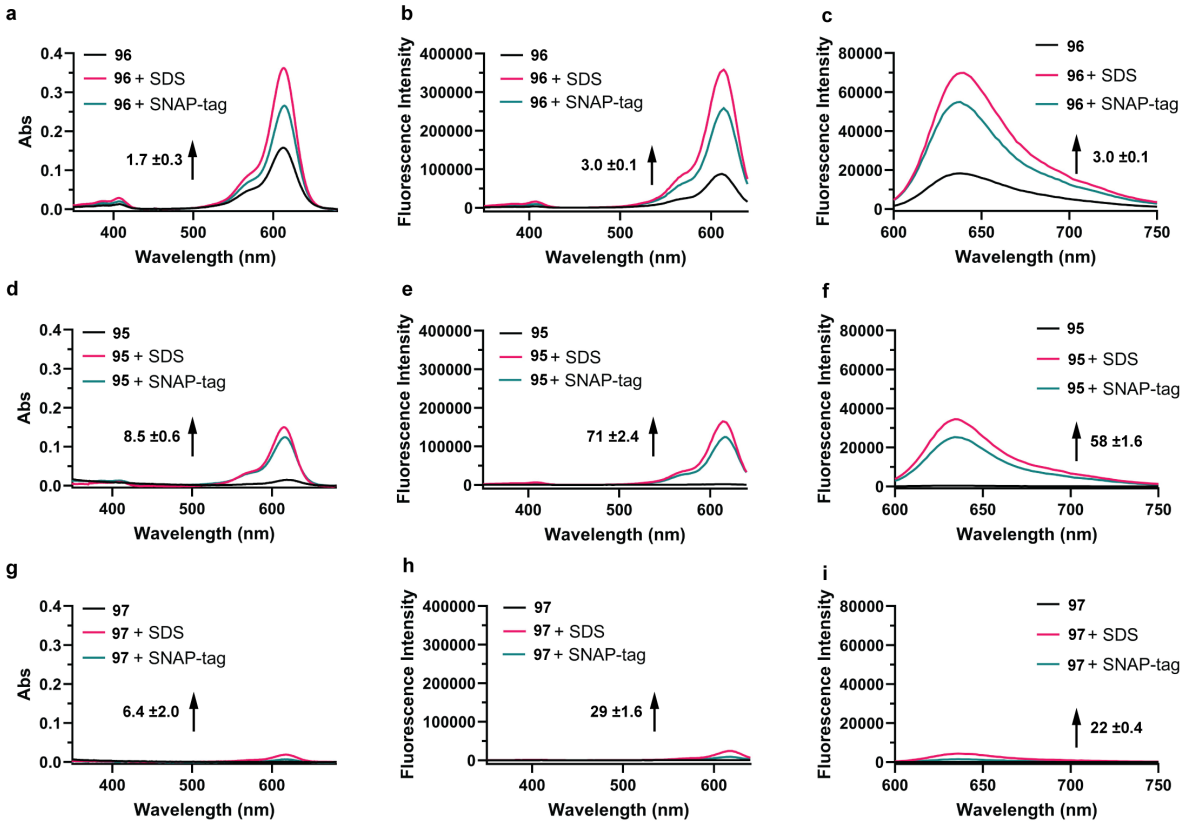

Supplementary Figure 9: Turn-on of carborhodamine SNAP-tag probes (**95 – 97**) upon labeling of SNAP-tag and interaction with SDS. Absorption (a, d, g), excitation (b, e, h) and emission (c, f, i) spectra of probes **95 – 97** (2.5 µM) measured in HEPES buffer (pH 7.3) in the absence and presence of SNAP-tag (5 µM) or SDS (0.1%) after 2.5 h incubation. The numbers represent the ratio of maximal absorbance and fluorescence intensities ($F_{protein}/F_0$) (emission: λ_{ex}: 580 nm, excitation λ_{em}: 660 nm) in the presence and absence of the SNAP-tag. Representative data for 3 experiments. Errors show ± s.d.

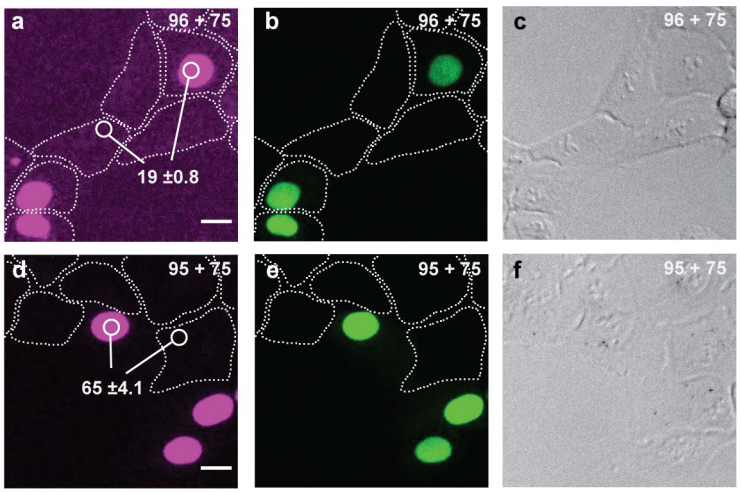

Supplementary Figure 10: Evaluation of fluorogenicity of carborhodamine SNAP-tag probes (**95** and **96**) in live-cell, no-wash confocal microscopy. Co-cultured U-2 OS FlpIn Halo-SNAP-NLS expressing cells and wild-type U-2 OS cells were labeled with **75** (200 nM) overnight and then labeled with **95** and **96** (500 nM) for 4 h. (a), (d) Live-cell, no-wash confocal images (sum projections of z-stacks) showing carborhodamine fluorescence and (b), (e) fluorescence of **75**. Wild-type U-2 OS cells are represented with dotted lines. (c), (f) Bright field images. The numbers represent the fluorescence ratios F_{nuc}/F_{cyt}. F_{nuc}: Nuclear carborhodamine signal in U-2 OS FlpIn Halo-SNAP-NLS expressing cells normalized to the nuclear signal of **75**. F_{cyt}: Cytosolic carborhodamine signal in wild-

type U-2 OS cells. In total, 180 cells were examined from 2 independent experiments for each probe. Errors represent ± s.e.m. Scale bar, 20 µm.

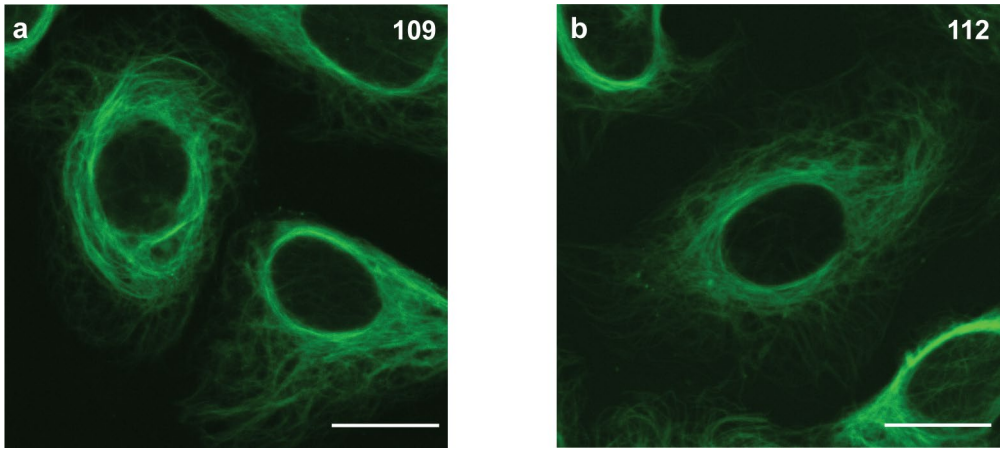

Supplementary Figure 11: Live-cell, no-wash confocal microscopy with rhodamine *500R* tubulin probes **109** and **112**.U-2 OS cells were incubated with **109** (a) and **112** (b) (500 nM) and verapamil (5 µM) for 3 h. Scale bars, 20 µm.

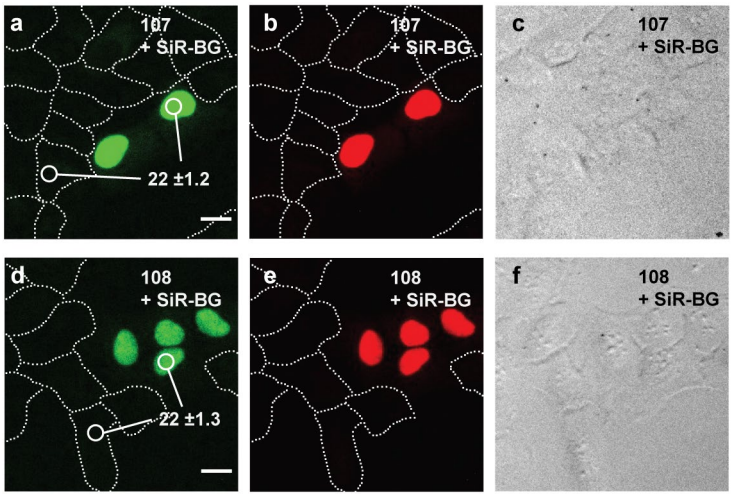

Supplementary Figure 12: Evaluation of fluorogenicity of rhodamine *500R* eDHFR probes (**107** and **108**) in live-cell, no-wash confocal microscopy. Co-cultured U-2 OS FlpIn SNAP-eDHFR-NLS expressing cells and wild-type U-2 OS cells were labeled with SiR-BG (500 nM) overnight and then labeled with **107** and **108** (200 nM) for 2.5 h. (a), (d) Live-cell, no-wash confocal images (sum projections of z-stacks) showing rhodamine *500R* fluorescence and (b), (e) fluorescence of SiR-BG. Wild-type U-2 OS cells are represented with dotted lines. (c), (f) Bright field images. The numbers represent the fluorescence ratios F_{nuc}/F_{cyt}. F_{nuc}: Nuclear rhodamine *500R* signal in U-2 OS FlpIn SNAP-eDHFR-NLS expressing cells normalized to the nuclear signal of SiR-BG. F_{cyt}: Cytosolic rhodamine *500R* signal in wild-type U-2 OS cells. In total, 180 cells were examined from 2 independent experiments for each probe. Errors represent ± s.e.m. Scale bar, 20 µm.

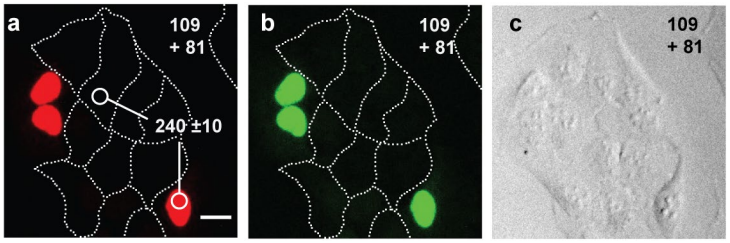

Supplementary Figure 13: Evaluation of fluorogenicity of SiR eDHFR probe (**109**) in live-cell, no-wash confocal microscopy. Co-cultured U-2 OS FlpIn SNAP-eDHFR-NLS expressing cells and wild-type U-2 OS cells were labeled with **81** (500 nM) overnight and then labeled with **109** (200 nM) for 2.5 h. (a) Live-cell, no-wash confocal image (sum projections of z-stacks) showing rhodamine *500R* fluorescence and (b) fluorescence of **81**. Wild-type U-2 OS cells are represented with dotted lines. (c) Bright field image. The numbers represent the fluorescence ratios F_{nuc}/F_{cyt}. F_{nuc}: Nuclear SiR signal in U-2 OS FlpIn SNAP-eDHFR-NLS expressing cells normalized to the nuclear signal of **81**. F_{cyt}: Cytosolic SiR signal in wild-type U-2 OS cells. In total, 180 cells were examined from 2 independent experiments. Errors represent ± s.e.m. Scale bar, 20 µm.

8.2. Supplementary Tables

Supplementary Table 1: Statistics from single-molecule assay.

Probe	On-time (mean over FOV) (ms)	Off-time (mean over FOV) (s)	Duty cycle (FOV)	Duty cycle (per cluster, median over FOV)	Photons	Localization precision (nm)
85	3.6 ±0.2	131 ±14	(2.8 ±0.4) · 10^{-5}	(3.2 ±0.5) · 10^{-5}	596 ±21	10.6 ±0.5
101	13.1 ±0.3	11 ±2	(1.3 ±0.2) · 10^{-3}	(1.9 ±0.3) · 10^{-3}	1864 ±33	4.4 ±0.3

The values are averages of 4 fields of view (FOVs), the errors report the standard deviation. The localization precision is reported as the position of the maximum of the distribution of the localization precision values. SMLM data were recorded and analyzed by Dr. Philipp Hoess (EMBL Heidelberg).

Supplementary Table 2: Photophysical properties of highly closed rhodamine *500R* (**62** and **64**) and TMR (**100**) derivatives.

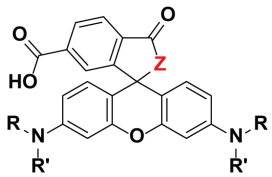

R, R' = CH_3 (100)
R = CH_2CF_3, R' = H (62, 64)

Z	Probe	λ_{abs} (nm)	λ_{em} (nm)	ε ($M^{-1}cm^{-1}$)	Φ
$NCON(CH_3)_2$	**62**	514_a	539_a	75000_a	0.94_a
NCH_2CF_3	**64**	512_a	535_a	26000_a	0.94_a
NCH_2CF_3	**100**	559_b	582_b	80000_b	0.39_b

$_a$ PBS buffer (pH 2.0), $_b$ PBS buffer (pH 3.0).

8.3. NMR Spectra and HPLC Traces

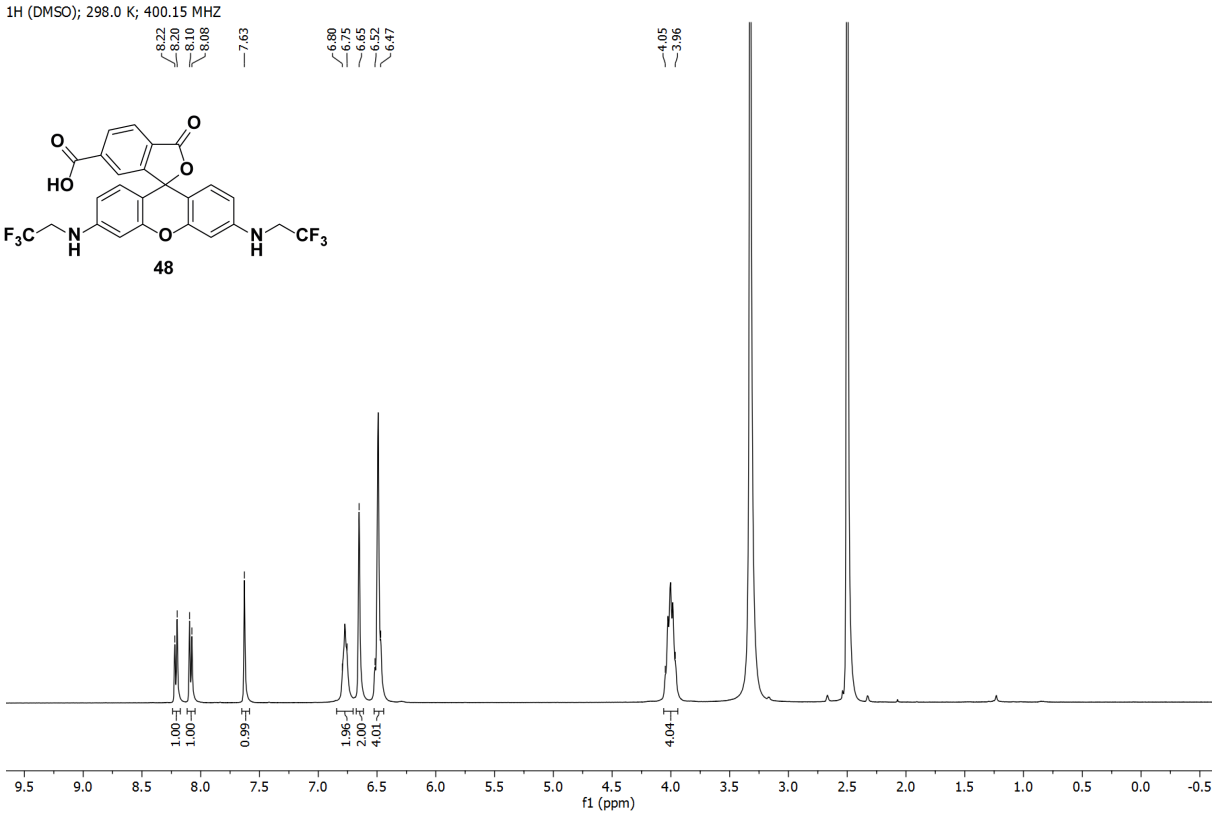

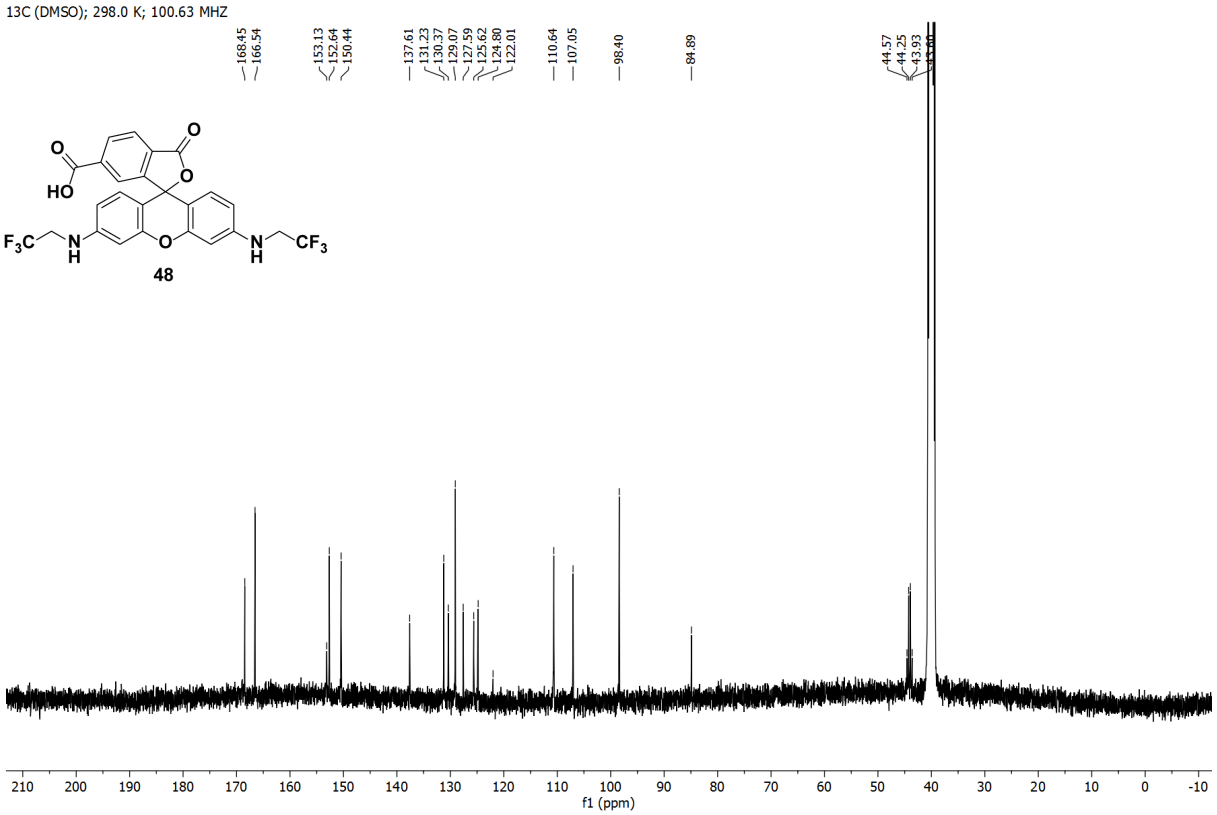

1H (DMSO); 298.0 K; 400.15 MHZ

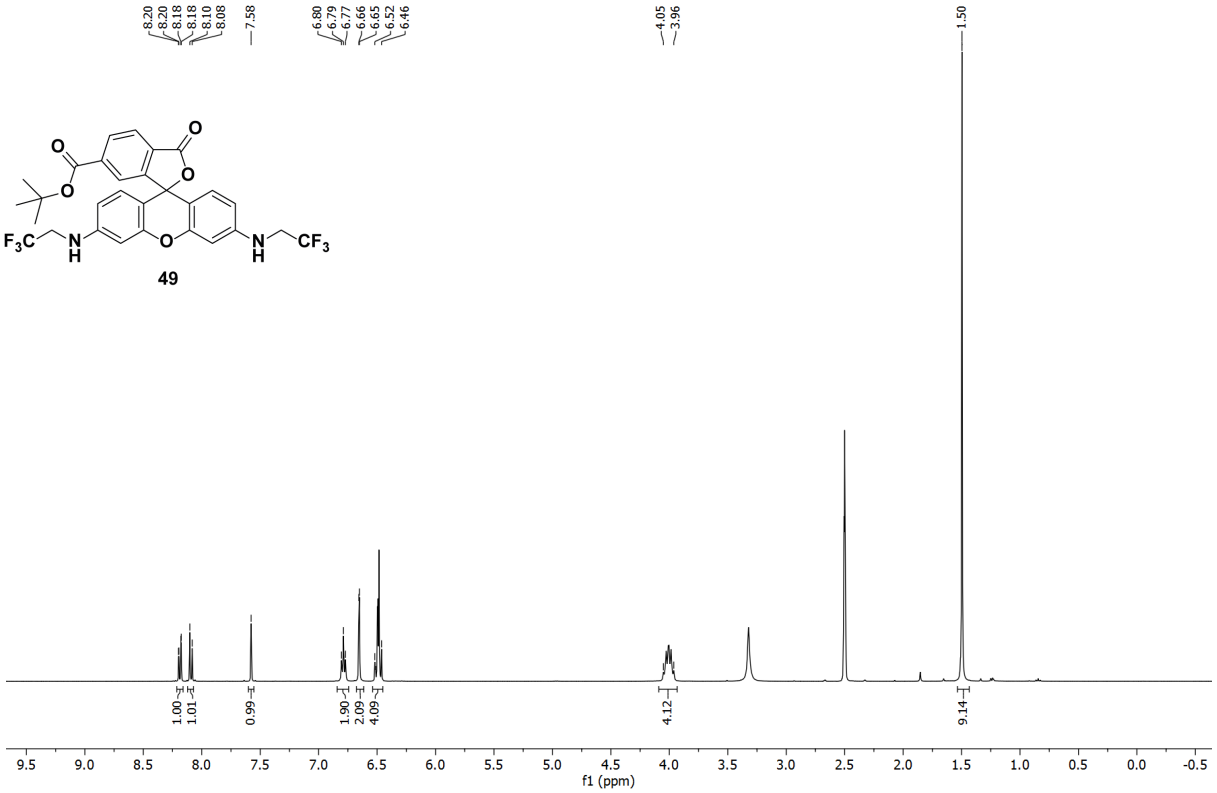

49

13C (DMSO); 298.0 K; 100.63 MHZ

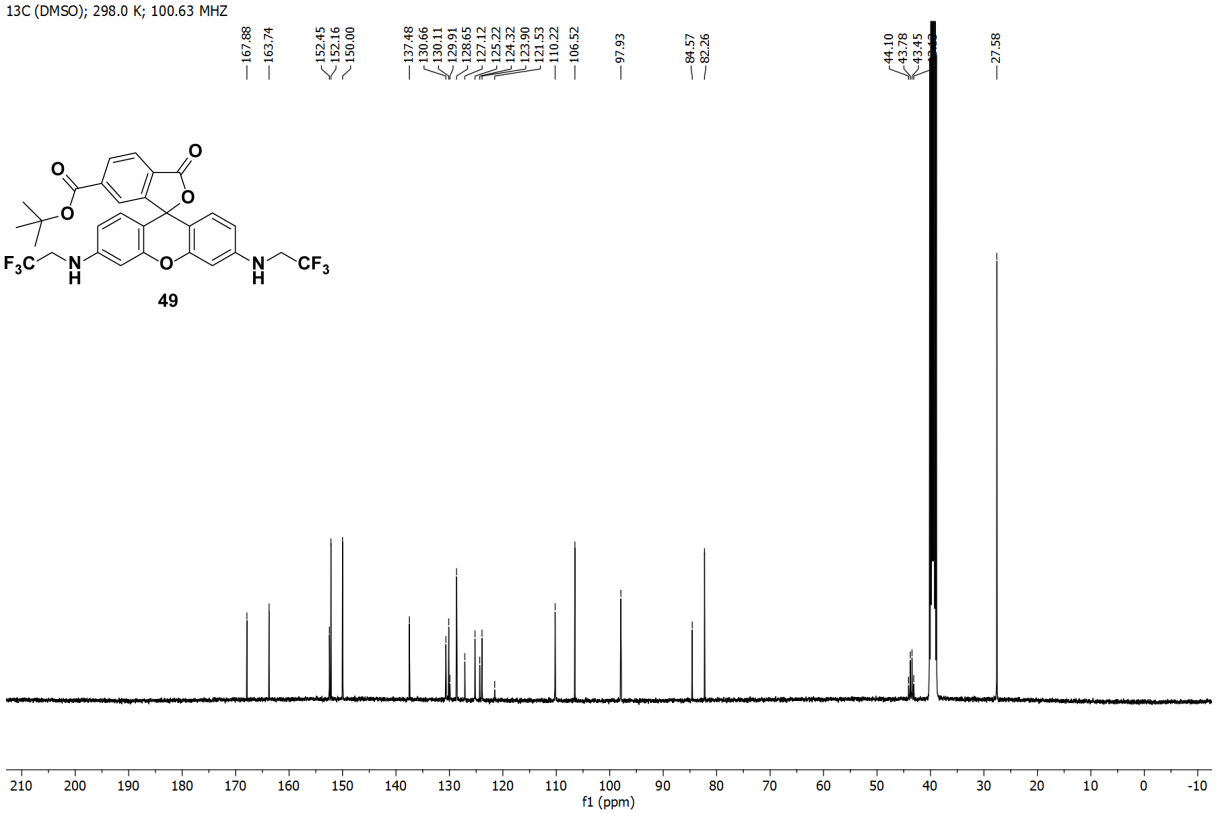

49

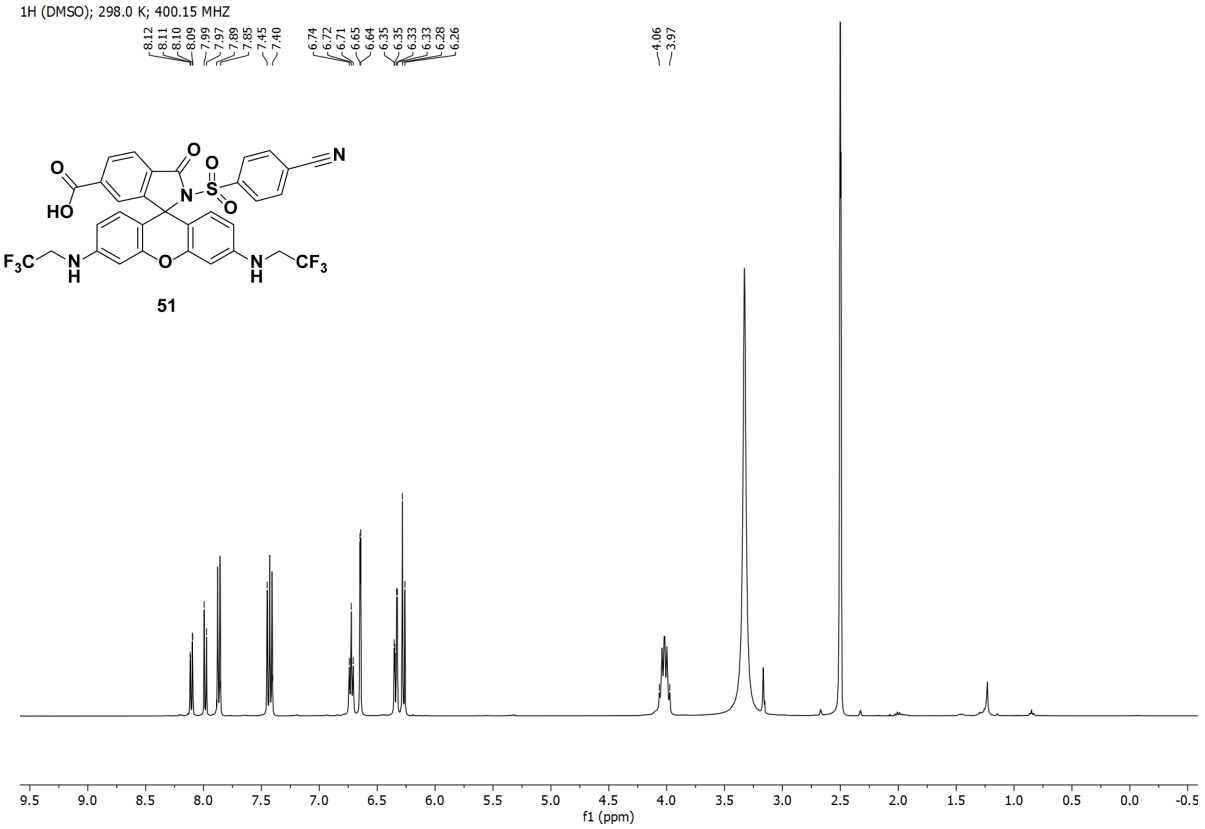
1H (DMSO); 298.0 K; 400.15 MHZ
8.12
8.11
8.10
8.09
7.99
7.97
7.89
7.85
7.45
7.40
6.74
6.72
6.71
6.65
6.64
6.35
6.35
6.33
6.33
6.28
6.26
4.06
3.97
51
f1 (ppm)

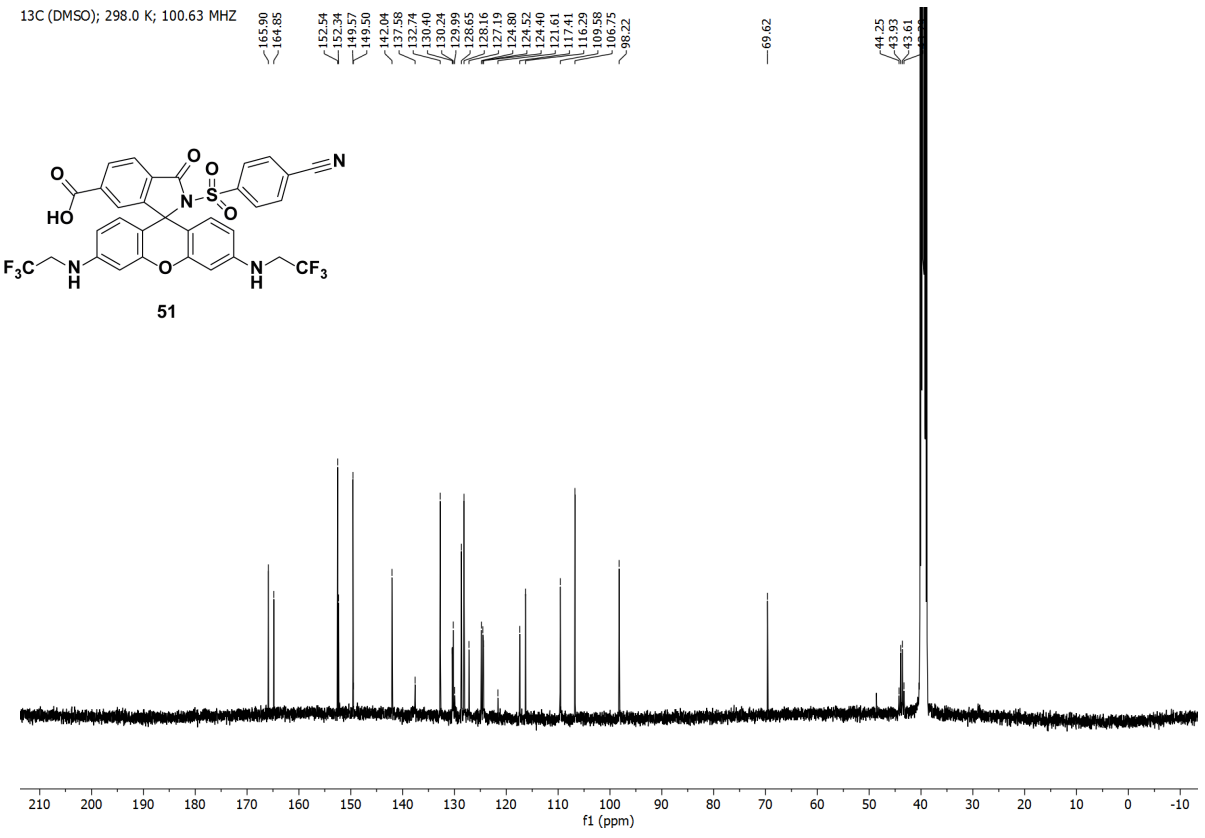
13C (DMSO); 298.0 K; 100.63 MHZ
165.90
164.85
152.54
152.34
149.57
149.50
142.04
137.58
132.74
130.40
130.24
129.99
128.65
128.16
127.19
124.80
124.52
124.40
121.61
117.41
116.29
109.58
106.75
98.22
69.62
44.25
43.93
43.61
51
f1 (ppm)

1H (MeOD); 298.0 K; 400.15 MHZ

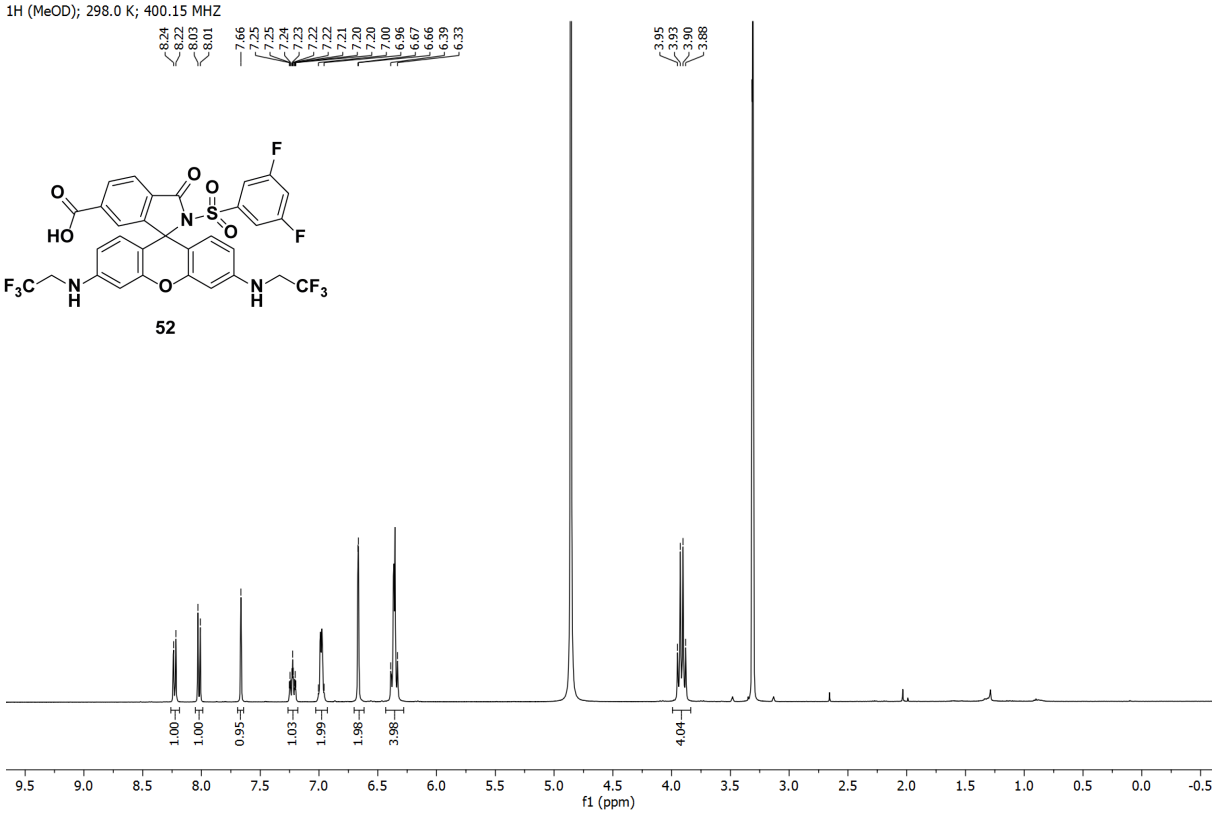

52

13C (MeOD); 298.0 K; 100.63 MHZ

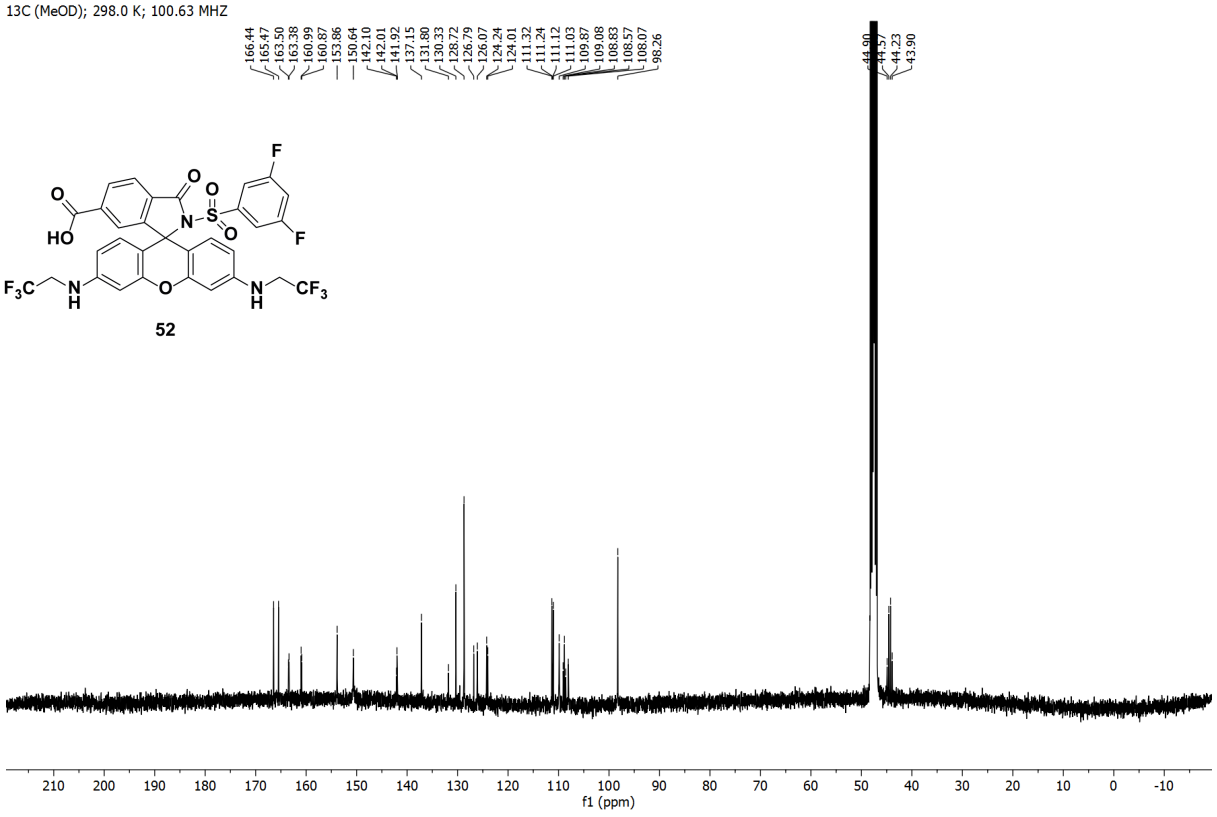

52

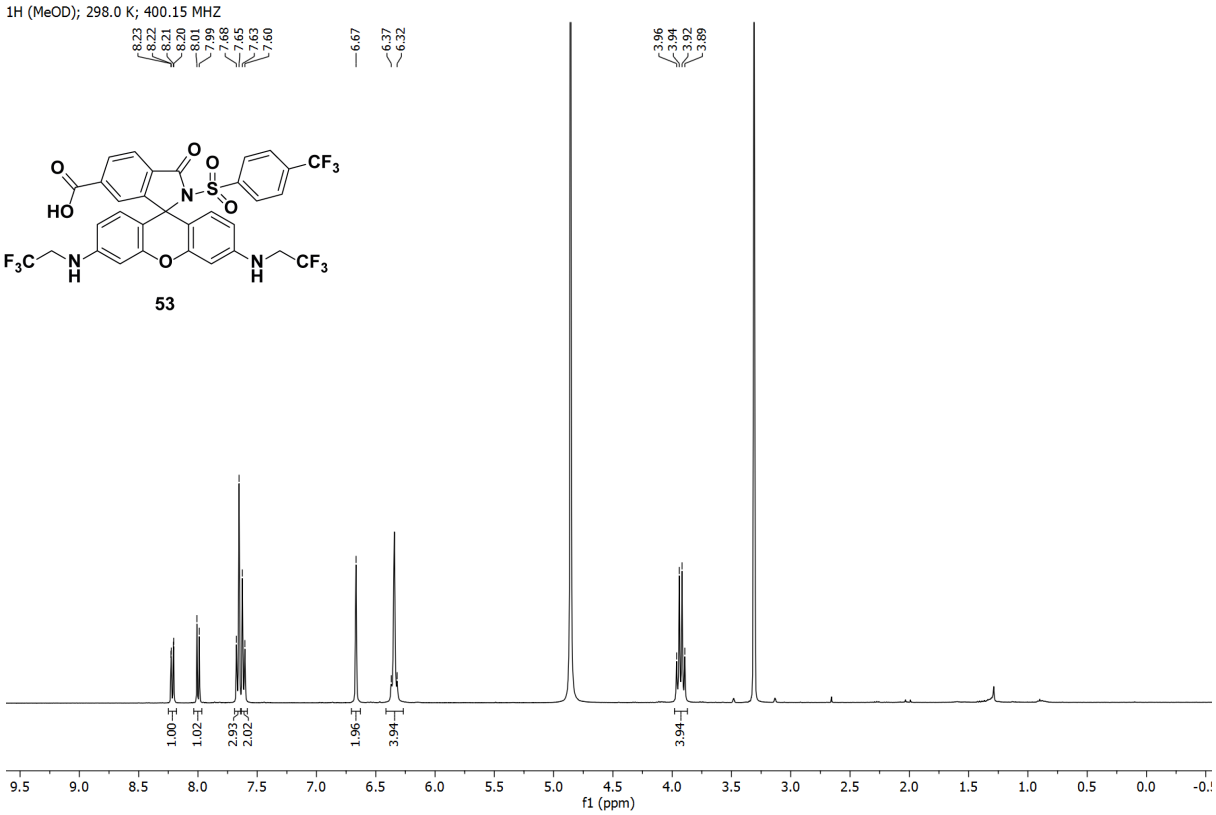
1H (MeOD); 298.0 K; 400.15 MHZ
8.23
8.22
8.21
8.20
8.01
7.99
7.68
7.65
7.63
7.60
6.67
6.37
6.32
3.96
3.94
3.92
3.89
1.00
1.02
2.93
2.02
1.96
3.94
3.94
f1 (ppm)

53

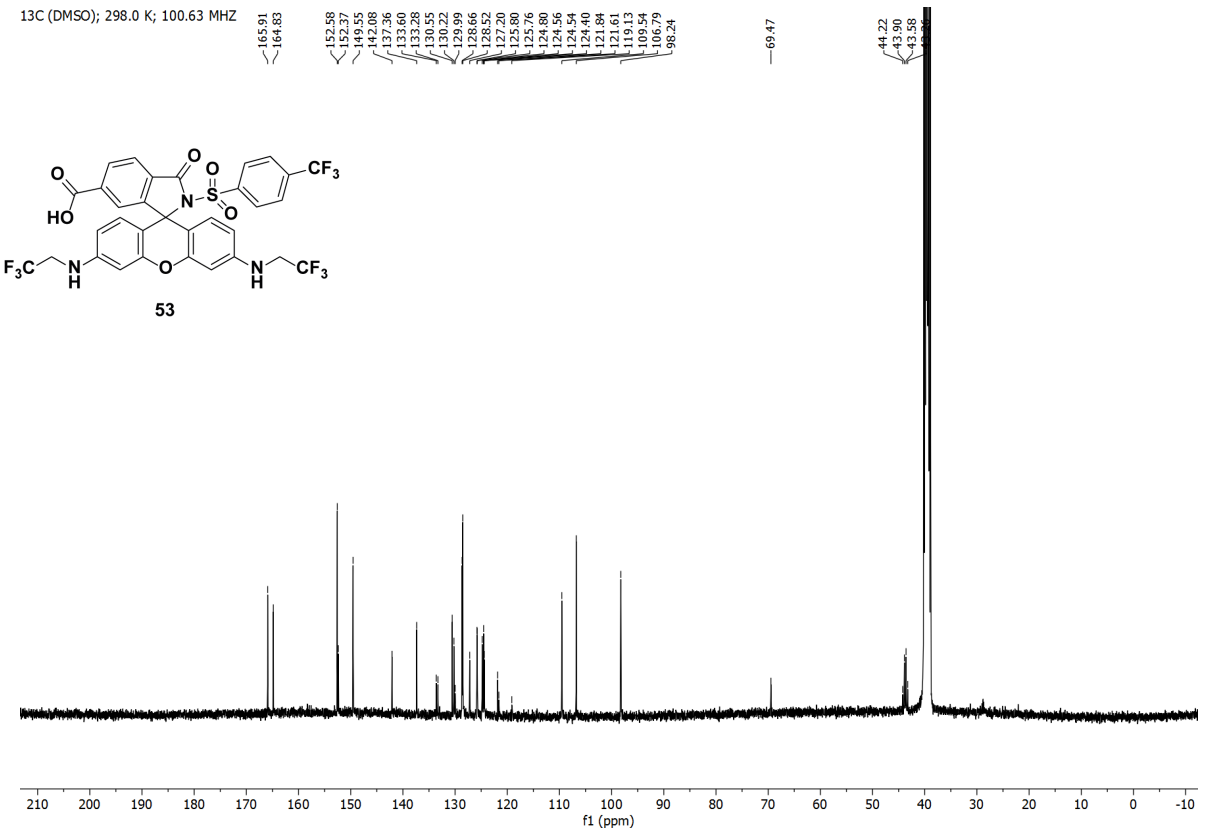
13C (DMSO); 298.0 K; 100.63 MHZ
165.91
164.83
152.58
152.37
149.55
142.08
137.36
133.60
133.28
130.55
130.22
129.99
128.66
128.52
127.20
125.80
123.76
124.80
124.56
124.54
124.40
121.84
121.61
119.13
109.54
106.79
98.24
69.47
44.22
43.90
43.58
f1 (ppm)

53

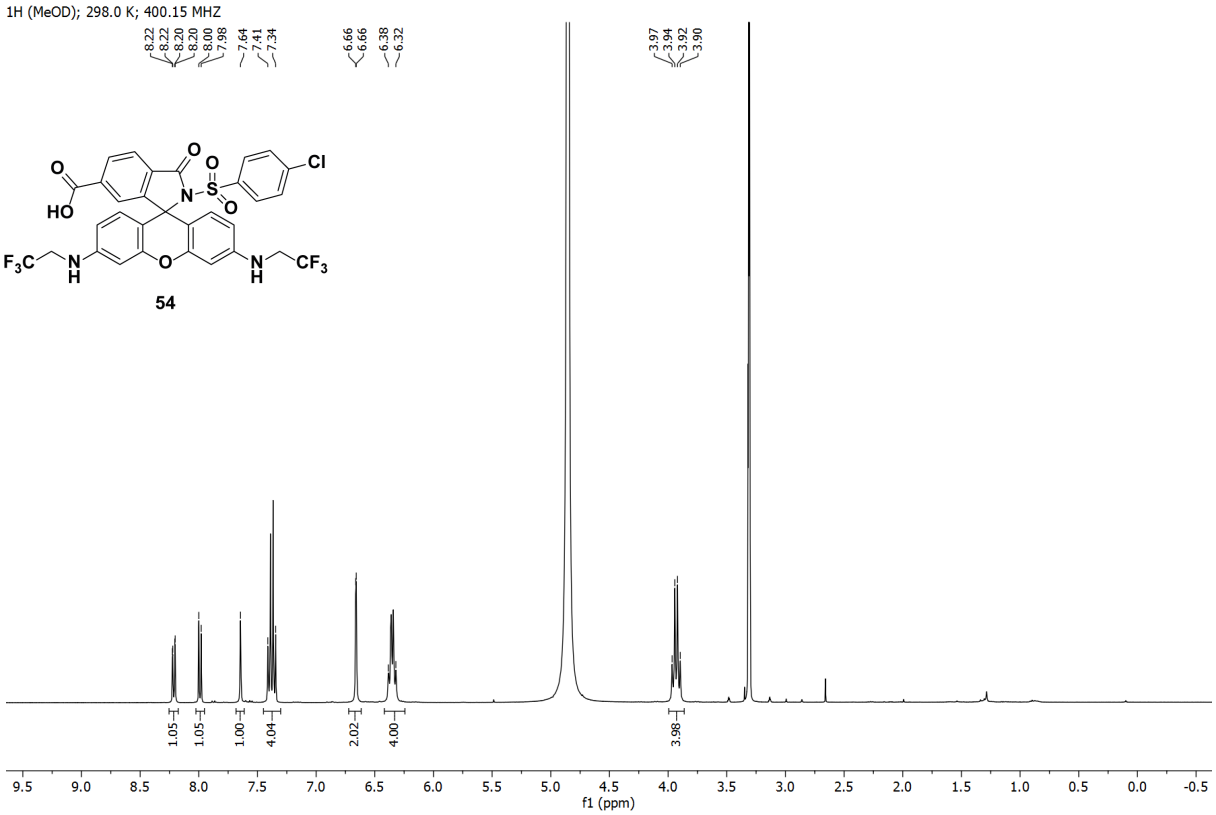
1H (MeOD); 298.0 K; 400.15 MHZ
8.22
8.22
8.20
8.20
8.00
7.98
7.64
7.41
7.34
6.66
6.66
6.38
6.32
3.97
3.94
3.92
3.90
1.05
1.05
1.00
4.04
2.02
4.00
3.98
f1 (ppm)

O
O
O
Cl
HO
N
S
O
F3C
N
H
O
N
H
CF3

54

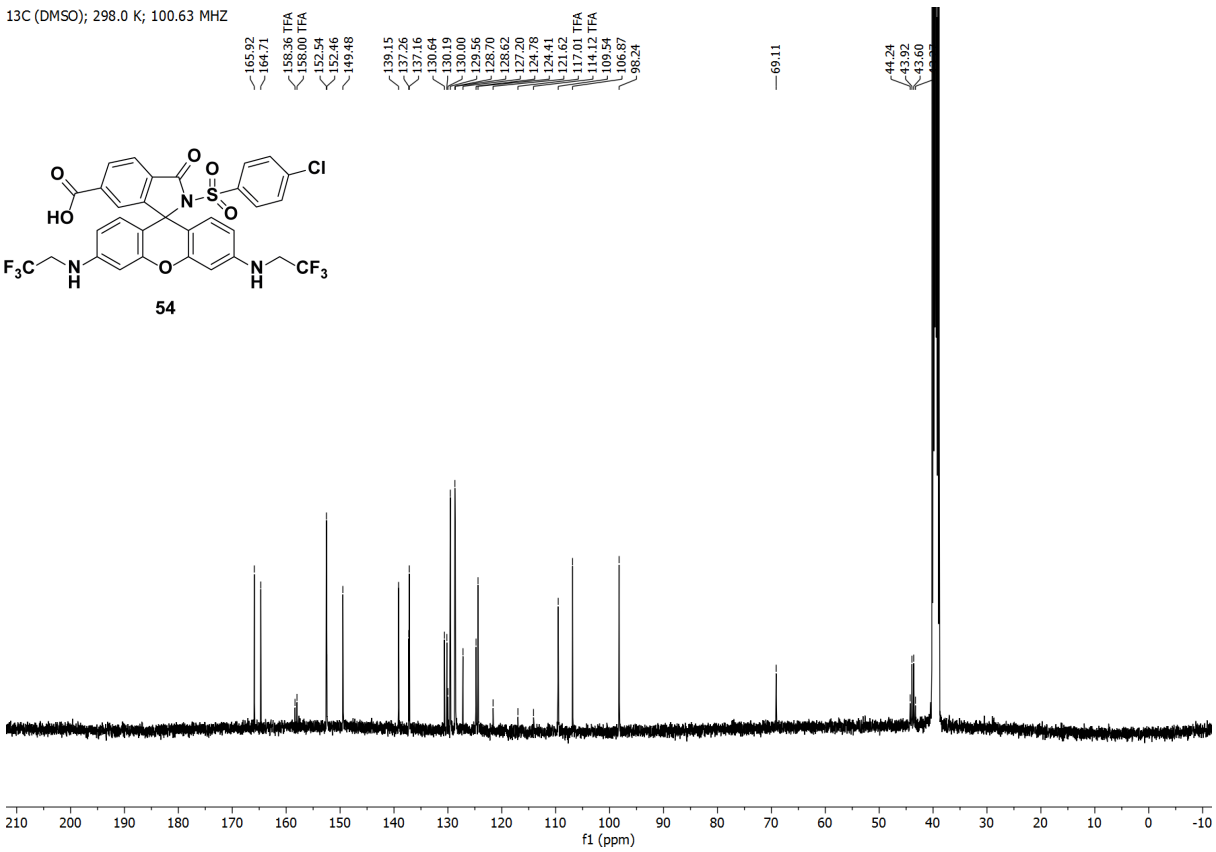
13C (DMSO); 298.0 K; 100.63 MHZ
165.92
164.71
158.36 TFA
158.00 TFA
152.54
152.46
149.48
139.15
137.26
137.16
130.64
130.19
130.00
129.56
128.70
128.62
127.20
124.78
124.41
121.62
117.01 TFA
114.12 TFA
109.54
106.87
98.24
69.11
44.24
43.92
43.60
f1 (ppm)

O
O
O
Cl
HO
N
S
O
F3C
N
H
O
N
H
CF3

54

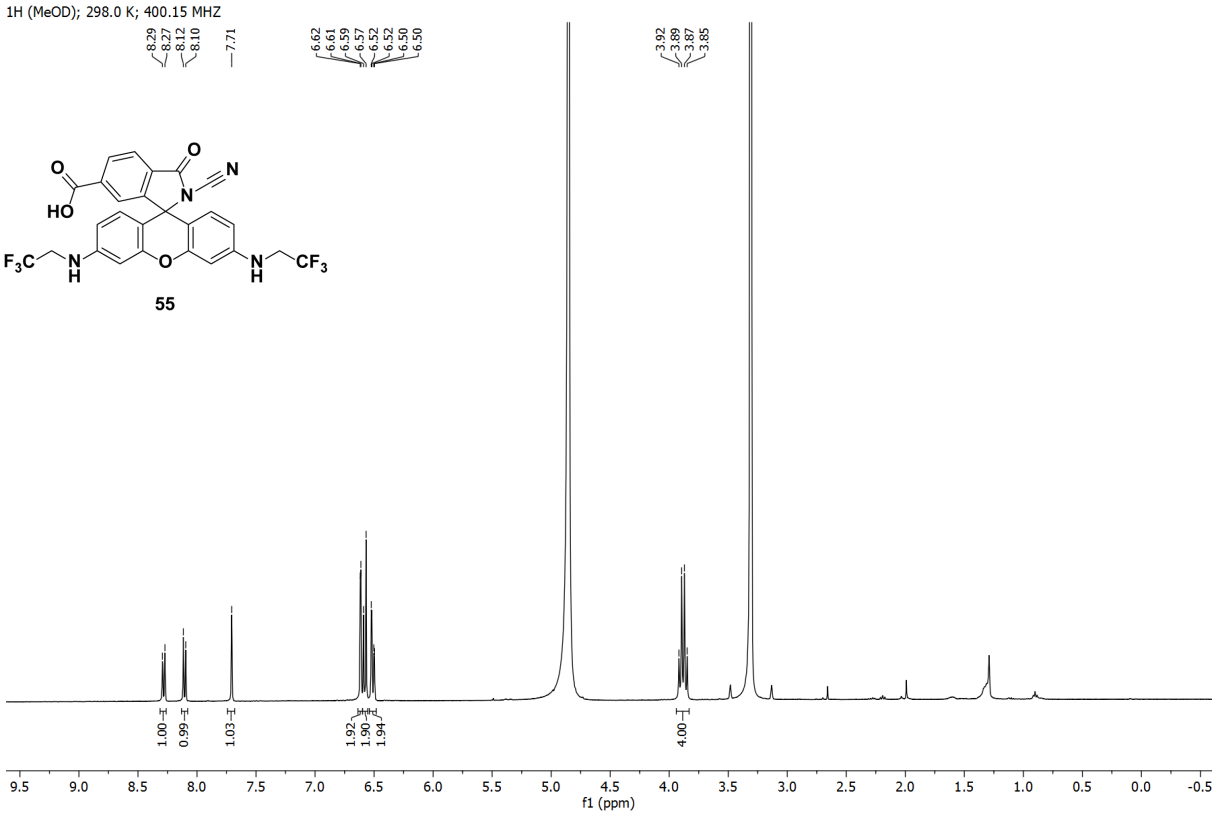
1H (MeOD); 298.0 K; 400.15 MHZ
8.29
8.27
8.12
8.10
7.71
6.62
6.61
6.59
6.57
6.52
6.52
6.50
6.50
3.92
3.89
3.87
3.85
55
1.00
0.99
1.03
1.92
1.90
1.94
4.00
f1 (ppm)

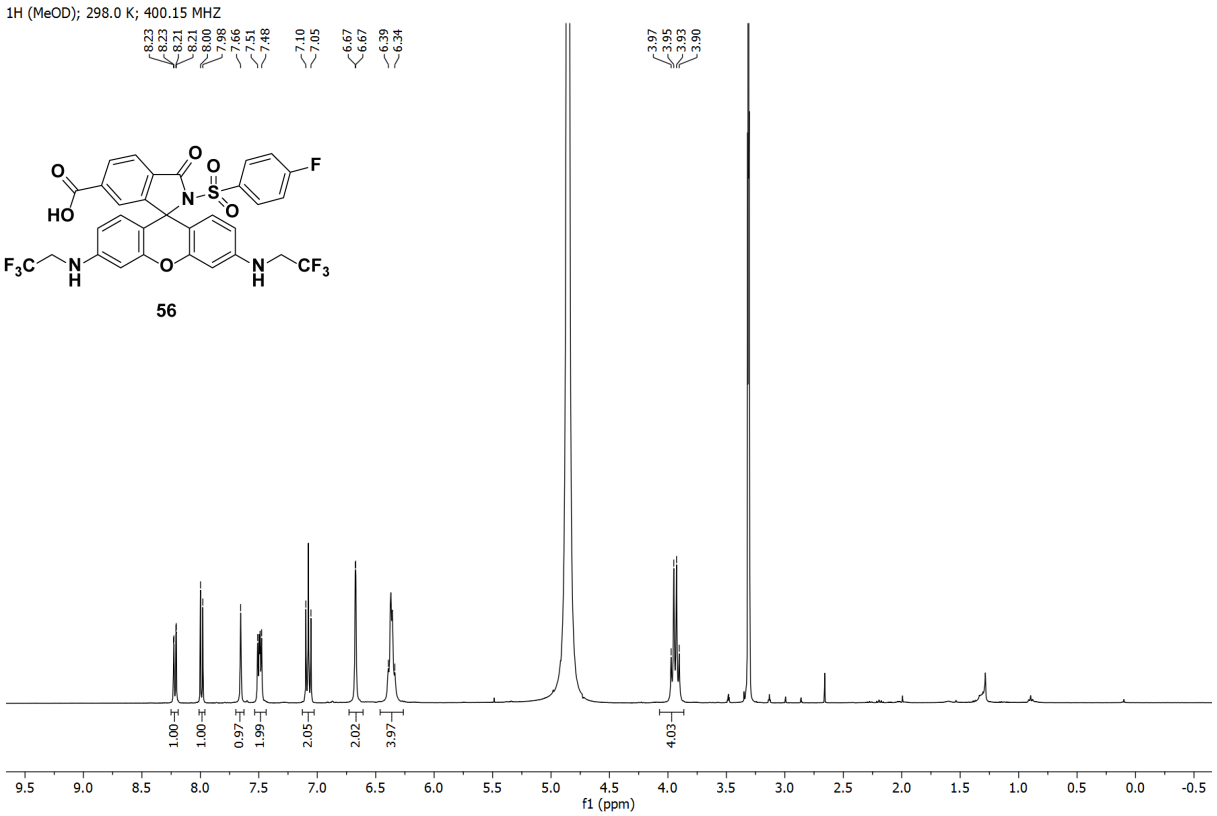
1H (MeOD); 298.0 K; 400.15 MHZ
8.23
8.23
8.21
8.21
8.00
7.98
7.66
7.51
7.48
7.10
7.05
6.67
6.67
6.39
6.34
3.97
3.95
3.93
3.90
56
1.00
1.00
0.97
1.99
2.05
2.02
3.97
4.03
f1 (ppm)

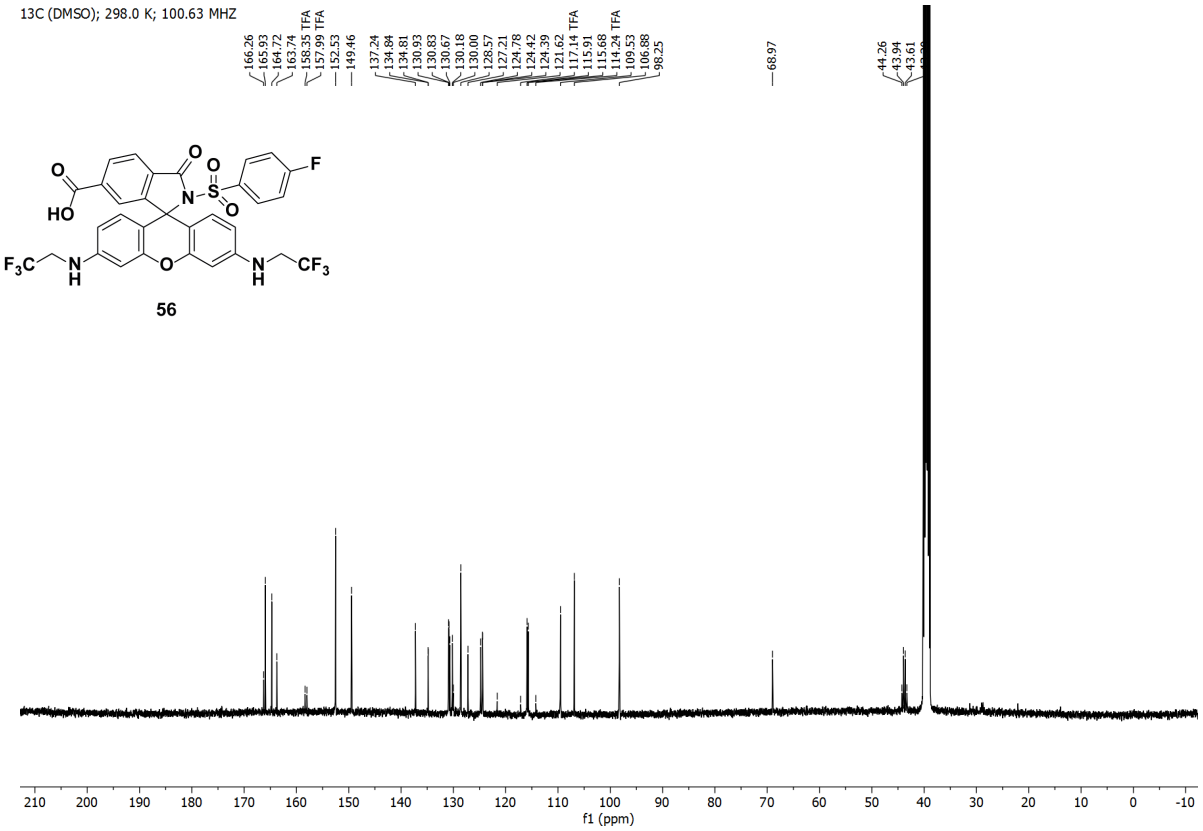
13C (DMSO); 298.0 K; 100.63 MHZ
166.26
165.93
164.72
163.74
158.35 TFA
157.99 TFA
152.53
149.46
137.24
134.84
134.81
130.93
130.83
130.67
130.18
130.00
128.57
127.21
124.78
124.42
124.39
121.62
117.14 TFA
115.91
115.68
114.24 TFA
109.53
106.88
98.25
68.97
44.26
43.94
43.61
f1 (ppm)

56

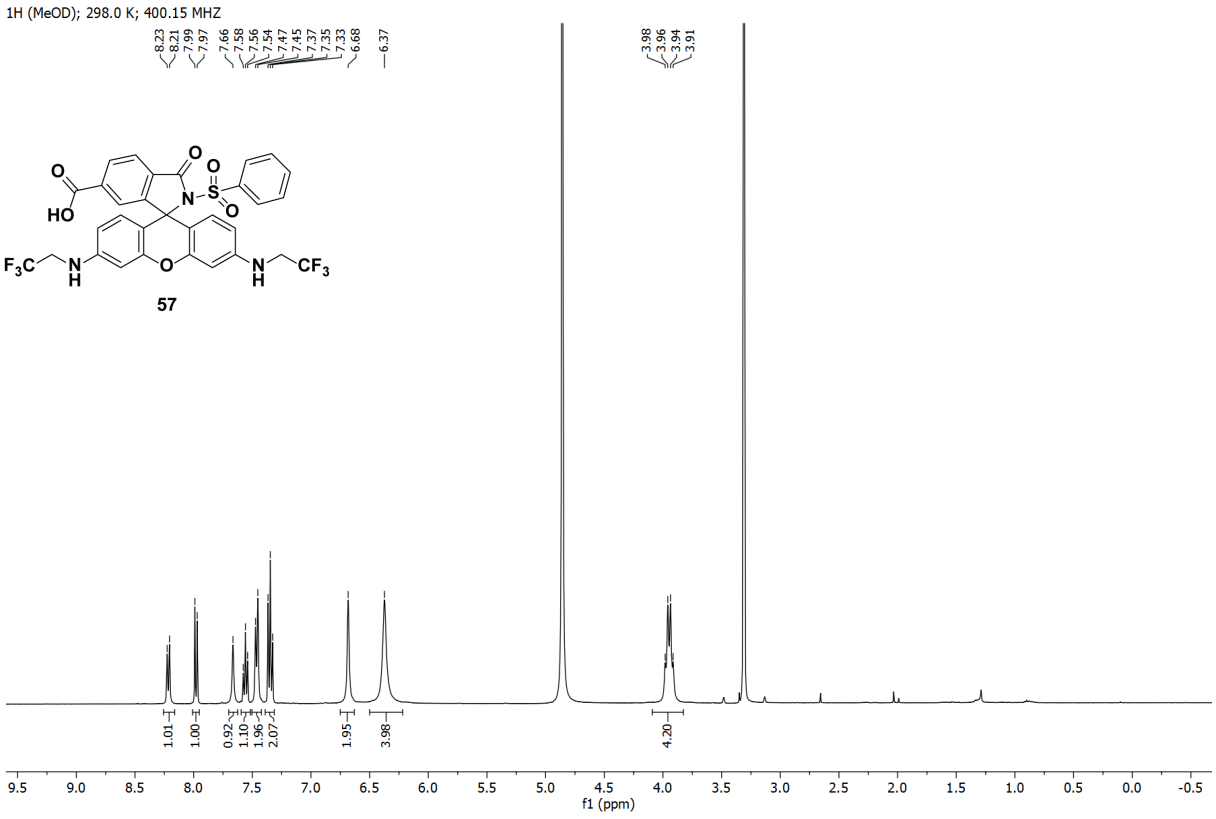
1H (MeOD); 298.0 K; 400.15 MHZ
8.23
8.21
7.99
7.97
7.66
7.58
7.56
7.54
7.47
7.45
7.37
7.35
7.33
6.68
6.37
3.98
3.96
3.94
3.91
1.01
1.00
0.92
1.10
1.96
2.07
1.95
3.98
4.20
f1 (ppm)

57

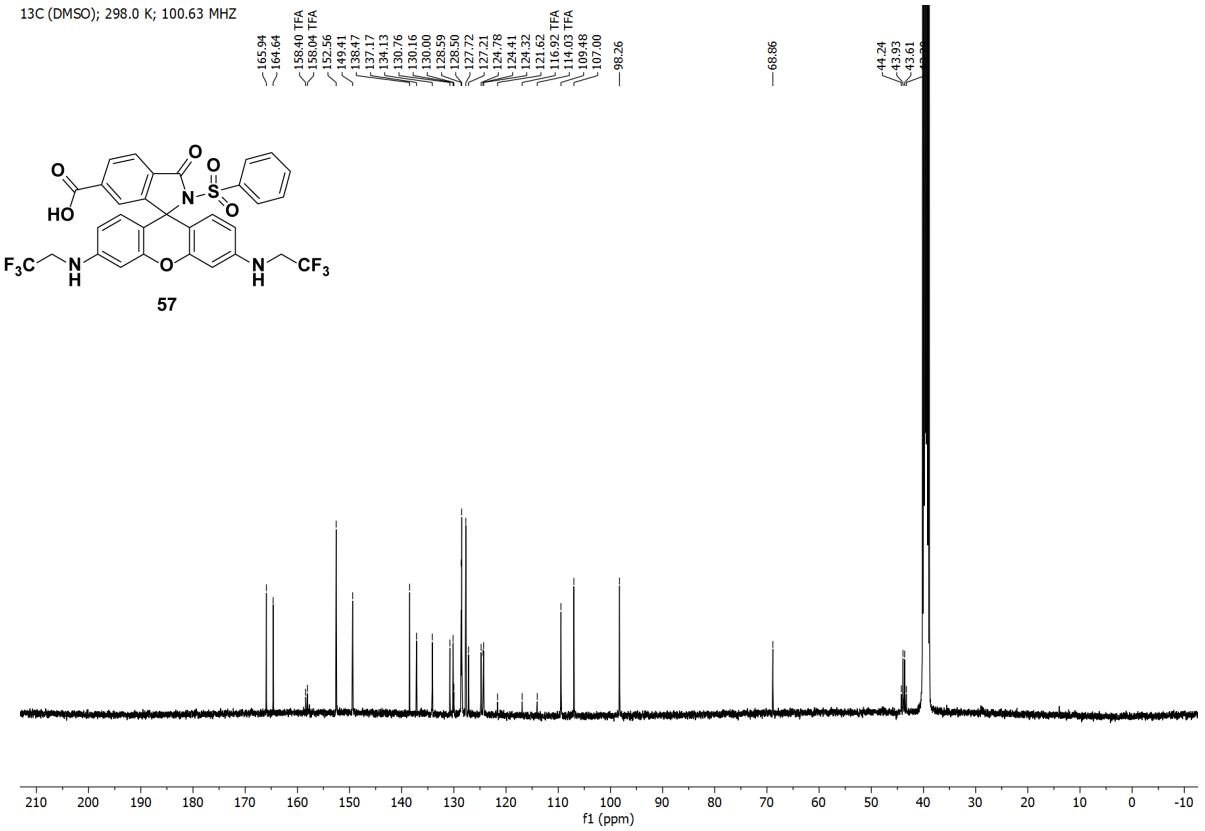
13C (DMSO); 298.0 K; 100.63 MHZ
165.94
164.64
158.40 TFA
158.04 TFA
152.56
149.41
138.47
137.17
134.13
130.76
130.16
130.00
128.59
128.50
127.72
127.21
124.78
124.41
124.32
121.62
116.92 TFA
114.03 TFA
109.48
107.00
98.26
68.86
44.24
43.93
43.61
f1 (ppm)

57

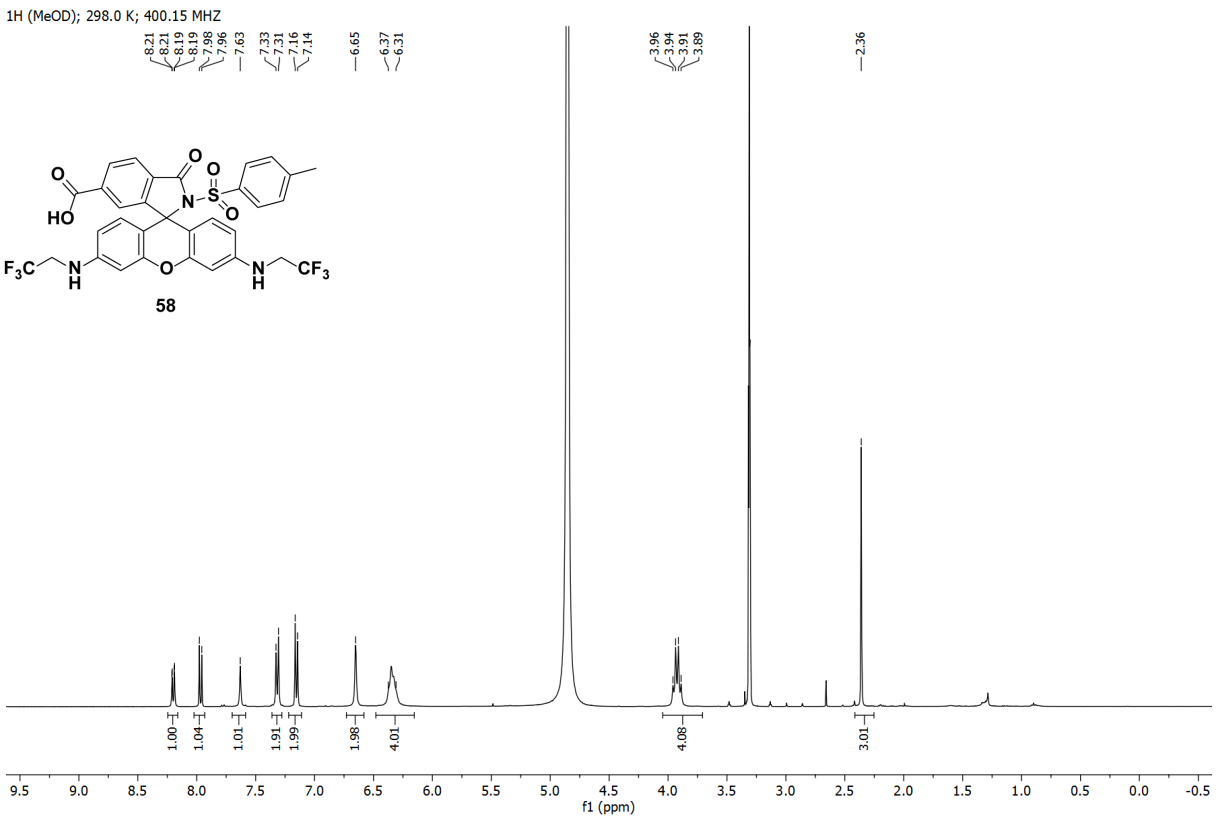
1H (MeOD); 298.0 K; 400.15 MHZ
8.21
8.21
8.19
8.19
7.98
7.96
7.63
7.33
7.31
7.16
7.14
6.65
6.37
6.31
3.96
3.94
3.91
3.89
2.36
1.00
1.04
1.01
1.91
1.99
1.98
4.01
4.08
3.01
f1 (ppm)

58

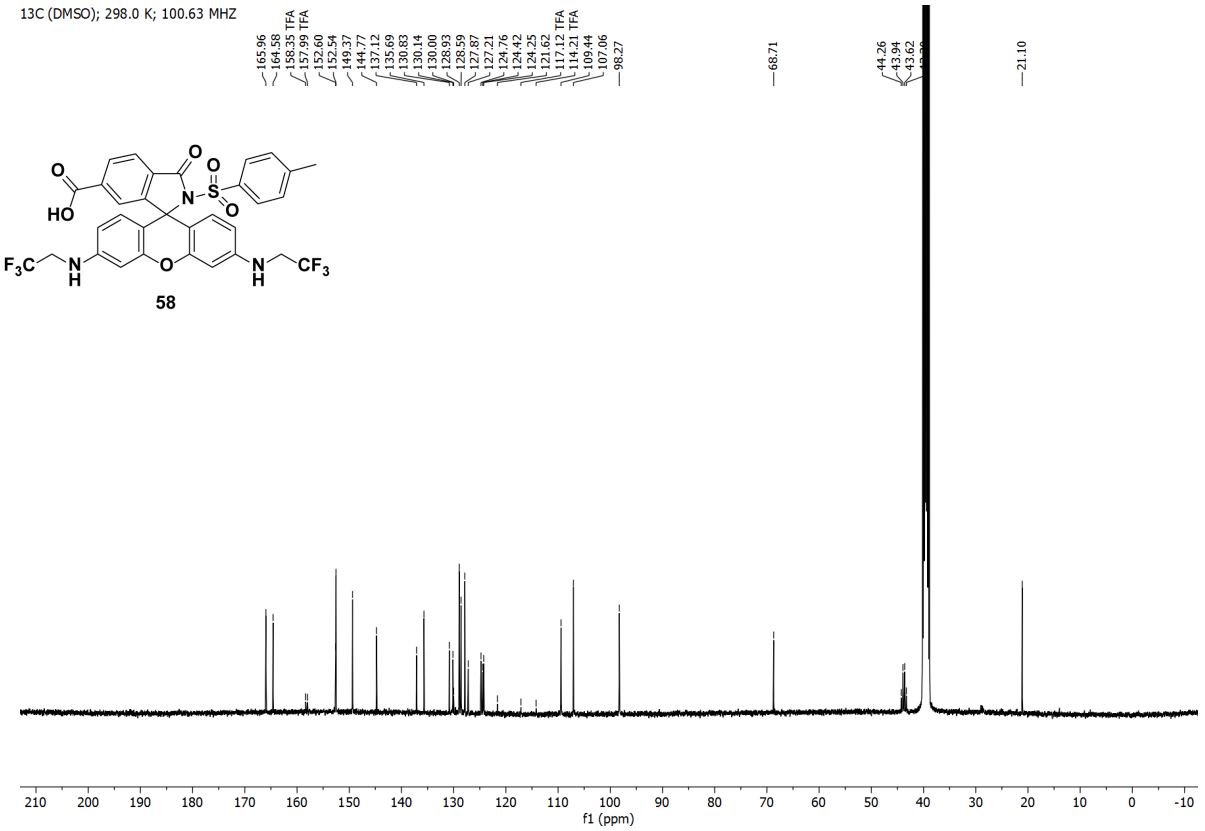
13C (DMSO); 298.0 K; 100.63 MHZ
165.96
164.58
158.35 TFA
157.99 TFA
152.60
152.54
144.37
144.77
137.12
135.69
130.83
130.14
130.00
128.93
128.59
127.87
127.21
124.76
124.42
124.25
121.62
117.12 TFA
114.21 TFA
109.44
107.06
98.27
68.71
44.26
43.94
43.62
21.10
f1 (ppm)

58

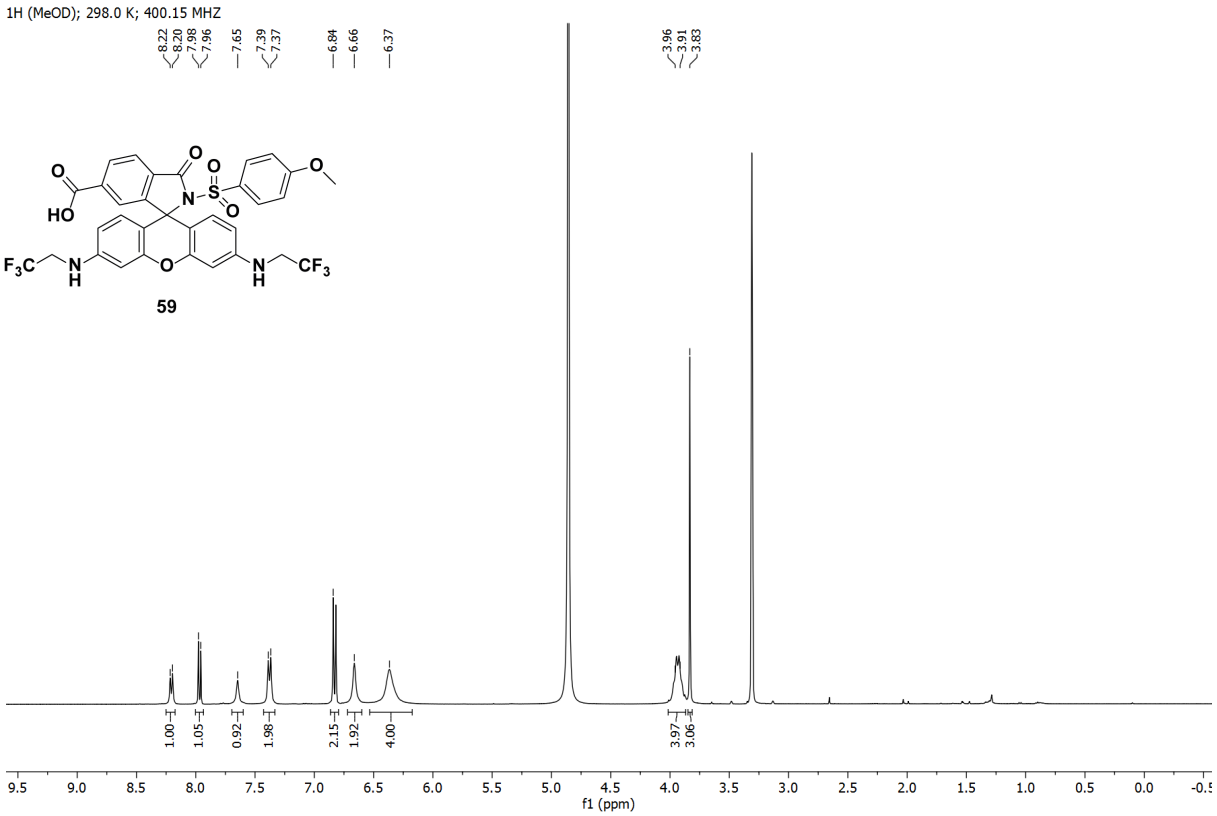
1H (MeOD); 298.0 K; 400.15 MHZ
8.22
8.20
7.98
7.96
7.65
7.39
7.37
6.84
6.66
6.37
3.96
3.91
3.83
1.00
1.05
0.92
1.98
2.15
1.92
4.00
3.97
3.06
f1 (ppm)

59

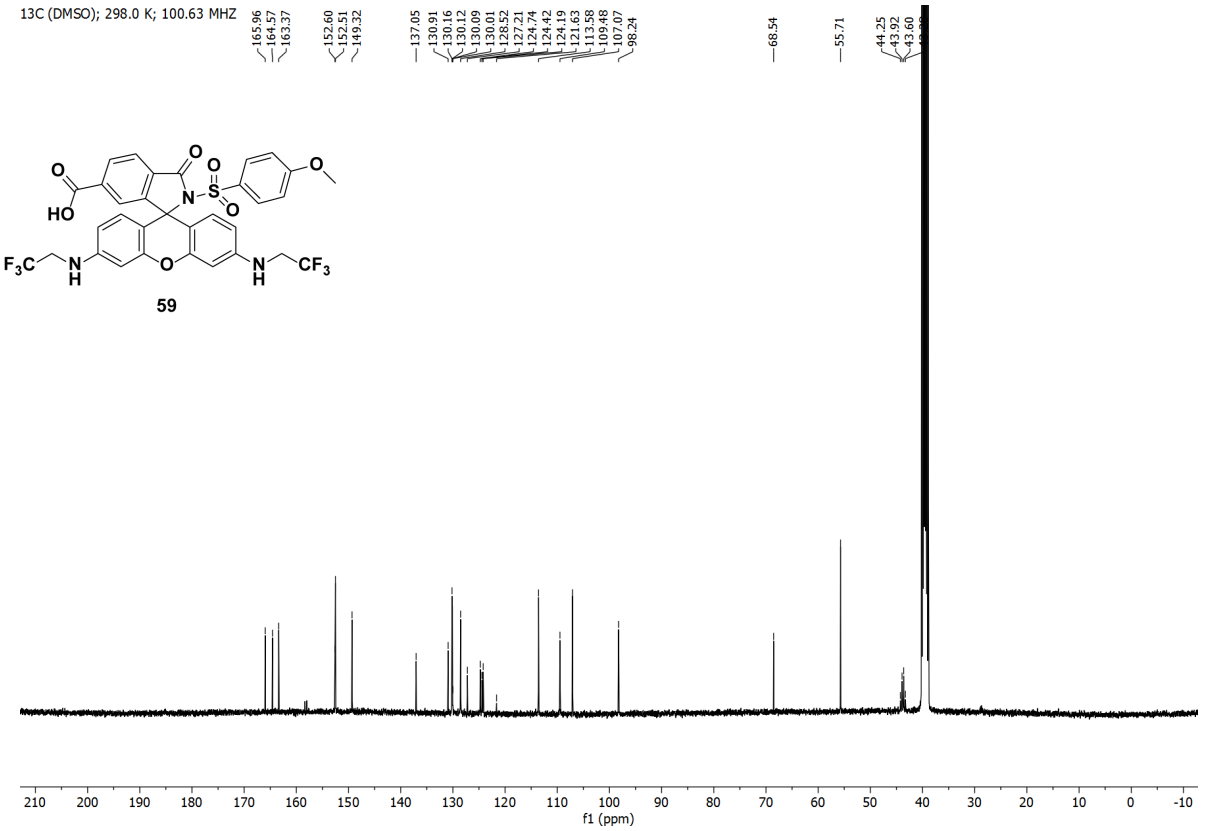
13C (DMSO); 298.0 K; 100.63 MHZ
165.96
164.57
163.37
152.60
152.51
149.32
137.05
130.91
130.16
130.12
130.09
130.01
128.52
127.21
124.74
124.42
124.19
121.63
113.58
109.48
107.07
98.24
68.54
55.71
44.25
43.92
43.60
59
f1 (ppm)

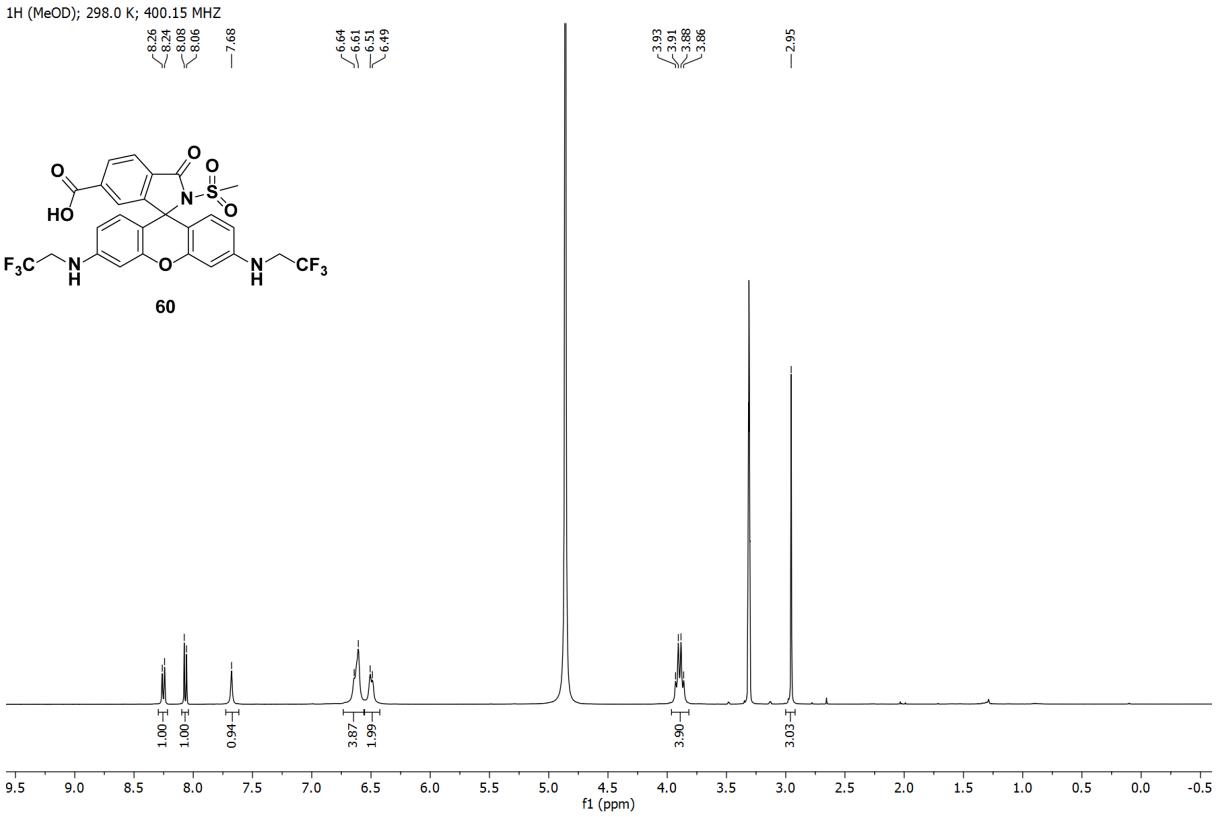
1H (MeOD); 298.0 K; 400.15 MHZ
8.26
8.24
8.08
8.06
7.68
6.64
6.61
6.51
6.49
3.93
3.91
3.88
3.86
2.95
60
1.00
1.00
0.94
3.87
1.99
3.90
3.03
f1 (ppm)

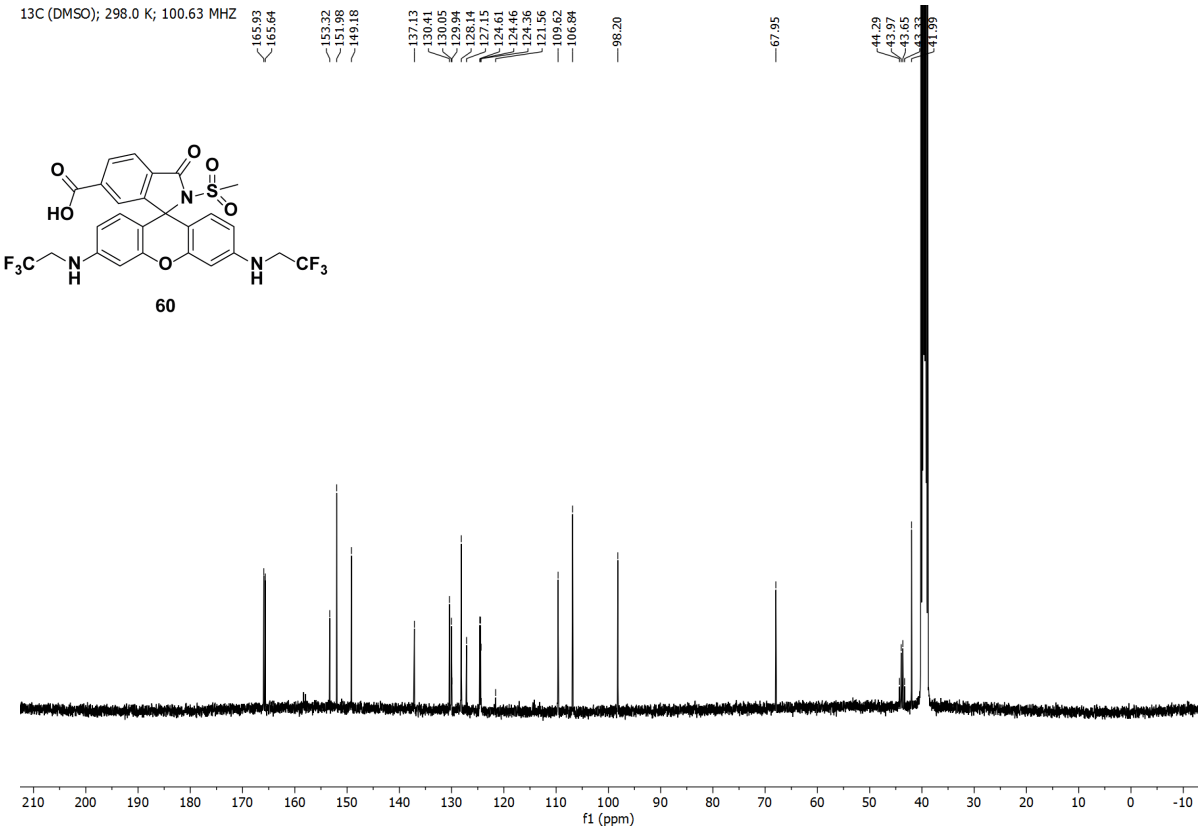
13C (DMSO); 298.0 K; 100.63 MHZ
165.93
165.64
153.32
151.98
149.18
137.13
130.41
130.05
129.94
128.14
127.15
124.61
124.46
124.36
121.56
109.62
106.84
98.20
67.95
44.29
43.97
43.65
43.33
41.99
f1 (ppm)

60

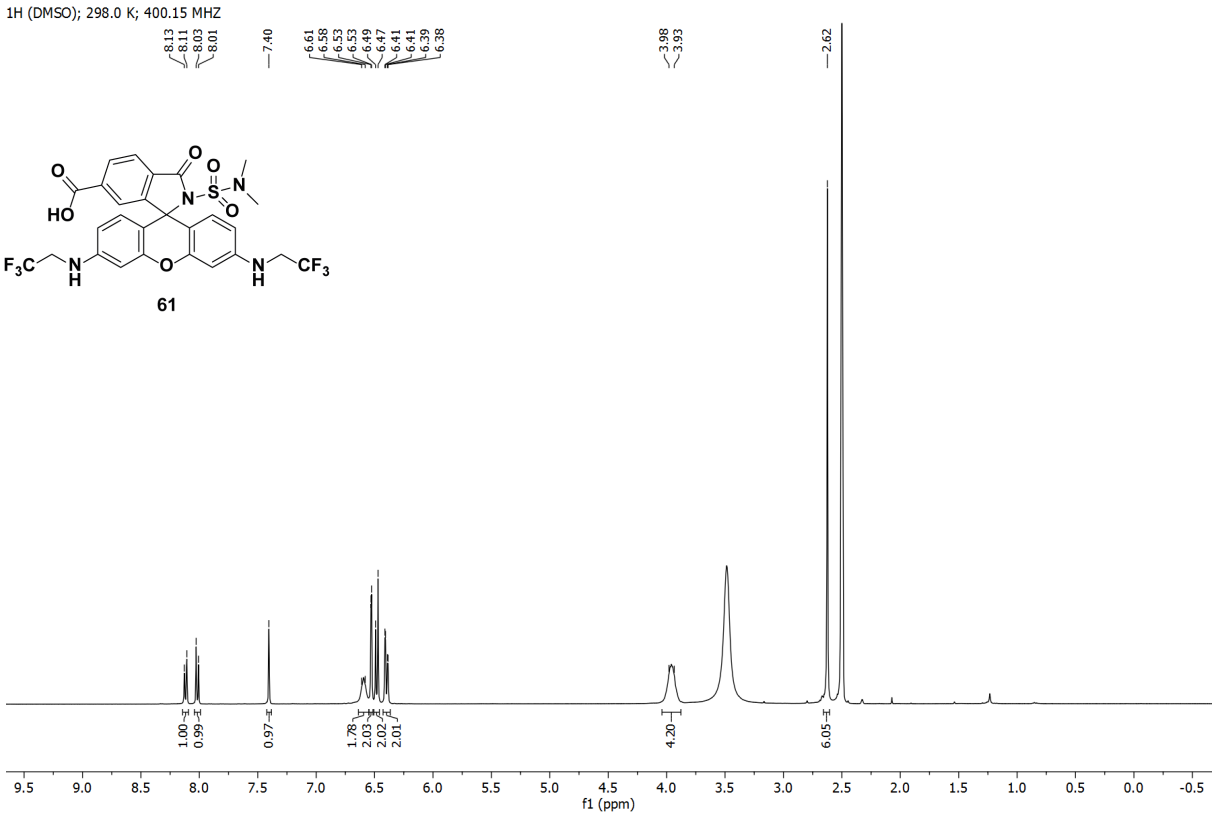
1H (DMSO); 298.0 K; 400.15 MHZ
8.13
8.11
8.03
8.01
7.40
6.61
6.58
6.53
6.53
6.49
6.47
6.41
6.41
6.39
6.38
3.98
3.93
2.62
1.00
0.99
0.97
1.78
2.03
2.02
2.01
4.20
6.05
f1 (ppm)

61

13C (DMSO); 298.0 K; 100.63 MHZ

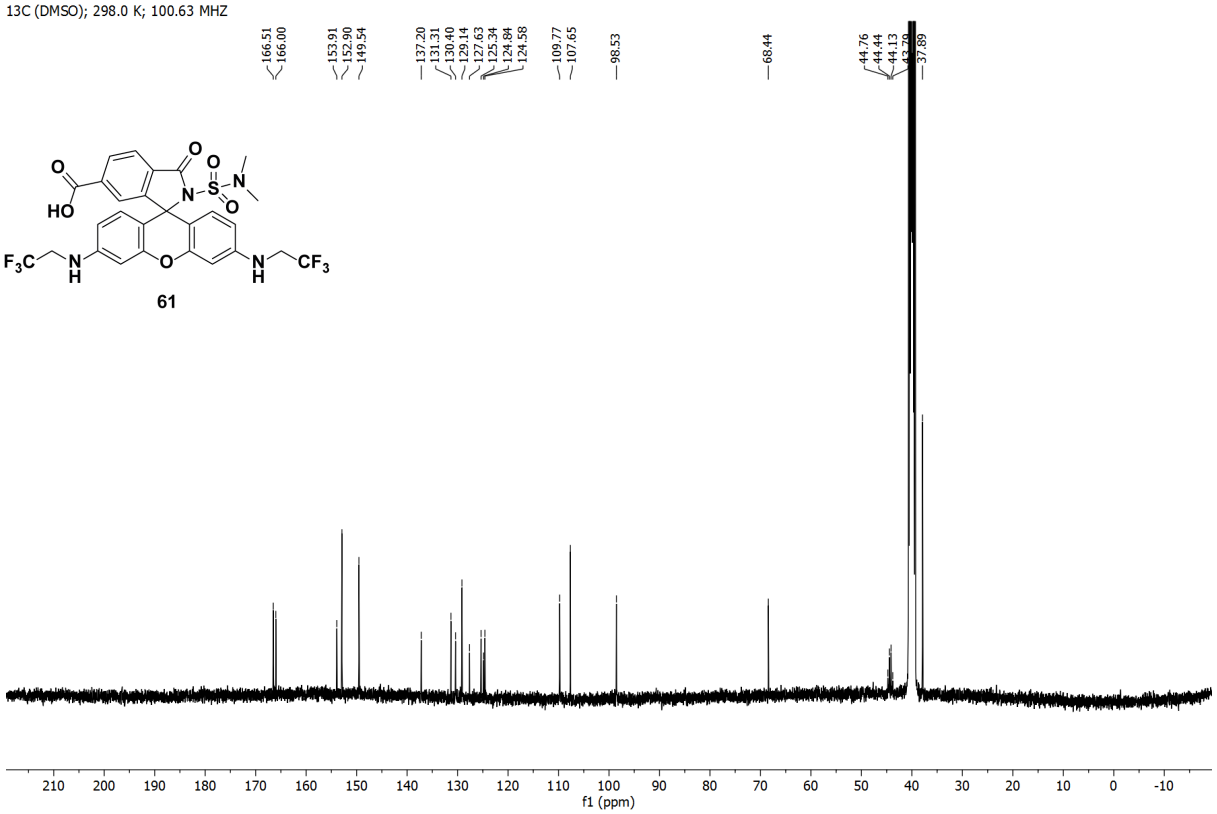

61

1H (MeOD); 298.0 K; 400.15 MHZ

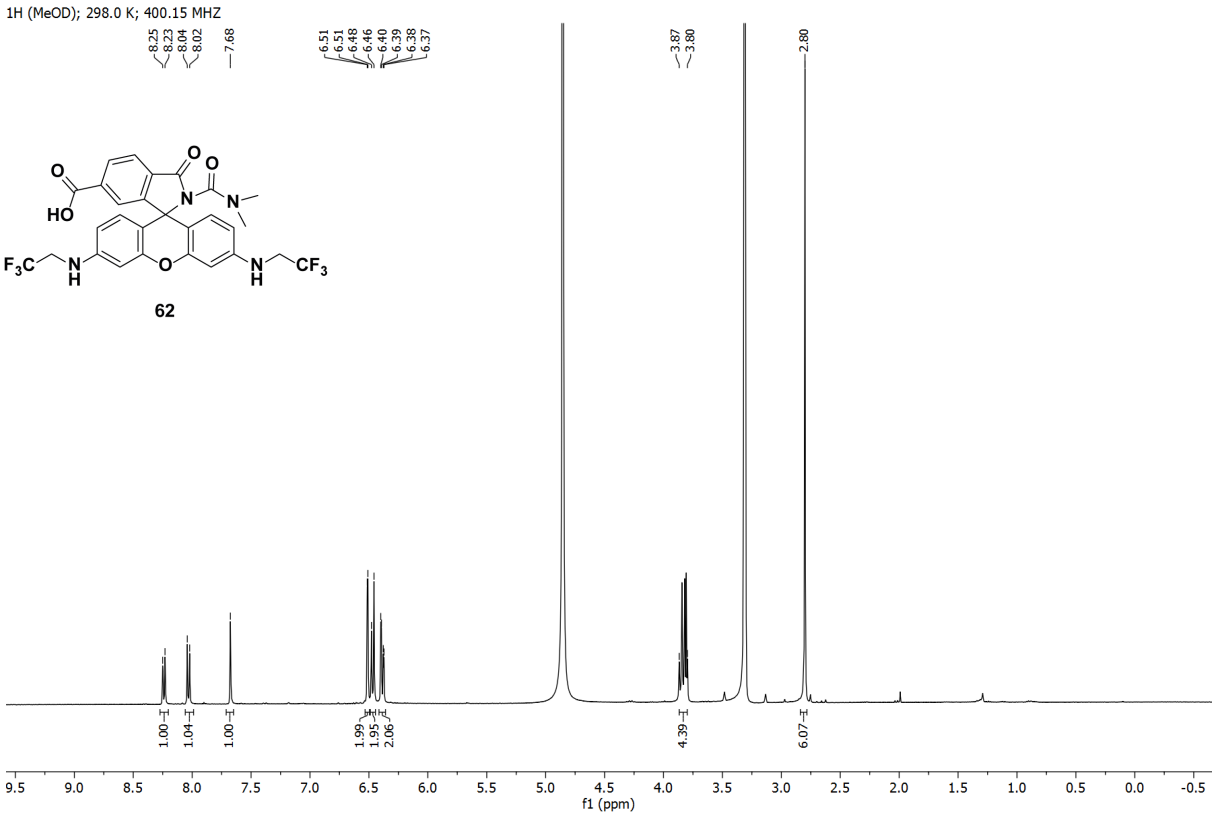

62

1H (DMSO); 298.0 K; 400.15 MHZ

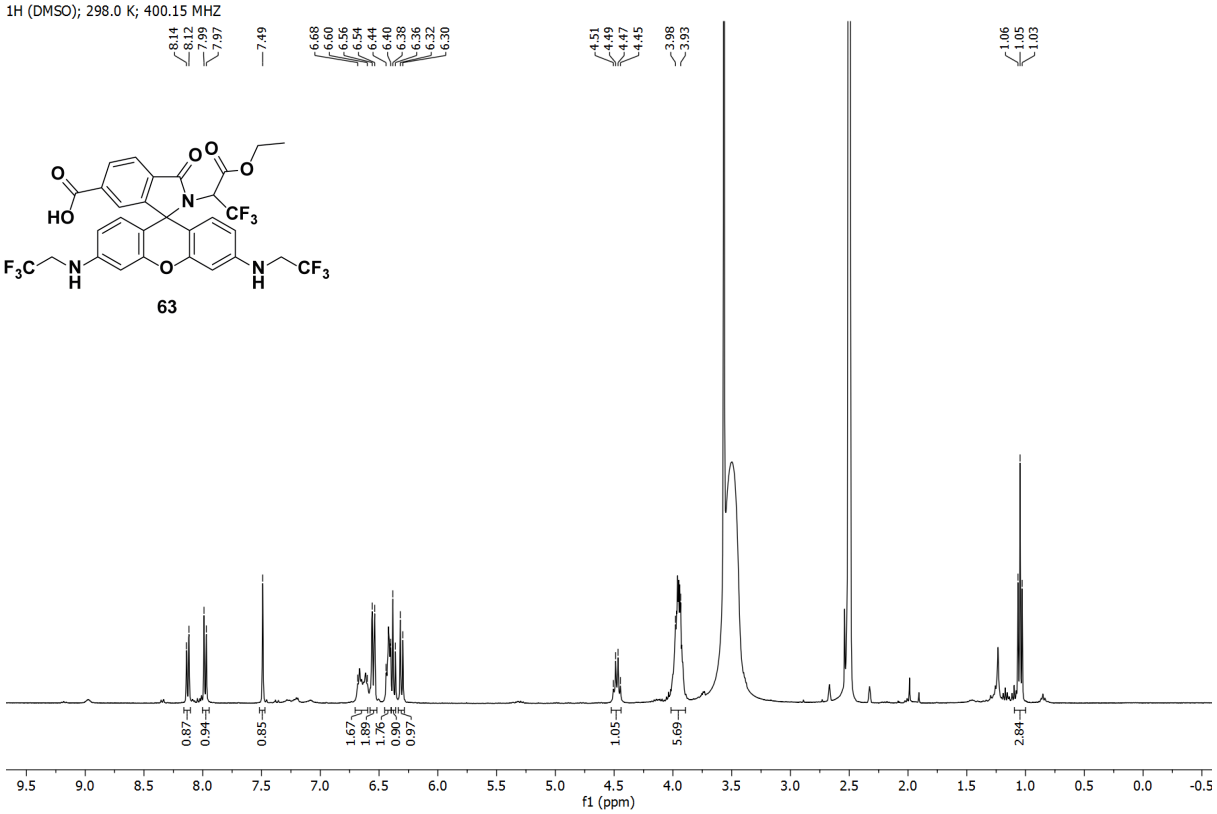

63

1H (DMSO); 298.0 K; 400.15 MHZ

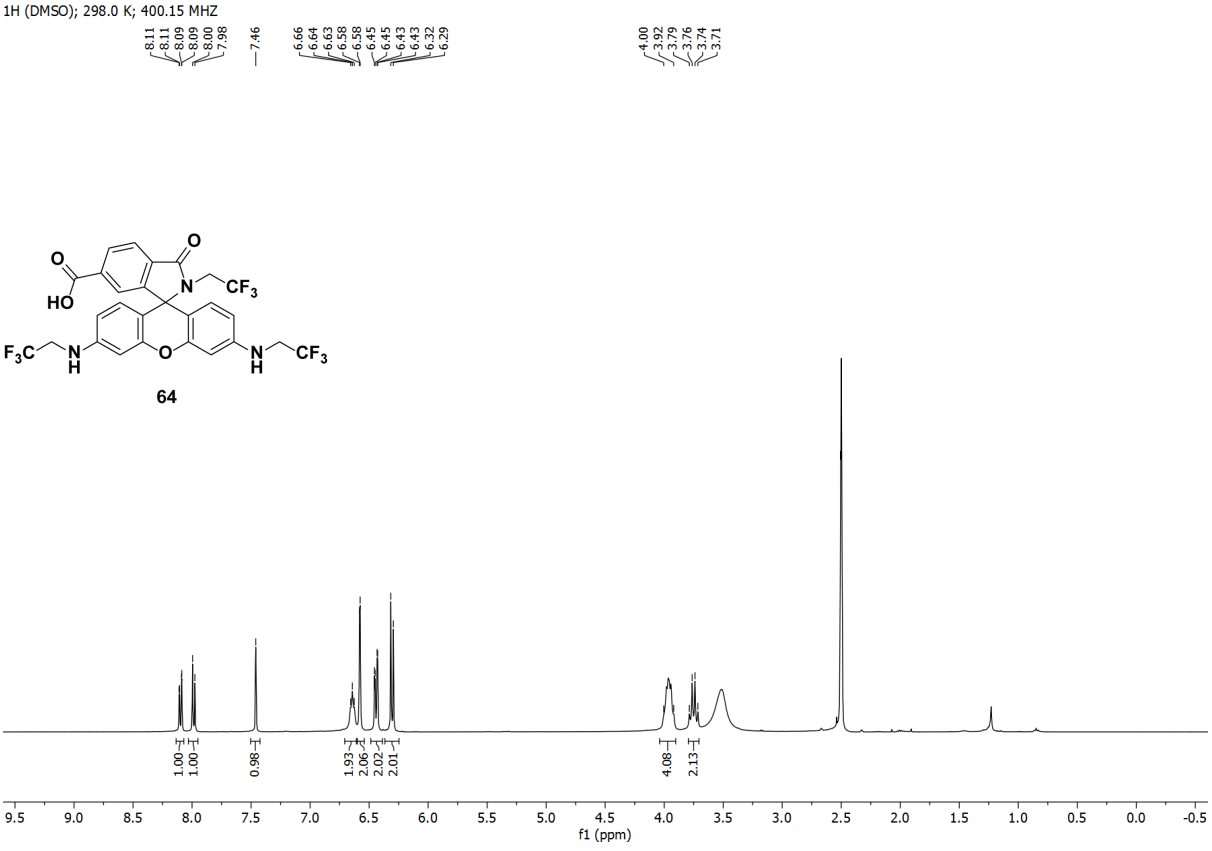

64

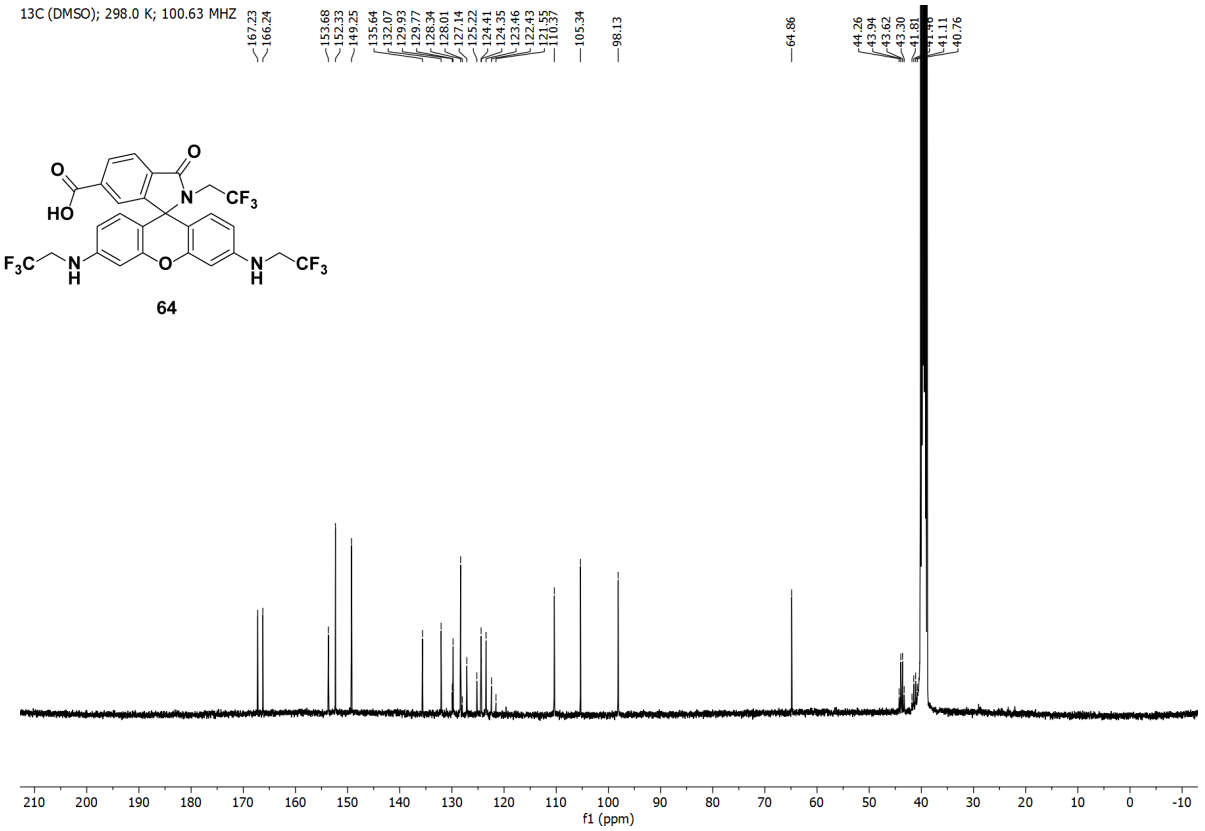
13C (DMSO); 298.0 K; 100.63 MHZ
167.23
166.24
153.68
152.33
149.25
135.64
132.07
129.93
129.77
128.34
128.01
127.14
125.22
124.41
124.35
123.46
122.43
121.55
110.37
105.34
98.13
64.86
44.26
43.94
43.62
43.30
41.81
41.38
41.11
40.76
f1 (ppm)

64

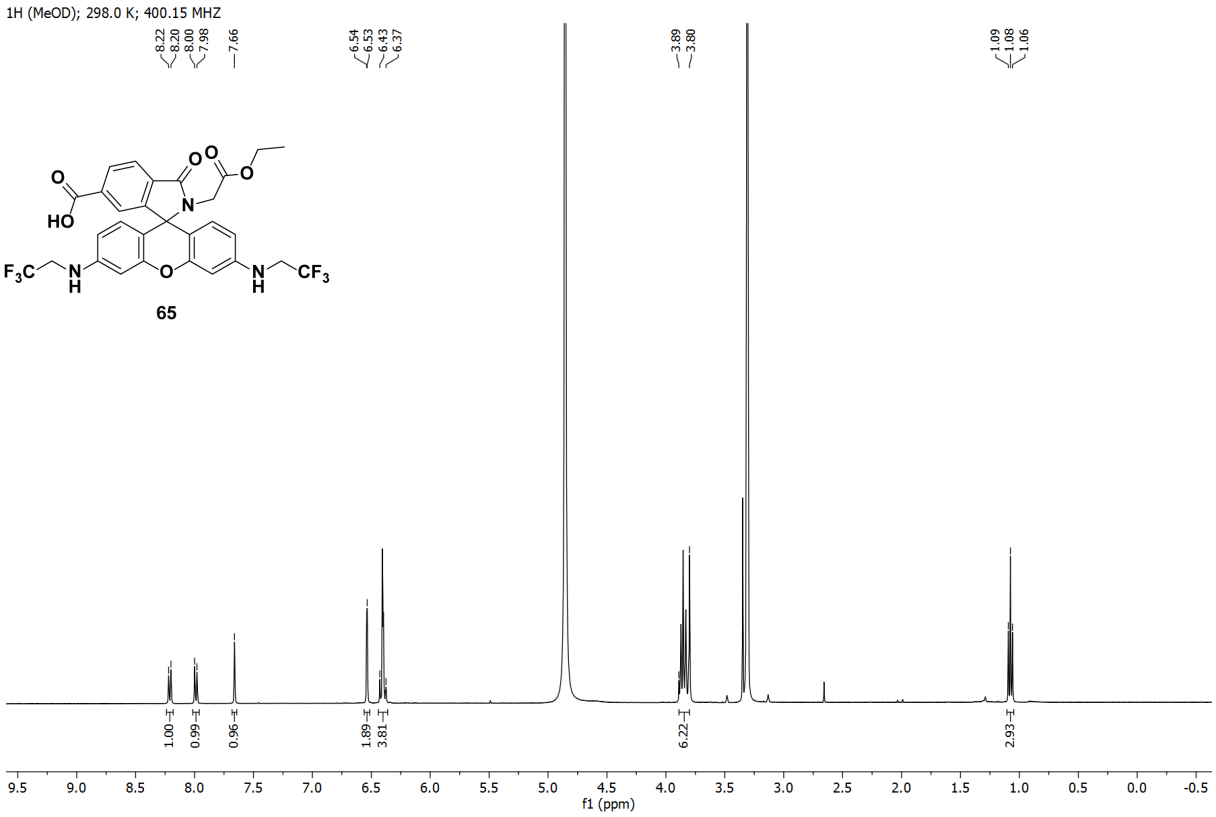
1H (MeOD); 298.0 K; 400.15 MHZ
8.22
8.20
8.00
7.98
7.66
6.54
6.53
6.43
6.37
3.89
3.80
1.09
1.08
1.06
1.00
0.99
0.96
1.89
3.81
6.22
2.93
f1 (ppm)

65

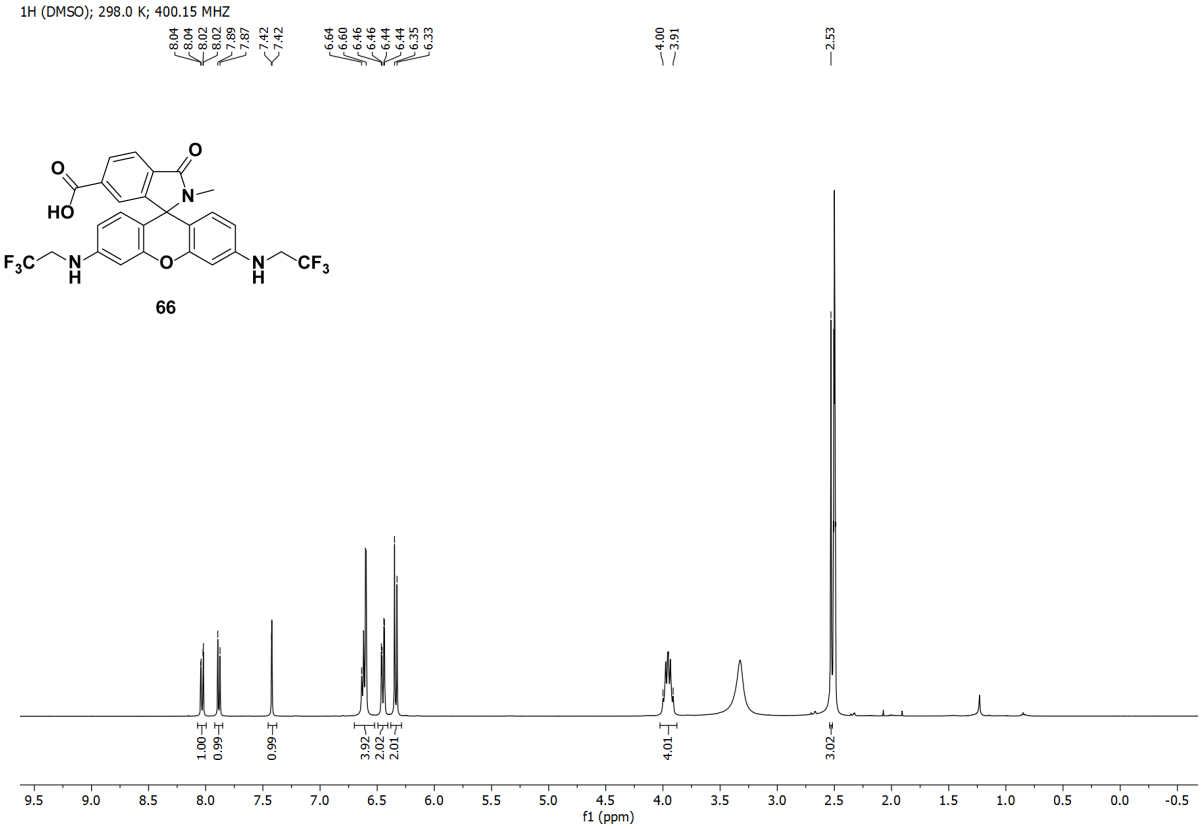
1H (DMSO); 298.0 K; 400.15 MHZ
8.04
8.04
8.02
8.02
7.89
7.87
7.42
7.42
6.64
6.60
6.46
6.46
6.44
6.44
6.35
6.33
4.00
3.91
2.53
1.00
0.99
0.99
3.92
2.02
2.01
4.01
3.02
9.5 9.0 8.5 8.0 7.5 7.0 6.5 6.0 5.5 5.0 4.5 4.0 3.5 3.0 2.5 2.0 1.5 1.0 0.5 0.0 -0.5
f1 (ppm)

O
O
HO
N
F3C
N
H
O
N
H
CF3

66

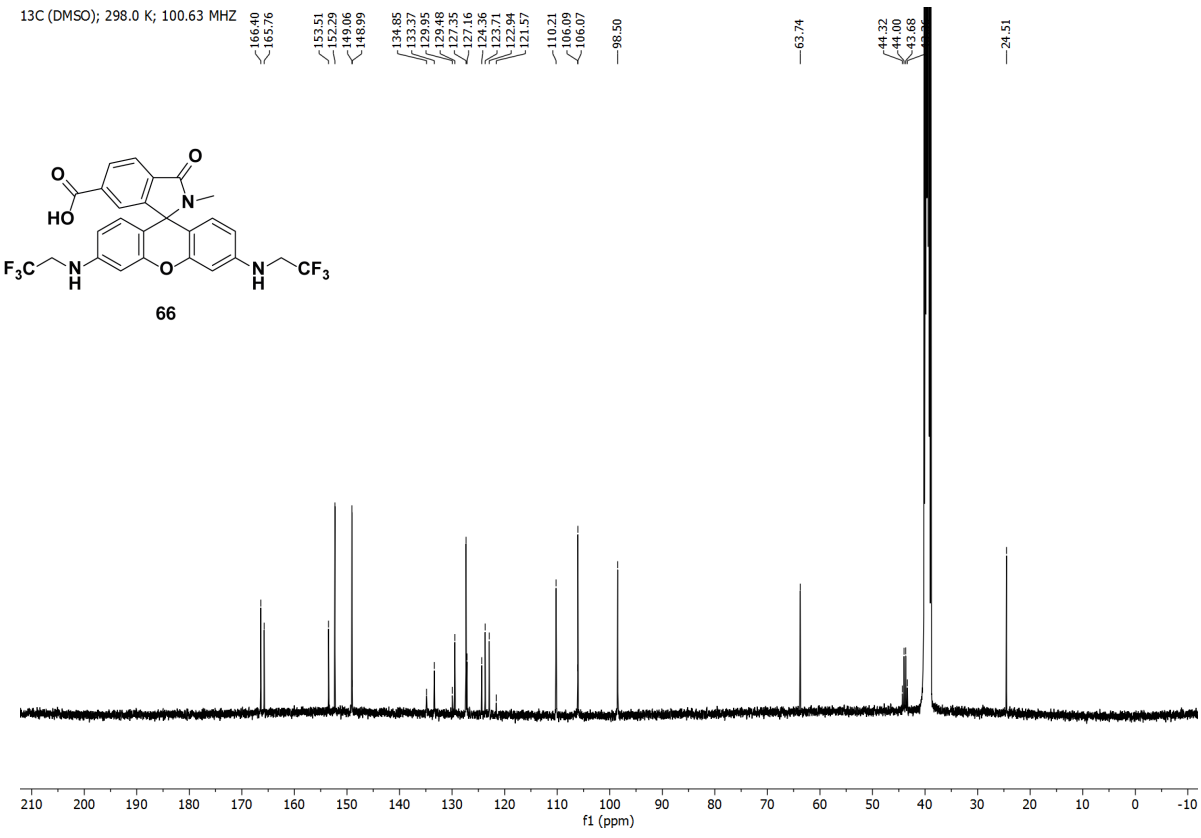
13C (DMSO); 298.0 K; 100.63 MHZ
166.40
165.76
153.51
152.29
149.06
148.99
134.85
133.37
129.95
129.48
127.35
127.16
124.36
123.71
122.94
121.57
110.21
106.09
106.07
98.50
63.74
44.32
44.00
43.68
24.51
210 200 190 180 170 160 150 140 130 120 110 100 90 80 70 60 50 40 30 20 10 0 -10
f1 (ppm)

O
O
HO
N
F3C
N
H
O
N
H
CF3

66

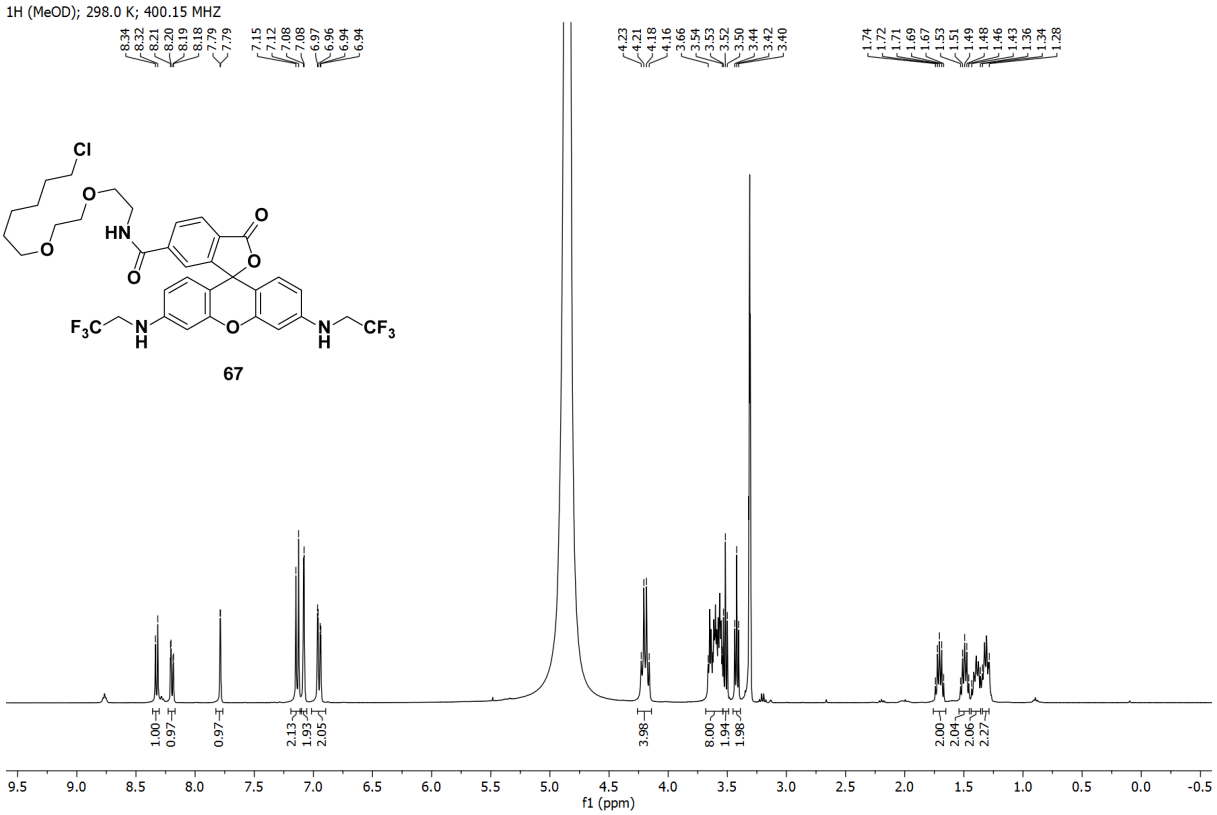

67

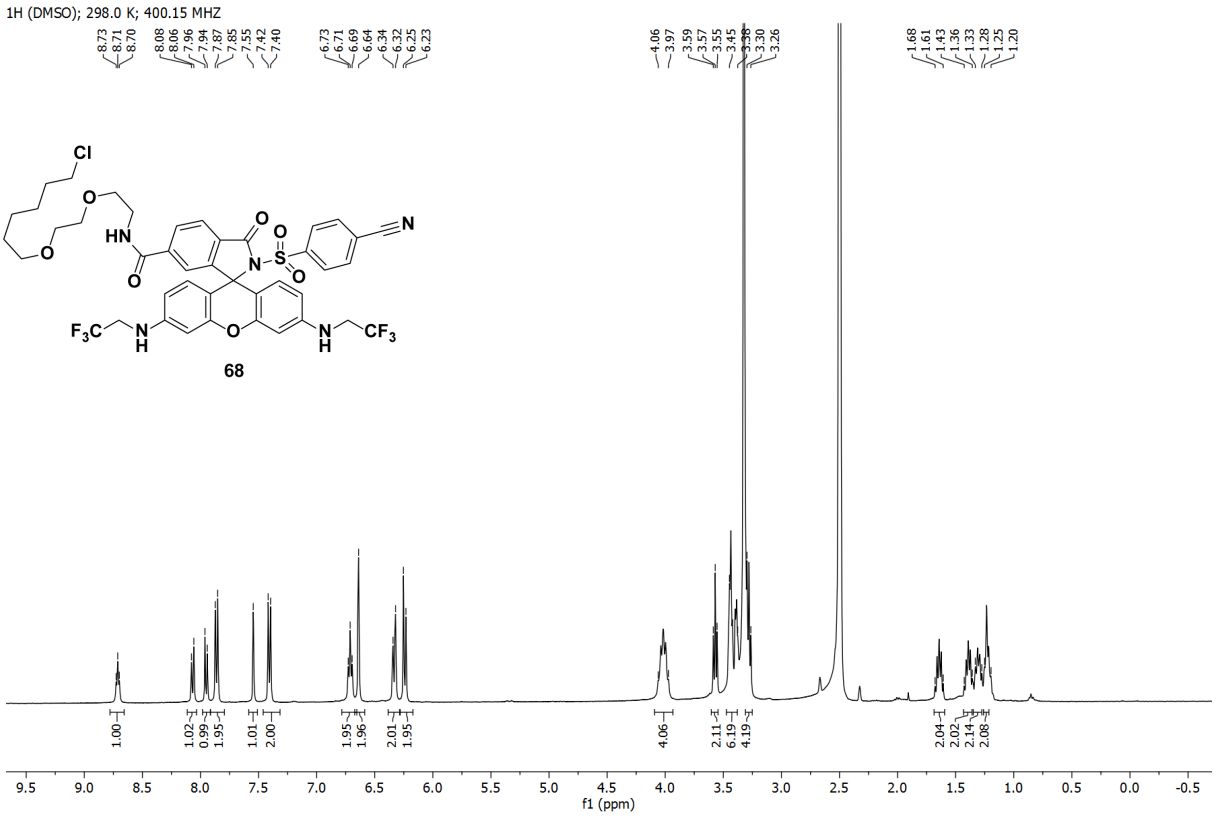

68

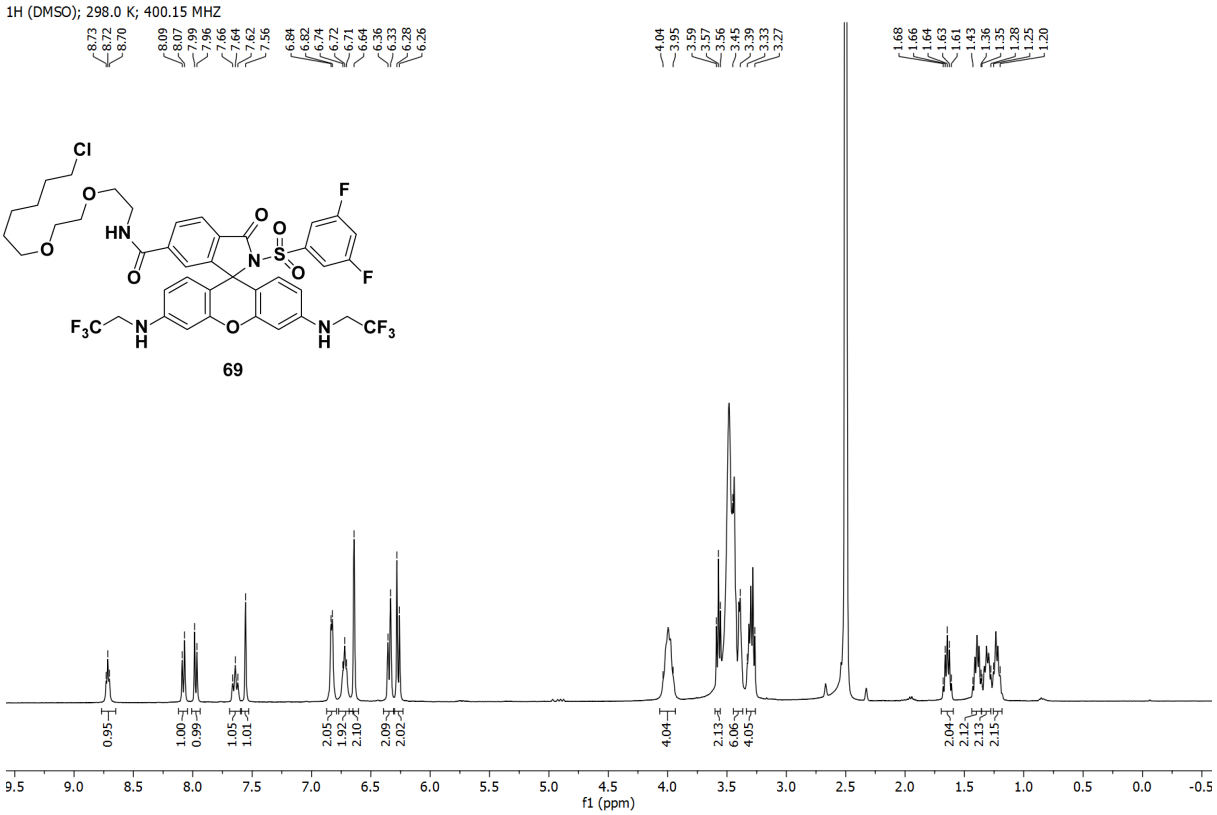

69

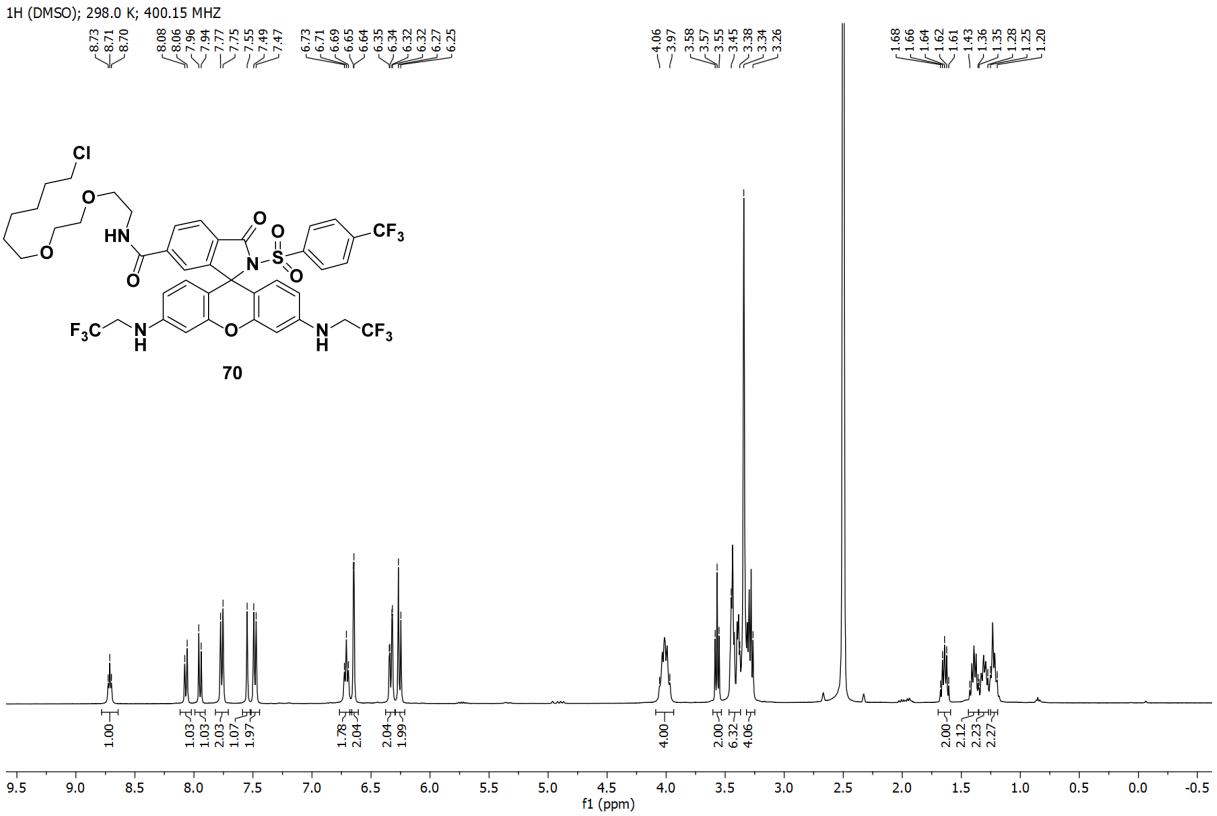

70

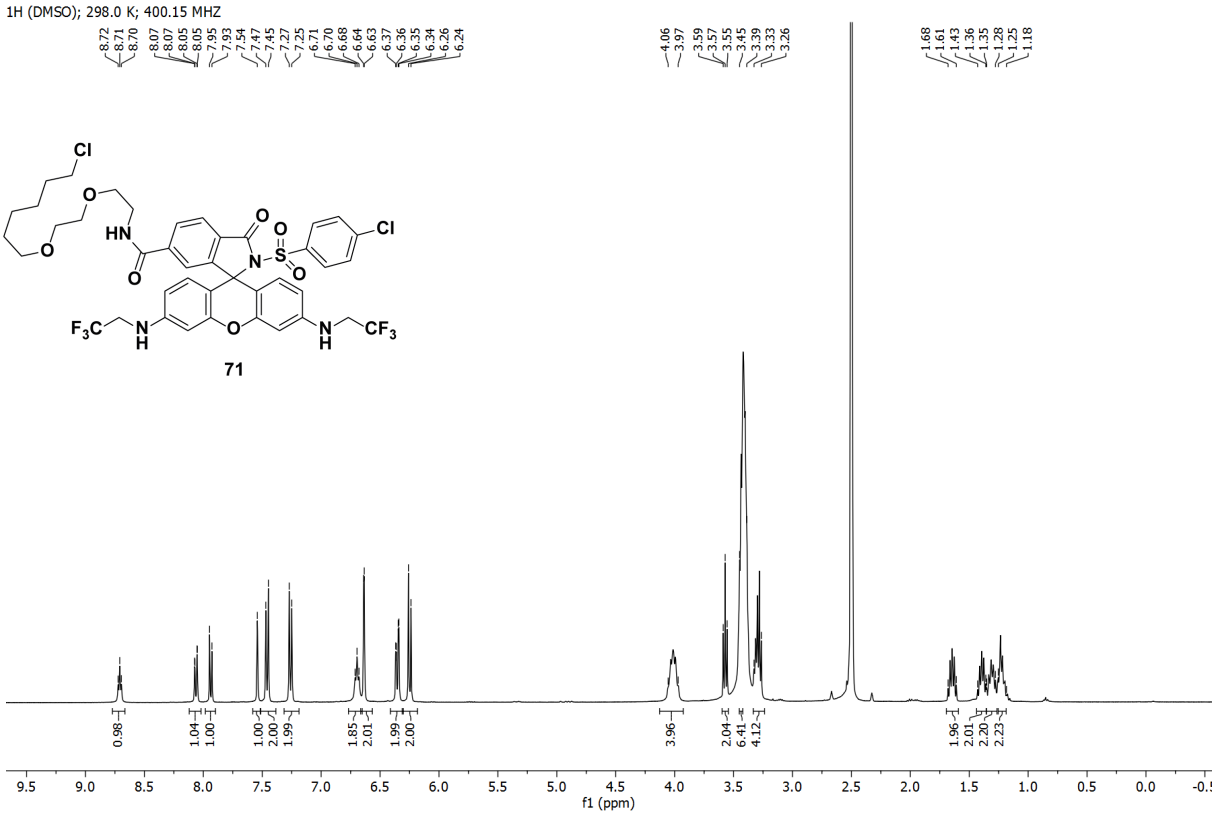
1H (DMSO); 298.0 K; 400.15 MHZ
71
f1 (ppm)

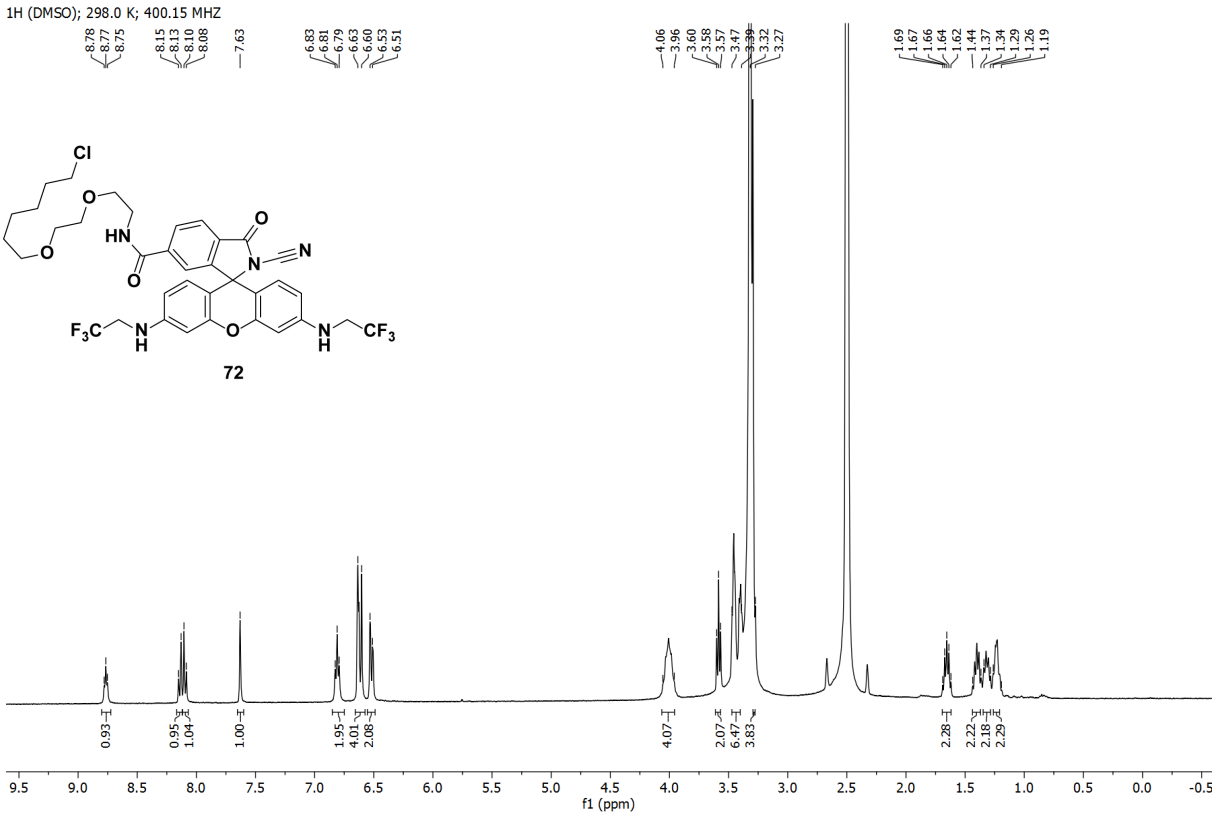
1H (DMSO); 298.0 K; 400.15 MHZ
72
f1 (ppm)

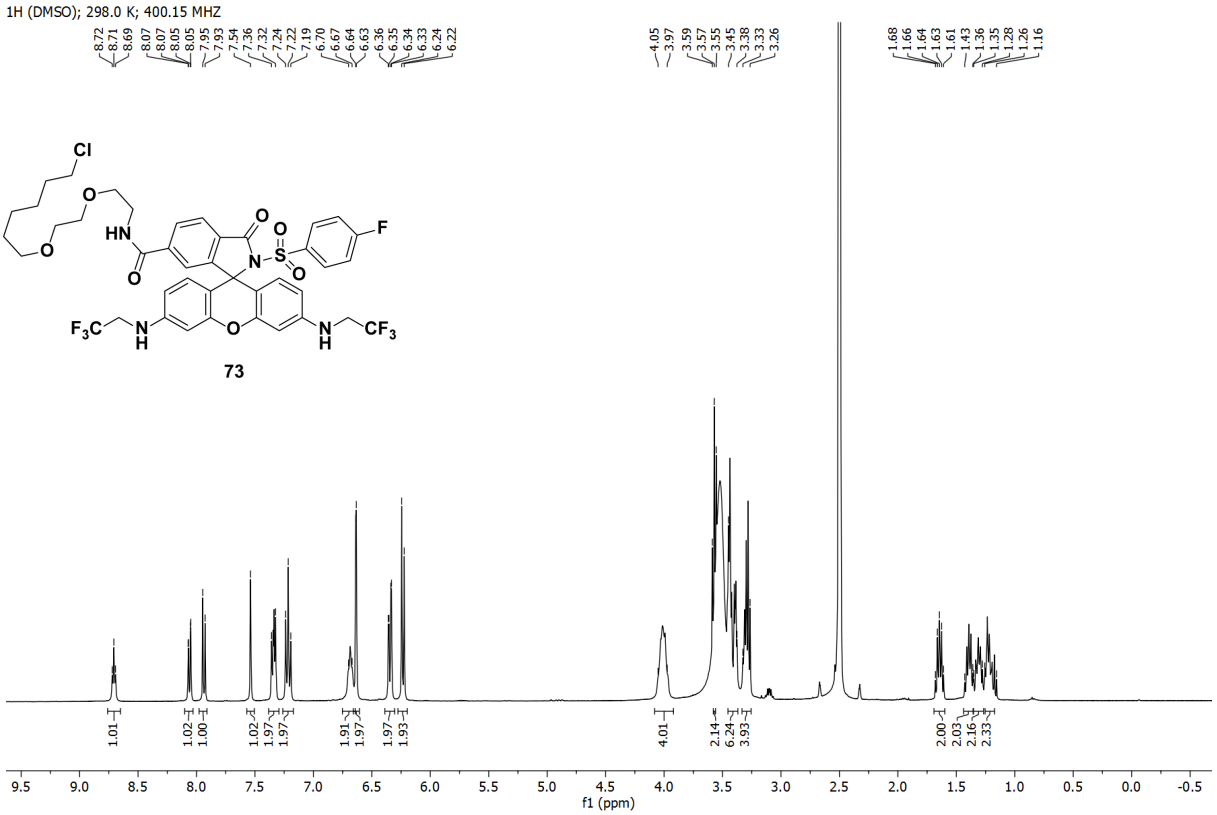

73

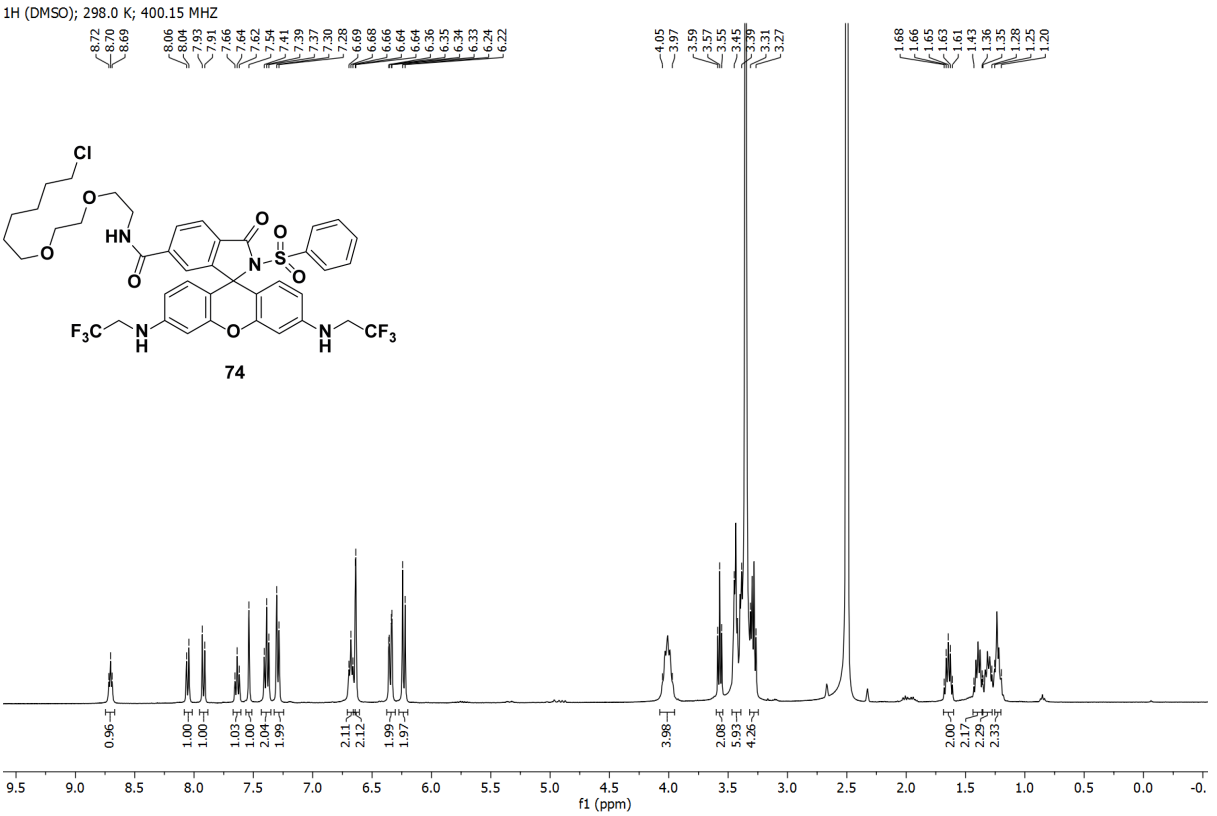

74

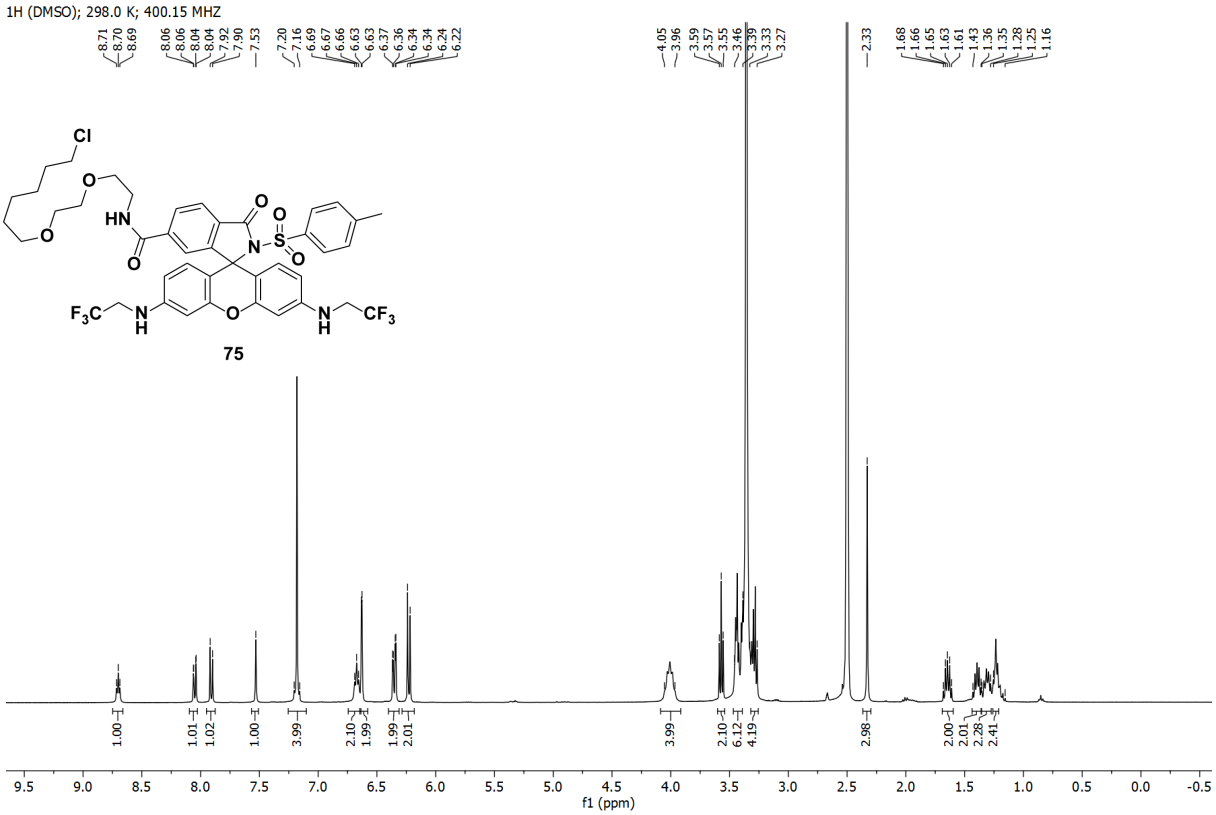

75

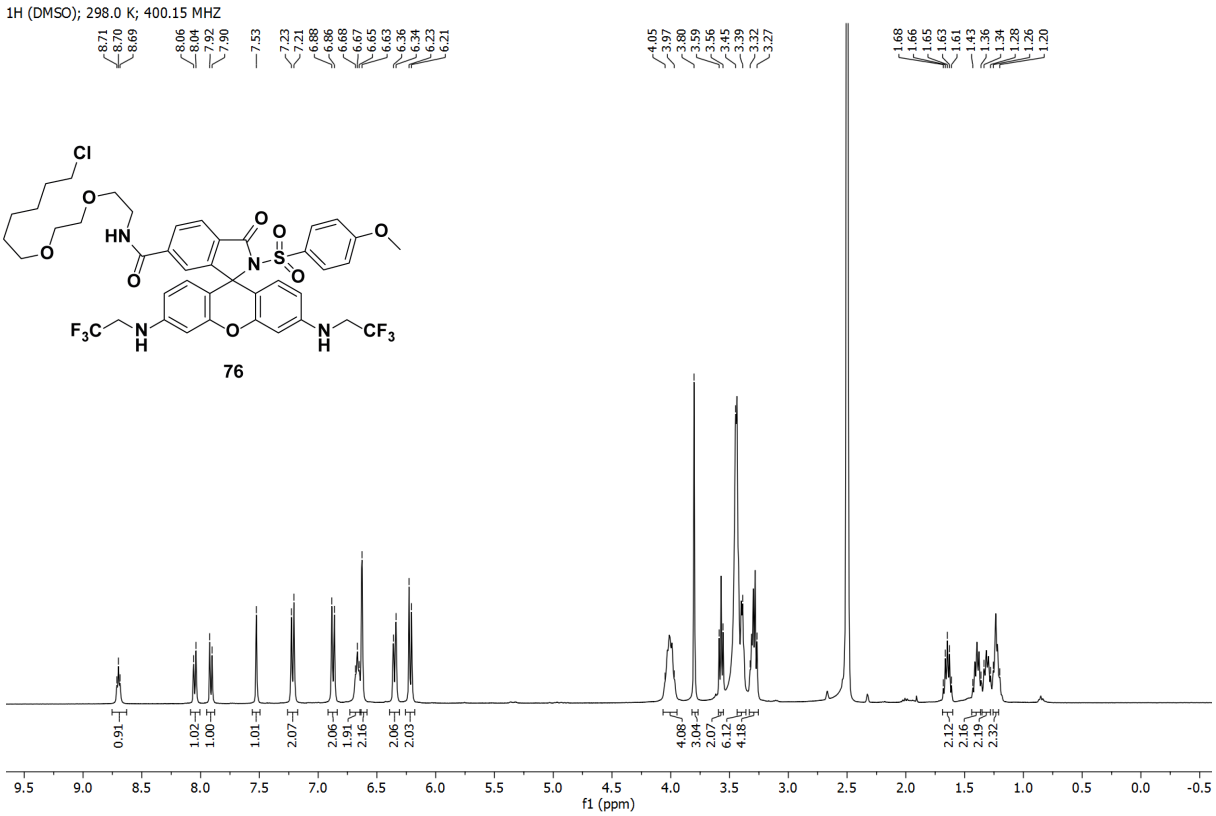

76

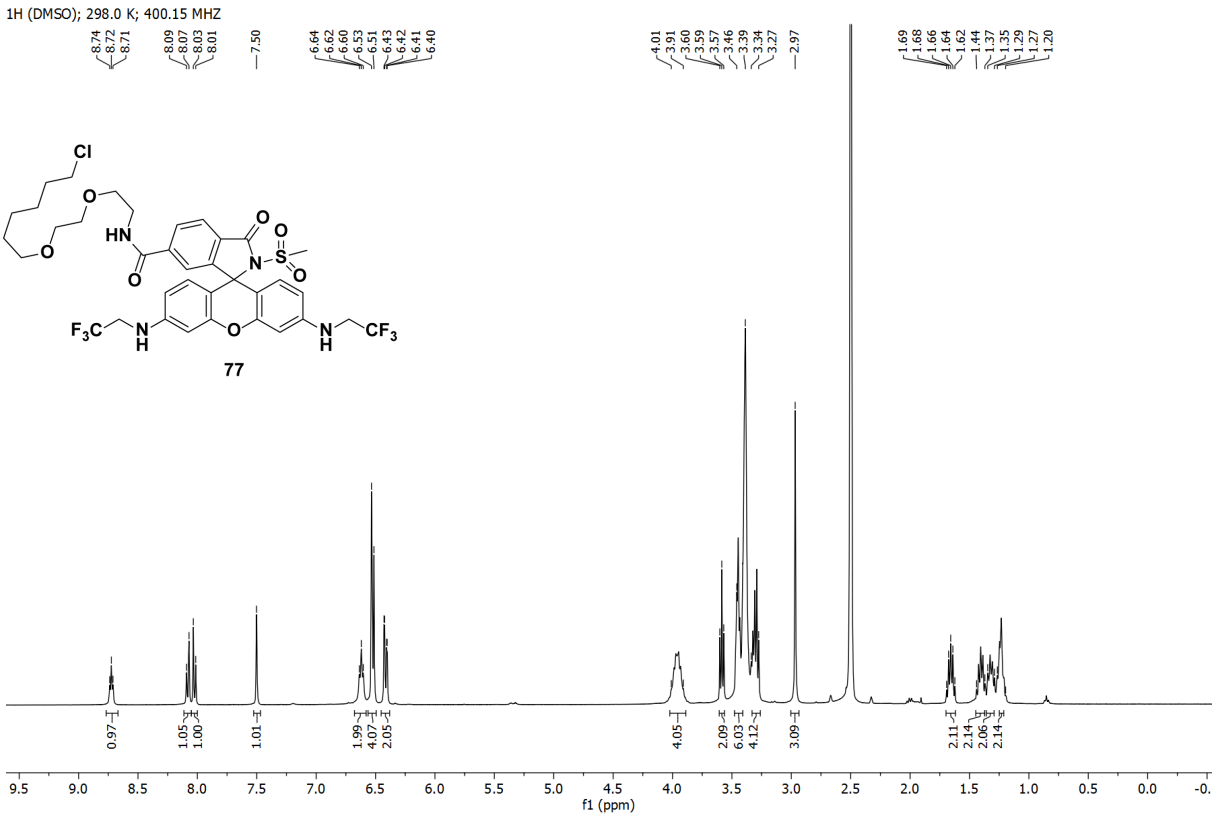

77

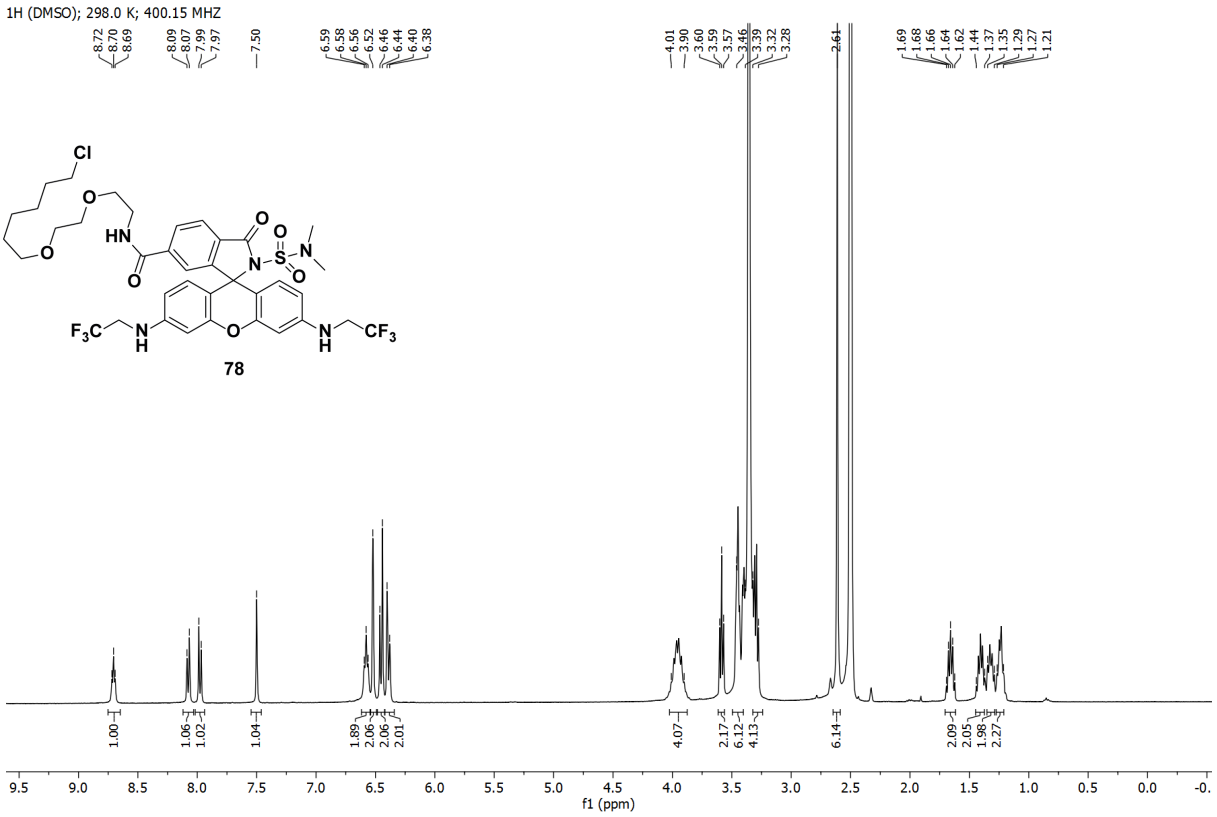

78

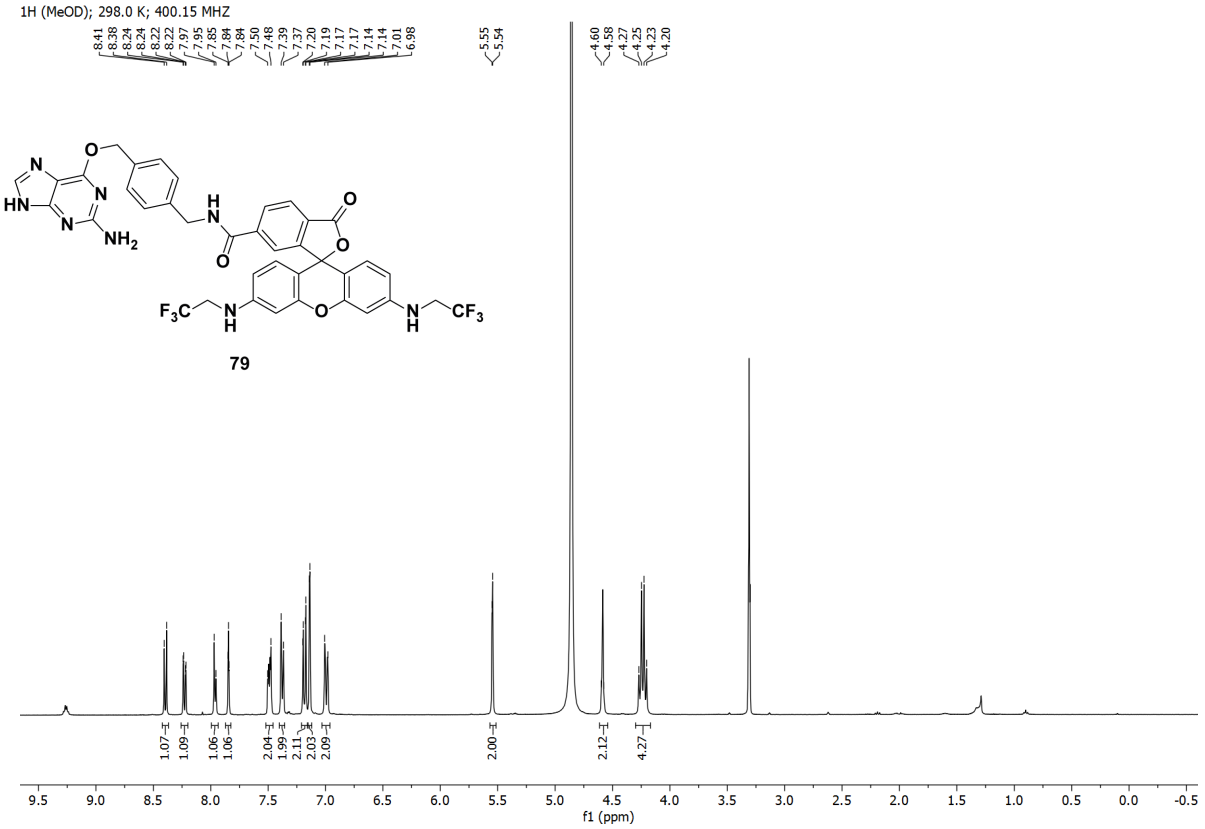

79

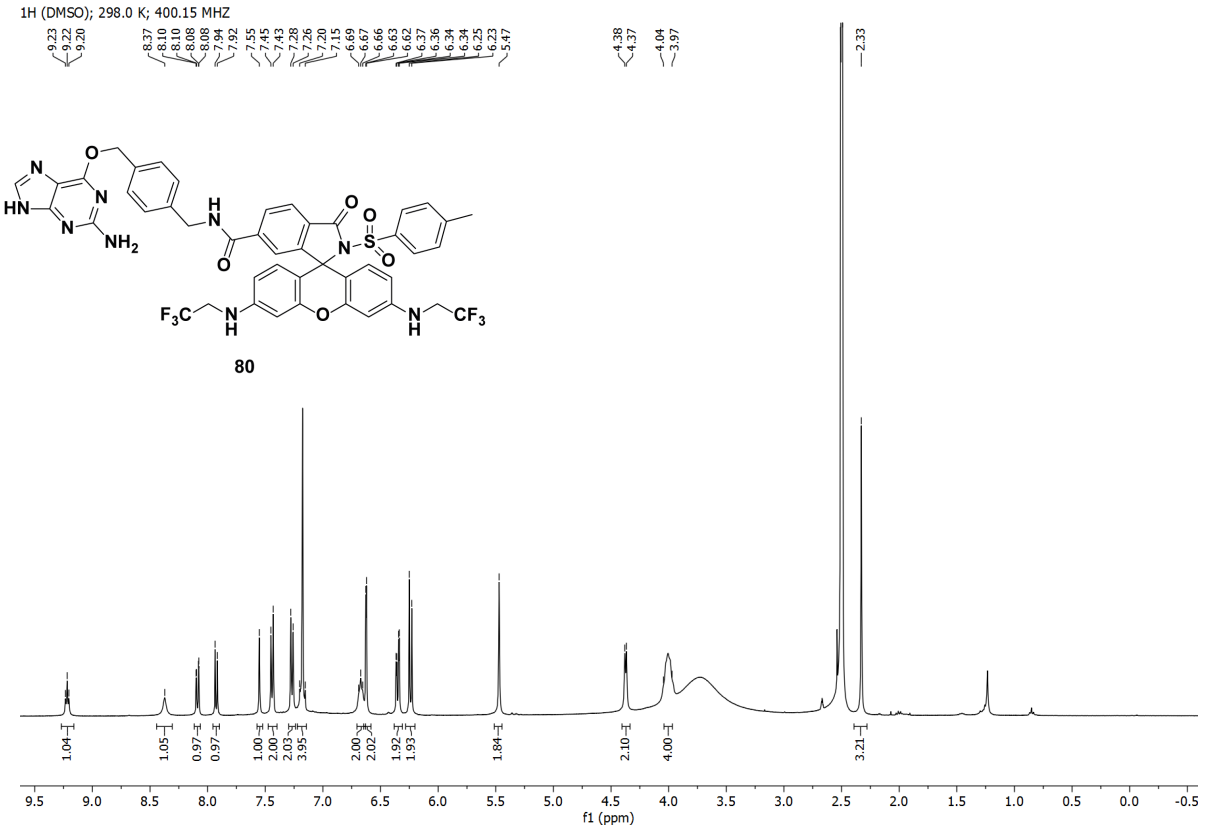

80

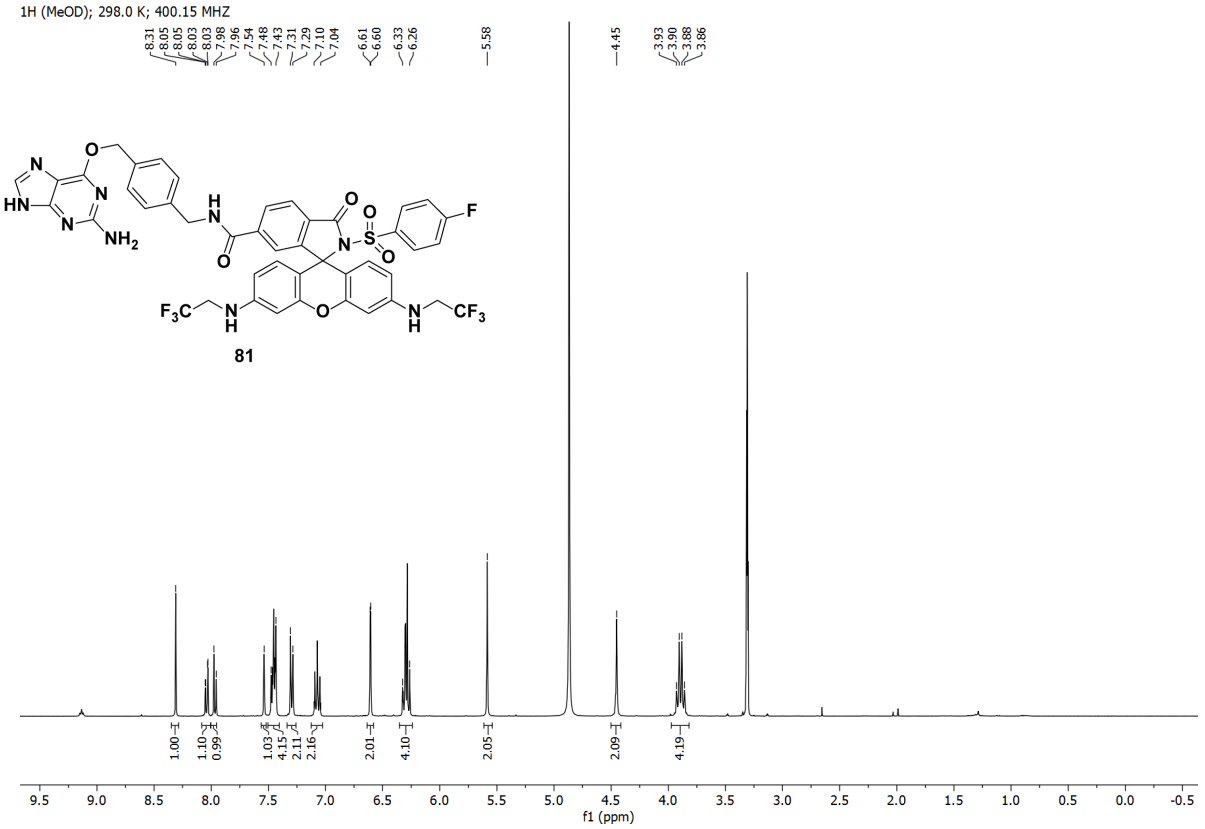

81

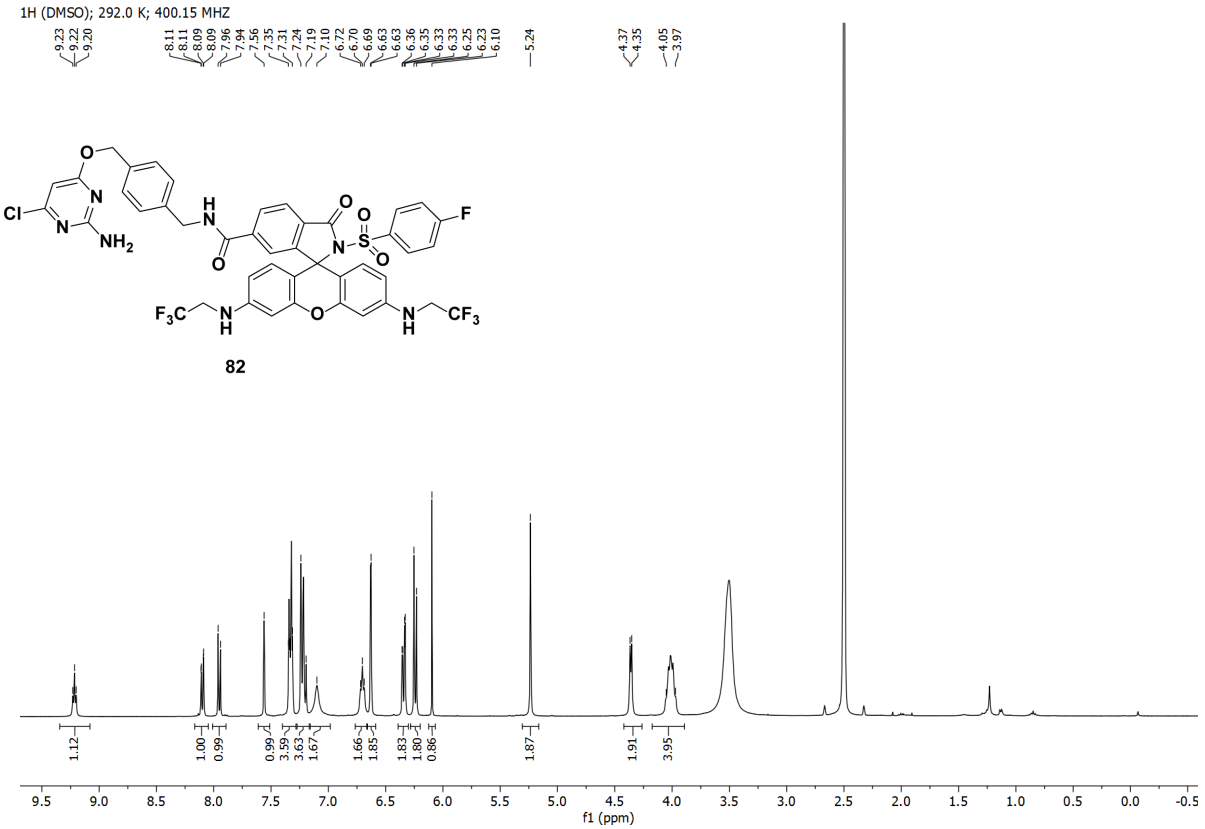

82

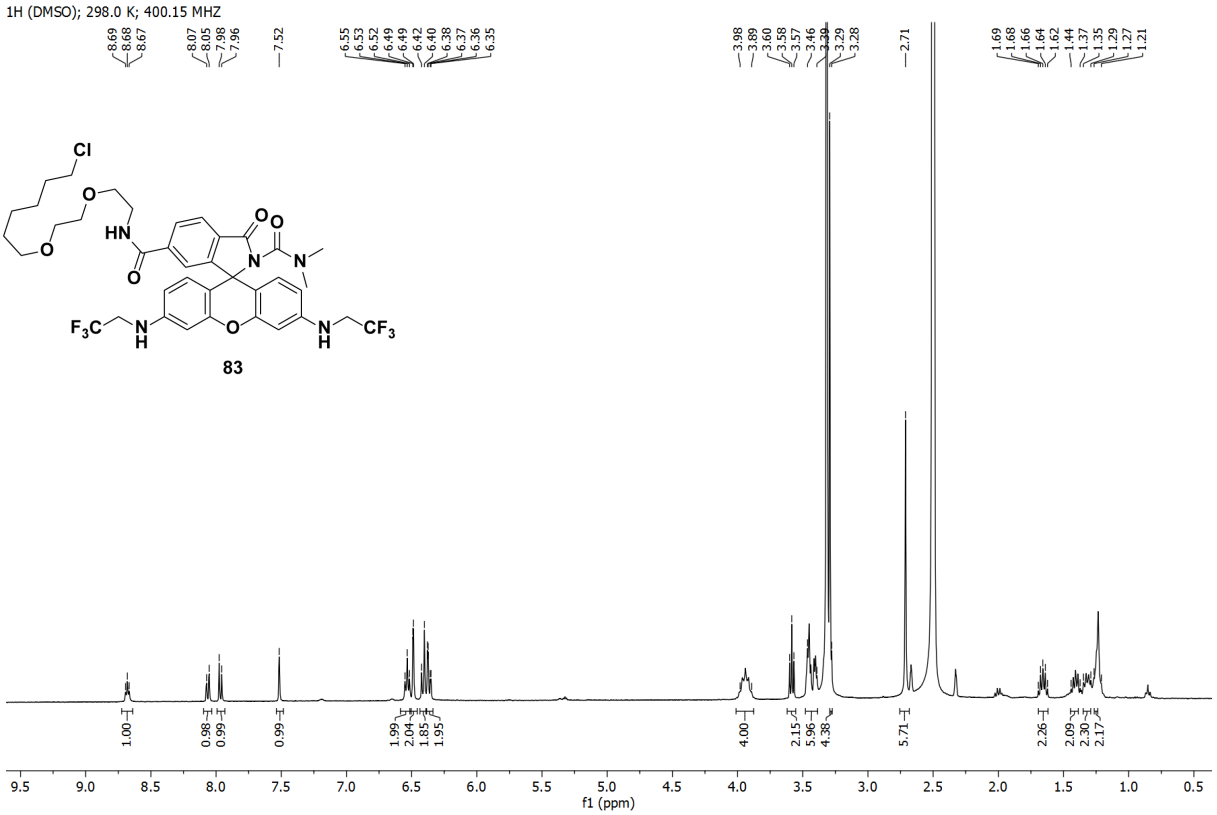

83

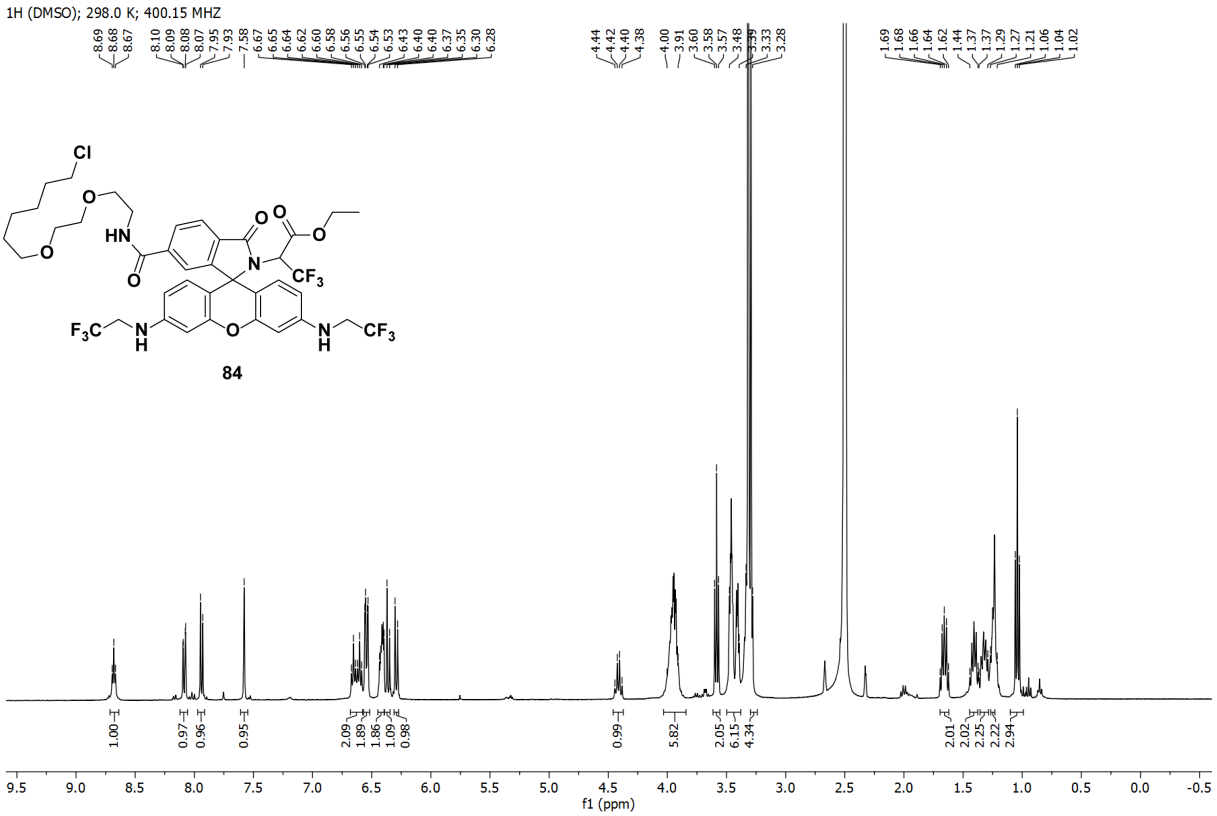

84

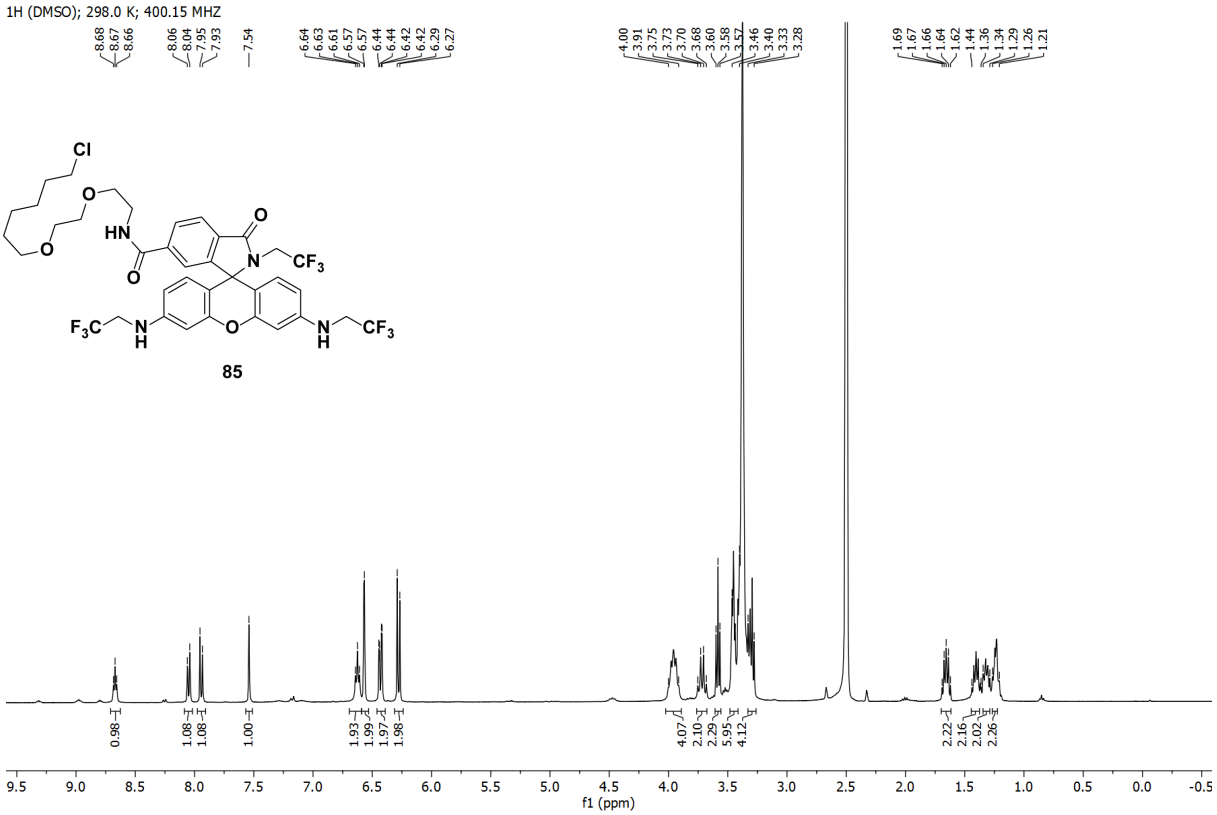

85

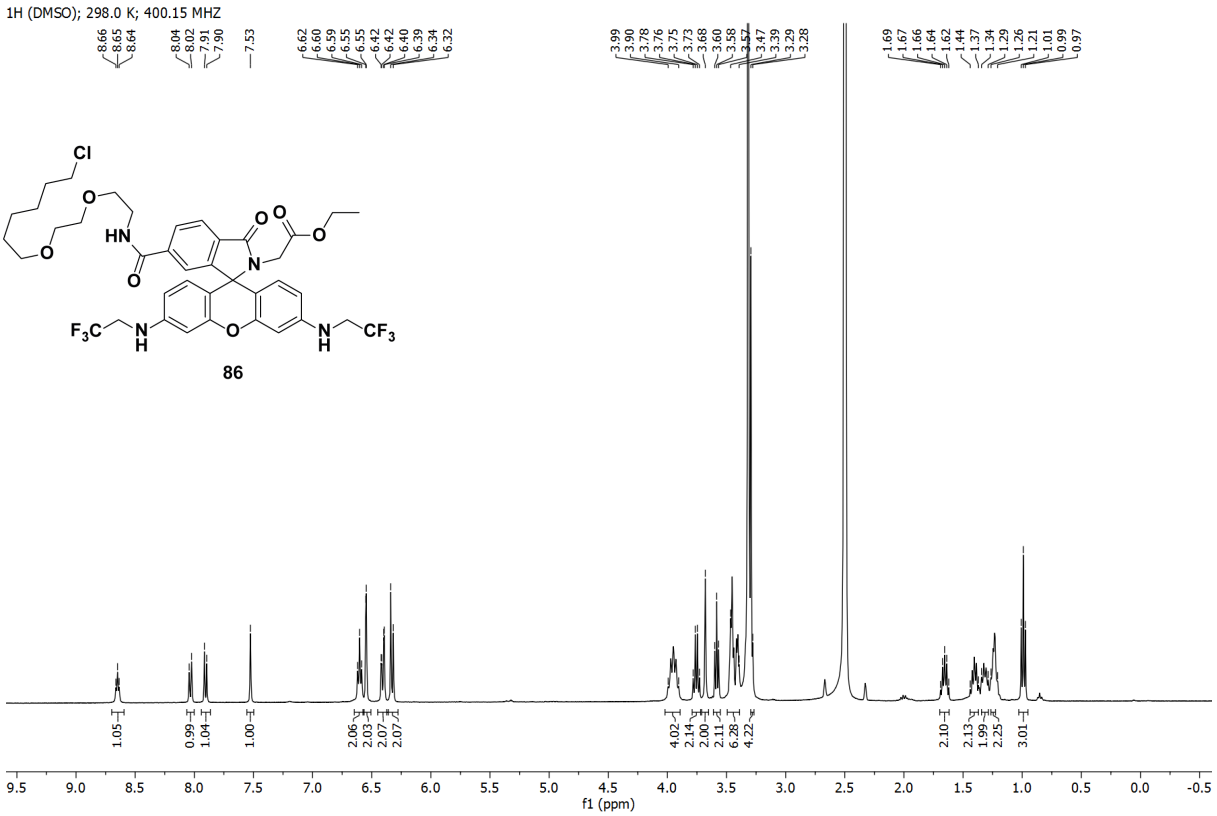

86

1H (CDCl3); 298.0 K; 400.15 MHZ

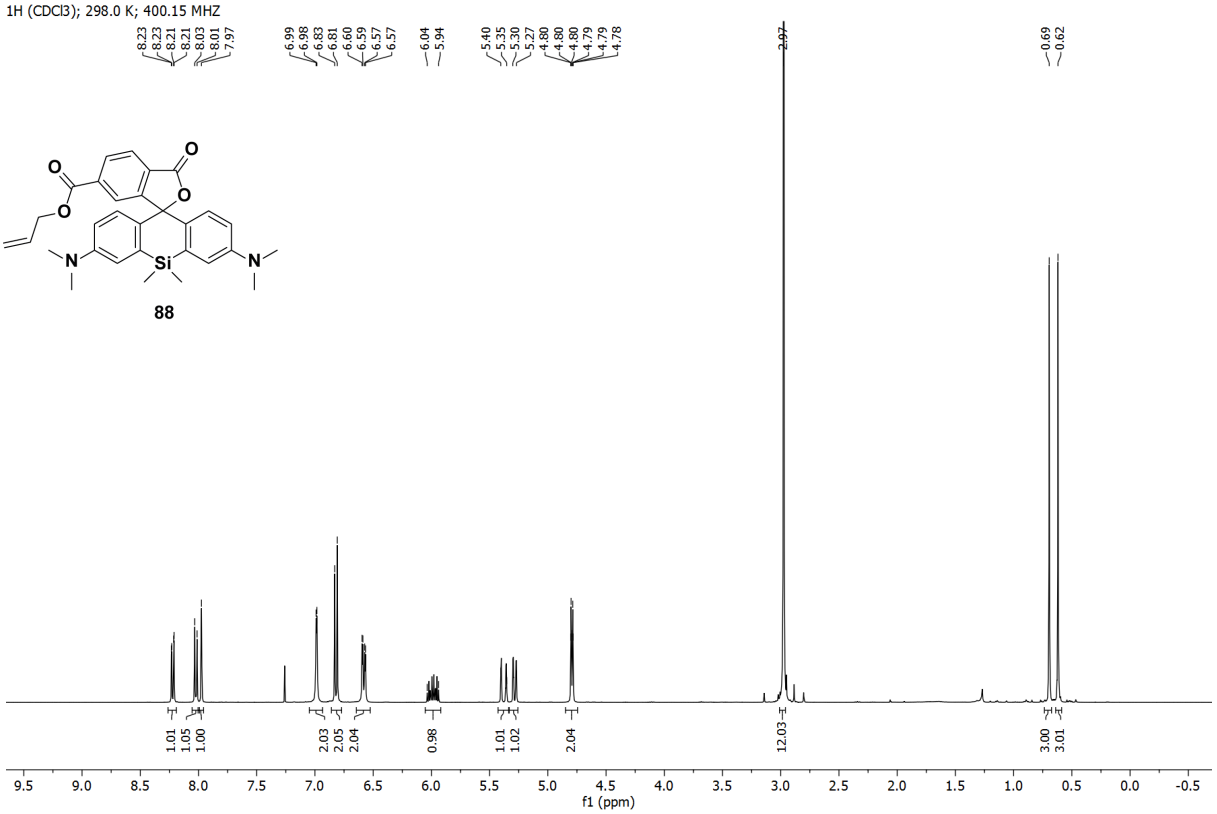

88

13C (CDCl3); 298.0 K; 100.63 MHZ

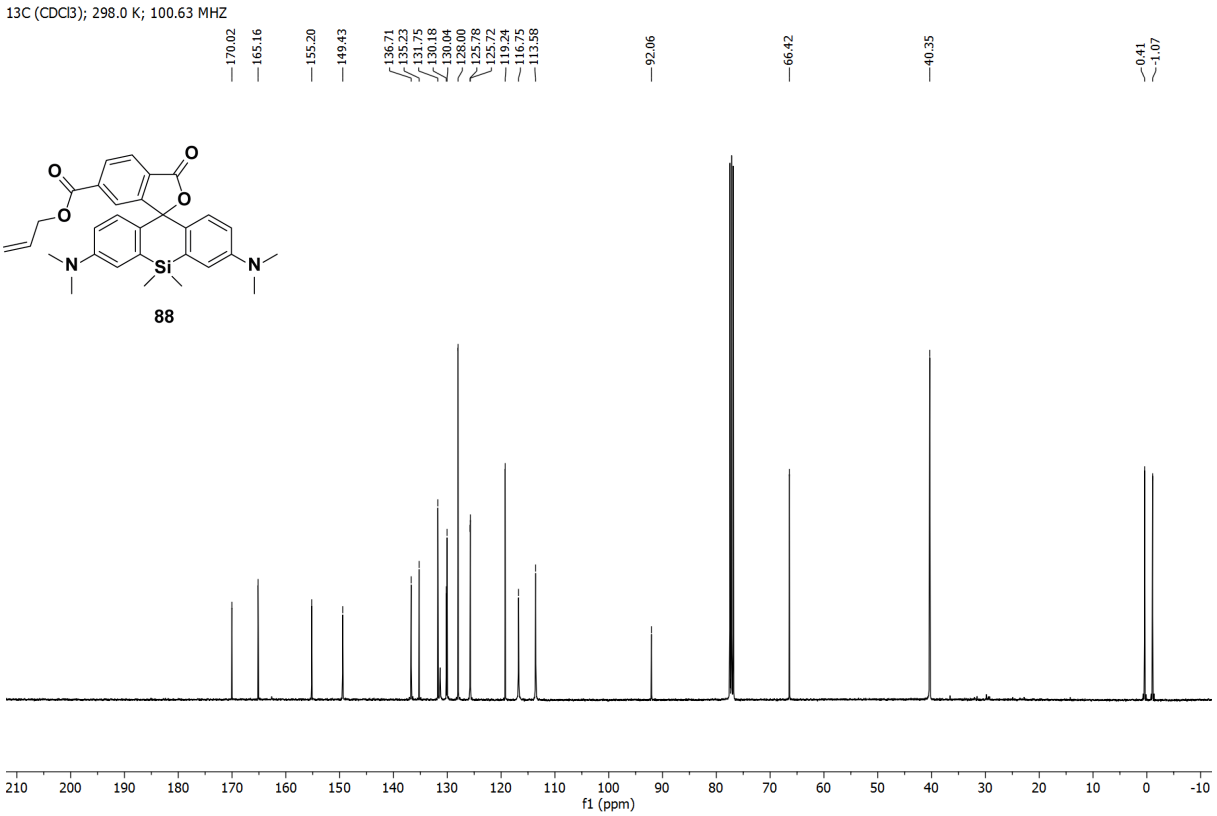

88

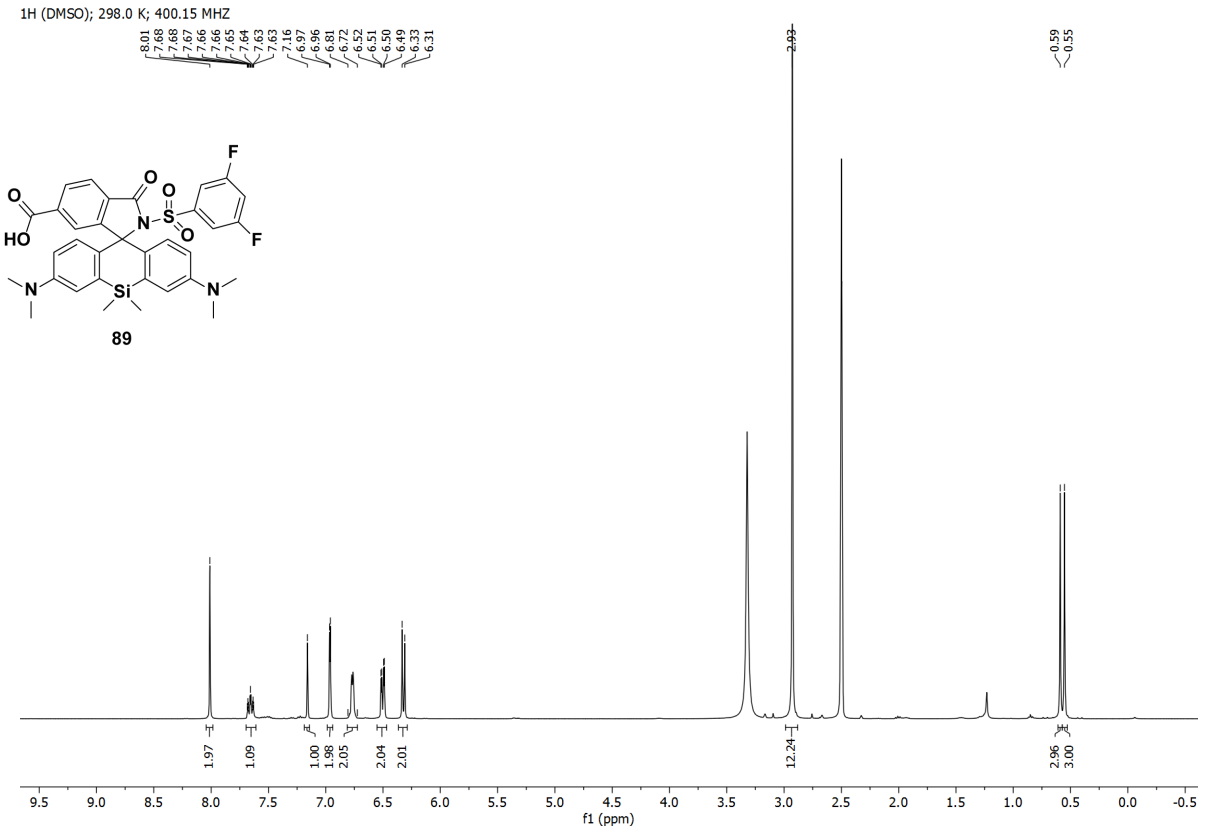
1H (DMSO); 298.0 K; 400.15 MHZ
8.01
7.68
7.68
7.67
7.66
7.66
7.65
7.64
7.63
7.63
7.16
6.97
6.96
6.81
6.72
6.52
6.51
6.50
6.49
6.33
6.31
2.93
0.59
0.55
F
O
O
O
HO
N
S
O
F
N
Si
N
89
1.97
1.09
1.00
1.98
2.05
2.04
2.01
12.24
2.96
3.00
9.5
9.0
8.5
8.0
7.5
7.0
6.5
6.0
5.5
5.0
4.5
4.0
3.5
3.0
2.5
2.0
1.5
1.0
0.5
0.0
-0.5
f1 (ppm)

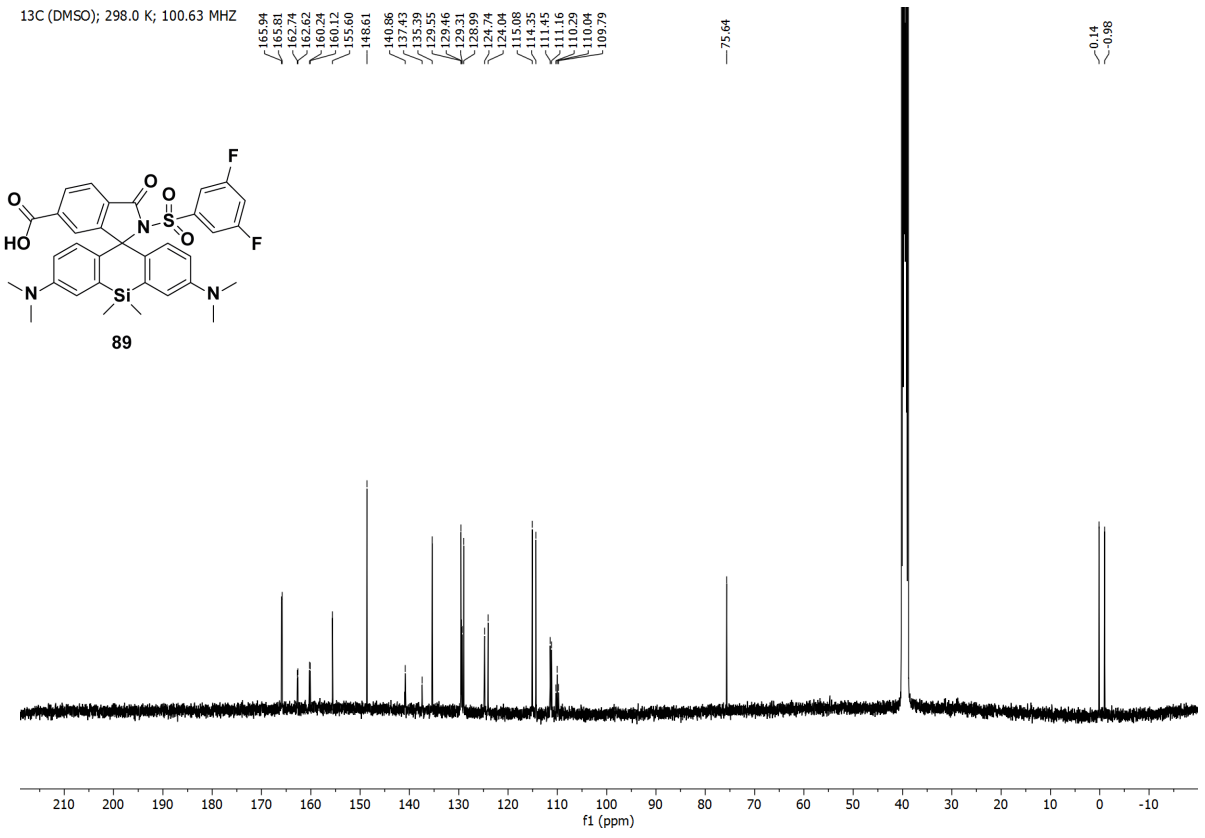
13C (DMSO); 298.0 K; 100.63 MHZ
165.94
165.81
162.74
162.62
160.24
160.12
155.60
148.61
140.86
137.43
135.39
129.55
129.46
129.31
128.99
124.74
124.04
115.08
114.35
111.45
111.16
110.29
110.04
109.79
75.64
0.14
-0.98
F
O
O
O
HO
N
S
O
F
N
Si
N
89
210
200
190
180
170
160
150
140
130
120
110
100
90
80
70
60
50
40
30
20
10
0
-10
f1 (ppm)

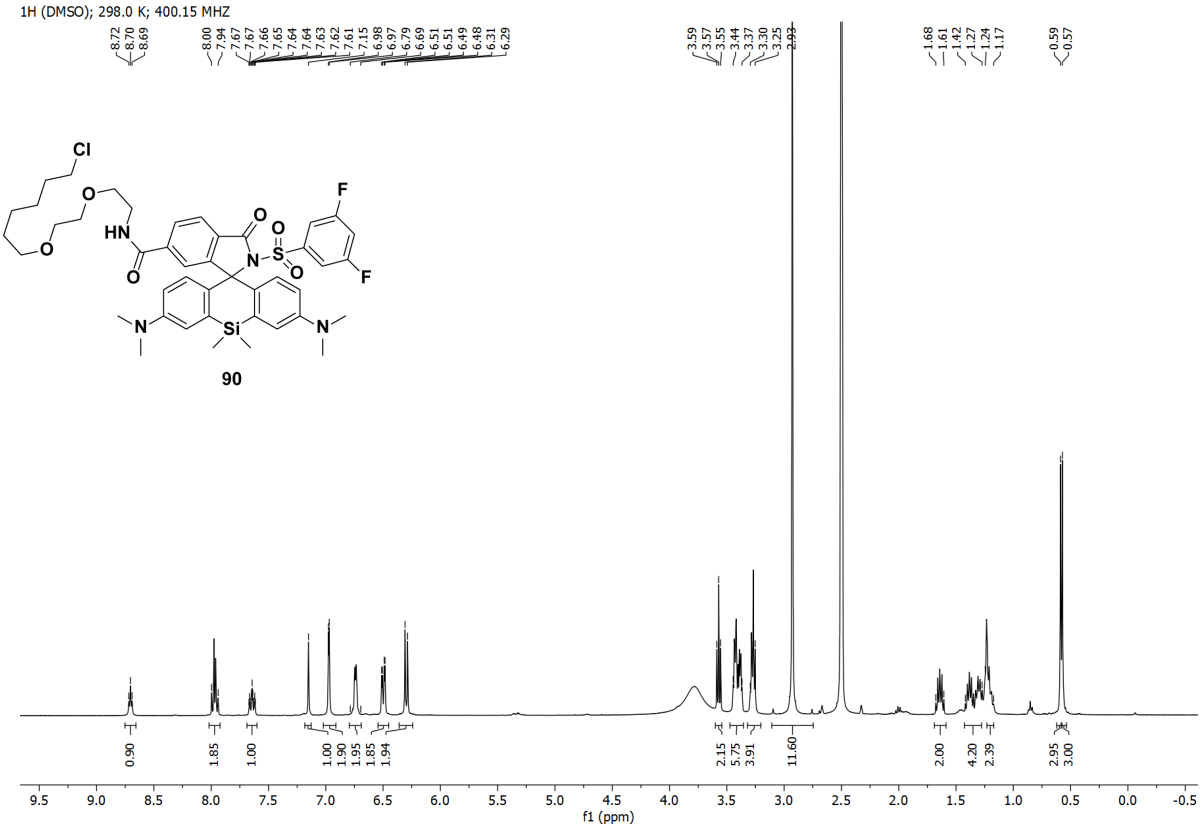

90

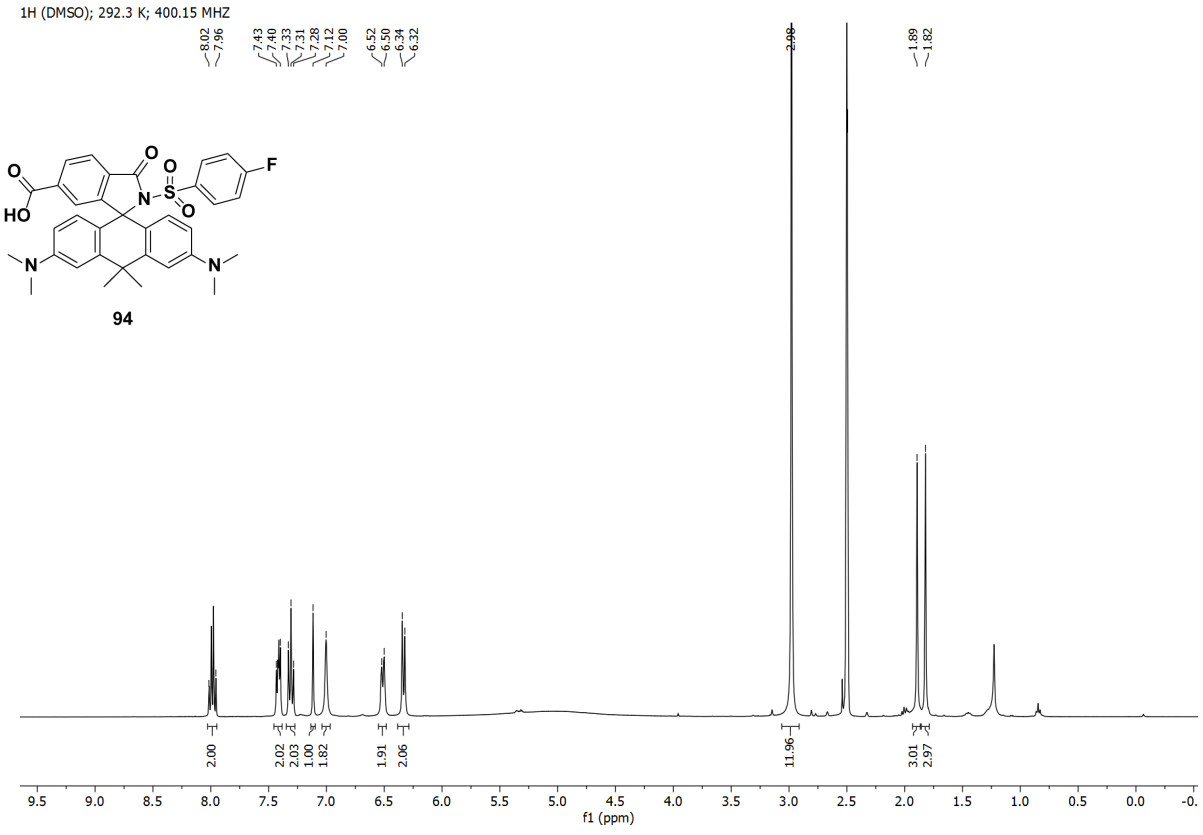

94

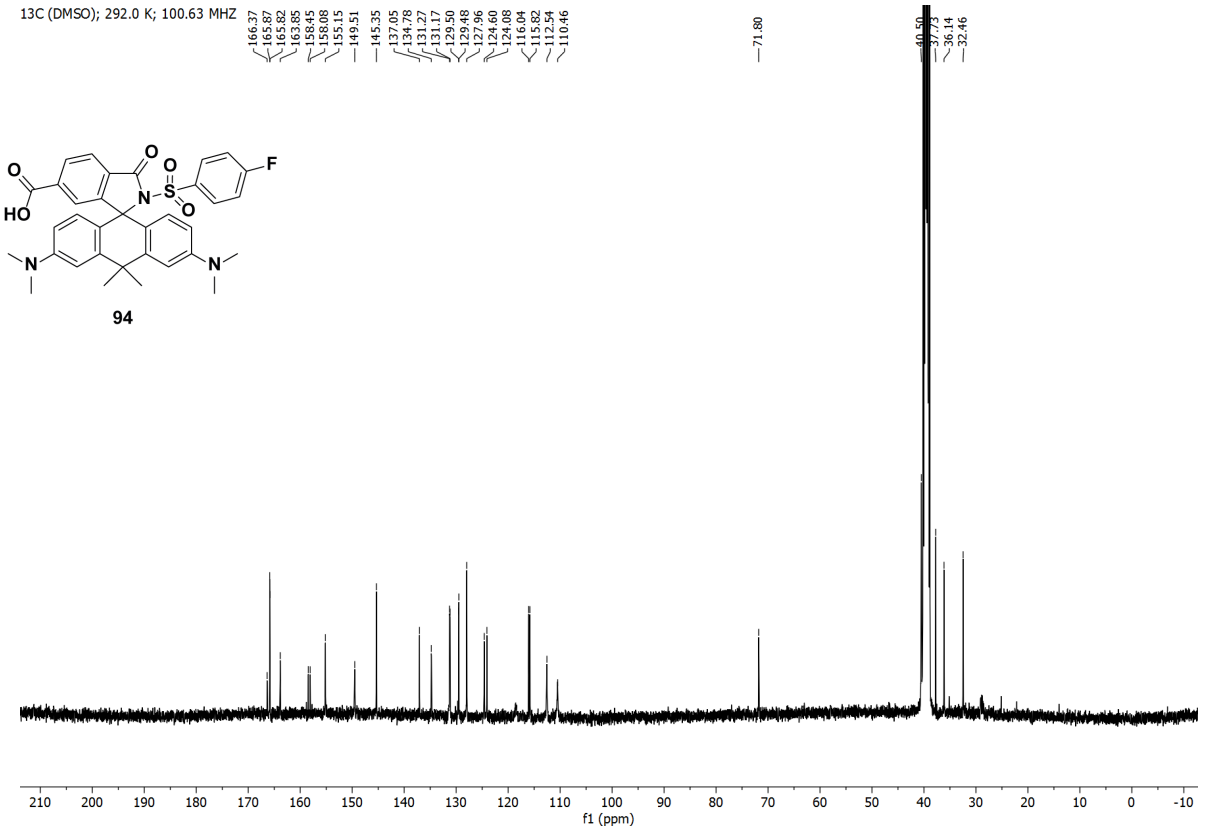
13C (DMSO); 292.0 K; 100.63 MHZ
166.37
165.87
165.82
163.85
158.45
158.08
155.15
149.51
145.35
137.05
134.78
131.27
131.17
129.50
129.48
127.96
124.60
124.08
116.04
115.82
112.54
110.46
71.80
40.50
37.03
36.14
32.46
f1 (ppm)

94

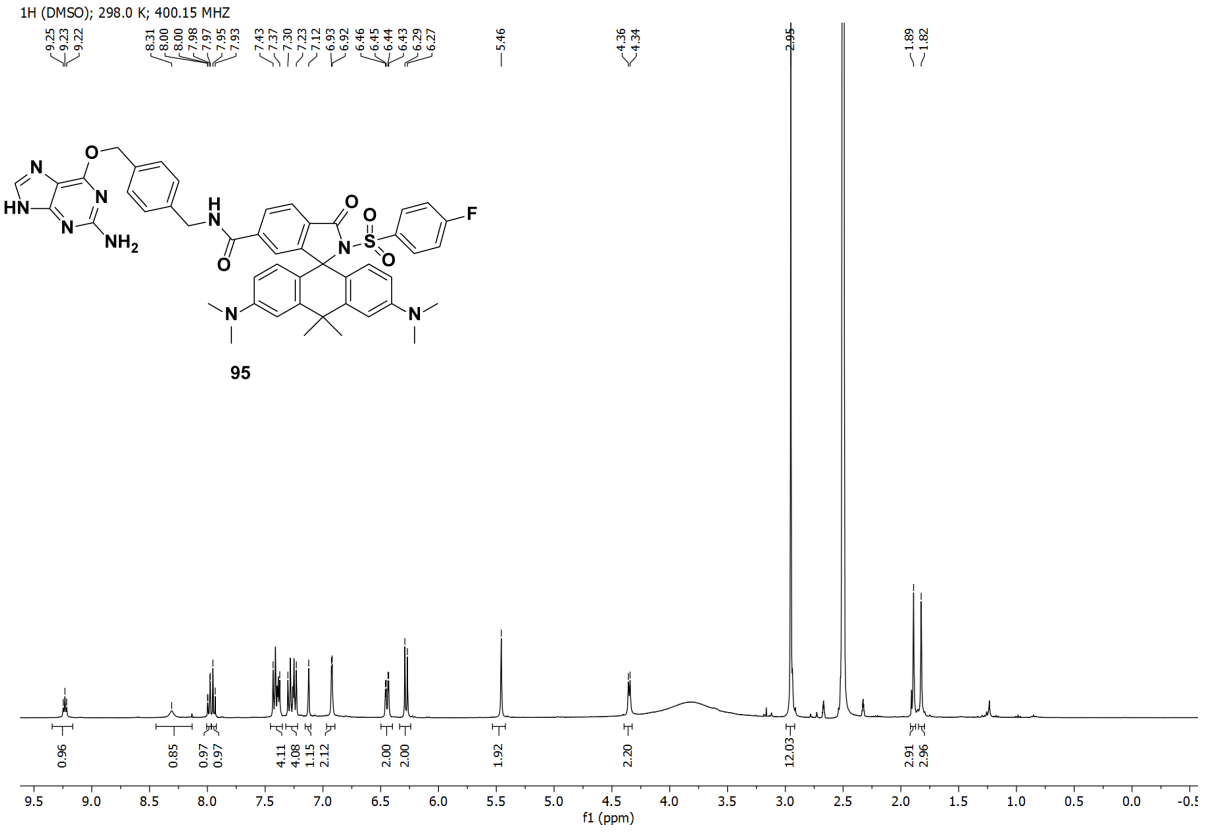
1H (DMSO); 298.0 K; 400.15 MHZ
9.25
9.23
9.22
8.31
8.00
8.00
7.98
7.97
7.95
7.93
7.43
7.37
7.30
7.23
7.12
6.93
6.92
6.46
6.45
6.44
6.43
6.29
6.27
5.46
4.36
4.34
2.95
1.89
1.82
0.96
0.85
0.97
0.97
4.11
4.08
1.15
2.12
2.00
2.00
1.92
2.20
12.03
2.91
2.96
f1 (ppm)

95

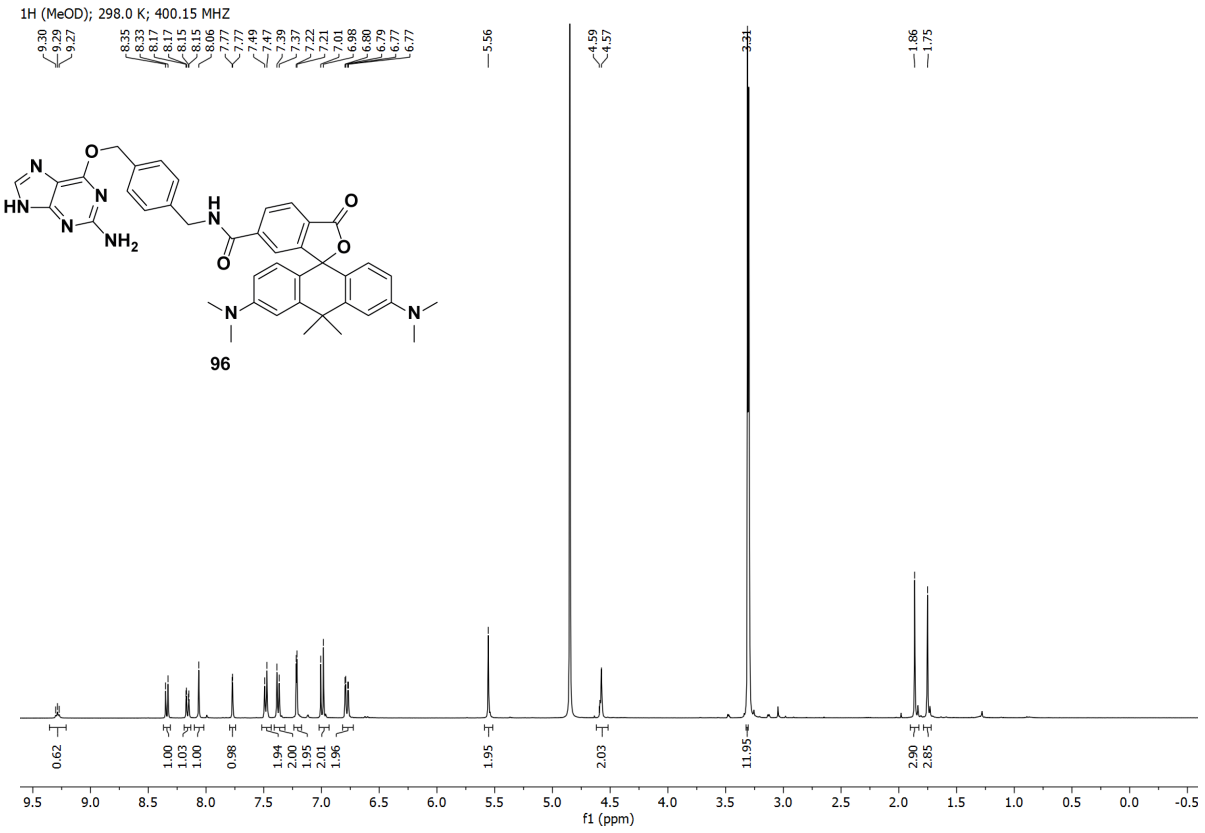
1H (MeOD); 298.0 K; 400.15 MHZ
9.30
9.29
9.27
8.35
8.33
8.17
8.17
8.15
8.15
8.06
7.77
7.77
7.49
7.47
7.39
7.37
7.22
7.21
7.01
6.98
6.80
6.79
6.77
6.77
5.56
4.59
4.57
3.31
1.86
1.75
0.62
1.00
1.03
1.00
0.98
1.94
2.00
1.95
2.01
1.96
1.95
2.03
11.95
2.90
2.85
f1 (ppm)

96

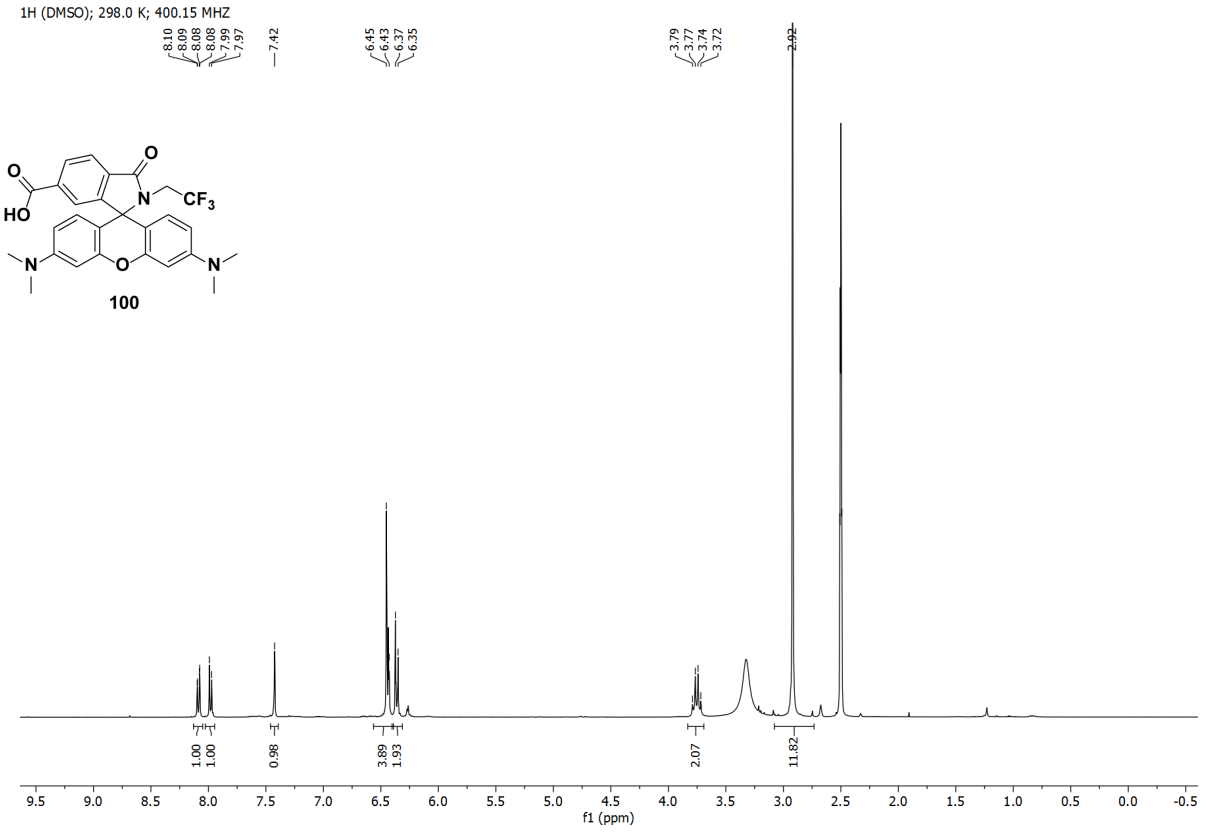
1H (DMSO); 298.0 K; 400.15 MHZ
8.10
8.09
8.08
8.08
7.99
7.97
7.42
6.45
6.43
6.37
6.35
3.79
3.77
3.74
3.72
2.92
1.00
1.00
0.98
3.89
1.93
2.07
11.82
f1 (ppm)

100

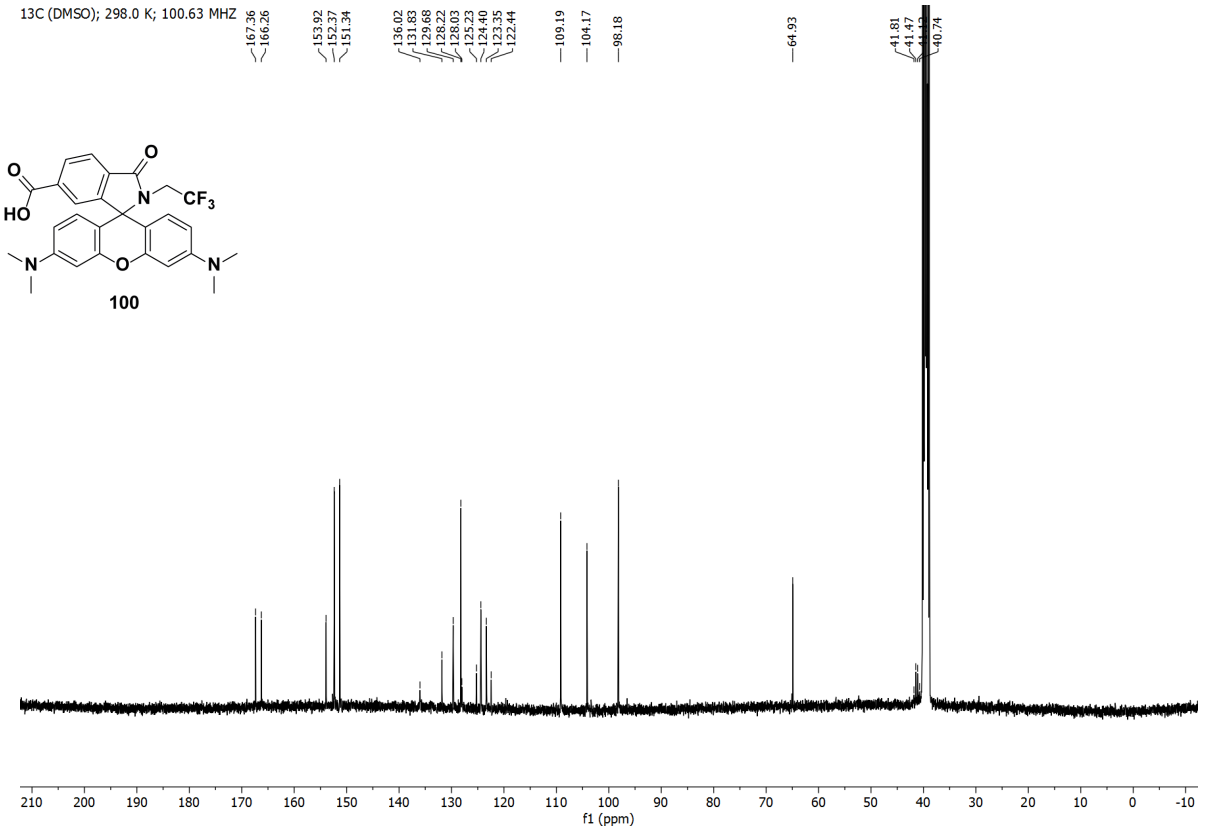
13C (DMSO); 298.0 K; 100.63 MHZ
167.36
166.26
153.92
152.37
151.34
136.02
131.83
129.68
128.22
128.03
125.23
124.40
123.35
122.44
109.19
104.17
98.18
64.93
41.81
41.47
40.74
100
f1 (ppm)

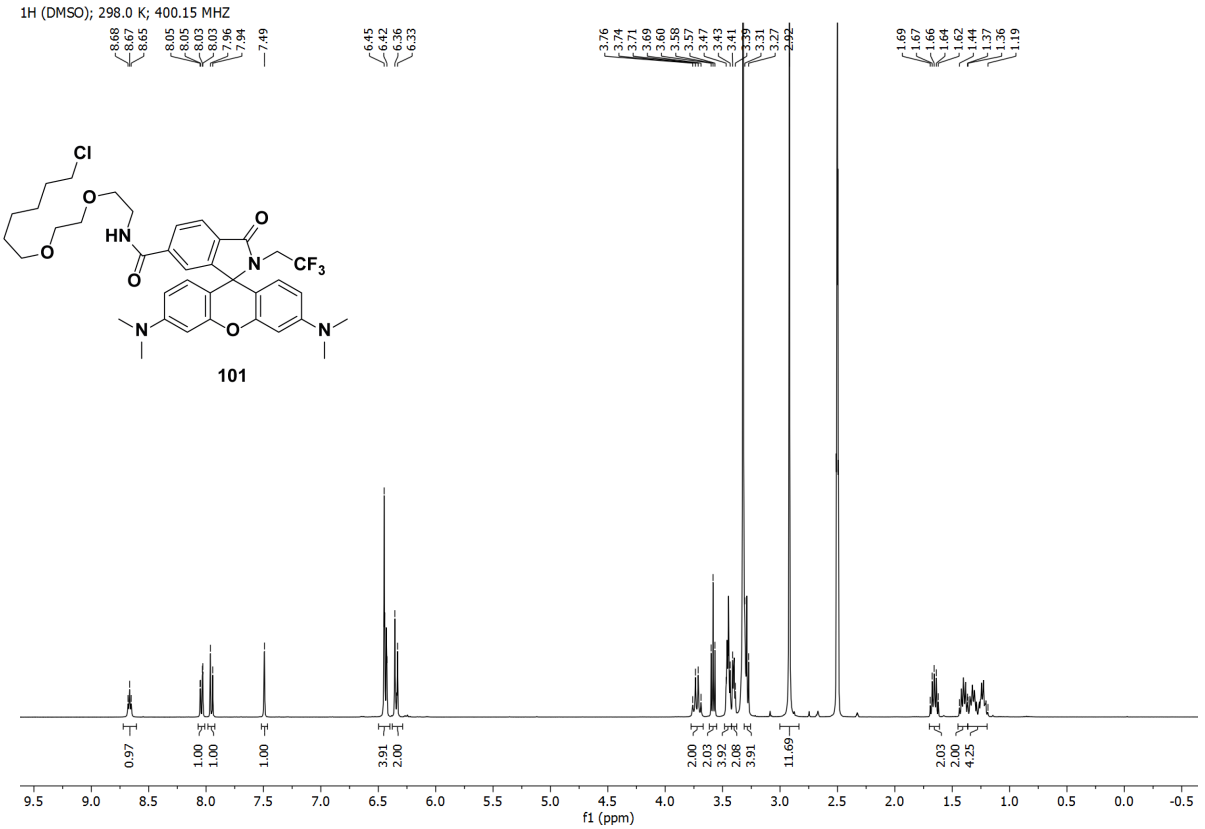
1H (DMSO); 298.0 K; 400.15 MHZ
8.68
8.67
8.65
8.05
8.05
8.03
8.03
7.96
7.94
7.49
6.45
6.42
6.36
6.33
3.76
3.74
3.71
3.69
3.60
3.58
3.57
3.47
3.43
3.41
3.39
3.31
3.27
2.92
1.69
1.67
1.66
1.64
1.62
1.44
1.37
1.36
1.19
0.97
1.00
1.00
1.00
3.91
2.00
2.00
2.03
3.92
2.08
3.91
11.69
2.03
2.00
4.25
101
f1 (ppm)

1H (MeOD); 298.0 K; 400.15 MHZ

102

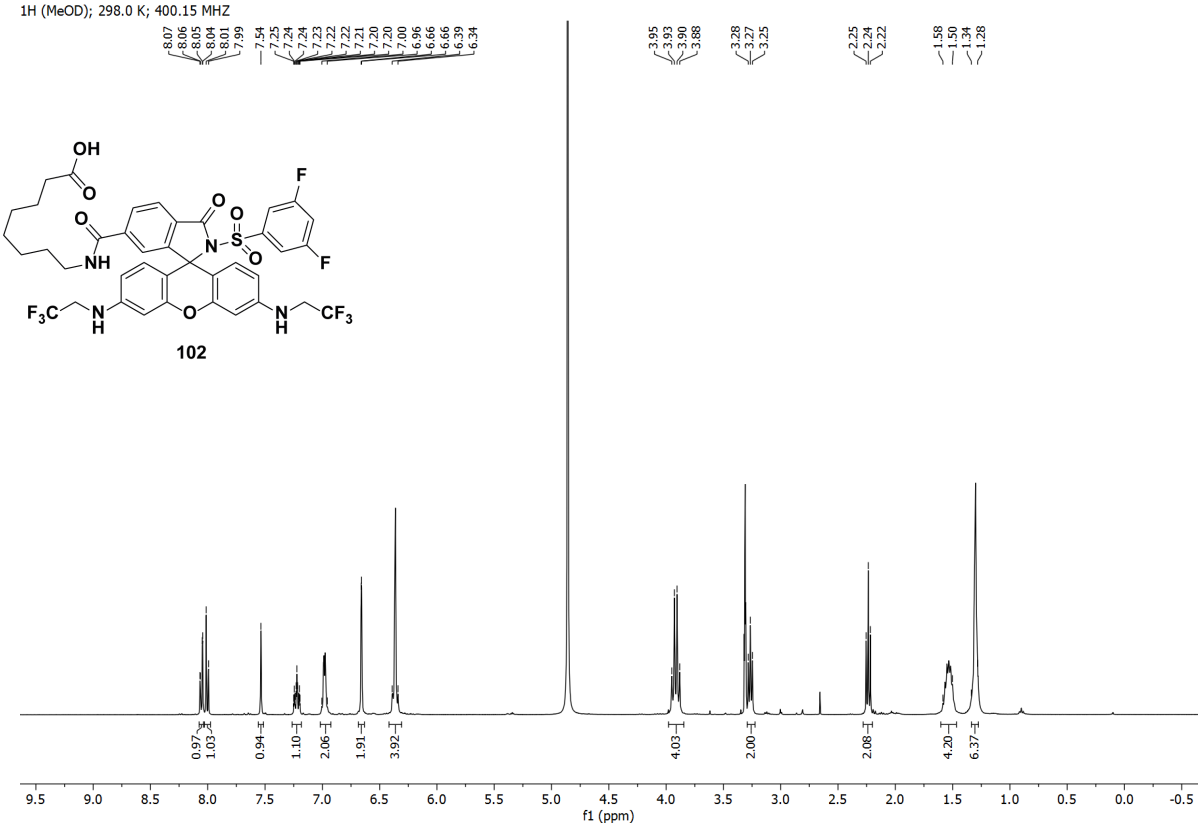

1H (MeOD); 298.0 K; 400.15 MHZ

103

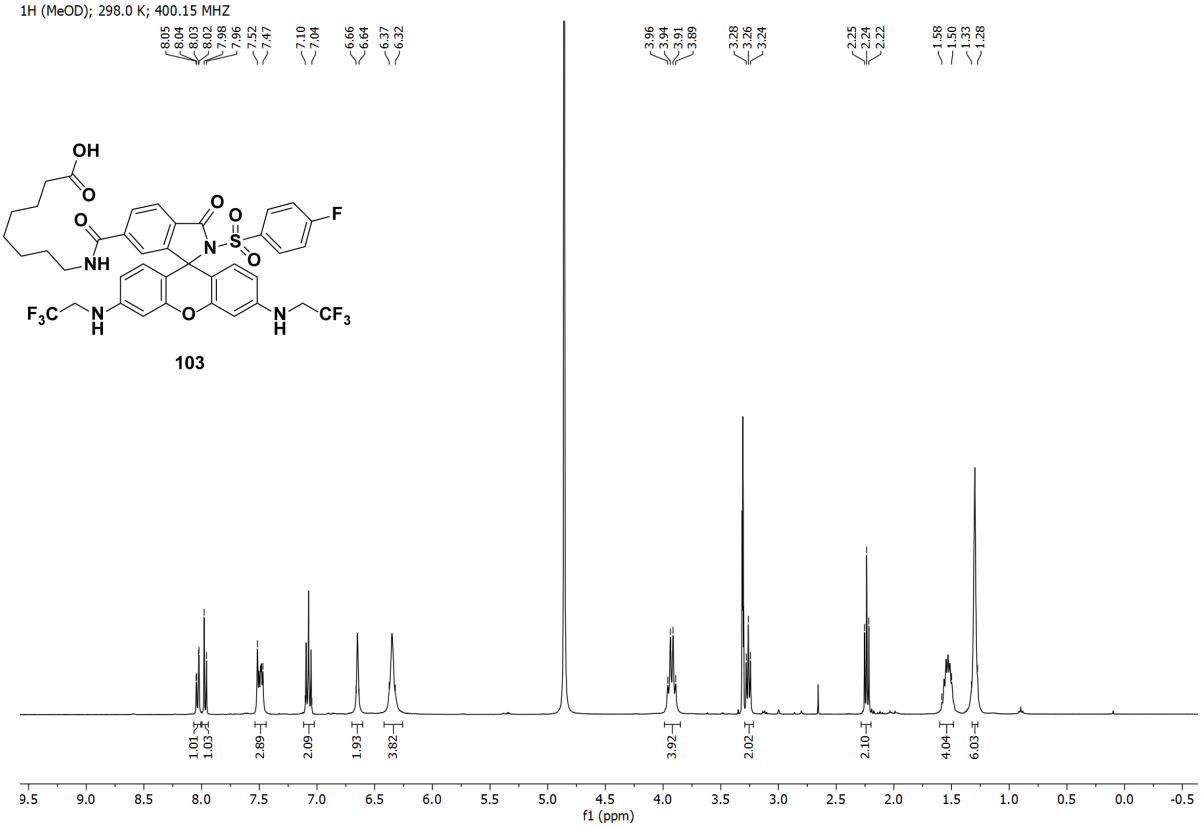

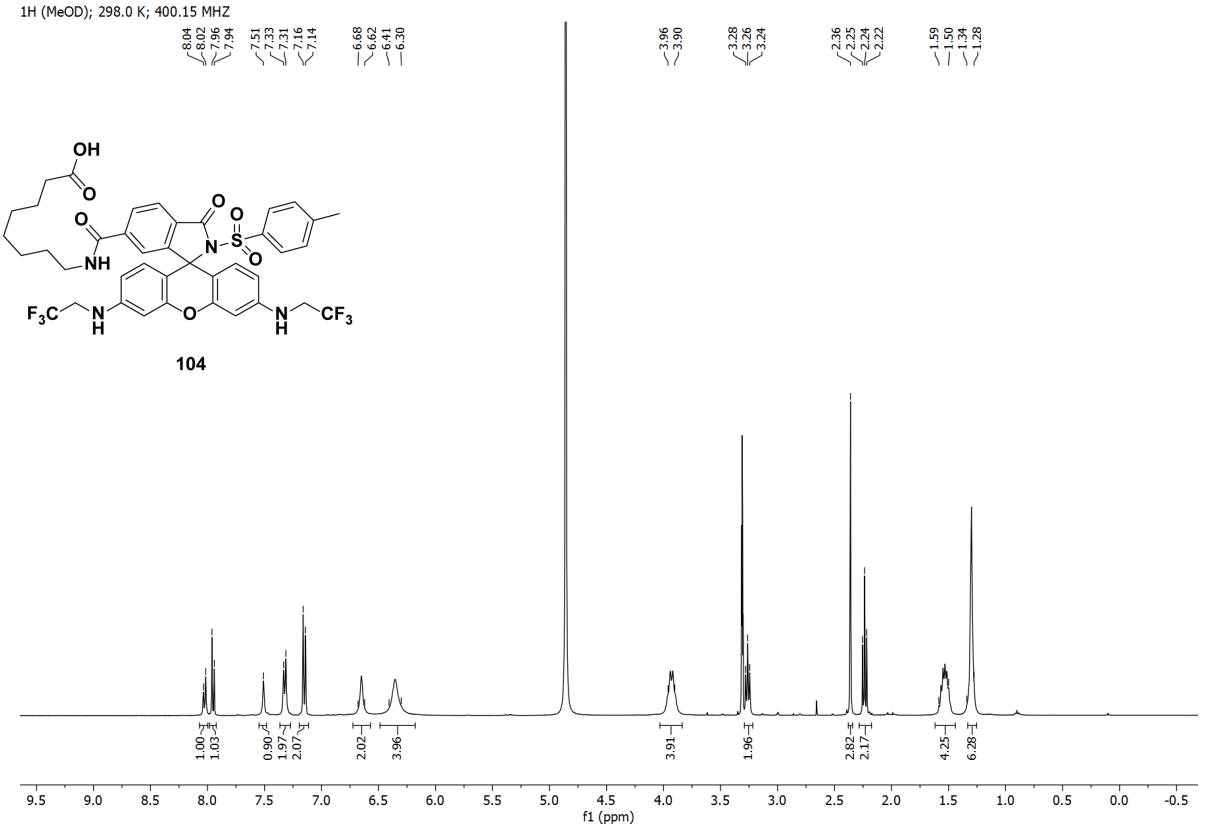
1H (MeOD); 298.0 K; 400.15 MHZ
8.04
8.02
7.96
7.94
7.51
7.33
7.31
7.16
7.14
6.68
6.62
6.41
6.30
3.96
3.90
3.28
3.26
3.24
2.36
2.25
2.24
2.22
1.59
1.50
1.34
1.28
1.00
1.03
0.90
1.97
2.07
2.02
3.96
3.91
1.96
2.82
2.17
4.25
6.28
f1 (ppm)

104

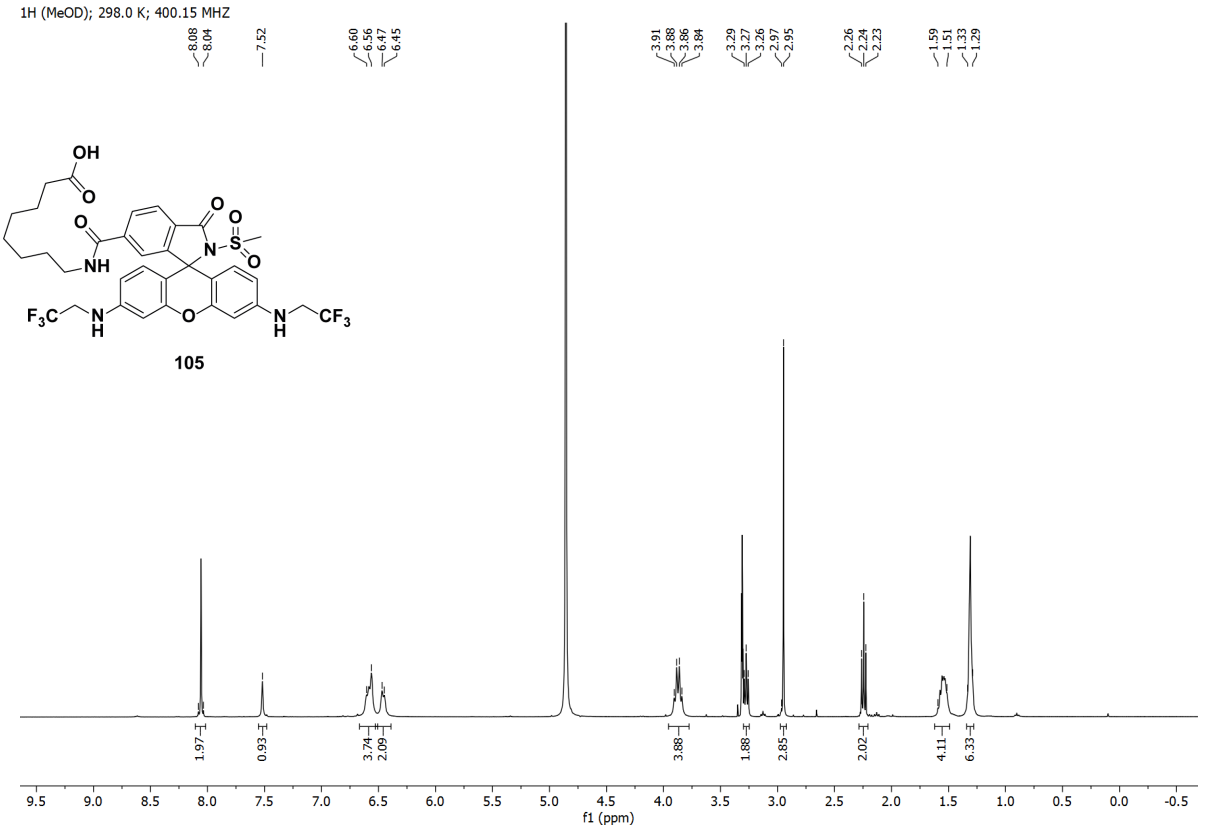
1H (MeOD); 298.0 K; 400.15 MHZ
8.08
8.04
7.52
6.60
6.56
6.47
6.45
3.91
3.88
3.86
3.84
3.29
3.27
3.26
2.97
2.95
2.26
2.24
2.23
1.59
1.51
1.33
1.29
1.97
0.93
3.74
2.09
3.88
1.88
2.85
2.02
4.11
6.33
f1 (ppm)

105

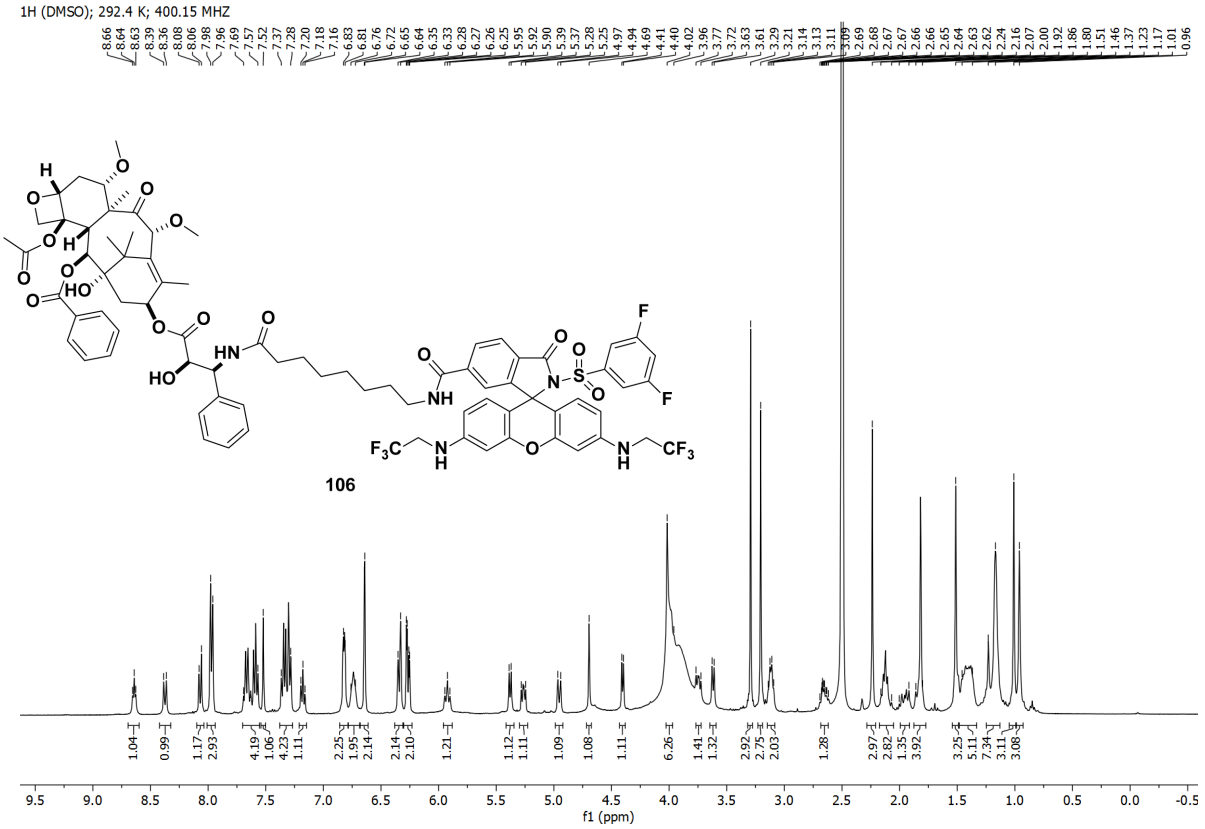
1H (DMSO); 292.4 K; 400.15 MHZ
106
f1 (ppm)

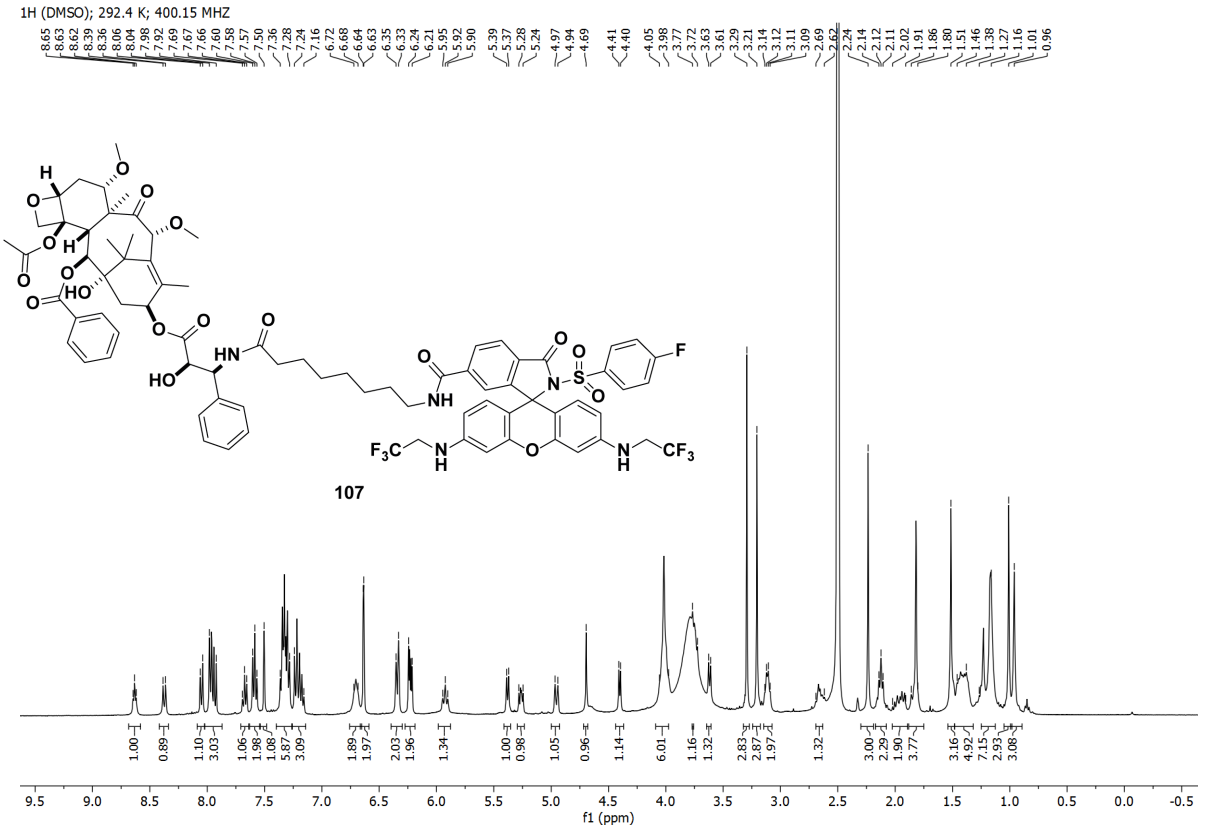
1H (DMSO); 292.4 K; 400.15 MHZ
107
f1 (ppm)

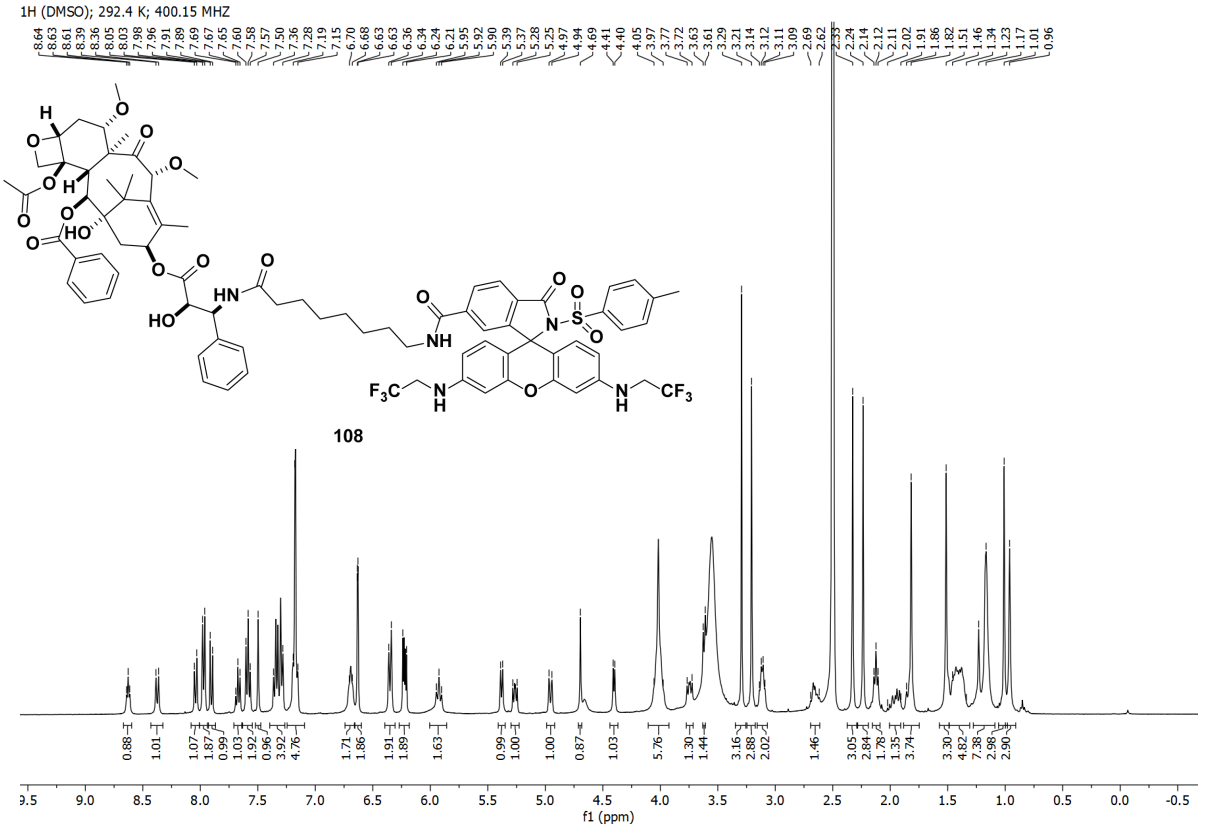
1H (DMSO); 292.4 K; 400.15 MHZ
108
f1 (ppm)

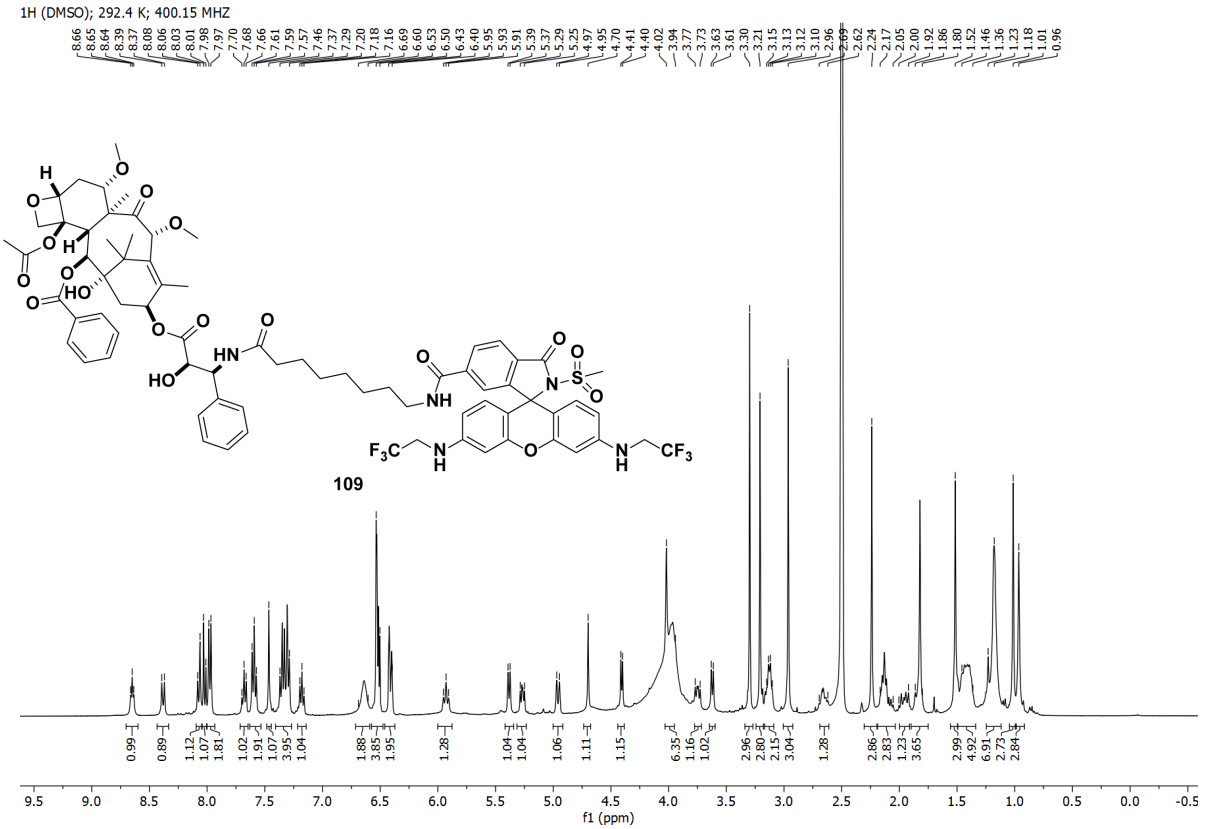
1H (DMSO); 292.4 K; 400.15 MHZ
109
f1 (ppm)

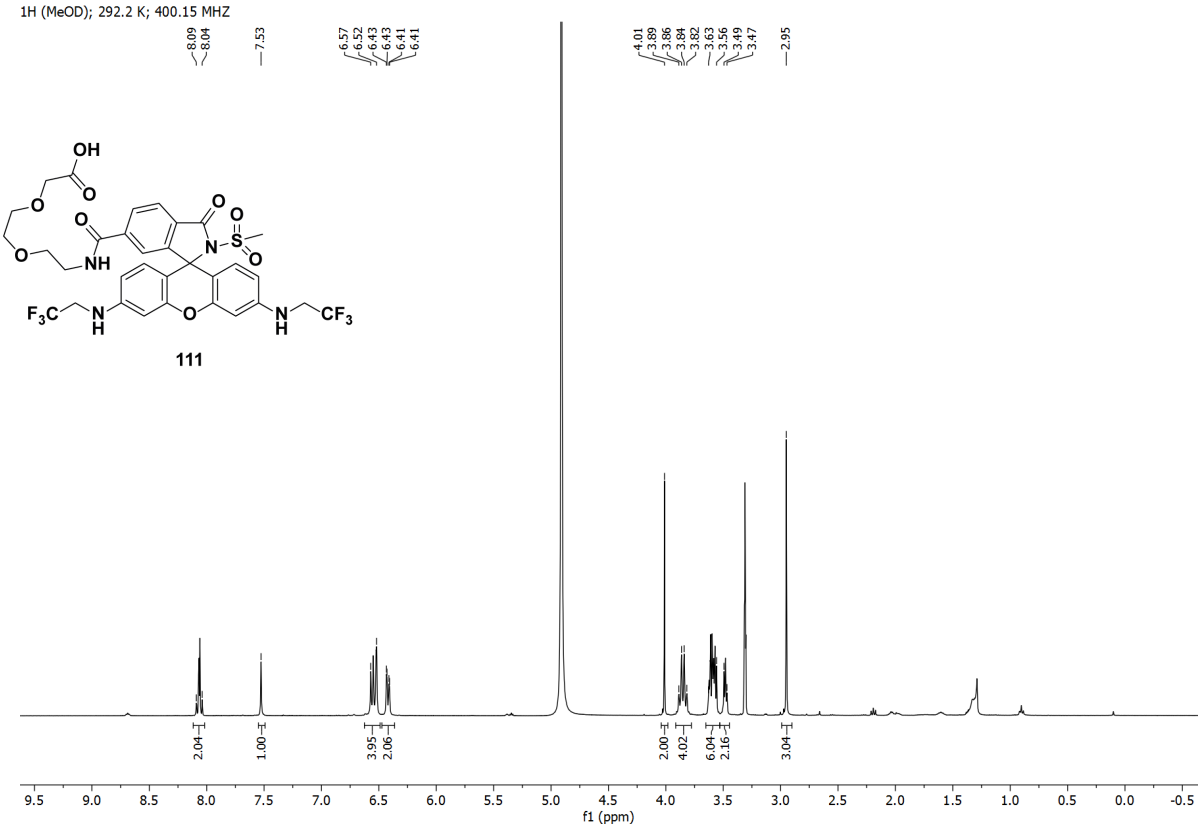

111

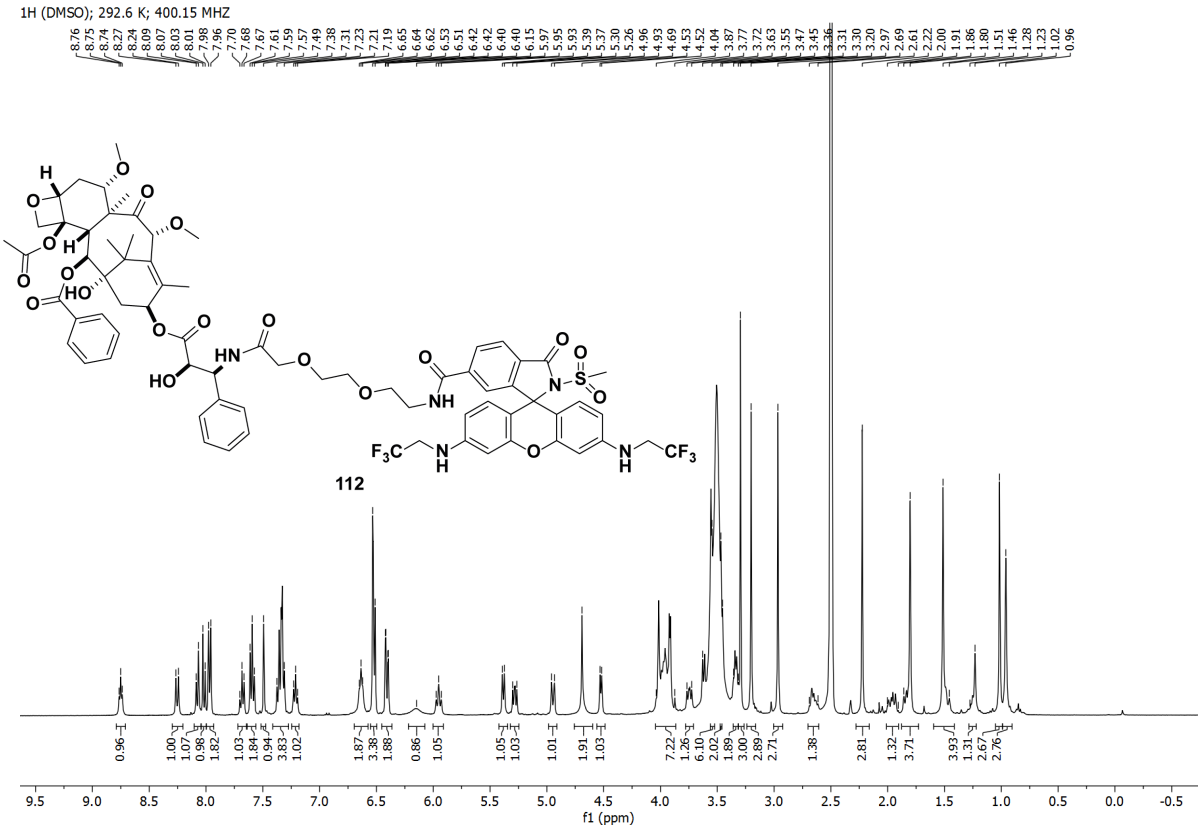

112

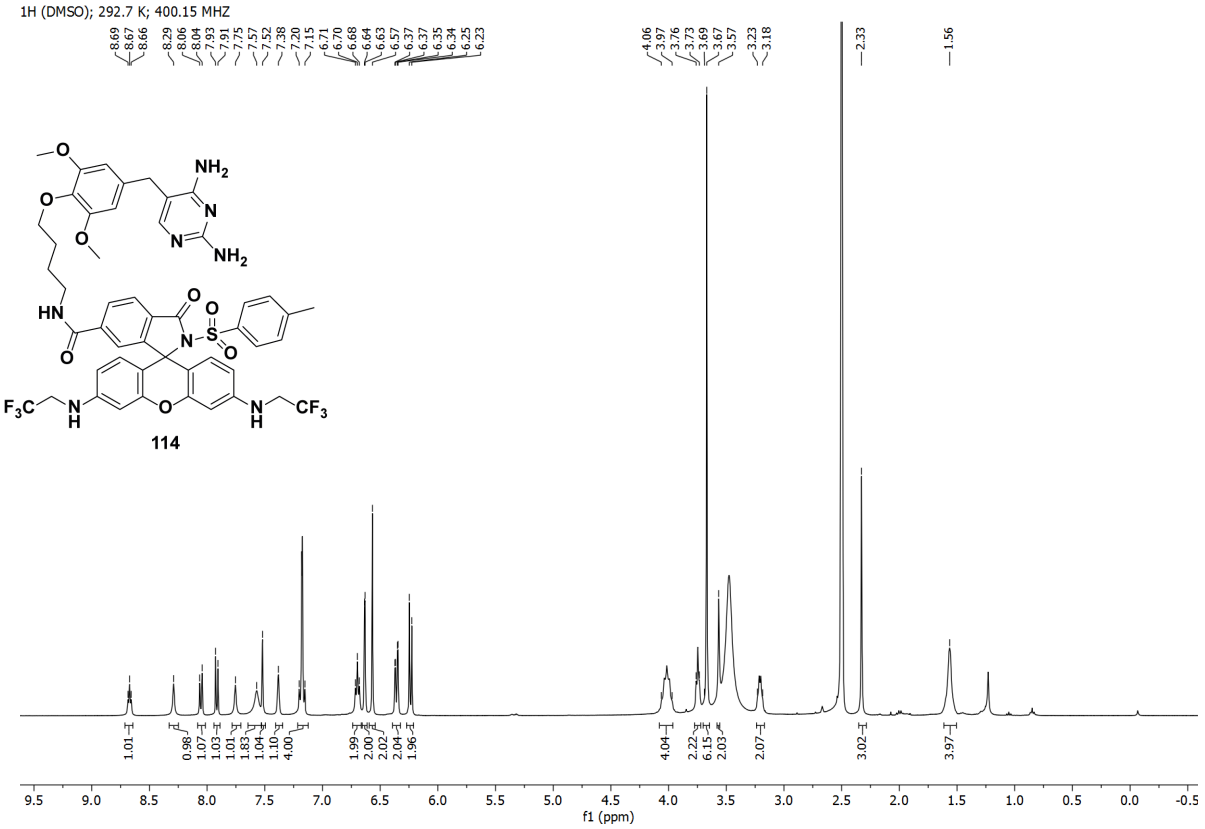

114

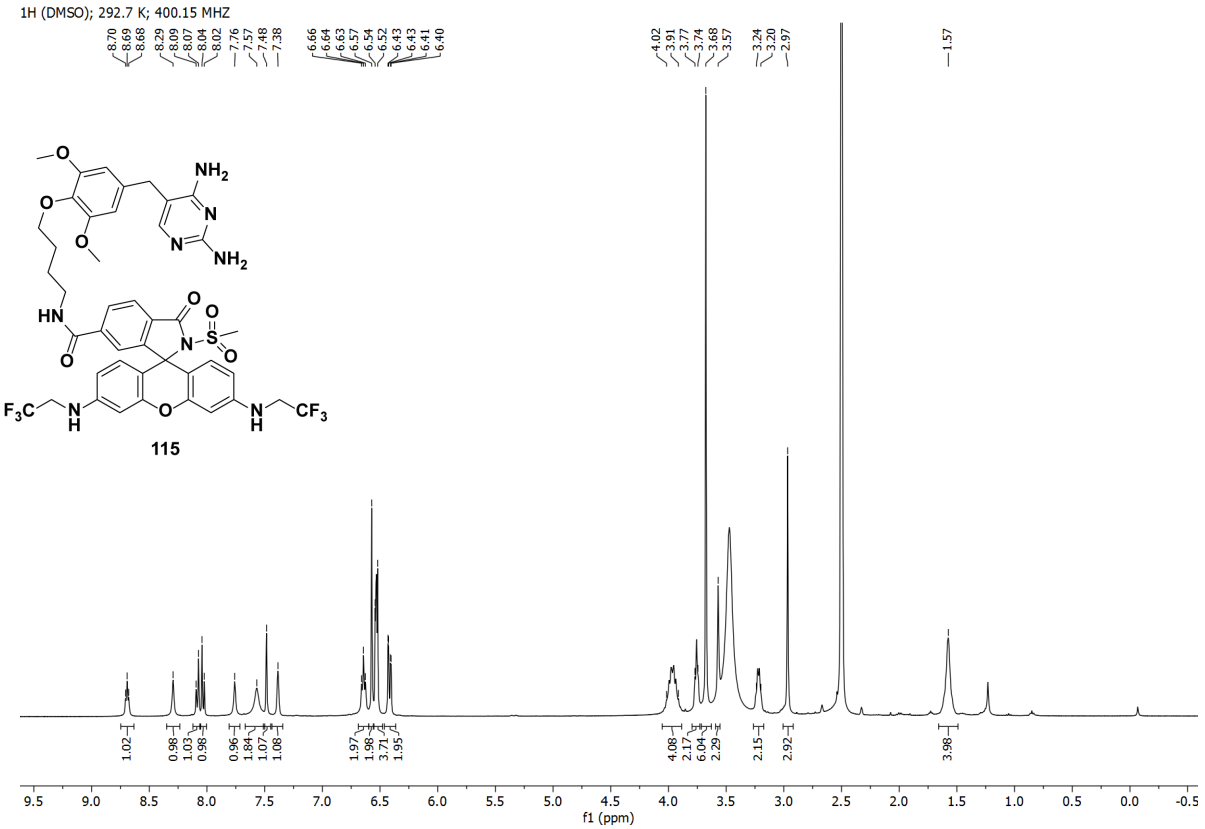

115

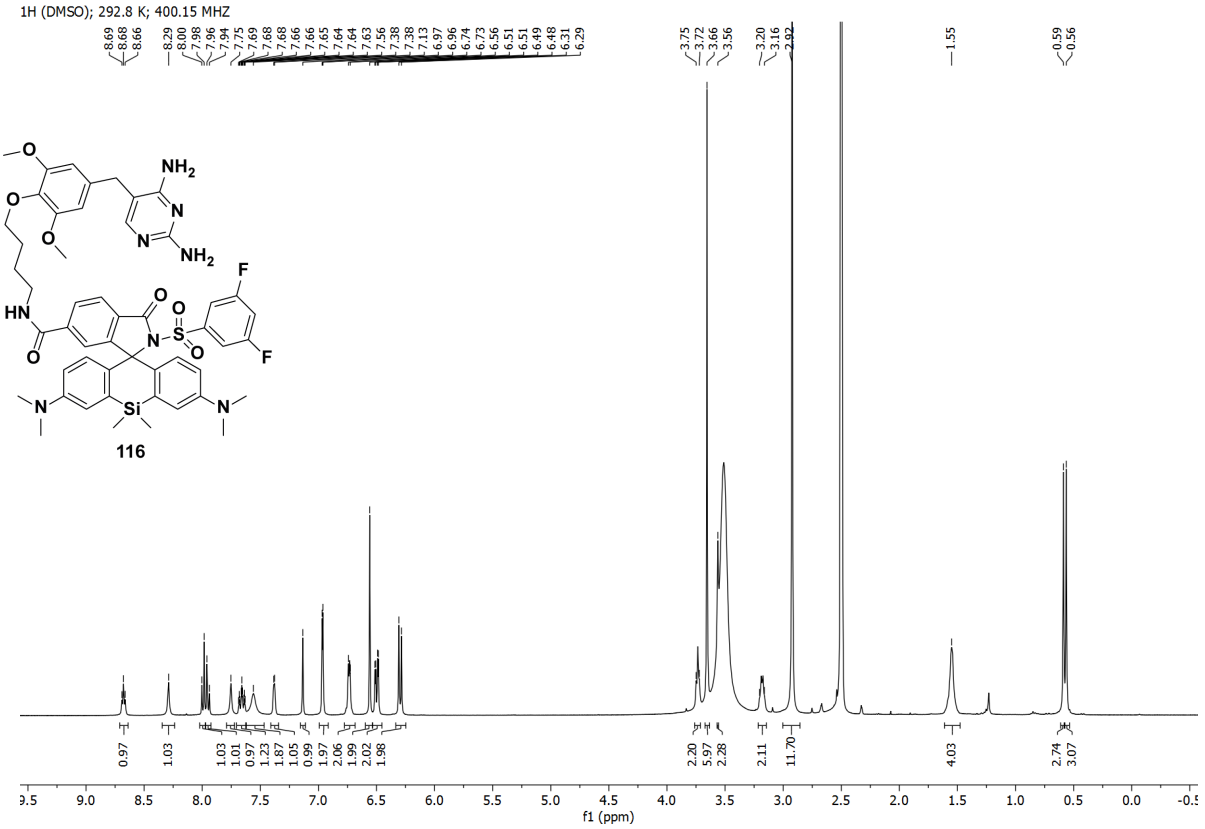

116

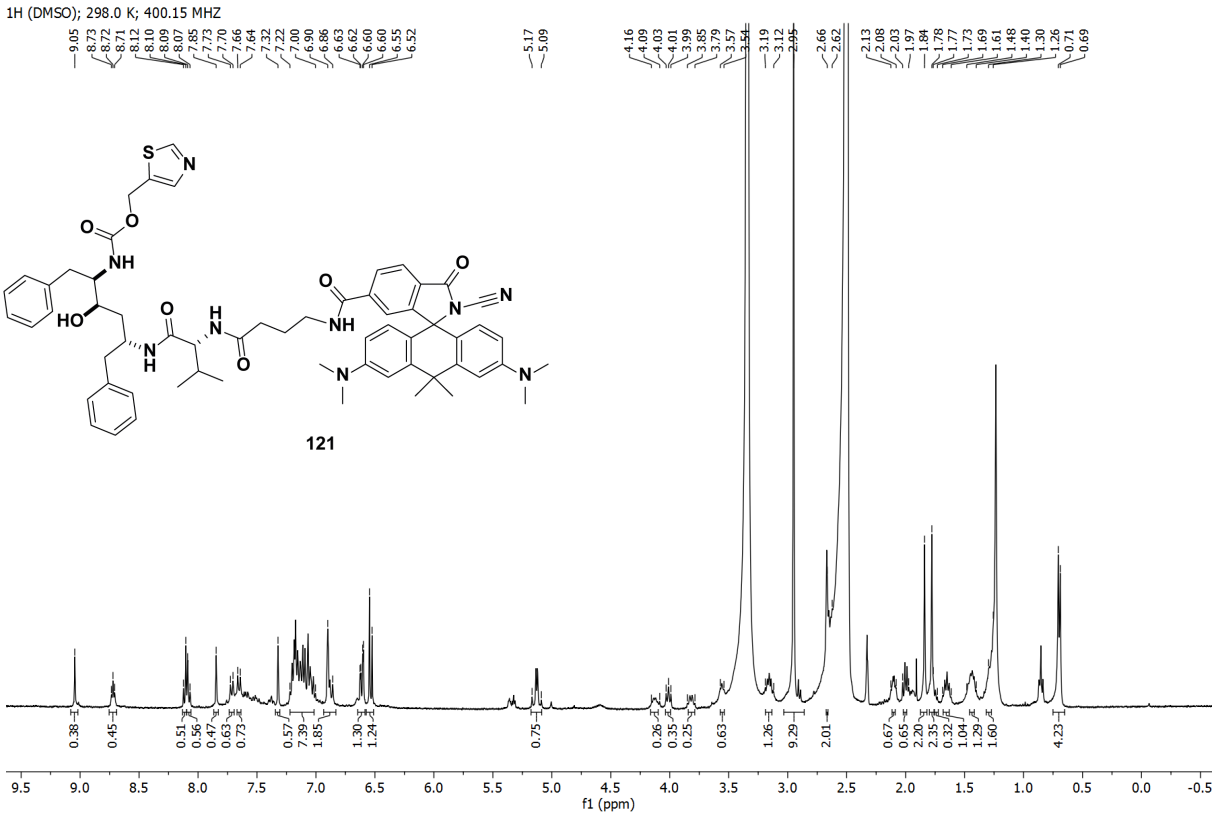

121

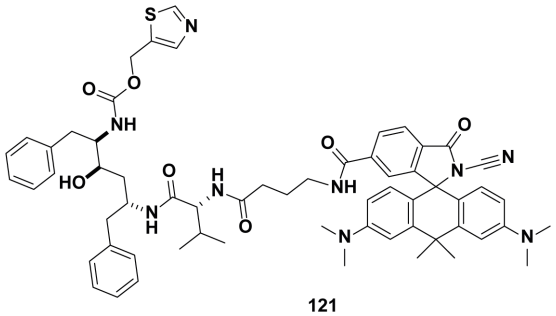

121

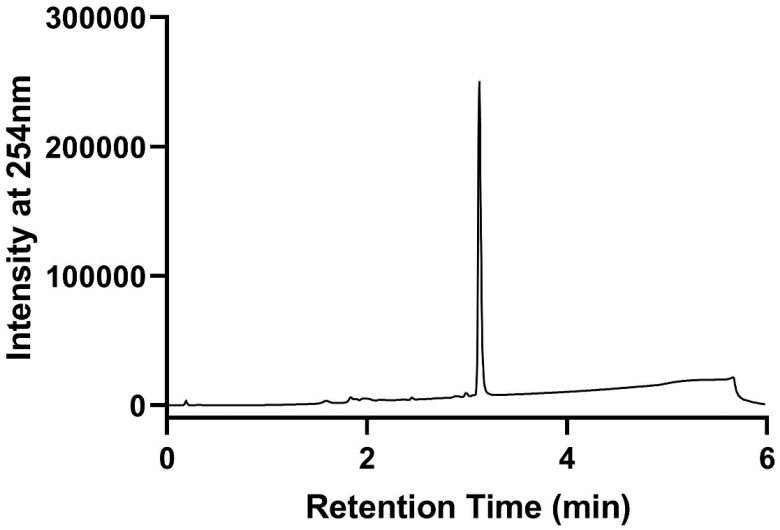
Intensity at 254nm
300000
200000
100000
0
0
2
4
6
Retention Time (min)

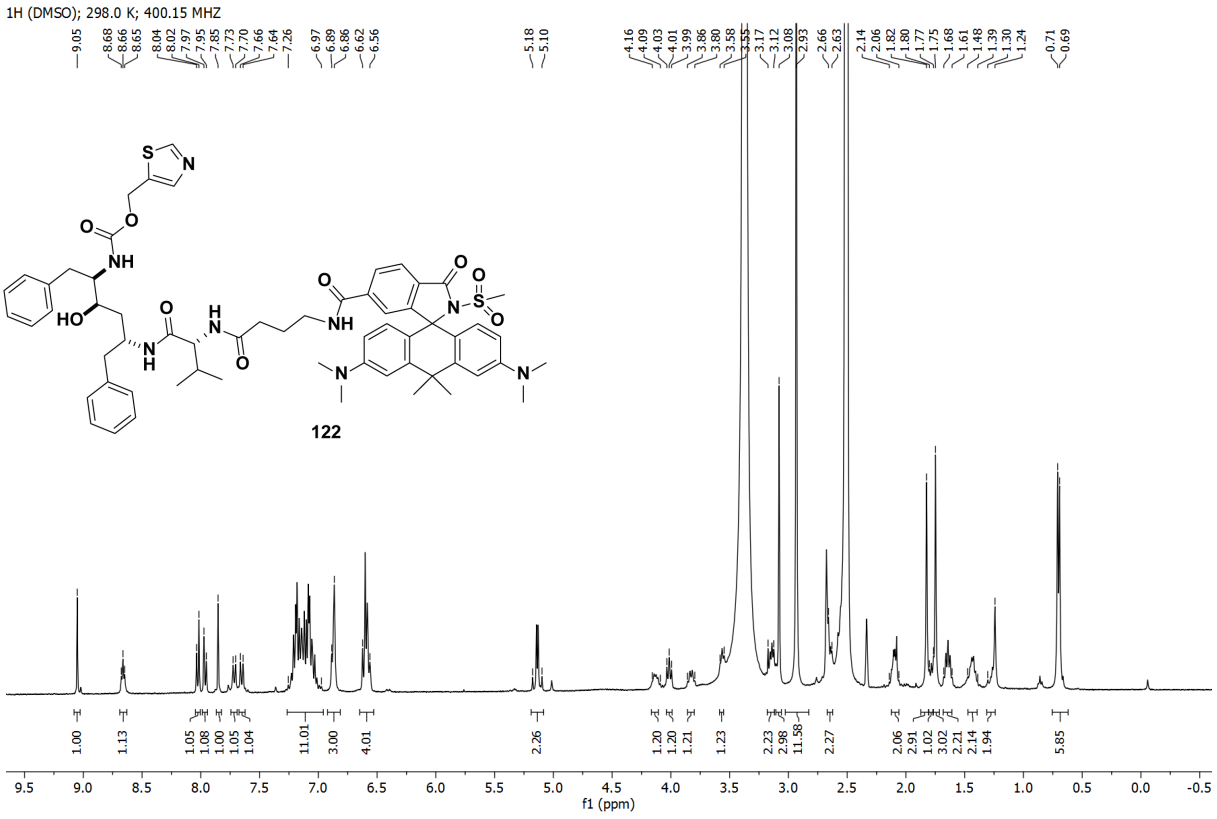
1H (DMSO); 298.0 K; 400.15 MHZ
f1 (ppm)

122

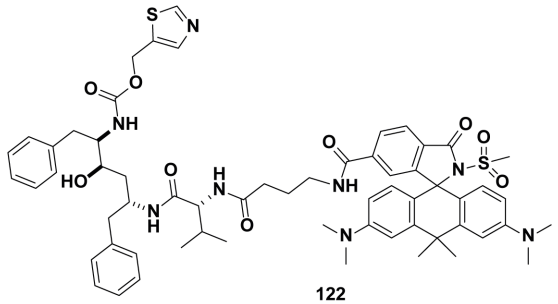

122

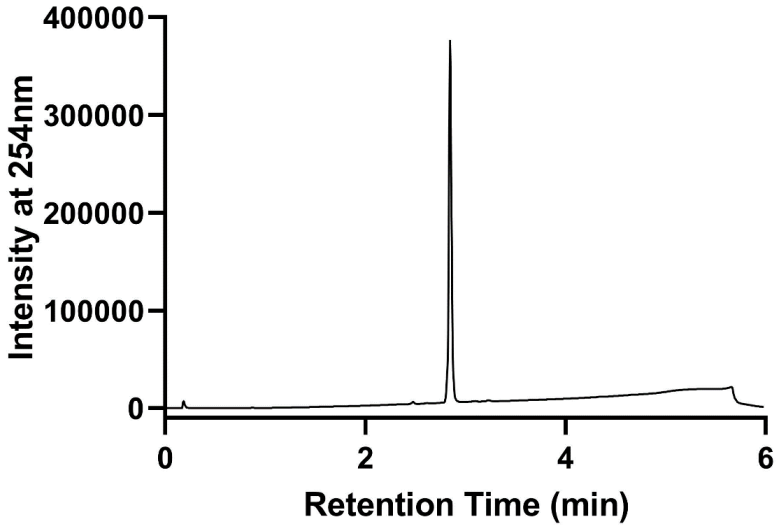
Intensity at 254nm
400000
300000
200000
100000
0
0
2
4
6
Retention Time (min)

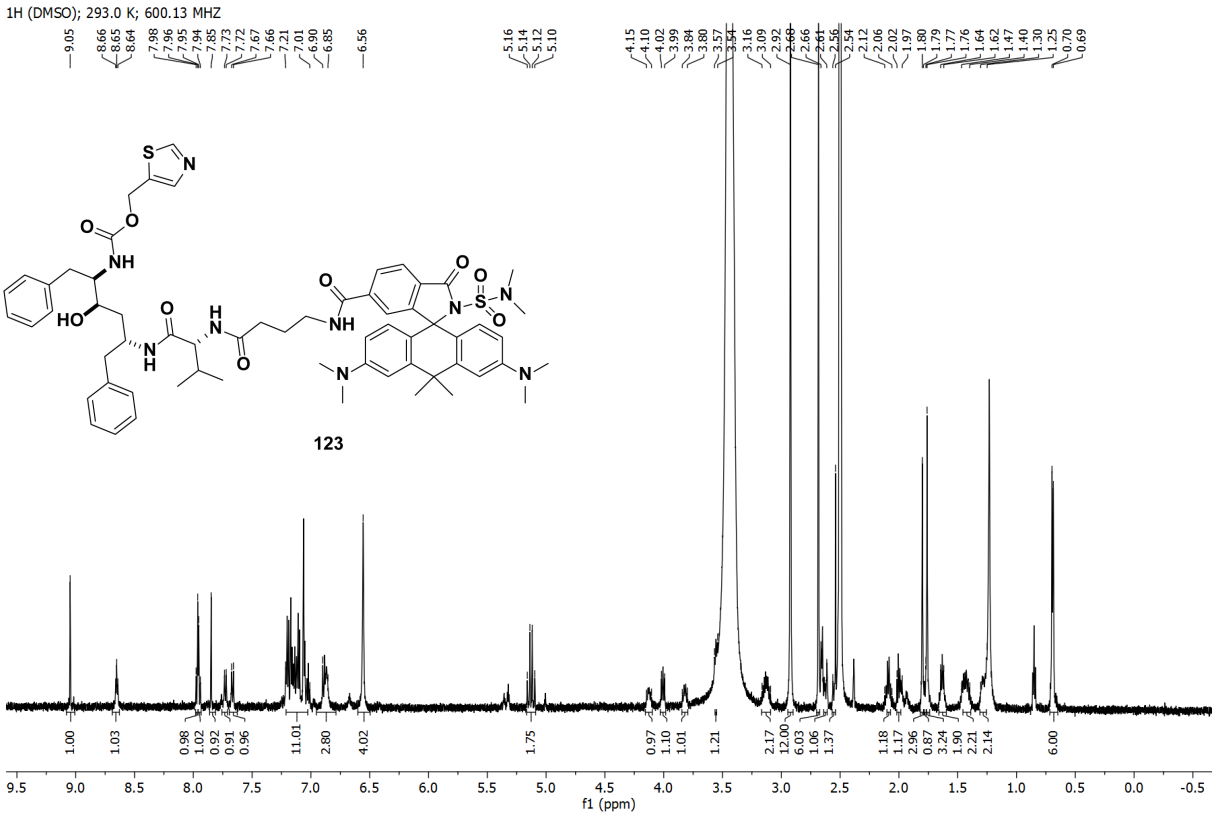
1H (DMSO); 293.0 K; 600.13 MHZ
f1 (ppm)

123

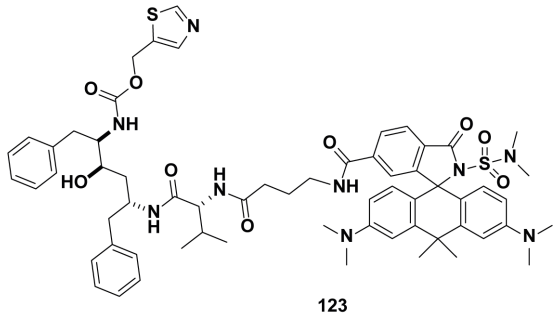

123

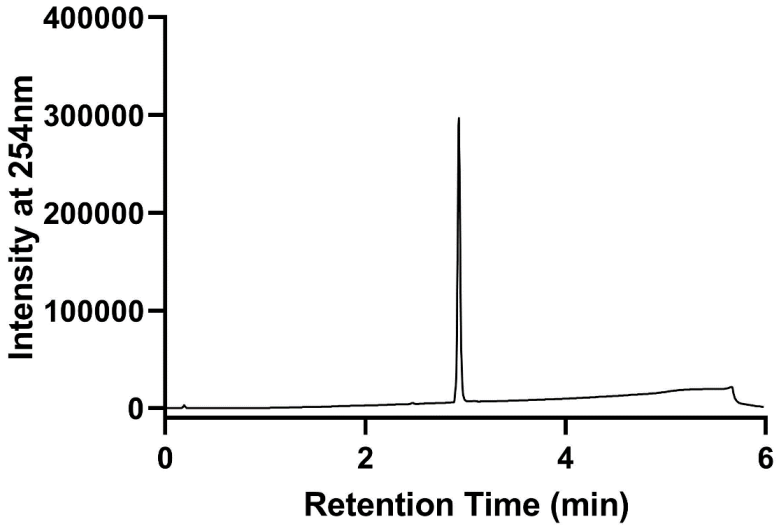
Intensity at 254nm
400000
300000
200000
100000
0
0
2
4
6
Retention Time (min)

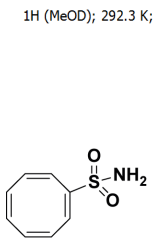

125

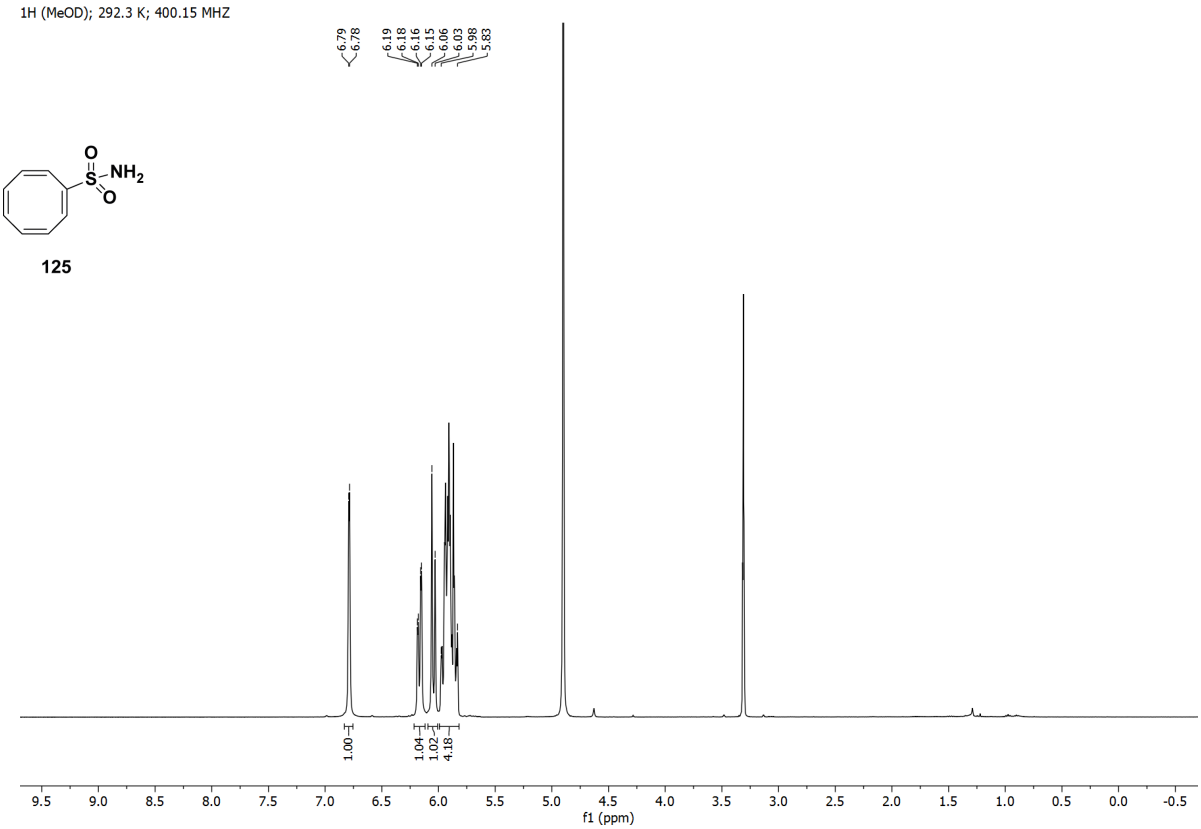
1H (MeOD); 292.3 K; 400.15 MHZ
6.79
6.78
6.19
6.18
6.16
6.15
6.06
6.03
5.98
5.83
1.00
1.04
1.02
4.18
9.5
9.0
8.5
8.0
7.5
7.0
6.5
6.0
5.5
5.0
4.5
4.0
3.5
3.0
2.5
2.0
1.5
1.0
0.5
0.0
-0.5
f1 (ppm)

13C (MeOD); 292.4 K; 100.63 MHZ

125

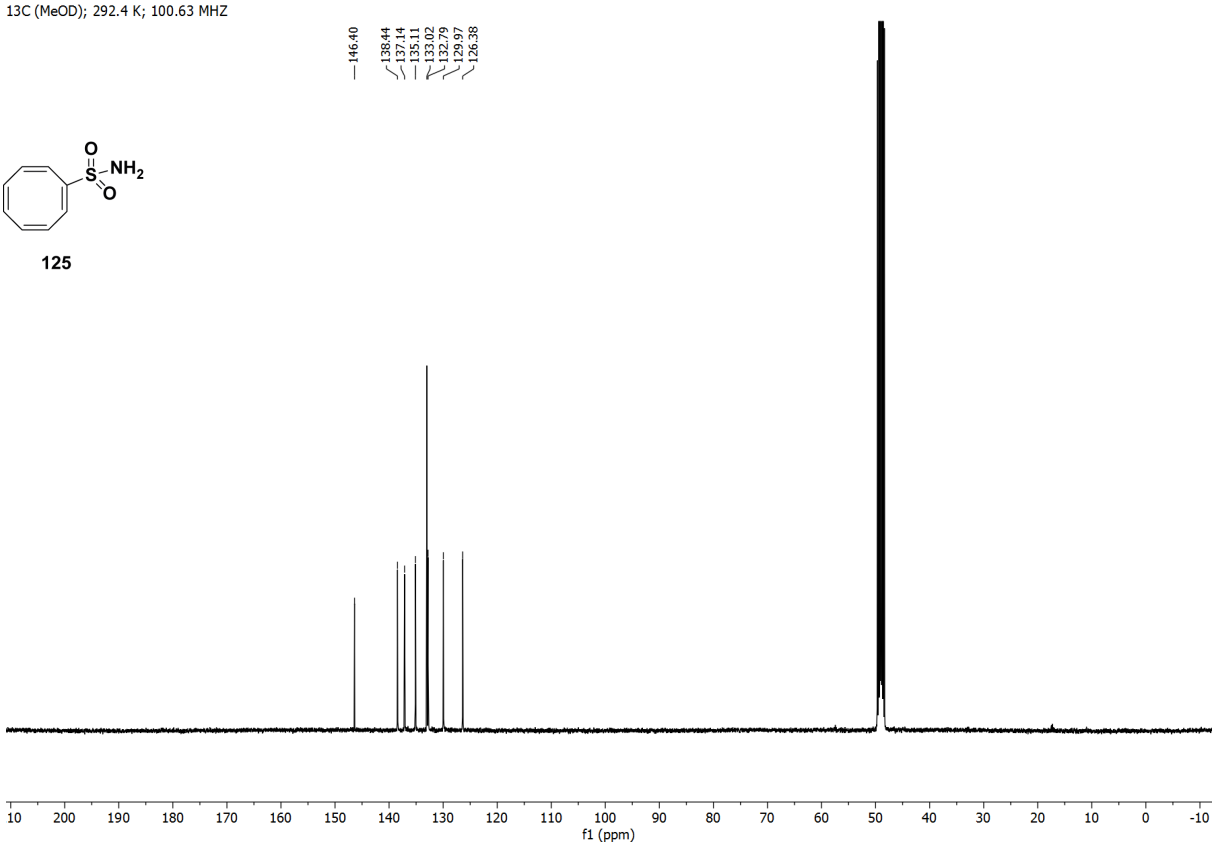

1H (MeOD); 292.2 K; 400.15 MHZ

127

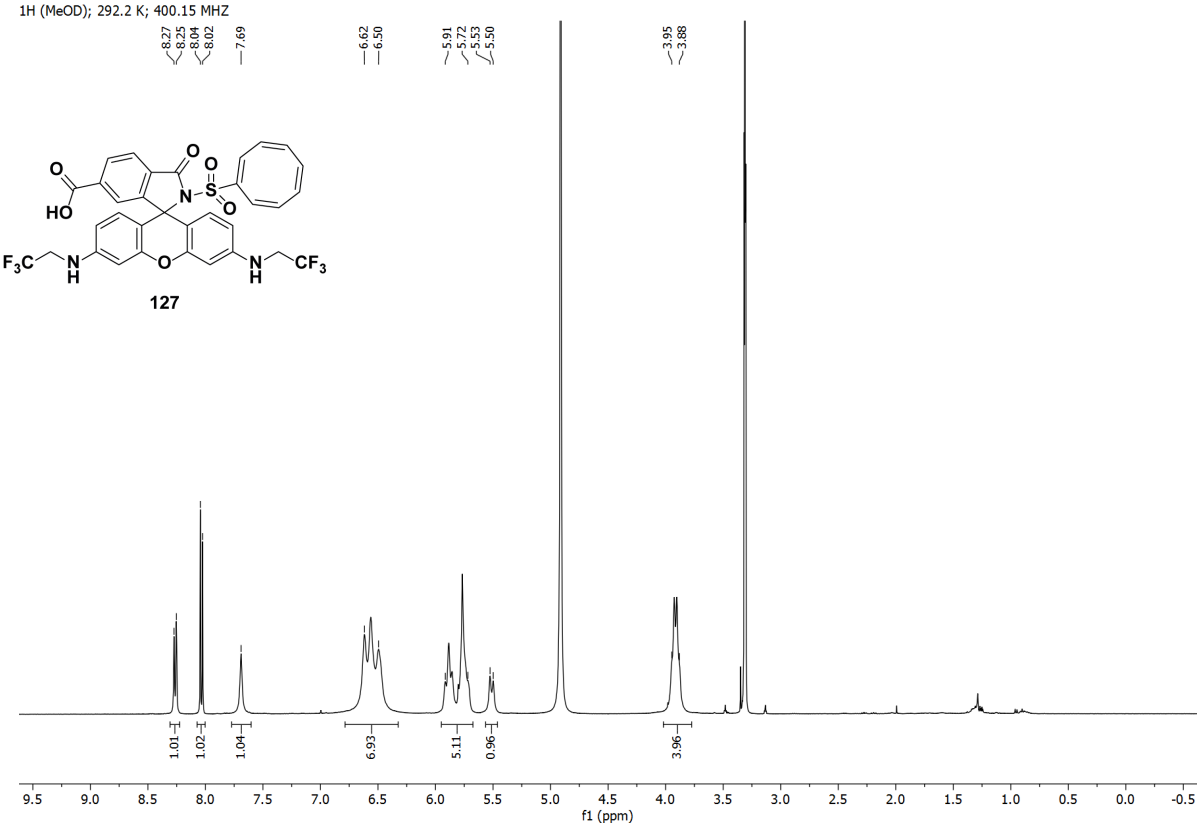

13C (DMSO); 292.2 K; 100.63 MHZ

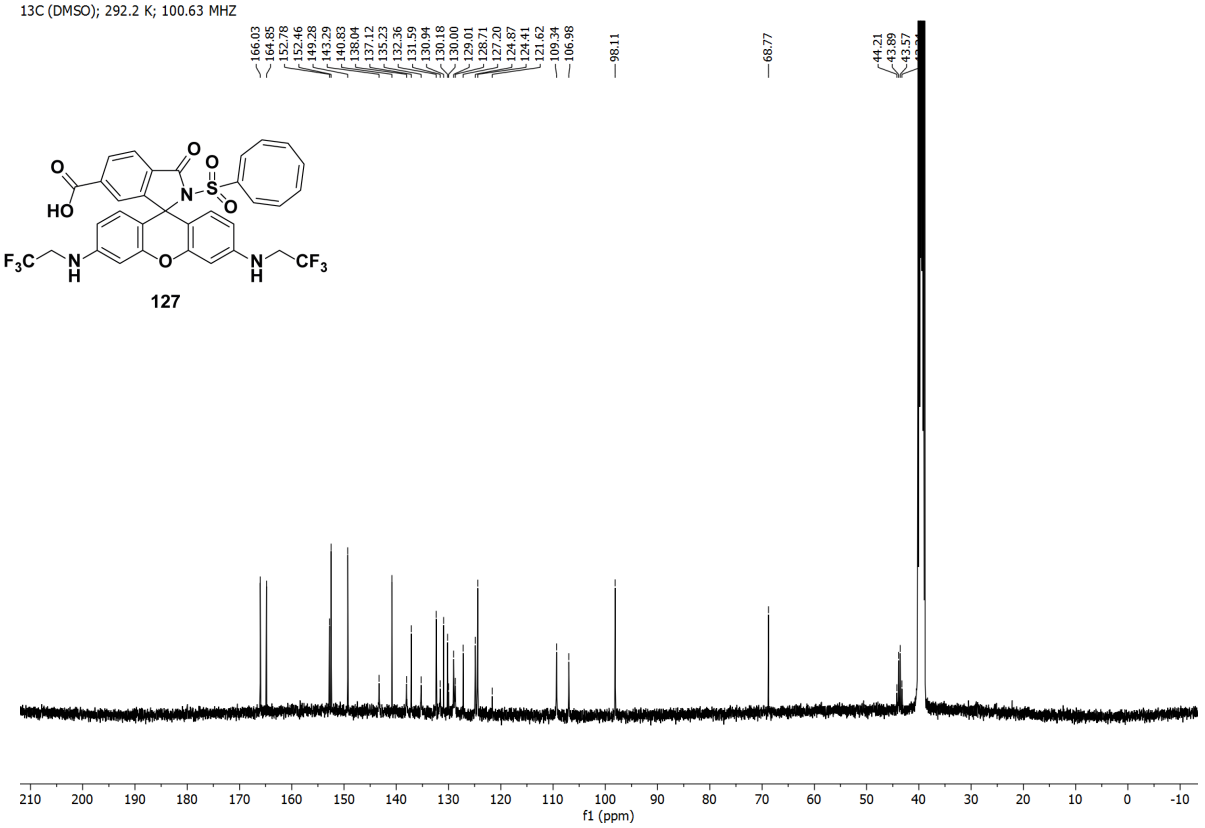

127

1H (DMSO); 292.6 K; 400.15 MHZ

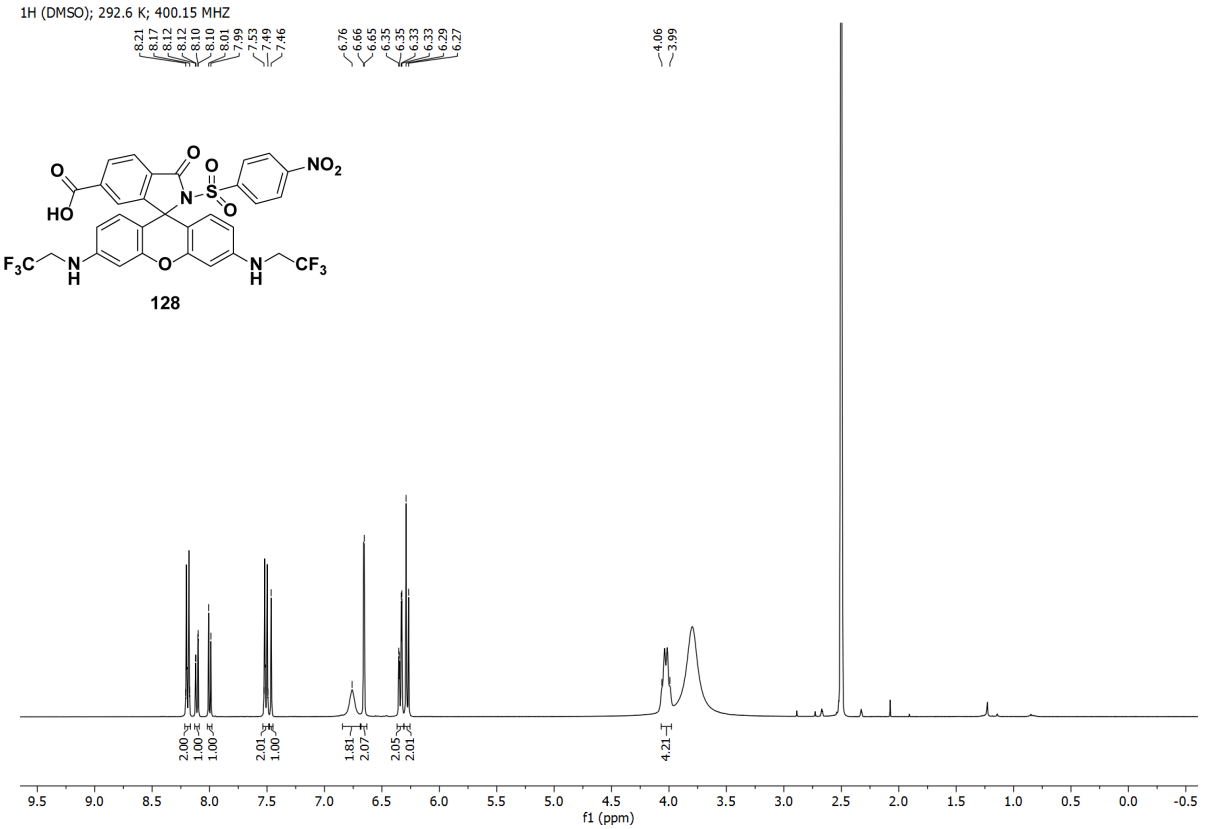

128

13C (DMSO); 292.2 K; 100.63 MHZ

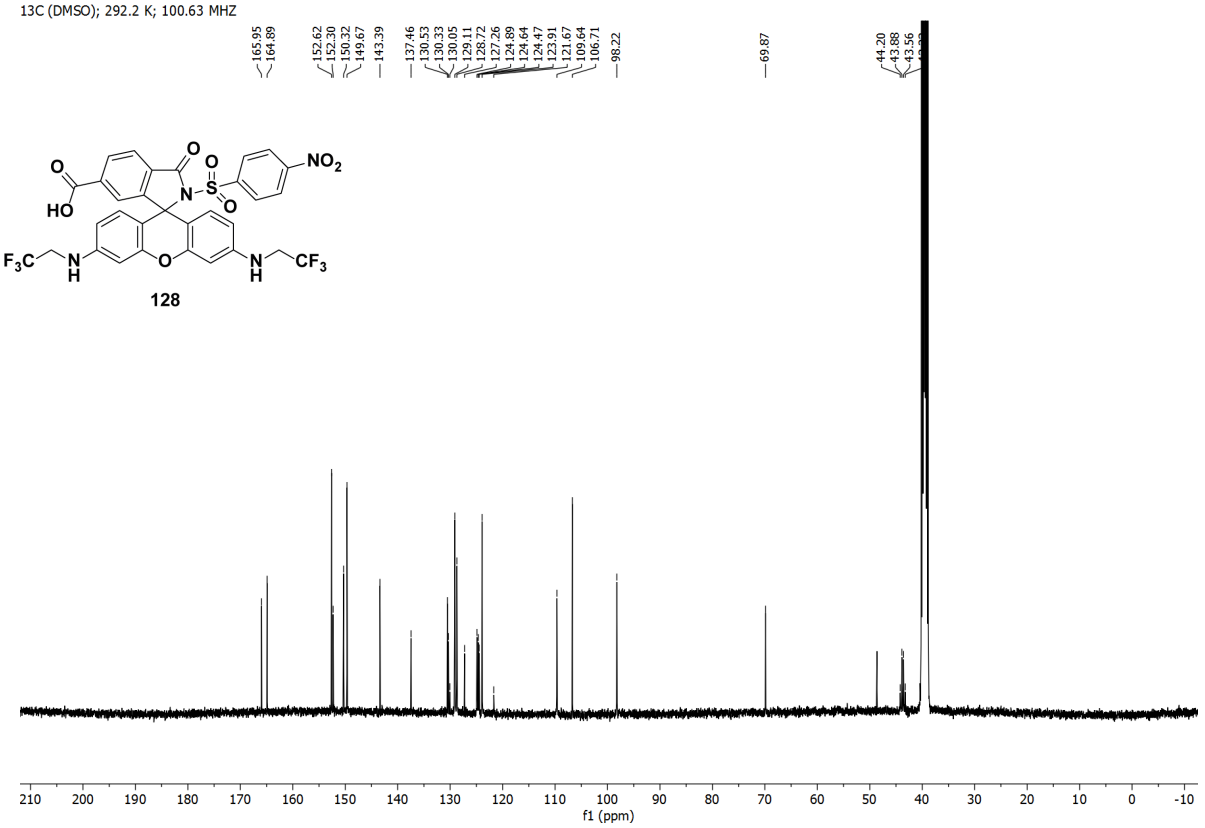

128

1H (DMSO); 292.0 K; 400.15 MHZ

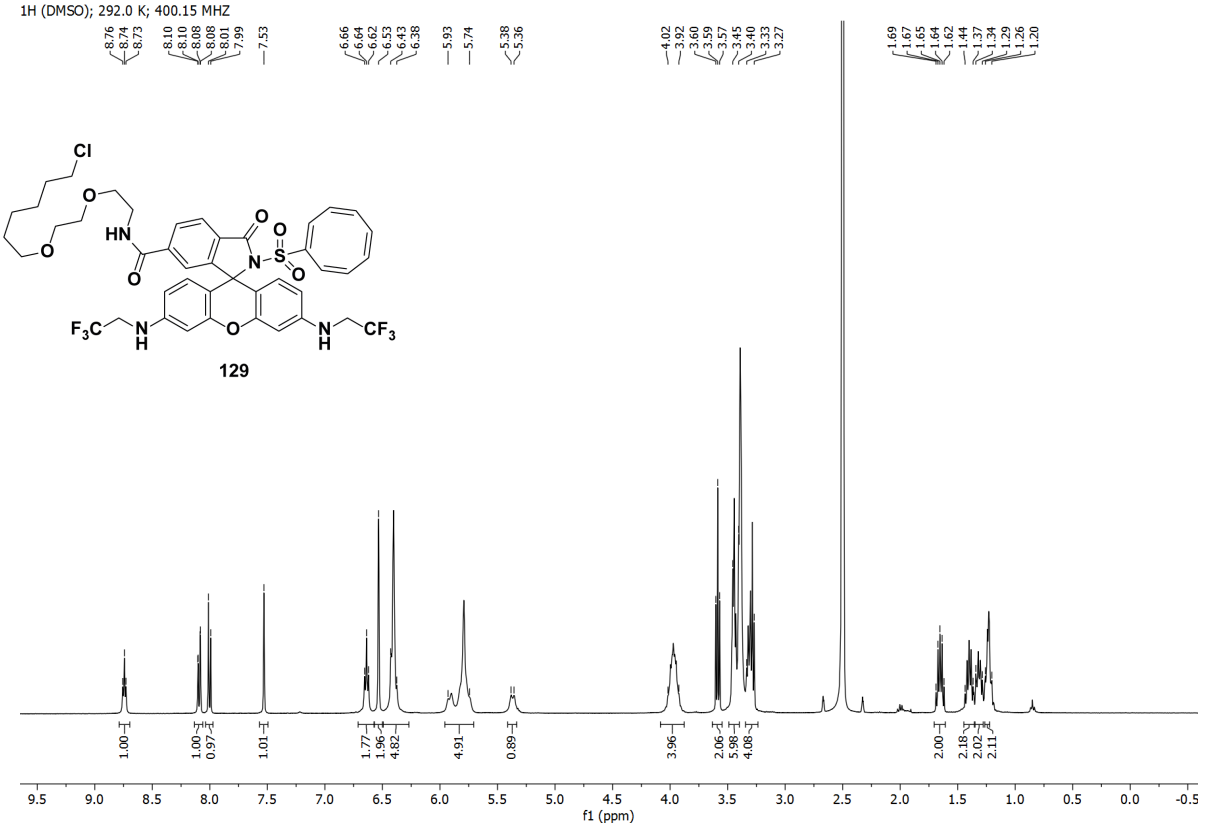

129

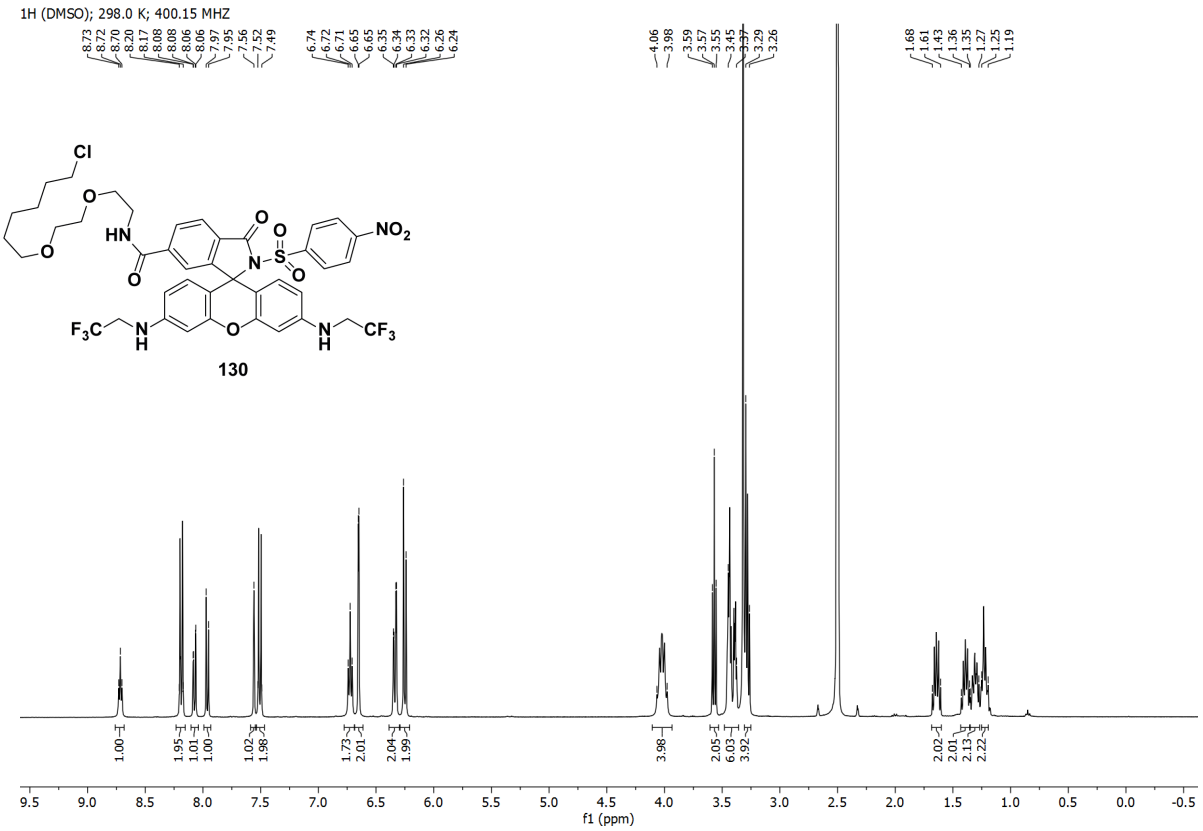

130

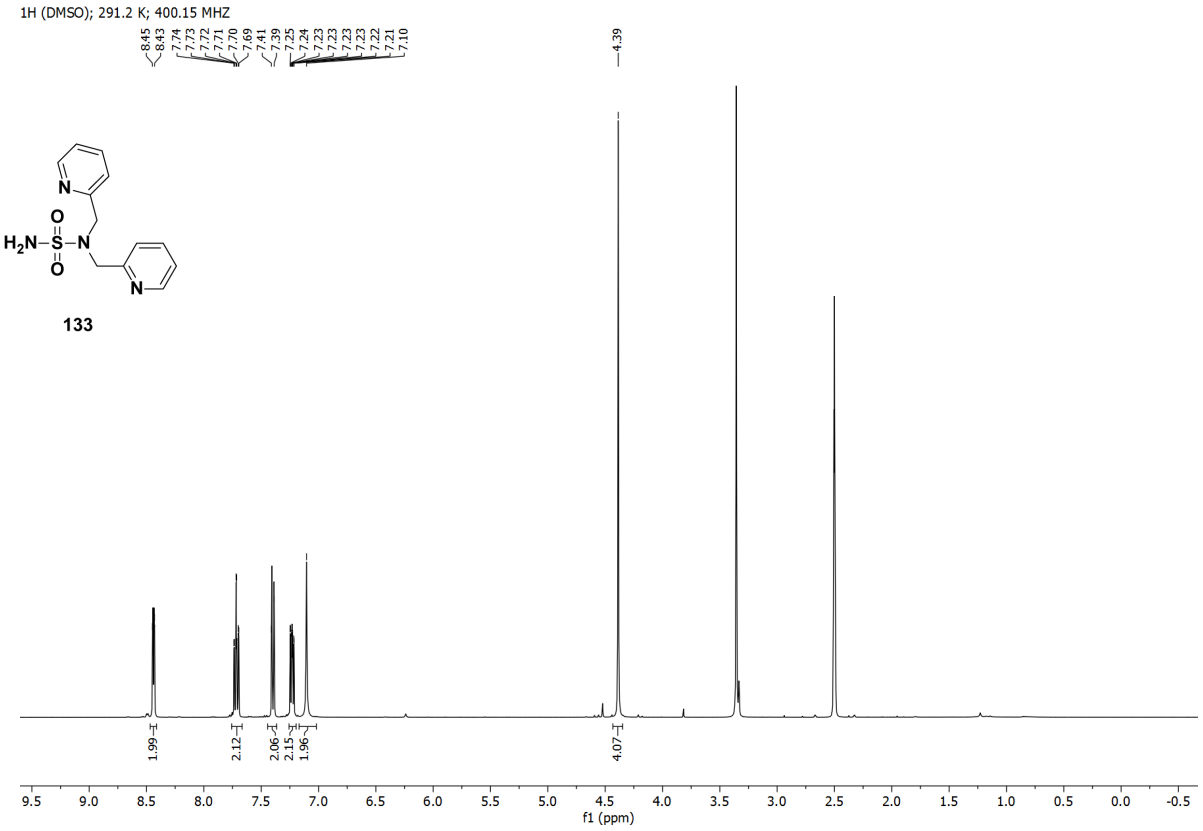

133

13C (DMSO); 291.5 K; 100.63 MHZ

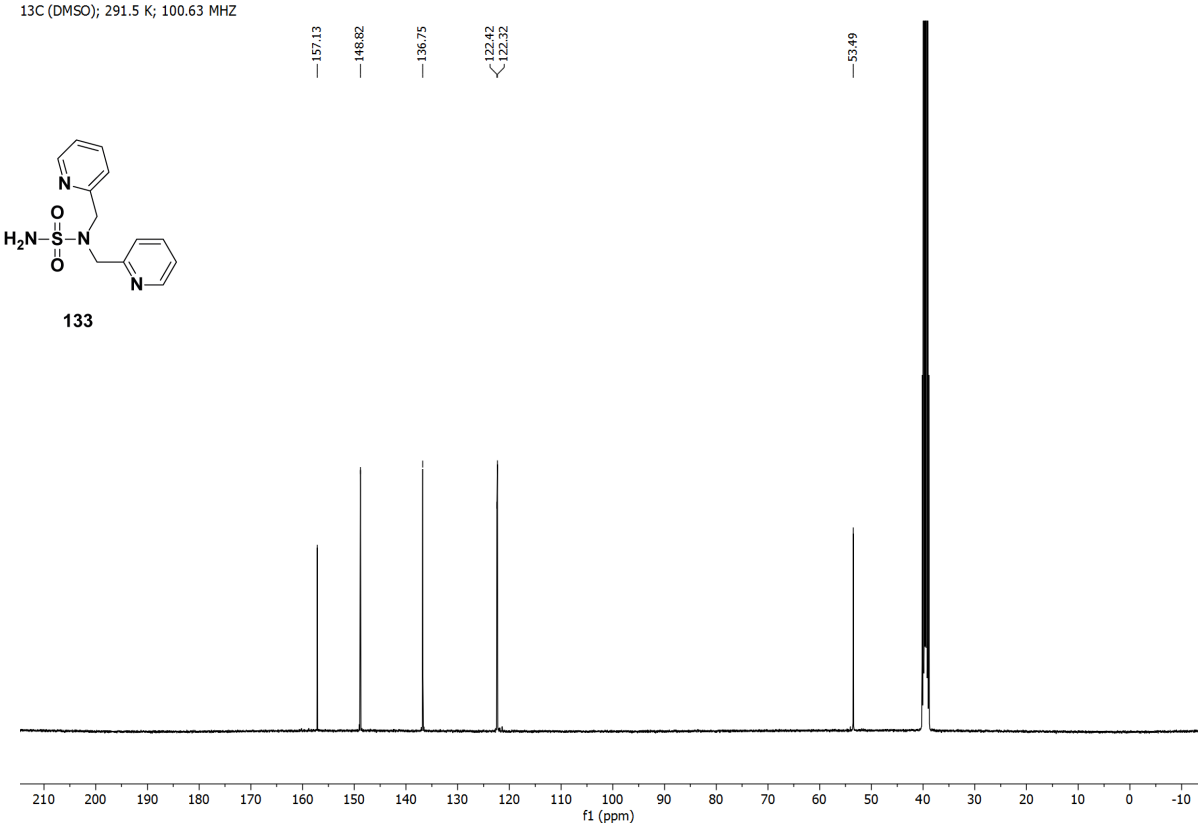

133

1H (MeOD); 298.0 K; 400.15 MHZ

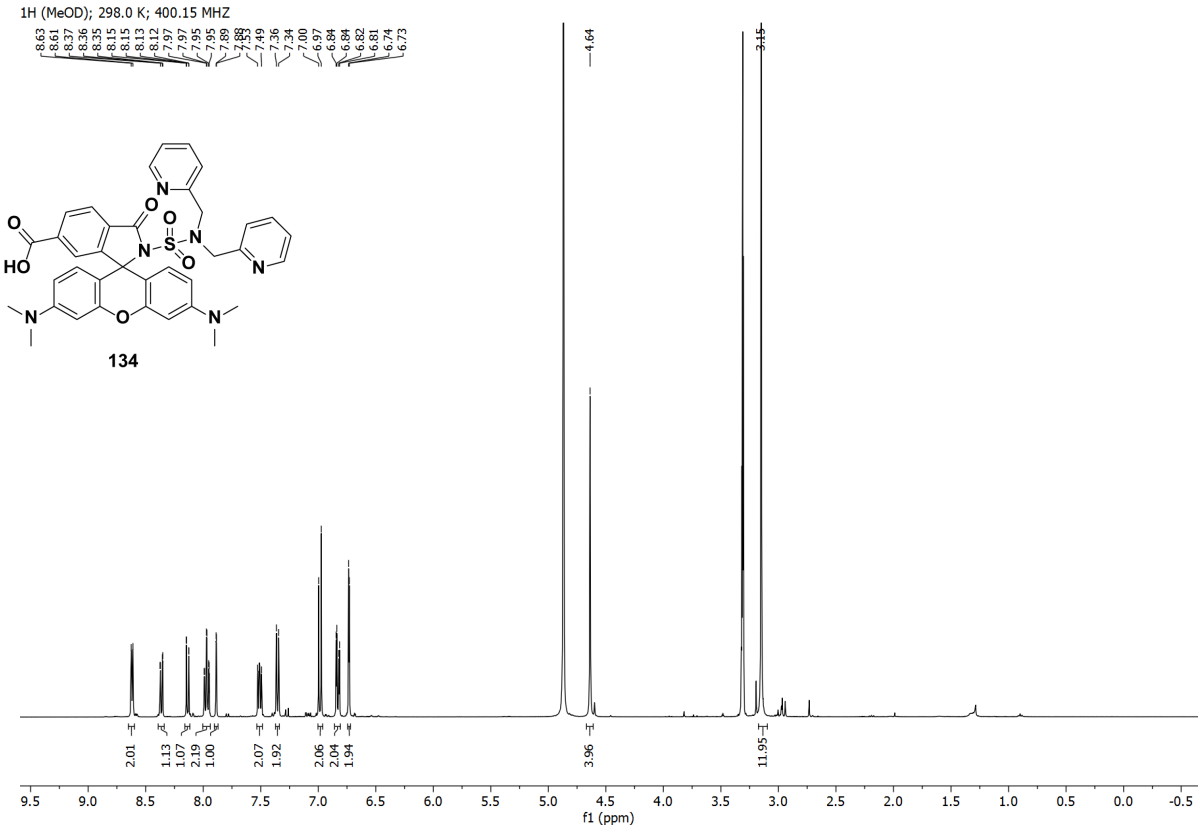

134

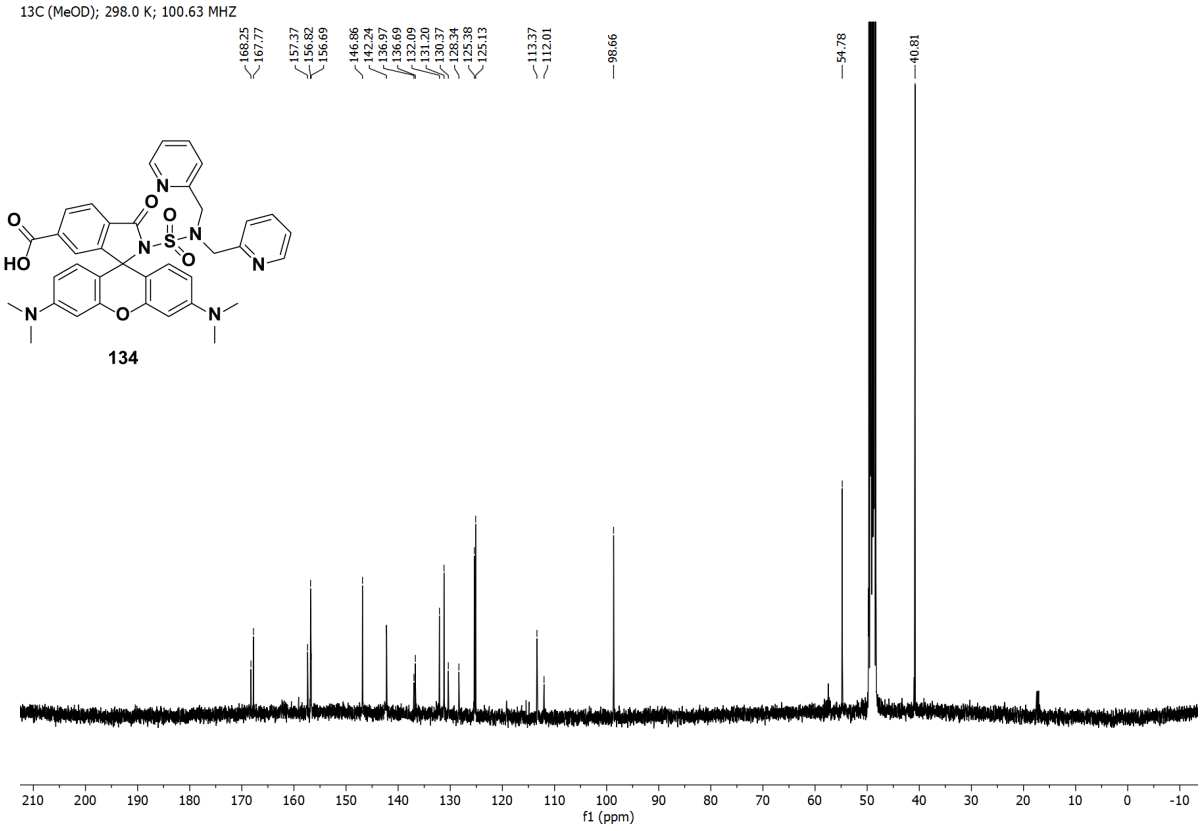
13C (MeOD); 298.0 K; 100.63 MHZ
168.25
167.77
157.37
156.82
156.69
146.86
142.24
136.97
136.69
132.09
131.20
130.37
128.34
125.38
125.13
113.37
112.01
98.66
54.78
40.81
f1 (ppm)

134

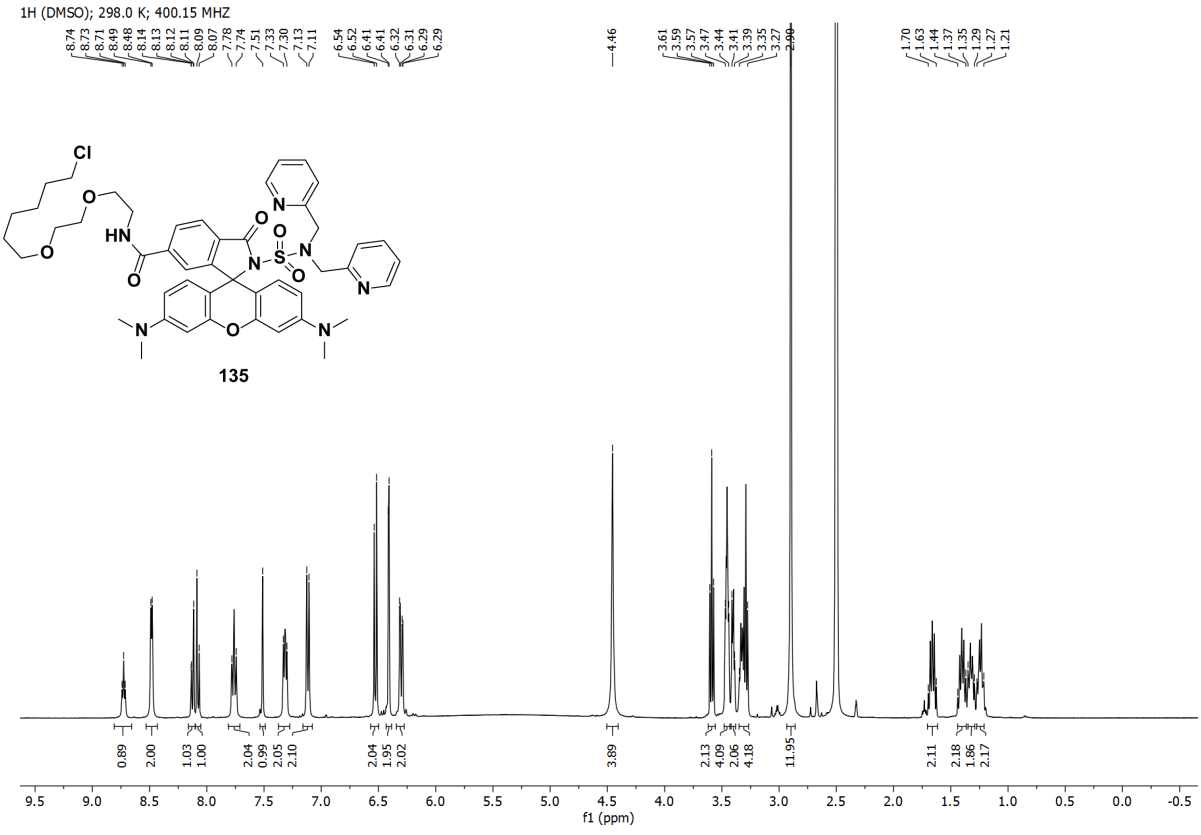
1H (DMSO); 298.0 K; 400.15 MHZ
8.74
8.73
8.71
8.49
8.48
8.14
8.13
8.12
8.11
8.09
8.07
7.78
7.74
7.51
7.33
7.30
7.13
7.11
6.54
6.52
6.41
6.41
6.32
6.31
6.29
6.29
4.46
3.61
3.59
3.57
3.47
3.44
3.41
3.39
3.35
3.27
2.90
1.70
1.63
1.44
1.37
1.35
1.29
1.27
1.21
0.89
2.00
1.03
1.00
2.04
0.99
2.05
2.10
2.04
1.95
2.02
3.89
2.13
4.09
2.06
4.18
11.95
2.11
2.18
1.86
2.17
f1 (ppm)

135

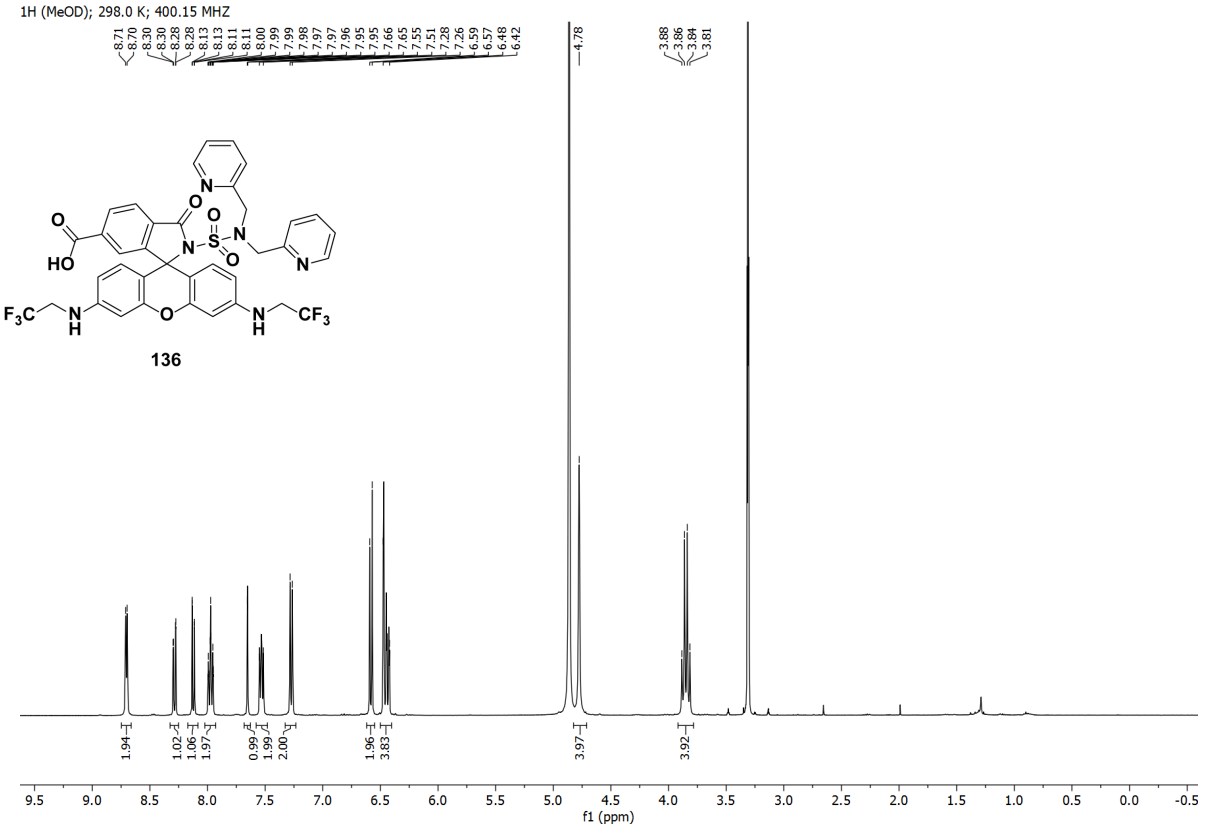
1H (MeOD); 298.0 K; 400.15 MHZ
8.71
8.70
8.30
8.30
8.28
8.28
8.13
8.13
8.11
8.11
8.00
7.99
7.99
7.98
7.97
7.97
7.96
7.95
7.95
7.66
7.65
7.55
7.51
7.28
7.26
6.59
6.57
6.48
6.42
4.78
3.88
3.86
3.84
3.81
1.94
1.02
1.06
1.97
0.99
1.99
2.00
1.96
3.83
3.97
3.92
f1 (ppm)

136

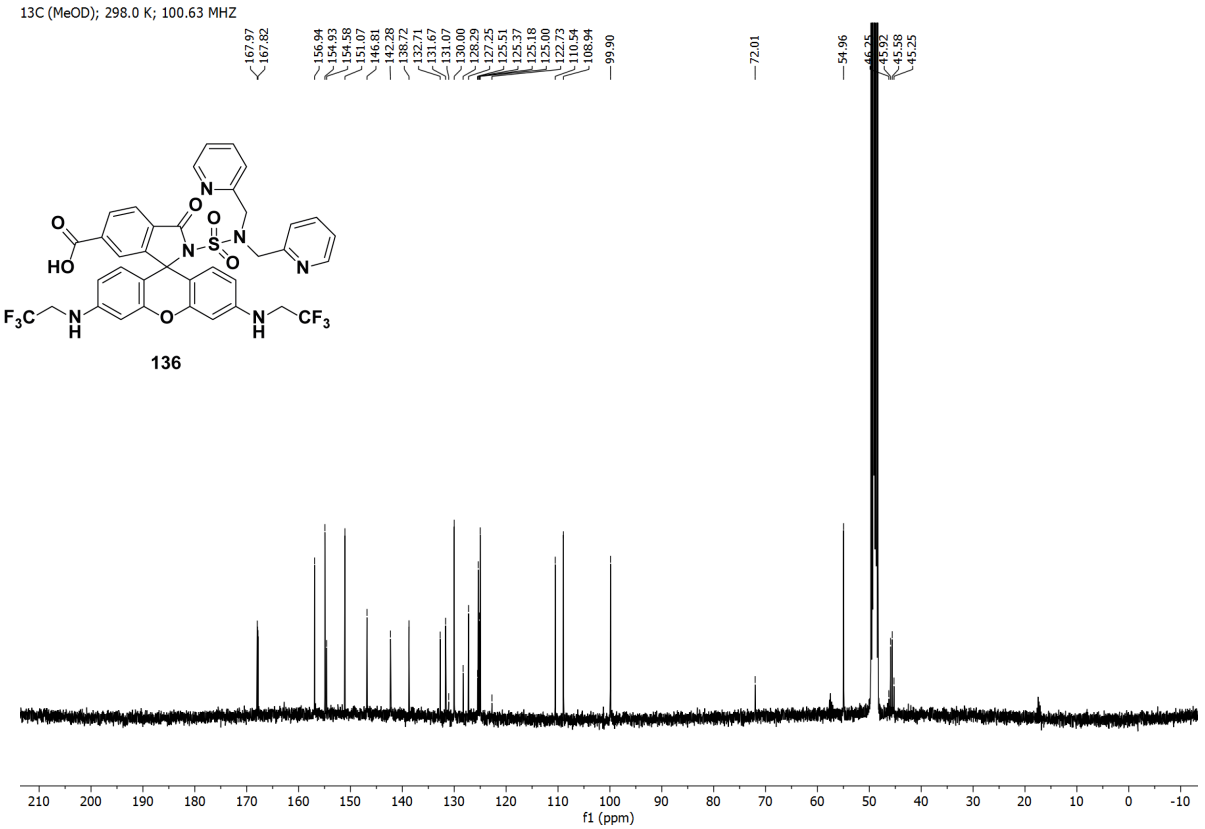
13C (MeOD); 298.0 K; 100.63 MHZ
167.97
167.82
156.94
154.93
154.58
151.07
146.81
142.28
138.72
132.71
131.67
131.07
130.00
128.29
127.25
125.51
125.37
125.18
125.00
122.73
110.54
108.94
99.90
72.01
54.96
46.25
45.92
45.58
45.25
f1 (ppm)

136

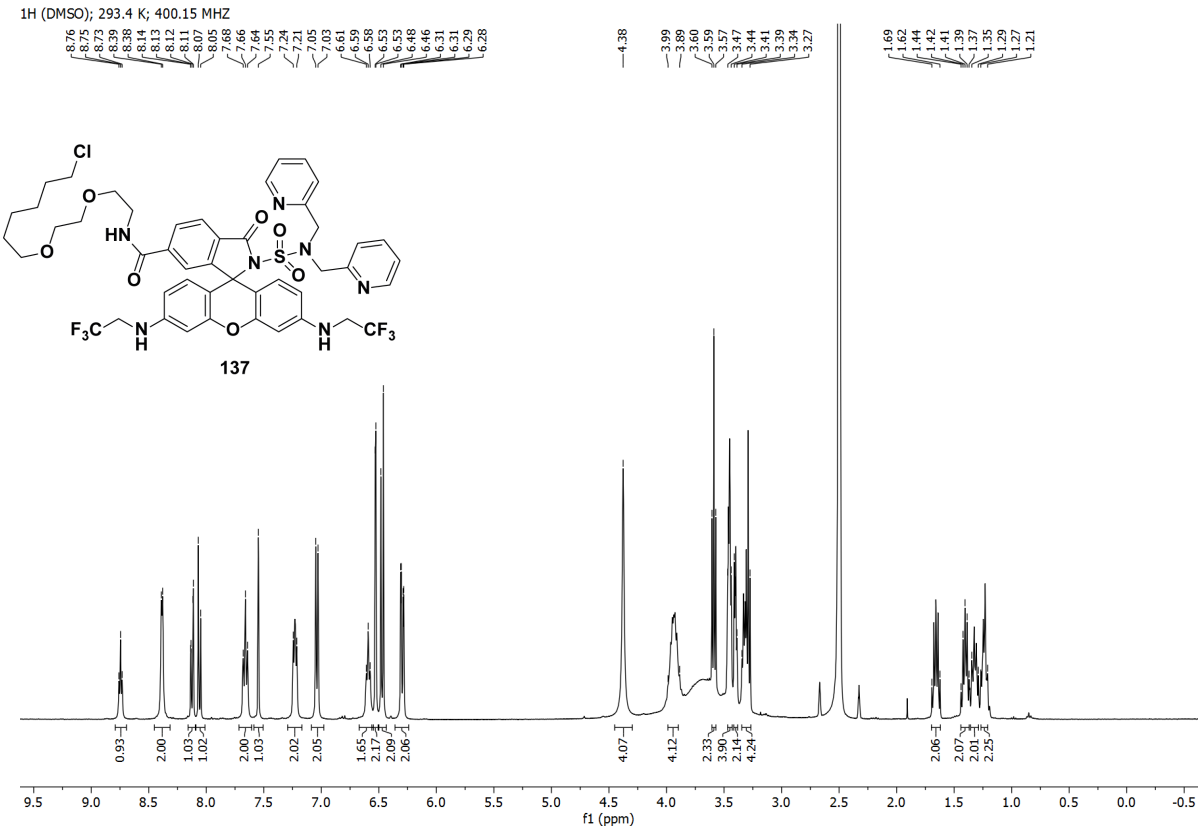
1H (DMSO); 293.4 K; 400.15 MHZ
137
f1 (ppm)

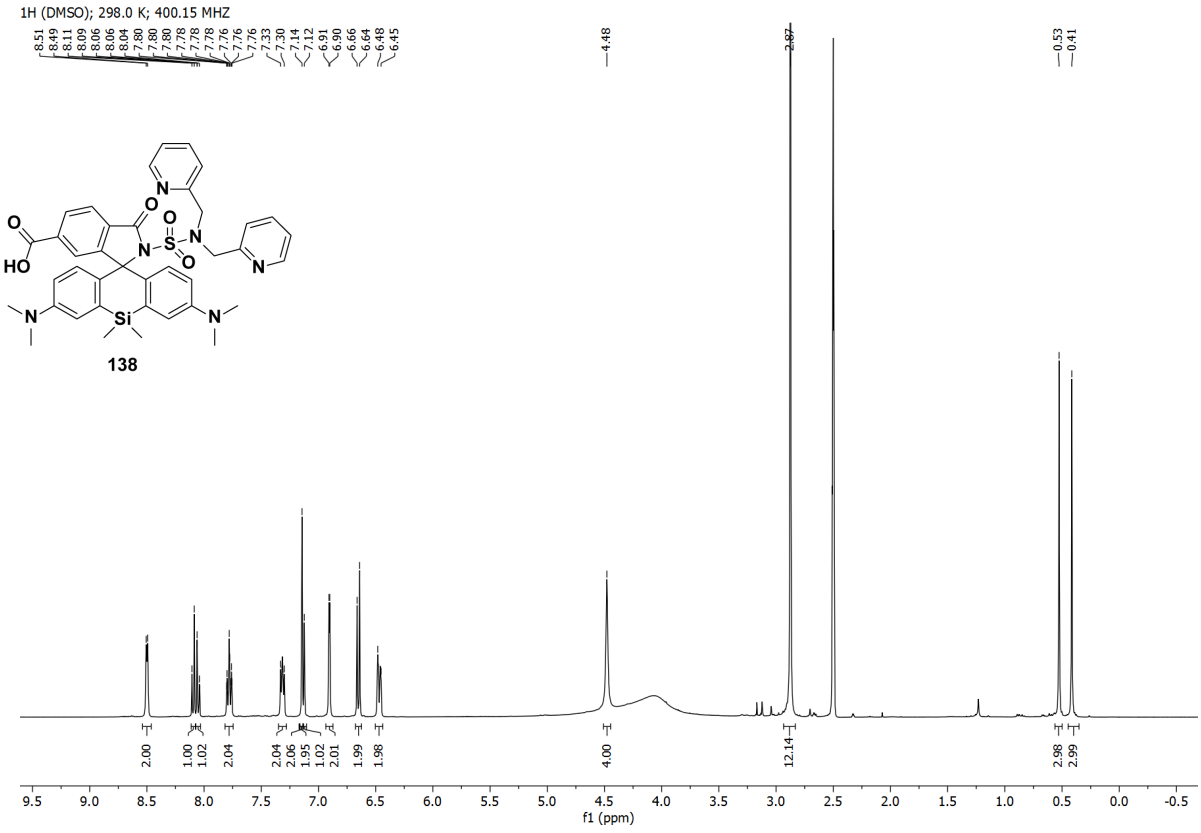
1H (DMSO); 298.0 K; 400.15 MHZ
138
f1 (ppm)

13C (DMSO); 298.0 K; 100.63 MHZ

138

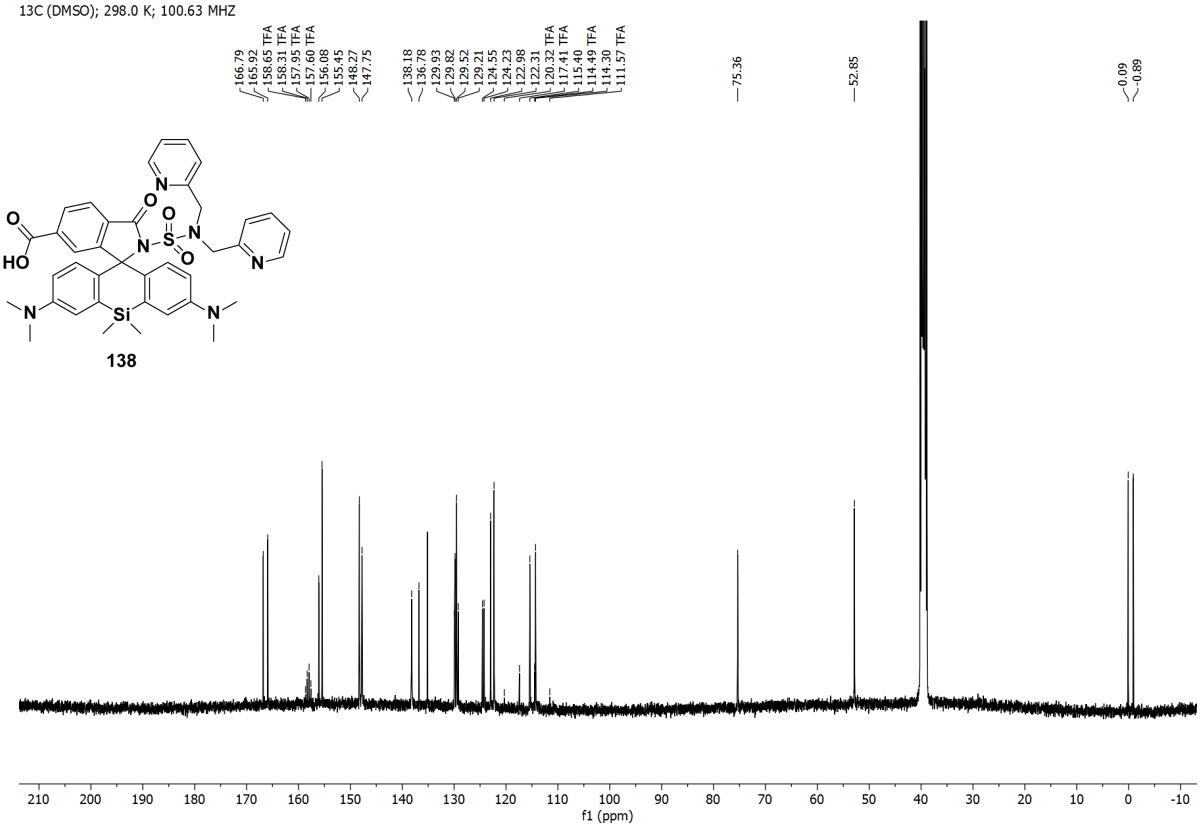

1H (DMSO); 298.0 K; 400.15 MHZ

139

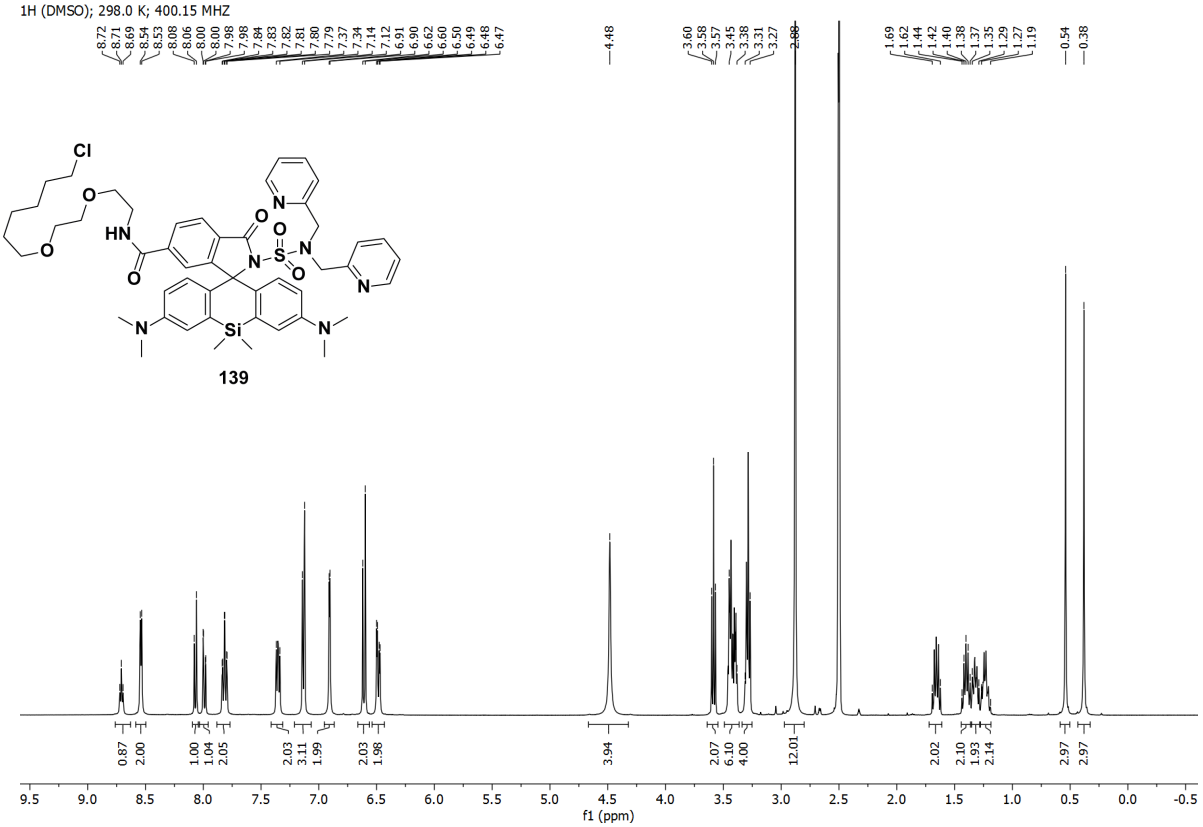

9. Eidesstattliche Versicherung

Eidesstattliche Versicherung gemäß §8 der Promotionsordnung für die Gesamtfakultät für Mathematik, Ingenieur- und Naturwissenschaften der Universität Heidelberg

1. Bei der eingereichten Dissertation zum Thema *Systematic Tuning of Rhodamine Spirocyclization* handelt es sich um meine eigenständig erbrachte Leistung.

2. Ich habe nur die angegebenen Quellen und Hilfsmittel benutzt und mich keiner unzulässigen Hilfe Dritter bedient. Insbesondere habe ich wörtlich oder sinngemäß aus anderen Werken übernommene Inhalte als solche kenntlich gemacht.

3. Die Arbeit oder Teile davon habe ich bislang nicht an einer Hochschule des In- oder Auslands als Bestandteil einer Prüfungs- oder Qualifikationsleistung vorgelegt.

4. Die Richtigkeit der vorstehenden Erklärungen bestätige ich.

5. Die Bedeutung der eidesstattlichen Versicherung und die strafrechtlichen Folgen einer unrichtigen oder unvollständigen eidesstattlichen Versicherung sind mir bekannt.

Ich versichere an Eides statt, dass ich nach bestem Wissen die reine Wahrheit erklärt und nichts verschwiegen habe.

....

Ort und Datum Unterschrift (Nicolas Marcel Lardon)